FEASIBILITY DESIGN OF AN INSTRUMENT SYSTEM FOR MEASUREMENT OF HORIZON RADIANCE IN THE CO_2 ABSORPTION BAND

Horizon Definition Study

May 1967

Prepared under Contract No. NAS 1-6010 by

HONEYWELL INC.
Systems & Research Division

Minneapolis, Minn.
Boston, Mass.
and

CONTROL DATA CORPORATION
Minneapolis, Minn.

for

NATIONAL AERONAUTICS AND SPACE ADMINISTRATION

FEASIBILITY DESIGN OF AN INSTRUMENT SYSTEM FOR MEASUREMENT OF HORIZON RADIANCE IN THE CO_2 ABSORPTION BAND

By   John C. Carson, Honeywell Inc.
Joseph S. Titus, Honeywell Inc.
Alden J. Mooers, Control Data Corp.
Ralph W. Peterson, Control Data Corp.
Charles N. West, Honeywell Inc.
Richard M. Jansson, Honeywell Inc.

HORIZON DEFINITION STUDY

May 1967

NATIONAL AERONAUTICS AND SPACE ADMINISTRATION

FOREWORD

This report documents Phase A, Part II of An Analytical and Conceptual Design Study for an Earth Coverage Infrared Horizon Definition Study performed under National Aeronautics and Space Administration Contract NAS 1-6010 for Langley Research Center.

The study was performed in two parts. Part I, which was previously documented, provided for the initial delineation of the experimental data required to define the earth's infrared horizon on a global basis for all time and space scales of interest. The capabilities of a number of flight techniques to collect the experimental data were then evaluated; a rolling-wheel spacecraft in a nominal 500-km polar orbit was selected as the baseline technique.

The Part II portion of the study, which this report documents, provides a more extensive analysis of the sampling requirements and operational methodology for the measurement program, including the evaluation of various system constraints. In addition, design requirements and conceptual designs are established for the overall system and its associated subsystems, including radiometer, attitude determination, data handling, communications, attitude control, electric power, structures and integration, flight vehicle operations and launch support.

Honeywell Inc., Systems and Research Division performed this study program under the technical direction of Mr. L. G. Larson. The program was conducted from 28 March 1966 to 10 October 1966 (Part I) and from 10 October 1966 to 29 May 1967 (Part II). This Part II portion of the study was the joint effort of Honeywell Inc., Systems and Research Division and Control Data Corp.

Gratitude is extended to NASA Langley Research Center for their technical guidance, under the program technical direction of Messrs. L. S. Keafer and J. A. Dodgen with direct assistance from Messrs. W. C. Dixon, Jr., E. C. Foudriat, H. J. Curfman, Jr., A. Jalink, Jr., T. B. McKee, W. Hodge, and T. M. Walsh as well as the many people within their organization.

CONTENTS

LIST OF ILLUSTRATIONS

LIST OF ILLUSTRATIONS (Continued)

LIST OF ILLUSTRATIONS (Continued)

LIST OF ILLUSTRATIONS (Continued)

LIST OF ILLUSTRATIONS (Continued)

TABLES

LIST OF TABLES (Continued)

FEASIBILITY DESIGN OF AN INSTRUMENT SYSTEM FOR MEASUREMENT OF HORIZON RADIANCE IN THE CO$_2$ ABSORPTION BAND

By   John C. Carson, Honeywell Inc.
     Joseph S. Titus, Honeywell Inc.
     Alden J. Mooers, Control Data Corp.
     Ralph W. Peterson, Control Data Corp.
     Charles N. West, Honeywell Inc.
     Richard M. Jansson, Honeywell Inc.

SUMMARY

A feasibility design of an instrument system to collect data of the earth's horizon radiance profile in the carbon dioxide absorption band has been developed. This system is the prime payload component of the Horizon Definition Study (HDS) spacecraft. The data gathered through the experiment performed by the spacecraft-borne instruments is to be used in determining the ultimate, obtainable horizon sensor performance and in increasing knowledge of the physics of the earth's atmospheric emission.

A radiometer, two starmappers, and two sun sensors constitute the primary elements of the experiment package. The radiometer utilizes a cooled Ge:Cd detector, in-flight calibration, and classical Newtonian optics. Radiometric requirements and constraints are analyzed in detail. Radiance profile data is referenced to a geocentric coordinate system and, thus, instantaneous attitude and position of the data-taking instrument must be known. While position information is obtainable from the ground, attitude must be measured from within the spacecraft. A passive starmapper, with a slit reticle and a photomultiplier detector, and a sun sensor, are the major components of the attitude determination system. Attitude determination is performed as a ground data processing task.

INTRODUCTION

Feasibility design of an instrument system for measurement of horizon radiance in the CO2 absorption band documented herein is a portion of the Horizon Definition Study (HDS) conducted for NASA Langley Research Center, Contract NAS 1-6010, Part II. The purpose of the Horizon Definition Study is to develop a complete horizon radiance profile measurement program to provide data which can be used to determine the earth's atmospheric state, especially at high altitudes. These data can then be effectively used in the many atmospheric sciences studies and in the design of instruments and measurement systems which use the earth's horizon as a reference.

Part I of the HDS resulted in the following significant contributions to the definition of the earth's radiance in the infrared spectrum:

- The accumulation of a significant body of meteorological data covering a major portion of the Northern Hemisphere.

- Computation of a large body of synthesized horizon radiance profiles from actual temperature profiles obtained by rocket soundings.

- Generation of a very accurate analytical model and computer program for converting the temperature profiles to infrared horizon profiles (as a function of altitude).

- An initial definition of the quantity, quality, and sampling methodology required to define the earth's infrared horizon in the CO_2 absorption band for all temporal and spatial conditions.

- An evaluation of the cost and mission success probabilities of a series of flight techniques which could be used to gather the radiance data. A rolling-wheel spacecraft was selected in a nominal 500-km polar orbit.

The Part II study effort was directed toward the development of a conceptually feasible measurement system, which includes a spacecraft to accomplish the measurement program developed in Part I. In the Part II HDS, a number of scientific and engineering disciplines were exercised simultaneously to conceptually design the required system. Accomplishments of Part II of the study are listed below:

- The scientific experimenter refined the sampling methodology used by the measurement system. This portion of the study recommends the accumulation of approximately 380 000 radiance profiles taken with a sampling rate that varies with the spacecraft's latitudinal position.

- A conceptual design was defined for a radiometer capable of resolving the earth's radiance in the 15-micron spectrum to 0.01 watt/meter^2-steradian with an upper level of response of 7.0 watt/meter^2-steradian.

- A starmapper and attitude determination technique were defined capable of determining the pointing direction of the spacecraft radiometer to an accuracy of 0.25 km in tangent height at the earth's horizon. The combination of the radiometer and starmapper instruments is defined as the mission experiment package.

- A solar cell-battery electrical power subsystem conceptual design was defined which is completely compatible with the orbital

conceptual design and experiment constraints. This system is capable of delivering 70 watts of continuous electrical power for one year in the sun-synchronous, 3 o'clock nodal crossing, 500 km orbit.

- A data handling subsystem conceptual design was defined which is capable of processing in digital form all scientific and status data from the spacecraft. This subsystem is completely solid state and is designed to store the 515 455 bits of digital information obtained in one orbit of the earth. This subsystem also includes command verification and execution logic.

- A communications subsystem conceptual design was defined to interface between the data handling system of the spacecraft and the STADAN network. The 136 MHz band is used for primary data transmission and S band is used for the range and range-rate transponder.

- A spacecraft structural concept was evolved to contain, align, and protect the spaceborne subsystems within their prescribed environmental constraints. The spacecraft is compatible with the Thor-Delta launch vehicle.

- An open-loop, ground-commanded attitude control subsystem conceptual design was defined utilizing primarily magnetic torquing which interacts with the earth's field as the force for correcting attitude and spin rates.

- The Thor-Delta as booster, which provides low-cost and adequate capability, was selected from the 1972 NASA "stable."

- Western Test Range was selected as the launch site due to polar orbit requirements. This site has adequate facilities except for minor modifications to handle the program and is compatible with the polar orbital requirements.

RADIOMETER

REQUIREMENTS

The purpose of the radiometer design study has been to establish the feasibility of the HDS experimental objectives. To accomplish this, it was first necessary to translate these objectives which are stated in terms of the functional relationship and its variability between radiance and tangent height into quantitative radiometric requirements.

Specifically, the quantities which define radiometric performance are:

- Sensitivity, expressed as Noise-Equivalent Radiance (NER) or that input radiance level required to produce a signal equal to the noise level at the radiometer output.

- Resolution or transfer function, the relationship between input and output expressed as a function of the spatial frequency content of the input.

- Radiometric accuracy, expressed in terms of signal-level-dependent (scale) and signal-level-independent (bias) components and distinguishing between constant, slowly varying, and rapidly varying contributors.

In addition, entities that define the conditions under which these three basic performance criteria apply are:

- Dynamic range, range of input radiance levels over which the requirements apply

- Spectral interval

- Mission constraints, determination of the relation between time and spatial frequencies, as well as definition of thermal, volume, and weight constraints.

Quantitative derivation of the above requirements and constraints from the experimental objectives determines the performance desired of the radiometer and becomes the grounds for the first-order assessment of feasibility. The method used was to synthesize both the phenomena to be measured and characteristics of the measurement instrument and to evaluate the resultant simulated measurement with respect to the degree to which the program objectives were achieved. This process is described in the following paragraphs.

In the following section, on system analysis, these requirements are used to develop a feasibility design concept and subsystem and component requirements to the degree necessary to assess their feasibility. Finally, the sections that follow are devoted to the detailed component design required to establish feasibility of the system.

Program Measurement Requirements

The basic radiometric objective is to obtain data upon the earth infrared horizon of sufficient quality for two applications: to determine the ultimate, obtainable horizon sensor performance as limited by the characteristics of the horizon itself; and to further develop the understanding of the physics involved in the emission of the earth atmosphere.

For the horizon sensor application, the desire is to determine the horizon variability that is random or effectively nondeterministic as opposed to that which can be explained, predicted and, hence, corrected. Synthesization of the infrared horizon radiance versus tangent height profiles was performed during Phase A, Part I, for a wide variety of conditions and as a function of spectral interval. The 14.0-to 16.28-μ spectral interval was chosen to provide the most stable horizon. The expected deterministic and nondeterministic variabilities within that interval were estimated and may be grossly summarized as follows:

- Maximum peak radiance = 7.0 W/m^2 - sr

- Minimum peak radiance = 3.0 W/m^2 - sr

- Maximum slope = 0.6 W/m^2 - sr-km

- Minimum slope = 0.02 W/m^2 - sr-km

- Maximum rate of change of slope = 0.15 W/m^2 - sr-km^2

The necessary data quality is defined in Table 1, where the affected radiometer characteristics have also been noted.

Mission Constraints

The constraints that the mission definition places upon the radiometer design result from two prime factors: (1) the spacecraft is a spin-stabilized, rolling-wheel configuration; and (2) the spacecraft is nominally in a 3 p.m., sun-synchronous, polar orbit (see Figure 1). The following considerations then apply

- Passive scanning is permitted.

- Thermal control and choice of operational temperatures can utilize the fact that one side of the spacecraft is never illuminated by the sun.

- The angle between the sun line and radiometer line of sight can be as small as 26°.

- Orbital altitude is 500 km which implies a conversion factor of ~ 0.02°/km tangent height

- Spin rate is three rpm which implies a scan rate of 18°/second or 800-km tangent height/sec.

TABLE 1.-PROGRAM MEASUREMENT REQUIREMENTS

Requirement	Source (a)	Affected Parameters
1. Spectral interval: 14.0 to 16.28 μ	I	Type of optics and detector operating temperatures
2. Resolve radiance signals ≤ 0.01 W/m²-sr at spatial frequencies up to 1.0 cycles/km.	I, II,	System transfer function (optics, detector, electronics). Sensitivity (NER)
3. Conform to (2) over the range of absolute radiance: 0.01 to 7.0 W/m²-sr	I, II	Dynamic range sensitivity (NER) Radiometric accuracy
4. Measured radiance assignable to tangent height accuracy of ± 0.25 km from -30 km to +80 km.	I, II	Attitude determination accuracy Transfer function Sensitivity Radiometric accuracy
5. Meet all requirements for one-year life in orbit	I, II	Applicable technology and hardware Operating temperatures
6. Azimuth resolution ≤ 25 km	I, II	Sensitivity

a
I.   Horizon sensor application
II. Atmospheric physics application

$\overset{\star}{\phi} = 3$ rpm (18° / sec)
h = 500 km
$\triangle\phi = 0.02°$ /km tangent height
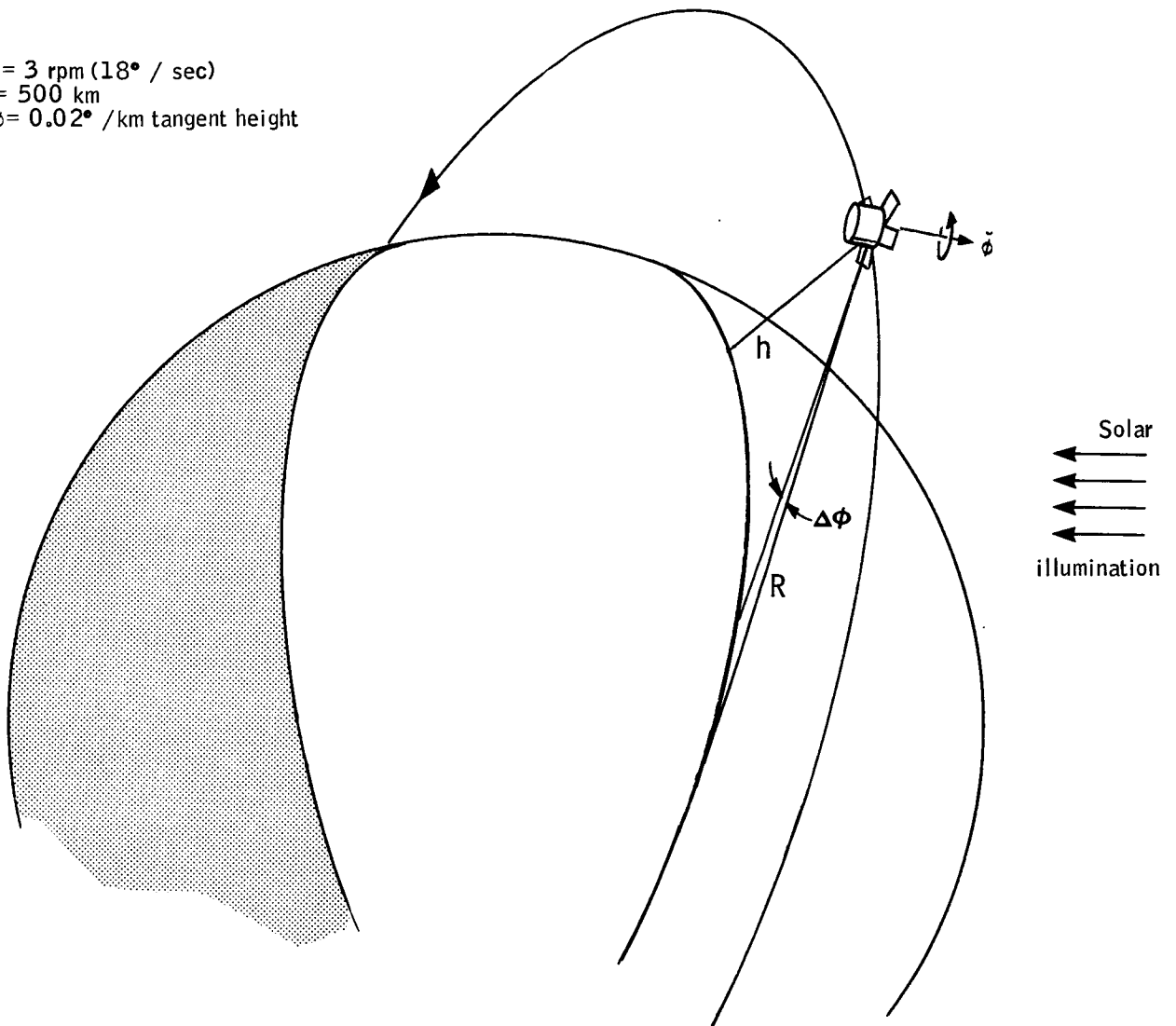
Figure 1. System Constraints

The launch vehicle is a Thor-Delta which will constrain the weight and size of the radiometer as will be seen in subsequent paragraphs.

Profile/Radiometer Synthesis Studies

Two types of studies were performed: the first to determine the effects of all of the possible types of radiometric error upon horizon detection capability versus the magnitudes of those errors; the second to quantify the errors attributable to system resolution or frequency response. Note that radiometric sensitivity (NER) will emerge as one of the contributors to radiometric accuracy.

Radiometer accuracy. -- Effects of radiometer errors on the data measurement requirements were determined by perturbing a set of 120 synthesized radiance profiles with the expected types and magnitudes of radiometer errors and calculating the resultant error in the located horizon as found by various horizon detection techniques.

The locations of the radiance profiles used are given in Figure 2, which shows the available locations and locations used and illustrates that the complete geographical area of the available data is covered. For each of the 30 locations shown, profiles for times in April, August, October, and January were used to include seasonal effects.

Each of these profiles was perturbed by four values of six different types of radiometer error. Radiometer errors were divided into two basic errors, scale and bias. Scale errors are percentage or fractional errors; bias errors are expressed in terms of radiance magnitude, e.g., radiometer noise equivalent radiance of $X.XXX$ W/m^2-sr, rather than percentage. These two kinds of errors affect radiance measurements in three different ways.

The first method of application of error is that the errors are constant in time, such as calibration errors. When a given radiometer is calibrated all of the actual errors, sometimes called nonlinearity, offset, etc., are calibrated out, but a residual calibration uncertainty remains.

By analysis, test, or otherwise, the maximum value of the uncertainty is known, but within this tolerance range the actual value of the uncertainty is not known. However, the value that existed at the time of calibration remains fixed for a given instrument. That is, if the calibration radiance is known to within ±1 percent, then for a given calibration, the input radiance is somewhere between 0.99 N_O and 1.01 N_O. If the input radiance is assumed to be 0.995 N_O, then a fixed calibration error of 0.5 percent exists which will exist for the instrument for all time. These fixed errors would seem to have no effect on local vertical because they affect all profiles in the same direction and subtract out when differences are taken to find local vertical. However, they do affect located horizons since they propagate into located horizon errors as a function of profile shape and magnitude. Then, although the radiometer error is a constant, the resulting located horizon error is not, and local vertical is affected.

8

Figure 2. Synoptic Data Map

9
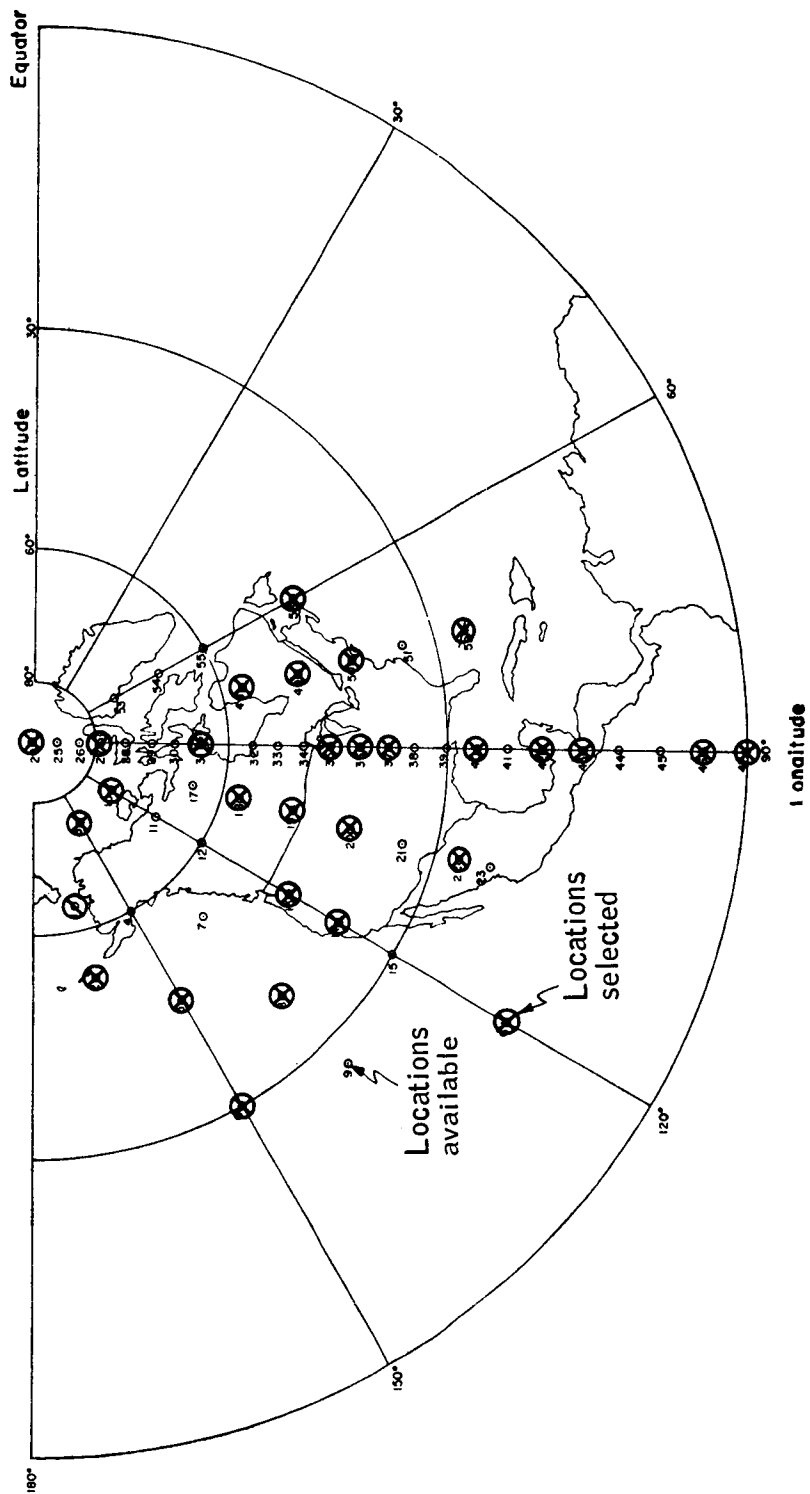
The magnitudes of this error investigated were selected to bracket the expected value of error to be associated with the HDS radiometer calibration. Thus, scale errors of 0. 4, 1, 2, and 5 percent and bias errors (all W/m^2-sr) of 0.001, 0.004, 0.01, and 0.04 were used.

The kinds of errors that vary over the operation of the devices have been referred to in discussions of precision, but since in-flight calibration will be done for the radiometer, this class of errors coming under precision or accuracy will be discussed further. Since repeated calibration is to be done, the stability of the calibration is critical; this stability includes that of the calibration source and of the radiometer response.

Instabilities are of two kinds, those that fluctuate rapidly like detector or electronics noise and those that fluctuate slowly like temperature-caused drift. Without discussing the specifics of frequency distributions, it is assumed for the HDS radiometer application that a slowly varying error, henceforth referred to as drift, is one which has a constant magnitude over a single profile measurement but which is different for some other profile measurement. A rapidly varying error, henceforth referred to as noise, is one which changes in magnitude from point to point on each profile being measured. Both of these are assumed to have gaussian amplitude distributions. The magnitudes chosen are the same as for calibration error.

For a given value of calibration error, all profiles were perturbed by a constant, e. g. , multiplied by 1. 05 for a five percent scale error. For a given value of drift, each profile was perturbed by a different error value selected from a gaussian distribution, e. g. , for five percent drift each profile was multiplied by (1 + X) where X was selected from a gaussian distribution with a σ of 0. 05. Perturbations were similar for noise, except that each radiance value on each profile was perturbed by a different error value selected from the applicable distribution.

Each type of error is determined by a variety of contributors within the radiometer and its associated calibration equipment. Examples of the various kinds of error sources are as follows:

Scale errors. --

Calibration: In terms of errors originating during, or as a part of, primary ground calibration:

- Calibration system optical transmission or reflectance uncertainty
- Calibration radiance source emittance or temperature uncertainty
- Source radiance level dependent stray radiation
- Geometrical - tilts and spacings - uncertainties

10

- Radiometer spectral response and source spectral content uncertainties and drifts

- Interaction between radiometer components and calibration equipment

and in terms of errors originating during, or as a result of, handling, and testing, and the environment from the time the instrument underwent primary calibration until the first secondary (in-flight) calibration on orbit:

- In-flight calibration system drift

- Radiometer optics reflectance and transmission changes

- Detector or electronic drifts (non-linear) that would affect interpolation between in-flight calibration levels

Drift:

- In-flight calibration system temperature and emittance uncertainties

- Interaction between telescope emission and detector responsivity

- Changes in optics reflectance and transmission

- Spectral response shifts

Noise:

- Stray radiation from neighboring resolution elements

- Detector temperature variations

- Detector bias variations

- System transfer function induced spurious modulation and/or smoothing (listed under scale errors since it is proportional to input signal modulation)

Bias errors. --

Calibration:

- Source radiation level independent stray radiation

- Finite sample size of zero-mean random phenemona such as detector noise, resulting in an error inversely proportional to the time spent in calibration

11

Drift:

- Stray radiation
- Finite sample size of noise and telescope emission during each in-flight calibration

Noise:

- Detector noise and short-term drifts
- Electronics noise and short-term drifts
- Stray radiation

The body of data operated on by different horizon detection techniques to determine horizon error consists of 24 different sets of 120 radiance profiles in each set. Each of these sets of profiles was operated on by four different threshold techniques with two threshold values used for each technique as summarized in Table 2 and Figure 3.

TABLE 2. - HORIZON DETECTION TECHNIQUES

Threshold technique	Threshold values
Radiance magnitude, (L1)	2.0, 3.0 W/m^2-sr
Normalized radiance magnitude, (L2), % of peak radiance	0.15, 0.90 (15%, 90%)
Integral of radiance, (L3)	4.5, 20.0 W-km/m^2-sr
Integral of normalized radiance, (L4)	2.5, 10.0 km

The results are presented in Table 3 which gives the located horizon error sensitivity coefficients in km/percent for scale error and in km/.01 W/m^2-sr for bias errors. Both error standard deviation, which is the contribution to horizon noise caused by the radiometer, and error mean value, which is an absolute accuracy indication, are given.

These horizon errors caused by instrument errors cause a degradation in the measurement program performance. A measure of program performance is the confidence level in obtaining a given confidence interval on the estimate of horizon noise obtained from the measured profiles. In the Part I study, data sampling requirements were determined which would produce a 95 percent confidence level of estimating the horizon noise to within ±0.5 km. Because of the added effect of instrument-caused horizon noise, this confidence interval must be reduced, or, alternately, the number of samples must be increased.
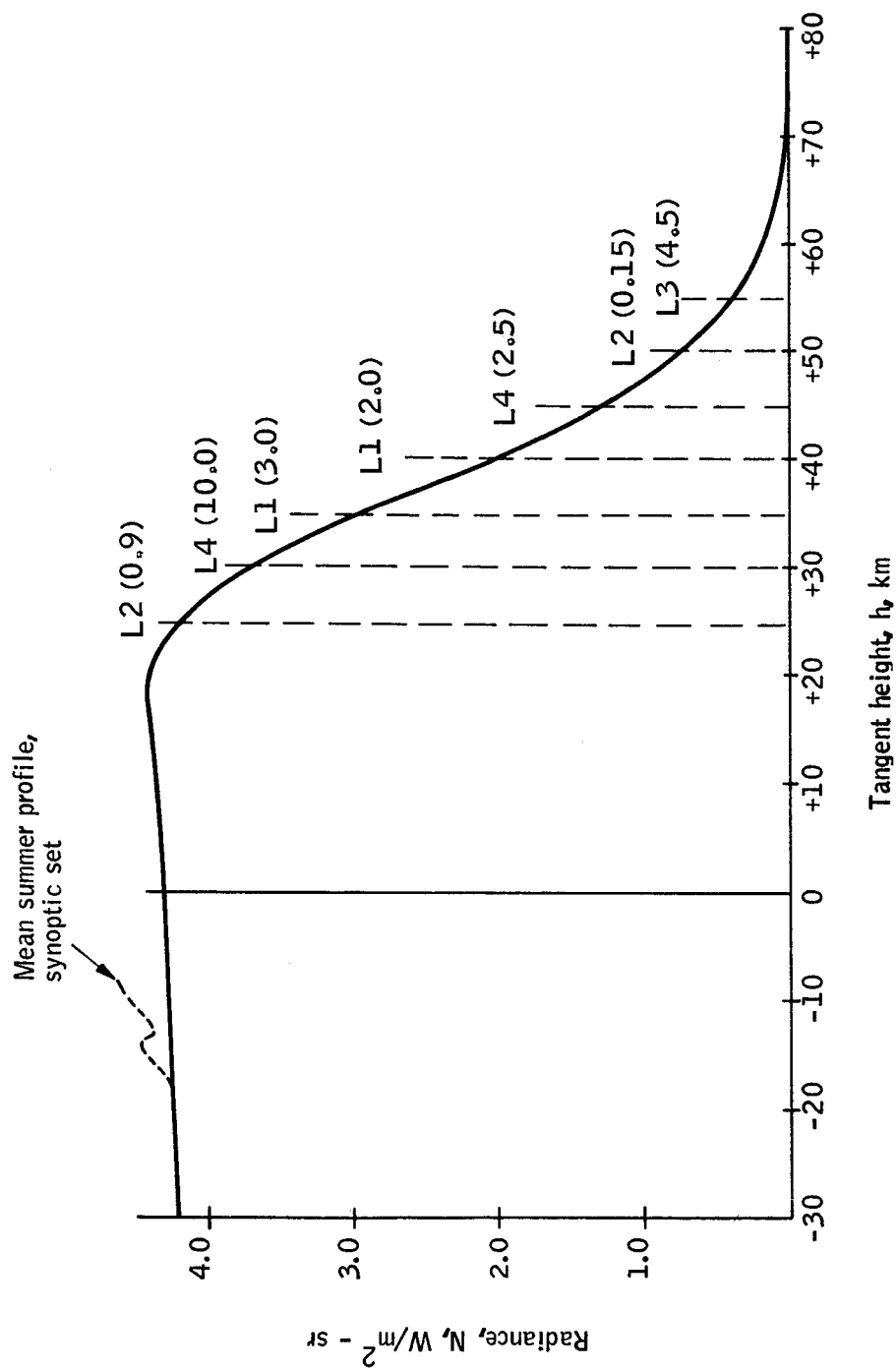
Figure 3. Mean Located Horizons for Selected Locators

TABLE 3. - SENSITIVITY COEFFICIENTS

	Standard deviation					
	Scale, km/%			Bias, km/.01 W/m^2-sr		
Locator	Cal	Drift	Noise	Cal	Drift	Noise
L1 (2.0)	.02	.13	.10	.01	.06	.05
L1 (3.0)	.04	.18	.13	.015	.05	.05
L2 (0.15)	0	0	.08	.02	.09	.08
L2 (0.9)	0	0	.48	.002	.008	.10
L3 (4.5)	.006	.07	.026	.06	.04	.15
L3 (20.0)	.008	.10	.023	.27	.19	.053
L4 (2.5)	0	0	.06	.04	.22	.07
L4 (10.0)	0	0	.08	.02	.10	.03
	Mean error					
L1 (2.0)	.12	-.02	.004	.06	-.006	-.01
L1 (3.0)	.15	-.03	-.004	.05	-.006	-.008
L2 (0.15)	0	0	-.116	.09	-.01	-.029
L2 (0.9)	0	0	-.625	.008	-.001	-.077
L3 (4.5)	.06	-.007	-.004	.41	-.038	-.006
L3 (20.0)	.09	-.01	0	.18	-.018	-.003
L4 (2.5)	0	0	-.12	.21	-.02	-.02
L4 (10.0)	0	0	-.19	.10	-.01	-.03

The analysis leads to the following equation which relates the parameters of interest.

$$I_c = \left[\frac{2\sigma^2 \left(1 + \frac{\sigma_1^2}{\sigma_2^2}\right)^2 + m(N-1)k^2 \frac{\sigma_1^2}{\sigma_2^2}}{m(N-1)(1 - P/100)} \right]^{1/2} \tag{1}$$

where:

I_c = confidence interval on the estimate of natural horizon noise

σ_2 = horizon noise in nature

σ_1 = instrument-caused horizon noise

m = number of time cells

N = number of samples per time-space cell

k = fractional uncertainty in the estimate of σ.

The approach taken here is to allow the confidence level to decrease to 90 percent from 95 percent rather than to increase the sample size. The resultant allowable instrument-caused horizon error is determined from Figure 4 which shows the confidence level P versus instrument caused error σ_1 for various values of horizon noise σ_2 and k, the fractional uncertainty in σ_1. At the 90 percent confidence level, allowable instrument-caused errors are

σ_1 = 0.3 km ±31.6%; 0.34 km ±20%; 0.38 km ±10%; and 4 km ±0%

To simplify the radiometer design problem, both the allowable error and its tolerance should be made as large as possible. However, as the allowable error increases, the allowable tolerance decreases, thus necessitating a compromise. The combination selected as being a reasonable compromise is an instrument-caused error σ_1 of 0.34 km known to within ±20 percent.

For this instrument-caused error the allowable values of radiometer scale and bias errors are determined from Table 3.

Using the sensitivity coefficients of Table 3, the locator exhibiting the maximum sensitivity for each error was constrained to produce a horizon error of $0.34/\sqrt{6}$ km in order to guarantee that the rss of the six errors did not exceed 0.34 km.
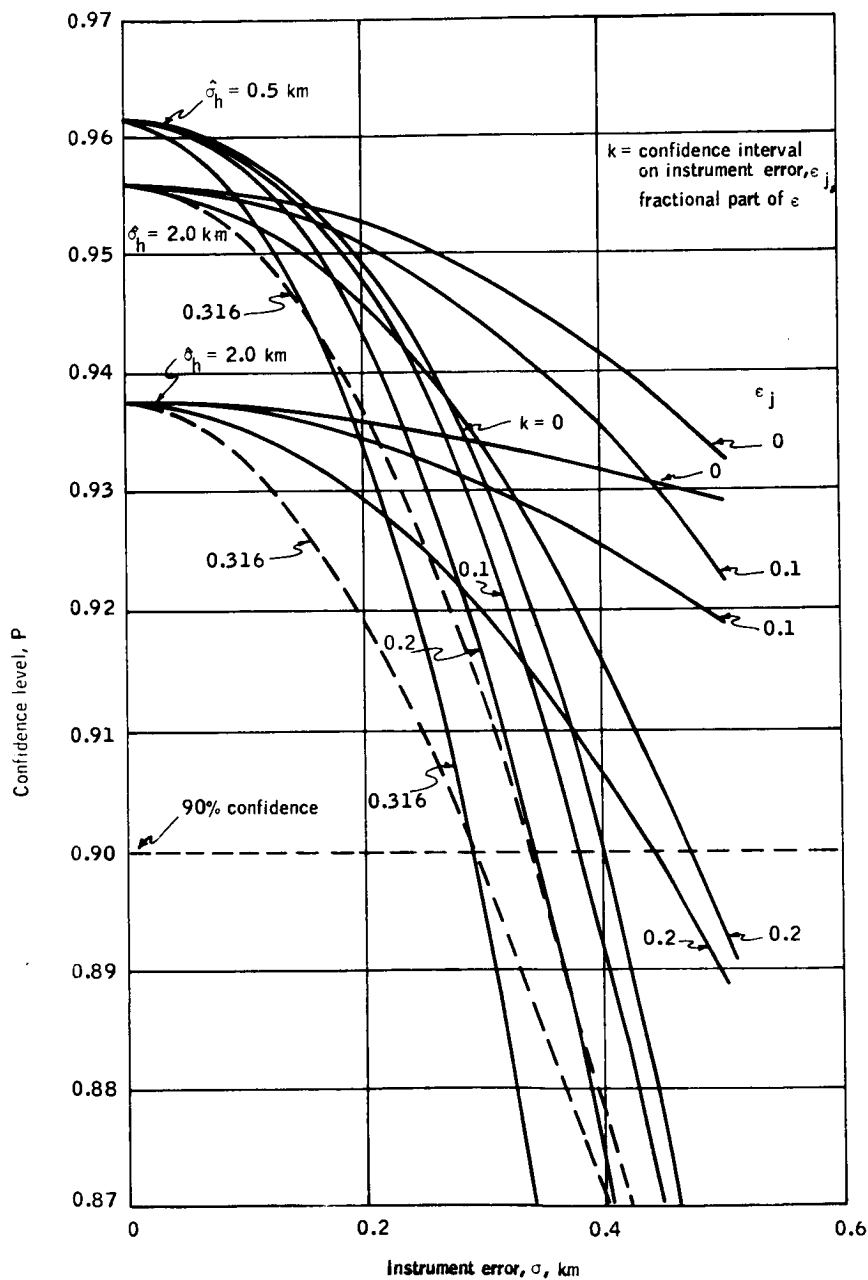
Figure 4. Confidence Level for Obtaining 0.5-km Interval Level on Horizon Standard Deviation versus Instrument Error and Instrument Error Confidence Interval

Since a given locator exhibits high sensitivity to one kind of error and low sensitivity to another (e. g. , Figures 5 and 6), the approach described above led to a root-sum-square horizon error considerably lower than the maximum allowable 0. 34 km. Adjustments were made in the errors known to cause difficulty in the radiometer design process to relieve the requirements and remain within the allowable 0. 34 km error.

The resulting allowable radiometer errors, the resultant root-sum-square-horizon standard deviation, and overall mean error are shown in Table 4.

These radiometer errors become radiometer specifications which define the maximum allowable (one σ) scale and bias errors for calibration, drift, and noise. For clarity they are restated here:

- Scale calibration: 3% (1. 0% design goal)
- Scale drift: 0. 72%
- Scale noise: 0. 27%
- Bias calibration: 0. 01 W/m^2 sr
- Bias drift: 0. 01 W/m^{-2} sr
- Bias noise: 0. 01 W/m^{-2} sr

Emphasis has been placed upon scale calibration accuracy for two reasons:

1. It is the largest single contributor to the mean error.
2. It is the one error that is not improved upon as the in-orbit data increases in quantity.

Radiometric Resolution Study. -- The radiometer resolution or frequency response is a function of the optical system collecting aperature diameter, the detector field of view, and the electronics bandwidth. The specific dependence is as depicted in Figures 7 and 8 which assumes that

1. The optical system is essentially diffraction limited, and
2. The detector time constant is sufficiently short that its effects can be ignored.

In order to evaluate the effects of the various combinations of radiometer parameters on the horizon measurement, the set of 120 profiles, discussed in the preceding paragraphs, was operated on by simulated radiometers. The resulting errors were then computed in terms of located horizon, local vertical, and the radiance tangent-height function itself. Twenty-seven cases were evaluated employing all combinations of the following parameters:
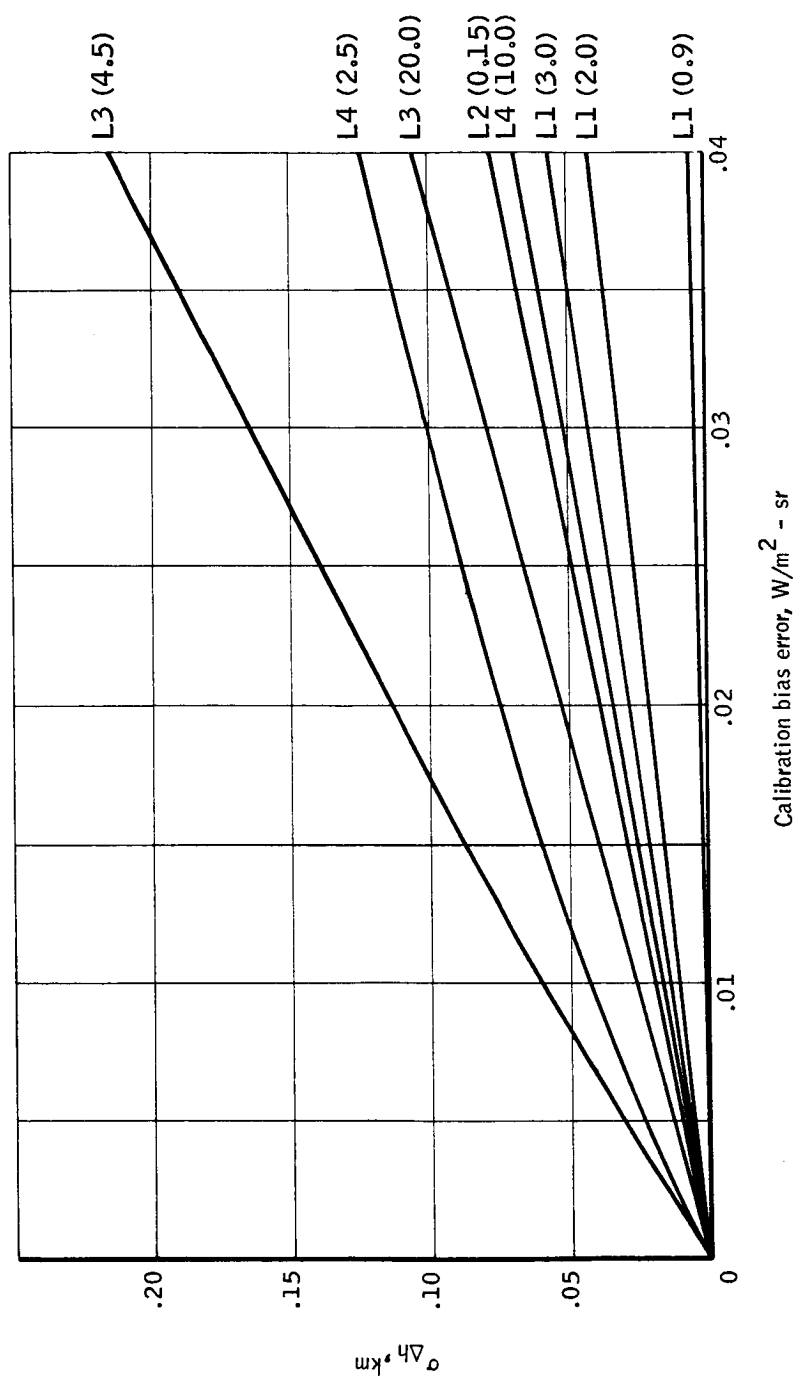
Figure 5.   Located Horizon Error Standard Deviation Caused
by Instrument Calibration Bias

18
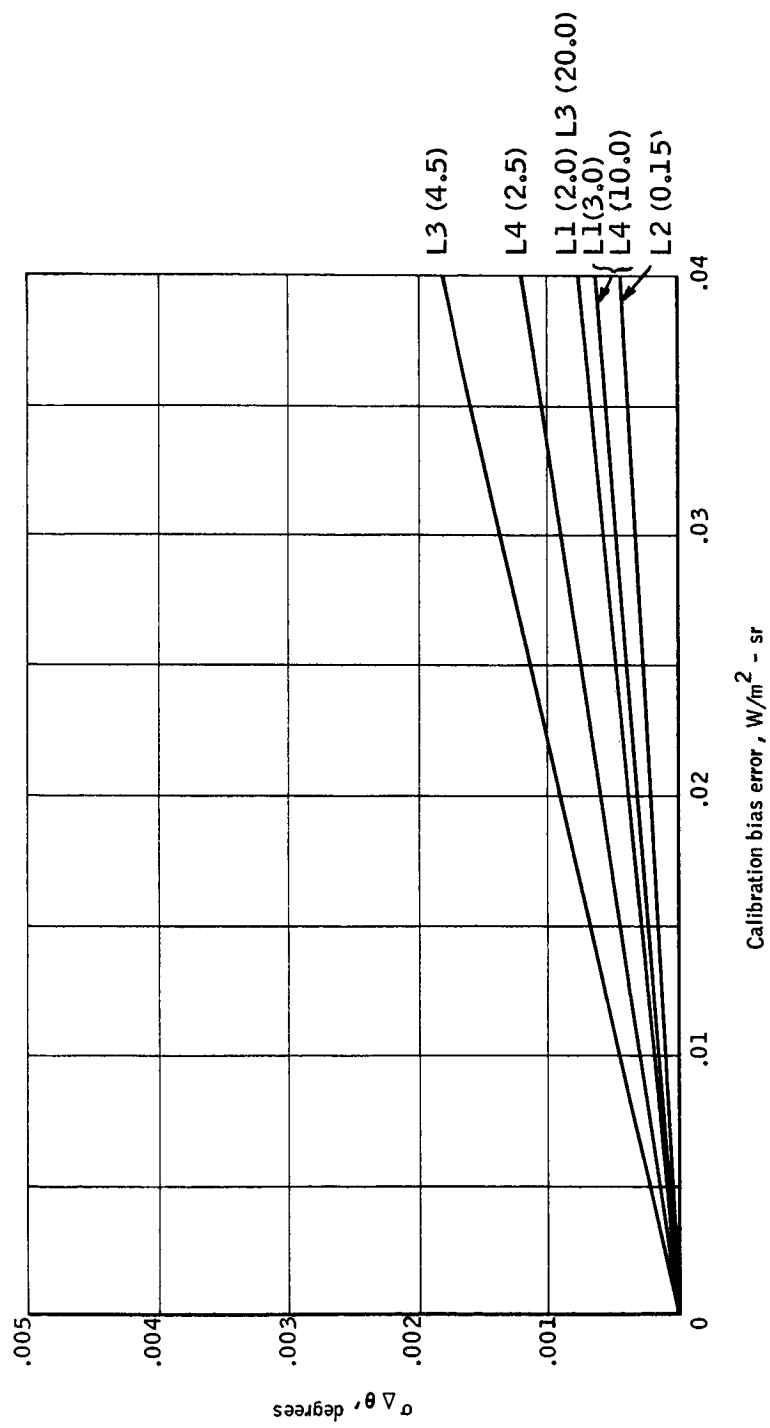
Figure 6. Local Vertical Error Standard Deviation Caused by Instrument Calibration Bias Error

19

TABLE 4. - ALLOWABLE INSTRUMENT-CAUSED HORIZON ERROR, STANDARD DEVIATION, AND MEAN

| Locator | rss | Standard Deviation | | | | | |
| | | Scale | | | Bias | | |
		Cal 3?	Drift 0.72?	Noise 0.27?	Cal	Drift	Noise
L1 (2.0)	.139	.06	.094	.027	.010	.060	.050
L1 (3.0)	.197	.12	.130	.035	.015	.050	.050
L2 (0.15)	.126	0	0	.022	.020	.090	.080
L2 (0.9)	.164	0	0	.130	.002	.008	.100
L3 (4.5)	.175	.018	.050	.007	.060	.040	.150
L3 (20.0)	.34	.024	.070	.006	.270	.190	.053
L4 (2.5)	.235	0	0	.016	.040	.220	.070
L4 (10.0)	.109	0	0	.022	.020	.100	.030

| Locator | Mean Error | | | | | | |
	Sum						
L1 (2.0)	.393	.36	-.014	.001	.06	-.006	-.01
L1 (3.0)	.463	.45	-.022	-.001	.05	-.006	-.008
L2 (0.15)	.019	0	0	-.032	.09	-.01	-.029
L2 (0.9)	-.239	0	0	-.169	.008	-.001	-.077
L3 (4.5)	.54	.18	-.005	-.001	.41	-.038	-.006
L3 (20.0)	.422	.27	-.007	0	.18	-.018	-.003
L4 (2.5)	.137	0	0	-.003	.21	-.02	-.020
L4 (10.0)	-.009	0	0	-.051	.10	-.01	-.030
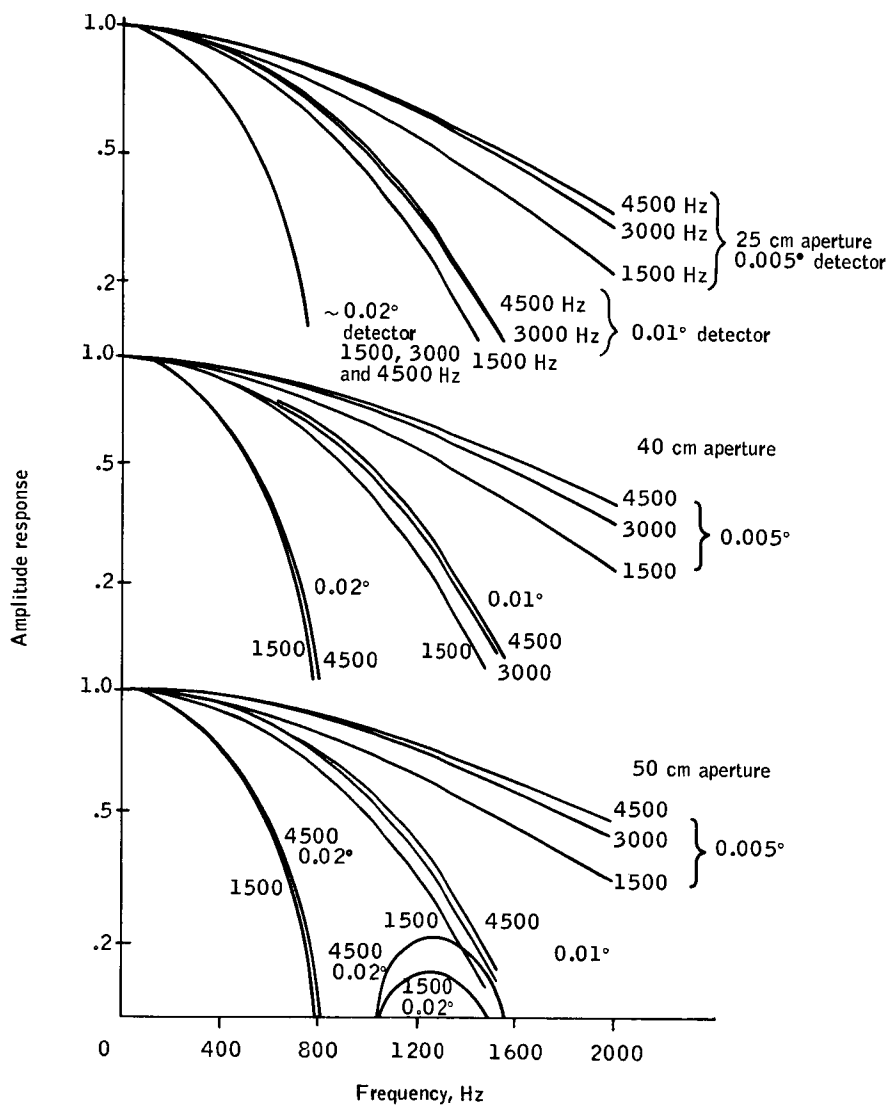
Figure 7. Frequency Response for Combinations of
Aperture, Detector, and Electronics
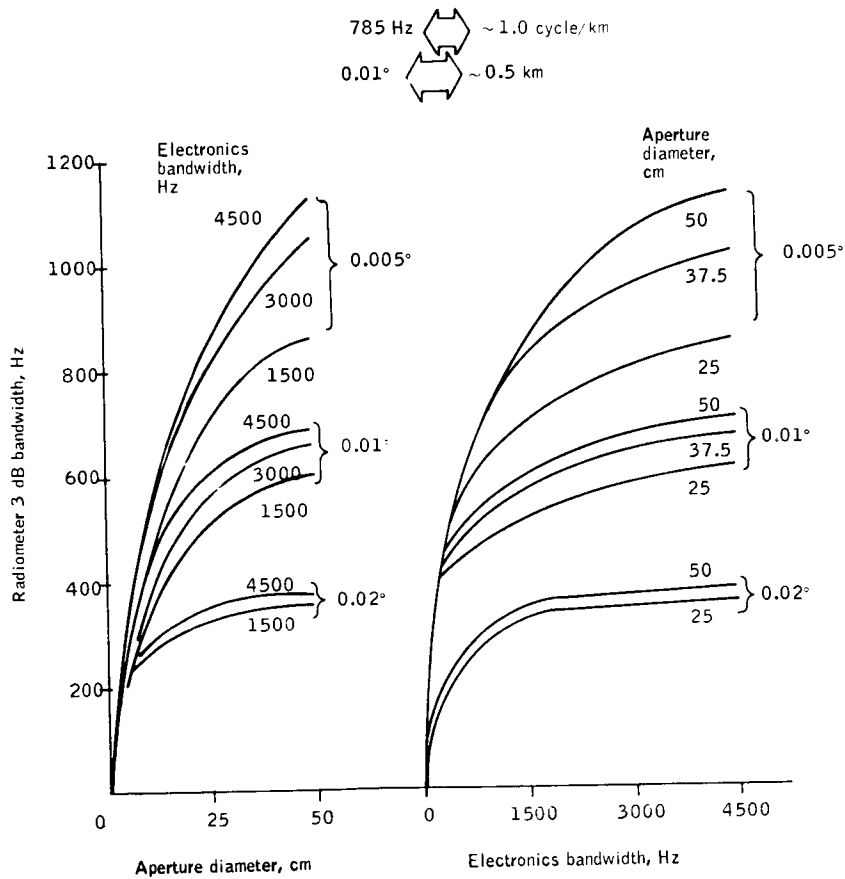
Figure 8. Frequency Response Relationships Between Optics,
Field of View, and Electronics Transfer Functions

- Optics diameter: 20, 40, and 60 cm.
- Detector field of view: 0.005°, 0.01°, and 0.02°
- Electronics 3-dB bandwidth: 750, 1500, and 3000 Hz
  (where 750 corresponds to 1 cycle/km)

which represents a variation in system bandwidth of from 1/3 to 1-1/3 cycles/km.

Other parameters used in the simulation were

- Scan rate: 18°/sec
- Altitude: 500 km
- Radiometer focal length: 40 cm

Output of the electronics was obtained by assuming that the detector time output is linear from point to point as the horizon profile is scanned in finite time increments. The electronics transfer function was assumed to be satisfactorily given by a single-order, low-pass filter. The output of the low-pass filter to each input ramp was calculated and summed to give the electronics output. For a given increment of time, the output is

$$E_o(t) = K(t - t_o) \left(1 - e^{-\frac{(t - t_o)}{\tau}} \right) t_o$$

where: t_o = scan time at the start of each ramp,

Δt = time increment until start of next ramp, and

K = slope of ramp.

Table 5 summarizes the mean located horizon errors and their standard deviation. Maximum mean errors are in the range 0.2 to 0.3 km and appear to be relatively independent of variation in aperture size or detector field. More thorough examination of the results indicate that this error is almost totally due to the low-frequency ($<$0.03 cycle/km) phase shift of the assumed linear, first-order electronics filter. It is, therefore[a], correctable to within its standard deviation, which does not exhibit a significant dependance upon electronic bandwidth. The error standard deviation in the range 0.01 to 0.05 km is strongly dependent upon optical resolution (aperture size).

---

[a] The phase shift can be removed by using knowledge of the filter phase versus frequency characteristic and by performing a frequency analysis of each profile which is unaltered by the phase shift. Alternatively an active filter can be employed to reduce the low frequency phase shift.

TABLE 5.-LOCATED HORIZON ERRORS FOR PARAMETER VARIATIONS (YEARLY AVERAGE)

			Yearly Average $dh(\sigma_h)$								
Δf_e HZ	Dc cm	Detector field, deg	$L^1(2.0)$	$L^1(3.0)$	$L^2(0.15)$	$L^2(0.9)$	$L^3(4.5)$	$L^3(20.0)$	$L^4(2.5)$	$L^4(10.0)$	Case
750	20	.005	.19(.04)	.17(.04)	.20(.05)	.15(.05)	.31(.02)	.23(.009)	.24(.01)	.20(.006)	1
		.01	.19(.04)	.17(.04)	.20(.05)	.15(.05)	.31(.02)	.23(.009)	.25(.01)	.20(.006)	2
		.02	.19(.04)	.17(.04)	.20(.05)	.15(.05)	.32(.03)	.23(.009)	.25(.01)	.21(.007)	3
	40	.005	.18(.02)	.17(.02)	.19(.03)	.16(.03)	.25(.02)	.20(.006)	.21(.008)	.19(.004)	4
		.01	.18(.03)	.17(.02)	.19(.03)	.16(.03)	.26(.02)	.20(.006)	.22(.008)	.19(.004)	5
		.02	.18(.02)	.17(.03)	.19(.04)	.15(.04)	.27(.02)	.21(.007)	.22(.008)	.19(.005)	6
	60	.005	.18(.02)	.17(.02)	.18(.03)	.16(.03)	.24(.02)	.19(.005)	.20(.007)	.18(.003)	7
		.01	.18(.02)	.17(.02)	.18(.03)	.16(.03)	.24(.02)	.20(.005)	.20(.007)	.18(.004)	8
		.02	.18(.02)	.17(.02)	.19(.03)	.16(.03)	.26(.02)	.20(.006)	.22(.008)	.19(.004)	9
1500	20	.005	.11(.03)	.09(.03)	.12(.05)	.07(.05)	.21(.02)	.14(.008)	.16(.009)	.12(.006)	10
		.01	.11(.04)	.09(.04)	.12(.05)	.07(.05)	.22(.02)	.14(.008)	.16(.009)	.12(.006)	11
		.02	.11(.04)	.09(.04)	.12(.05)	.07(.05)	.22(.02)	.14(.008)	.16(.009)	.12(.006)	12
	40	.005	.10(.02)	.08(.02)	.10(.03)	.07(.03)	.16(.01)	.11(.005)	.12(006)	.10(.003)	13
		01	.10(.02)	.08(.02)	.10(.03)	.07(.03)	.16(.01)	.12(.005)	.13(.006)	.10(.003)	14
		.02	.10(.02)	.08(.02)	.11(.03)	.07(.03)	.17(.02)	.12(.006)	.13(.006)	.11(.004)	15
	60	.005	.09(.02)	.08(.01)	.10(.02)	.08(.02)	.14(.01)	.11(.003)	.11(.005)	.10(.003)	16
		01	.09(.02)	.08(.02)	.10(.02)	.08(.02)	.14(.01)	.11(.004)	.12(.005)	.10(.003)	17
		.02	.10(.02)	.08(.02)	.10(.03)	.07(.03)	.16(.01)	.12(.005)	.13(.006)	.10(.003)	18
3000	20	.005	.06(.03)	.04(.03)	.08(.04)	.03(.05)	.17(.02)	.10(.007)	.11(.008)	.07(.005)	19
		.01	.06(.03)	.04(.03)	.08(.04)	.03(.05)	.17(.02)	.10(.007)	.11(.008)	.07(.005)	20
		.02	.07(.04)	.04(.04)	.08(.05)	.03(.05)	.18(.02)	.10(.008)	.12(.009)	.08(.006)	21
	40	.005	.05(.02)	.04(.02)	.06(.02)	.03(.03)	.11(.01)	.01(.004)	.08(.005)	.06(.003)	22
		.01	.05(.02)	.04(.02)	.06(.03)	.03(.03)	.11(.01)	.01(.004)	.08(.005)	.06(.003)	23
		.02	.06(.02)	.04(.02)	.06(.03)	.03(.03)	.13(.01)	.08(.005)	.09(.005)	.06(.004)	24
	60	.005	.05(.01)	.04(.01)	.05(.02)	.04(.02)	.09(.008)	.06(.003)	.07(.003)	.05(.002)	25
		.01	.05(.01)	.04(.01)	.05(.02)	.04(.02)	.10(.009)	.06(.003)	.07(.004)	.06(.002)	26
		.02	.05(.02)	.04(.02)	.06(.02)	.03(.03)	.11(.01)	.07(.004)	.08(.005)	.06(.003)	27

[a]Number is mean error in km, number in ( ) is std. deviation.

A technique for compensating the mean error is to estimate the value of the expected mean error by simulation and to bias the experiment results accordingly. The uncertainty in the estimate of the mean σM is given by

$$\sigma_M = \frac{\hat{\sigma}_{\Delta h}}{\sqrt{m-1}} \tag{3}$$

where:

$\hat{\sigma}_{\Delta h}$ = standard deviation about the expected mean

M = number of samples used to calculate the mean and standard deviation

Of greater utility than the located horizon error analysis was a detailed analysis of the radiance errors versus tangent height for selected profiles. Figures 9 through 12 illustrate such analysis for a representative profile. Because this error is perfectly describable as bias noise, the maximum allowable value has been set at 0.01 W/m^2-sr. This should actually be taken as at least a 3 σ value, since, as will be seen later, there are five contributors of comparable size to the bias noise error.

The curves of Figures 9 through 12 indicate that the electronic phase shift is relatively constant. The curves also indicate, to the extent that this profile is representative, that a 40-cm aperture and a 0.5-km detector field constitute a reasonable combination which fulfills the measurement objective.

Summary and Conclusion

The foregoing discussions have implied that the one remaining parameter NER would naturally emerge from the error analysis. This parameter is one of the contributors to noise bias errors and as such should be maintained at no greater than 1/3 the total error allotment, i.e., of ≤ 0.003 W/m^2-sr. This is also consistent with the program measurement requirements of detecting a minimum absolute radiance of 0.01 W/m^2-sr as well as measuring fluctuations of the same amount regardless of absolute radiance level.

Requirements and constraints developed in this section are summarized as follows:

- Spectral interval: 14.00 to 16.28μ

- NER: ≤ 0.003 W/m^2-sr

25
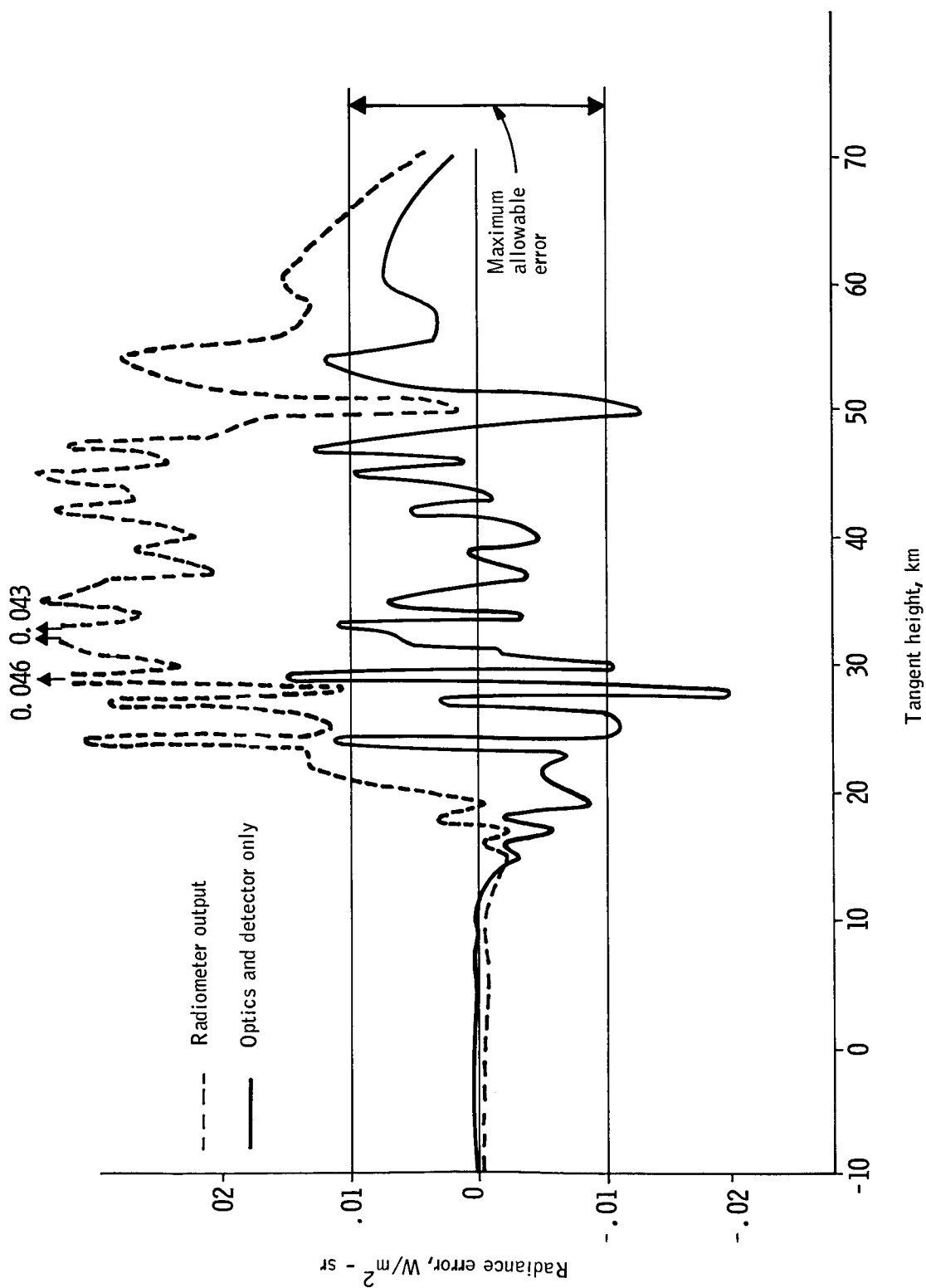
Figure 9. Radiometer Error for 20 cm Aperture, 1.0 km Field of View, and 1.0 Cycle/km (-3db) Electronic Bandwidth

26
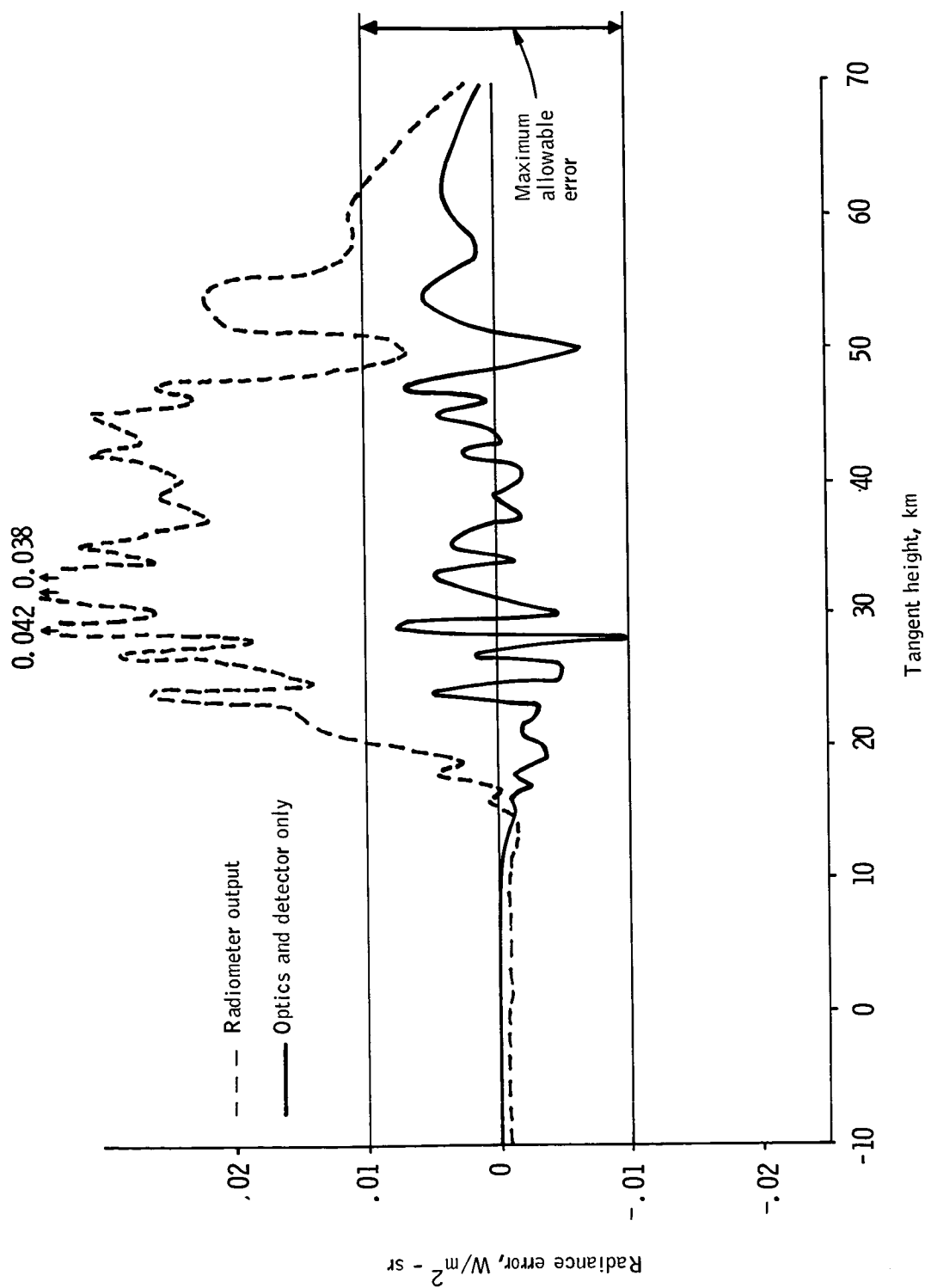
Figure 10. Radiometer Error for 40 cm Aperture, 0.5 km
Field of View, and 1.0 cycle/km (-3db)
Electronic Bandwidths

27
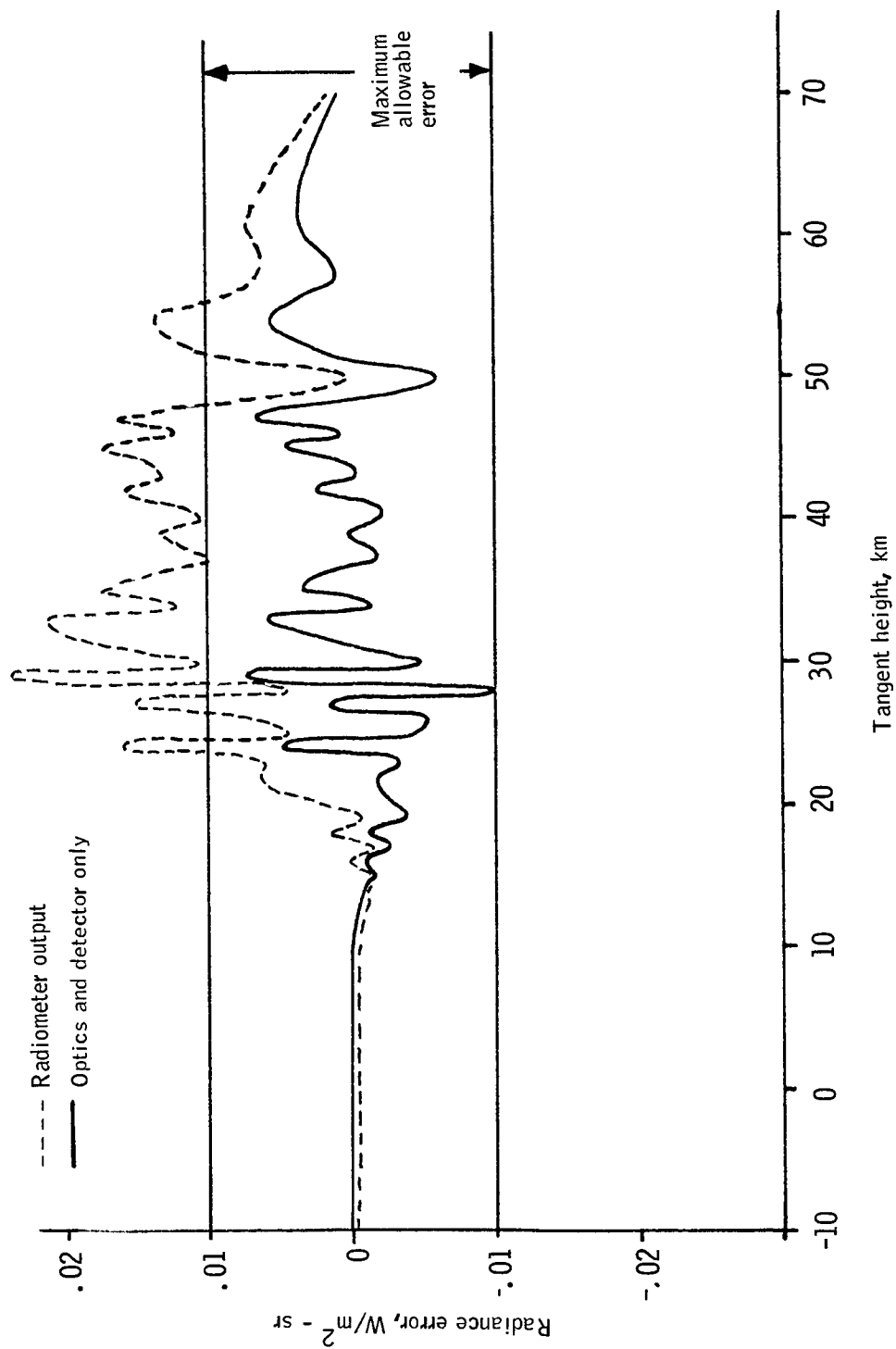
Figure 11. Radiometer Error for 40 cm Aperture, 0.5 km Field of View, and 2.0 cycles/km (-3db) Electronic Bandwidth

28
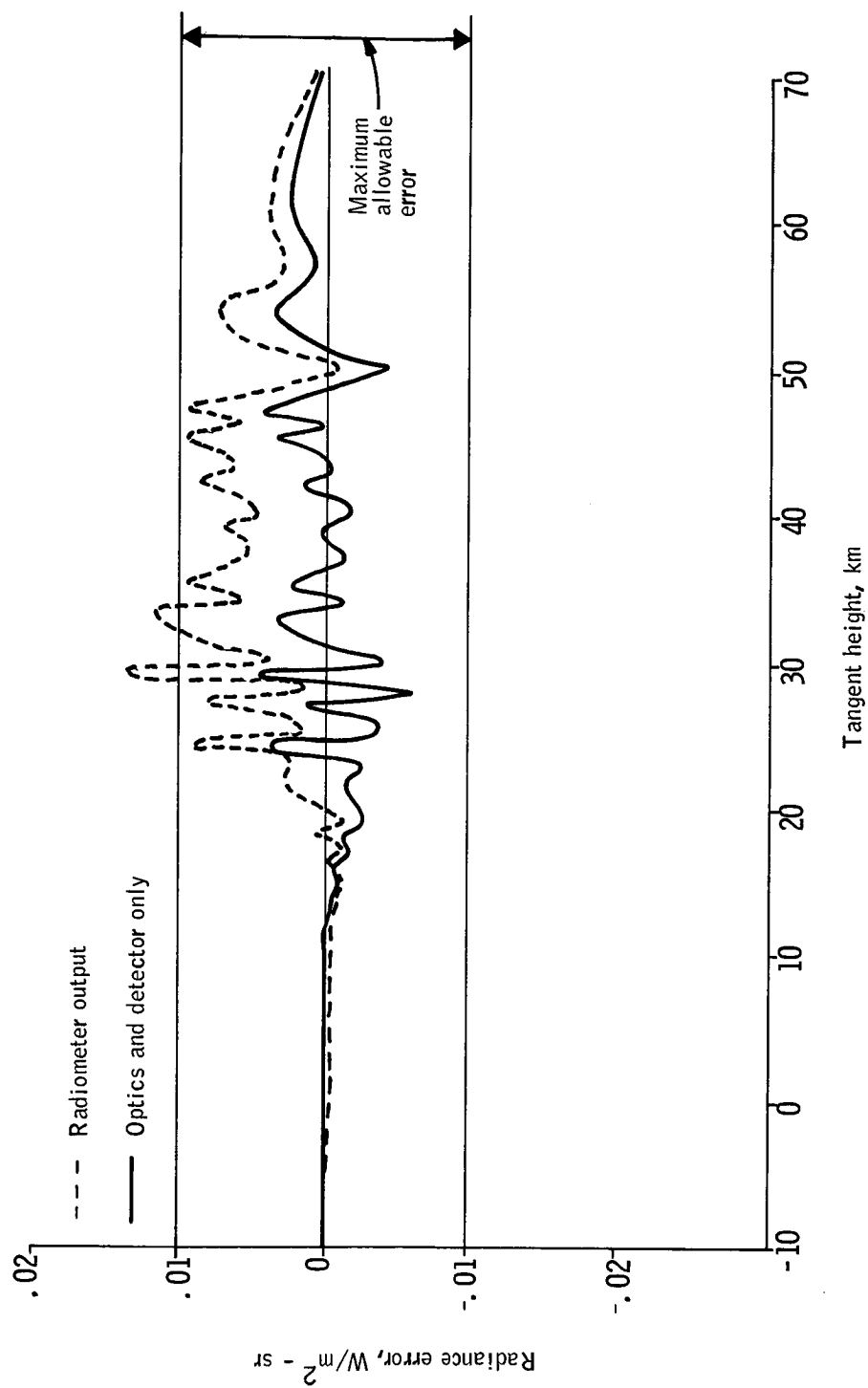
Figure 12. Radiometer Error for 60 cm Aperture, 0.25 km Field of View, and 4.0 cycles/km (-3db) Electronic Bandwidths

29

- System transfer function

  Frequency response[a]: $\leq 10^{-4}$ to ≥ 0.75 cycle/km (post-detection)

  Low end chosen to keep "droop" at frequency
  $\sim \dfrac{1}{\text{profile length}} \leq 1.$

  Phase shift (uncorrectable): $\dfrac{2\pi}{30}$ radians cycle/km of spatial frequency.

  ($0 < f_s < 1$ cycle/km)

- Radiometric accuracy - Scale % bias, W/m^2-sr

		Scale %	bias, W/m^2-sr
Calibration	$\leq$	3.0	0.01
Drift		0.72	0.01
Noise		0.27	0.01

- Dynamic range: NER to 7.0 W/m^2-sr

- Minimum aperture diameter: 40 cm ($\pm$ 10)

- Maximum detector field: 0.5 km ($\pm$ 0.25)

- Altitude: 500 km

- Scan rate: 18°/sec

SYSTEM ANALYSIS

The feasibility of attaining the radiometer performance objectives has been demonstrated by the development and evaluation of a feasibility design concept. This was accomplished in the following steps:

1. Parametric analysis to relate the parameters defining radiometer performance to those defining its configuration to provide a basis for quantitative evaluation of the effects of design decisions upon the expected performance.

2. Tradeoff and design analyses to define a preferred configuration by which to establish the feasibility of the performance requirements. These analyses do not optimize the design concept with respect to anything except that it be the most straightforward and demonstrative means of establishing feasibility.

---

[a] The low frequency of 10^{-4} cycle/km maintains the "droop" at frequencies corresponding to the profile fundamental ($\sim 10^{-2}$ cycle/km) to less than 1 percent.

3. Detailed design and analyses of subsystems and components where necessary to establish feasibility.

4. Derivation of the expected performance characteristics of the preferred design and comparison with the basic requirements. As a result of this effort, critical problem areas are defined along with the required design and development upon which the feasibility of the design ultimately is predicated.

Parametric Analysis

The two performance parameters of interest are sensitivity and transfer function. The latter was discussed in the previous section, and the resultant parametric constraints noted. The radiometric sensitivity is given by

$$NER = \frac{4}{\pi} \frac{f/no. \sqrt{\Delta f}}{D^* D_c \sqrt{\Delta \Omega}} \qquad (4)$$

where:

f/no.	=	optics effective f number
Δf	=	post-detection noise equivalent bandwidth
D_c	=	aperture diameter
D^*	=	detector detectivity normalized to unity area and bandwidth
$\Delta \Omega$	=	detector field of view
	=	$\Delta \theta$ (az) x $\Delta \phi$ (el.)
δ	=	system efficiency

since:

$$\Delta f = k (\Delta \phi)^{-1} \dot{\phi}$$

where:

$\dot{\phi}$	=	scan rate and
k	=	constant of proportionality of electronics cutoff in terms of resolution elements/sec; then, an alternate form of equation (4) is

$$NER = \frac{4}{\pi} \frac{f/no. \sqrt{k \dot{\phi}}}{D^* D_c \Delta \phi \delta \sqrt{\Delta \theta}} \qquad (4a)$$

Now $\delta = \delta_o \qquad \delta_e$

$\qquad\qquad$ optics $\qquad$ electronics

and $\qquad \dfrac{k}{\delta_e} \simeq$ constant $\pm 5\%$, $1/2 < k < 2$;

therefore, we can take any k in that range and the corresponding δ_e for the purpose of computing NER. [Note, there are other factors involving the choice of sampling rate, memory size, etc. that enter into the actual value of k.] In particular, k can be taken as 1, and δ_e computed for the specific electronic operations utilized.

The quantity f/no. can reasonably be taken to be 1 for the purpose of this analyses. The scan rate $\dot\phi$ is 18°/sec.

The azimuthal resolution $\Delta\theta$ can be as great as 25 km (~ 10 mr). However, since the elevation resolution will be between 0.25 and 1.0 km, and since aspect ratios on the detector of greater than 5 - 10 will be difficult to achieve, $\Delta\theta$ will be taken as equivalent to 2 km (0.8 mr). Owing to the required low frequency response, the system will undoubtedly employ a chopper implying a 50% energy loss/resolution element. Further losses are in the spectral filter ($\sim 40\%$) and optics ($\sim 40\%$), which taken with δ_e (~ 0.80) yield a system efficiency in the range 10 - 15%. Using 0.15, the following relation is yielded:

$$NER = \frac{1.7 \times 10^2}{D^* D_c \Delta\phi} \; W/cm^2 - sr$$

D^* in cm $- Hz^{1/2}/W$, D_c in cm, $\Delta\phi$ in radians

This quantity is plotted in Figure 13, for a range of D^* corresponding to the applicable technology in detectors and coolers. Note that to get a room temperature system onto the same graph required giving it a 25 km azimuthal resolution, so that the difference between it and the other two temperature regimes is quite real. Such is not the case between the lower two bands which can be made to converge by means of straining the aspect ratio somewhat.

The area devoted by "required region of operation" is bounded by the maximum allowable NER and minimum allowable aperture, the latter being determined by resolution requirements (see the section on radiometric resolution study).
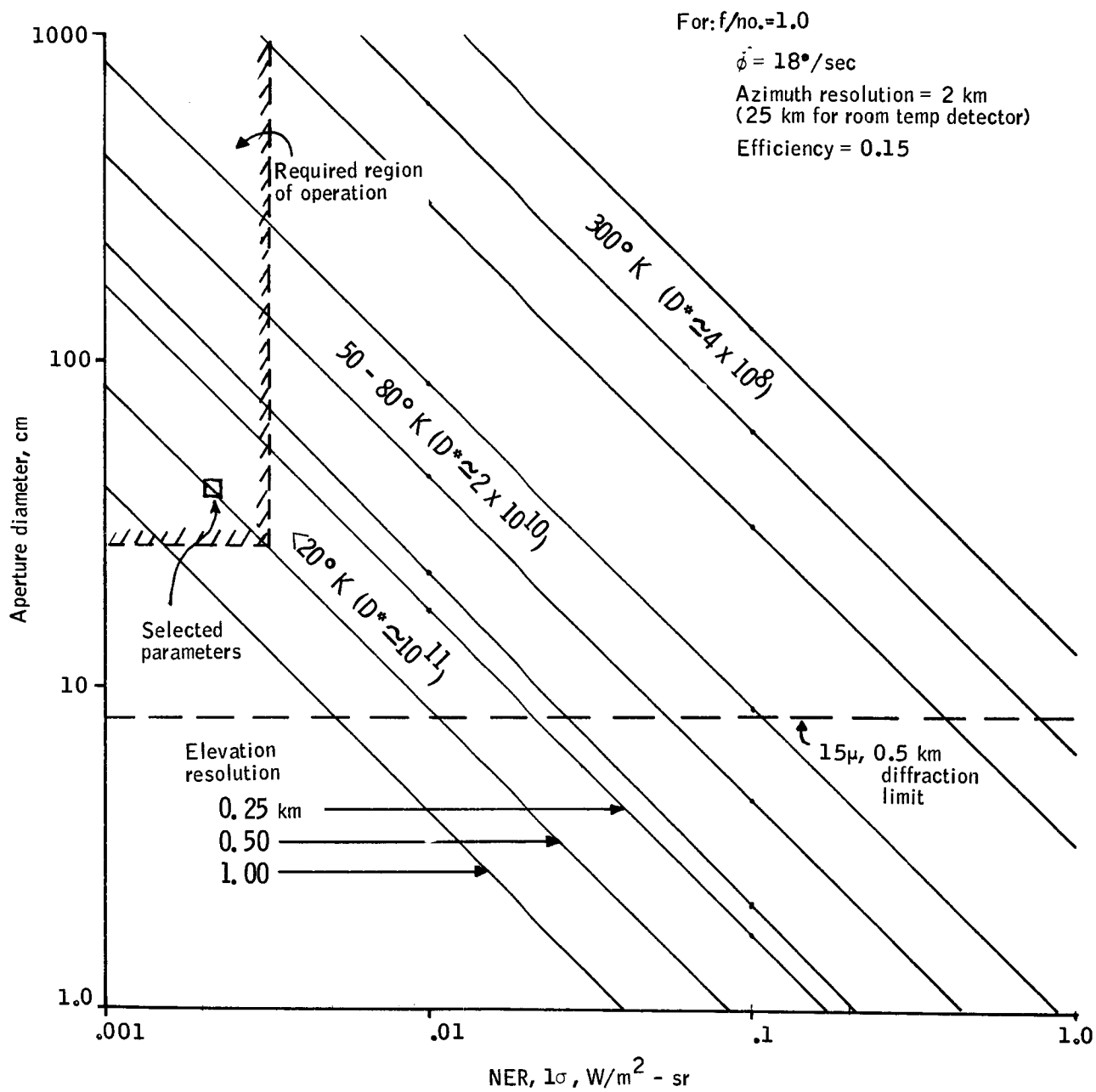
Figure 13. Minimum Detectable Radiance

System Design

To define the radiometer configuration the following must be determined:

- Type of detector
- Type of optical system
- Operating temperatures
- Primary calibration technique
- In-flight calibration technique
- Redundancy

As soon as the type of detector is chosen, by immediate reference to Figure 13, virtually all of the remaining characteristics can be determined. This choice is governed by the necessary D^* and the associated cooling required. Owing to the developmental character of Hg: Cd: Te for this wavelength region, and the extreme cooling requirement of Ge: Cu, Ge: Cd was chosen as the detector material. The following parameters may then be defined:

- Detector type: Ge: Cd
- Detector temperature: 15 to 20° K
- $D^*_{15\mu,\ 1500,\ 1}$: $\gtrsim 1 \times 10^{11}$ cm - $Hz^{1/2}$/W
- Aperture diameter: 40 cm
- f/no. : f/1.0
- Detector field of view: $0.2 \times 0.8 \ (mr.)^2$
- Electronic bandwidth: 1600 Hz

(0.1 - 1600 Hz post detection)

($f_c \pm 1600$ Hz pre-detection where f_c = chopping frequency)

Actually, the requirement upon aperture size is sufficiently loose from the point of view of resolution and, since the radiometer NER is really proportioned to $\frac{D\delta o}{f \#}$, the latter quantity should be specified as whole rather than in terms of its components. To meet the NER requirement of 0.003 W/m^2-sr, with the D^* and other parameters defined as above, $\frac{D\delta o}{f \#}$ must be ≥ 25 cm.

The type of optics, calibration techniques, and the detailed design tradeoffs are discussed in the relevant sections. Two radiometer system design areas are important to the choice of configuration: redundancy, and operating temperature.

Redundancy -- The radiometer consists of three basic types of components in terms of the types of failures that are important: (1) those that are vulnerable to breakage and degradation in the launch/orbit environment as typified by the optics; (2) those that fail with time in a more or less random fashion due to interaction between materials characteristics, production flaws, and operating loads as typified by the detectors and electronics; and (3) those that are most susceptable to predictable wear-out over the mission life as typified by the stored cryogen type of detector cooler. Of the three, only type (2) really profits significantly from redundancy and in the radiometer includes all of the electronics, choppers, secondary calibration systems, but not the optics or cooler. Owing to the fact that virtually all of the system weight and volume are consumed in the optics and cooling subsystems, a major design problem will be how to achieve the required redundancy without being redundant unnecessarily in these two areas. This consideration will dictate heavily in favor of optical systems with wider fields of view than absolutely necessary to permit separate detectors and choppers within a single optical system.

Operating temperature -- In a long wavelength radiometer such as this is, thermal emission within the instrument can produce signals greater than that due to the horizon itself. Figure 14 illustrates the various effects of this thermal emission on the radiometer. These spurious signals are theoretically constant in time and can be subtracted from the data and, hence, no error will theoretically be produced. However, spurious modulation, such as by the chopper, will produce unknown signal components and, hence, errors. To demonstrate feasibility, the operating temperature of the radiometer will be set as low as practical for the spacecraft.

Radiometer Design Summary

The major areas of design where special emphasis was required to assure feasibility were:

- Thermal control

- Radiation chopping: how performed without spurious signal production

- Detector bias power: minimize D^* degradation

- Detector mounting

- Stray radiation supression: baffling required to supress radiation from earth beyond instantaneous field
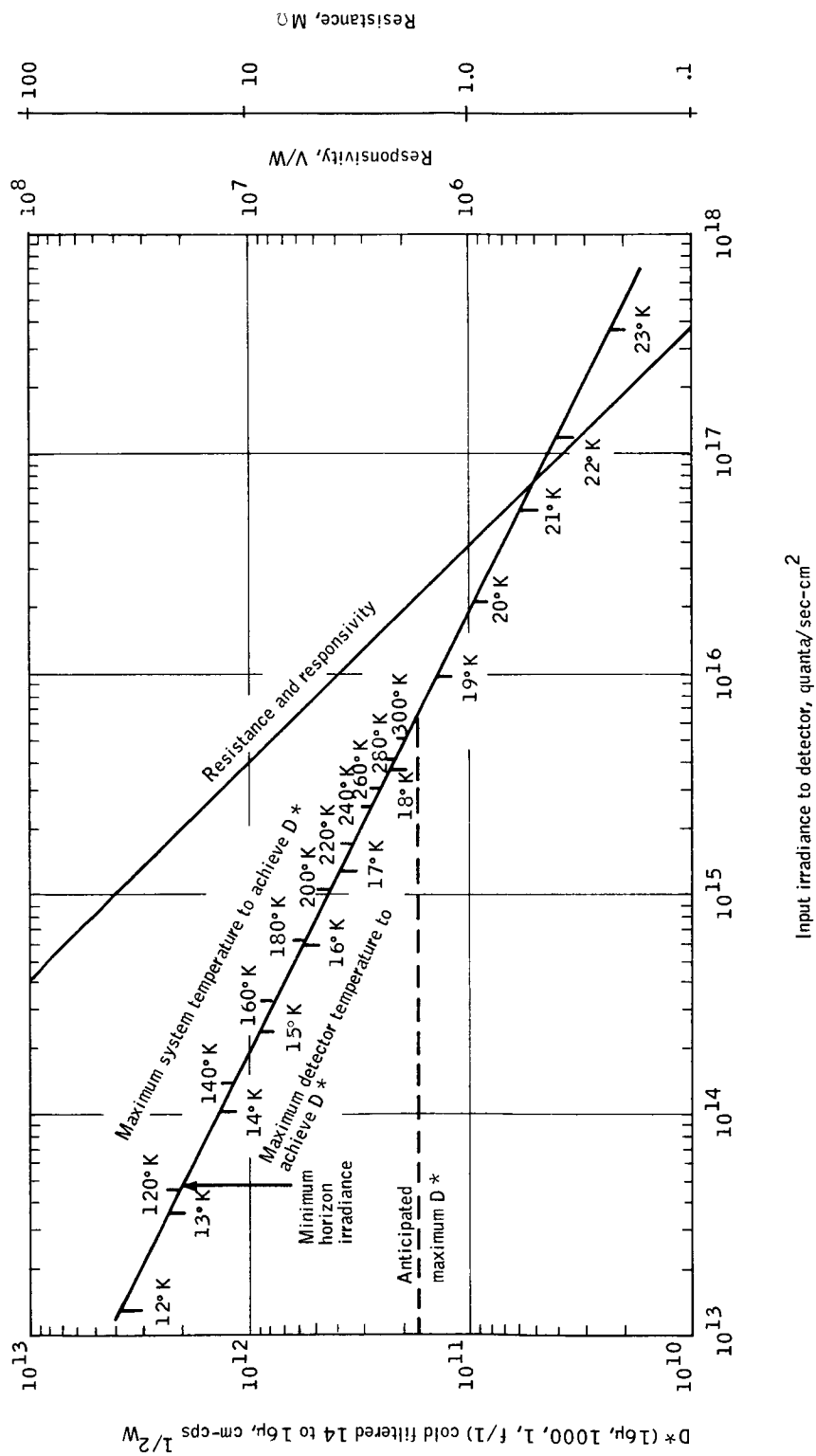
Figure 14. Variation of Responsive Properties of Ge:Cd
With Input Irradiance

36

- In-flight calibration: stability, non-interference with measurement

- Redundancy: how achieved at no compromise in performance

- Primary calibration: source/technique/facilities required

- Detector cooling

All but the last two items were demonstrated to be feasible in terms of both analysis and comparison to similar hardware applications. In the areas of primary calibration and detector cooling, the design approaches involved the use of standard techniques, but in new application and combinations such that feasibility can only be said to have been established analytically.

The feasibility design concept is illustrated in Figures 15 and 16 and incorporates the following design features:

- Type of optics system: Classical Newtonian f/1.0 (f/2.0 primary) 40-cm aperture diameter

- Detector: Ge: Cd at 16° K; 0.2 x 0.8 $(mr)^2$ field

- Cooling: Solid neon primary coolant
  Solid methane secondary coolant

- Operating temperature: 200°K ± 20°K

- Chopper: Torsional pendulum at 2500 cps (generates 5000 "chops"/second)

- In-flight Calibration: 3 levels through entire system
  4th and highest level near detector, coated platinum sources, platinum thermometer control

- Redundancy: Calibration subsystems and chopper, detector, electronics channels

The radiometer subsystems and their interrelationships are as shown in the block diagram of Figure 17. All elements inside the dotted line denoted "thermal control shroud" are at the radiometer operating temperature of 200°K.

The approach to primary calibration is shown in Figure 18 and has the following features:

- Calibration sources: One fixed radiance, fixed temperature - Hg freezing point
  One adjustable temperature
  One fixed temperature (Sn freezing point), adjustable radiance

37
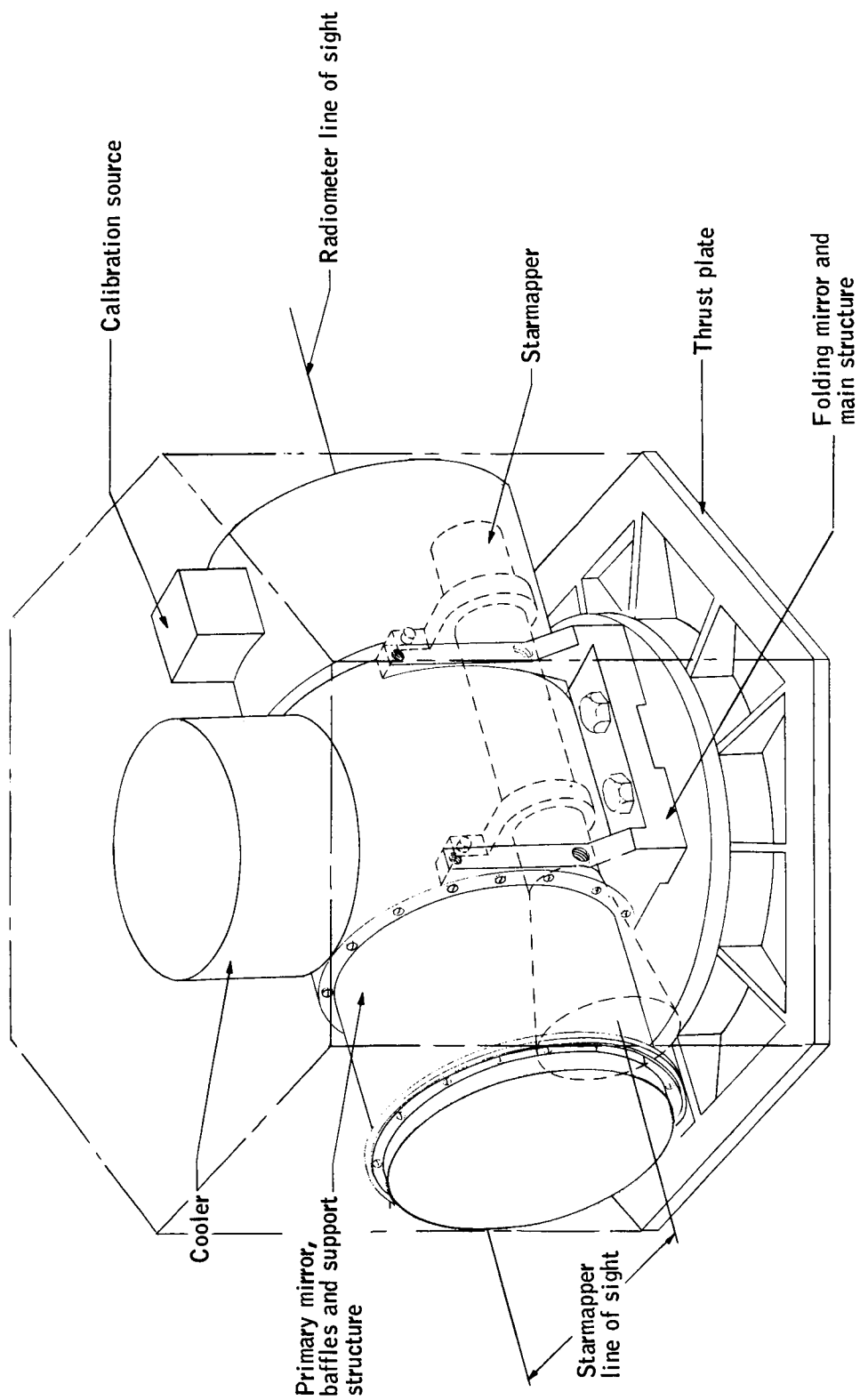
Figure 15. Radiometer Conceptual Design

38

Calibration electronics

Calibration source

Shutter actuator

Aperture actuator

Collimator parabola

Line of sight

Baffles

Thrust plate

Cooler

Detector

Field lens

Chopper actuator

Field stop

Folding mirror

Primary mirror
and mounting
structure
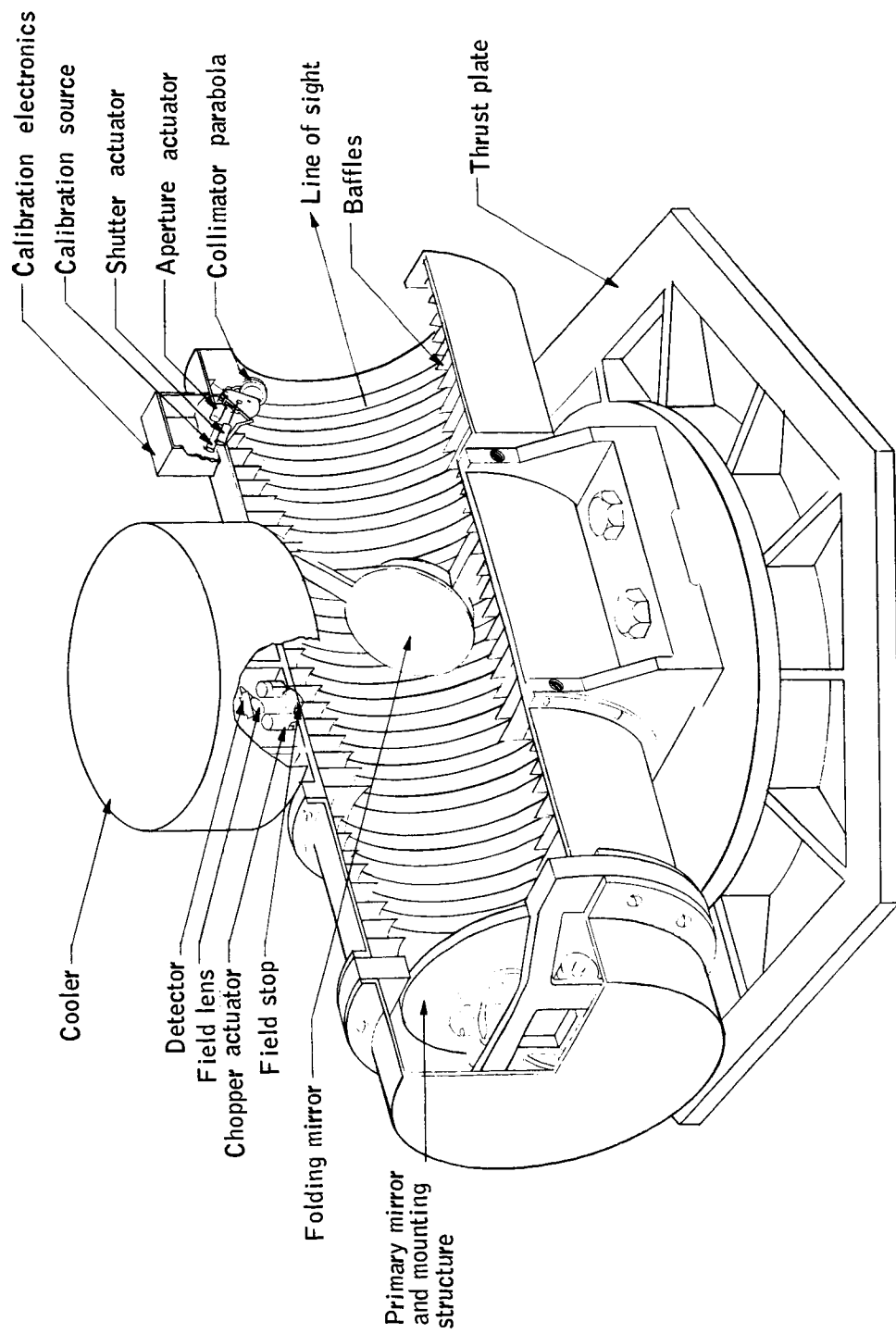
Figure 16.   Radiometer Conceptual Detail Design
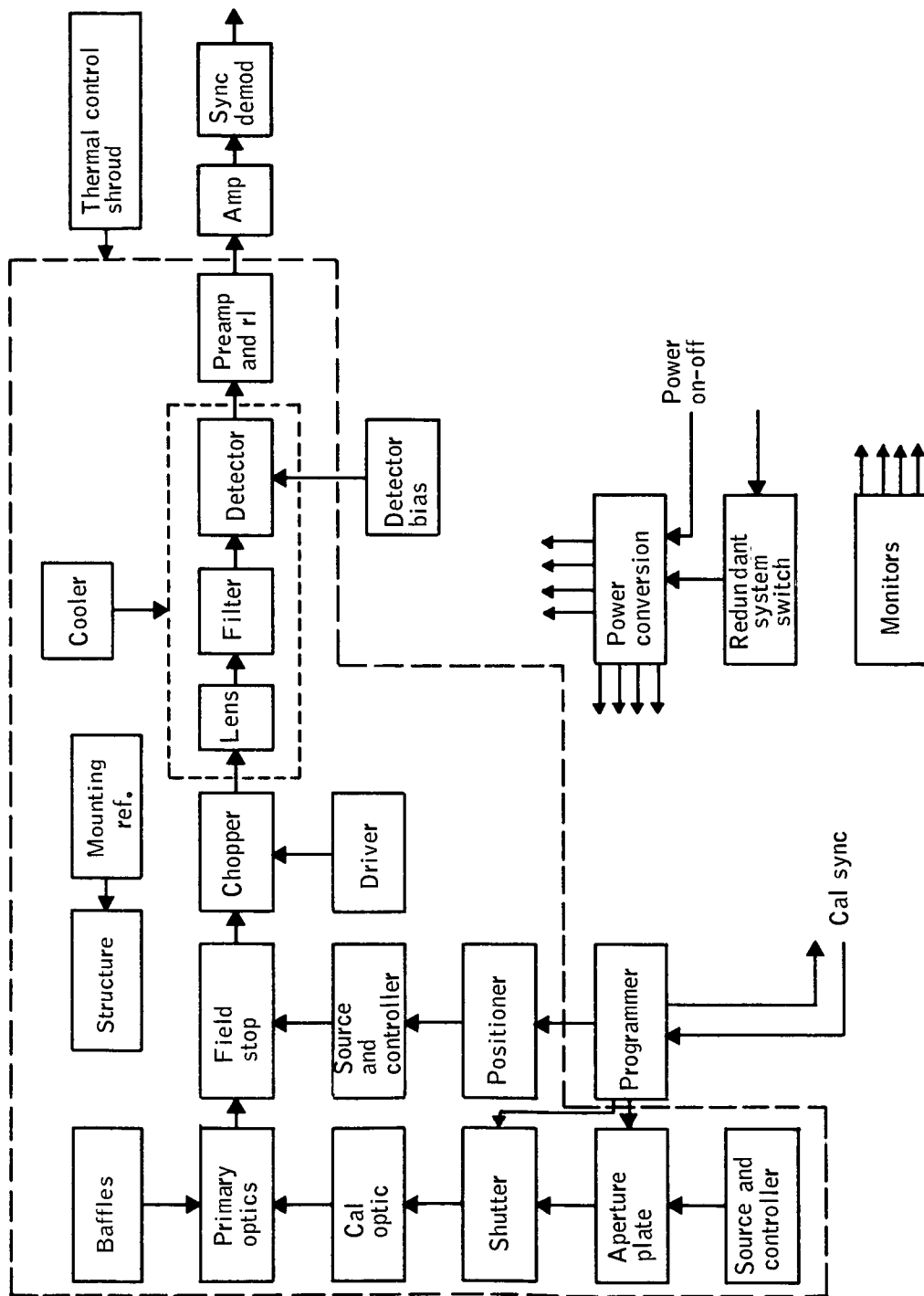
Figure 17. Radiometer Schematic Block Diagram

40
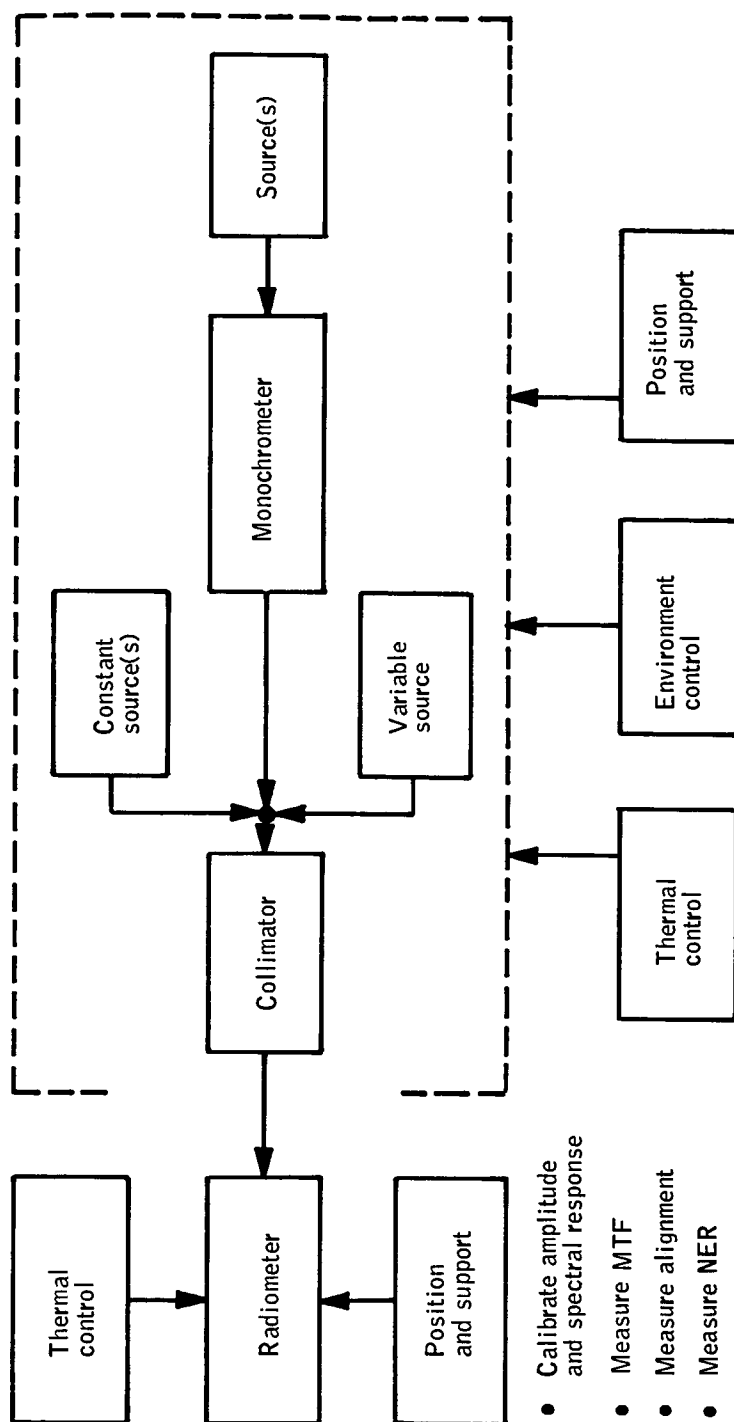
Figure 18. Primary Calibration Schematic Block Diagram

41

- Spectral calibration: Sn freezing point (NBS) source and mono-chromator

Thermal control is required to accurately position and vary the radiometer temperature and to maintain the source surroundings and optical elements near liquid nitrogen temperatures to avoid errors due to their emission.

Performance Summary

Sensitivity. -- from equation (4):

$$NER = \frac{4}{\pi} \frac{f/no. \sqrt{\Delta f}}{D^* \; D_c \; \delta \sqrt{\Delta \Omega}}$$

$f/no.$ = 1.0

Δf = 1600 Hz

D^* = 1×10^{11} cm - Hz$^{1/2}$/W

D_c = 40 cm

$\sqrt{\Delta \Omega}$ = 0.4 mr

δ = product of 0.98 = primary mirror refl.
0.98 = secondary mirror refl.
0.80 = obscuration
0.92 = optics transfer function
0.9 = lens transmission
0.6 = spectral filter transmission
0.5 = chopper transmission
0.7 = electronic transfer function and NF effect combined

δ = 0.13

NER = 0.0024 W/m^2-sr

Measurement Accuracy. -- The expected absolute radiometric measure-ment accuracy is as tabulated in Table 6. Although the noise bias and drift scale errors slightly exceed specification, they are more than compensated by the degree to which the other types of errors and below their specified value. As was noted before, these errors are, to a degree, tradeable against one another.

Some of the error sources should be further clarified:

- primary optics: Scale is primarily non-uniform reflectivity variation, bias is stray light

TABLE 6. - ABSOLUTE RADIOMETRIC MEASUREMENT ACCURACY

Error source	Magnitude		Error type: noise (n), drift (d), cal. (c)
	Scale, %	Bias, W/m^2-sr	
1. Primary calibration	0.5	0.0006	c
2. In-flight calibration	0.4	< 0.0001	d d
3. Primary optics	0.2	0.0015	d n
4. Chopper	0.1	N.A.	d, n
5. Spectral filter	<< 0.1 (a)	N.A.	d
6. Detector / cooler	0.1	0.0015	d d
7. Detector bias	<< 0.1	0.0003	d n
8. Signal conditioning electronics	0.1	0.0015	n n
9. System transfer function	< 0.1	0.003	d n
10. Sensitivity	N.A.	0.003	n
Linear sum: Noise (rss)	0.2 (0.14)	0.012 (0.006)	
Drift	0.8 (0.5)	0.0015 (0.0015)	
Cal.	0.5 (0.5)	0.0006 (0.0006)	

[a]Against an idealized source, i.e., taking into account only instrument errors, as opposed to validity of assumptions about interaction with variability in spectral content of the horizon radiance.

- chopper: Synchronization and amplitude variations

- detector/cooler: Temperature versus responsivity affects

Spectral Calibration. -- The spectral calibration will be performed at the radiometer system level using the 500°K (NBS) tin freezing point black body and a monochromator. Between the 10% points of the system spectral band, the relative response will be measured with a spectral resolution of 0.02μ (1/100 of the total band) and a relative accuracy of ≤5% per wavelength increment. To achieve the necessary signal-to-noise requires a special purpose integrating amplifier with about a 10 Hz bandwidth.

The out-of-band resolution will be degraded proportionately to the filter attenuation to maintain relatively constant signal-to-noise level at which the system would be rejected for insufficient out-of-band suppression.

Operating Temperature. -- As performance of long wavelength radiometers has been traditionally limited by their internal self-emission, and since the requirements upon the HDS radiometer are very much more stringent than those of any of its predecessors, a decision was made early in the design study to make the radiometer operating temperature as low as is practical. The lowest temperature attainable within spacecraft and orbital constraints is 200°K with a tolerance (analytical accuracy) of ±20°K.

These numbers, however, could be quite conservative owing to the orientation of the study around an objective of an absolute guarantee of feasibility.

Disadvantages of 200°K operation: The disadvantages of operating the radiometer, and, hence, the entire measurement system at 200°K include the following:

1. Assembly, Calibration, and Test Complexity - The system may have to be focused and aligned while at or near 200°K, involving the use of remote manipulating devices.

2. Temperature Cycling - The equipment will be cycled many times from 200°K to 300°K during the time from fabrication to launch, bringing up the possibility of plastic deformation and irrevocable loss of alignment and possibly even focus.

The first disadvantage will not be removed by elevating the temperature to 300°K. The system must be operated, during calibration and most of performance testing, in a vacuum or, at best, a dry, inert atmosphere. Thus, remote manipulation is still desirable. The only real inconvenience is the loss of time required to achieve thermal soak, possibly 1-2 days. This could at most be a factor of two in time required to prepare for the test measurement sequences (at least 1 day to pump down or flush).

The second disadvantage is more serious and was identified early as a potential problem area, resulting in a great deal of structural design analysis. The two preferred structural approaches were both oriented about solving just this problem.

44

Plastic deformation will occur primarily as a result of differential rates of expansion between structural elements of the measurement system, resulting in stresses beyond elastic limits. The preferred structural design was to use only aluminum throughout. The problem then revolves about the differential rates between the aluminum primary mirror and its coating. Our survey of vendors having experience with this problem indicate that solution of this problem is within the current state of the art.

The second approach is to use fused silica or pyrex or the primary mirror (qualified over the required temperature range) and compensating structures. A total of at least three different types of materials is involved. The approach in this case was to perform analyses and design to assure sufficiently small plastic deformation. Admittedly, the assurance one gets from the analysis is not as great as with the preferred design, really requiring breadboarding to demonstrate capability of meeting the requirement. In terms of a mechanical engineering problem, there are examples of similar requirements having been met; however, in terms of this particular application, no similar program exists that has produced qualified hardware, although several are in early procurement phases.

The net result of the design study was analytical confirmation of the feasibility of both design approaches and partial experimental confirmation with respect to the preferred approach.

Effects on radiometer performance of 300°K operation: The following performance parameters are affected:

1. Noise-equivalent-radiance (NER): D^* and noise produced by modulated spurious radiation.

2. Calibration, primary and in-flight.

3. Detector cooler size and weight and/or life.

The detector is not expected to operate in BLIP condition with its environment (except for spectral filter, which is at the detector temperature) at 200°K.

The BLIP D^* is $\sim 8 \times 10^{"}$ whereas the expected D^* is $\sim 1 \times 10^{11}$, implying that the internally generated thermal noise is eight times that produced by background photon fluctuations. The photon rate is increased by a factor of five for a temperature change from 200° to 300°K. Thus, noise then increases by $\frac{5^2 + 8^2}{1^2 + 8^2}$, or 1.17 reducing D^* to 8.5×10^{10}. This is certainly not in itself a serious effect.

The optics self-emission produces a signal in the range of 20-50 times NER when at 200°K. This increases to a factor of 100-250 if the optics are at 300°K. This signal is nominally a d-c offset that produces no error as it is accounted for when the radiometer views space. However, any modulation of that signal produced by the chopper during each chop will appear as noise. At 200°K the worst case implies a maximum allowable modulation less than

2 percent which reduces to 0.5 percent at 300°K. Sources of this kind of noise are emissivity and temperature gradients, particularly at the chopper and field stop since these are imaged onto the detector (although somewhat scrambled by the recollector lens). The factor of five makes a somewhat difficult but achievable (demonstrably, from extant data) allowable emissivity gradient into a requirement that requires demonstration specifically for this program to assure feasibility.

The effect on primary calibration is to increase the back-radiation reflection from the diffuser, raising the offset level to 14 x NER. This is not particularly troublesome. In-flight calibration presents a more serious problem. The shutter (or aperture plate, if no shutter were used) is effectively part of the source, in that the signal from its emission varies with calibration level. For 200°K optics, this signal is 1/10 that from the source and, hence, its temperature must be known to 1/10 as good accuracy or ±0.5°. For 300°K optics, this value reduces to ±0.1°, and the number of shutter temperature increments for which ground calibration is performed increases by a factor of five.

The cooler, if its outer shell temperature becomes 300°K, increases in size and weight by a factor of approximately five. The design would have to be re-optimized, perhaps using a different secondary coolant such as ethylene, and a lower weight and size penalty could result. The cooler design proceeded conservatively, also; hence the absolute magnitude of the affect may be deduced. To establish feasibility now, however, the factor of five will have to be assumed, resulting in a weight penalty of approximately 100 pounds. It is not desirable to run the cooler at 200°K and the optical system to which it is rigidly mounted at 300°K considering the optical alignment problems and other effects of large thermal gradients.

Conclusions: From the foregoing considerations, feasibility cannot be demonstrated at 300°K; conversely, it cannot be demonstrated to be impossible at 300°K. However, as the purpose of this study is prove feasibility, the temperature has been set as low as spacecraft constraints permit, 200°K. The ultimate decision tests upon results of further work in the following areas:

- Detailed structural design and worst case thermal analysis.

- Development and test of samples of low, uniform emissivity surfaces, particularly for the chopper and field stop.

- Further design of the inflight calibration system, optimized with operation at 300°K in mind.

- Cooler breadboarding to evaluate the degree of conservation in the design.

The problems associated with internal optical emission are sufficiently great that should the structural design continue to appear satisfactory after the above mentioned effort, it is strongly recommended that the operating temperature of the radiometer be as low as is practically obtainable from the point of view of spacecraft thermal control considerations.

46

Interface Characteristics

The radiometer will employ two redundant signal channels, each consisting of a chopper, detector, detector bias supply, preamplifier, and amplifier. Redundant calibration sources and power supplies will be capable of functioning with either signal channel. At no time will more than one calibration source or chopper be in operation. Whether or not power is supplied simultaneously to both signal channels, exclusive of one of the choppers, depends on reliability and thermal tradeoffs and has not yet been determined. Pending that decision, however, and to assure a sufficient power allowance, it has been assumed that power is applied to both channels at the same time.

Prelaunch. -- The radiometer must at all times be maintained in a dust-free, low humidity environment. The cooler may be charged at any convenient time prior to launch but, after charging, must be continuously supplied with refrigerant (typically liquid helium) until a maximum of seven days prior to launch.

The radiometer may be maintained at local ambient temperature provided it is never directly illuminated by sunlight.

To purge the system of CO_2, it should be flushed for several hours with a dry inert gas (nitrogen or argon) and maintained at a positive pressure of that gas through launch.

On-orbit. -- After launch, the system may take as much as 7 to 14 days to reach thermal equilibrium.

The data taking sequence will be as illustrated in Figure 19. The radiometer shall be designed such that profiles may be taken in an earth-to-space mode as well as space-to-earth.

Weight and balance. -- The radiometer weight estimate is 294 pounds. The c.g. is located one inch toward the primary mirror along the optical axis from the intersection of that axis with the spin axis. The cooler is, of course, located such that its axis of symmetry coincides with the spin axis.

The calibration system contains three moving components generating angular impulses during each calibration period (not simultaneously, however). Each motion reverses itself during the period. Estimates for these are as follows:

1. Forward - 0.0018 in-lb-sec
    Backward - 0.0165

2. Forward and back - 0.063

3. Forward and back - 0.0072
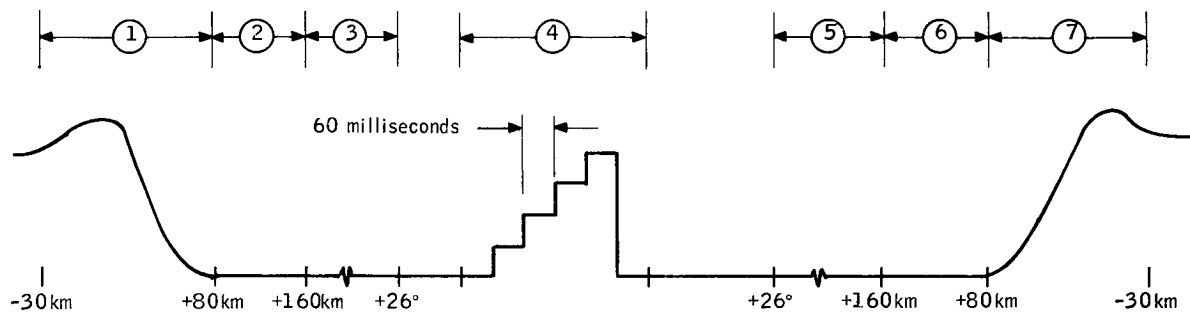
① Earth-to-space profile

② Take 10 samples over this interval

③ Take 10 samples, each averaged over 60 msec
} record when recording 1

④ Calibration - record average at each level, including the ② space measurement at beginning and end: record when recording 7

⑤ and ⑥ As in ② and ③

⑦ Space-to-earth profile

Figure 19. Data Taking Sequence

Power. -- The estimate for the radiometer power, including power conversion and regulation for each item, consumption is:

Detector bias	-	0.4 watt
Preamplifier, amplifier and synchronous demodulator	-	1.2 watts
Chopper	-	0.4 watt
Calibration source	-	1.0 watt
Monitors	-	4.0 watts
		7.0 watts, continuous
Calibration system programmer, drivers	-	3.0 watts, short-term transient

Thermal interface. -- The following constraints are necessary for the radiometer to perform as required:

- Points at which the radiometer is directly conductively coupled must be maintained at a temperature of less than 195°K.

- Direct sunlight shall never be permitted to fall on the entrance aperture.

- Any surface which has a finite projection onto the entrance aperture shall be maintained at a temperature of less than 200°K.

Magnetic. -- The only source of a significant magnetic field from the radiometer is the chopper driver which is estimated to generate a field strength between one and ten milligauss one inch from its housing.

Data interface. -- The radiometric data appearing at the output of either of the two redundant signal channels will be analog and have the following characteristics:

Bandwidth - 1600 Hz

Voltage range - 2 millivolts - 5 volts

Responsivity - Nominally 0.6 volt/W/m^2-sr

Output impedance - 10 killohms

Anticipated monitoring requirements are:

Mounting pad temperature   (3)

Primary mirror temperature   (4)

Relay lens temperature   (1)

Telescope temperatures   (8)

Cooler temperatures   (4)

Detector temperature   (2)

Field stop temperature   (2)

Power supply voltage   (2, only one at a time)

Power supply current   (2, only one at a time)

(All of the above may be recorded very infrequently - e.g., 2-4
times/orbit or only when a nominal range has been exceeded; also,
3-bit resolution should be adequate.)

Calibration level   (2, one at a time) - assumed recorded as
                                                  a part of cal sequence

Calibration source current   (4, two at a time)

Calibration source voltage   (4, two at a time)   read once for each cal-
                                                   ibration cycle; 50-100
                                                   part resolution

Calibration source temperature
                             (4, two at a time)

Detector bias current   (2, one at a time)
                                                 read once for each
Detector bias voltage   (2, one at a time) recorded profile; 10-20
                                                 levels

Chopper frequency   (2, one at a time) - read once/orbit

Ground commands. --

1) On-off power

2) Initiate calibration

3) Switch to redundant system (3 command lines)

DETECTOR

The largest single contributor to the capability of the radiometer in meeting its sensitivity (NER) requirement is the detector detectivity. Obtaining a high detectivity, however, generally results in cooling and other requirements that, while maximizing detector performance, may compromise system performance. The major tradeoff in this area is, then, to obtain a combination of sufficiently high detectivity without jeopardizing system feasibility.

Requirements

The specific requirements upon the detector are:

- Spectral interval: 14.0 to 16.28μ

- Detectivity ($D^*_{15\mu, \ f, \ 1}$): $\geq 1 \times 10^{11}$ cm-Hz$^{1/2}$/W, design goal

                                   $\geq 2 \times 10^{10}$ cm-Hz$^{1/2}$/W, absolute minimum

- Frequency interval: 5000 ± 1600 Hz

- Size: 80 x 320 microns

- Number: 2, separated by 320 microns in the direction of the largest detector dimension.

- Optics f/number: f/1.0, effective

In addition, the following qualitative factors shall be observed:

- Maximization of responsivity

- Minimization of cooling requirements in terms of both temperature and bias power heat load

- Minimization of responsivity variations as a function of operating temperature and input radiation levels

State-of-the-Art Detectors

The possible choices of detectors for the radiometer within the current state of the art are:

a) Bolometers

b) Cadmium-doped germanium

c) Copper-doped germanium

Mercury- and gold-doped germanium are not satisfactory because their detectivity in the 15-micron band is insufficient, and the standard mercury cadmium telluride (Hg:Cd:Te) does not qualify because it also has a cutoff at approximately 13 microns. Bolometers are unstable in operating characteristics and are orders of magnitude less sensitive than the minimum required. The cooling requirements for copper-doped germanium make it a qualified but marginal choice by virtue of its extremely low temperature requirements. Its operating characteristics are extremely sensitive to the variation in the coolant temperature from 14° to 16° Kelvin.

A detector possibility not listed above is a composition-modified Hg:Cd:Te detector with the ratio of mercury to cadmium adjusted to extend the long wavelength cutoff to 16 microns. This detector, while representing a major advance toward meeting all the HDS radiometer requirements at the least penalty in terms of cooling, is essentially a research detector at this time and cannot be recommended as the prime approach for the radiometer. However, it will be included in some parts of the discussion to show the impact of this different type of detector upon the design.

Cadmium-doped germanium has been chosen as the prime detector approach and the detailed analysis necessary to apply this detector has been performed. Subsequent sections of the report discuss the details of the analysis.

Cadmium-Doped Germium Detector

BLIP performance -- The theoretical maximum performance at 15 microns for any infrared photoconductor is a function of the photon flux density from the background and is given by

$$D^*_{BLIP} = \frac{\lambda}{2\, hc\, Q_b^{1/2}} \quad cm\text{-}Hz^{1/2}/watt \qquad (5)$$

where hc/λ is the energy of the 15-micron quanta, and $Q_b^{1/2}$ is the fluctuation in the photon flux density. The factor of 2 is related to the details of the g-r noise spectrum which for a photoconductor is due to fluctuations in both the number of carriers and their lifetime. Equation (5) has been evaluated in terms of input quantum irradiance to the detector from the optics for $I_Q = \varepsilon(\Omega/\pi)\, Q_b$ and f/1 optics. This relationship is shown in Figure 20.

52
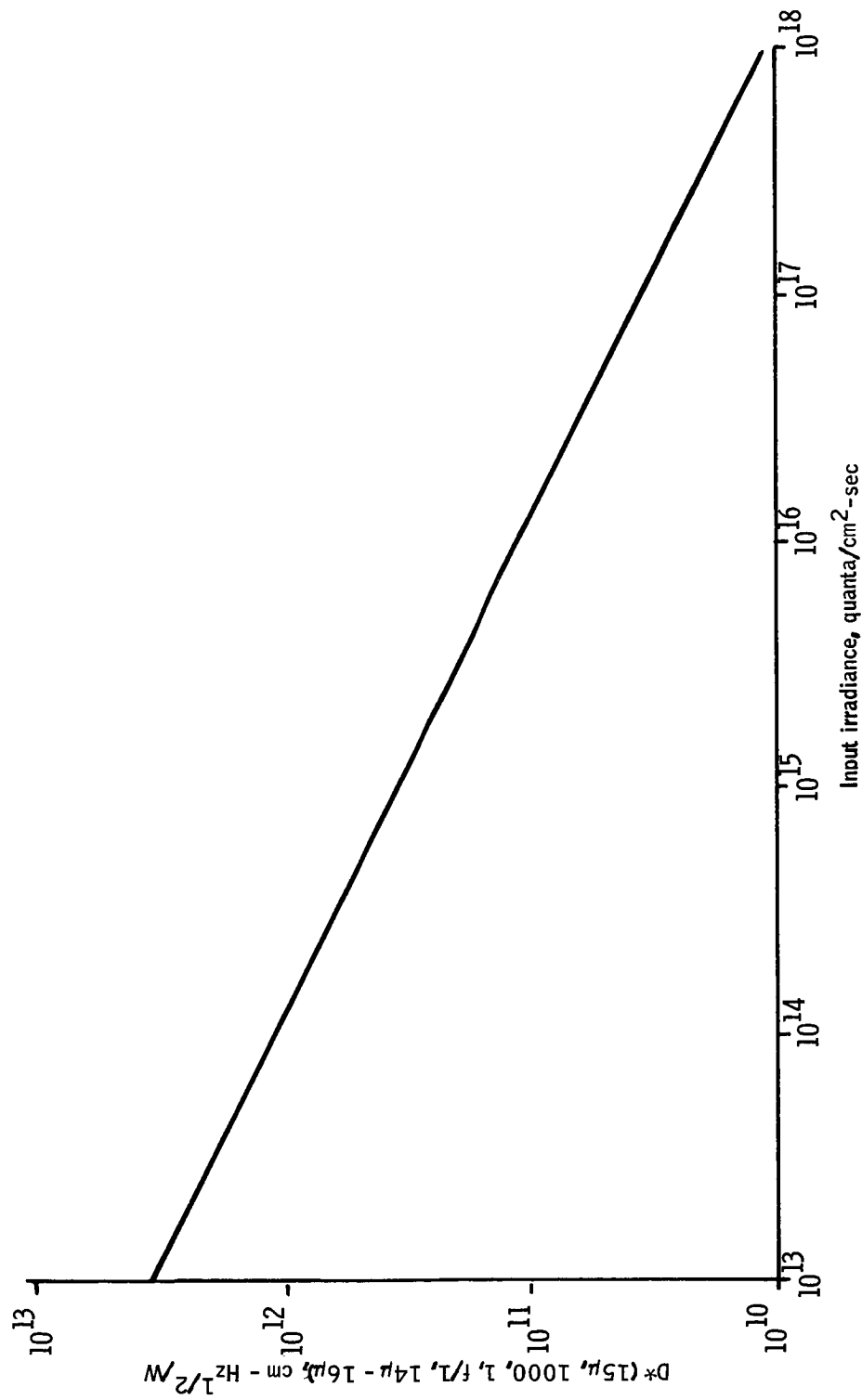
Figure 20. Peak Specific Detectivity for Cadmium-Doped Germanium Detector as a Function of Input Irradiance

53

If the spectral coverage of the detector is limited by a cooled narrow spectral-band filter and a cooled aperture, the theoretical maximum detectivity is increased because it is proportional to the reciprocal of the square root of the photon flux density, and extremely high detectivities can be predicted (as shown in Figure 21). In practice, however, the low-energy acceptor impurities in the germanium (e. g. , copper, zinc, and stoichiometric defects or germanium vacancies which are always present in the detectors) limit the ultimately achievable detectivity under conditions of very narrow spectral, cold filtering and aperturing. Residual impurities may be viewed as an "equivalent internal optical bias" and treated as background irradiance. Attempts at reduction of the external irradiance from the background, such as by cooling the optics, below the internal optical bias irradiance will not improve the detectivity. In the HDS radiometer, the effective internal optical bias due to residual impurities in the cadmium - doped germanium sets the limits of the wavelength band of the spectral filter and the required temperature of the optics. The optics are the major source of background irradiance. In general, if the optics are at a temperature lower than the temperature at which their quantum irradiance in the 14-to 16-micron band is equal to that of the equivalent optical bias within the detector, the operating characteristics of the detector become decoupled from their dependence on optics temperature. The input irradiance from the optics as a function of emissivity and temperature has been evaluated and is shown in Figure 22.

Detector equivalent internal optical bias. -- The thermally generated dark current in cadmium-doped germanium is due to thermal ionization of the cadmium atoms and impurities such as copper, zinc, and stoichiometric defects. If the dark current concentration is known, the equivalent internal optical bias may be determined as the equivalent input irradiance from the background that generates about 1/10th the concentration of carriers, i. e. ,

$$I_Q \, \eta \, \tau \, A_D \; = \; N_{TH} \; (V/10)$$

or

$$I_Q \; = \; \frac{N_{TH} \; (V/A_D)}{10 \, \eta \, \tau}$$

where the ratio V/A_D is the absorption depth for a "bare" element or the ratio of the detector volume to the entrance aperture area for a detector within an integrating chamber.

For a bare Ge:Cd detector element, the following are reasonable estimates:

$$V/A_D \; = \; 0.2 \; cm,$$

$$\eta \; = \; 0.5,$$

and thus,

54
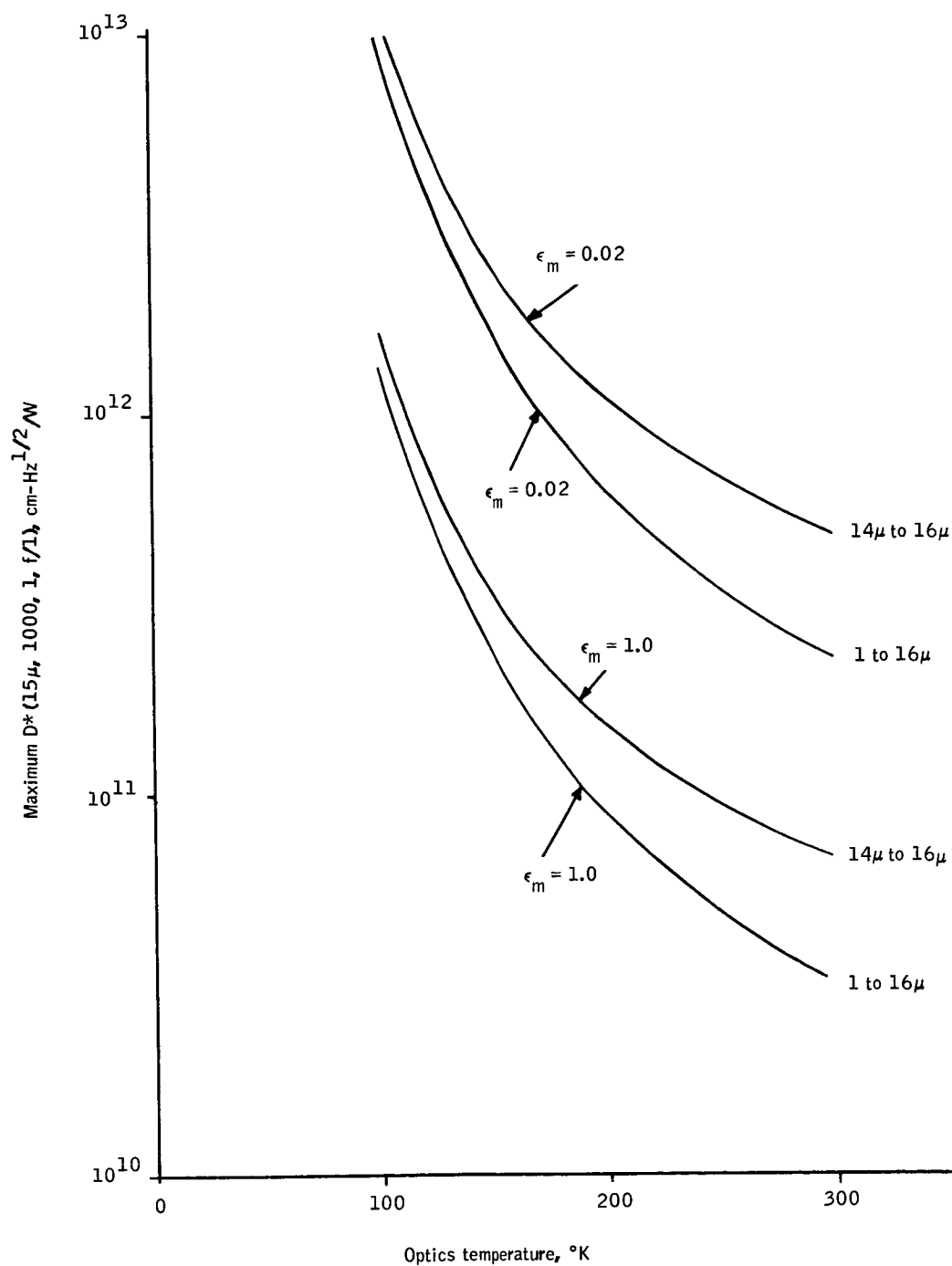
Figure 21.   Theoretical Maximum Peak Detectivity for Varying
Conditions of Cold Filtering and Mirror Emissivities
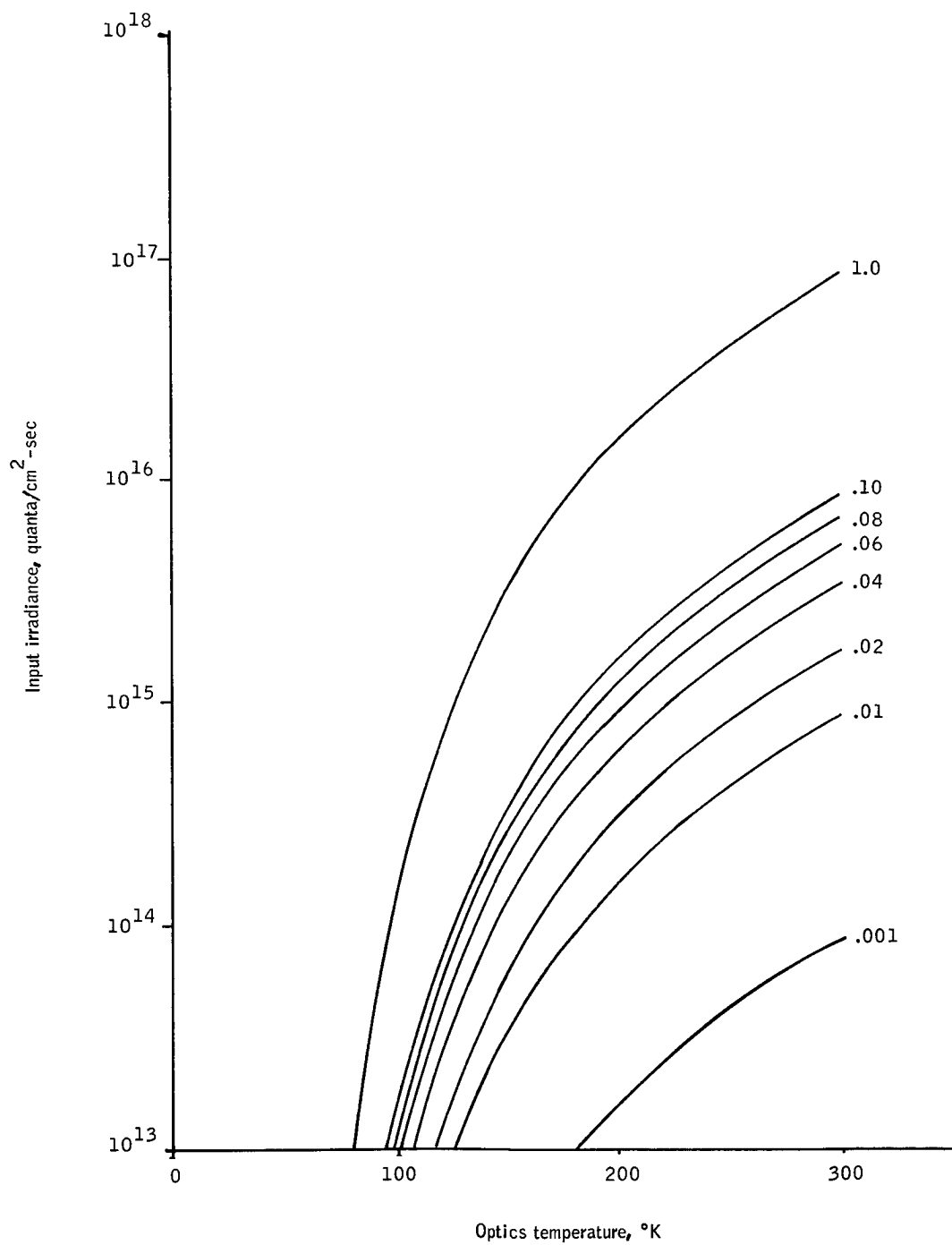
Figure 22. Input Irradiance at Detector as a Function of Optics Emissivity and Temperature

$$\tau = 10^{-7} \text{ sec,}$$

$$I_Q = 4 \times 10^6 \, N_{TH} \text{ quanta/cm}^2\text{-sec}$$

For a Ge:Cd detector within an integration chamber, substituting

$$V = 0.008 \text{ cm}^3,$$

$$A_D = (8 \times 10^{-3} \text{ cm}) (3.2 \times 10^{-2} \text{ cm}) = 2.56 \times 10^{-4} \text{ cm}^2,$$

$$\eta = 0.5, \text{ and}$$

$$\tau = 10^{-7} \text{ sec}$$

then

$$I_Q = 6.25 \times 10^8 \, N_{TH} \text{ quanta/cm}^2\text{-sec} \tag{6}$$

Comparing these two cases, the minimum equivalent internal optical bias irradiance occurs for a bare detector element. The high equivalent internal optical bias irradiance is essentially the major problem in the use of integrating chambers with doped-germanium detectors. However, using the integration-chamber approach for a "worst-case estimate", the thermally generated carrier concentration for Ge:Cd for an electronic model has been evaluated using

$$N_{TH} = N_{Zn} + \left(\frac{2\pi \, m_2 * K \, T_D}{h^2} \right)^{3/2} \left[\frac{N_{Cu} - N_D}{N_D} \exp \left(- \Delta Ecm/KT_D \right) \right] \tag{7}$$

with

$$N_{Cd} \cong 10^{16} \text{ atoms/cm}^3$$

$$N_{Donor} \cong 10^{11} \text{ atoms/cm}^3 \text{ (due primarily to arsenic leached out of the glassware)}$$

$$N_{Cu} \cong 10^{13} \text{ atoms/cm}^3$$

$$N_{Zn, \text{ etc.}} \cong 10^7 \text{ to } 10^9 \text{ atoms/cm}^3 \text{ (low ionization energy}$$
$$\text{residual impurities)}$$

Equation (7) substituted in (6) determines Figure 23 which shows the relationship between the equivalent internal optical bias irradiance as a function of the Ge:Cd detector operating temperature and concentration of carriers due to low ionization energy residual impurities. Over the temperature range from 10 to 14°K, the level of equivalent irradiance is determined by the residual, low-energy impurities. Above the 20°K this level is set by the concentration of copper impurities, and (not shown in Figure 23) the level of the BLIP temperature for ordinary Ge:Cd, is set by ionization of the cadmium atoms above approximately 25°K. (Note: The parallel, residual impurity concentration curves of Figure 23 are equivalent to the residual carrier concentrations at low temperature determined by measuring the Hall effect. In the case of the Hall effect measurements, $\log (1/q \, R_H)$, which is proportional to N_T, is plotted against $1/T$ not T as in this figure. The $1/T$ plot allows the determination of the ionization energy from the slope.)

A reasonable level of carriers due to residual low energy impurities is cercertainly on the order of 10^7 carriers/cm^3. Using this value the irradiance of the equivalent internal optical bias is approximately 6×10^{15} quanta/sec-cm^2, and the maximum detectivity at 15 microns is greater than 10^{11} cm-Hz$^{1/2}$/W. From Figure 22 the temperature of the optics, at which the equivalent internal optical bias irradiance is approximately equal to the optics irradiance, is approximately 275°K for an emissivity of 0.10. The emissivity required here is the effective emissivity due to all the emitting and reflecting optical elements within the field of view of the detector. An effective emissivity in the range of 0.05 to 0.10 appears to be reasonable. The optics should be maintained at a nominal 200°K to render essentially insignificant influence on the detectivity of the Ge:Cd detector. At this temperature, the effect is less than 10 percent.

Detector responsive properties. -- The anticipated responsive properties of the cadmium-doped germanium detectors of the HDS radiometer are:

1. D^* (15µ, 1000, 1, f/1, 14µ to 16µ) $\geq 1 \times 10^{11}$ cm-Hz$^{1/2}$/W

2. Spectral response without cold filter and with cold filter as shown in Figures 24 and 25 respectively.

3. Responsivity $\cong 10^4$ to 10^5 volts/watt

4. Resistance $\leq 10^6$ ohms.
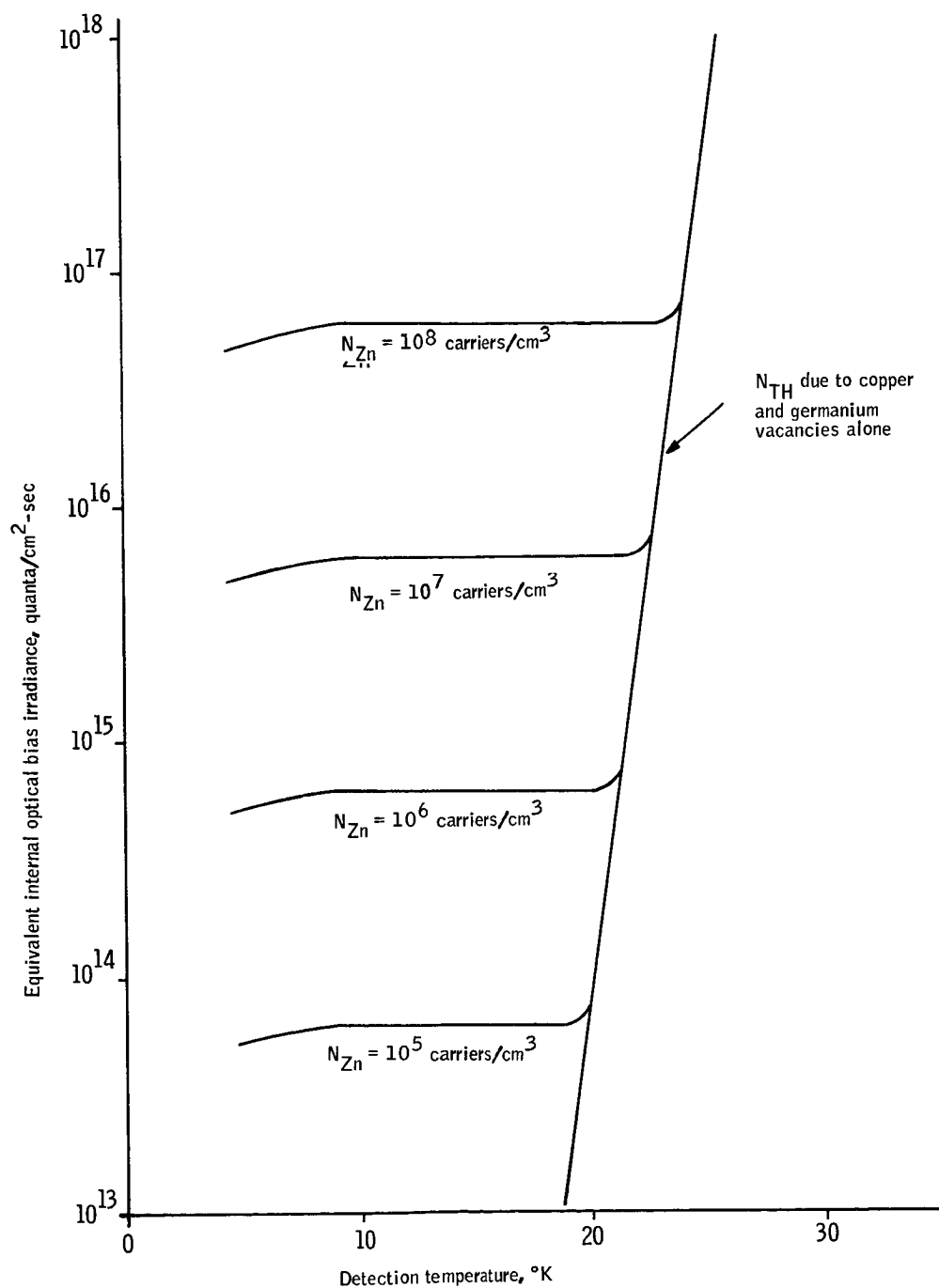
Figure 23. Equivalent Interval Optical Bias Irradiance as a Function of Detector Temperature
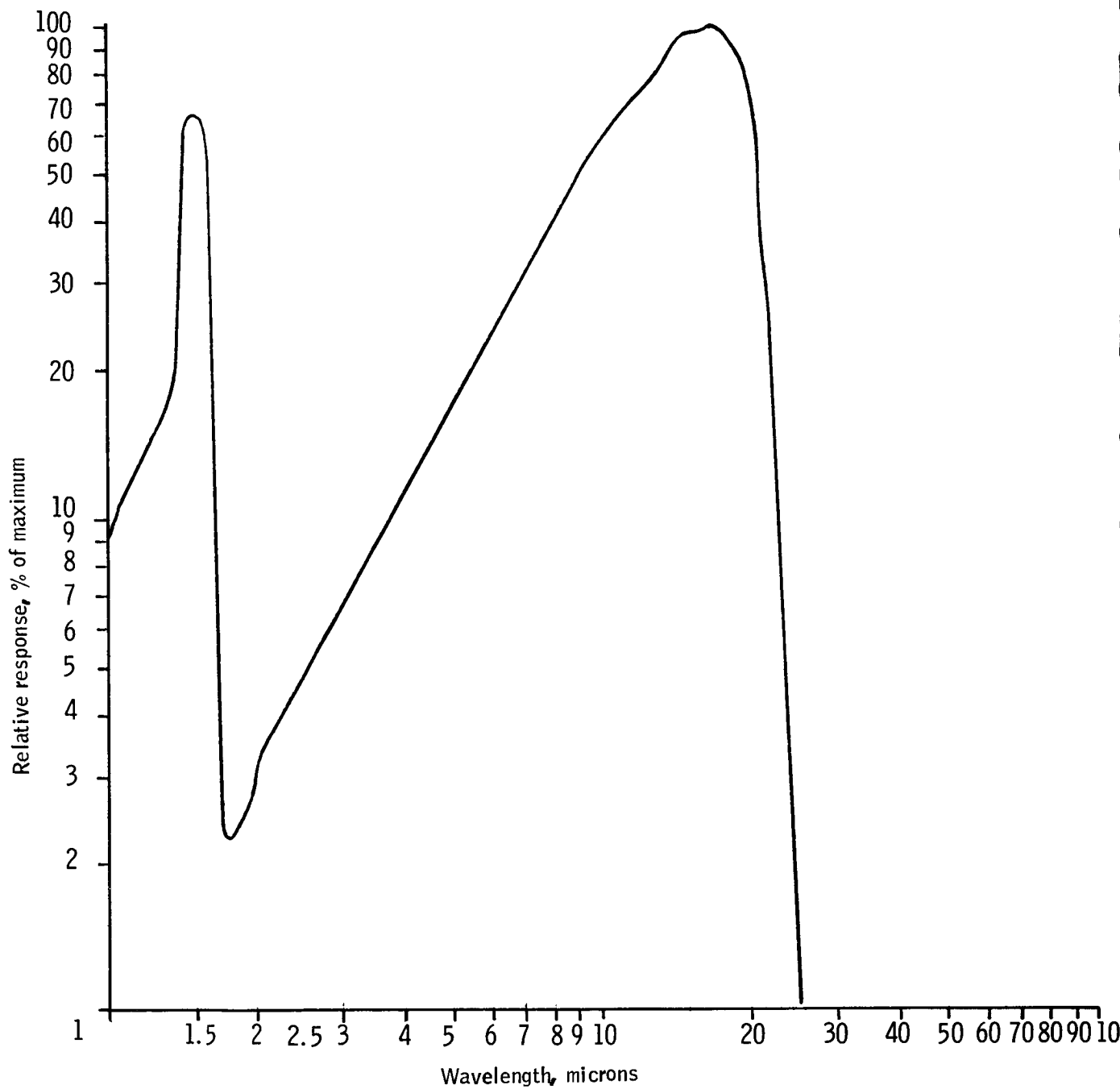
Figure 24. Typical Relative Spectral Response for Cadmium-
Doped Germanium Detector
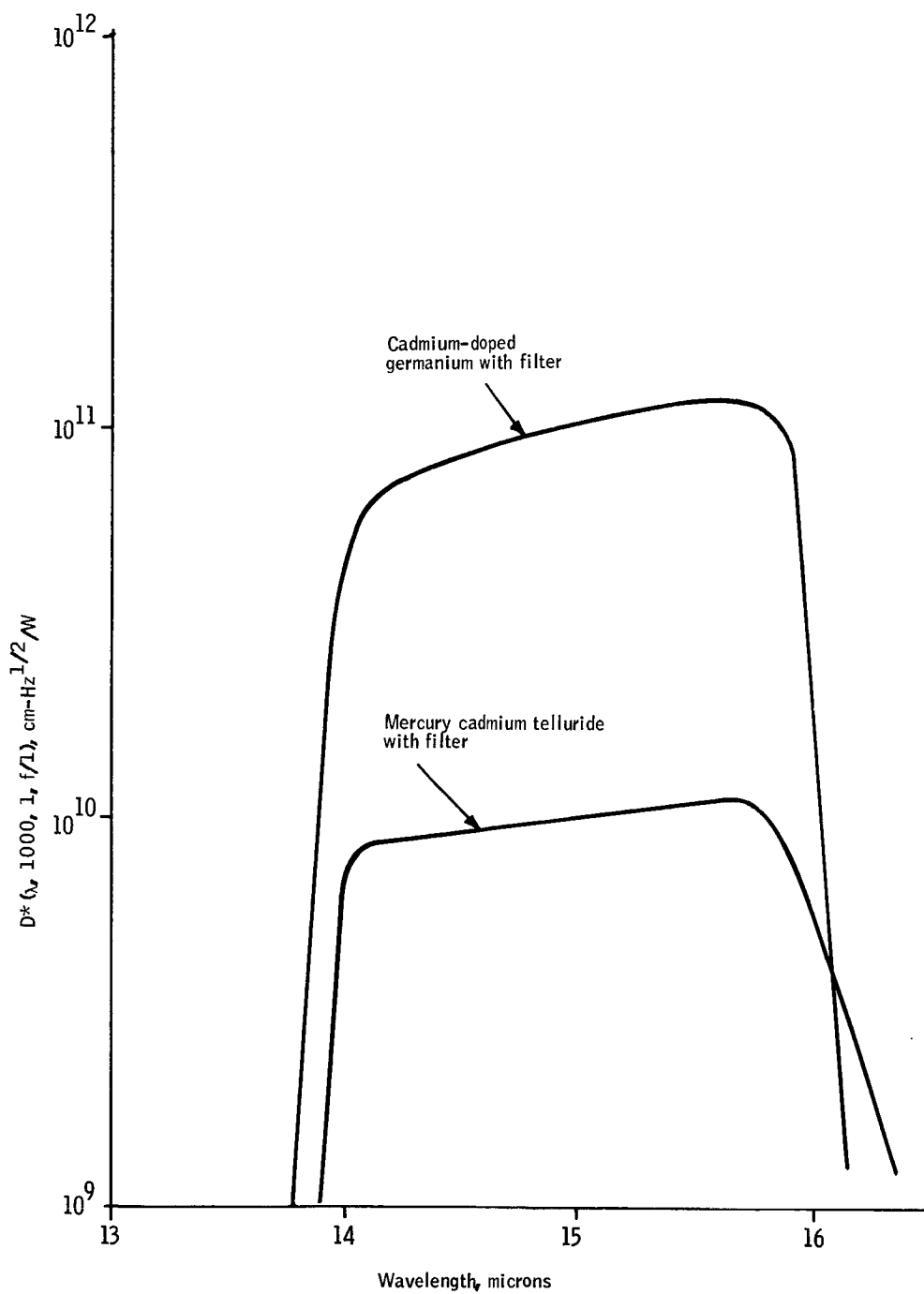
Figure 25. Typical Spectral Detectivity for Ge:Cd and Hg:Cd:Te with Cold Filters

5. Bias current range = 10 to 50 microamperes.

6. Detector time constant < 1 microsecond.

7. Operating temperature $\geq$ 20°.

8. Bias power dissipation = 2.5×10^{-3} watt/element

9. 1/f noise g-r noise crossover frequency $\cong$ 100 to 200 Hz

10. Detector noise $\sim$ 20 x Johnson noise.

11. Noise power spectrum as follows:

    a. 1/f noise to approximately 200 Hz

    b. g-r noise limited from 200 Hz to about 1.5 MHz

    c. 6 dB/octave high frequency roll off with a half-power point at 1.5 MHz

12. Noise bandwidth effects - The use of the usual $\sqrt{\Delta F}$ to estimate the effects of the electrical bandwidth on signal to noise will over estimate integrated noise because the g-r noise has a gradual drop-off in magnitude at high frequencies as contrasted with the usual flat noise spectrum.

Detector Transfer Function

Typical transfer function diagrams of the HDS radiometer are shown in Figures 26 and 27. The source of infrared radiance in the 14- to 16-micron band is either the earth's infrared horizon or a calibration standard with suitable attenuators to cover the range of irradiance values to be encountered in the use of the equipment. The optical system receives the radiance from the source and is then modulated.

The modulated irradiance from the in-flight calibration source or the infrared horizon is focused on the detector through a cooled infrared window, infrared filter, and defining aperture as shown in Figure 27. All objects within the optical path of the detector must be cooled to avoid noise from their infrared emission. Objects behind the modulator, which is usually a chopper with an equal number of open and opaque sectors, need not be cooled as much as the chopper blade and objects in the optical path in front of the chopper. The detector absorbs the irradiance and generates an output voltage in proportion to the input irradiance. To operate the detector at its maximum detectivity requires a source of low temperature, supplied by the solid-cryogen cooler, and a source of bias current, shown as originating in the detector bias supply. Both the bias current and temperature should be essentially constant over the calibration/measurement cycling time. The output of the detector consists of a time-varying voltage which is the input for the radiometer electronics.

62
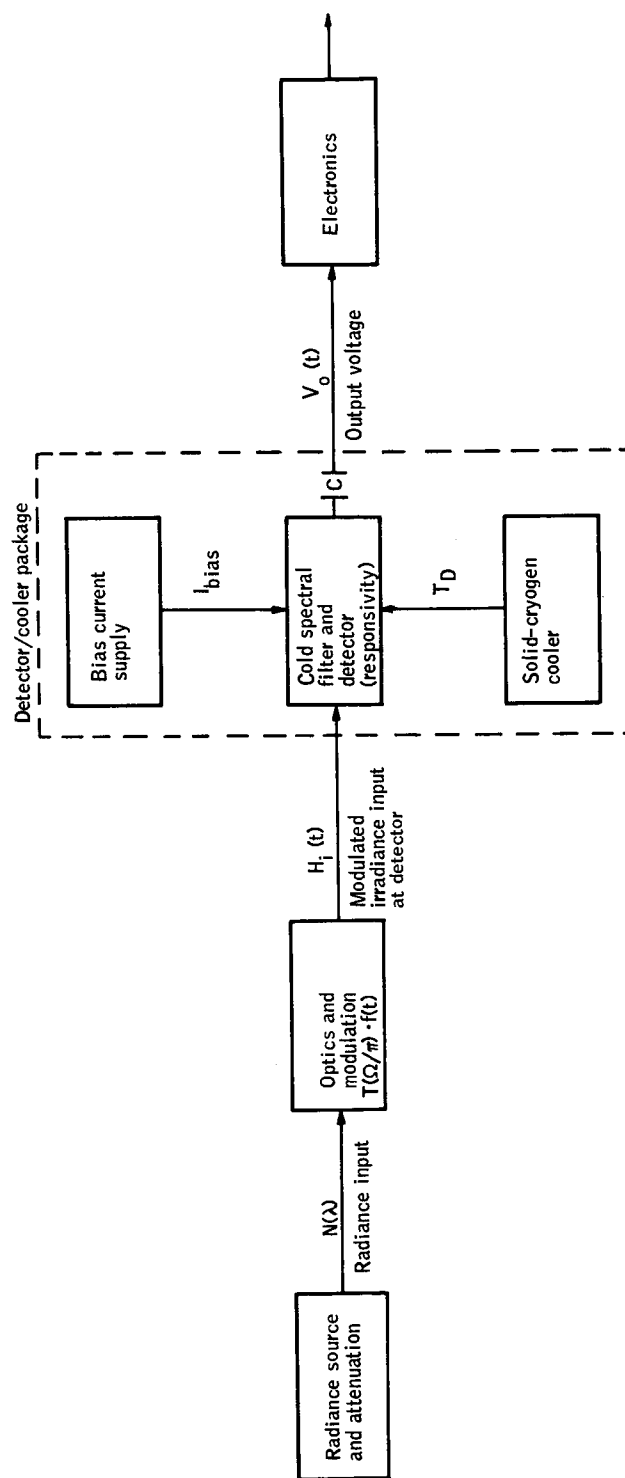
Figure 26. Typical Functional Diagram for the HDS Radiometer
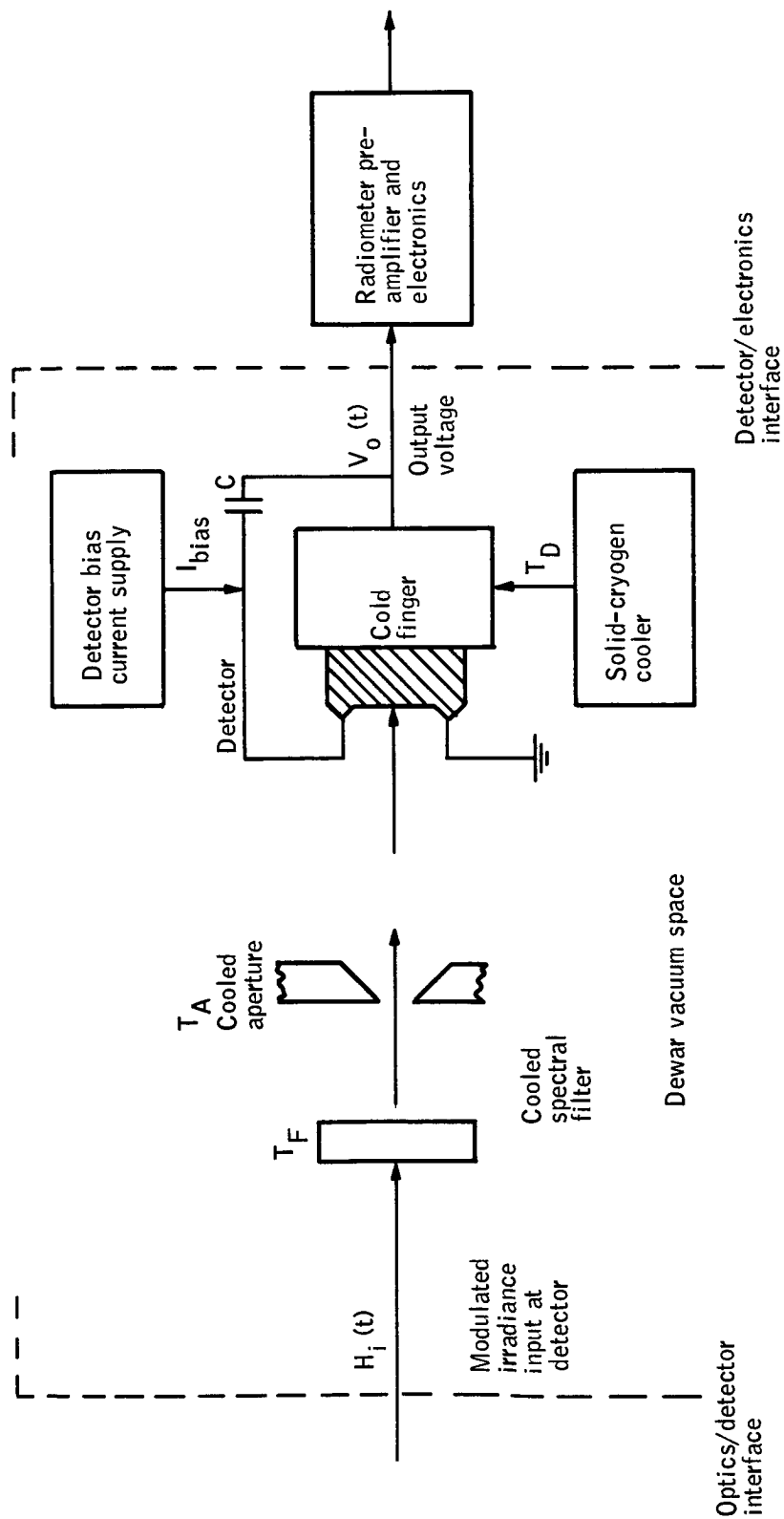
Figure 27. Essential Functional Components for Detector/Cooler Package

The transfer function for the detector is related to the detector responsitivity by

$$K = \frac{V_o(t)}{H_i(t)} = (T_W)(T_V)(T_A) R_H \frac{\text{volts}}{\text{watt}/\text{cm}^2}$$

where the factor R_H is the detector irradiance responsitivity. In terms of detector parameters the detector irradiance responsivity is given by

$$R_H = \frac{I_o R_D}{H_i(t)} \frac{N_H(wt) + N_M + N_T}{N_c(wt + \pi) + N_M + N_T} \cdot \frac{1}{(1 + w^2 \tau^2)^{1/2}}$$

where:

I_o is the bias current;

R_D is the detector resistance when obscured by the coppper blade;

$H_i(t)$ is the instantaneous irradiance from the horizon;

and

N_H, N_M, N_C, and N_T are the density of carriers generated in the detector by the horizon irradiance, mirror irradiance, chopper irradiance, and detector internal thermal processes.

Since the chopper modulates the irradiance from the horizon and is itself a source of modulated irradiance these terms have a time dependence, the emission from the chopper is, however, 180° out of phase with the signal of the horizon.

For an input signal of $H_i(t)$ with $w\tau << 1$, detector output voltage is given by

$$V_{out}(t) = I_o R_D \frac{1 + \dfrac{N_H f(wt)}{N_M + N_T}}{\dfrac{N_C f(wt + \pi)}{N_M + N_T}} \quad \text{volts}$$

The total density of current carriers generated in the detector by each of the mechanisms is given in the following paragraphs on (infrared horizon and mirror irradance).

Infrared horizon. --

$$N_H(t) = W_H(\Omega_i)\left(\overline{\frac{\lambda}{hc}}\right)\left(T_o\right)\left(\frac{A_{Optics}}{A_D}\right)(\eta\tau/d) \ f(wt) \ carriers/cm^3$$

where the average photon energy from the horizon is

$$\int\overline{\frac{\lambda}{hc}} = \frac{\displaystyle\int_{14}^{16}\overline{\frac{\lambda}{hc}} \ W_H \ d\lambda}{\displaystyle\int_{14}^{16} W_H \ d\lambda}$$

and

W_H =   horizon radiance in watts/cm^2-sr

Ω_i =   instantaneous FOV of the detector in sr

T_o =   transmission of the optics

A_{optics} =   entrance pupil area of the optics

A_D =   detector area

η =   detector conversion efficiency, carriers/photon

τ =   carrier lifetime

d =   detector thickness

f =   modulation waveform

Mirror irradiance. -- For large f number optics[a], the quantum irra-diance at the detector for a single mirror surface is given by

---

[a]Appendix A contains a more rigorous calculation of the effect of obliquity of the mirror edge which shows that the use of $1/f \ (f/no.)^2$ slightly over-estimates the mirror irradiance for small f/no. optics.

$$H_C = \frac{\epsilon_M (\Delta_{14-16})}{(f/no.)^2} \quad W_M \quad \frac{\overline{\lambda}}{hc}$$

where:

ϵ_M = mirror quantum emissivity

Δ_{14-16} = fraction of the mirror irradiance contained in the 14- to 16-μ band

W_M = radiance for a blackbody at T_M, the mirror temperature

and the other parameters have the definitions given above.

The current carrier density generated in the detector is

$$N_M = H_Q \, \eta \, \tau / d, \text{ carriers/cm}^3$$

Chopper irradiance. -- Similar to the calculation for the mirror irradiance, the density of the carriers generated in the detector by the chopper is

$$N_c = \frac{\overline{T}_o \, \epsilon_c \, (\Delta_{14-16}) \, W_c}{4 \, (f/no.)^2} \quad \cdot \quad \frac{\overline{\lambda}_c}{hc} \, \eta \tau / d \, f \, (\text{wt at } \pi), \text{ carriers/cm}^3$$

where:

$\overline{T}_o$ = optics transmission

ϵ_c = chopper quantum emissivity

W_c = radiance from a blackbody at the chopper temperature, T_c.

Thermal generation of carriers in the detector. -- The density of thermally generated carriers is a complicated function of detector temperature and the physical properties of the semiconductor. For a simple, spherical-band semiconductor which is a good approximation for cadmium-doped germanium, the density of thermally generated carriers is given by the usual

$$N_T = (2\pi \, m_v \, KT/h^2)^{3/2} \quad \frac{N_A - N_D}{N_D} \quad \exp(-\Delta E/KT), \text{ carriers/cm}^3$$

At the operating temperature available with a solid-hydrogen cryogenic cooler, it can be shown that the thermal generation term is small compared with the mirror generation time. Therefore, the output voltage takes the form

$$V_{out}(t) = (I_o R_D) \; \cfrac{1 + \cfrac{N_H f(t)}{N_M}}{\cfrac{N_C \, f(wt + \pi + \phi)}{N_M}}$$

where ϕ is a phase error introduced in the detector by lifetime fluctuation since

$$N_H \cong \left(\frac{1}{10}\right) N_M$$

due to the limits of optics temperature available, the output voltage may be expanded as

$$V_{out}(t) = I_o R_D \left[1 + \frac{N_H \, f(wt)}{N_M} - \frac{N_c \, f(wt + \pi + \phi)}{N_M} - \frac{N_H \, N_c}{N_M^2} \, g(\phi) + \ldots\right]$$

The quadratic term $(I_o R_D) \dfrac{N_H \, Nc}{N_M^2} \, g(\phi)$ is essentially a phase-error term.

If the chopper irradiance can be made small with respect to either the horizon or mirror irradiance, the third and fourth term of the expansion may be neglected, and the output voltage is linear with respect to input irradiance, i.e.,

$$V_{out} = I_o R_D \; 1 + \frac{N_H \, f(wt)}{N_M}$$

The first term is a dc-offset term which usually is removed by the electrical circuit; the second term is the linear term described above, i.e.

$$V_{out} = I_o R_D \; \frac{N_H}{N_M} \, f(t)$$

68

or

$$V_{out} = \frac{I_o R_D H_i}{\varepsilon_M \Delta_{14-16} W_M / 4 \, (f/no.)^2}$$

since

$$H_i = W_H \cap_i \overline{T}_o \, (A_{optics} / A_D)$$

Therefore, the detector transfer function under the assumptions discussed above is

$$K = \frac{T_W T_F T_A I_o R_D}{\varepsilon_M \Delta_{14-16} W_M / 4 \, (f/no.)^2} , \quad volts/watt/cm^2$$

Detector Mechanical Parameters

The mechanical design of the cadmium-doped germanium detector assembly must have good thermal conductivity and low thermal mass. Two design approaches, dual integration chambers and dual elements, are being considered for the radiometer. In the integration chamber approach the cadmium-doped germanium detector elements are in the form of cubes, 2 mm on a side. These are attached to copper screws which are inserted into integration chambers as shown in Figure 28. The access wire for each element is brought out of the integration chamber by a hollow insulated feedthrough. The integration chamber consists of cylindrical cavity of machined copper. The cavity is highly polished and is coated with gold. The radiation to be detected is incident on a rectangular aperture which attaches at the top of the integration chamber sealing it "light-tight". The area of the aperture defines the effective sensitive area (80 microns x 320 microns) of the detector in the integration-chamber approach.

The alternate approach to the integration chamber is shown in Figure 29. This approach uses discrete cadmium-doped germanium detector elements with the frontal area of the elements being the sensitive area of the detector. Electrical contact to the detector element is along the long sides as shown in Figure 30. The detector element is approximately 2 mm deep with the bottom shaped to allow total internal reflection of radiation within the detector element. The detector elements will be made and tested individually and positioned in a frame with Mylar-film insulators as shown in Figure 29.

Figure 31 illustrates another possible mechanical configuration which is a typical design for mercury-cadmium telluride detector elements. This

69

Effective sensitive area
$(80\mu \times 320\mu)$

Highly reflecting
integration chamber

Access electrodes

Detector element
mounting screw
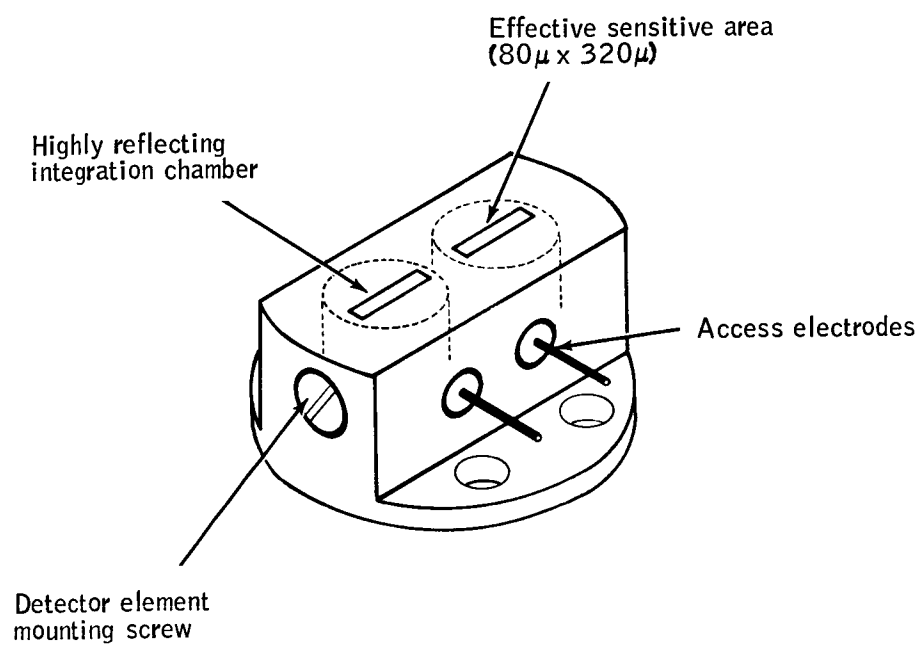
Figure 28.   Sketch of Integration Chamber Configuration
for Cadmium-Doped Germanium

0.005 inch Mylar insulator

Kovar backup mounting plates (6)

Typical Ge:Cd detector, 80μ x 320μ x 2mm thick

Access electrodes
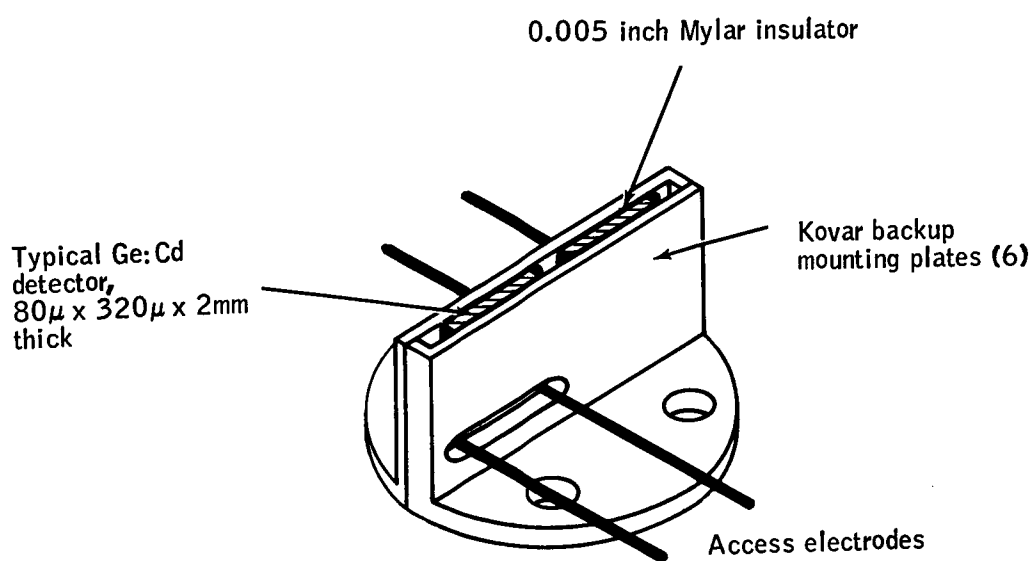
Figure 29. Sketch of Cadmium-Doped Germanium Discrete Detector Element Assembly
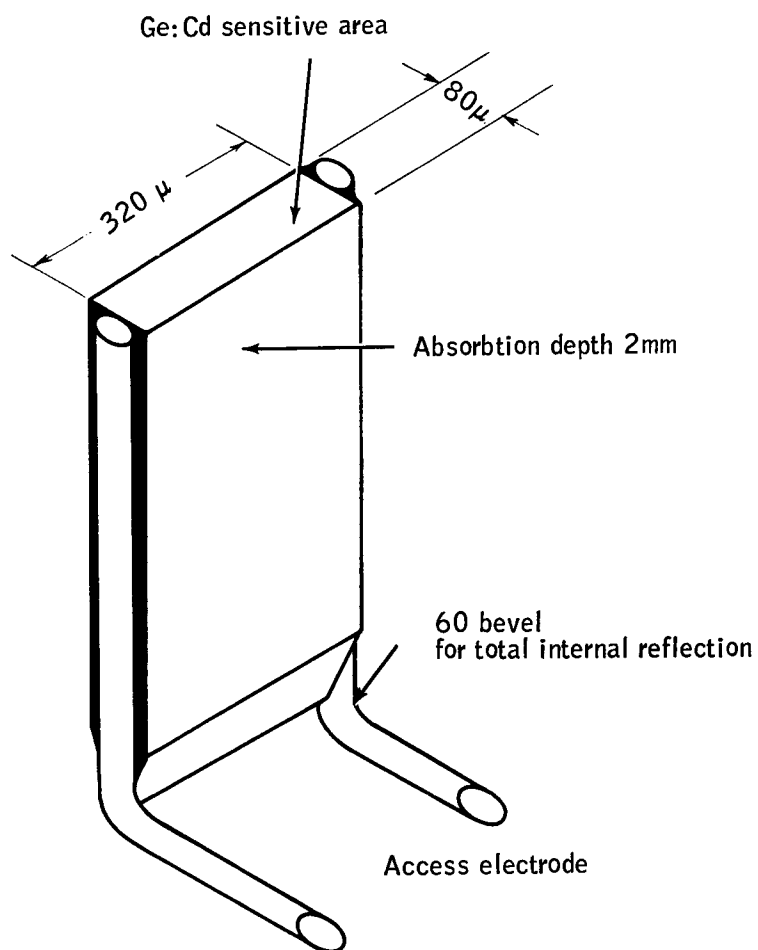
Figure 30. Sketch of Cadmium-Doped Germanium Detector Element

Typical Hg:Cd:Te detector, $80\mu \times 320\mu \times 10\mu$ thick

Kovar alloy mounting plate

Access electrodes

Germanium substrate
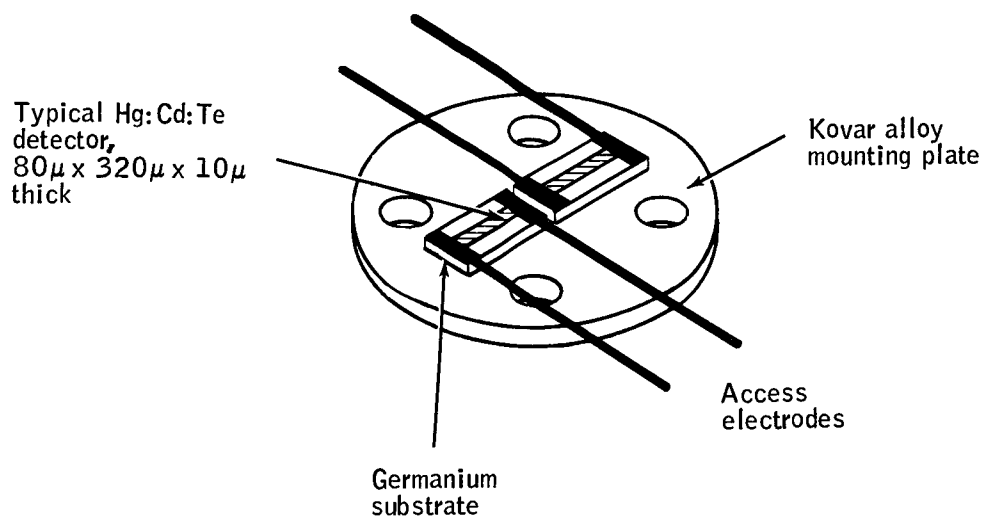
Figure 31. Sketch of Hg:Cd:Te Detector Element Assembly

73

design is of great simplicity. Thicknesses of the Hg:Cd:Te detector elements range from 10 to 20 microns; these elements can be handled as thin-film detectors attached to a backing substrate (germanium). The access wires are micro-welded to small metal films which define the length of the detector element sensitive area. The width of the detector sensitive area is defined by the mechanical width of the Hg:Cd:Te.

Each of these design approaches is capable of achieving detector elements of 80μ x 320μ in sensitive area, which is the requirement for the HDS radiometer.

Quantum Efficiency of Detector Mounts

The efficiency for the integration chamber for the cadmium-doped germanium detector shown in Figure 32 is given by (ref. 1)

$$\eta = \frac{2 \, N_{Cd} \, A_{cs} \, V}{A_A + A_L + A_W \, (1-r) + 2 \, N_{Cd} \, A_{cs} \, V}$$

where:

A_{cs} = absorption cross section of a cadmium atom in germanium, cm^2

N_{Cd} = concentration of cadmium atoms in the detector, cm^{-3}

V = volume of the detector element, cm^3

A_A = integration chamber entrance aperture area, cm^2

A_L = total area of extraneous radiation loss within the integration chamber such as feed-throughs and mechanical joints, cm^2

A_W = wall area, cm^2

r = wall reflectance

The factor of two is related to the geometric fact that cadmium absorption centers receive radiation from 4π steradians while the other absorbers receive radiation from only 2π steradians.

For the case being considered here of a BLIP detector, there is no "optimum volume" as derived in reference 1. The best volume for the Ge:Cd element is the largest volume consistent with the mechanical design constraints.
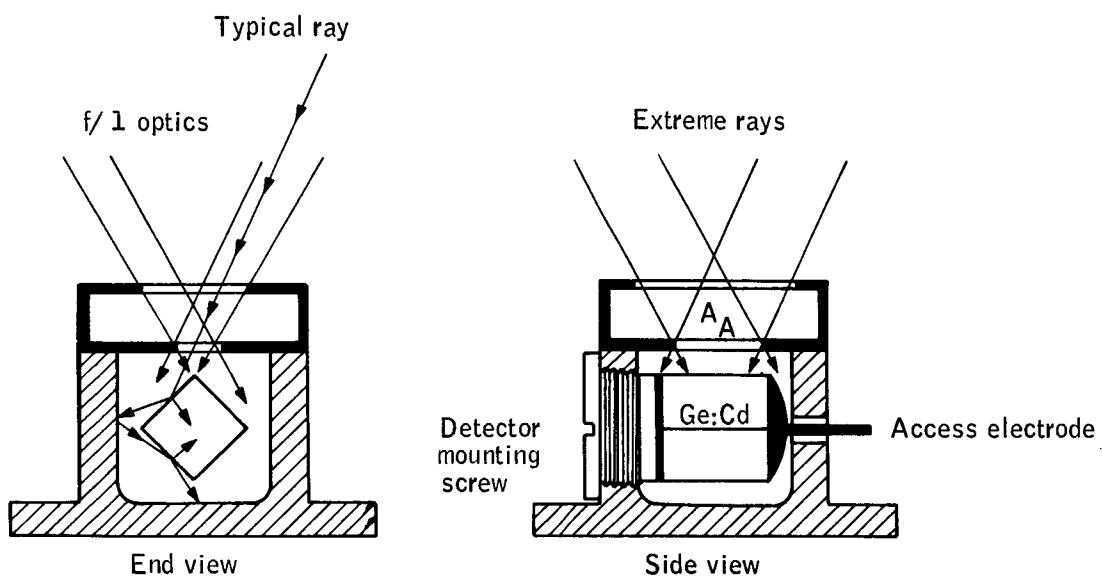
Figure 32. Sketch of Typical Integration Chamber for Cadmium-Doped Germanium Detector

Substituting the following typical parameters for cadmium-doped germanium:

$$A_{cs} = 10^{-16} \text{ cm}^2$$

$$N_{Cd} = 5 \times 10^{15} \text{ cm}^{-3}$$

$$V = 0.027 \text{ cm}^3$$

$$A_A = 2.56 \times 10^{-4} \text{ cm}^2$$

$$A_L = 10 \, A_A = 2.56 \times 10^{-3} \text{ cm}^2$$

$$A_W = 1 \text{ cm}^2$$

$$r = 0.98$$

The cross section for losses out the integration-chamber aperture and extraneous losses is 2.83×10^{-3} cm^2. The useful absorption cross section is 27.0×10^{-3} cm^2, and the effective cross section for wall losses is 20×10^{-3} cm^2. The integration chamber efficiency is, therefore,

$$\eta = \frac{27.0 \times 10^{-3}}{49.8 \times 10^{-3}} = 0.54$$

For the self-integrating design shown in Figure 33, the following geometric relationship for angles shown in Figure 34 are easily derived.

The conditions for total internal reflection are:

$$\sin \theta_M = \frac{1}{2 \, fn_o} \qquad\qquad \theta_M = 0.525 \text{ radian}$$

$$\sin \theta = (n_1/n_2) \sin \theta_M \qquad\qquad \theta = 0.130 \text{ radian}$$

$$\sin \theta_C = n_1/n_2 \qquad\qquad \theta_C = 0.255 \text{ radian}$$

$$\phi_1 = (2\beta + \theta - \pi/2) \qquad\qquad \phi_1 = 0.400$$

$$\phi_2 = (2\beta - \theta - \pi/2) \qquad\qquad \phi_2 = 0.660$$

$$\alpha_1 = (\pi/2 - \beta - \theta) \qquad\qquad \alpha_1 = 0.924$$

$$\alpha_2 = (\pi/2 - \beta + \theta) \qquad\qquad \alpha_2 = 1.185$$
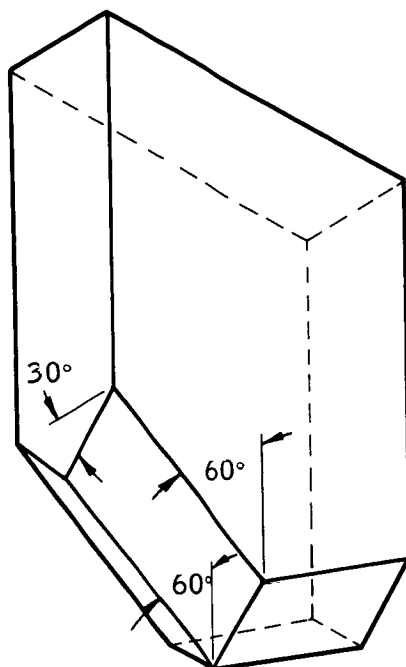
Figure 33.   Details of Bottom Facets of Self-Integrating Cadmium-
Doped Germanium Detector
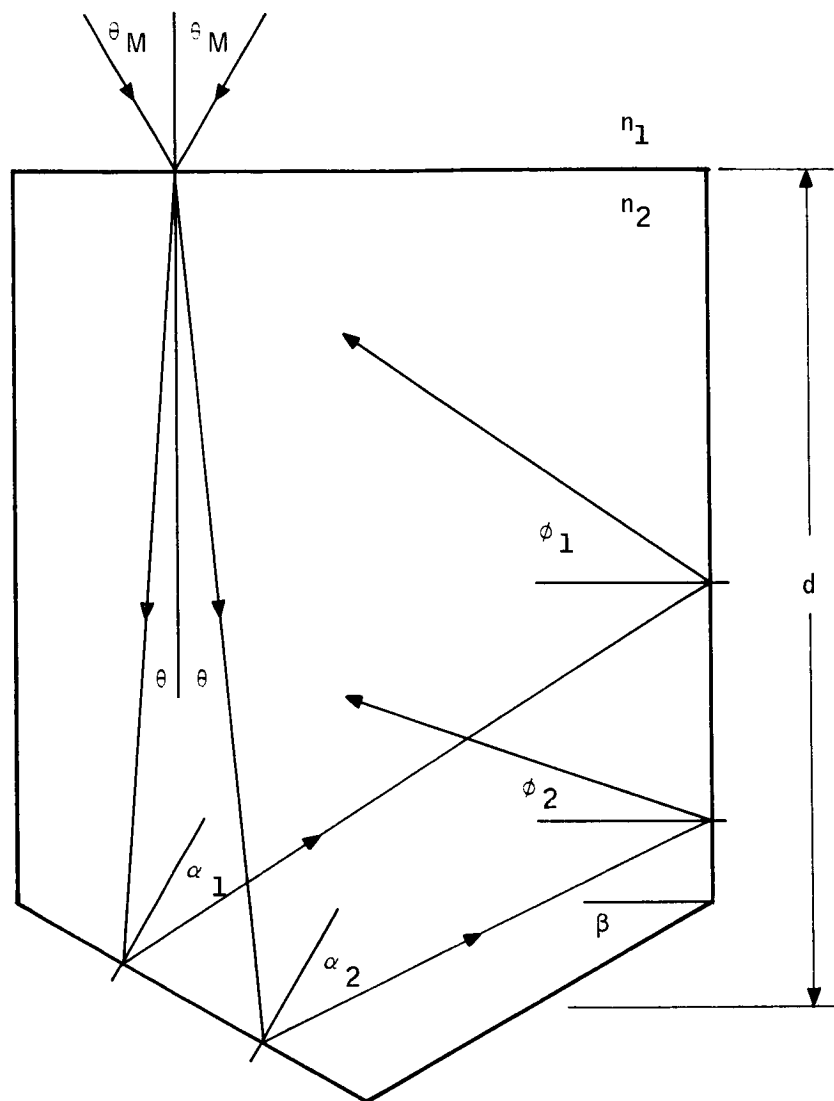
Figure 34. Typical Angular Relationships for TIR in Self-Integrating Ge:Cd Detector Element

78

Since

$$n_1 = 1,$$

$$n_2 = 4,$$

$$\beta = \pi/6 = 0.525 \text{ radian, and}$$

$$f/no. = 1,$$

the most stringent condition for the inequalities is easily seen to be

$$\phi_1 \geq \theta_c$$

which yields $\beta_{max.} = 0.598$ radian or 34.2°. If β were greater than $\beta_{max.}$ (due to surface irregularities), the condition for total internal reflection would be lost. A good engineering compromise value is $\beta = 30°$. From the geometry shown in Figure 34 for a detector element of geometric depth d, the effective depth de may be shown to be

$$d_e \cong d \left[\frac{2}{\cos \theta} + \frac{4}{\sin \phi_1 + \sin \phi_2} \right]$$

where it is assumed that all angles between ϕ_1 and ϕ_2 are equally probable.

Therefore,

$$\frac{d_e}{d} = 6$$

Since

$$\cos \theta = 0.9916$$

$$\sin \phi_1 = 0.3894$$

$$\sin \phi_2 = 0.6131$$

For $\beta = 30°$, the effective length is, therefore, about 6 times the geometric length.

It can be shown (ref. 2) that the net absorption or quantum efficiency for the self-integrating Ge:Cd detector element is given by (assuming every quanta absorbed results in an electron-hole pair):

$$\eta = (1-R) \; - \; \left[\frac{(1-R)^2 \, e^{-2 \, \alpha \, d_e}}{1 - R \, e^{-2 \, \alpha \, d_e}} \right]$$

where the reflectivity at the bottom is 1 and the reflectivity at the top surface is 12.

Since $d_e = 6 \, d$, therefore,

$$\eta = (1-R) \; - \; \left[\frac{(1-R)^2 \, e^{-12 \, \alpha \, d}}{1 - R \, e^{-12 \, \alpha \, d}} \right]$$

or

$$\eta = \frac{(1-R) \, (1 - e^{-12 \, \alpha \, d})}{1 - R \, e^{-12 \, \alpha \, d}}$$

This equation has been evaluated as a function of R, α and, d and is tabulated below.

The quantum efficiency of the detector for t = 4 mm and 8 mm is plotted in Figure 35. For an absorptivity of 0.5 cm^{-1} which is a reasonable assumption (ref. 1), the quantum efficiency is about 0.89 for an anti-reflection coated detector for either thickness. For an uncoated detector the quantum efficiency for either thickness is about 0.59. It is important, therefore, to anti-reflection coat the front side of the detector element to achieve a high quantum efficiency with the self-integrating Ge:Cd detector.

The following quantum efficiencies are estimated for the Ge:Cd detector configurations being considered for HDS radiometer:

Integration chamber	$\eta = 0.54$
Uncoated SIC	$\eta = 0.59$
Anti-reflection coated SIC	$\eta = 0.89$
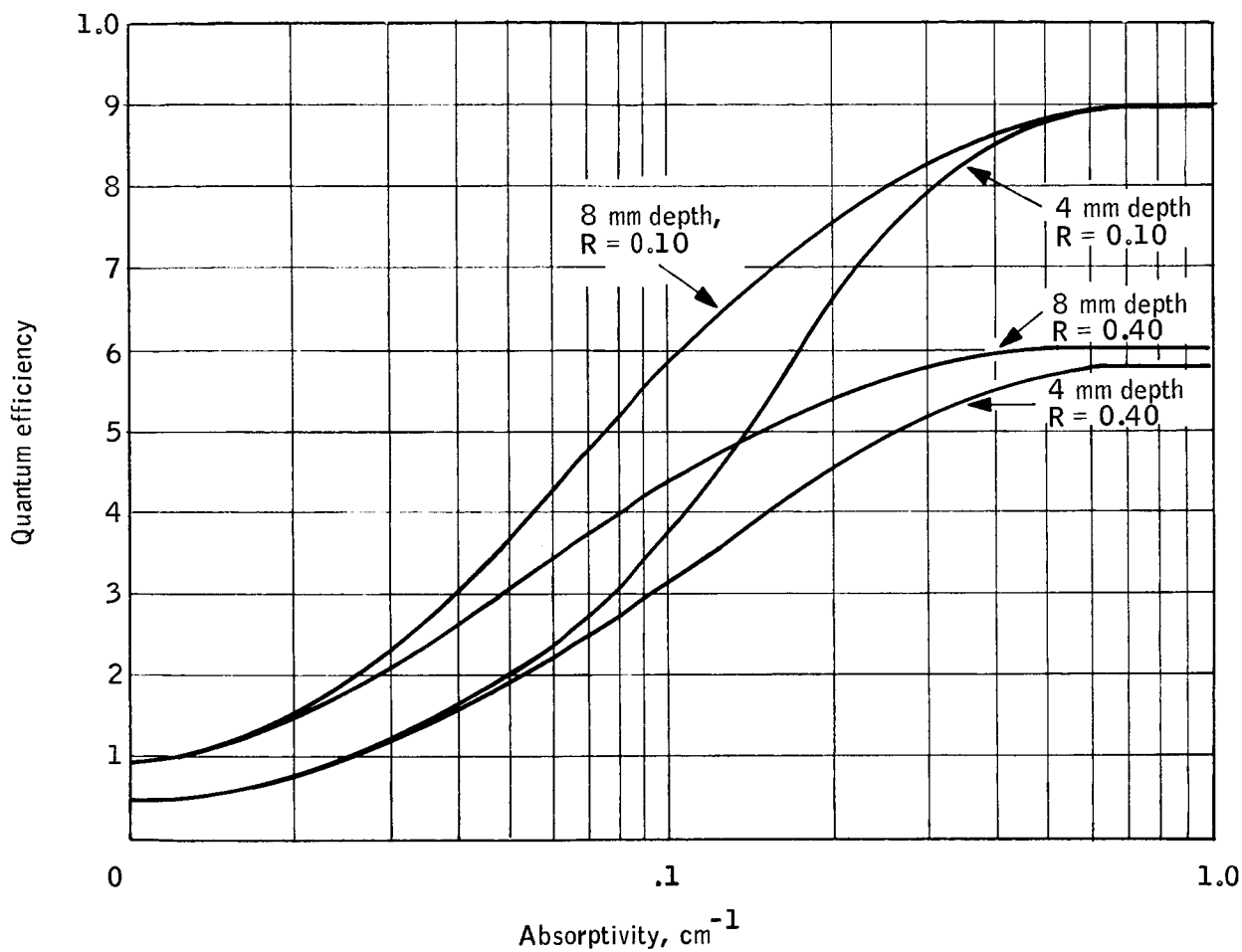
Figure 35. Quantum Efficiency of Self-Integrating Ge:Cd Detector

Ratio of Ge:Cd Detector g-r Noise to Johnson Noise

The square of the ratio of the open-circuit generation-recombination noise N_{g-r} to the Johnson noise N_j for the cadmium-doped germanium detector for $\omega\tau << 1$ is

$$\left(\frac{V_{g-r}}{V_u}\right)^2 = I_o^2 \; \frac{\tau R}{KTN}$$

where:

$$V_{g-r} = \frac{2 I_o (\Delta f \tau)^{1/2}}{N^{1/2} (1 + \omega^2 \tau^2)^{1/2}} \; , \; \text{rms volts}$$

$$V_j = (4KT \Delta fR)^{1/2} \; , \; \text{rms volts}$$

and

I_o = bias current, amps,

τ = hole lifetime, seconds,

R = detector resistance, ohms,

K = Boltzman's constant, 1.38×10^{-23} joules/°K,

T = detector temperature, °K, and

N = total number of carriers in the detector element

For a cadmium-doped germanium clement of cross section A_{cs} and length ℓ contained within an integration chamber with entrance aperture area A_{A6},

$$R = \frac{\ell^2}{Ne\mu_+}$$

and the ratio becomes

82

$$\left(\frac{V_{g-r}}{V_j}\right)^2 = \frac{I_o^2 \, \tau \ell^2}{N^2 \, e\mu_+ KT}$$

Since

$$N = N_{TH} + N_{BKG}$$

and

$$N_{TH} = (N_A - N_D) \, A_{cs} \, \ell$$

$$N_{BKG} = F \, A_A \, \eta\tau \int_{\lambda_1}^{\lambda_2} Q_b \, (\lambda_1 T_b) \, d\lambda$$

therefore,

$$\left(V_{g-r}/V_j\right)^2 = \frac{I_o^2 \, \tau \, \ell^2}{\left[N_{TH} + (F \, \eta \, \tau \, A_A) \displaystyle\int_{\lambda_1}^{\lambda_2} Q_b(\lambda_1 \, T_b) \, d\lambda\right]^2 e\mu_+ \, KT}$$

where the optimum bias current I_o is a measured physical parameter of the Ge:Cd material used to make the detector element, and the other factors have their usual definitions.

For the particular operating conditions of the Ge:Cd detector in the HDS radiometer with the detector spectral coverage limited to the 14 to 16 micron band and a 200°K optics background, it has been shown that

$$N_{TH} \gg N_{BKG}$$

and $N_{TH} \approx 10^7$ carriers/cm^3 due to ionization of residual, low-energy impurities. Therefore,

$$\frac{V_{g-r}}{V_j} = \frac{I_o \ell}{N_{TH}} \left(\frac{\tau}{e\mu_+ KT} \right)^{1/2}$$

Substituting the following representative values:

$$I_o = 10^{-5} \text{ amp}$$

$$N_{TH} = 10^7 \text{ carriers/cm}^3$$

$$\ell = 0.2 \text{ cm}$$

$$\tau = 10^{-8} \text{ sec}$$

$$\mu_+ = 5000 \text{ cm}^2/\text{volt-sec}$$

$$T = 15°K$$

Then, $V_{g-r}/V_j = 50$ at $I_o = 10^{-5}$ amp. Since the ratio is linear with bias current, the bias current where V_{g-r} equals V_j is 0.2×10^{-6} amp.

Since the two noise sources are uncorrelated, the total noise as a function of bias current is

$$V_T = V_j \left[1 + (V_{g-r}/V_j)^2 \right]^{1/2}$$

For a 500 K ohm detector operating at 15°K, the Johnson noise is 2×10^{-8} rms volts/$Hz^{1/2}$. Quantitatively, the total noise is essentially Johnson noise below bias currents of 0.2 microampere. Above this value, the total detector noise is g-r noise.

The cadmium-doped germanium detector may be operated at any bias current in the range from 2 to 10 microamperes with no significant change in detectivity. The responsivity, however, is linearly proportional to the bias current in the same bias current range. The total detector noise will be a factor of from 10 to 50 times the Johnson noise of the detector in the same bias current range.

ELECTRONICS

Primary functions performed by the radiometer electronics are to provide bias power to the photoconductive infrared detector and to condition the resultant output signals in a form suitable for sampling, quantizing, and storage. These

functions and their interrelationships are depicted in the block diagram of Figure 36. Incoming, modulated radiation varies the resistance of the detector which, as a result of the bias power and load resistor, is presented to the preamplifier as a voltage signal variation, which is ac coupled to the detector. Power gain of the preamplifier provides a low source impedance to the high-gain filter amplifier. The demodulator removes the carrier frequency and provides bandpass filtering to limit the output signal frequencies to the desired information bandwidth. Radiometer output to the data-handling subsystem of the spacecraft is then, the unmodulated, low frequency coupled horizon profile signal waveform. A tradeoff exists here as to whether the highest accuracy results from performing demodulation on the ground or within the radiometer as is assumed here. Feasibility of the radiometer and data-handling subsystems is not critical with respect to the outcome of this tradeoff, however; therefore, for the purpose of the feasibility design study, demodulation has been included in the radiometer design with which it is directly and functionally associated.

The specific requirements and constraints upon the radiometer electronics are as follows:

- Noise -- Electronics noise from all sources shall be minimized such that the rms noise voltage at the radiometer output is no more than 10 percent greater than detector noise alone in the same bandwidth and at the same gain.

- Transfer function -- The post-detection (after demodulation) bandwidth is from 0.1 to 1600 Hz (-3 dB points) and shall be -20 dB at 2500 Hz. Phase shift shall be less than 1/4 that of an ideal first-order low-pass filter from 1 to 200 Hz or about $\frac{2\pi}{30}$ radians/Hz/km. The 0.1 Hz corresponds to 10^{-4} cycle/km and maintains low frequency droop to less than 1 percent from beginning to end of a profile.

- Dynamic range -- $\geq 2100:1$ minimum; 3000:1 design goal

- Detector impedance -- $\cong 500$ K ohm.

- Drift -- 0.1 percent of signal level or 1/3 noise level, whichever is greater over any 10-second period.

The detector bias, preamplifier, and demodulator networks will require feasibility demonstrations with respect to the noise requirement and the implications of the approach to achieve it.

Input

The detector output, including its noise, must be essentially reproduced at the radiometer output. The detector Johnson noise is approximately 2×10^{-8} volts-Hz$^{-1/2}$ which, in the required bandwidth, is an rms voltage level of about 0.8 μV. The actual detector noise is g-r noise, however, which
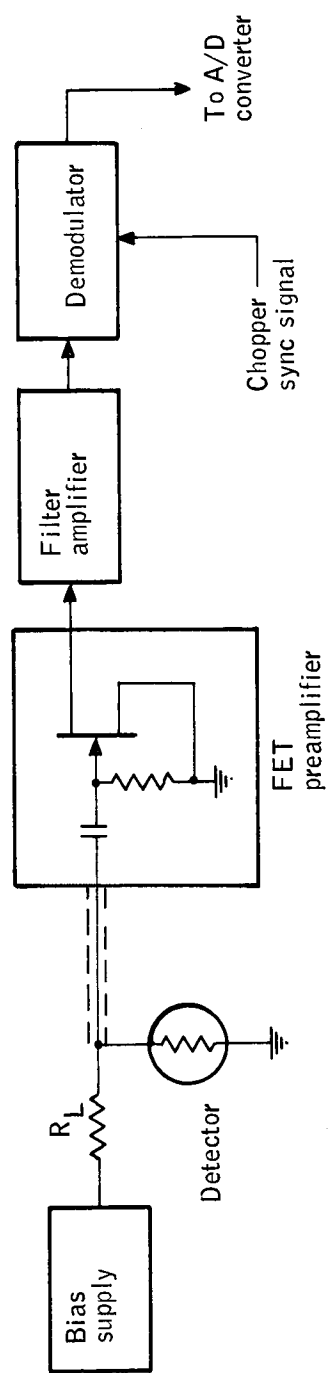
Figure 36. Radiometer Electronics Block Diagram

is bias dependent and can be raised to as much as 40 times Johnson noise. In determining the operating level, a tradeoff must be made. At a high bias level, the heat load due to bias power dissipated by the detector is placed upon the detector cooler. This must be weighed against the strain placed upon bias-supply regulation and noise rejection as well as the preamplifier and amplifier noise figures at a low bias level. A level of 20 times Johnson noise (about 16 μV) has been selected as placing a sufficiently small load (less than 2.5 milliwatts) on the cooler. Note that detectivity is virtually constant over the range of from 5 to 40 times Johnson noise.

With the noise level this high, the detector load resistor need not be at the same temperature as the detector and will, in fact, be integrated into the preamplifier.

This requires a shielded cable to carry the detector signal to the input of the preamplifier. A problem is introduced by this signal lead due to vibration and flexure which changes the capacitance and due to induction of charges on the dielectric caused by friction with the center conductor or shielding. When a bias potential exists across the cable insulation, capacitance changes cause current which flows through the preamplifier input resistor to appear as noise voltage. This problem is solved by the use of a cable which is treated with conductive materials between the outside sheaths and the dielectric insulation and, as far as possible, between the center conductor and the dielectric. These conductive coatings dissipate the charge induced by friction and maintain reasonably constant capacitance.

Detector Bias Supply

The detector bias supply is of particular concern because of the low noise level requirement over the signal frequencies of interest. Bias power is required due to the current of 10 to 50 microamperes flowing into the 500 K ohm detector, i.e., 10 to 12 volts across the detector. The bias supply consists of essentially two separate functional circuits; namely, (1) a high-voltage power supply inverter of reasonably low noise, and (2) a dc regulator loop with special emphasis on noise rejection. The inverter section consists of an astable multivibrator driving a bi-stable multivibrator with transformer output to develop a rectified dc voltage. The inverter frequency is considerably higher than the signal frequencies of interest to preclude ripple terms directly in the signal bandwidth. Although these ripple terms will contribute to the overall noise level, they will be relatively easy to filter because of the high-ripple frequency and the subsequent attenuation in the signal channel. Inverter ripple will also be lowered by maintaining symmetry in the duty cycle which results from a single astable trigger reversing the bi-stable state. Inverter output will be limited by zener and catching diodes to clip the noise spikes and will be L-C filtered to a noise level of not more than 100 mV including ripple terms. The regulator section will be a series-type dc regulator having constant gain from approximately 1 to 10 kHz and a unity-gain crossover of approximately 2 MHz.

Due to amplifier drift, dc regulation is on the order of ±0.1 percent; this is more than adequate for the detector supply. Regulation of the noise perturbations, however, is at least -80 dB across the regulator which results in less than a $10\mu V$ rms noise being introduced across the detector and load resistor. The noise generation of the control amplifier and reference circuit is approximately $5\mu V$ for an equivalent noise bandwidth of 15 kHz for a 3-dB noise figure control amplifier and network, which amounts to a $10\mu V$ rms contribution to voltage bias. The vector sum of these uncorrelated terms appearing across the detector is approximately $7\mu V$ ($\approx$ 15 kHz noise bandwidth).

Stabilizing the loop by means of a linear, second-order, low-pass filter with a zero near the unity-gain crossover region should pose no particular problem for $\beta = 0.5$ and $A = 86$ dB; the resulting loop gain is approximately 80 dB. Using the numbers discussed above, the total noise appearing across the detector due to the bias supply is approximately

$$V_{\text{noise at detector}} = \frac{R_{\text{det}}}{R_{\text{det}} + R_s} \sqrt{\frac{\Delta \bar{V}_R}{\beta} + \frac{\Delta \bar{V}_1}{A_\beta}}$$

$$= 1/2 \sqrt{\left(\frac{5 \times 10^{-6}}{0.5}\right)^2 + \left(\frac{100 \times 10^{-3}}{1 \times 10^4}\right)^2}$$

$$= 1/2 \sqrt{200 \times 10^{-12}} = 7\mu V \quad (15 \text{ kHz noise band})$$

Considering the signal channel to be of 6 ± 1 kHz bandwidth (or approximately 3 kHz effective noise bandwidth instead of the 15 kHz bandwidth over which the regulator is operative), the equivalent noise through the signal channel will be reduced by $\sqrt{\frac{15 \text{ kHz}}{3 \text{ kHz}}} = \frac{1}{0.45}$ or to approximately $3\mu V$ (3 kHz noise bandwidth).

The bias power supply block diagram is shown in Figure 37.

Bias Supply Test Results

A bias supply of the type to be used in the radiometer was built and tested, and the results are described in the following paragraphs. The low-noise bias supply consists of a high-frequency inverter ($\approx$ 20 kHz) with a zener pre-regulator and a passive ripple filter followed by an active-type regulator with

88
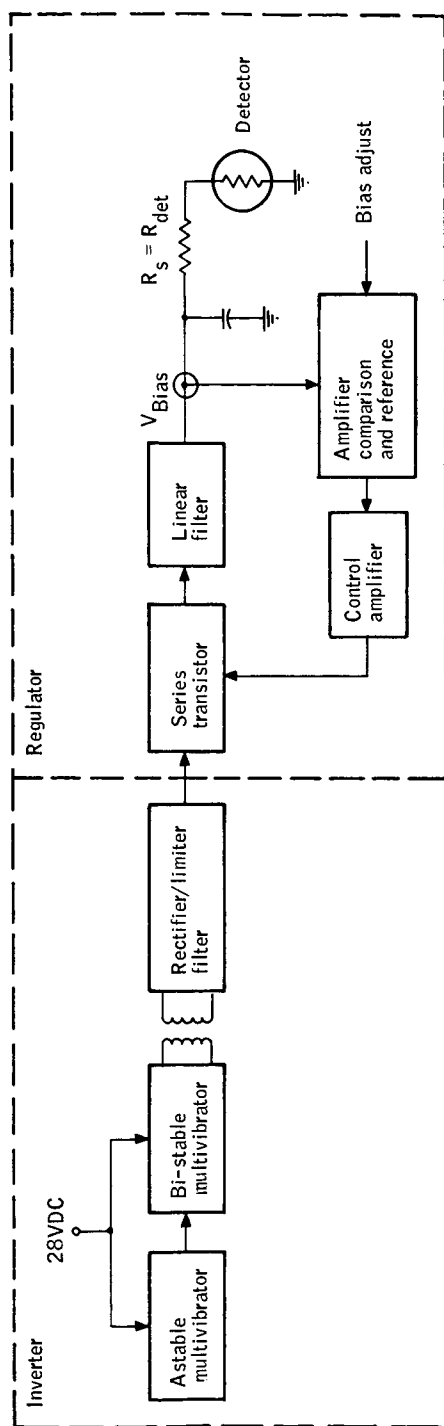
Figure 37. Radiometer Bias Supply Block Design

further filtering to remove primarily the noise generated in the series control element. The pre-regulator output is 46 ± 1 vdc with a total noise of 2.5 mV rms measured at 12 kHz with a noise equivalent bandwidth of 3 kHz. With the regulator output set to 30 vdc, the noise output measured $\approx$ 54μV at the same frequency and bandwidth. The inverter was replaced with a 45-volt battery whose noise was below 1μV in a 3-kHz bandwidth, and the regulator output measured $\cong$ 25μV. Therefore, the regulator output has approximately 25μV due primarily to the series control element and approximately 50μV attributable to the inverter, assuming a correlation factor near zero.

Measurement of dc regulation at higher levels subsequently showed the regulation to be 2 percent for the regulator alone and approximately 0.1 percent for the inverter, pre-regulator, and regulator. An inverter noise reduction of 50 times in the regulator agrees with the measured regulation of 2 percent and, although the comparison amplifier noise is rather small, the series control element noise requires that an additional filter be incorporated in or following the regulator. A low-pass filter was attached to the regulator output (2.7 K and 1μF), and the total regulator output noise measured approximately 250 nV rms at a center frequency of 12 kHz and Δf = 3 kHz. Since the inverter ripple falls outside the signal pass band, this noise should be fairly uniform, and wave analyzer measurements at various frequencies over the 3 kHz bandwidth show this to be true. Consequently, the bias supply described can be adequately represented by a noiseless dc source in series with a noise generator equivalent to a 20 K ohm thermal noise source ($\cong$20 nV/ Hz). This is equal to the detector nominal Johnson noise level or about 20 times less than its actual noise level; hence, this bias supply noise should cause negligible degradation of performance. Finally, the bias supply was operated in conjunction with a detector test station, and no perceptible difference could be discerned with a low-noise battery and the regulated bias supply described above.

Preamplifier

Selection of the field effect transistor (FET) as a low-noise device is based on consideration of the two noise components of a transistor; voltage noise and current noise. The voltage noise component is independent of the source impedance, but the current noise component is not. When source resistance is very high, current noise becomes more significant than voltage noise. Important characteristics of the FET are very low current noise with high input impedance. Here again, the FET was chosen over the conventional transistor as the device to match the HDS radiometer detector for optimum noise figure. Optimum noise figure is a function of the source resistance, and comparison of the conventional transistor with the FET optimum source resistance shows the transistor R_g(opt) too low for HDS requirements. However, the FET R_g(opt) requirement is nearly an optimum match.

Optimum noise figure of the FET is also a function of frequency. A typical case (for the 2N2500 FET) shows R_g(opt) to be approximately 0.8 megohms at 3 kHz, and the noise figure is at approximately its lowest value at this frequency.

90

The amplifier input impedance, as shown in Figure 38, has a value of $Z_{in}=10^7$ ohms to 1.6 kHz and a value of $Z_{in} = 1.6 \times 10^{10}/f$ when above 1.6 kHz.

As seen by the detector, this impedance will be high.

If the 1/f noise break frequency is plotted using three selected points from typical available FET specifications such that:

1. Point one is well within the 1/f region,

2. Point two is on the "knee", and

3. Point three is well within the plateau region,

then the 1/f noise break frequency is less than 100 Hz which is about half an order of magnitude lower than most transistors.

Figure 39 was drawn from transistor specification sheet parameters of spot noise figure (NF) specified at three frequencies. A fourth point is known where NF is three dB higher than the intersection point of the two asymptotes.

For 1/f noise the source generator resistance is of importance, since at lower frequencies, $R_g(opt)$ increases. In the FET, the 1/f noise can take the form of a single noise-voltage generator in series with the input and e_n. As frequency is reduced, the total voltage in series with the input increases and the optimum source resistance also increases to yield the optimum value of NF. The 1/f noise break frequency of less than 100 Hz is typical for an R_g of 0.5 megohm, which will be approximately the detector impedance. The 1/f noise breaks in a cadmium-doped germanium detector at approximately 200 Hz, which again makes the FET an ideal matching device.

In the proposed preamplifier, the FET input stage is followed by two amplifier stages using conventional transistors. The second stage is designed to have a low current flow to minimize "shot-noise". Minimization of noise in this stage is important since nothing can be done to the system to reduce the total noise factor below that of this second preamplifier stage. Shot noise is given by the Schottky formula

$$I_s^2 = 2qI_N\Delta f$$

where q is the charge of an electron and I_N is the dc (noise-producing) collector current.

Shot noise is thus seen to increase with collector current flow. The direct current flowing through the second stage is only 10 microamperes. The noise figure of the amplifier is $\cong 0.6$ dB.
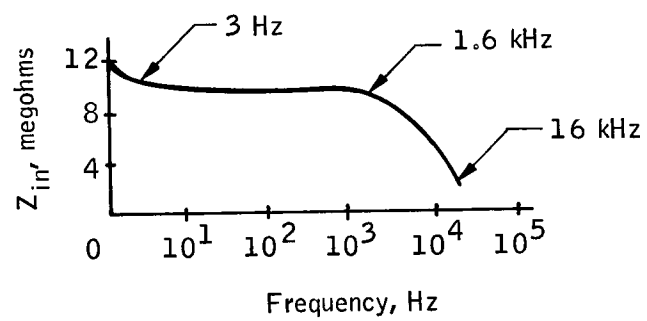
Figure 38.   Amplifier Input Impedance
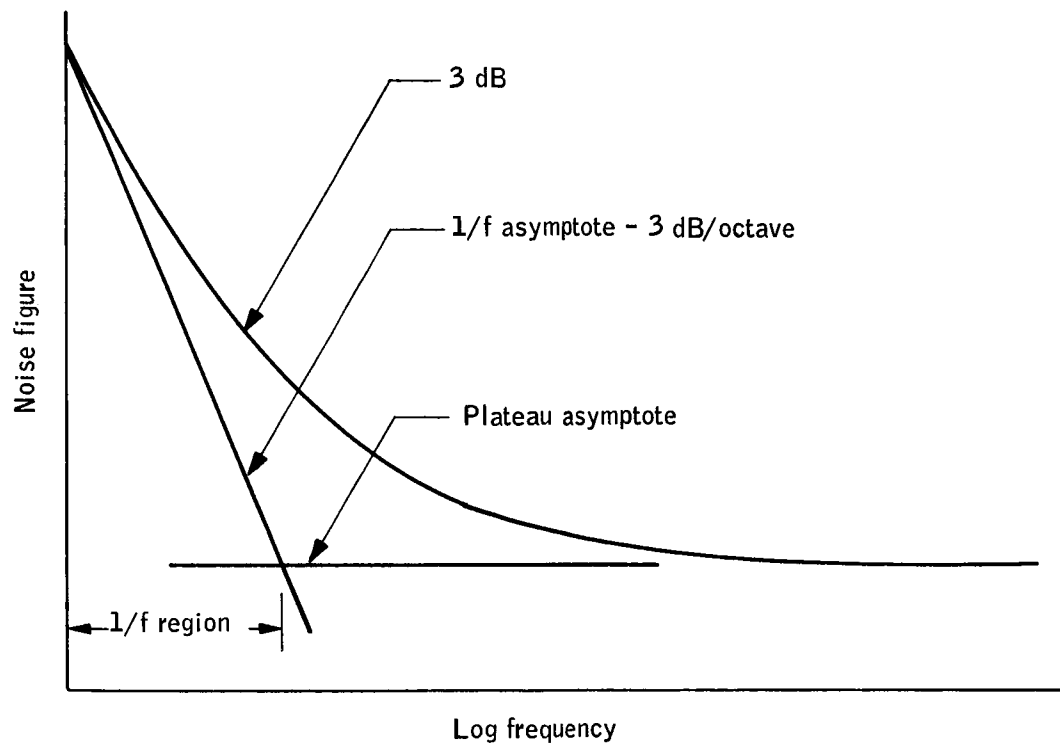
Figure 39. I/F Noise Characteristics for the FET

For a source resistance R_g = 0.5 x 10^6 ohms and a bandwidth Δf = 1.6 x 10^3 Hz, the noise e_n in a 500 K ohm resistor at 200°K is given by

$$e_n = (4 \times 1.38 \times 10^{-23} \times 200 \times 1.6 \times 10^3 \times 0.5 \times 10^6)^{1/2} = 2.97 \ \mu V$$

Amplifier noise (e_{NA}) with NF = 0.6 dB is

$$e_{NA} = \sqrt{10.1 - 8.8} = 1.14 \ \mu V$$

As stated above, the noise from the detector will be 16μ volts; hence, the amplifier will contribute very little to the overall noise voltage.

The amplifier has a voltage gain of 500. The first transistor stage following the FET preamplifier has a current gain of 20, and the last stage has a current gain of 5. The transistor in the drain of the FET is a constant-current source. Frequency response is essentially flat from a few Hz to 16 kHz.

Demodulator

There are two possible methods of demodulation to obtain the horizon profile waveform from the modulated (chopped) signal; synchronous, and non-synchronous demodulation.

Synchronous . -- In this system, the demodulator is driven synchronously with the chopper so that phase as well as amplitude is recovered. The output is related to the cosine of the difference in phase angle between reference and signals. Since it is synchronized to the chopper, the chopper can change rate without having any appreciable effect on signal output.

Nonsynchronous. -- The nonsynchronous method is accomplished in an incoherent detection system using a nonlinear device and a diode rectifier and followed by a low-pass filter. This system would recover the horizon profile waveform by averaging over several chopper cycles. The incoherence effectively doubles the required bandwidth, and the nonlinearity near zero has an attendant signal-to-noise and noise-to-noise heterodyning, both of which effects result in signal-to-noise losses in this type of system.

Description of recommended method. -- The modulated signal processed from the detector through the preamplifier and amplifier is the input signal to the demodulator. The switching circuitry of the demodulator is driven by the phased, synchronized signal from the chopper. This synchronized switching of the differential amplifier input results in recovery of the horizon profile waveform as the output signal.

Analysis of recommended demodulator. -- The switching system of the demodulator requires high-quality transistor switching which exhibits sufficiently small "on" voltages and "off" currents. In the "on" state, transistor switches exhibit a small voltage source between collector and emitter. This is commonly known as "offset" voltage V_{CE} (offset) for normal operation and V_{EC} (offset) for inverted operation. The back bias which turns the device off creates temperature-dependent leakage currents. These effects produce noise and nonlinearities in circuits using transistor switches. An estimate of the lowest noise power to which the transistor can be reduced is given by the product of the "on" offset voltage and the "off" leakage current. The optimum impedance to be seen by the transistor is approximately the "on" offset voltage divided by the "off" leakage current.

Practically, the opposing actions of a pair of transistors are generally required to obtain high-quality switching performance. Connecting two transistors back-to-back tends to cancel "on" offset voltage at the expense of doubling the "on" resistance, which is not serious since load resistance is usually many orders of magnitude larger. This back-to-back connection can achieve offset matching below a $50\mu V$ difference for matched, single transistors over a temperature range of -55 to 100°C. A double-emitter transistor which consists of a single base and a single collector sharing two symmetrically placed emitters can match offset difference below $20\mu V$ from -55 to 100°C. The advantages of this double-emitter transistor over two selected back-to-back connected transistors are: (1) the proximity of its emitter-base junctions; and (2) the single, base-collector junction. The first gives greater uniformity and extremely close thermal tracking. The second improves uniformity and eliminates external collector-to-collector connections that can add error voltages which are produced by temperature differences and by the flow of base current through contact resistance. In the "off" state, this double-emitter transistor, connected as a series switch, looks very nearly like an ideal open circuit for voltages applied in either direction. However, "shunt" switching is utilized, and switching is never required to "open-circuit" either the source or the load. Overshoot, commonly called "spikes" which occur at the end of the rise or fall of the input signal, is another switching problem and is primarily the result of junction capacitance which couples fast change in base drive voltage into the load. Junction capacitances might be considered the most important parameters in transistor switching since switching time will be slow and the spikes large if junction capacitances are large. Good switching performance is predicted from parameters C_{ib} and C_{ob} which are the zero-biased junction capacitances and from f_T which is the frequency at which the magnitude of hfe (forward current gain transfer ratio) is numerically "one" for a collector current of one mA or less. When this frequency f_T is six MHz and the junction capacitances are each 10 pF, the switching times are fair and improve as F_T is increased and junction capacitances are reduced. The double-emitter transistor has very small junction capacitances and high f_T; e.g., 4 pF for C_{ib} and 60 MHz for f_T.

The shunt switching used here, showing a short circuit rather than an open circuit to either the source or the load, presents a low contrast to impedance levels and should give no transient problems.

The switching system is followed by a high-performance, low-drift differential amplifier microcircuit with capacitive feedback. This differential amplifier will provide both gain and the post-detection filtering. The amplified output will be designed to feed the converter in the data-transmission module.

OPTICAL SYSTEM

The performance of the optical system is defined by the following parameters:

- Resolution

- Effective aperture

- Thermal emission

- Stray radiation

- Alignment stability

- Spectral response

Requirements on these parameters have been developed in the previous discussion on system analysis and will be summarized here.

The optical resolution should be essentially diffraction limited for an angular resolution element of 2×10^{-4} radian diameter. The actual resolution element size will be a maximum of 2×10^{-4} radian in elevation and a minimum of 6×10^{-4} radian in azimuth. For the purposes of the feasibility design, the azimuth resolution will be taken at 8×10^{-4}. Optical resolution will be such that at least 90 percent of the energy, excluding transmission losses, from the resolution element in object space is contained in the corresponding, resolution element at the focal surface. This requirement is to be met for an optical system temperature of $200 \pm 20°K$. This resolution requirement is derived from the system transfer function analysis and its effects upon sensitivity and accuracy, not resolving power. From that analysis it is apparent that this requirement can be traded against other contributors to the system transfer function and, moreover, that the accuracy and sensitivity are not particularly sensitive to small variations in the optics transfer function.

Specifically, with respect to controlling defocus a degradation to 80 percent of the energy in a resolution element is certainly tolerable.

The effective aperture is expressed as $\dfrac{D\delta_o}{f/no.}$, where D is the geometrical aperture diameter, δ_o is optical transmission including all losses up to the spectral filter, and $f/no.$ is the f/number of the optics.

The requirement is:

$$\frac{D\delta_o}{f/no.} \geq 25 \text{ cm}$$

In addition, the requirement on resolution indicates a minimum diameter of 40 cm.

Both accuracy and sensitivity performance of the radiometer can be jeopardized by thermal emission characteristics of the optics and their associated mechanical structures. Steady-state emission can limit the detector D^*; temporal variations may perturb detector response linearity; and spatial variations can appear as spurious signals if they are chopped. Therefore, the emissivity of the optical system elements and temperature and emissivity gradients shall be minimized.

As a design goal, sufficient baffling shall be introduced to reduce the effects of radiation from all sources originating from beyond the instantaneous field of view to below the level equivalent to detector noise.

The alignment of the optical line of sight shall be maintained and known with respect to a defined reference surface to within ± 4 seconds of arc. This requirement applies through launch and when the system is at its nominal operating temperature of 200° ± 20° K.

The spectral response of the instrument shall extend from 14.0 to 16.28μ over which band the integrated transmission of the spectral filter shall be at least 50 percent. Outside of the band, transmission shall decrease to 10 percent of peak in the first 0.1μ and to $< 5 \times 10^{-7}$ at wavelengths shorter than 2.5μ.

Alternate Approaches

Refractive system. -- A refractive primary element for the radiometer was discarded primarily because of its comparatively heavy weight and chromatic aberrations. If it is assumed that the objective is a germanium, symmetrical biconvex lens with a 40-cm diameter, an 80-cm focal length, and a 10-cm thickness, the weight may be approximated by calculating the volume of a half cylinder of the same thickness. Thus,

$$V = \frac{\pi D^2 t}{4}$$

$$= \frac{10\,\pi}{4} \quad (40)^2$$

$$= 40\,000\,\pi$$

$$= 12\,560\ cm^3$$

The density of germanium is 5.327 g/cm^2 at 27°C; thus the weight of the objective lens at sea level is 37 000 or 147 pounds. This is an optimistic estimate as achromatizing would probably require two such lenses.

This value may be compared to the weight of an aluminum parabolic reflector of the same diameter. A parabola may be described by the equation, $y = x^2$. Since y would be one half the diameter or 20 cm, the depression x would equal $\sqrt{20}$ or 4.5 cm. If it is assumed that the thickness of the mirror blank is 1.5 times that of the depression, a cylinder results which is 6.75 cm deep by 50 cm in diameter with a depression in the middle. The depression volume is

$$vol. = \int_0^{4.5\ cm} \pi y^2\ dx$$

$$= \pi \int_0^{4.5} x^4\ dx = \frac{\pi}{5}\ x^5 \Big|_0^{4.5}$$

$$= 1130\ cm^3$$

The cylinder volume is

$$\frac{\pi D^2 t}{4} = \frac{2500 \times 6.75 \times \pi}{4} = 13\,200\ cm^3$$

Net volume is then 13 200 - 1130 = 12 070 cm^3.

The weight, therefore, is 2.7 g/cm^3 x 12 070 cm^3 = 32 700 g (2.2 x 10^{-3} lb/g)

$$= 73.5\ pounds$$

98

The refractive system, at the very least, is twice as heavy as the reflector mounting; fabrication difficulties are greater; and the amount of scattered radiation also increases. In addition, the refractive system has no resolution advantages; therefore, a reflector was chosen for the objective element of the optical system.

Reflective systems. - The four types of reflective optical systems (Cassegrain, on-axis Newtonian, classical Newtonian, and off-axis parabolic) were investigated as possibilities for the radiometer and are shown schematically in Figures 40 through 43. The Cassegrain and the on-axis Newtonian are unacceptable because they require one additional folding mirror and will allow only one half the baffle length of the other two systems. The axis of symmetry of the cryogenic cooler for the detector must coincide with the spin axis of the spacecraft so that the center of gravity of the spacecraft will only shift along this axis during flight. Figures 40 and 41 show that this restriction dictates that the parabolic reflector of the Cassegrain and off-axis Newtonian systems must be placed in front of the center line of the spacecraft. These systems may be compared with Figures 42 and 43 where the reflector may be placed well behind the center line. For optimum baffling of stray radiation, the baffle tube in front of the reflector must be as long as possible. The Cassegrain and the on-axis Newtonian systems were eliminated because they use only one half the length of the spacecraft for baffling, whereas the classical Newtonian and the off-axis paraboloid use the entire length.

The classical Newtonian and the off-axis paraboloid were analyzed to establish their resolution capabilities. The spot diagrams of the three systems analyzed are shown in Figures 44 through 46. Figure 44 is for a classical Newtonian with an 80-cm focal length and a 40-cm diameter at four off-axis field positions of the object, 0.2, 0.5, 0.7 and 1.0 milliradian. Figure 45 is the spot diagram of a classical Newtonian with a 60-cm focal length and a 40-cm diameter (f/1.5) for the same four field angles. Figure 46 is the result of an off-axis paraboloid with a focal length of 60 cm and diameter of 40 cm for objects at the four field positions. Because an off-axis paraboloid is fabricated by cutting the reflector out of the radius of a larger paraboloid, the maximum f number of the system is one half the focal ratio or

$$\text{f-number}_{\text{max.}} = \left(\frac{60}{40}\right) (0.5) = 0.75$$

This, however, is not a practical configuration because the image is located on the axis which originates at the rim of this reflector. The system which was analyzed was an f/0.5 paraboloid which is the largest practical focal ratio such as is shown in Figure 43.

The scale of the spot diagrams is distance in image space measured in centimeters; therefore, the linear dimension of a resolution element in image space must be known to compare the diagrams. One resolution element subtends 0.2 milliradian which equals 0.012 cm in image space for the two
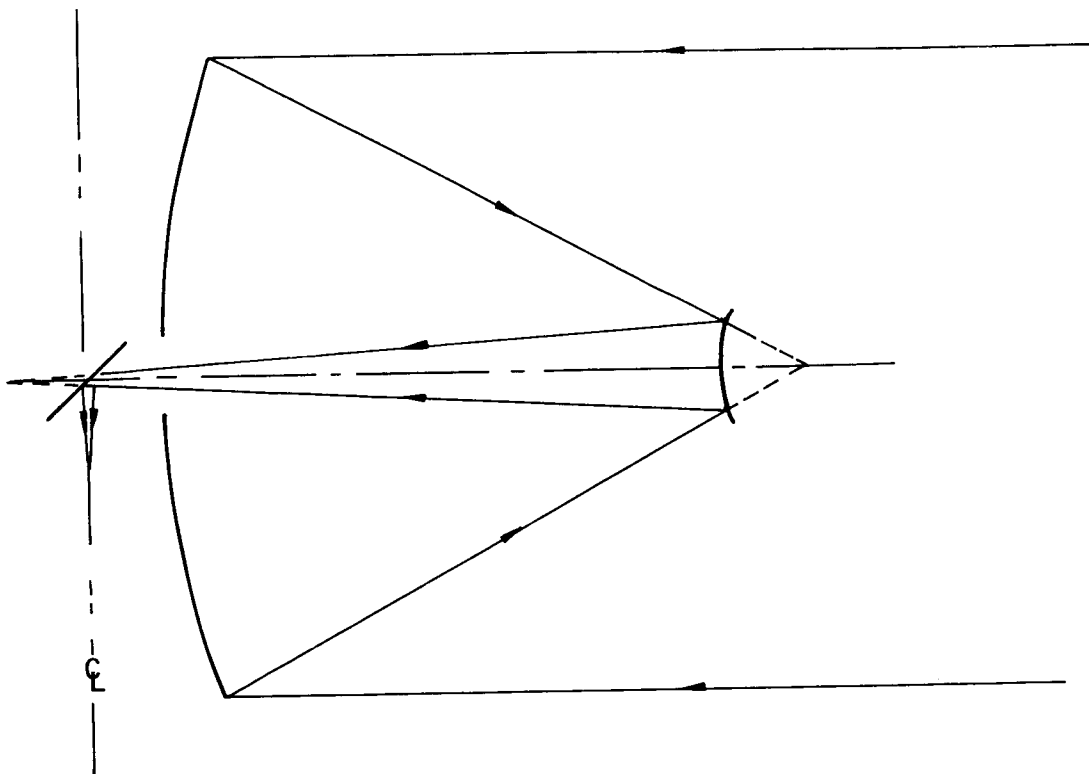
Figure 40.   Cassegrain Reflective Optical System
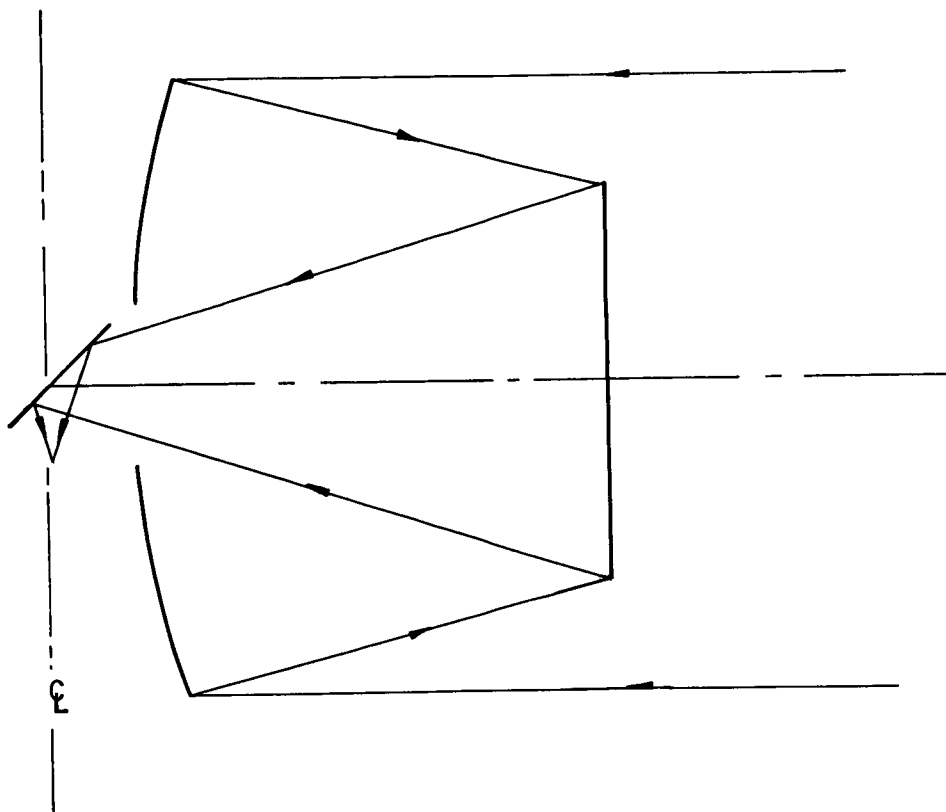
Figure 41. On-Axis Newtonian Reflective Optical Systems
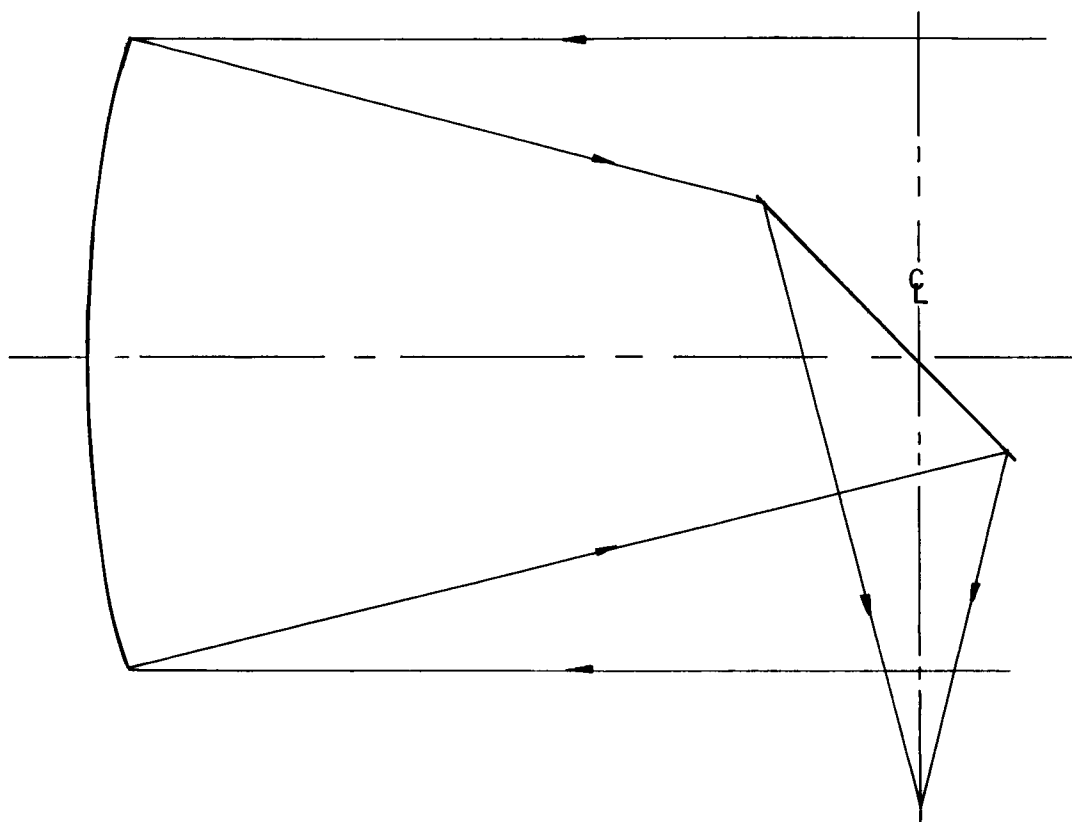
Figure 42. Classical Newtonian Reflective Optical System
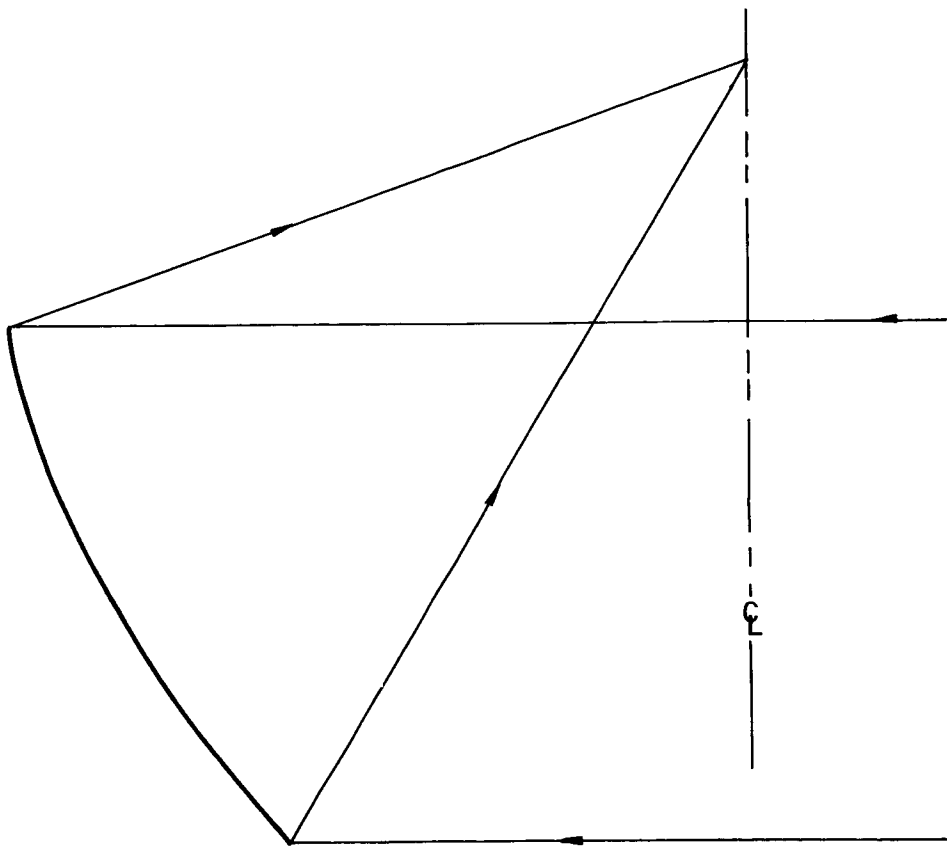
Figure 43.   Off-Axis Parabola Reflective Optical System
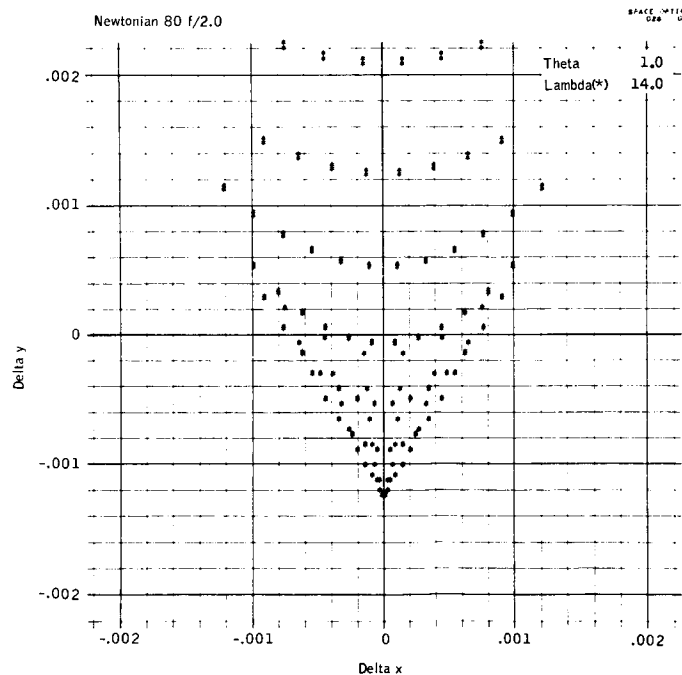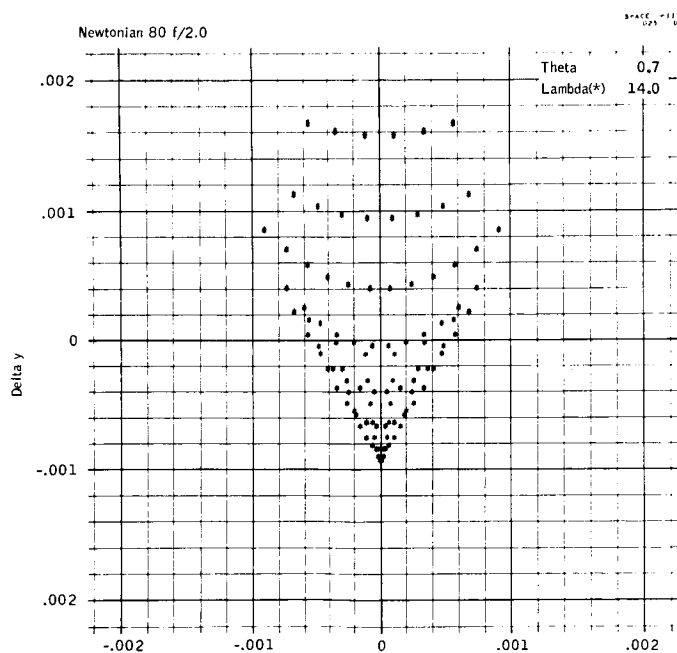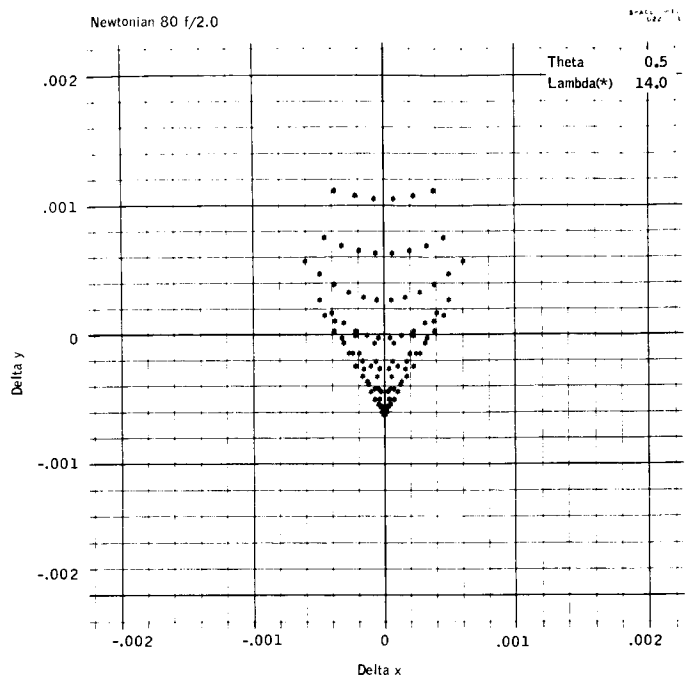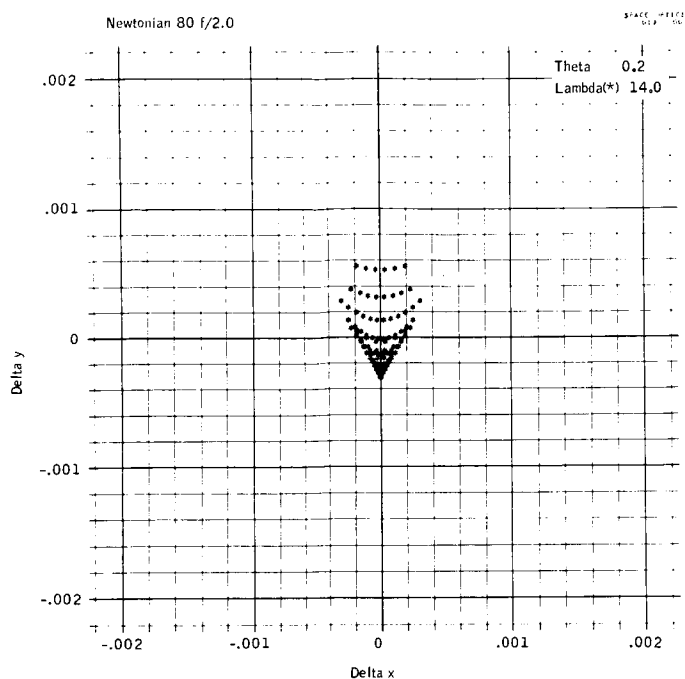
Figure 44. Spot Diagrams of Classical Newtonian with an 80-cm
Focal Length and a 40-cm Diameter, f/2.0
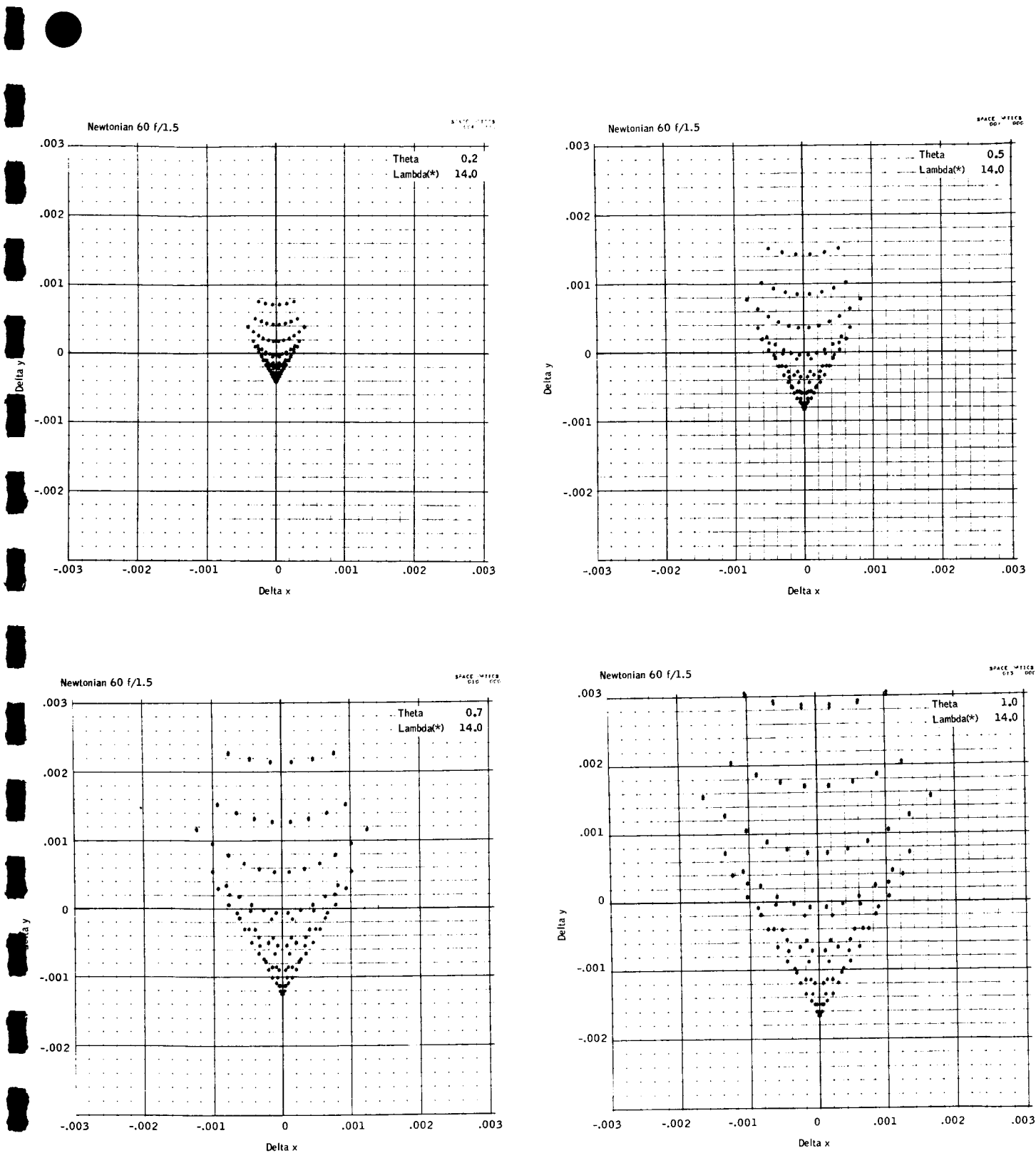
Figure 45. Spot Diagrams of Classical Newtonian with a 60-cm
Focal Length and a 40-cm Diameter, f/1.5
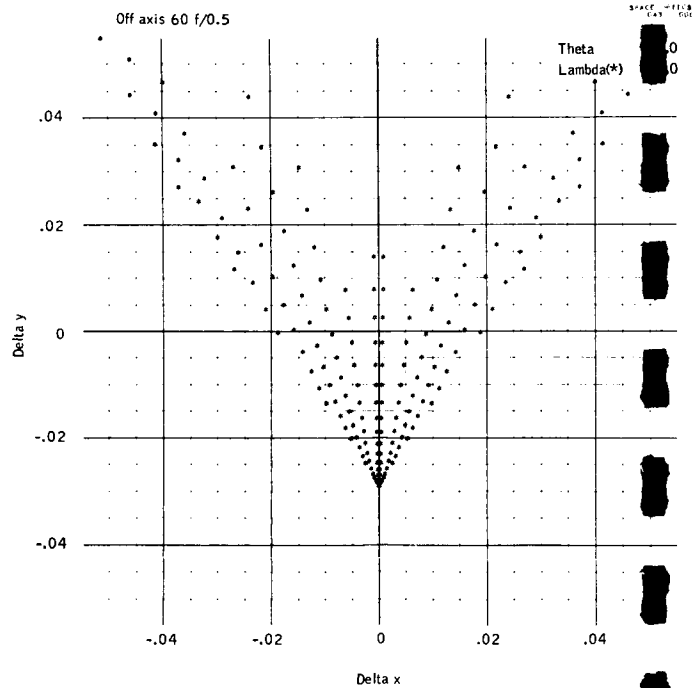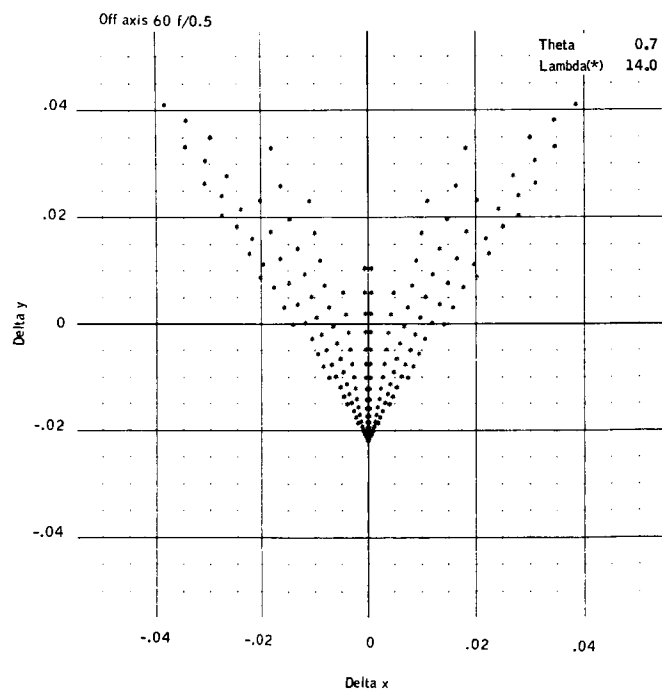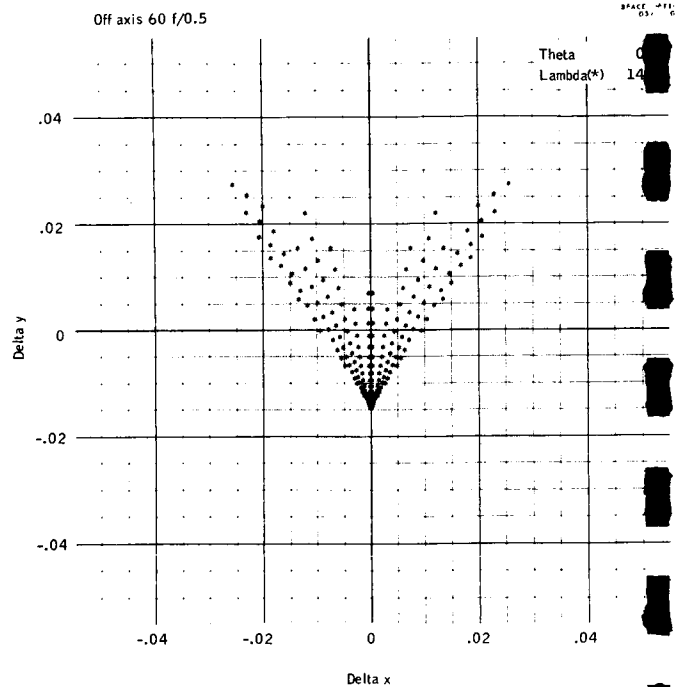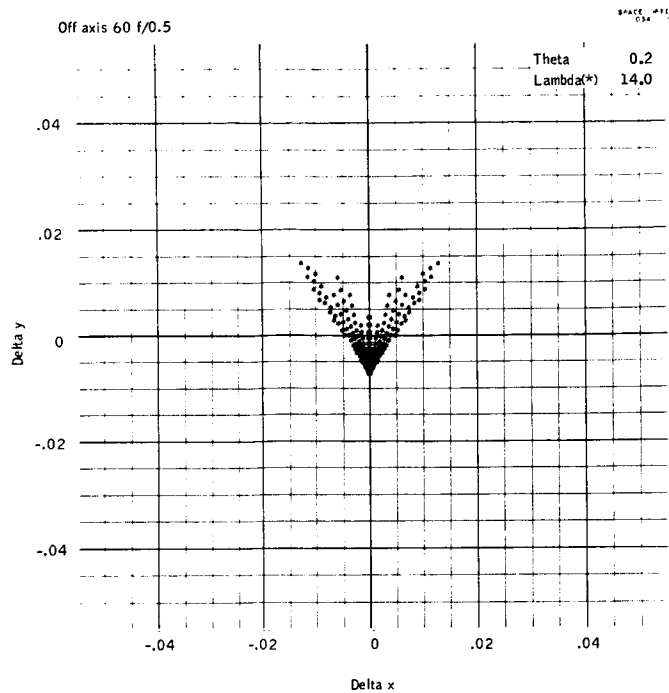
Figure 46. Spot Diagrams of Off-Axis Paraboloid with a 60-cm
Focal Length and a 40-cm Diameter, f/0.5

60-cm focal length systems and 0.016 cm for the 80-cm focal length system. The spot diagrams may be compared by their diameters with that of the diffraction pattern. Because all three systems use a 40-cm entrance pupil, the angular radius of the diffraction pattern to the first dark ring may be found by the equation for Fraunhofer diffraction by a circular aperture. This angle is

$$\theta_1 = (1.22) \frac{\lambda}{D}$$

$$\theta_1 = 0.046 \text{ milliradian}$$

Angular radius corresponds to a linear diameter of 0.0055 cm in image space for the two 60-cm focal length systems and 0.0073 cm for the 80-cm focal length system.

Comparison of the spot diagrams shows that with the f/2 classical Newtonian system with a focal length of 80 cm, the geometric blur diameter measures approximately 30 percent of the resolution eelment size and 65 percent of the diffraction pattern radius at the worst case of one milliradian off axis. The spot diagram for the 60-cm focal length, f/1.5 classical Newtonian system shows that the geometric blur is approximately 55 percent the size of a resolution element and approximately equal to the size of the diffraction pattern at the one milliradian off-axis position. The spot diagram for the f/0.5, off axis paraboloid shows that at the best case of an object 0.2 milliradian off axis the geometric blur is approximately the same size as the resolution element, which is equal to twice the diameter of the diffraction pattern. As Figure 46 demonstrates, the diameter of the spot diagram increases rapidly for objects further off-axis; the geometric blur for 100 percent of the energy for an object 1.0 milliradian off-axis is approximately ten times the size of a resolution element. Table 7 summarizes the data by showing the angular diameter of the geometric blur for the three systems at five values of percent of encircled energy.

Further data concerning the resolution of the three systems are contained in the modulation transfer functions which are shown in Figures 47 through 49. These functions present much the same type of information as found in the spot diagrams. They are calculated by integrating the spot diagram in one direction to form the spread function

$$A(x) = \int_{\infty}^{\infty} a(x, y) \, dy$$

The sine and cosine Fourier transforms of the spread function are then calculated for each desired spatial frequency ν for example,

TABLE 7. - COMPARISON OF RESOLUTION OF REFLECTIVE SYSTEMS

System	Field angle off-axis, mrad	Blur radius (mrad) at % encircled energy				
		10%	30%	50%	80%	100%
Newtonian, 60-cm focal length, D = 40 cm, f/1.5	0.0	0.0	0.0	0.0	0.0	0.0
	0.25	0.0050	0.0072	0.0090	0.0132	0.0266
	0.50	0.010	0.0142	0.0182	0.0270	0.0536
	0.75	0.0150	0.0216	0.0272	0.0402	0.0802
	1.00	0.0202	0.0290	0.0362	0.0536	0.1072
Newtonian, 80-cm focal length, D = 40 cm, f/2.0	0.0	0.0	0.0	0.0	0.0	0.0
	0.25	0.0026	0.0040	0.0050	0.0074	0.0146
	0.50	0.0056	0.0080	0.0100	0.0124	0.0294
	0.75	0.0084	0.0120	0.0152	0.0224	0.0444
	1.00	0.0112	0.0160	0.0202	0.0300	0.0592
Off-axis parabola, 60-cm focal length, D = 40 cm, f/0.5	0.0	0.0	0.0	0.0	0.0	0.0
	0.25	0.0840	0.1326	0.1710	0.2736	0.6266
	0.50	0.1680	0.2652	0.3568	0.5470	1.2522
	0.75	0.2520	0.3976	0.5300	0.8196	1.8766
	1.00	0.3360	0.5300	0.7060	1.0922	2.5002
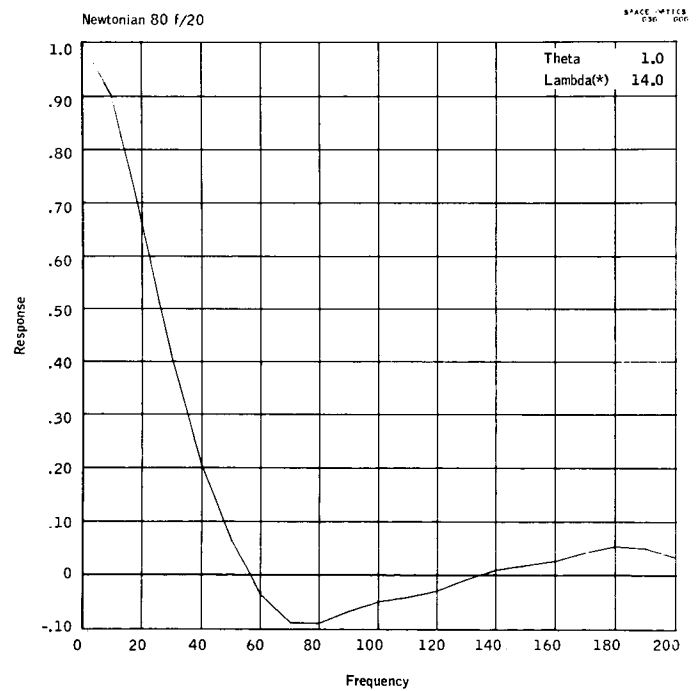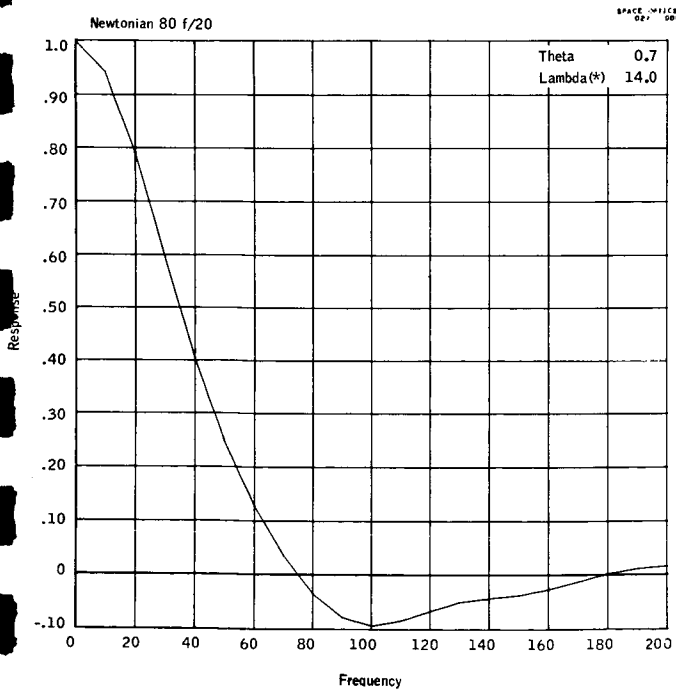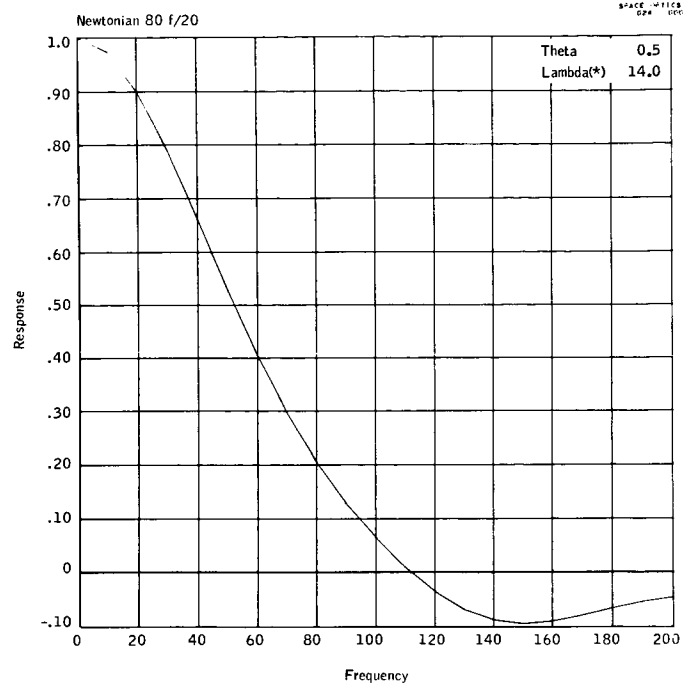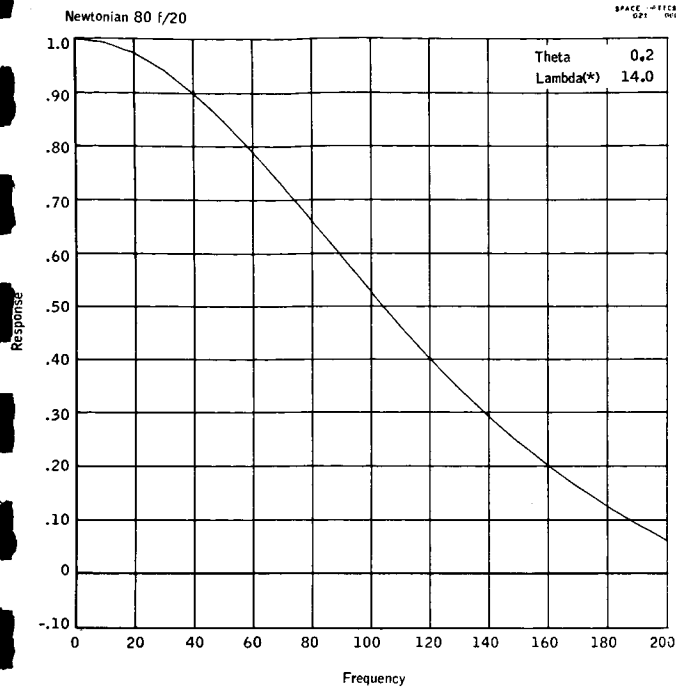
Figure 47. Modulation Transfer Functions of Classical Newtonian
with an 80-cm Focal Length and a 40-cm Diameter, f/2.0
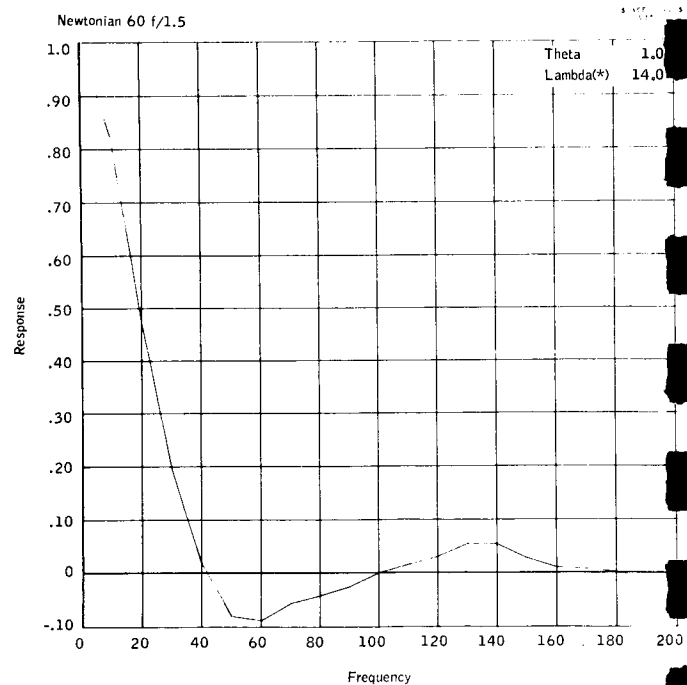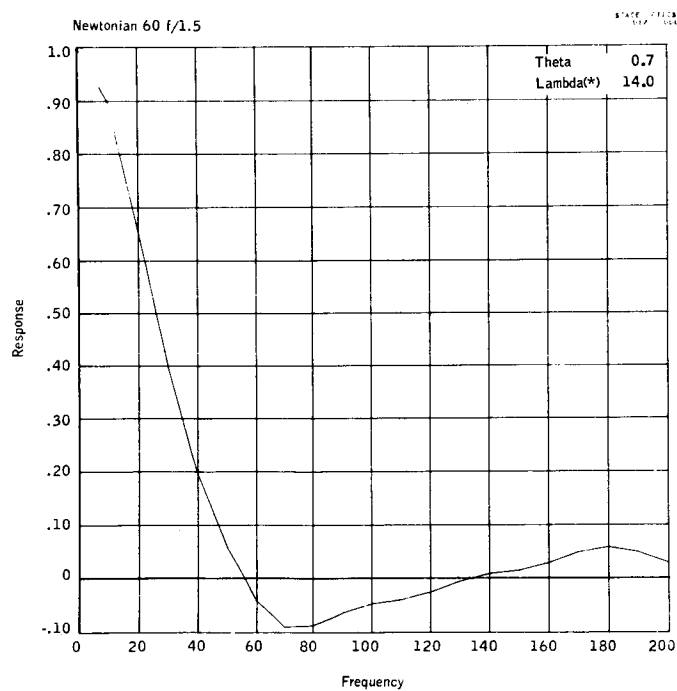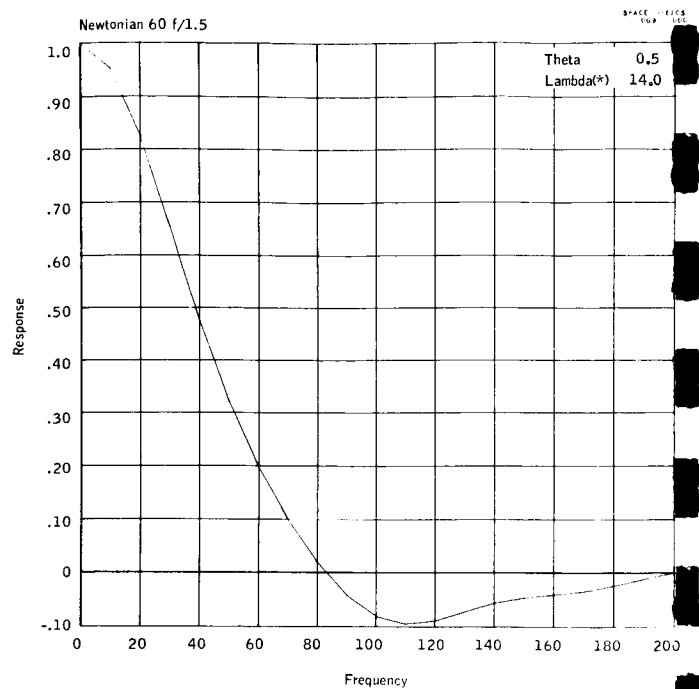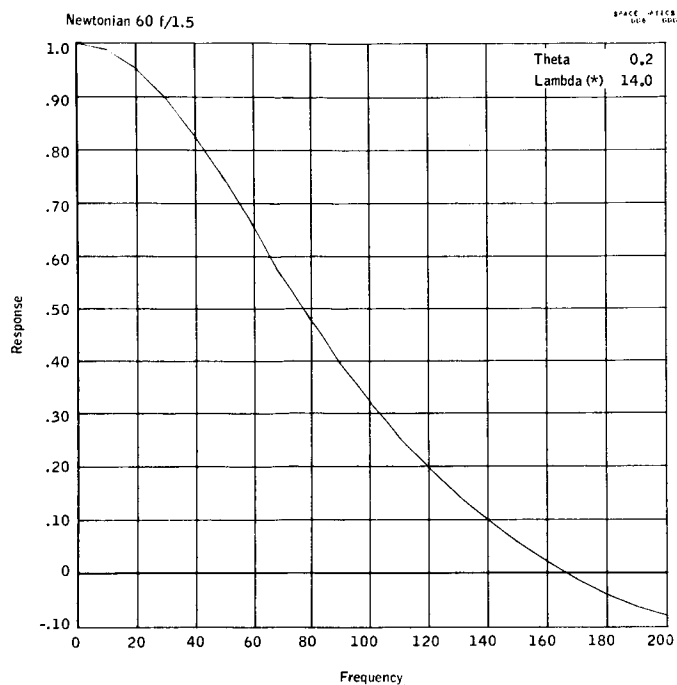
Figure 48. Modulation Transfer Functions of Classical Newtonian
with a 60-cm Focal Length and a 40-cm Diameter, f/1.5
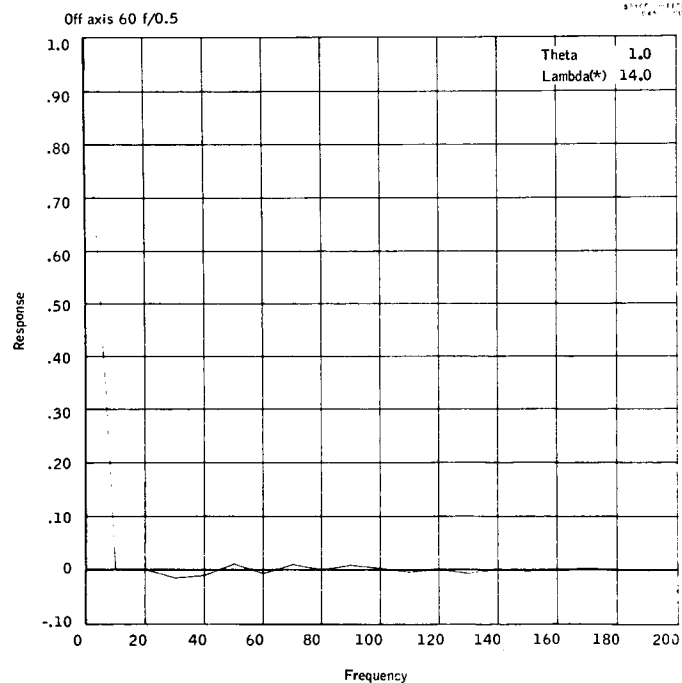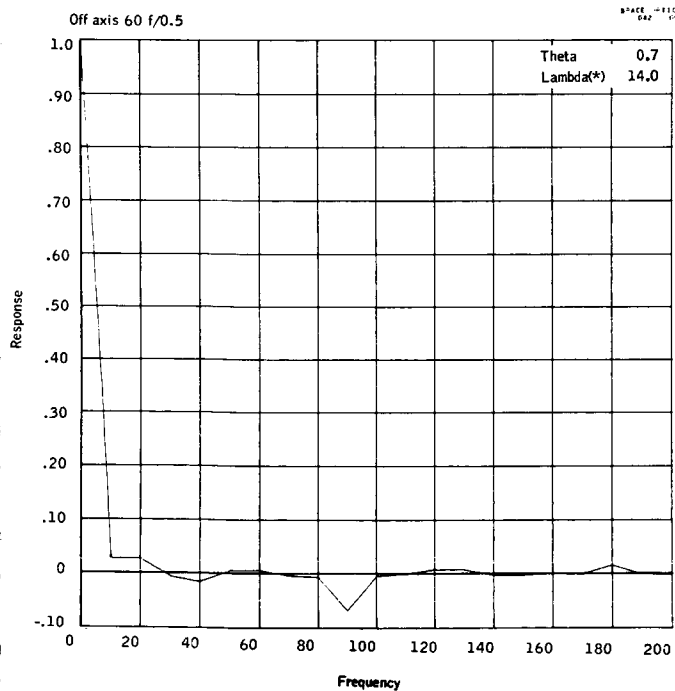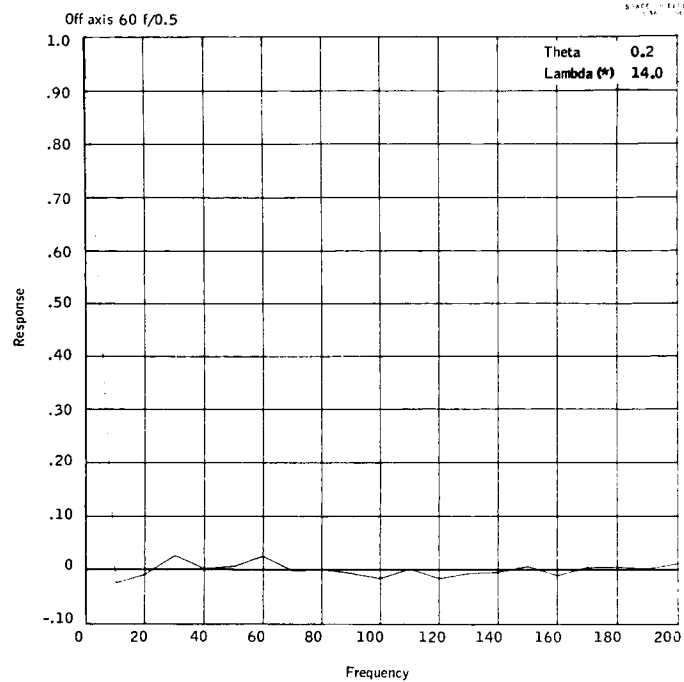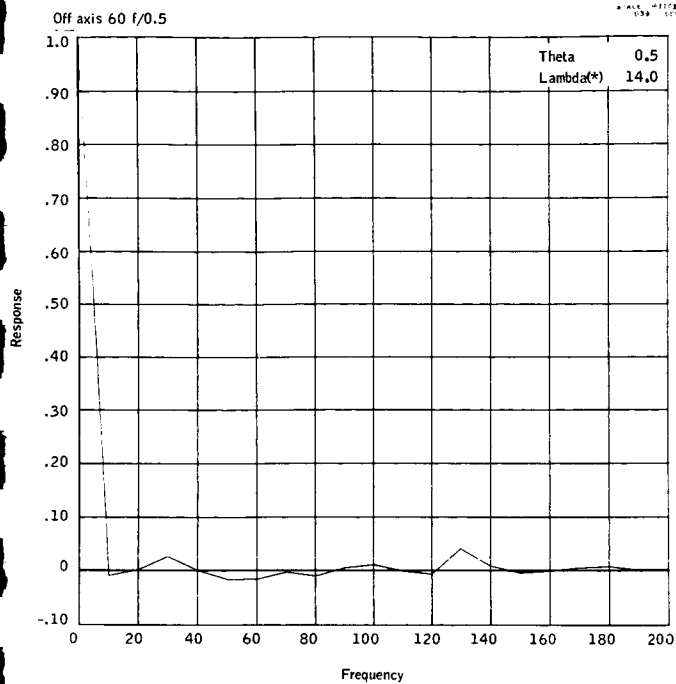
Figure 49. Modulation Transfer Functions of Off-Axis Paraboloid with a 60-cm Focal Length and a 40-cm Diameter, f/0.5

111

$$A^{\#c}(\nu) = \int_{\infty}^{\infty} A(x) \cos 2\pi \nu\, x\, dx$$

The transforms are then treated as mutually orthogonal vectors whose resultant is the value of the modulation transfer function at each spatial frequency.

Of particular interest in these functions is the response at the spatial frequency which corresponds to a resolution element which is 0.2 milliradian (or 5 milliradian^{-1}). Linear spatial frequency as shown in Figures 47 through 49 is 6.26 mm^{-1} for the 80-cm focal length system and 8.34 mm^{-1} for the two 60-cm focal length systems. Summarized in Table 8 are the responses of the three systems at this frequency. The values given for the off-axis parabola may be rather inaccurate due to the high negative slope of the functions. In addition, the geometric blur due to abberrations and the energy distribution from Fraunhofer diffraction by the aperture have been treated separately in this analysis, whereas the true system response is a convolution of the two effects.

Recommended System

The configuration of the recommended optical system must be chosen by consideration of the following requirements:

1) The components in which a failure can occur must be made redundant, either by the use of two complete radiometers, or by duplicating only the chopper, detector and in-flight calibration sources.

2) The radiometer(s) including all structures, mounts, and stray radiation baffles must fit within the 54-inch diameter hexagonal spacecraft.

3) The field of view must be 0.2 milliradian in the direction of the earth's radius and sufficiently large in the other direction to assure that the radiant power on the detector is at least equal to the three-sigma noise level of the detector when measuring the point of minimum radiance of the horizon.

4) The field of view cannot be extended beyond the point where the off-axis geometric aberrations (coma) at the edge of the field significantly affect the size of the resolution element.

5) The optical design of the system should use as few elements as possible to minimize the amount of thermal emission radiation on the detector.

6) The system should be simplified as much as possible to increase the ease and accuracy of alignment.

TABLE 8. - MODULATION TRANSFER OF THREE REFLECTIVE
SYSTEMS AT FIVE CYCLES/MILLIRADIAN

System	Half-field angle, milliradians	Response
Newtonian, 80-cm focal length, f/2.0	0.2	.99
	0.5	.97
	0.7	.96
	1.0	.93
Newtonian, 60-cm focal length, f/1.5	0.2	.98
	0.5	.96
	0.7	.92
	1.0	.86
Off-axis parabola, 60-cm focal length, f/0.5	0.2	(.15)
	0.5	(.15)
	0.7	(.15)
	1.0	(.15)

Initial considerations of the classical Newtonian and the off-axis paraboloid alternatives show that the greatest advantage of the off-axis paraboloid is that it fulfills the fifth and sixth requirements and eliminates the folding mirror of the Newtonian system.

Interpolation of the data of Figure 50 indicates that the half-field angle for an off-axis paraboloid cannot exceed 0.1 milliradian if 90 percent of the geometric blur diameter is to fall within the 0.2 milliradian resolution element. The maximum field of view for this system then would be 0.2 x 0.2 milliradian. Figure 51 shows that a much larger field of view could be used if necessary with the f/2.0 Newtonian system. The extrapolation shown indicates that for an object 1.4 milliradian off axis 100 percent of the energy of the geometric blur would fall well within the 0.2 milliradian resolution element.

The two systems may now be compared to find the required system efficiency with the given values of the field of view by calculating the noise equivalent radiance (NER) for the radiometer for each case. The NER of the detector is found by
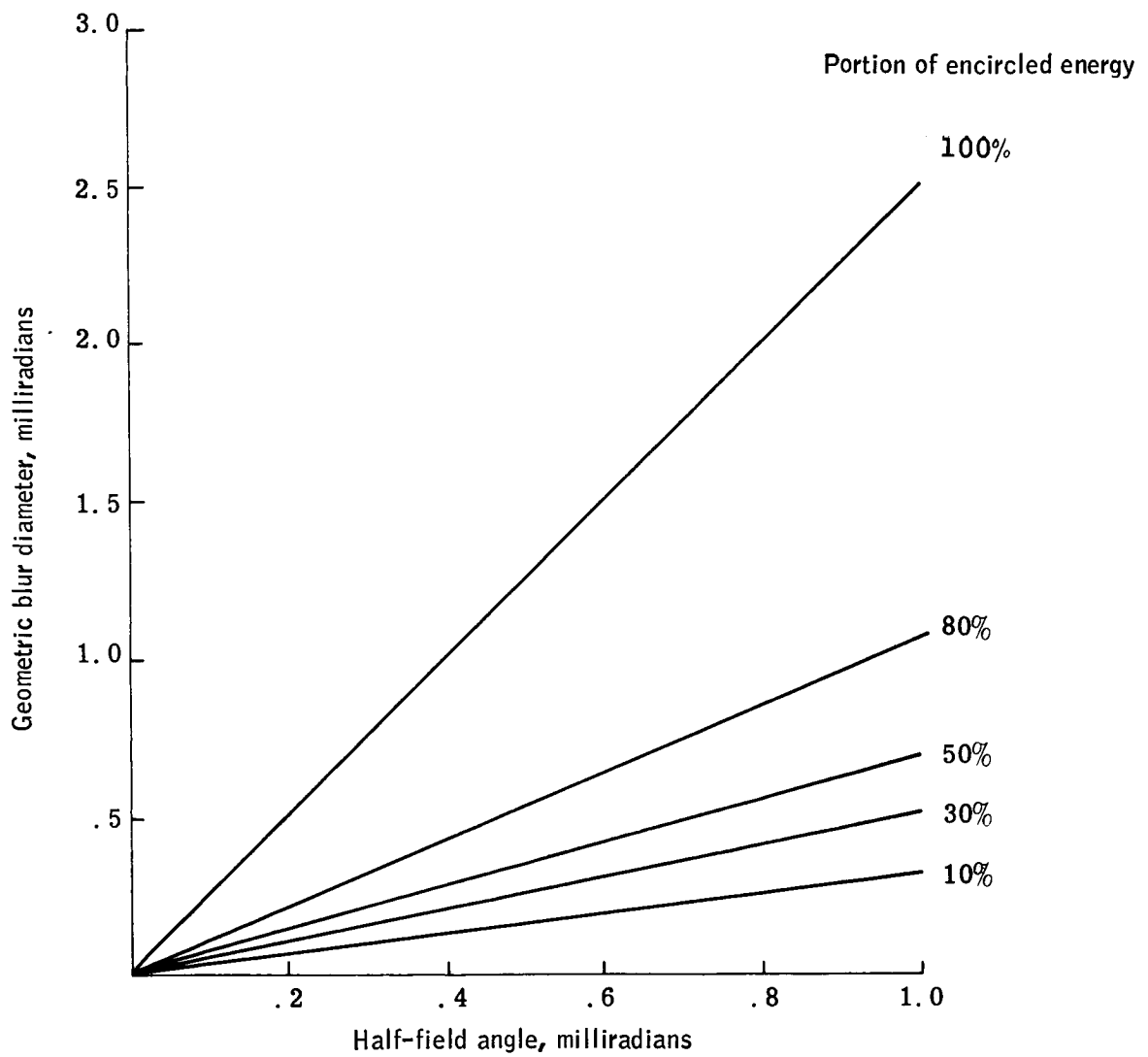
Figure 50. Geometric Blur Diameter for a f/0.5 Off-Axis Paraboloid

114
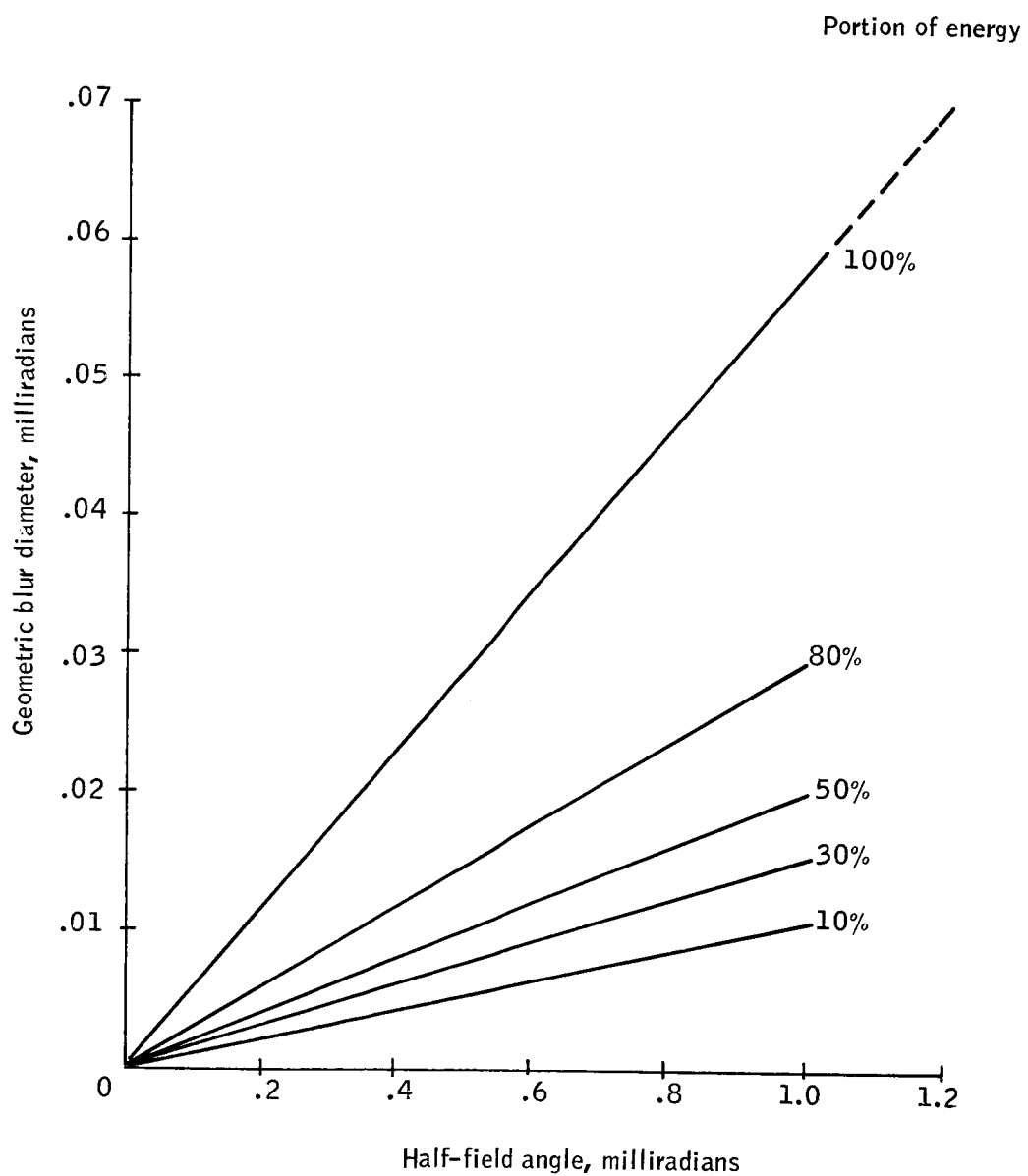
Figure 51. Geometric Blur Diameter for a f/2.0 Classical
Newtonian Design

$$NER = \frac{\sqrt{A_o} \sqrt{\Delta f}}{D_\lambda^* \ \Delta\Omega \ \delta \ A_c}$$

where:

A_o = area of the detector

Δf = system bandwidth

D_λ^* = detectivity of the detector

A_c = collecting aperture area

δ = system efficiency

$\Delta\Omega$ = detector field of view

From the assumptions that:

(1) The minimum practical length for a side of a detector is 80μ;

(2) A re-collector lens would be used with either system to focus the energy onto the smallest possible detector; and

(3) Both systems use the same collecting aperture size.

The differences can only be in the factors $\Delta\Omega$ and δ. As tabulated below, these are:

	$\Delta\Omega$, mrad	δ
Classical Newtonian	0.2 x 0.8	$0.8 \times (0.98)^2 \delta_r$
Off-axis parabola	0.2 x 0.2	$0.8 \times 0.98 \ \delta_r$

Where δ_r is the loss common to both systems. The difference in δ is solely due to the central obscuration in the classical Newtonian. Since detector size is proportional to $\Delta\Omega$, the net decrease in NER is proportional only to the square root of the ratio of the $\Delta\Omega$'s. Thus, the classical Newtonian is approximately 1.5 times as effective as the off-axis parabola for the same aperture size.

The next comparison of the two systems is the method of duplicating the critical components. It is apparent that there is no necessity to duplicate the primary mirror because any possible failure due to the space environment is experimenced by both mirrors. Therefore, only the chopper, the detectors and the in-flight calibration source need be redundant. Figure 52 diagramatically illustrates the advantage of using a single primary. This is a top view of the spacecraft
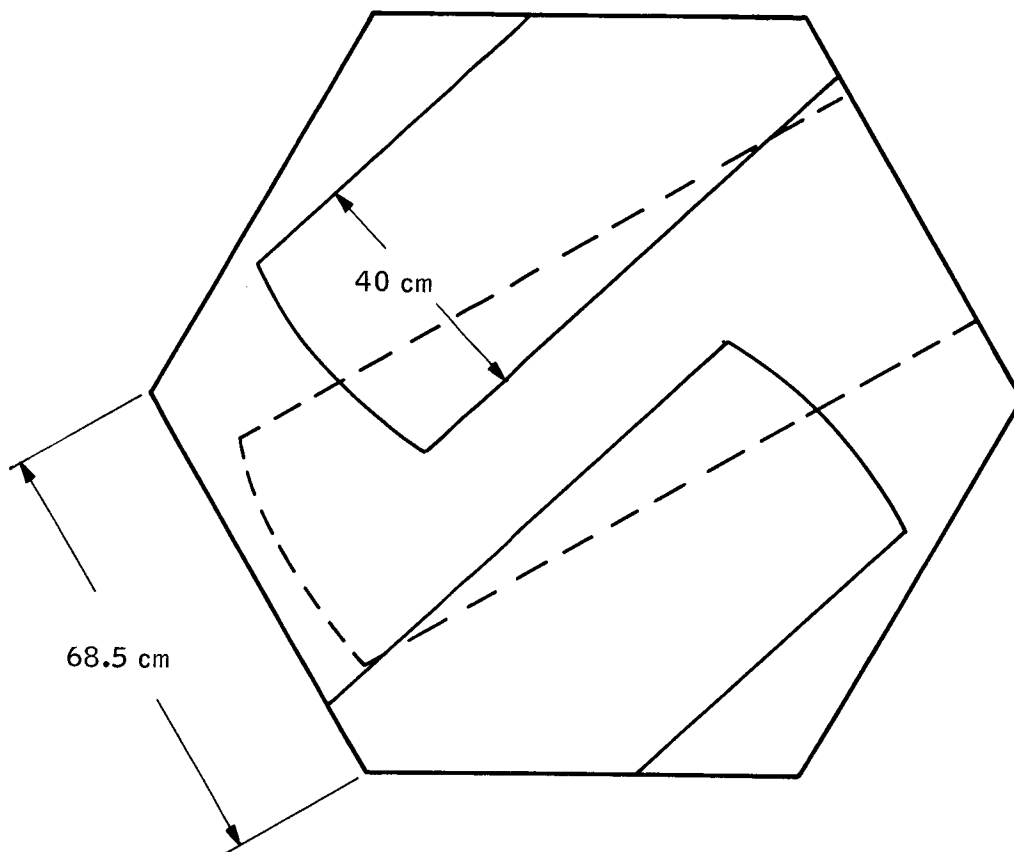
Figure 52. Layout of Single and Dual Radiometers within the Spacecraft

showing the necessary placement of the two primary mirrors if they were duplicated as compared with a single primary mirror system. The placement of the two primaries decreases the available baffle length as well as increasing the difficulty of alignment because of the lack of orthoganality.

The method of duplicating the critical components without duplicating the primary is to place two field stops side by side in the focal plane of the primary mirror. These two stops are symmetrical about the optical axis with a separate chopper for each. A single re-collector lens is placed behind the field stops which focuses them onto the two detectors. This method is illustrated in Figure 53. Consideration of the field-of-view requirements shows that this method could not be used with the off-axis paraboloid. The resolution requirements have dictated that a point can be no more than 0.1 milliradian off axis with the paraboloid; however, with the dual field-stop configuration, each stop must be at least 0.2 milliradian from the axis to allow sufficient separation of the choppers. Therefore, if a classical Newtonian design is used, a single primary with redundant choppers and detectors is possible; if an off-axis paraboloid is used, two complete systems will be necessary.

Description of a Recommended System

Consideration of all of the comparisons of the two optical systems has lead to the selection of an 80-cm focal length, f/2.0 classical Newtonian design. A drawing of this system is shown in Figure 54. This design uses a single primary parabolic mirror which is 40 cm in diameter and 80 cm in focal length.

The optical path is folded by a flat secondary mirror onto the two field stops which are situated in the image plane of the primary. The field of view of each field stop is 0.2 x 0.8 milliradian and they are separated by 0.025 inch or 0.8 milliradian. Mirror choppers are located in front of each of the two field stops to modulate the signal. Radiant energy is focused onto the two detectors by a re-collector lens at a magnification of 0.5. The detectors therefore, are the size that would be used with an f/1 system which is 80 x 320μ. The geometric aberration blur diameter is, of course, a function of the off-axis angle which extends from 0.4 milliradian to 1.2 milliradians. The spot diagrams for four positions across the field stop are shown in Figure 44, and the blur diameter data are summarized in Figure 47. As previously mentioned, at the full field position 1.2 milliradians off-axis blur diameter is approximately 35 percent of the resolution element size. The modulation transfer function for this system, as shown in Figure 51, will vary from 0.97 at 0.4 milliradian and may be extrapolated and found to be 0.91 at 1.2 milliradians.

The thermal emission of radiation by the optical components is of concern primarily from those elements which precede the chopper, i.e., the primary and secondary mirrors. This power may be calculated by deriving an equation for the system. Radiant power from the thermal emission of the primary mirror which falls within the area of one of the field stops is given by

118
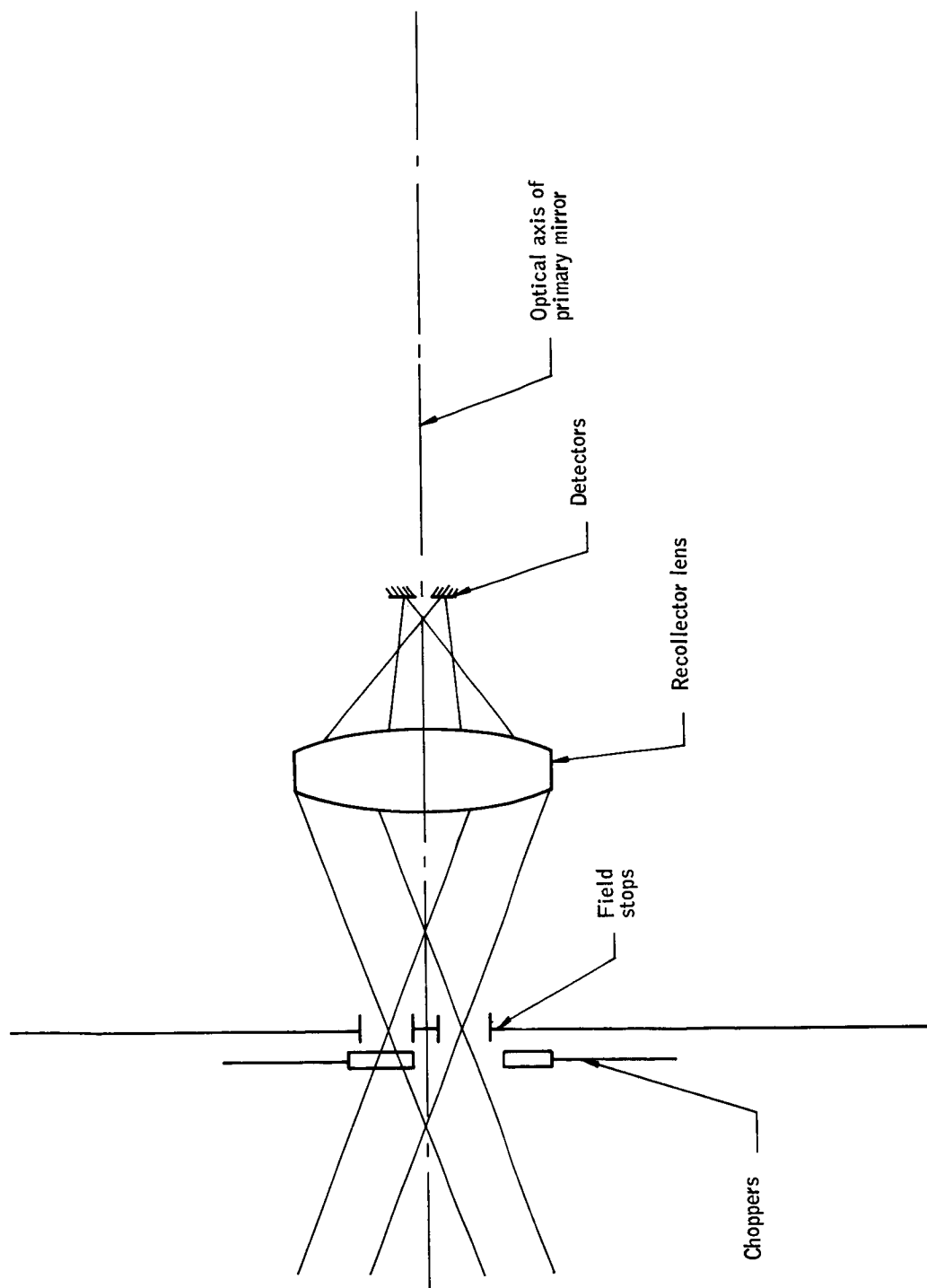
Figure 53. Sketch of Redundant Chopper and Detector System

Optical axis of primary mirror

Detectors

Recollector lens

Field stops

Choppers
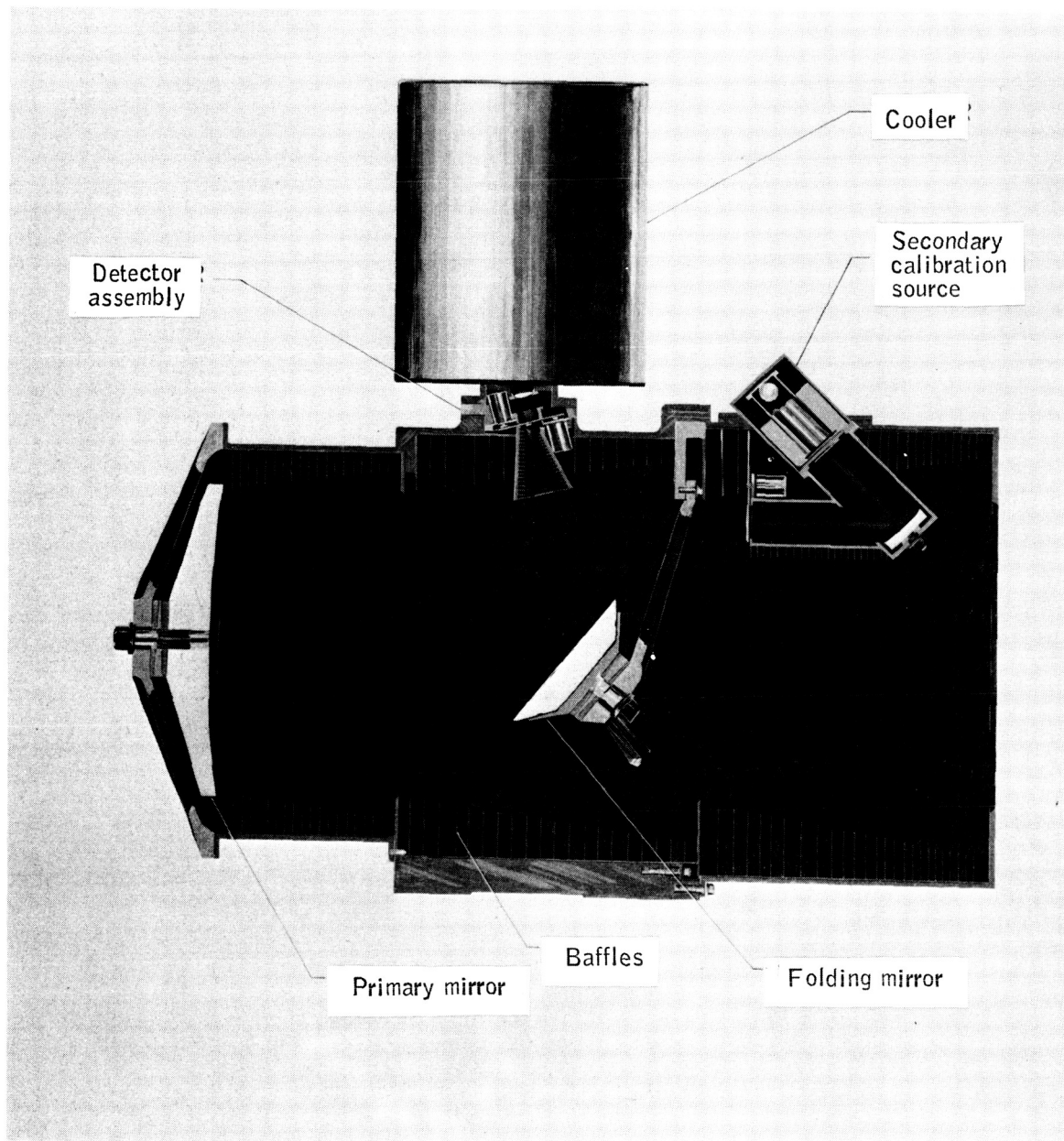
Figure 54. Radiometer

$$P_p = N_p A_p \Omega_{Fp} \rho_s$$

N_p = radiance of the primary in the 14-to 16-μ band.

A_p = area of the primary,

Ω_{Fp} = solid angle subtended by the field stop from the primary, and

ρ_s = reflectance of the secondary mirror.

The secondary mirror radiates in the same way. Thus,

$$P_s = N_s A_s \Omega_{Fs}$$

where the symbols have the same meaning as above with the exception of the area of the mirror which in this case is the projected area as seen from the field stop. Assuming the radiance of the primary and secondary to be equal, the two equations may be combined to give the total radiant power which reaches the detector from the emission of the two mirrors. This power is

$$P = N \left(A_p \Omega_{Fp} \rho + A_s \Omega_{Fs} \right)$$

Assuming the two mirrors to be Lambert radiators at 200°K with an emissivity of 0.02, their radiance may be calculated by standard radiometric equations and found to be 5.22×10^{-6} watts/cm^2 - sr^1 in the 14-to 16-μ band. The reflectance of the secondary mirror may be assumed to be 0.98, and the following geometric values are taken from Figure 54.

$$A_p = (\pi) \ (20 \ cm)^2 = 1255 \ cm^2$$

$$\Omega_{Fp} = \frac{1.05 \times 10^{-3} \ cm^2}{(80 \ cm)^2} = 1.6 \times 10^{-7} \ sr$$

$$A_s = (\pi) \ (7.4 \ cm)^2 = 172 \ cm^2$$

$$\Omega_{Fs} = \frac{1.05 \times 10^{-3} \ cm^2}{(28.3 \ cm)^2} = 1.32 \times 10^{-6} \ sr$$

Substituting these values into the equation results in 2.22×10^{-9} watt as the total radiant power on the field stop from the thermal emission of the primary and secondary mirrors.

The radiant power which falls within the field stop when measuring the minimum horizon radiance may be found by

$$P = N \; A_p \; \Omega O_s \; \rho^2 \; D$$

where: N = the minimum horizon radiance in the 14- to 16-μ band

              = 10^{-6} W/cm^2 - sr

      Ω = the solid angular field of view of the system

              = $(2 \times 10^{-4}$ rad$) \times (8 \times 10^{-4}$ rad$)$ = 1.6×10^{-7} sr

      O_s = the obscuration factor by the secondary mirror

              = $1 - \dfrac{A_s}{A_p}$ = $1 - \dfrac{172}{1255}$ = 0.864

      P = the reflectance of the two mirrors = 0.98

      D = the fraction of the energy of the diffraction pattern which falls within the field stop = 0.94

Substituting these values into the equation results in 1.56×10^{-10} watt as the power on the field stop when measuring the minimum horizon radiance. Comparing the value of power from the horizon with the power from the mirror shows that 14.2 times more power will fall within the field stop from the mirror emission than from the minimum horizon radiance. This is about 45 times that associated with the system noise level.

The nominal value for mirror emissivity, 0.02, upon which this ratio is based appears to be a conservative estimate.

Bennett, Bennett, and Ashley (ref. 3) report reflectance data for silver in the 0.55 to 32μ region is accurate to ± 0.1 percent and these films, they report, are reproducible to 1 percent. Additionally, they list the following:

λ, μ	ρ (fresh)	ρ (aged in air)
14	.9861	.9830
16	.9868	.9838

Storage in dry nitrogen can almost stop the aging. Bennett and Ashley (ref. 4) have reported further on reflectivities of gold and silver and gave higher values (again with an accuracy of ±0.1 percent):

λ, μ	ρ	ϵ	
14	.9955	.9945	silver
16	.9956	.0044	
14	.9940	.0060	gold
16	.9940	.0060	

They say, "The problem of a reflectance decrease during aging occurs only with silver... the reflectance of one ultrahigh vacuum silver film stored in dry nitrogen dropped by less than 0.1 percent... in 42 days." Table 9 gives the radiant power on the detector which would result from other values of mirror emissivity and temperature. These again may be compared to 1.56×10^{-10} watt, the radiant power on the detector when the minimum horizon is being measured. For example, if the data of reference 3 is correct, an emissivity of 0.0060 could be achieved with gold coating. Assuming a mirror temperature of 200°K, the ratio of power from the mirror to power from the minimum horizon would be 4.25. Although the effect of mirror radiation will be eliminated by the in-flight calibration procedure in any case, the accuracy of measurements would be increased by these low emissivity coatings.

Efficiency of the optical system will depend upon the accuracy of alignment of the various components, any misalignment will cause a loss of radiant energy on the detector.

These mechanical tolerances have been established, and their effect upon system efficiency has been calculated by first-order optical theory. These tolerances and their effect is summarized in Table 10. Assumptions upon which these energy losses are based are as follows:

(1)   Field stop to detector spacing - the error (0.0002 inch) has been evenly divided between the distances on either side of the re-collector lens to give the maximum increase in the magnicantion which could result.

(2)   Centering - each component was decentered in the direction which causes the greatest loss of the effective area of the field stop or detector.

(3)   Tilting of primary and secondary mirror - each mirror was tilted in the direction which causes the greatest loss in the effective area of the field stop.

(4)   Recollector lens tilt - any rotation of this lens will be about its nodal point.

TABLE 9. - RADIANT POWER IN WATTS FROM THE MIRROR
OPTICS WHICH FALLS WITHIN THE DETECTOR AREA

ϵ	190°K	200°K	210°K	220°K
.002	1.84×10^{-10}	2.22×10^{-10}	8.42×10^{-10}	9.95×10^{-10}
.004	3.67×10^{-10}	4.44×10^{-10}	1.68×10^{-9}	1.99×10^{-9}
.006	5.51×10^{-10}	6.66×10^{-10}	2.52×10^{-9}	2.78×10^{-9}
.01	7.65×10^{-10}	1.11×10^{-9}	4.21×10^{-9}	4.97×10^{-9}
.02	1.84×10^{-9}	2.22×10^{-9}	8.4×10^{-9}	9.95×10^{-9}

TABLE 10. - MECHANICAL TOLERANCE OF OPTICAL
COMPONENTS AND THEIR EFFECT UPON
SYSTEM EFFICIENCY

Type of tolerance	Component	Tolerance	Worst-case energy loss
Axial spacing	Primary to field stop	±0.0015 in.	12.9%
	Field stop to detector	±0.0002 in.	0.06%
Centering	Primary	0.0005 in.	8 %
	Re-collector	0.0005 in.	8 %
	Detector	0.0003 in.	9.5%
Tilting	Primary	3 sec	14.5%
	Secondary	5 sec	8.7%
	Re-collector	20 sec	no effect
	Detector	5 sec	negligible

124

(5)   Detector tilt - the only inefficiency results from the decrease in the projected area of the detector (cos θ).

Radiometer Structure and Spacing

The selection of the mechanical structure configuration of the proposed radiometer design is based upon consideration of both structure and thermal requirements. A description of the boundary conditions of the design and its operational parameters is as follows:

1.   The operating temperature during the flight will be 200° ±20°K.

2.   The temperature change from manufacturing to flight will be 100°K.

3.   The environment includes operation through a "soft" launch; all pertinent environmental specifications are relative to a Thor or Agena vehicle. Final operation in orbit involves a zero "g" condition at an altitude of approximately 260 nautical miles.

4.   Spacing, centering, and tilt tolerances are as specified in Table 10.

5.   The 40-cm diameter, f/2; parabolic primary is assumed to be equivalent to a spherical mirror having a radius of curvature of 160 cm.

These are two basic structural systems available:

1.   The optical elements are spaced by the structure itself, and the structure material and design is such that any change in the focal point of the primary mirror is matched by the change in structure (see Figure 55).

2.   The optical elements are spaced by a system of thermal compensating rods and structure with a portion of the structure thermally isolated from the optical elements (see Figure 56).

     Structure spacing. -- From Figure 55 the focal length (FL) of the system is defined as

$$FL = C - (A + B) + D$$

The change in the focal length over an excursion of temperature must be matched by the corresponding change in the structure over the same temperature excursion. That is,

$$\Delta FL = \Delta C - (\Delta A + \Delta B) + \Delta D$$

125
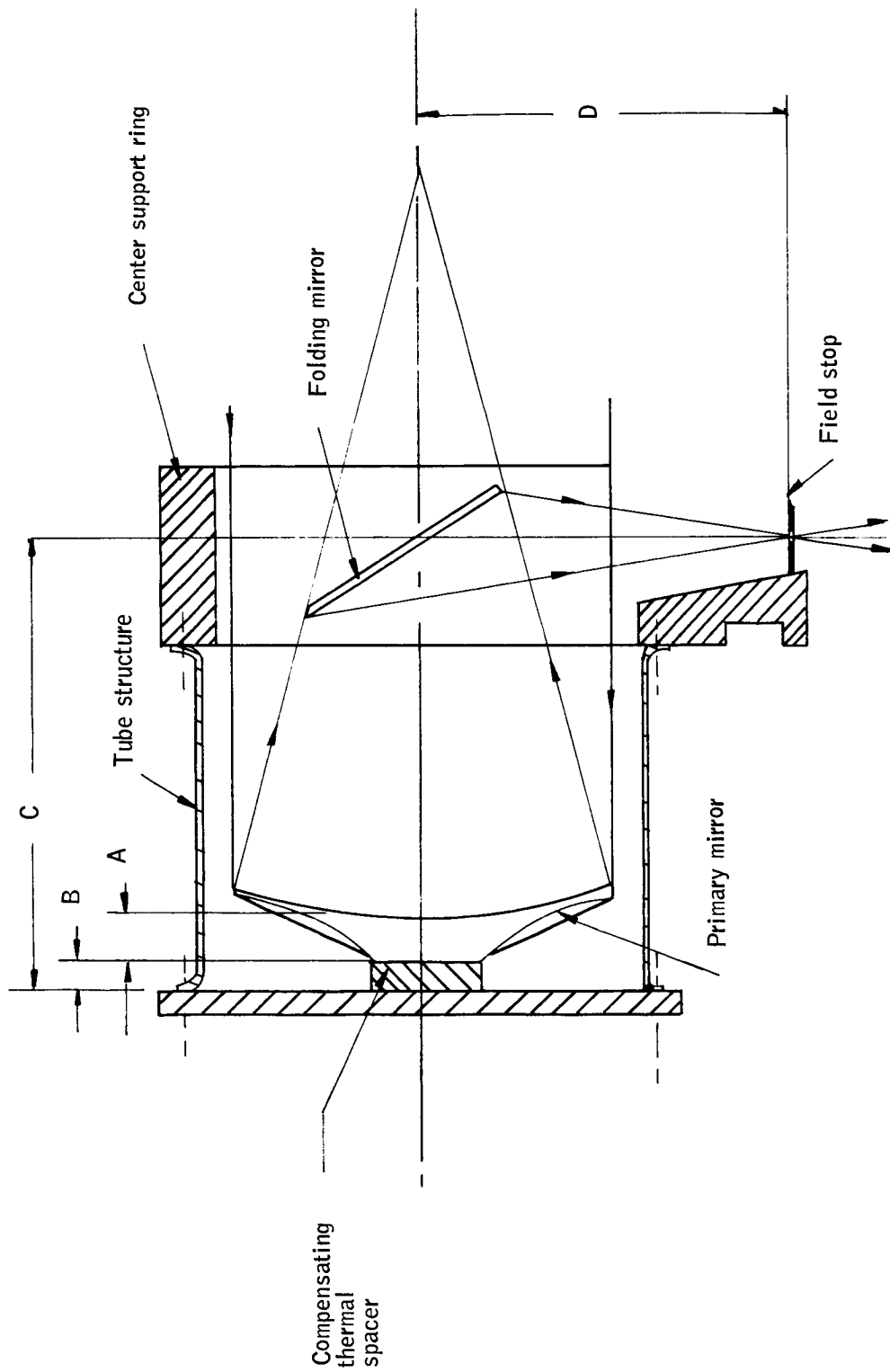
Figure 55. Optical Element Spacing by Structure
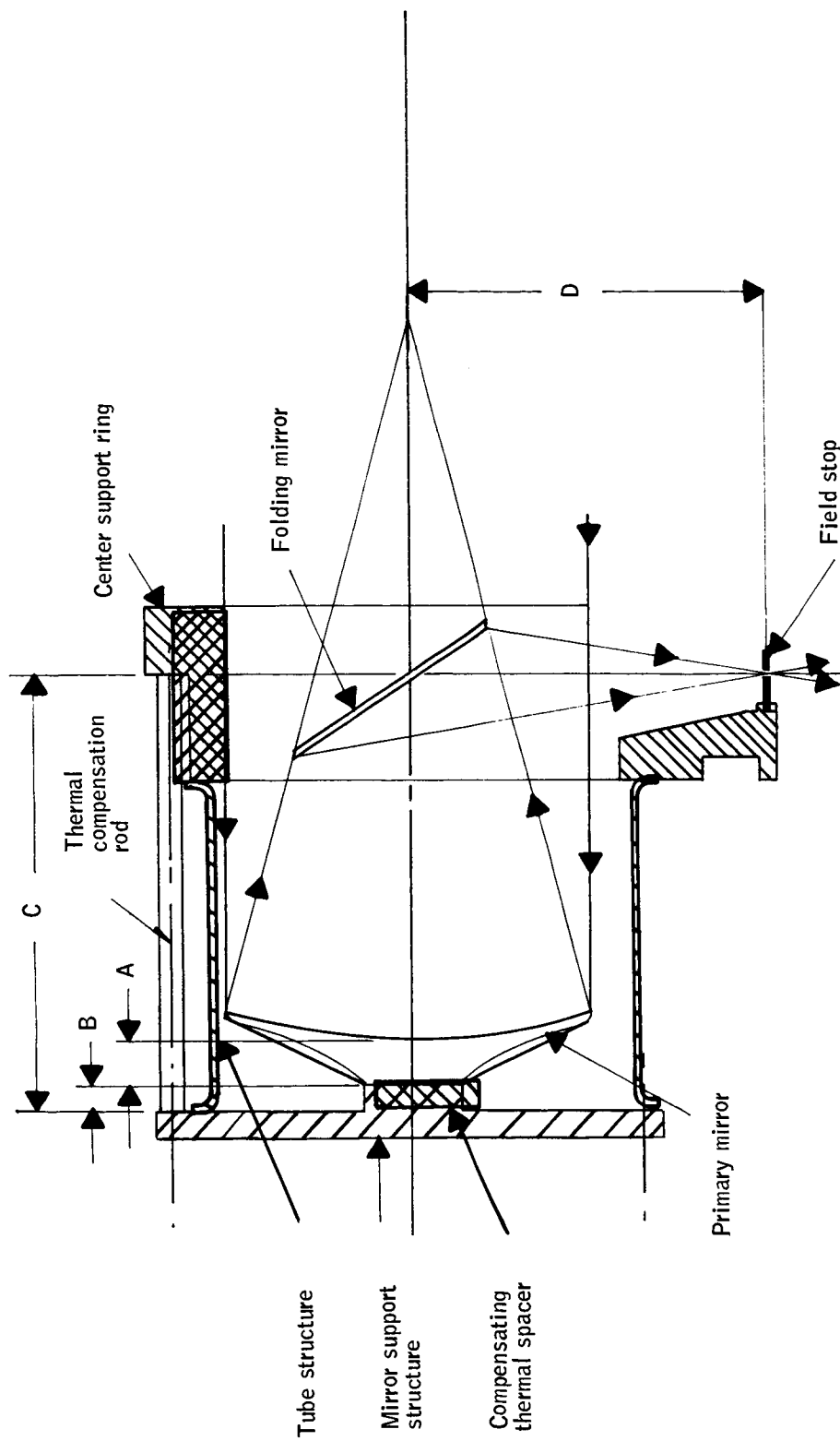
Figure 56. Optical Element Spacing by Thermal Rods and Structure

127

$$\Delta FL = \frac{R_o}{2} \alpha_A \Delta T$$

$$\Delta A = A \alpha_A \Delta T$$

$$\Delta B = B \alpha_B \Delta T$$

$$\Delta C = C \alpha_C \Delta T$$

$$\Delta D = D \alpha_D \Delta T$$

where R_o is the radius of curvature of the primary; and A, B, C, and D are the structural dimensions at ambient conditions; i.e., prior to a ΔT excursion. The coefficient of expansion value for each element, optical or structure, is denoted by α_n as shown.

Combining,

$$\frac{R_o}{2} \alpha_A \Delta T = \left[C \alpha_C - \left(A \alpha_A + B \alpha_B \right) + D \alpha_D \right] \Delta T$$

or

$$\frac{R_o}{2} + A \quad \alpha_A = C \alpha_C - B \alpha_B + D \alpha_D$$

By hypothesis, the material denoted by C is made identical to the material denoted by D. As such, $\alpha_C = \alpha_D$, and

$$\left(\frac{R_o}{2} + A \right) \alpha_A = (C + D) \alpha_C - B \alpha_B \tag{8}$$

The mechanical/optical layout of the classical Newtonian systems as outlined in Figure 55 gives the following approximate dimensional data:

$$R_o = 160 \text{ cm}$$

$$A = 7 \text{ cm}$$

$$C = 59 + B$$

$$D = 28 \text{ cm}$$

128

The relationship between the focal-point shift and the structure change over a ΔT reduces equation (8) to

$$\left(\frac{160}{2} + 7\right) \alpha_A = (59 + B + 28) \alpha_C - B \alpha_B$$

$$87\alpha_A = 87 \alpha_C + B \alpha_C - B \alpha_B$$

then

$$B = \frac{87 (\alpha_C - \alpha_A)}{\alpha_B - \alpha_C}$$

By inspection, the relationship $\alpha_B > \alpha_C > \alpha_A$ must exist between the coefficients of expansion

The choice of material for the primary mirror includes:

- Fused silica (quartz)
- Pyrex
- Berryllium
- Aluminum

while structural material choices include:

- Titanium
- Aluminum
- Magnesium
- Stainless steel

Table 11 is a matrix analysis comparing the four mirror materials with the four structural materials relative to equation (8).

As concluded from Table 11, the only combinations of mirror and structural materials that are thermally compatible are: (1) aluminum throughout; and (2) a beryllium mirror, titanium structure, with a magnesium compensating thermal spacer.

Thermal compensating rod spacing. -- As is shown in Figure 56, the focal length change over an excursion of temperature must be matched by the corresponding change in the structure over the same temperature excursion, that is,

$$\Delta FL = \Delta C - (\Delta A + \Delta B) + \Delta D$$

TABLE 11. – MATERIALS COMBINATION MATRIX FOR STRUCTURE SPACING

Mirror material	Structural material	α_C (structure) cm/cm/°C×10⁻⁶	Basic equation	Specific mirror-structure equation	For minimum B, material for B must be as noted	B cm	Judgement
Fused silica (quartz) $\alpha_A = 0.5 \times 10^{-6}$	Titanium	12.8		$B=1070/(\alpha_B - 12.8)$	Mg	67	No
	Stainless steel	18.7		$B=1583/(\alpha_B - 18.7)$	Mg	157	No
	Aluminum	24.7		$B=2150/(\alpha_B - 24.7)$	Mg	524	No
	Magnesium	28.8		$B=2506/(\alpha_B - 28.8)$			No
Pyrex $\alpha_A = 3.2 \times 10^{-6}$	Titanium	12.8	$B = 87 \dfrac{(\alpha_C - \alpha_A)}{\alpha_B - \alpha_C}$	$B=835/(\alpha_B - 12.8)$	Mg	52	No
	Stainless steel	18.7		$B=1349/(\alpha_B - 18.7)$	Mg	134	No
	Aluminum	24.7		$B=1870/(\alpha_B - 24.7)$	Mg	456	No
	Magnesium	28.8		$B=2230/(\alpha_B - 28.8)$			No
Beryllium $\alpha_A = 11.5 \times 10^{-6}$	Titanium	12.8		$B=113.1/(\alpha_B - 12.8)$	Alum. or Mg	7.07	Yes
	Stainless steel	18.7		$B=626/(\alpha_B - 18.7)$	Mg	61	No
	Aluminum	24.7		$B=1149/(\alpha_B - 24.7)$	Mg	280	No
	Magnesium	28.8		$B=1505/(\alpha_B - 28.8)$			No
Aluminum $\alpha_A = 24.7 \times 10^{-6}$	Titanium	12.8		$B=1035/(12.8 - \alpha_B)$	Quartz	84.2	No
	Stainless steel	18.7		$B=1390/(18.7 - \alpha_B)$	Quartz	76.3	No
	Aluminum	24.7		$B=0$	Aluminum	0	Yes
	Magnesium	28.8		$B=182.7/(\alpha_B - 28.8)$			No

This expression, as in the previous exercise, reduces to

$$\left(\frac{R_o}{2} + A\right) \alpha_A = C \, \alpha_C - B \, \alpha_B + D \, \alpha_D$$

By hypothesis, the material denoted by B is made identical to the materials denoted by D . As such, $\alpha_B = \alpha_D$, and

$$\left(\frac{R_o}{2} + A\right) \alpha_A = C \, \alpha_C - (B - D) \, \alpha_B$$

Again, as in the previous exercise, the following approximate dimensional data exists:

R_o = 160 cm

A = 7 cm

C = 59 + B

D = 28 cm

The relationship between the focal point shift and the structure change over ΔT reduces from the equation above to

$$\left(\frac{160}{2} + 7\right) \alpha_A = (59 + B) \, \alpha_C - (B - 28) \, \alpha_B$$

$$87\alpha_A = (59 + B) \, \alpha_C + (28 - B) \, \alpha_B$$

A typical material that may be used for the thermal compensation rod material is Invar, since this material can serve both as a thermal compensator and as a structural element. Kovar is also a possibility, but is essentially represented by Invar.

Referring to Figure 56, it can be seen that the design approach includes the following premises:

1. Thermal compensation is accomplished along only that portion of the focal length that lies between the primary mirror and the folding mirror.

2. In order to eliminate radical distortions, the mirror support structure and the center support ring are of the same material.

3. The mirror support structure and the Invar thermal compensating rods are matched to effect the required thermal compensation.

131

Choices of material for the primary mirror include:

- Fused silica (quartz)
- Pyrex

The structural material choices include:

- Titanium
- Aluminum
- Magnesium
- Stainless steel

A matrix analysis comparing the two mirror materials with the four structural materials relative to the equation above is contained in Table 12. It may be concluded from Table 12 that the best mirror and structural material combination available is pyrex and titanium with Invar rods as the thermal compensating structure member.

Material analysis -- From the two preceding paragraphs, the following facts have been ascertained:

1. Spacing the optical elements by the structure is thermally possible. The combination of materials that are acceptable are (from Table 11) as follows:

   Mirror: Beryllium

   Structure: Titanium

   Spacer: Magnesium

   or:

   Mirror: Aluminum

   Structure: Aluminum

   Spacer: None

2. Spacing the optical elements by the thermal compensating rod technique is also thermally possible. The combination of materials that effects a minimum telescope size is:

   Mirror: Pyrex

   Structure: Titanium

   Rods: Invar

A tabulation of the six materials involved and their characteristics pertinent to their study is listed in Table 13.

TABLE 12. - MATERIALS COMBINATION MATRIX FOR COMPENSATING ROD SPACE

Mirror material	Structural Material B & D	Structure, $\alpha_B = \alpha_D$ cm/cm/°C x 10^{-6}	Basic equation $\alpha_C = 1.98 \times 10^{-6}/°C$	B, cm	Judgement
Fused silica (quartz) $\alpha_A = 0.5 \times 10^{-6}$	Titanium	12.8		40.0	No
	Stainless steel	18.7	$B = \dfrac{73.3 + 28\,\alpha_B}{\alpha_B - 1.98}$	35.7	No
	Aluminum	24.7		33.7	No
	Magnesium	28.8		32.8	No
Pyrex $\alpha_A = 3.2 \times 10^{-6}$	Titanium	12.8		18.2	Yes
	Stainless steel	18.7	$B = \dfrac{28\,\alpha_B - 161.6}{\alpha_B - 1.98}$	21.7	No
	Aluminum	24.7		23.3	No
	Magnesium	28.8		24.1	No

133

TABLE 13. -MATERIALS COMBINATION MATRIX FOR STRUCTURE SPACING
AND COMPENSATING ROD SPACING

Design	Mirror material	Structural material	Thermal compensating spacer material	Thermal compensating rod material	Isotrophic characteristic	Density, lb/in^3	Modules of elasticity E x 10^6, psi	Specific stiffness, E/ρ	Thermal coeff. of expansion per °C x 10^{-6}	Specific strength 10^3 in	Thermal conductivity, Cal/sec/cm/°C
Structure spacing	Aluminum	Aluminum			Isotrophic	.1	10.6	106	24.7	765	.54
	Beryllium	Titanium	Magnesium		Non-isotropic Non-isotropic Isotropic	.067 .165 .064	44.0 19.0 6.5	657 111 102	11.5 12.8 28.8	821 1500 462	.385 .00 .184
Thermal compensating rod spacing	Pyrex	Titanium		Invar	Isotropic Non-isotropic Isotropic	.083 .165 .291	9.1 19.0 21.5	114 111 72	3.2 12.8 1.98	38 1500 240	.002 .00

From thermal considerations, the choice of mirror material has been limited to pyrex, beryllium, and aluminum.

Pyrex mirror: From space-envelope considerations, it is impossible to accept the "B" dimension of Figure 56 as dictated by the use of pyrex. The B dimension called for in Figure 56 and Table 12 is 18.2 cm or 7.2 inches. This requirement exceeds the maximum space allowed. As a result, the thermal compensating rod technique as shown in Figure 56 is eliminated as a consideration.

The B requirement can be met by introducing a new structural concept as shown in Figure 57. This technique simply shifts the structural dimension required to the other end of the system where there is no space-envelope restriction.

Figure 58 shows the thermal expansion of Invar (ref. 5). Over a temperature excursion of ±20° F about a mean of -100° F the thermal coefficient of expansion is not constant. As a result of this, Invar, as shown in Table 12, requires a B dimension that differs by 1.5 cm over the 40°F temperature shift. This effect rules out the use of Invar and, as a consequence, rules out the use of a pyrex mirror.

Suppliers have been contacted relative to this problem. It has been affirmed that the coefficient of expansion can be made constant within the temperature range desired. However, even admitting the possibility of this affirmation being true, the approach cannot be recommended without development since the material is an unknown.

Beryllium and aluminum mirrors: To effect the reflectivity required in the 12- to 16-μ region, both beryllium and aluminum mirror surfaces must have a Kanigen chemical nickel coating with a chrome deposit over which is a gold finish deposit. This technique provides the highly specular low emissivity surface required. Te Corporation, Santa Barbara, California has fabricated a mirror that has operated at low temperatures. Dr. Robert Neiswander of the Te Corporation has stated that they have fabricated an aluminum mirror which has been successfully temperature cycled to liquid-nitrogen temperature and maintained a 0.5 mrad resolution. This particular unit had a 5-mil Kanigen coating. Further, it was his opinion that because of the nonisotropic characteristic of beryllium, they had not been successful in any beryllium mirror fabrication operating over this kind of temperature excursion. Itek Corporation, Lexington Massachusetts, has not been successful with aluminum mirrors. Itek has not been able to keep the Kanigen coating intact over this kind of a temperature swing. In their opinion, however, the use of a beryllium mirror should not be ruled out; one could be developed to perform satisfactorily at 200° K

Conclusions. -- From a mechanical/thermal point of view, a system to satisfy orbiting operation requirements is feasible.
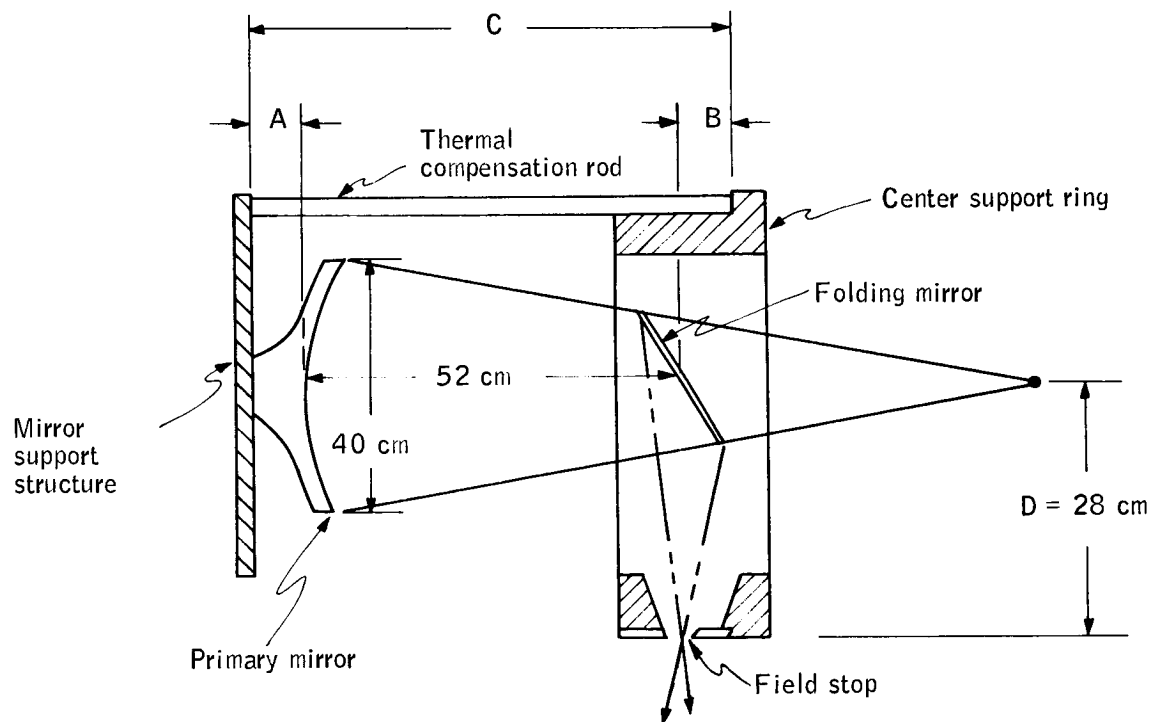
Figure 57. Alternate Structure Approach
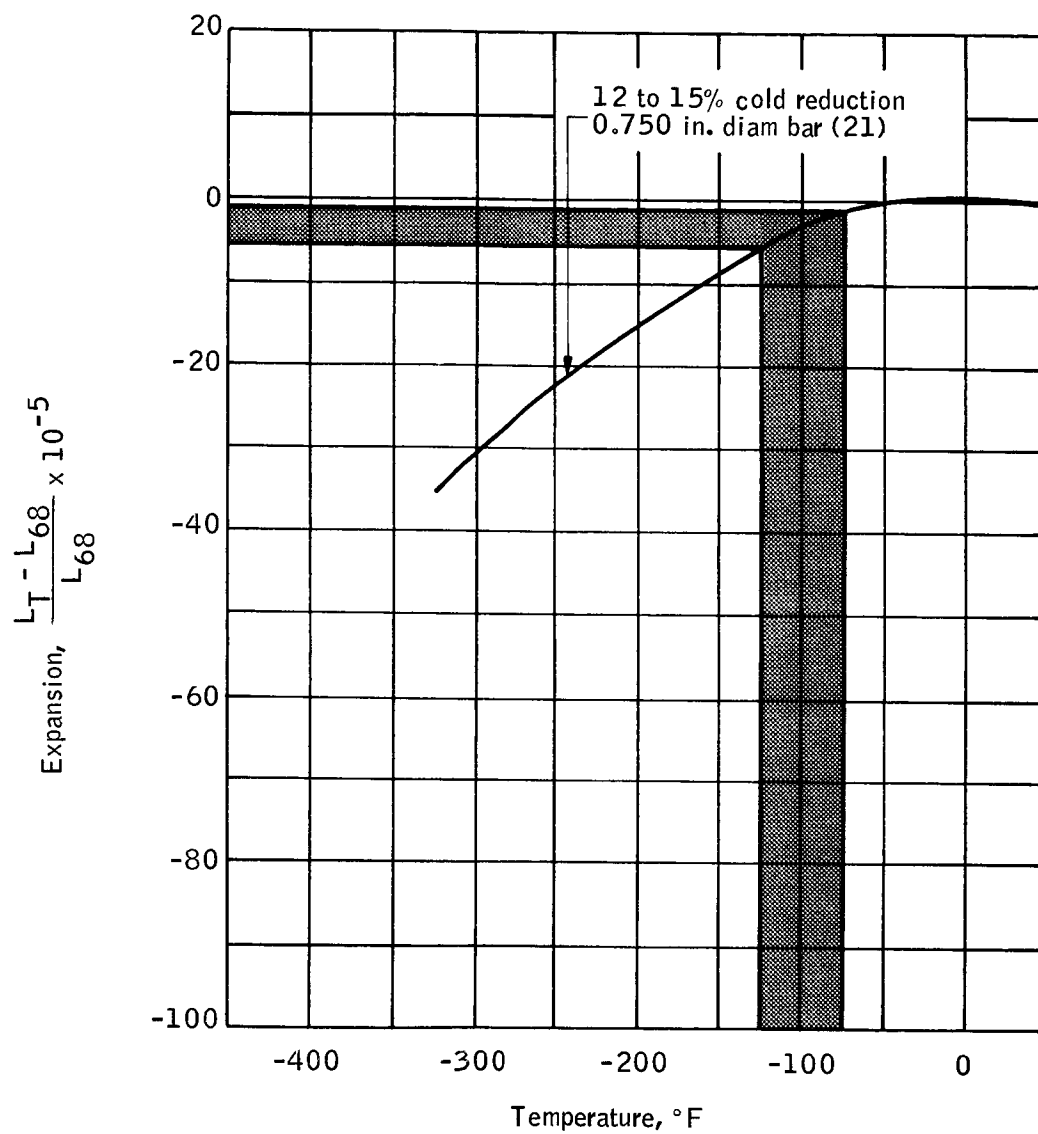
Figure 58.   Thermal Expansion of Invar

137

The study completed leads to an optimum material/structure configuration of an aluminum primary with an aluminum structure serving both as a structure and as the optical spacing element. All data indicate that the use of aluminum has the following advantages:

1. An essentially constant coefficient of expansion from ambient to 200° K.

2. The most superior thermal expansion/conductivity ratio of all materials.

3. It is isotropic.

4. Strength and stiffness characteristics compatible with the environmental excursions expected.

5. A mirror has been successfully fabricated with an aspheric figure compatible with the optical requirements and with test data existing showing that it has been cycled to liquid N_2 temperature maintaining a 0.5 mrad resolution with every expectation of improvement at 200° K.

Baffling

Baffle techniques. -- In any telescopic optical system, it is virtually impossible to prevent radiation from outside the field of view from entering the system, reflecting off internal surfaces, and causing a loss of contrast in a visual system or undesirable "noise" in an electronic photodetection system.

Energy absorbing baffles are provided to attenuate the undesirable off-axis radiation which enters the system. With any baffling system, the possible sources of undesirable radiation falling on the detector(s) are

1. Direction radiation

2. Radiation from side of baffle

    a. Diffuse

    b. Specular

3. Radiation from edges of baffle

    a. Diffuse

    b. Specular

138

4. Radiation from other surfaces

    a. Lens, mirror, and window edges

    b. Mounting surfaces

Baffles are provided on surfaces which cannot be shielded from off-axis radiation coming directly from outside the optical system. The purpose, in general, of any baffling system is to absorb and/or redirect the incident off-axis radiation such that it either will not get to the detector(s) or, when reaching the detector, it is greatly attenuated so as not to exceed the detector noise.

To attenuate incident radiation, the surface of a baffle must be treated so as to absorb as much of the incident energy as possible. Reflection from baffle surfaces can be made specular or diffuse. Figure 59 illustrates typical baffle approaches. Incident radiation impinging upon a baffle surface can be specular as shown in Figures 59a and 59b, diffuse as shown in Figure 59c, both specular and diffuse as shown in Figure 59d, and a cone trap as shown in Figure 59e.

A baffle surface that is made specular has the following characteristics:

1. The first reflection is directed down into the baffle.

2. The reflected energy is attenuated by the multiple reflections, the number of reflections being a function of the incident angle θ and the l/d ratio of the baffle design.

3. The direction of the reflected energy is controlled and can be directed away from the field of view of the detectors.

A baffle surface that is made diffuse has the following characteristics:

1. Diffusely reflecting baffles reradiate incident energy in a forward hemisphere (first reflection) and a rearward hemisphere (second reflection).

2. The reradiated energy is uncontrolled.

3. Attenuation is exclusively a function of the absorptivity of the baffle surface during the first impingement as a worst case.

In addition to the incident off-axis radiation impinging directly upon the walls of the telescope tube, there is an off-axis reflection from the primary that also strikes the telescope walls. Consider Figures 60 and 61.

Figure 60 shows the radiometer in its orbital path above the earth. While orbiting, the radiometer is rotating about an axis as shown. When the radiometer is 90° away from the on target line of sight, earth radiance starts being received within the telescope barrel.

139
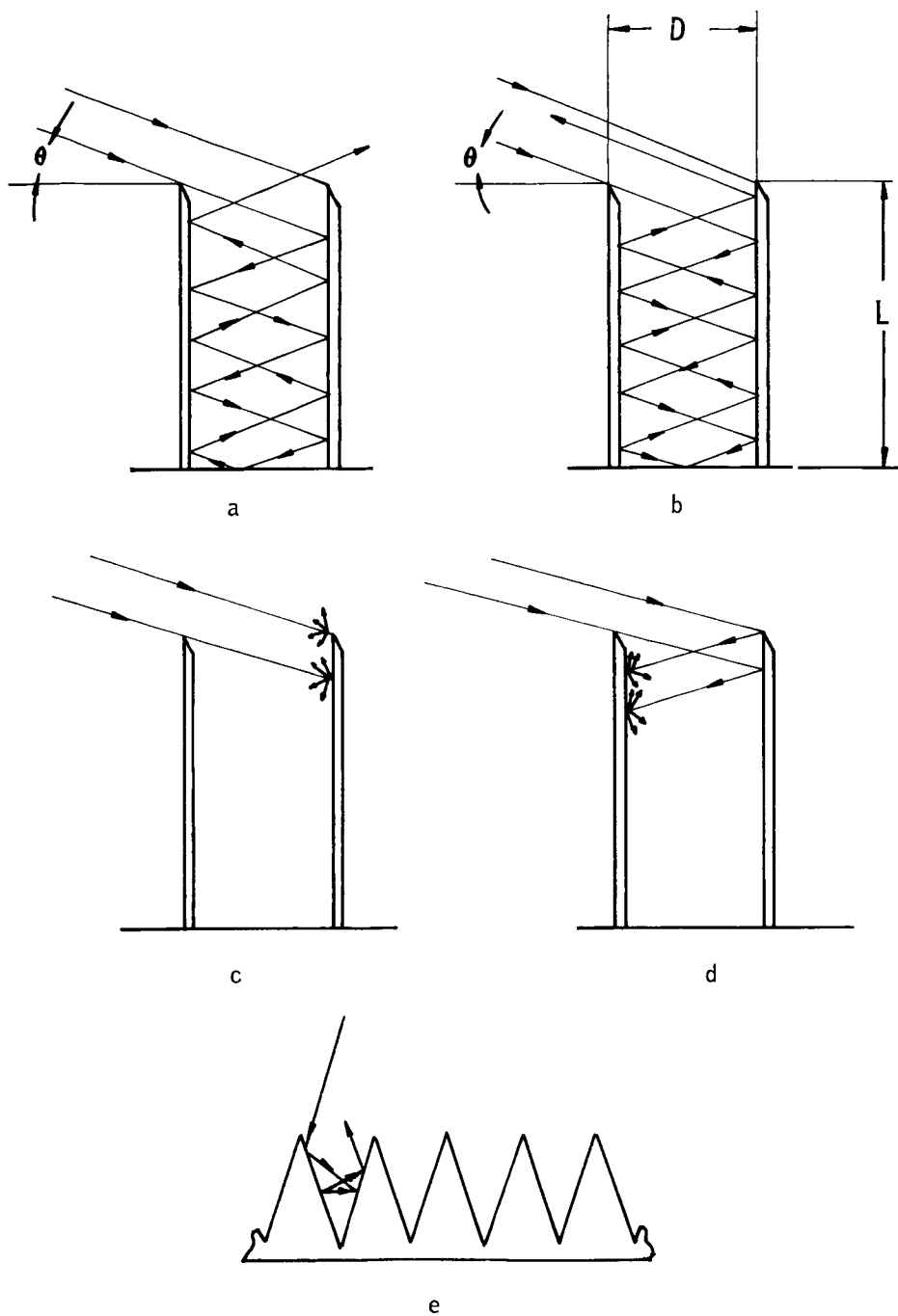
Figure 59.   Typical Baffle Techniques
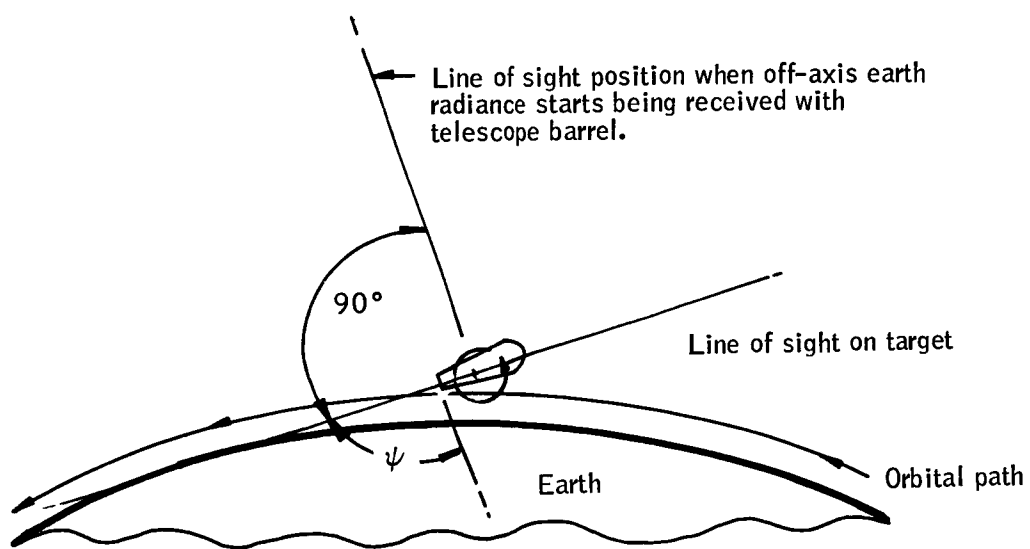
Figure 60. In-Flight View of Radiometer
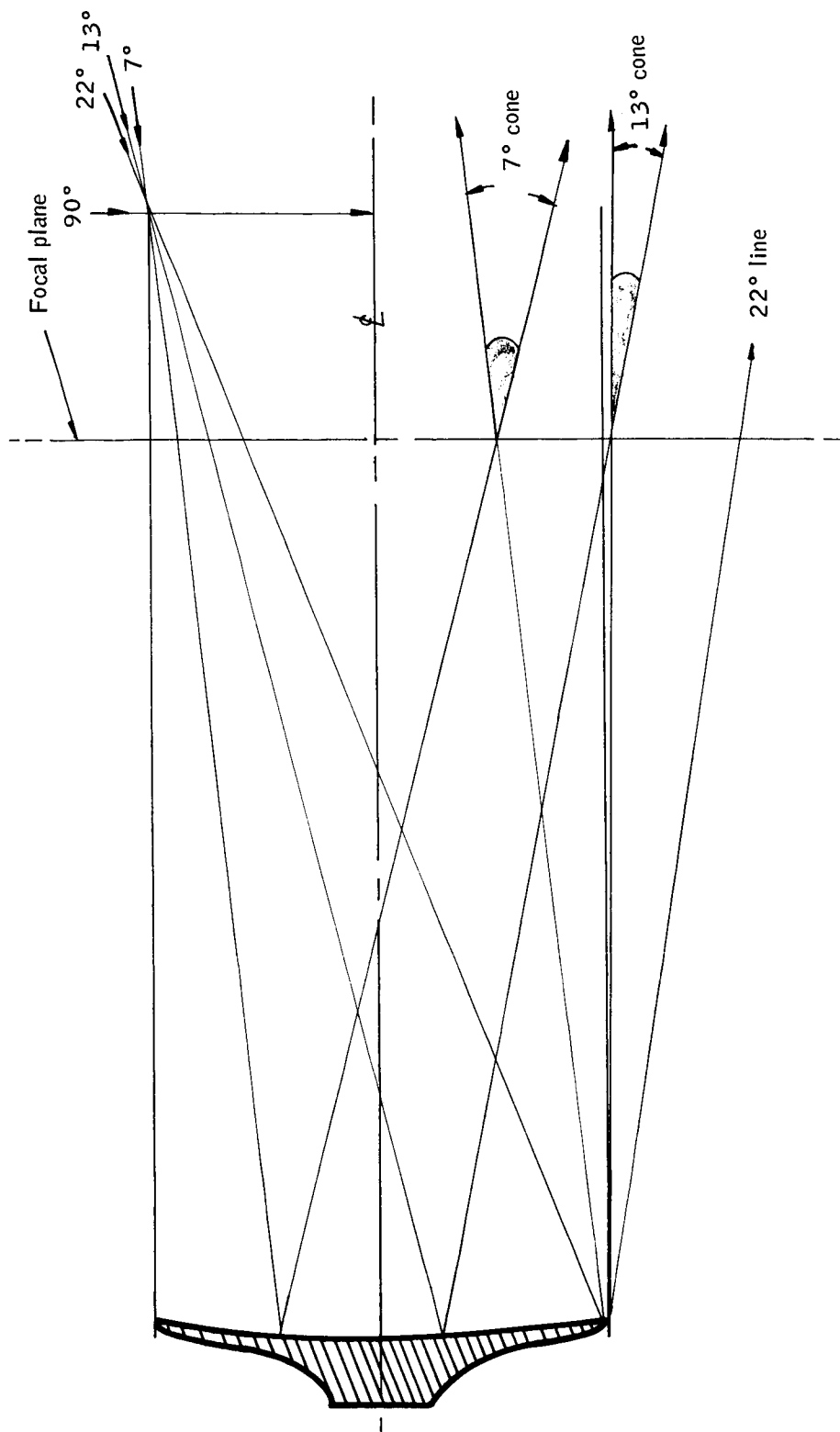
Figure 61. Off-Axis Deflection from the Primary Mirror

142

From Figure 61, it can be seen that the earth radiance impinges only on the telescope walls when the line of sight is between 90° and 22° from target. From 22° to line of sight on target (0°), off-axis energy impinges on the primary mirror. This energy is reflected back towards the focal plane (where it converges) and beyond. Figure 61 examines energy coming in at 22°, 13° and 7°. The energy being received at 7° comes to a focus and is reflected out of the telescope opening, clearing the telescope walls. This condition, obviously, is similar for all energy being received at angles from 0° to 7° and up to approximately 10°. From 10° to 22°, as illustrated by the 13° trace, the energy is impinging upon the telescope wall.

The baffle design technique must accommodate both forms of incident, off-axis energy; direct and reflected.

The conventional procedure relative to baffle design is to incorporate concentric rings with the ring i.d. conforming to the field of view, the spacing and ℓ/d ratio in accordance with the attenuation requirements. This approach does not take into consideration the off-axis energy reflected by the primary mirror.

The ideal baffle technique for attenuation of both direct and reflected off-axis energy is a baffle edge that conforms to the outermost reflected ray - in this case the 22° line as shown in Figure 61. Reflected energy from the primary would be collected by a baffling technique as shown in Figure 59. Since the largest possible spacecraft space envelope will not permit this luxury, a step baffle arrangement evolved in accordance with Figure 62.

Design analysis of recommended baffle configuration. -- The primary requirement of the baffle system is that off-axis stray radiation be attenuated so it does not exceed the radiant power reaching the detector when measuring the minimum horizon radiance or 1.56×10^{-10} watt.

Baffle cavity: Design analysis of any baffle cavity configuration begins with an analysis of the value of off-axis energy being received. Reference to Figure 60 shows that as the spacecraft rotates in the assumed ccw direction, for any given approach rate of the line of sight of the radiometer to the horizon (target), the maximum exposure of earth radiation occurs when the radiometer is on target. The possible angle of incident earth radiation on the inside of the radiometer telescope ranges from 90° at the telescope opening to 21.6° at the full depth of 40 inches as is shown in Figure 63.

Each angle has been converted to a solid angle as is shown in Table 14.

The earth radiance has been given as

$$N = 700 \times 10^{-6} \text{ W/cm}^2\text{- sr}$$
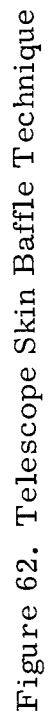
Figure 62. Telescope Skin Baffle Technique

144
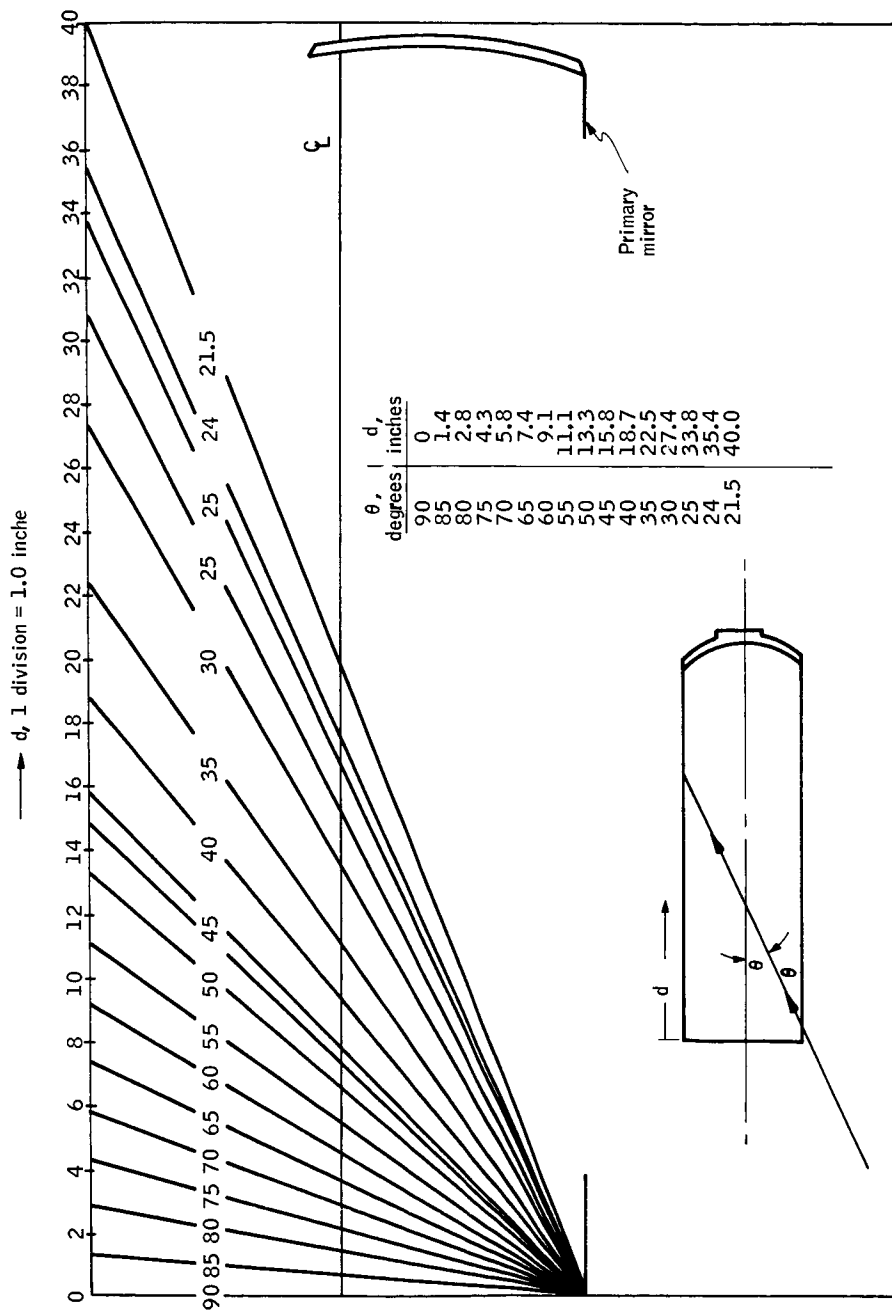
Figure 63. Incident Angle versus Depth Inside Telescope

TABLE 14. - SOLID ANGLE OF STRAY RADIATION ON
THE RADIOMETER TUBE CALCULATION

θ, deg	$\frac{\theta}{2}$, deg	$\cos \frac{\theta}{2} = S$	$h = 1 - S$	A, sr
21.5	10° 45'	0.98245	0.01755	0.1105
24	12°	0.97815	0.02185	0.1373
30	15°	0.96593	0.03407	0.2141
35	17° 30'	0.95372	0.04628	0.2908
40	20°	0.93969	0.06031	0.3789
45	22° 30'	0.92388	0.07612	0.4783
50	25°	0.90631	0.09369	0.5887
55	27° 30'	0.88701	0.11299	0.7099
60	30°	0.86603	0.13397	0.8418
65	32° 30'	0.84339	0.15661	0.9840
70	35°	0.81915	0.18085	1.1363
75	37° 30'	0.79335	0.20665	1.2984
80	40°	0.76604	0.23396	1.4700
85	42° 30'	0.73728	0.26272	1.6507
90	45°	0.70711	0.29289	1.8403

Knowing the solid-angle for energy impingement for points within the tele-scope, the irradiance for each point was computed (Table 15) from the follow-ing relationship:

$$H \text{ (irradiance)} = 700 \, (\theta) \times 10^{-6} \, W/cm^2$$

where θ is expressed in steradians (Table 14)

Figure 64 is a plot of Table 15 and gives the irradiance in W/cm^2 for any point inside the telescope barrel when the telescope line of sight is tangent to the earth's surface.

The ℓ/d ratio that is required for the baffles is defined by the following relationships:

1. Power into a baffle cavity x (surface reflectivity)^n = power out.

2. Power into a baffle cavity = H (W/cm^2) x area subtended by the baffle cavity (cm^2).

3. Power out = 1.56×10^{-10} W, by definition.

4. n = the number of specular reflections required within the baffle cavity.

Figure 65 shows a folded layout of a typical baffle such that, for a given incidence angle of energy, the number of reflections within the baffle cavity is defined as

$$\tan \theta = \frac{2L}{nD} \quad n = \frac{2L}{D \tan \theta}$$

where

θ = incidence angle of impinging energy,

L = depth of baffle,

D = spacing of baffle plates (rings), and

n = number of reflections within the baffle cavity defined by L and D

If a point on the telescope barrel wall is selected, an irradiance value at this point may be taken from the graph presented in Figure 64. For any given D spacing requirement, the value of the H selected can be assumed to remain constant over the D spacing within a reasonable approximation. Finally, D can be multiplied by 1 cm in order to establish an area of impinging energy.
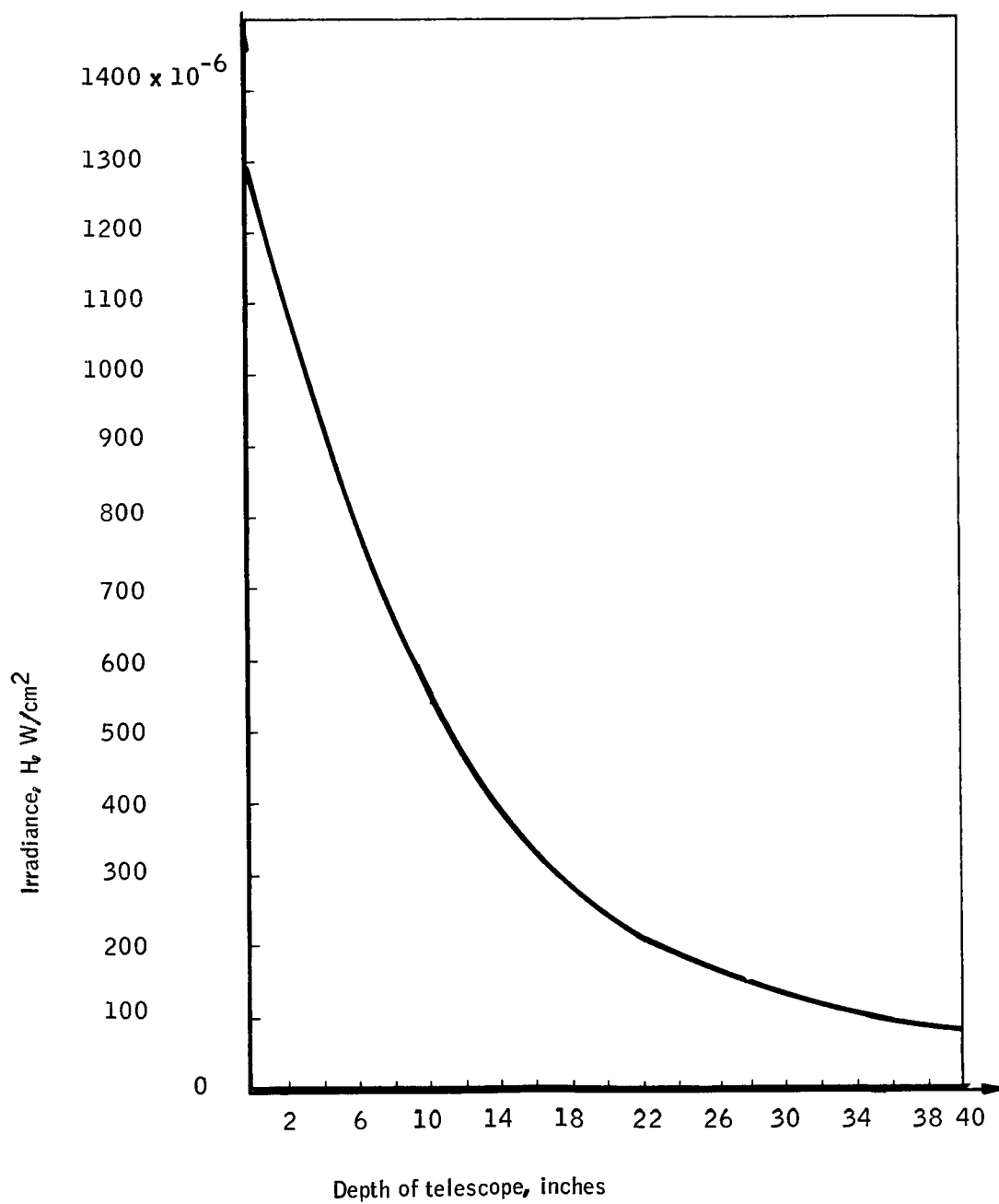
Figure 64.   Earth Irradiance versus Depth Within Telescope Barrel

TABLE 15. - IRRADIANCE FROM EARTH ON RADIOMETER
TUBE CALCULATION

θ, deg	θ, sr	$H = 10^{-6}$ W/cm^2
21.5	0.1105	77.2
24	0.1373	96.1
30	0.2141	150
35	0.2908	204
40	0.3789	265
45	0.4783	335
50	0.5887	412
55	0.7099	497
60	0.8418	589
65	0.9840	689
70	1.1363	795
75	1.2984	909
80	1.4700	1029
85	1.6507	1155
90	1.8403	1288

$$N = \frac{2l}{d \times \tan \theta}$$

Where: l = Length of baffle
         d = Width of baffle
         θ = Angle of incidence
         N = Number of bounces
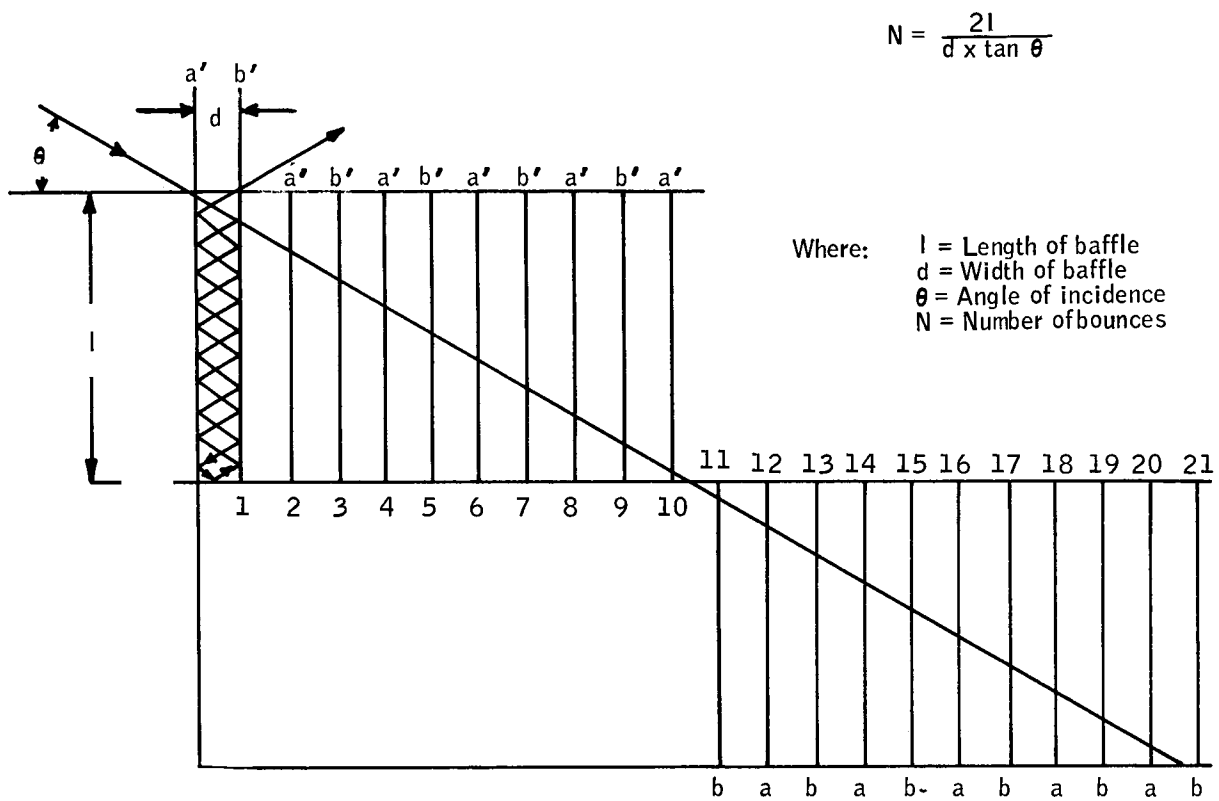
Figure 65.   Layout of a Baffle System

The relationship between H and the L/D ratio can now be expressed as:

$$(\text{Power In}) \ (\text{reflectivity})^n \ = \ \text{power out}$$

$$H(W/cm^2) \ x \ D \ x \ 1 \ (cm^2) \ x \ (\rho)^n \ = \ 1.56 \ x \ 10^{-10} \ \text{watts}$$

$$HD \ (\rho)^n \ = \ 1.56 \ x \ 10^{-10}$$

where, from Figure 65, $\quad n \ = \ \dfrac{2 \, L}{D \tan \theta}$

Taking the natural log of both sides of the above equation gives the workable expresion:

$$\ln H + \ln D + \frac{2 \, L \, \ln \rho}{D \tan \theta} \ = \ -10 \, \ln 1.56$$

For the given point selected on the telescope wall, a value for H is available from Figure 64. The angle $|\theta|$ can be scaled by the use of Figure 62. Reflectivity can be assumed to be 0.10 as a conservative estimate. It is convenient to assign a value to D and solve for L, adjusting D to attain a suitable L/D ratio. The analysis of the baffle problem involves a feasible solution as shown in Figure 62.

The results of the analysis are not trivial. The proposed solution is unique and constitutes an approach that virtually eliminates stray light from the telescope walls as a source of error. The step-function baffle edge with the L/D ratio incorporated includes the following design features:

1. The L/D ratio used in each of the three sections is that ratio defined by the worst-case $|\theta|$ within the section. As an example, consider the mid-baffle section shown in Figure 62. The worst-case angle is 46° 48', this angle dictates the largest irradiance as seen by the field of view of the edge of this baffle segment. For the entire mid-baffle section the L/D ratio is defined by 46° 48'. As such, the minimum baffle (the one shown by the reflected ray trace) has the same L/D ratio as the last baffle cavity towards the primary mirror within the mid-baffle section. As can be seen, the baffles are not uniformly spaced. The spacing is a function of the L/D ratio dictated within each section. This approach provides a step increase in baffle spacing with a minimum number of baffles required, and in addition, provides a conservative rather than a marginal design.

2. From Figure 62, the edge-effect analysis can be seen to include only three baffle edges: the first at the aperture of the radiometer, the second at the end of the mid-baffle section, and the third at the beginning

of the third baffle section (adjacent to the primary mirror).

3. The recommended finish of each baffle surface is a specular coating with maximum reflectance of 10 percent. This may be readily obtained by using black enamel on both sides of each baffle ring.

Baffle Edges: In the baffle design shown in Figure 62, there are three edges that could get into the field of view since the rest of the baffles are, by the step design, outside the field of view. The design analysis will consist of determining the energy falling on these edges and the radius of edge required such that the power delivered to the detector from off-axis radiation will not exceed the minimum target signal. This exercise is somewhat academic as each edge in the proposed design can be pulled back from the field of view outline defined by the primary so that baffle edge reflections will not impinge upon the detector array.

Figure 66 depicts the three baffle edges involved in the analysis. Each edge has an associated irradiance that is a function of the edge depth within the radiometer barrel (see Figure 64). Associated with each edge is an area of energy impingement which is defined in terms of a radius edge R. The total reflected power from each edge is listed in Table 16.

Total power on the detector is the summation of the reflected power from each edge in accordance with the relationship

$$\frac{\text{Power on detector}}{\text{Total reflected power (edge)}} = \frac{0.2 \times 0.8 \times 10^{-6} \, (\text{rad})^2}{\alpha \times \pi (\text{rad})^2}$$

where α = angle subtenting the exposed edge expressed in radians is shown in Figure 66.

Table 17 represents the analysis that includes the total power due to off-axis radiation within the field of view of the detector from the specular reflection from the three baffle edges considered. This power is related to the baffle edge radius as follows:

$$\text{Total power on detector from edges} = 57.4 \, \rho R \times 10^{-10} W$$

The maximum power permitted has been given as 1.56×10^{-10} W.

therefore

$$1.56 \times 10^{-10} = 57.4 \, \rho R \times 10^{-10}$$

and

$$R = \frac{1.56}{57.4 \, \rho}$$

152

Edge no. 1 (opening of telescope)
energy impinges upon entire hemispheric area

$$\text{Area} = \pi R \times \frac{40\pi}{2} = 20R\pi^2 \text{ cm}^2$$

Note: aperture = 40 cm
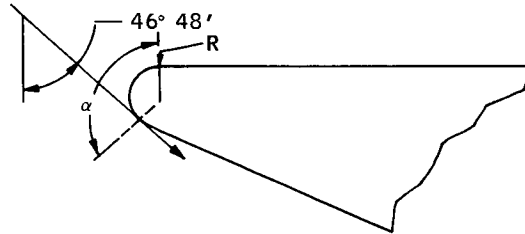
Edge no. 2 (first step in baffle edge line)

$$\text{Area} = 20 R \pi^2 \times \frac{(90 + 48.8)}{180} = 15.5 R \pi^2 \text{ cm}^2$$

46° 48′

27° 18′
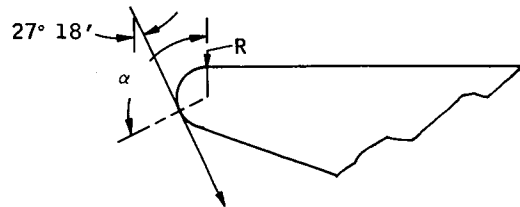
Edge no. 3 (second step)

$$\text{Area} = 20 R \pi^2 \frac{(90 + 27.3)}{180} = 13.1 R \pi^2 \text{ cm}^2$$

Figure 66. Baffle Edge Effects

153

TABLE 16.- EDGE-REFLECTED POWER ANALYSIS

A	B	C	D	E	F	G
Edge no.	Incident angle	Depth within telescope	Irradiance W/cm^2	Area cm^2	Power on edge, watts (column D x column E)	Total reflected power, watts F x ρ, W (a)
1	90°	0 in.	1290×10^{-6}	$20R\pi^2$	0.25464 R	0.25464 ρ R
2	46° 48'	14.8 in.	370	$15.5R\pi^2$	0.05660 R	0.05660 ρ R
3	27° 18'	30.7 in.	130	$13.1R\pi^2$	0.01681 R	0.01681 ρ R

a ρ = reflectivity

TABLE 17. – POWER ON DETECTOR – SPECULAR ANALYSIS

$$\frac{\text{Power on detector (watts)}}{\text{Total reflected power (edge)}} = \frac{0.2 \times 0.8 \times 10^{-6} \ (rad)^2}{\text{Angle subtending exposed edge} \times \pi \ (rad)^2}$$

Edge no.	Total reflected power, W (column G of Table 3)	Column B x 16×10^{-8}	Angle subtending edge, deg.	π x angle sub-tending edge, $\frac{\pi(\text{column D})}{52.3}$, rad^2	Power on detector $\frac{\text{column C}}{\text{column E}}$, W
1	.25464 ρR	$4.07424 \ \rho R \times 10^{-8}$	180°	9.89	$41.3\rho R \times 10^{-10}$
2	.05660 ρR	0.90560	(90+48.8) 138.8°	7.61	11.9
3	.01681 ρR	0.26896	(90+27.3) 117.3°	6.43	4.2

Σ power = 57.4 ρR x 10^{-10} W

where ρ = reflectivity. Assuming a reflectivity of ρ = 0.1,

R = 0.272 cm = 0.107 inches

Thus the baffle edge may be defined by a radius of 0.107 inches if all reflections are specular.

Spectral Filtering

The ideal spectral response function of a radiometer for this measurement would be perfectly rectangular with no sensitivity on either side of the 14.0-to 16.28-μ band if such were also possible for horizon sensors.

This ideal case may be approximated by the use of a spectral filter within the radiometer system which minimizes errors due to radiation from beyond the band limits.

The spectral response function of the radiometer is given by the general equation

$$R(\lambda) = \rho(\lambda)^2 \; \tau(\lambda)_R \; \tau(\lambda)_F \; S(\lambda)$$

where

$\rho(\lambda)$ = spectral reflectance of the surfaces of the primary; and secondary mirrors

$\tau(\lambda)_R$ = spectral transmittance of the re-collector lens

$\tau(\lambda)_F$ = spectral transmittance of the filter

$S(\lambda)$ = detector spectral response function

Therefore, the required $|\tau(\lambda)_F|$ may be calculated only after the actual spectral sensitivity of the detector and the spectral characteristics of the other components have been determined.

The two mirrors are polished or gold-coated aluminum to achieve low emissivity, high reflectance surfaces. A single lens, the re-collector, forms the front window of the dewar. This lens is fabricated from germanium on which is deposited a wide-band spectral filter to reduce the heat load on the detector assembly components. Mounted directly in front of the detector is the multilayer-type spectral filter.

156

Material for the re-collector and filter substrates. -- A study of mater-ials which transmit in the 14.0- to 16.3-μ interval has been made to determine the best substrate to use for the filter and the best material for the re-collector lens. Mechanical stability, spectral transmittance, fabrication experience, repeatability of performance, and related physical characteristics have been studied. Germanium has the best combination of characteristics for both, the filter and re-collector lens (ref. 6).

General spectral transmittance characteristics of germanium at various temperatures are shown in Figure 67 (ref. 7). The curves may be inter-polated in an approximate manner to find the function for the recollector lens which is at 200 °K and the filter substrate which is at approximately 20°K.

Transmittance is a function of the thickness, and its value may be found by the solution of Bouguer's Law

$$\tau(\lambda) = e^{-a\,x}$$

where

  a is the absorption coefficient, and x is the sample thickness.

Total transmittance in the spectral band of interest is found by

$$T = \frac{\int_{14}^{16.23} \tau(\lambda)\,d\lambda}{\int_{14}^{16.23} d\lambda}$$

An empirical solution to Bouguer's Law as measured on a spectroradiometer is shown in Figures 68 and 69, for two thicknesses of germanium at room temperature. It may be seen that there is an absorption dip at ~ 650 cm^{-1} which could interfere with the desired radiometer response function. Figure 67, however, shows that at the operating temperature of both the re-collector and the spectral filter, the absorption of the germanium is so small that the dip should have a negligible affect upon the response function. Verification of this during the final design of the radiometer will be neces-sary.

Two other materials have been considered for use as the filter substrate or the re-collector lens. The materials and their characteristics are

    1)   Polycrystalline zinc sellenide (Kodak Irtran 4)
        This material has been used for substrates and lens elements which operate in the radiometer's spectral region. There are no absorption bands in the spectral transmittance function which, however begins slowly decreasing at 15 microns as shown in Figure 70. Interference filters and antireflection coatings have been placed on Irtran 4 and are available from several manufacturers; however, there is some doubt as to the filter adherence at low temperatures.

157
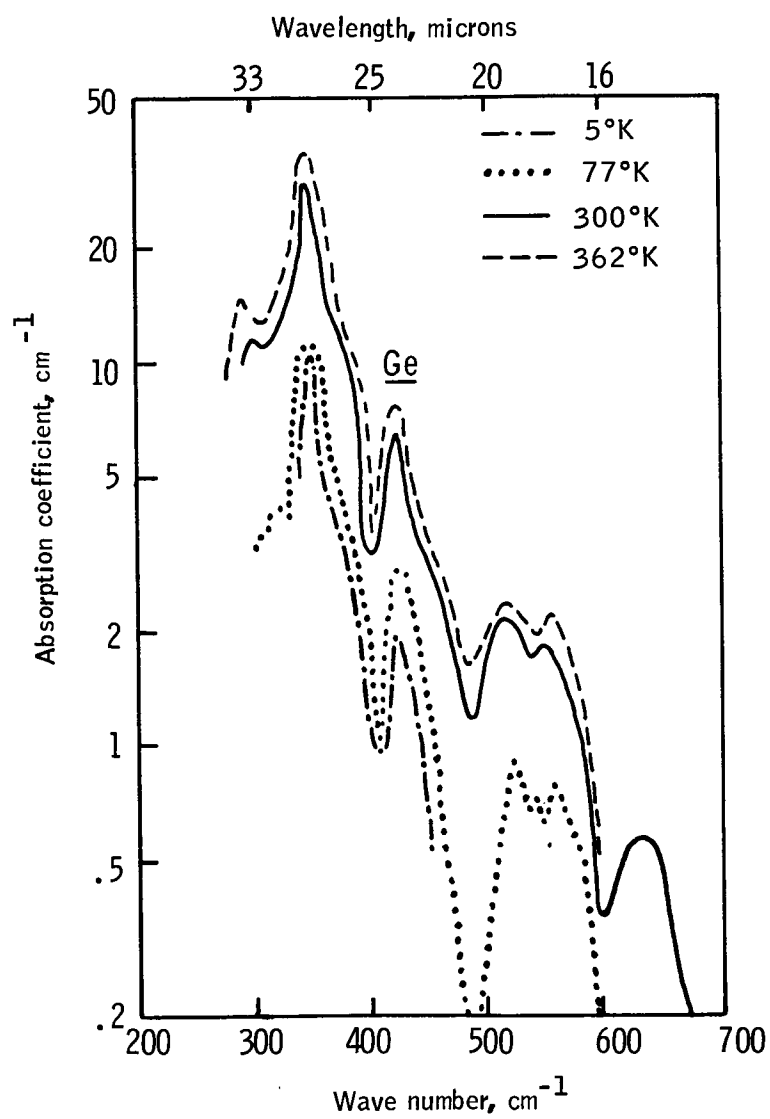
Figure 67. Lattice Vibration Adsorption in Germanium (Ref. 7)
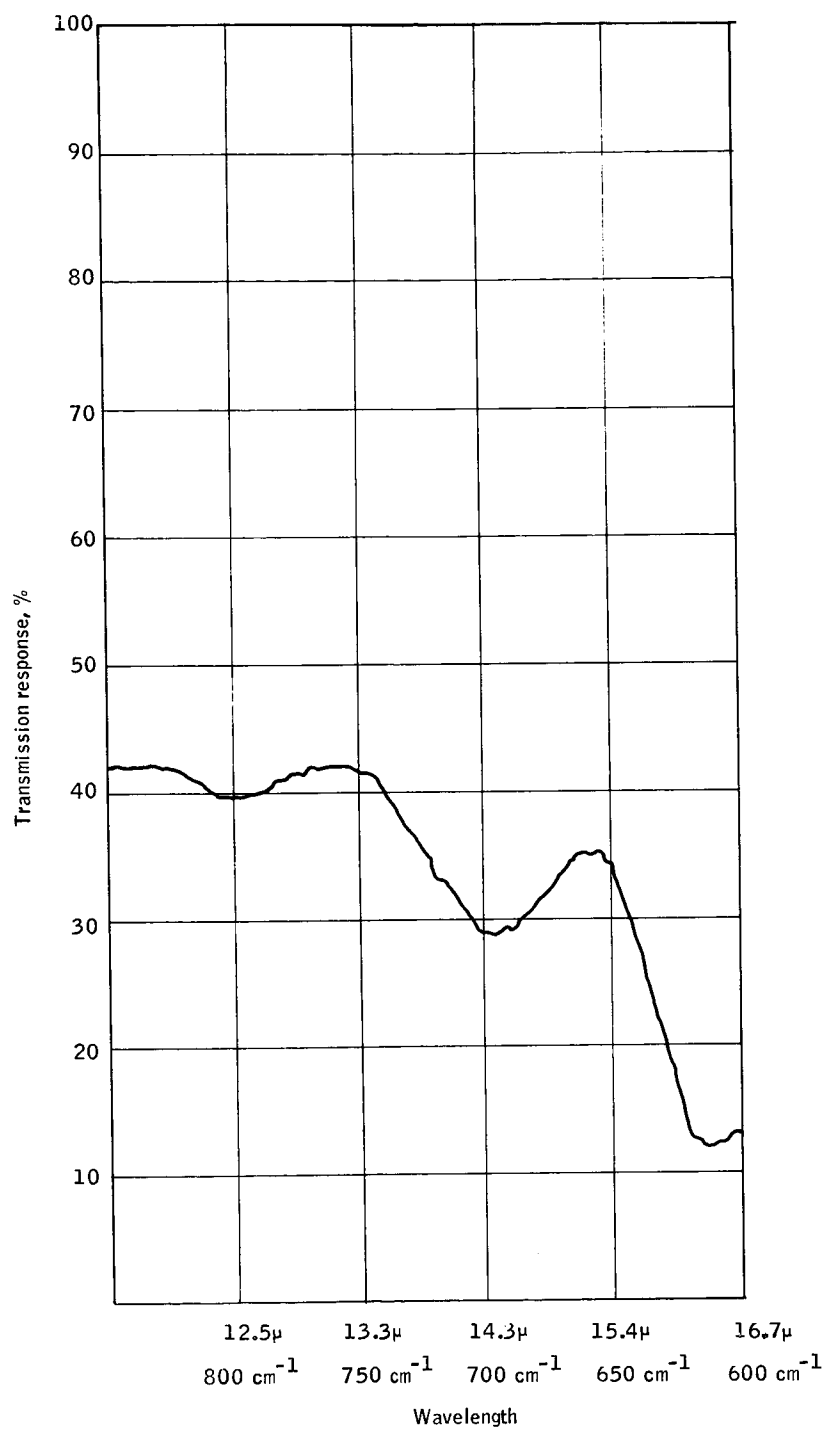
Figure 68. Spectral Transmittance of Germanium 0.250-inch Thick
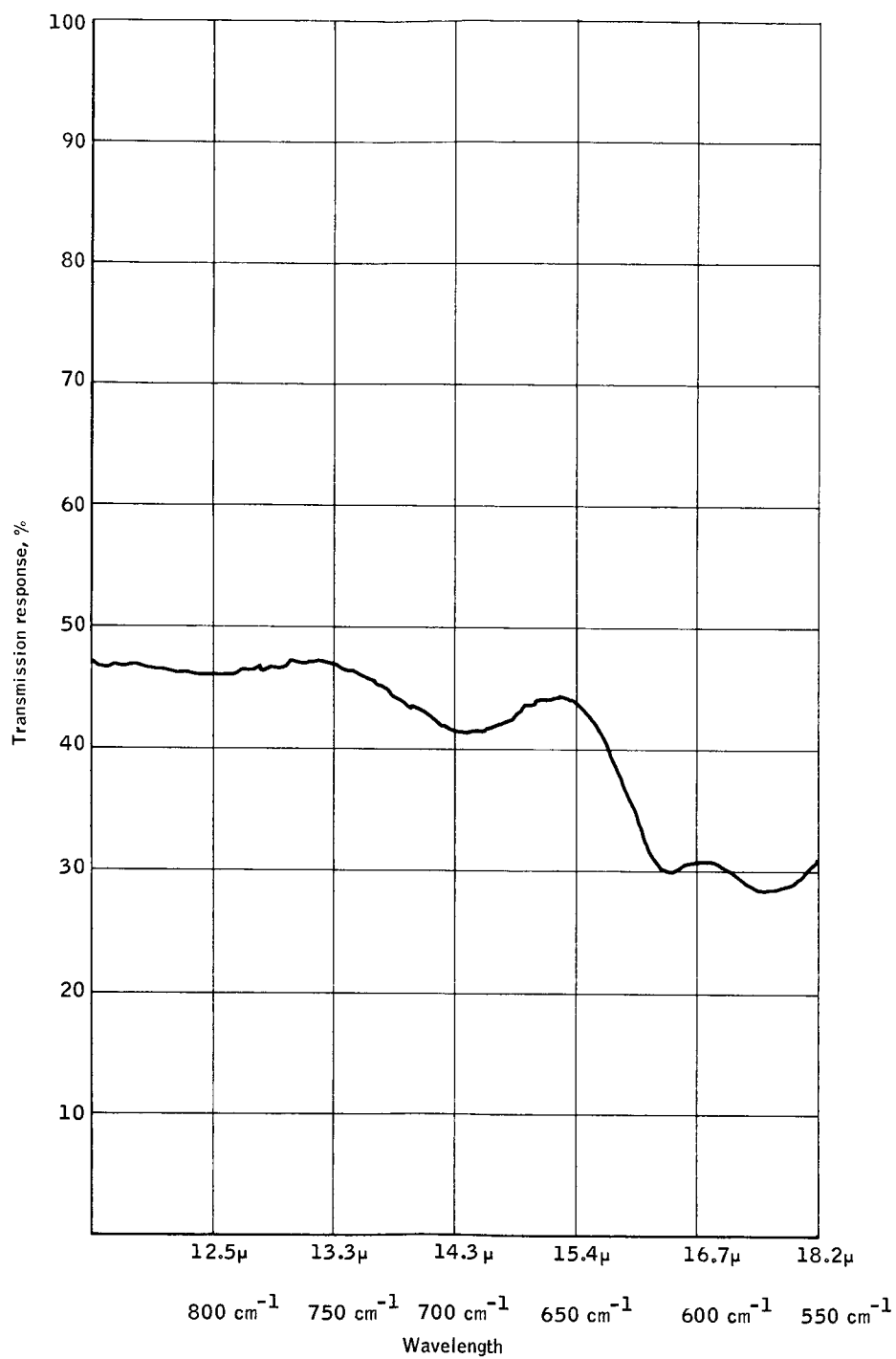
Figure 69. Spectral Transmittance of Germanium 0.080-inch Thick
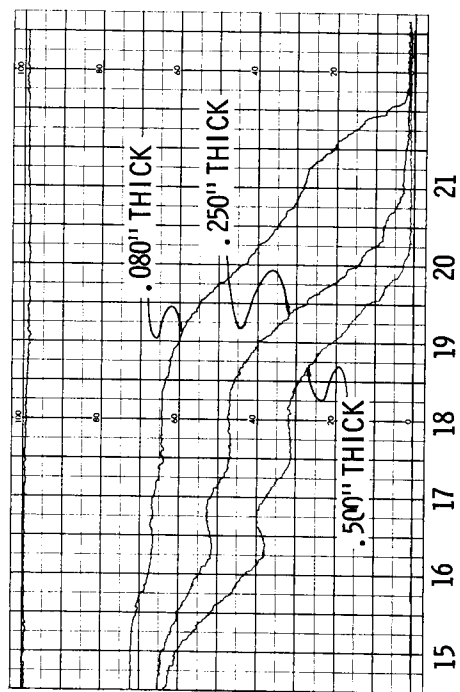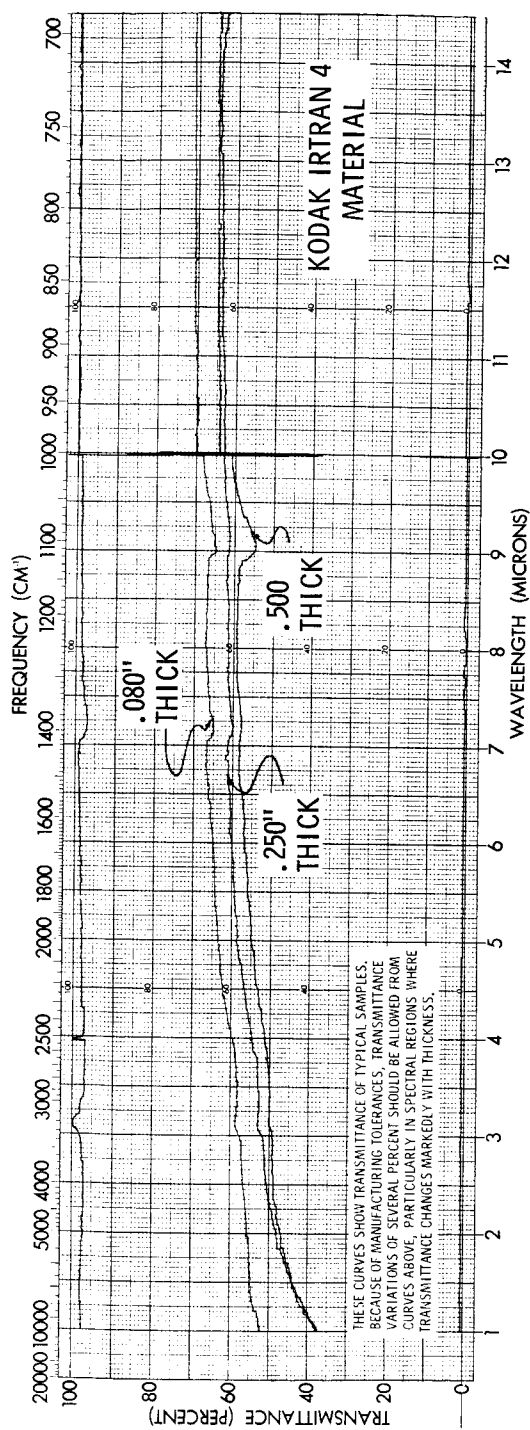
Figure 70. Irtran 4 Spectral Transmission

2)   Polycrystaline cadmium telluride (Kodak Irtran 6)
     Since this is a relatively new material for use in infrared systems,
     there are very little data on its characteristics available at this
     time.   Further investigation of its characteristics will be neces-
     sary, however, before it may be chosen or rejected.   Appendix B
     presents a summary of the data which is presently available.

     Spectral filter. -- As was previously discussed, the ideal radiometer
spectral response would be a rectangular function between 14.0 and 16.23μ
with no response in any other spectral region.

Preliminary analysis of the spectral transmittance of germanium indicates that
it may, for a first approximation [a], be considered constant over the spectral
region of interest.   The spectral reflectance of the gold or aluminum mirrors
may be assumed constant; thus, the response equation may be reduced to

$$R(\lambda) = \tau(\lambda)_F S(\lambda) \tag{9}$$

The spectral response of the Ge:Cd detector, $S(\lambda)$ was shown in Figure 24,
and the 14-to 16.3-μ region of this function has been enlarged and is shown
in Figure 71.   Assuming the ideal response for $R(\lambda)$, equation 9 may be
solved for $\tau(\lambda)_F$.   The result of this calculation is shown in Figure 72, the
desired spectral transmittance function of the spectral filter.

The filter which will approximate this function is composed of layers of
quarter-wave thickness with alternate high and low indexes of refraction.

The simple stacking of low and high index films yields progressively narrower
bandwidths; however, the simple stack also has passbands at wavelength
multiples of the fundamental wavelength.   If these multiple pass bands occur
within the sensitive spectral range of the detector, they may be blocked by
additional filter layers.   One method of providing this blocking is to use
long-wavelength filters to block wavelengths shorter than the desired wave-
length.   Short-wavelength pass filters can be used to block all wavelength
longer than the desired wavelength.

The use of a long-pass and a short-pass filter pair can define a bandpass.
Usually the resulting filter slopes are rounded and do not provide a precise
spectral interval.

For applications requiring a broad spectral interval with sharply defined
edges, a "square band" filter design is possible by using the general layer pat-
tern of $(HL)^m LL(HL)^m \ldots LL(HL)^m$.   The overlapping filter skirts of the
different $(HL)^m$ stacks result in a rapid decrease in transmission outside of
the desired pass band.

A series of graphs selected from reference 8 illustrate the differences be-
tween the various types of filters.   These graphs, which are shown in Appen-
dix C, are for shorter wavelengths than will be utilized in the radiometer;
however, similar characteristics can be obtained.

[a] The recollector lens will be of the order of 0.10 to 0.15 inches thick result-
in a variation in spectral transmittance of 15-30 percent over the band room
temperature, certainly much less at 200°K.   The filter will be of less thick-
ness and at 15°K should be quite constant over the band.

162
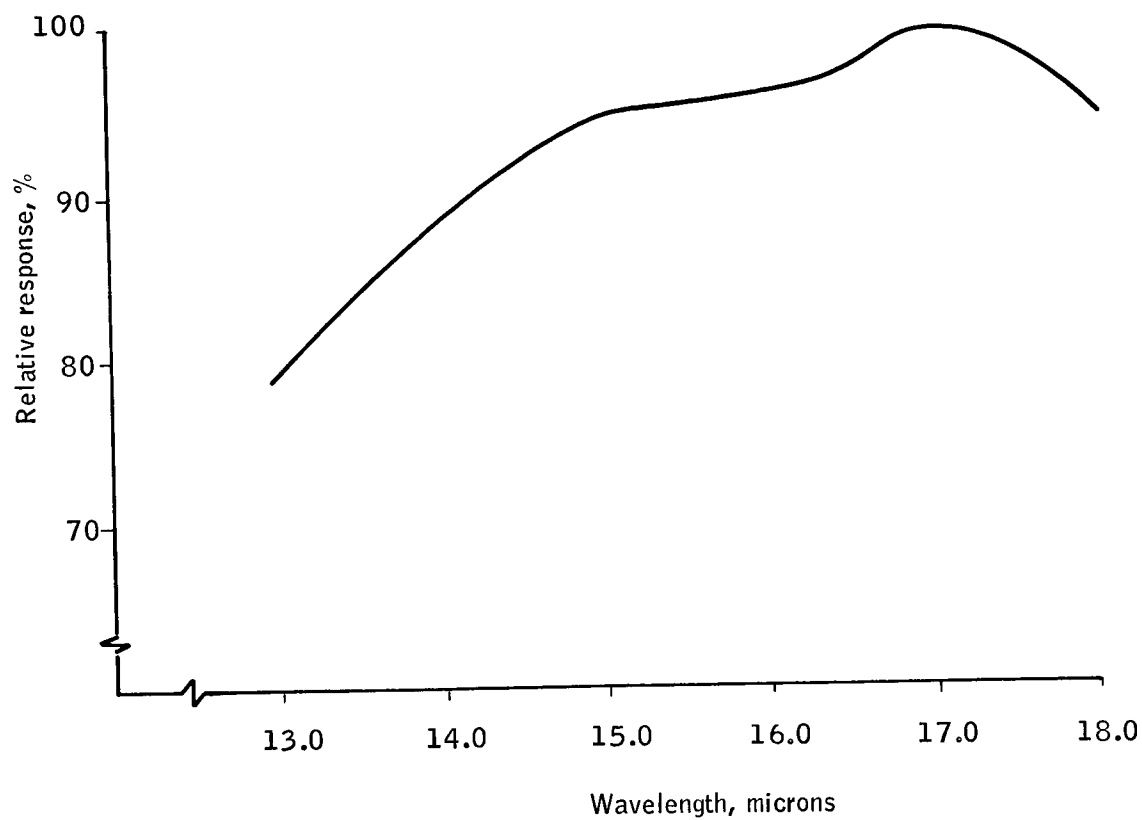
Figure 71. Spectral Response of Ge:Cd Detector
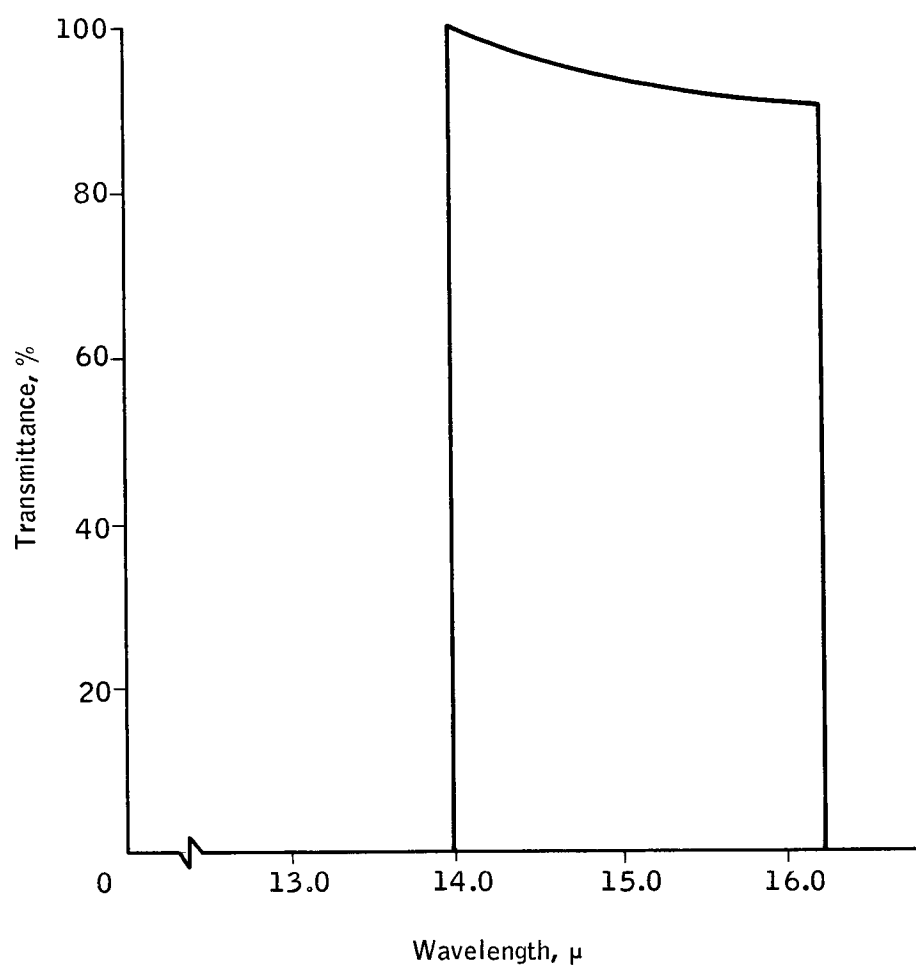
Figure 72. Spectral Transmittance of Ideal Filter

164

Figure 73 shows the relative spectral energy distribution $N(\lambda)$ of a 194°K blackbody source, approximation to the atmospheric CO_2 emission characteristic. The response of the radiometer when measuring this source will be

$$R = \int_0^\infty N(\lambda)\, S(\lambda)\, \tau(\lambda)_F\, d\lambda$$

For simplification it may be assumed that $N(\lambda)$ is constant over the 14-to 16-μ region. The error in this assumption may be calculated by

$$E = \frac{\int_{14}^{16} d\lambda - \int_{14}^{16} N(\lambda)\, d\lambda}{\int_{14}^{16} d\lambda}$$

$$\approx \quad 0.25\%$$

Utilizing this assumption, the radiometer response may be reduced to

$$R = \int_0^\infty S(\lambda)\, \tau(\lambda)_F\, d\lambda$$

where, as above $S(\lambda)$ is the spectral sensitivity of the Ge: Cd detector, and

$\tau(\lambda)_F$ is the spectral transmittance of the spectral filter.

The ideal rectangular response function was shown to be achieved with the Ge:Cd detector and the filter transmittance of Figure 74. Appendix C data shows that this spectral response function may be approximated with the exception of the infinite slope of the sides of the function. Therefore, the approximate error may be calculated by assuming sides of nominal shape for the spectral transmittance function $\tau(\lambda)_F$. This calculation was performed with the filter function shown in Figure 74. Shown here are the ideal function, as in Figure 72, and the assumed function for a filter that could be fabricated. If the filter were assumed to have the ideal transmittance function when, in fact, it had the assumed function of Figure 74, the error may be calculated by solving the equation

$$R = \int_0^\infty N(\lambda)\, S(\lambda)\, \tau(\lambda)_F\, d\lambda$$

for each of the two filters. This calculation shows that a one percent error would result which is equivalent to requiring radiation in that region to have 100 percent modulation to produce a one percent uncertainty in the in-board measurement. Comparison of the assumed function of Figure 74 and the
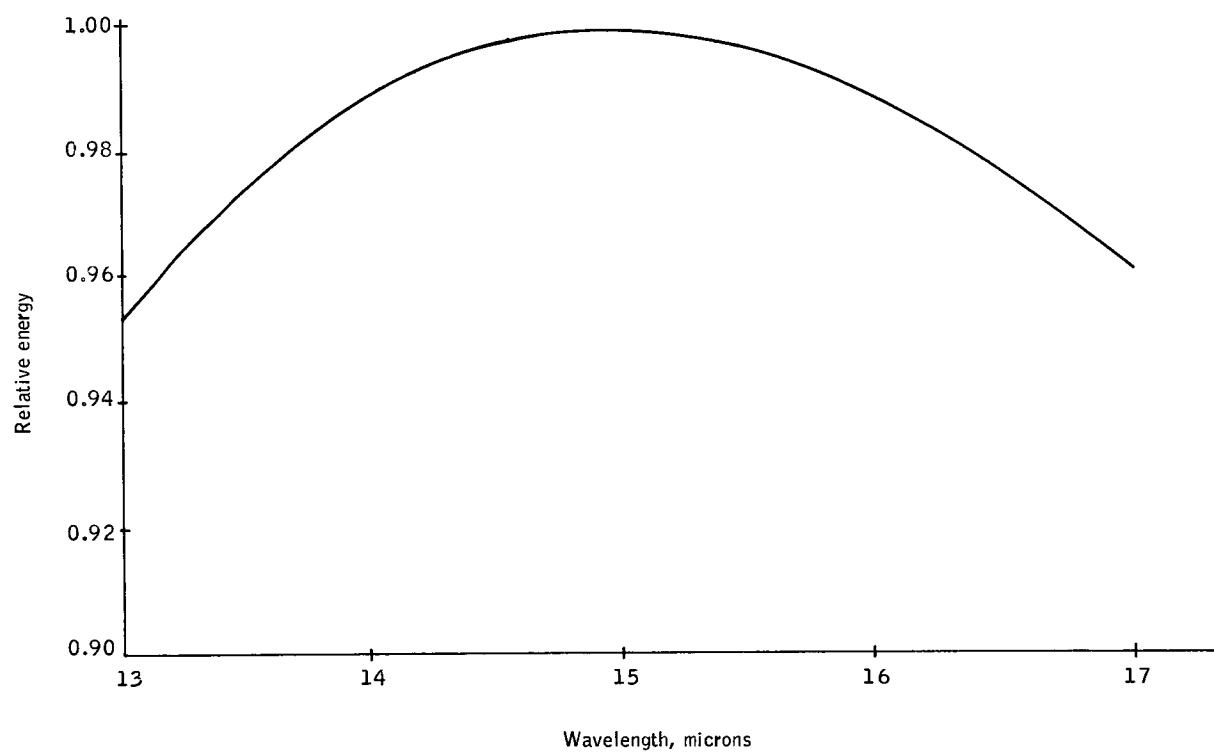
Figure 73.   Relative Spectral Energy Distribution of a
             Blackbody at 194 °K
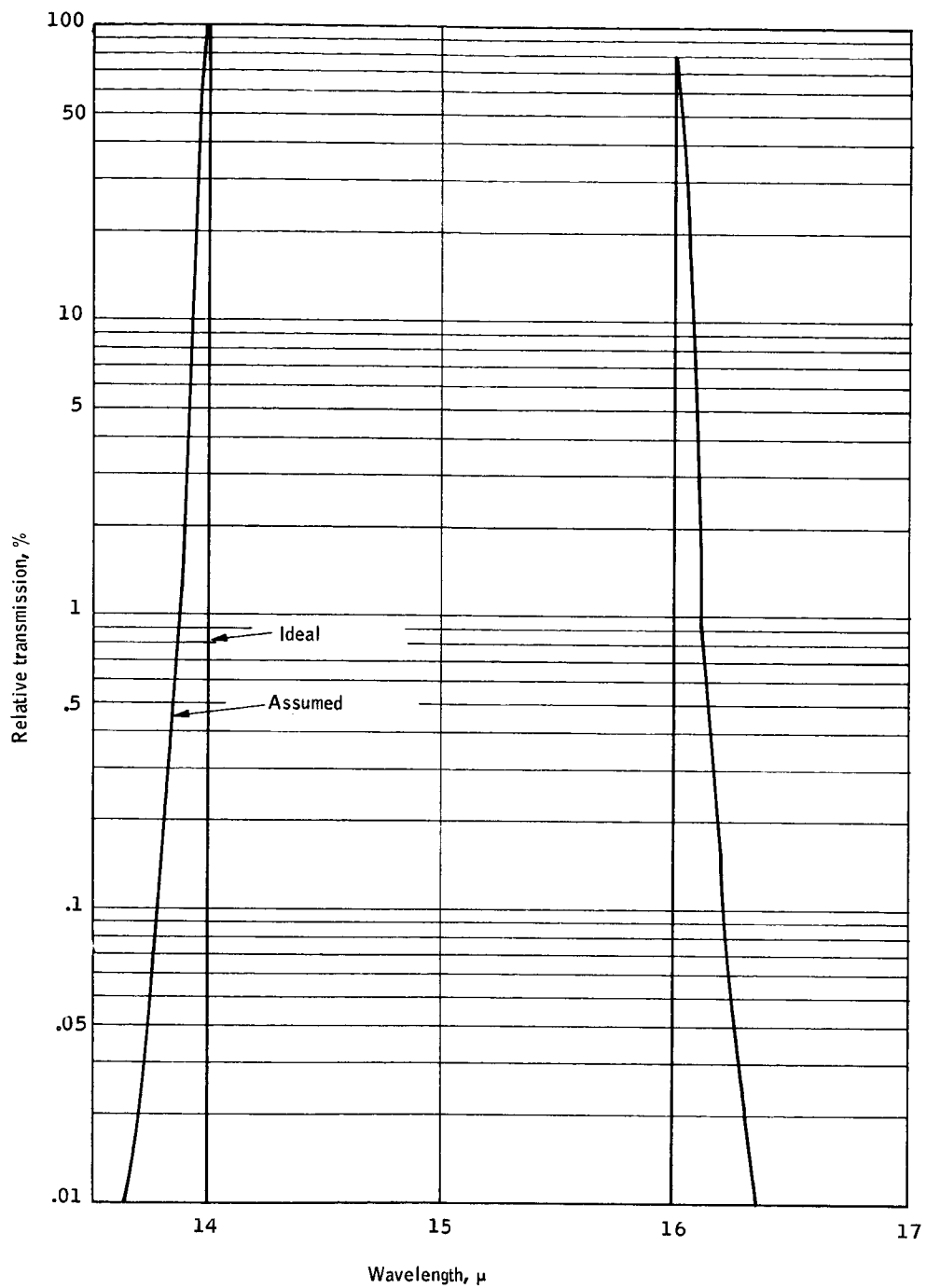
Figure 74. Spectral Transmittance of Ideal and Assumed Filter

function shown in Appendix C, Figure C2 will show that the slope of the sides of the two curves are approximately the same; thus this filter can be fabricated.

Although the spectral filtering system will be designed to match this ideal response as closely as possible, the spectral response function of the radiometer will be measured as part of the calibration procedure. The only residual error will then be the accuracy of this measurement. This is the error against a rather idealized source, the 194°K blackbody, which is a gross approximation to the actual spectral content of the horizon radiance. The latter is highly structured in the band, can vary its effective temperature as a function of tangent height, and be highly modulated by other atmospheric constituents in neighboring spectral intervals. Demonstration of the total measurement error due to convolving the instrument spectral response with the spectral characteristics of the horizon radiance will have to be done by computer simulation over the range of applicable variables, including tangent height, latitude, season, etc. as well as for various filter shape and skirt attenuation factors. The intent of the foregoing analysis was to indicate feasibility of the requirement considering just the uncertainties associated with the instrument characteristics.

Effect of filter temperature at angle of incidence. -- The spectral transmittance of a filter is usually calculated for normal incidence, collimated radiation. When the filter is used in a converging or diverging cone of radiation, there will be a shift in spectral bandpass. Since those rays which are incident off the normal traverse a longer path through the filter layers, the spectral transmission shifts towards the shorter wavelengths. This effect is, however, not as severe as oblique collimated radiation measurements would indicate since only a portion of the energy is incident at the full cone angle.

Cooling a filter increases the germanium substrate transmittance slightly and decreases the film thickness; as a result, the peak transmittance shifts toward shorter wavelengths. Therefore, the filter design must be matched to both the incident angle and the operating temperature.

Appendix D (ref. 9) contains details on the effects of incident angle and temperature on the filter characteristics.

A broad-band filter will be coated on the surface of the re-collector lens to reduce the head load on the detector assembly elements. If it is assumed that a 12-to 18-µ filter is used, approximately 1/3 of the radiation from the horizon will impinge on the cold filter so that the heat load on the detector cooler is reduced by this factor. The data of Appendix D show that variations in the angle of incidence or variations in temperature shift the entire bandpass of the filter with very little effect upon the shape of the spectral transmittance function; therefore, no error will result from these variations since the pass band of the re-collector's filter will be considerably wider than the 14-to 16-µ bandpass which is being measured.

168

The spectral filter itself will not introduce an error from temperature variations since it is cooled by the solid-cryogen cooler. The data in Appendix D show that rather large temperature variations are necessary to affect any noticeable change of the spectral transmittance of the filter. Since the detector cooler controls the temperature of the filter, such large variations are not possible.

An error could result from the variation in the angle of incidence with which the radiation impinges on the spectral filter. This effect can be eliminated however, by coating the filter on a curved substrate. If the radius of curvature of the substrate is equal to the distance from the substrate to the detector, all rays from the re-collector lens will strike the filter at normal incidence. The back surface of this filter substrate can also be curved so that its radius of curvature is equal to that of the front surface. This configuration will result in a classical lens design with zero power.

CHOPPER

The chopper function is to translate the information bandwidth which extends from dc to 1600 Hz to a sufficiently high center frequency such that the system is free from the effects of low frequency detector noise and drifts. This is done by optically modulating the incoming radiation prior to its incidence upon the detector.

The most straightforward chopping technique from system considerations has resultant modulation from a value, which can validly be referred to as zero, to the value of radiance to be measured. When, however, the incoming radiation includes spurious, varying components, this becomes impossible. In the current radiometer design, spurious radiation is of two types: stray radiation from points on the earth and other sources outside the instantaneous field of view, and internal emission from elements of the radiometer. If these sources are essentially constant over and just prior to a profile measurement, they can be measured and become the zero reference. This is indeed the case, provided the chopping technique itself introduces no additional modulation of the spurious radiation.

Two chopping techniques were investigated. In one, the instantaneous field of view is continuously deflected into space and back to the horizon; in the other the detector alternately views itself and the horizon. The first approach besides being extremely difficult to implement, suffers in that from chop to chop the detector views slightly different parts of the radiometer interior. The second approach is relatively simpler to implement but suffers from gradients or hot spots on the optical elements which may be chopped at the signal frequency. This latter difficulty is resolved if the chopping is performed at the primary focus of the optical system at which point the gradients are sufficiently smoothed and mixed by the optics transfer function as to be immeasurable. Based upon these considerations the second approach was chosen.

169

Chopper Requirements

The chopper parameters to be defined are chopping frequency, excursion, and thermal/optical constraints.

Frequency. -- If the amplifier bandpass filter had a perfectly sharp cut-off at 1600 Hz, the required chopping frequency, based upon the Shannon limit, would be twice that frequency or 3200 Hz. Errors or noise due to the filter not being perfectly sharp are approximately equal to the value of the integral of the shaded area divided by the information bandwidth Figure 75.

This is an rms error, however, where the associated probability function is decidedly non-gaussian. A more useful description of the error is the amplitude at the crossover point of the two curves. The only spectra involved in the crossover region are those of the detector and amplifier noise as the system transfer function has a much sharper roll-off. Hence, it is only necessary to reduce this error to, say, 10 percent or 20 dB down from the peak.

A barely practical filter would reach a slope of 36 dB/octive at 2000 cps at which point it would be approximately 12 dB down. Then, the 20 dB point would occur at about 2500 Hz, implying a chopper frequency of at least 5000 Hz. Should the chopper be marginal at this frequency, from the analysis in the section on systems analyses, a tradeoff remains against where the 3 dB point of the filter is to be placed. A significantly lower frequency could be used with little compromise to system performance.

Excursion. -- At an 80-cm focal length, the minimum detector dimension is 16×10^{-3} cm. It is desirable that the null position of the chopper be in the totally "off" condition, implying a peak-peak excursion of 32×10^{-3} cm plus whatever is necessary to account for the diverging characteristics of the optical beam. With this approach, two chopping cycles occur for each cycle of chopper motion.

Thermal Optical Constraints. -- To avoid the chopper producing spurious signals the following constraints apply:

1. As little as possible of the chopper blade outside that covered by a resolution element shall be visible to the detector in order to minimize chopping of structure emission and stray radiation.

2. The emissivity of the chopper shall be minimized, preferably less than 0.01, and certainly no greater than that of the field stop.

3. The chopper blade temperature shall be within ±1°K of the field stop temperature.

4. The vicinity of the chopper shall be baffled to avoid optical crosstalk between adjacent resolution elements.

170
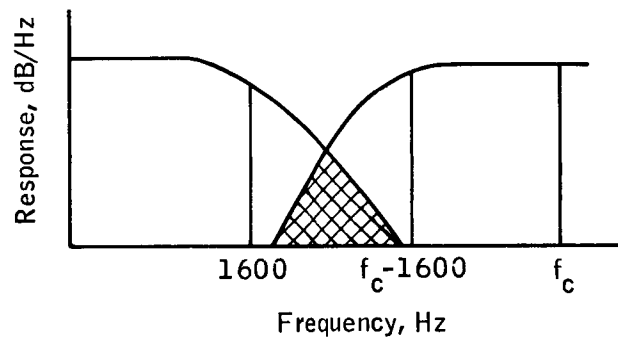
Figure 75. Sideband Overlap

Alternate Chopper Mechanisms

The initial effort for the development of a resonant chopper studied a reed-type three to five kHz chopper with a germanium wedge attached to the tip to deflect the field of view. By setting up a series of approximations for the mathematical model of the chopper, it was determined that the reed-type chopper, utilizing an efficient electrodynamic vibrator drive, was limited to frequencies of 2500 Hz or less. The manufacturer's literature confirms that tuning fork choppers are limited to frequencies below 3000 Hz at an excursion which would permit only one "chop" per chopper cycle and violate the criterion that null position should be the off-position.

Because a higher frequency is required other choppers were investigated. The American Time Products, Division of the Bulova Watch Company, have recently upgraded a torsional pendulum scanner, to 6000 Hz with an angular excursion of 4°, peak to peak. The radius arm above the upper torsional mass is one quarter of an inch in length, thus providing a total tangential excursion of 0.0175 inches. With a mirror on the end of one arm and a counter weight placed at the end of the opposite arm, the frequency would be lowered to not less than 3000 Hz, and the excursion would be 0.015 inches. The mass of the mirror and its distance from the center of oscillation are the operational factors required to determine its chopper's performance characteristics. An experiment was conducted using a piece of brass approximately 0.040 x 0.040 x 0.125 inch at the end of one arm, with a similar weight of brass, as a counter weight placed at the end of the opposite arm. The frequencies and amplitude were above 3000 Hz and 0.015 inch respectively. Therefore, the frequency would be above 5000 Hz with a 0.01 x 0.01 x 0.08 -inch aluminum or berryllium mirror and counter weight mounted at the tips of the arms. The power required was approximately 200 mW.

A third chopper mechanism which was considered is a rotary disc which contains alternating mirrors and apertures. The disc which would be manufactured from 0.003-inch beryllium copper is photoetched to provide the necessary chopper spacing. A 1.4-inch diameter disc would contain two-hundred 0.010-inch wide mirrors and spaces so that a 6000 Hz chopping rate could be achieved by a 1800 rpm angular velocity. Although the rotating mechanism does achieve the required chopping rate, chopper emissivity variations over a large surface, bearings, and motor reliability cause this system to be secondary to the torsional pendulum chopper.

Description of Recommended Chopper

The chopper consists of a torsion rod, a driving arm, a base, two electro-magnetic coils, and two pole pieces. (See Figure 1). The torsion rod is firmly attached to the base, similar to a classic torsional pendulum. A driving arm, made of a highly permeable steel, is affixed through and centered on the lower portion of the rod and coil is placed on each side of the arm. The two pole pieces extend from the end of one arm, across the chopper to the end of the other arm. These are both permanent magnets, with their poles opposed, and with the end of the driving arms placed in the air gaps. By inducing a current in the coils, the arm is polarized. It will, therefore, be attracted to the opposite pole, which creates a torque, causing the rod to twist. By introducing an alternating current into the coils, the

driving arm will oscillate between the pole pieces, which will create an os-
cillatory angular motion in the torsion rod. The amplitude ratio will be a
function of the driving torque, the resonant frequency of the system, the
driving frequency, the damping factor, and the moment of inertia of the
torsional mass.

Because of the high frequencies involved and the many damping variables,
only an estimate of the chopper performance can be calculated. This
relationship follows the relationship of an oscillating motion exciting the
base of the system where the base is considered as the mass immediately
above the driving arm as is shown in the following equation.

$$\left|\frac{\theta}{\nu}\right| = \frac{\sqrt{1 + \left(2\delta \frac{\omega}{\omega_n}\right)^2}}{\left[1 - \frac{\omega}{\omega}\right]^2 + \left[2\delta\frac{\omega}{\omega_n}\right]^2} \tag{10}$$

Where:

ω is the induced angular frequency

ω_n is the natural frequency

ν is the motion of the base

θ is the response of the torsional mass

δ is the damping factor

$\frac{\theta}{\nu}$ will be greater than 1.0 up to a frequency of $\omega_n \sqrt{2}$.

Within this region, a small base motion will give a noticeable deflection
to the torsional mass, especially near resonance.

The motion will be sinusoidal and will follow the relationship:

$\theta = \theta \sin(\omega t - \phi)$

where ϕ is the phase angle, induced by the system damping, between the
base and the mass. For the best response, the damping should be small.

The motion of the base can be calculated from the torque introduced into the
lower portion of the rod. This, however, becomes a two degree of freedom
system, which tends to introduce complexities unless it is assumed that the
lower portions are much stiffer than the upper portion and, therefore, trans-
mits only the induced motion caused by the torsional oscillations of the
driving arms.

These units can be made to withstand the environment of space without having to undergo major changes. The primary change would be to use a different lacquer on the coil windings. American Time Products has produced choppers for the MIT Instrumentation Laboratory for use in the Apollo guidance and navigation system, and also for other satellite applications. They are, therefore, familiar with the rigors of this environment, and what must be done to protect instrumentation against it. Because there are essentially no moving parts in contact, the chopper life expectancy depends solely upon the failure rate assumed for the coils.

The chopper, Model No. L44, which is shown in Figure 76 has a weight of 4 ounces and is 0.5-inch square by 3-inches high. It comes in a small, sheet metal case which may be discarded if it is operating within a temperature range of -55° C to 85° C. The temperature limits can be extended by the fabrication of special units, with a different coil insulation. To keep the cross arm, or the base, out of the line of sight of the optical system, the mirrors will be placed at a small angle to the cross arm. (See Figure 77). This angle will be minimized to keep the motion of the mirror nearly planar. In conjunction with the small angular excursion of the arm, the variation from a plane motion will be extremely small.

Cooling of the chopper mirror can be accomplished by heat sinking the aluminum base to the spacecraft structure to conduct most of the heat developed by the electromagnetic driving coils. By placing a cooling jacket around the torsional shaft (which is made of beryllium copper) above the driving coils, the shaft can be kept cool. By making the cross arm of a light metal, the mirror can also be cooled by conduction. It will be necessary for the cooling jacket to cool the torsion shaft solely by radiation. Otherwise, if physical contact is made for conductive cooling, energy would be lost from the vibrating system with a resulting decrease in frequency.

Although the acceleration forces at the ends of the arms are high (above 5000 g) the mass of the mirrors is very low (5 x 10^{-7} lb.). The shear stresses on an adhesive under these conditions would be low. Therefore, bonding of the mirror to the cross arm is primarily a question of selecting an adhesive suitably adapted to the vacuum and temperature conditions encountered in this particular spacecraft. A high strength adhesive is not required for this application. American Time Products will bond the mirror to the cross arms to make the proper frequency adjustments to their chopper. The adhesive will be selected and tested under operating conditions to ensure that it meets the environmental specifications.
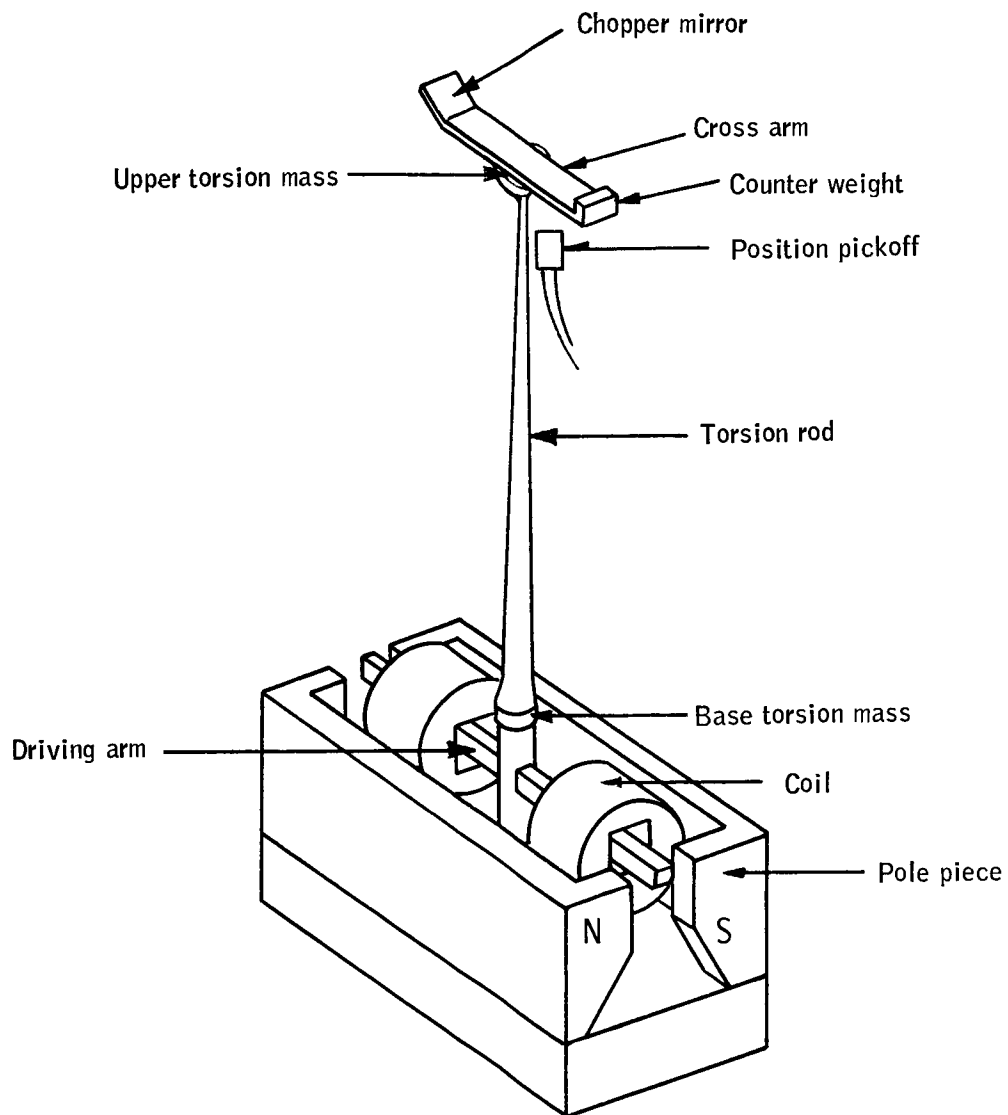
Figure 76. Sketch of Torsional Pendulum Chopper
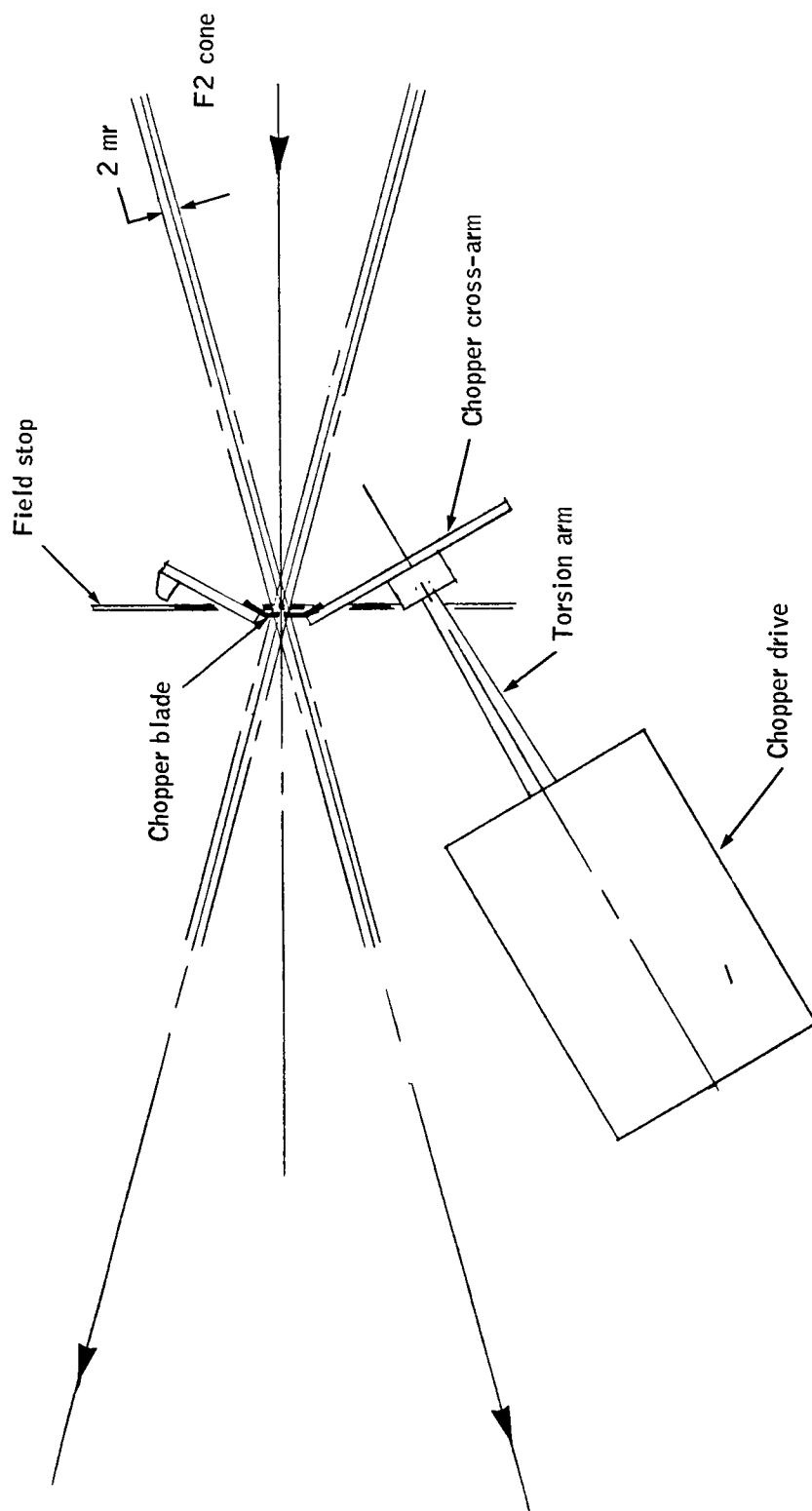
Figure 77. Sketch of Chopper Mechanism within Optical System

176

DETECTOR COOLING

The feasibility of meeting the radiometer performance requirements is critically dependent on achieving necessary detector temperatures during the orbital life of the mission. In the following paragraphs, a cooling system design is developed to demonstrate feasibility and to define and evaluate problem areas. Although requiring a development program to conform to the specific needs of this program, the cooling system defined is within the current state of the art.

The detector cooling requirements may be summarized as follows for the two applicable detector materials:

Cadmium-doped germanium (first choice)

- Operating temperature   15 to 20° K

- Bias power dissipation   5 milliwatts

Mercury cadmium telluride

- Operating temperature   50 to 65° K

- Bias power dissipation   5 to 10 milliwatts

The ambient temperature shall be 200° K for both cases. In addition to meeting the above requirements, the cooling system must handle the heat loads imposed by refrigerator insulations, by detector mounting and leads, and through the optical path to the detector. The cooling system must meet all requirements over a one-year operating life in orbit.

Comparison of Alternate Types

Several methods have been considered for refrigerating the radiometer detector to the required temperatures. The methods considered, and detailed below, encompassed three basic techniques: passive radiation cooling to space, closed-cycle refrigeration machines, and open-cycle stored refrigerants.

Radiation cooling. -- Studies have been made for several different space-craft missions on the feasibility and design of detector coolers based on the principle of passive radiation cooling to free space. Successful radiation cooling techniques requires careful consideration and minimization of all heat inputs from the earth, sun, and spacecraft.

A free panel (such as the baseplate of the HDS spacecraft) can reach temperatures in the range of 180°K to 200°K by merely applying coatings that minimize the albedo absorbtion and also have a high infrared emittance. Obtaining lower temperatures on this panel (which is never irradiated directly by the sun) is prohibited by the radiant heat transfer between the panel and earth.

Cooling of panels to lower temperatures requires that the earth input be reduced either by increases in orbital altitude or specially designed shielding techniques.

Construction of an adequate radiation cooler for the spinning HDS spacecraft is not practical. If the spacecraft were operated in an earth-oriented mission mode, a cooler and shield could be designed to achieve 70°K to 30°K temperatures. Highly sophisticated designs have also been conceived to reach temperatures as low as 40°K for an earth-oriented spacecraft in a 600 n. mi. orbit.

Radiation cooling of the doped-germanium type of detectors, with operating temperatures in the 4°K to 30°K range, cannot be practically considered, and the HDS mission rules out practical radiactive cooler designs for 80°K operation.

Closed-cycle refrigeration. -- Consideration has been given to the use of miniature, closed-cycle refrigeration machines operating on Sterling or Brayton cycle principles. These machines, with input powers in the range of 20 to 40 watts, are now available for ground-based operations and cool detectors to the 50°K to 80°K region. Operating reliability generally rules out the use of these closed-cycle machines; the best projected operating lifetimes is in the range of 1000 to 3000 hrs.

There are other developments being made in the long-lifetime, closed-cycle refrigerator concept, but they are not yet reduced to practical and operational equipment. In addition, these machines are generally not applicable for the low temperature requirements of doped-germanium detectors.

Open-cycle stored refrigeration. -- Two general forms of open-cycle refrigeration are presently available: Joule-Thompson expansion of high-pressure stored gas, and stored solid or liquid cryogens. No further consideration will be given to the Joule-Thompson expansion process, since the gas storage requirements for one-year operation are not practical.

Stored liquid cryogen is a commonly used method of refrigeration for ground-based operations, but would suffer in a zero-gravity environment due to the problems of providing a proper liquid-vapor phase separation. However, a properly designed solid-cryogen refrigerator is capable of retaining the refrigerant while dissipating by sublimation the thermal inputs to the refrigerator.

It is in this principle of the expendable solid-cryogen storage refrigerator that suitable means for cooling of the doped-germanium detector will be found. There remains the significant problems of the proper conception and execution of a refrigerator design that will satisfy the HDS mission requirements. In an effort to define a suitable refrigerator, a design study has been performed and is reported in the following paragraphs.

Design Analysis of Solid-Cryogen Refrigerators

Introduction. -- The only systems presently capable of providing practical refrigeration of on-board infrared detectors for long-term missions are those employing either solid or liquid cryogens. Of the two systems, a cryogen in the solid state is more favorable than the same cryogen in the liquid state for the following reasons:

- In the zero gravity conditions of spacecraft, there is no venting problem in the case of solid; whereas for the liquid phase, there could be two phase or liquid venting.

- In the solid system, the latent heat of fusion is available for refrigeration. This is a 10- to 15-percent gain in refrigeration capacity for most cryogens. Also, there is a 10- to 15-percent gain in density in the solid phase which permits construction of a smaller, lighter system.

Basically, a solid-cryogen refrigeration system consists of a container initially filled with a solid cryogen which is coupled thermally to an external load in this case an infrared detector by means of a link of high thermal conductivity extending from a heat exchanger within the cryogen container. The cryogen is chosen so that the desired detector temperature is maintained at some appropriate value by controlling the vapor pressure over the solid. Pressure control is achieved by controlling the venting rate of the subliming vapor to the surrounding space environment. All extraneous heat leaks to the solid cryogen should be minimized in order that the principal thermal load on the solid cryogen is due to the infrared detector. This is accomplished by isolating the solid cryogen from its warm surroundings by a vacuum space filled with a multilayer insulation.

The aim of the present design analysis is to provide two different, optimal solid-cryogen refrigerator systems. Each system is to provide approximately 5 mW of infrared detector cooling; one system is to provide cooling at 15 to 20°K, whereas the other system is to provide the requisite cooling at 60 to 70°K. These systems are to be optimized from the standpoint of possessing minimum volume and weight and having high reliability. At the same time, the vapors of the cryogens to be used should not have any infrared absorption characteristics in the 14-to 16-µ region; otherwise, the refrigerator system might interfere with the infrared system for which it is used.

The choice of the optimum cryogen depends on the particular detector operating temperature desired. Thermodynamic characteristics of the various cryogens having high latent heats of vaporization are indicated in Table 18. For a given cryogen, the highest operating temperature of the solid phase is defined by its triple-point temperature; the lowest is defined by the vapor pressure over the solid required to vent the flow of vapor due to the total heat load on the solid. The vapor venting rate is limited either by venting line conductance or the presence of choked (sonic) flow in the venting line. If the diameters of the venting lines are significantly increased to permit venting at a lower vapor

TABLE 18. - REPRESENTATIVE SOLID-CYROGEN CHARACTERISTICS

[From refs. 9, 10, and 11]

Cryogen	Operational solid temperature range, $K°$ (a)	Latent heat of sublimation, cal/cm^3 (b)	Density g/cm^3 (b)
Hydrogen	13.8 - 8.3	9.71	0.09
Neon	24.5 - 13.5	25.2	1.495
Nitrogen	63.1 - 43.4	58.8	0.98
Carbon monoxide (c)	68.1 - 45.5	75	1.04
Argon	83.9 - 47.8	82.1	1.7
Methane	90.7 - 59.8	73.5	0.5
Ethylene	104 - 95	123	0.73
Carbon dioxide	217.5 - 125	246	1.7
Ammonia	195.4 - 150	350	0.73

[a]Lower operating temperature point taken as solid temperature corresponding to equilibrium vapor pressure of 0.1 Torr.

[b]Values of latent heat of sublimation and solid density taken at lowest temperature point.

[c]Values for latent heat of sublimation and density taken below solid phase change at 62°K.

pressure, or an equivalently lower solid temperature, then an increased radiation heat leak to the solid via this enlarged opening will result. As a practical rule of thumb, the lowest solid-vapor pressure is in the 0.1 to 0.01 Torr range. In Table 18, a solid temperature corresponding to solid-vapor pressure of 0.1 Torr is arbitrarily considered to be the lowest solid operating temperature. If lower operating temperatures are desired for a particular solid cryogen, a careful analysis of the largest venting line conductance permissible must be made by taking into account the change in system thermal performance due to its presence. However, at the pressure considered here, a decade reduction in the vapor pressure results only in approximately 10 percent reduction in the solid temperature. At the same time, for a fixed venting tube length, the cross-sectional area is increased by a factor of approximately three.

It is evident from Table 18 that for infrared detector systems operating in the 60 to 70°K temperature range, methane is the best choice for a coolant since it possesses a latent heat of vaporization per unit volume approximately as high as any competitive cryogen and yet has a very low density. At the same time, neither methane nor neon have infrared absorption in the wavelength region between 14 and 16 microns. Methane has absorption bands in the region of 2.3, 3.3, and 7.7 microns only (ref. 12). A solid-methane cryogen refrigerator will, therefore, be chosen in the optimization of an infrared detector cooler unit for 60 to 70°K detector cooling in the present study.

It is apparent from Table 18 that the solid cryogens for which temperatures below 20°K may be readily obtained, i.e., hydrogen and neon, have much lower latent heats of sublimation per unit volume than the higher temperature solid cryogens listed in the same table. This makes dual-cryogen refrigerator systems possible in which a cryogen possessing a lower latent heat of sublimation is used for the lower temperature detector cooling while a higher temperature, higher latent heat cryogen is used as a thermal guard material. In a dual-cryogen system, the cryogen used for the detector cooling will be designated as the primary coolant; whereas, the cryogen used in its thermal protection system will be designated as the secondary coolant. The supports for the primary container are thermally grounded to the secondary-coolant container so that the temperature difference between their ends and, therefore, the heat flow from the secondary to the primary coolant is small. The only other significant heat input besides the detector cooling to the solid primary coolant is due to radiation from the low-emittance boundary surrounding the primary-coolant container, which is maintained at secondary-coolant temperature. As will be later discussed in detail an optimal system for the present detector cooling requirements is a dual-cryogen refrigerator system using solid neon for the 15 to 20°K detector cooling and a solid-methane thermal protection system maintained at 60°K. The neon-methane system will require approximately 6.6 lbs (3000 g) of neon which will occupy a container volume of 2200 cm^3.

If hydrogen were used in place of neon, its weight, for the same detector heat load, would be only one lb (refer to Table 18). This would apparently rule strongly in favor of hydrogen instead of neon. However, the container volume required for hydrogen would be 5700 cm^3, which represents significant increase in refrigerator volume. As refrigerator volume increases, the area of outer insulation and the heat transfer to the secondary cryogen also increase. Thus,

the required mass of the secondary cryogen increases as well as its container insulation weight. Altogether, this additional weight is about four lbs. Thus, for a hydrogen system there is a system weight reduction of about 2.3 lbs. However, this reduction in the refrigerator weight (approximately 10 percent) is believed to be offset by the corresponding increase in system volume, the increased difficulty in servicing a solid-hydrogen unit, and the added hazards associated with hydrogen. In regard to the servicing operation, as will be discussed later, approximately 100 liters of liquid helium are required for the production of solid neon and solid methane in a neon-methane refrigerator. Over 500 liters of helium would be required in a hydrogen-methane refrigerator, due to the high, gaseous specific heat of hydrogen. Not only is this an inordinate amount of helium, but also the servicing time would probably be lengthened from two to three hours to ten hours or more. Thus, in the present system, neon was chosen as the primary coolant in the 15 to 20°K refrigerator. Neon is a monotomic gas, and thus has no molecular vibrational modes. No definitive data have been located by inspection of the standard reference books. However, the knowledge that electronic absorption is accompanied by high-energy transitions tends to confirm the inference of the reference books that no neon infrared absorption occurs for wavelengths longer than one to two microns.

Good thermal contact between the detector and solid cryogen is provided by a link of high thermal conductivity extending from the detector to a heat exchanger embedded in the solid cryogen. The heat exchanger between the solid cryogen and the thermal link to the detector is formed either from thin sheets of copper foil or sections of expanded copper foam soldered to the thermal link rod and embedded in the solid cryogen. It can be shown that as the subliming solid recedes from the heat-exchanger surface for normal detector refrigeration loads the gaseous conductivity of cryogen vapor is such that a reasonably small, total heat-exchanger area ($\cong$ several square feet) is sufficient to keep the detector within a few tenths of a degree Kelvin of its operating temperature. If better long-term temperature control is required, then a servo-controlled throttle valve, keyed to the detector temperature, can be used to control the venting-line conductance for long-term temperature regulation.

The temperature of the solid cryogen can be regulated either by direct control of the pressure over the solid or by controlling the mass venting rate of the subliming vapor. Direct pressure regulation is obtained by controlling the venting with a pressure-actuated diaphragm located at the vapor venting line inlet; however, this technique does not operate well at low pressures. Fortunately, the principal heat load on an infrared detector is due to the steady heat dissipation produced by the detector bias current plus the heat flow through the system insulation and supports. Changes in the radiant heat load incident on the detector results in small fluctuations of the total solid-cryogen heat load. These power fluctuations can be accommodated by a simple, passive temperature regulation scheme. In this system, the venting line for the cryogen vapor is critically sized so that for a specified cryogen vapor pressure, which determines the detector temperature, the resulting mass flow of vapor due to the total cryogen heat load is just accommodated by the vent line conductance. If the heat load to the detector is then increased or decreased, a new equilibrium vapor pressure must be established over the solid to accommodate the new mass flow rate. It can be shown that the resulting required temperature changes are small.

182

The structural and thermal design of a spacecraft sublimating solid refrigerator are not two independent tasks. In fact, the rigidity required of structures to withstand the ascent environment is in distinct contrast to the thin-walled, low-conductivity supporting members used in cryogen storage containers. Hence, in any minimum weight, flight-qualified, solid-cryogen refrigerator system there must be a strong counterplay between the thermal and structural requirements of the systems. In the present system, emphasis will be placed on titanium or dacron taut-wire suspension systems and support columns of glass filament wound, epoxy-reinforced materials. These systems and/or materials provide high strength support systems possessing low thermal conductivity.

Thermal design of solid cryogen refrigerator. -- The thermal design aspects of two different solid-cryogen refrigerators are discussed below. One system provides infrared detector cooling in the 15 to 20°K temperature range, while the other unit provides 60 to 70°K detector cooling. These systems are optimized from the standpoint of satisfying the above detector cooling requirements with systems having minimum volume and weight. Basic thermal ground rules assumed in this optimization are that 5 mW of cooling must be provided in each unit for the infrared detector bias current heating and that the refrigerator will view 200°K surroundings.

Thermal design of solid-cryogen refrigerator for 15 to 20°K operation: As discussed earlier, the primary coolant for a solid-cryogen refrigerator for 15 to 20°K infrared detector cooling must be either neon or hydrogen. A system employing neon was chosen for the present infrared detector cooling requirement of 5 mW. The basic configuration of the refrigerator for this analysis is shown in Figure 78. The container for the solid neon is surrounded by an annular container for the secondary cryogen. The inner walls of this container along with end plates provides a low temperature radiative boundary for the solid neon coolant. The neon container is supported by a taut-wire suspension system from the secondary-cryogen container. A low temperature difference is thus provided across the ends of this support system and, therefore, low thermal conduction along these members to the neon container. The secondary cryogen is thermally isolated from its 200°K surroundings by a blanket of high-performance multilayer insulation two-inches thick. The entire refrigerator is supported by a single, tapered, glass filament wound, epoxy-reinforced column which extends from the plate at the upper end of the secondary-cryogen container to the refrigerator mounting flange. All fill and vent lines for the cryogens, as well as the thermal link to the detector, are routed up the interior of this column.

All of the cryogens listed in Table 18 with the exception of neon and hydrogen are potential candidates for the secondary cryogen used for the thermal protection system. However, in order to reduce the radiant heat load on the neon and, therefore, the neon mass, the secondary-cryogen temperature should definitely be kept below 100°K. This fact eliminates carbon dioxide and ammonia as candidates. Of the remaining cryogens, methane and ethylene are the best candidates since they have high latent heats of sublimation per unit volume and
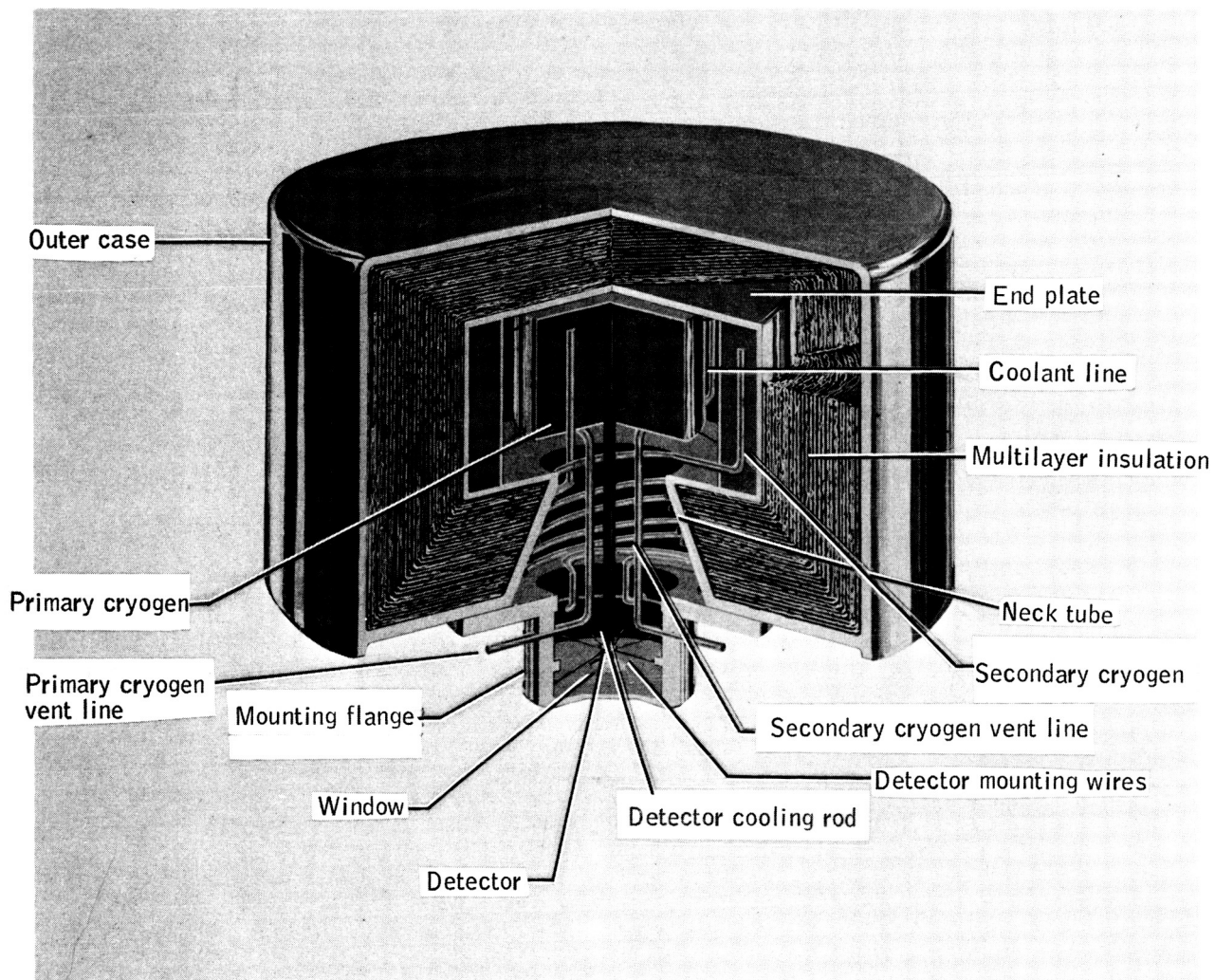
Figure 78. Conceptual View of Two-Cryogen Refrigerator

yet possess very low densities and thus lead to a low-weight thermal protection system. As indicated, the secondary cryogen is contained in an annular container surrounding the neon container. The inner diameter of this secondary-cryogen container is fixed by the diameter of the neon container and the additional requirement for a 1.85-cm (0.725-inch) gap between the containers as indicated in Figure 79. This gap provides a space for routing the various fill, vent, and coolant lines, as well as for the neon-container support system. The height of the annular, secondary-cryogen container has been chosen arbitrarily to be 25 cm. Thus, the volume of the secondary-cryogen container is basically a function of its outer diameter. Figure 80 shows a comparison of the mass requirements of methane and ethylene as the secondary cryogen for the neon-thermal protection system. For both methane and ethylene, curves are presented in Figure 80 indicating the mass of each of these cryogens contained in the annular secondary-cryogen container as a function of its outer diameter. Also curves are presented indicating methane and ethylene mass requirements for one-year operation as a function of the heat load on the secondary-cryogen container. As will be subsequently discussed in detail, this total heat load is determined by two factors:

- A fixed thermal energy transport due to radiation and conduction down the refrigerator support column.

- The heat load through the insulation system which is a function of the container size.

These heat loads are not the same for methane and ethylene. In the case of methane, the temperature difference across the support and insulation system is 200-60 = 140°K; whereas for ethylene, this temperature difference is 200-90 = 110°K. The intersection point, for each cryogen, between the curves in Figure 80 defines the mass requirements for each cryogen for one-year operation. The methane mass requirement is 3.82 lbs (1730 g); whereas, the ethylene mass requirement is 2.42 lbs (1100 g). Thus, the methane mass requirement is 1.40 lb (630 g) greater than the ethylene mass requirement. The increased methane mass and resulting increased refrigerator volume for methane as compared to ethylene increases the total refrigerator weight, excluding the neon weight, by 3.4 lbs (1.4 lbs methane, 0.2 lb methane container, 0.2 lb insulation, and 1.6 lbs refrigerator vacuum container) over the ethylene case. Although the weight requirements for the thermal protection system are greater in the methane case than the ethylene case by 3.4 lbs, the lower operating temperature of methane, 60°K as opposed to 90°K for ethylene, reduces the radiant heat load on the neon by a factor of 6.5 and the conductive heat load through the support system by 40 percent. The additional heat load on the neon for an ethylene-thermal protection system would increase the neon mass requirement by 5 lbs or more. This latter factor rules in favor of a methane thermal protection system.

▶ Sizing of Primary Cryogen Mass

Sufficient neon must be provided to withstand all heat loads for an operating period of one year. The thermal loads on the neon are due to:
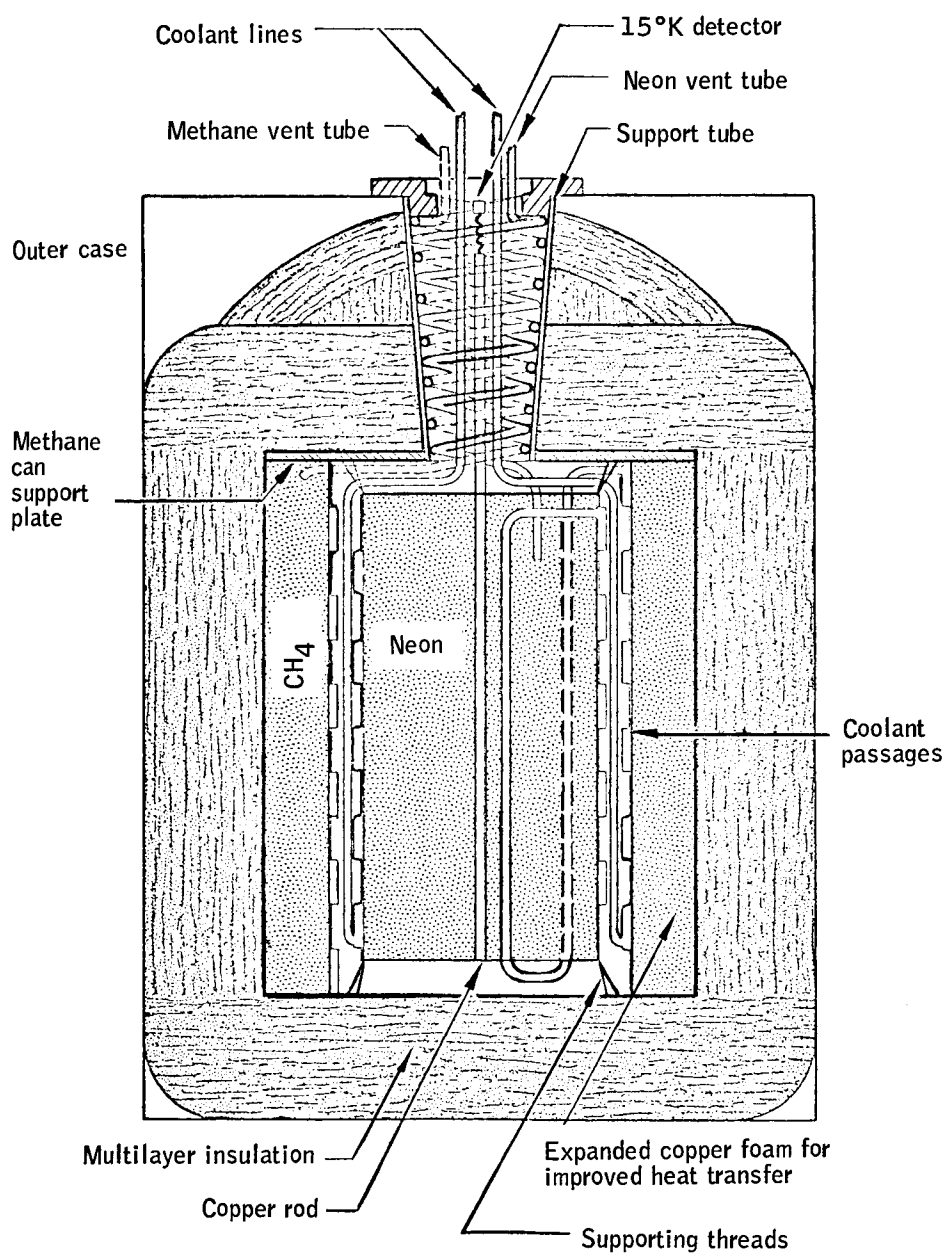
Figure 79. Schematic of Neon-Methane Refrigerator
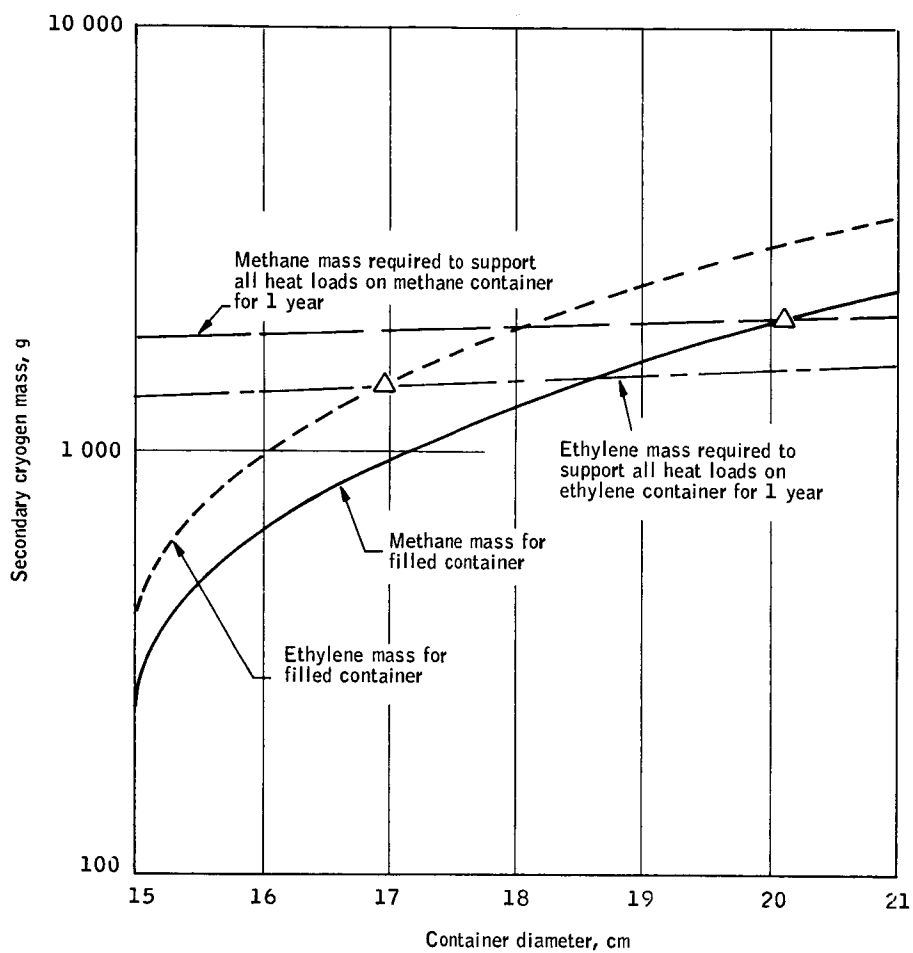
Figure 80. Secondary Cryogen Mass Requirement for Neon
Thermal Protection System

- Detector, including conduction through supports and radiation to the detector, and radiation to the copper rod, as well as the resistive heating from the bias current.

- Radiation exchange with the secondary cryogen.

- Conduction through supports system.

An efficient parametric approach is possible provided the radiation is considered at the outset. For either diffuse or specular radiation inside the concentric cylinders, the net radiative exchange to the neon is given by

$$q_{12} = \sigma A_1 F_{12} (T_1^4 - T_2^4) \tag{11}$$

where the exchange factor is given by

$$F_{12} = \frac{\epsilon_1 \epsilon_2}{\epsilon_2 + \dfrac{A_1}{A_2}(1-\epsilon_2)\epsilon_1} \tag{12}$$

The formula for q_{12} is accepted as a reasonable estimate of the radiation, even in the case of finite cylinders, because the separation is small. The surfaces are gold coated to provide for very low emittance, particularly at temperatures below 100°K. Taking ϵ_2 = 0.02 (60°K) and ϵ_1 = 0.01 (15°K) (both conservative values) - see Figure 81 and a nominal value of A_1/A_2 = 0.8, then F_{12} = 0.007. Taking A_1, the area of the neon container, a value of 1000 cm^2, a value which is typical of the final design value, it follows that q_{12} = 0.65 mW It is convenient to adopt a constant, conservative value for the radiation to the neon so that the detector and support thermal loads can be studied parametrically. The value of q_{12} calculated above is assumed to provide conservative design, only to be less than 1 mW for a 65°K secondary of cryogen.

Figure 82 shows the mass of neon required for the various detector loads (bias, conduction, and radiation) as a function of heat conduction through the neon container supports. The data for Figure 82 is for a low pressure (< 1 Torr) heat of sublimation for neon of 105.2 joules/g. The actual cooling requirements for the detector assembly are summarized below:

Detector bias current heating	5.0 mW
Radiation to detector	0.91
Radiation to thermal link	0.11
Conduction through detector supports	0.42
Total	6.44 mW
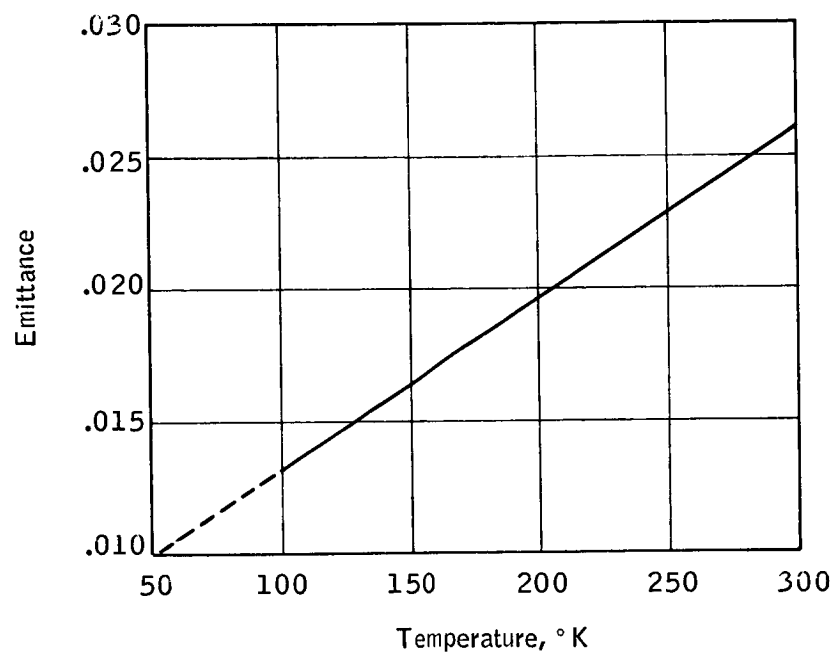
Figure 81. Emittance from Chemically Deposited Gold
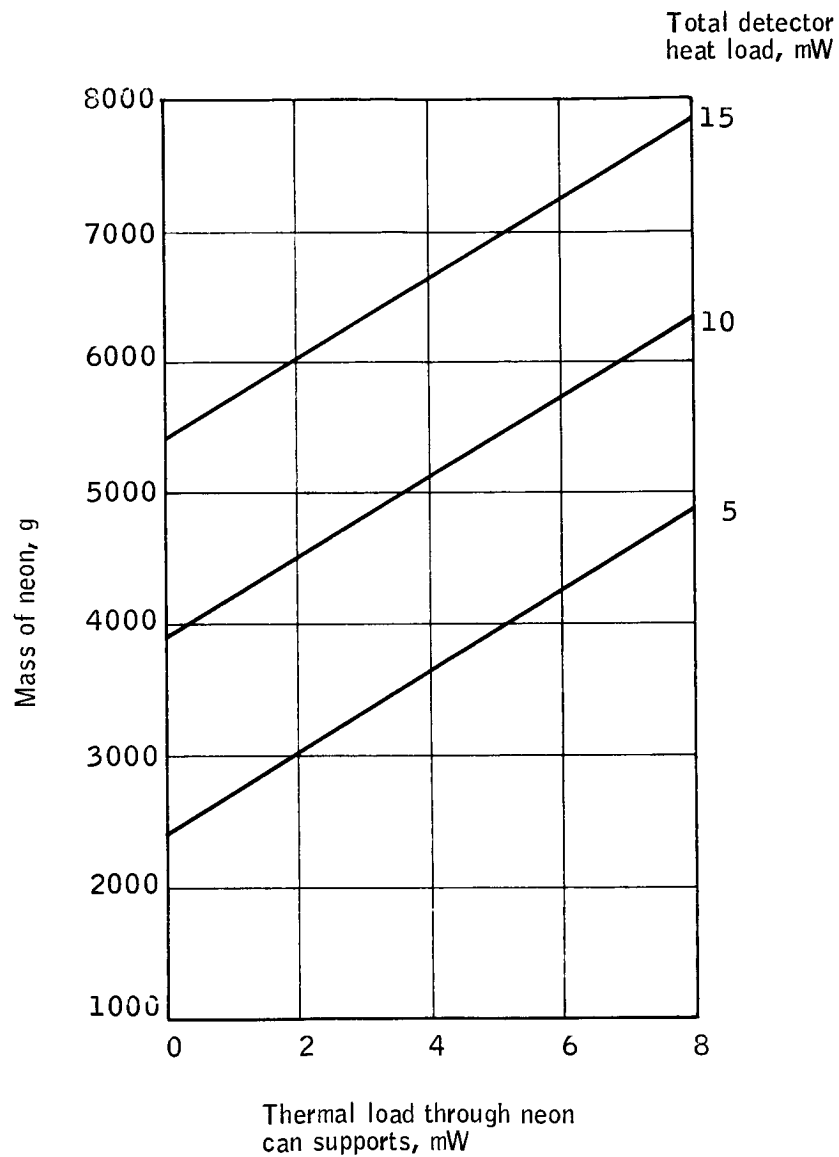
Figure 82. Mass of Solid Neon Required as a Function of the Support and Detector Heat Loads

190

The various heat inputs to the detector assembly, excluding the bias current heating which is simply an assumption in the thermal design, will be justified in detail subsequently in the present analysis.

It will be shown that a support system of 16 Dacron filaments 0.024 inch in diameter will provide sufficient support for the neon container. These filaments will support the neon container from the methane container. Each support is 1.15-inches long (2.9 cm), the temperatures at the ends of each of these supports are 15°K (solid-neon temperature) and 60°K (solid-methane temperature), and the total heat transfer through each support is less than 0.18 mW The value for this conduction term will be taken to be 2 mW. The heat leak down the heat-exchanger tubing is calculated to be 0.6 mW, comprising 0.5 mW from the exterior and 0.1 mW from the neon can - methane can link. The heat leak along the vent tube is neglected at this stage since the venting gas will eliminate it almost entirely. Then, the total heat load on the neon will be taken to be 1 mW (radiation) + 2 mW (supports) + 0.6 mW (heat-exchanger lines) + 6.44 mW (detector) = 10.04 mW (total heat load). Therefore, for 5 mW bias on the detector, the total thermal load on the neon is taken to be 10 milliwatts, a conservative value for this particular bias current rent heat rate. This means that 3000 g (6.6 lbs) of neon are needed. The 3000 g of neon is contained in a cylinder whose length L is twice the diameter, D. The dimensions are L = 22.4 cm (8.64 in) and D = 11.2 cm (4.32 in) where the container is 10 percent oversize to provide for internal heat exchangers and achievement of less than maximum neon density. The high density of neon means that minor increases in the mass of the neon made by increasing the neon-container diameter-will not alter its dimensions significantly . Finally, it is noted that the surface area of this neon container is about 900 cm² which justifies the earlier assumption of the area used in the estimate of the radiation to the neon container.

▶ Sizing of the Secondary Cryogen Mass

The thermal load on the methane container is from the following three sources:

- Conduction and radiation through the multilayer insulation system.

- Conduction down the access column..

- Radiation down the access column.

Some of the energy entering via the access column is intercepted by the venting gases. A calculation of this convection cooling is made at the end of this section.

An estimate of the effective thermal conductivity k_e of a multilayer insulation system applied to the refrigerator is based on the following considerations. Double aluminized mylar multilayer insulation systems using Tissuglas resulted in insulation conductivities of 5.2×10^{-7} W/cm-°K (3×10^{-5} Btu/hr-ft-R) when applied to previous solid-cryogen refrigerator systems operating

with a 300°K outer-boundary temperature. Further, the conductivity of this insulation system has been determined as function of outer-boundary temperature in a number of tests. Based on this knowledge, the multilayer insulation conductivity for the present design should be 1.3×10^{-7} W/cm-°K $(0.75 \times 10^{-5}$ Btu/hr-ft-°R). However, a more conservative insulation conductivity of 2.17×10^{-7} W/cm-°K $(1.25 \times 10^{-5}$ Btu/hr-ft-°R) is utilized for the present design. The conduction and radiation through the insulation is given by

$$q_{ins} = k_e A \frac{\Delta T}{\Delta X} \tag{13}$$

where $|A|$ is the average area of the insulation in cm^2. This average area is conservatively calculated using the average area of the methane, container, and the outer area of the insulation, where the area of the insulation is that required to provide an insulation blanket two-inches thick on the refrigerator. Taking the diameter of the neon container to be 4.4 in. (11.2 cm), its height to be 8.8 in. (22.4 cm), and making provision for an 0.73 in. (1.85 cm) clearance between the neon and methane containers (See Fig. 79), it follows that the average insulation area in cm^2 is given by

$$A = \frac{\frac{\pi}{2}D_o^2 + 25\pi D_o + 2(D_o + 10)^2 + 35\pi D_o}{2}$$

$$= \frac{\pi}{2}D_o^2 + 35\pi D_o + 25\pi \tag{14}$$

where D_o is the outer diameter of the methane container in cm. The total heat load on the methane container in one year is

$$q = 3.17 \times 10^7$$

where q_{ins} is defined in equation (13) and $|q_c|$ is the total thermal load by conduction and radiation down the support column which will be shown to be 16.8×10^{-3} W|(16.8 mW). The mass of methane required to support this one year's total heat on the methane container is given by

$$= \frac{q}{\mathcal{L}} = 3.17 \times 10^7 \frac{q_c + q_{ins}}{\mathcal{L}} \tag{15}$$

where $|\mathcal{L}|$ is the latent heat of sublimation of methane in J/g (6.15 J/g). On the other hand, the total mass of methane in grams contained in the annular methane container is given by

192

$$m = e \cdot \left\{ \frac{\pi}{4} D_o^4 \ (25) - \frac{\pi}{4} (14.9)^2 \ (25) \right\}$$

$$= 6.25 \ \pi \ e \ (D_o^2 - 222) \tag{16}$$

where $| \ e \ |$ is the density of methane in g/cm^3 (0.49 g/cm^3) The simultaneous solution of equations (15) and (16) is accomplished graphically in Figure 80 for methane and ethylene. The results for both systems appear in Figure 80.

The support column is a slightly tapered (conical), reinforced (glass filament wound), epoxy material. A mean thermal conductivity of 2.08×10^{-3} W/cm-°K (0.12 Btu/hr-ft°R) in the 60 to 200°K range is a reasonable value (ref. 14). From structural considerations, a tube of 0.020-inch thickness and 1.19-inch mean inside diameter with a length of 4.5 inches is acceptable. (This structural analysis will be discussed later. Under these conditions the cross-sectional area for heat transfer is 0.48 cm^2, and for the ΔT of 138°K, the thermal load due to conduction is 14 milliwatts.

To estimate the radiation down the support column, the results of a Lockheed study for radiation down tubes is used (ref. 15), Figure 83 shows pertinent data for conduction and radiation down a tube. This figure indicates a function of the dimensionless ratio of "radiation conduction" to solid conduction for various L/D ratios of tubes and the ratio of the solid conduction plus radiation heat transport down a tube to the solid conduction. This data, therefore, constitutes a solution of the coupled radiation and solid conduction heat transport down a tube. The various parameters entering into this analysis are defined as follows:

D = outer diameter of tube

L = tube length

δ = tube-wall thickness

k = thermal conductivity of tube-wall material

T_{so} = temperature at tube hot end

T_{si} = temperature at tube cold end

ϵ_E = effective emittance of tube hot end

ϵ_w = effective emittance of tube cold end

Using an emittance ratio (see Figure 83) of 1.0 and taking $| \ \epsilon_E = 0.1$, the

Combined conduction and radiation heat transfer through straight pipes for an emissivity ratio of 1.0

$$q_{cond} = \frac{\pi k \delta (D-\delta)(T_{so}-T_{si})}{L}$$

$$\epsilon_E/\epsilon_w = 1$$

$$T_{so}/T_{si} = 10$$
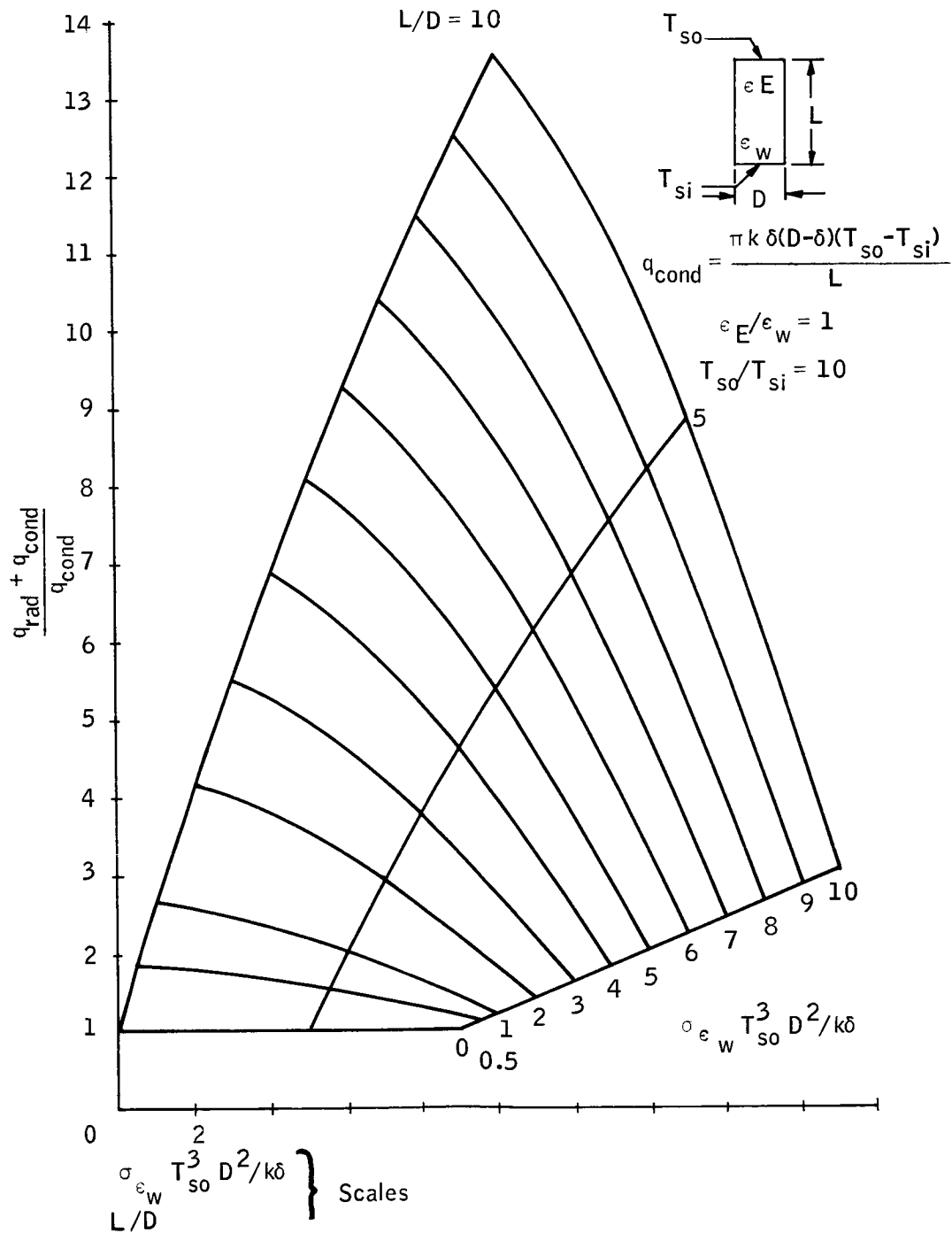
Figure 83. Data for Coupled Radiation and Conduction Heat Transfer in a Tube

194

parameter $|\sigma \epsilon_w T_{so} | D^2/k\delta |$ has a value of 0.12 so that the curves give $(q_{rad} + q_{cond})/q_{cond} = 1.2$ so that $| q_{rad} = 2.8$ mW. Total radiation and conduction is approximately 16.8 mW The above value of $|q_{rad}|$ is relatively insensitive to the exact values of $|\epsilon_E, \epsilon_w,$ and $|T_{so}/T_{si}|$ so that the present value of $|q_{rad}|$ should be quite exact.

● Thermal Capacity - Convection Capability of the Vented Gases

Considerable heat can be intercepted by the vented gases provided capability for heat transfer exists. Very low flow rates and low Reynolds numbers, on the order of one (1), limit the size of the convective heat transfer coefficients. From the classical Graetz-Nusselt problem, an estimate of the Nusselt number is provided by

$$\frac{hD}{k} \approx N_u \approx 4 \qquad (17)$$

which can be converted into expressions in terms of tube diameter expressed in cm:

$$h_{15,N} = \frac{0.6}{D} , \frac{\text{milliwatts}}{\text{cm}^2 - °K} \quad (\text{neon, } 15°K)$$

$$h_{200,N} = \frac{1.48}{D} , \frac{\text{milliwatts}}{\text{cm}^2 - °K} \quad (\text{neon, } 200°K)$$

$$h_{60,M} = \frac{0.12}{D} , \frac{\text{milliwatts}}{\text{cm}^2 - °K} \quad (\text{methane, } 60°K)$$

$$h_{200,M} = \frac{0.8}{D} , \frac{\text{milliwatts}}{\text{cm}^2 - °K} \quad (\text{methane, } 200°K)$$

Assuming $D \approx 0.5$ cm for each gas, average convective coefficients of 2, and 0.9 milliwatts/cm²-°K for the neon and methane, respectively are calculated. For tubes of 10 cm in length, and $\Delta T_N \approx 20°K$ for the neon and $\Delta T_M = 10°K$ for the methane, the transfer capability is much larger than needed. Actually, this shows that the thermal capacity of the neon and methane is the limiting quantity. By a straightforward calculation, the total capacity on the flowing neon and methane is

$$\dot{\mathcal{E}} = \dot{\mathcal{E}}_{neon} + \dot{\mathcal{E}}_{methane} \approx 25 \text{ milliwatts}$$

Unfortunately, the radiation load of 2.8 milliwatts down the interior of the main support tube is the only heat rate that the tubes can intercept without providing some means of thermal contact with the support column. If such provisions were made, the net heat load down the column could be almost totally intercepted.

► Sizing of the Copper Thermal Link

A copper rod is used to conduct the thermal energy from the detector to the neon refrigerant. Using the relation

$$A = \frac{KA\Delta T}{\Delta X}$$

and assuming a rod length of 12 cm, a conductivity of 12 W/cm-°K, for copper at 15 to 20°K and a detector heat load of 7 mW, then, for an allowed temperature drop down the rod given by $\Delta T = 0.5°K$ the rod diameter is 1.3 mm. Since 1.3 mm is rather slender, a link diameter of 2 mm has been selected. The radiation heat load on the thermal link may be calculated utilizing equations (11) and (12). In this case $A_1/A_2 = 0.132/2.5$

$= 0.053$, $\epsilon_1 = 0.01$, $\epsilon_2 = 0.1$, $T_2 = 200°K$, and $T_1 = 15°K$; this

assumes the interior of the support column is coated with a low emittance surface. This gives $q_{12} = 0.25$ mW; this was assumed to be 0.35 mW to be conservative in the previous analysis of the total neon heat load.

► Vent-Tube Sizing and Establishment of the Primary and Secondary Cryogen Temperature

The mass flow rates through the vent tubes are extremely small and the flow is laminar. Indeed, for a 5 mW detector heat load design, the mass flow rates of the neon and methane are respectively $\dot{m}_{neon} = 7.3 \times 10^{-5}$ g/sec and $\dot{m}_{methane} = 5 \times 10^{-5}$ g/sec, and the Reynold' numbers are of the order of unity (1) for venting tubes greater than 0.2 cm in diameter.

The flow relationship for the tubes is as follows:

$$P - P_o = \frac{128 \, \dot{m} \, \mu \, L}{\bar{\rho} \, D^4}$$

where $\bar{\rho}$ and $\bar{\mu}$ the gas density and viscosity, are evaluated at some mean temperature. Venting is to a vacuum so $P_o \cong 0$. The density obeys the perfect gas relation, $\bar{\rho} = \overline{P}M/RT = \overline{P}M/2RT|$ where a mean temperature

and pressure of the venting gas is used and $|M|$ is the molecular weight. Expressing these results in terms of the vent-tube sizing factor D^4/L, it follows that

$$\frac{D^4}{L} = \frac{256 \, \dot{m} \, RT\mu}{\pi M P^2} \qquad (18)$$

For the particular case of the neon can: -

$$\overline{T} = 90°K \, (\overline{P} = 0.2 \text{ Torr})$$

$$\overline{\mu} = 100\mu \text{ poise } (=10^{-4} \text{ g/cm-sec})$$

$$\dot{m} = 8.314 \times 10^7 \text{ ergs/mole-°K}$$

$$\frac{D^4}{L} = \frac{1.26 \times 10^{-4}}{P^2}, \qquad (19)$$

where P is in Torr

Figure 84 indicates the vapor pressure of neon as a function of temperature. For example, if P = 0.2, which as indicated in Figure 84 corresponds to a neon temperature of approximately 14.5°K, then, from the above equation D^4/L = 31.5 cm³ and for L = 30 cm (which is the anticipated venting tube length for the refrigerator) D = 0.56 cm. In Figure 85, the solid-neon operating temperature is for various values of the venting tube length. The curve for L = 30 cm should be characteristic of the present design. The neon operating temperature, is therefore, simply fixed by a choice of the dimensional characteristics of the venting tube.

For the particular case of the methane can:-

$$\overline{T} = 100°K$$

$$\overline{\mu} = 50\mu \text{ poise}$$

$$\dot{m} = 55 \times 10^{-5} \text{ g/sec}$$

$$\frac{D^4}{L} = \frac{5.94 \times 10^{-4}}{P^2}, \qquad (20)$$

where P is in Torr

197
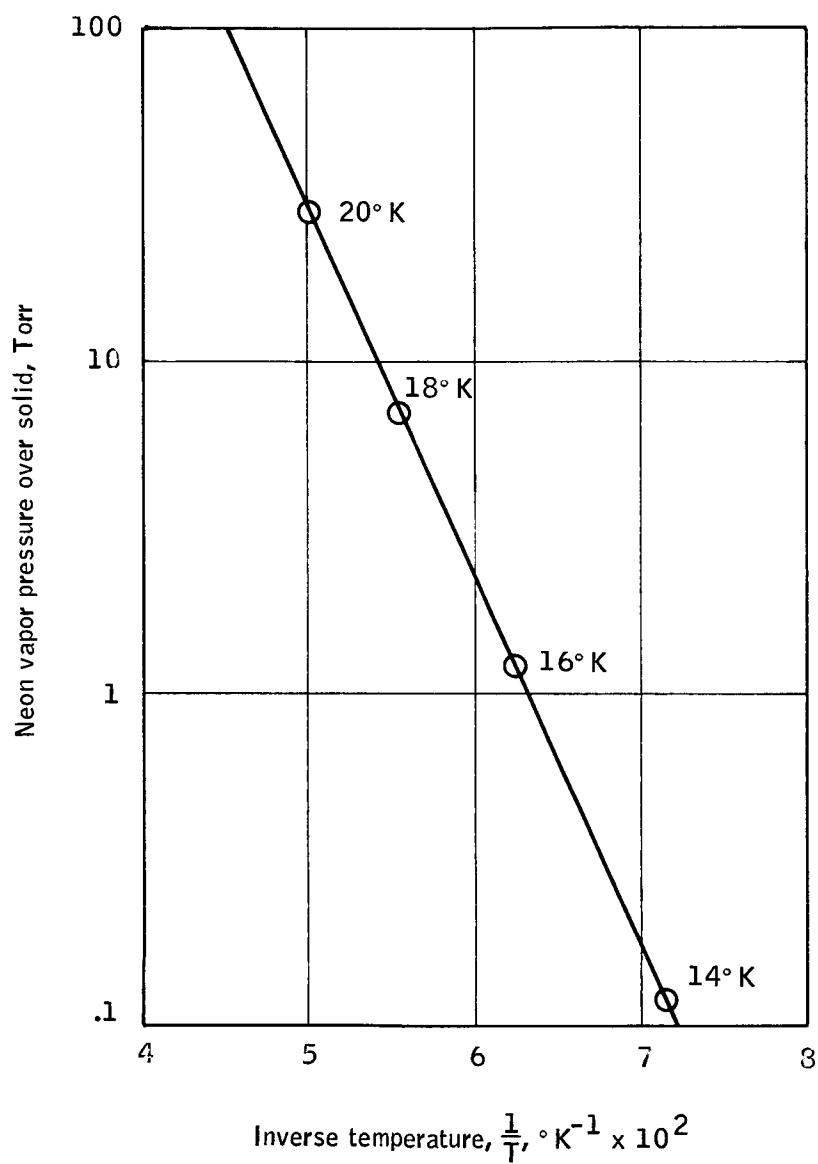
Figure 84. Pressure Temperature Characteristic for a Neon
Vapor-Solid Equilibrium System
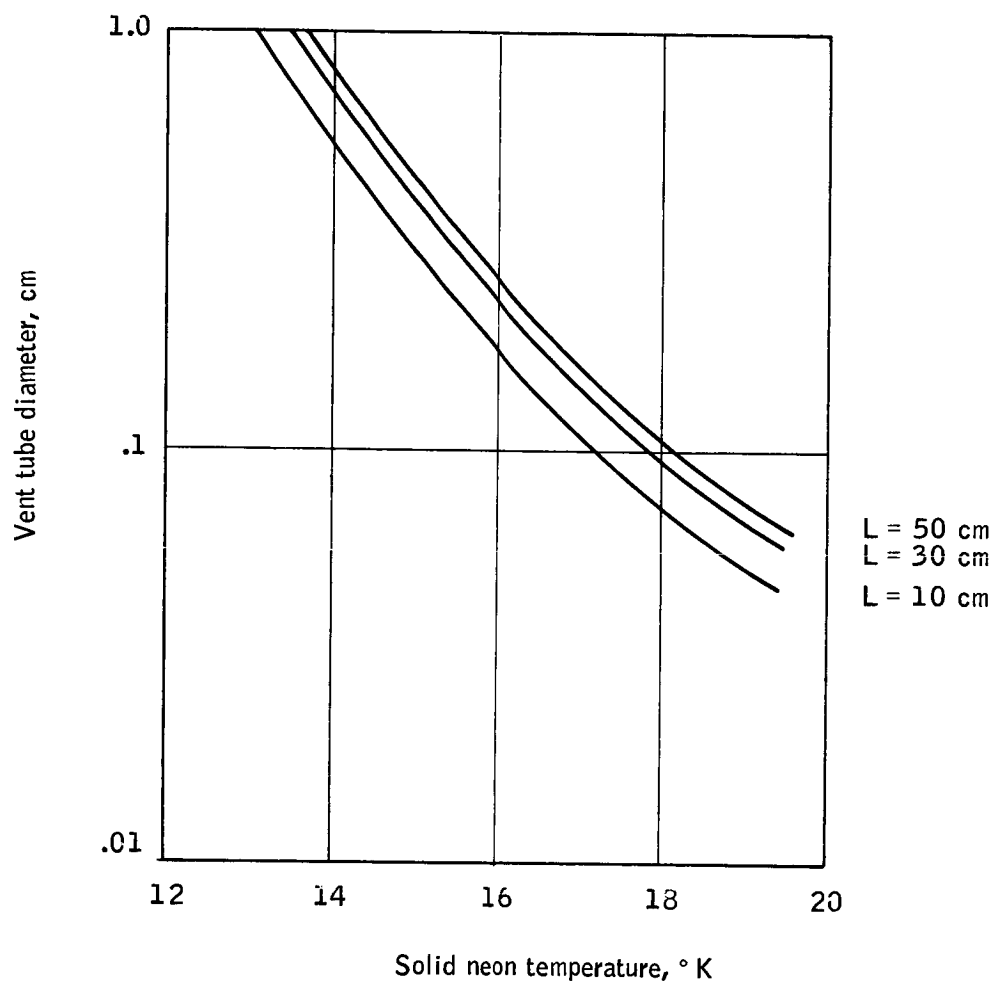
Figure 85.   Tube Sizing for Neon Venting

The operating temperature for methane should be fixed as low as is possible. This is because the lower the methane temperature, the lower the radiation load on the neon and, therefore, the lower the neon mass requirement. A graph showing methane vapor pressure versus temperature is presented in Figure 86. As indicated by this graph, using the rule of thumb discussed previously, that the lowest operating pressure is fixed by the venting system at approximately 0.1 Torr, it can be seen that the lowest operating temperature for the methane would be about 60°K. In Figure 87, the methane venting line sizing given by equation (20) is presented graphically. It can be seen that for venting tube lengths of 30 cm, which is the anticipated venting tube length for the present system, and for a venting tube diameter of 0.7 cm, the methane operating temperature would be 60°K. The narrowest part of the support tube has a diameter of about one inch, thus, there may be a geometrical conflict if all the vent and service lines are to pass through this member with good clearance. A possible solution would be to use shorter overall lengths, a choice which should be made during the design of hardware. The present calculations may be used in making choices at that time.

Design characteristics of the solid-neon, solid-methane system are summarized in Table 19. The insulated refrigerator will be approximately 12 inches in diameter and 16 inches in height. Total weight of the neon-methane system will be approximately 26 pounds.
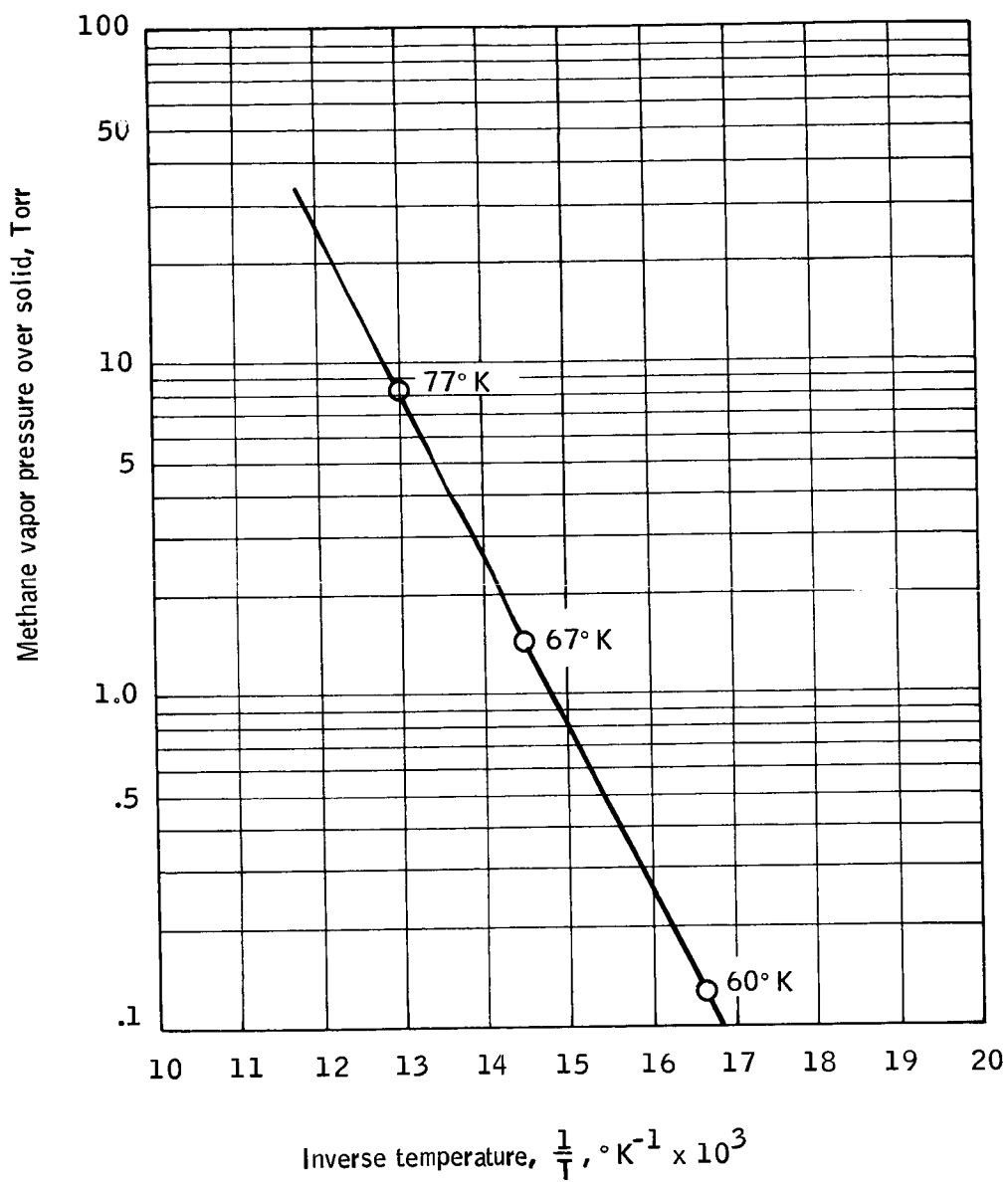
Figure 86. Pressure-Temperature Characteristic for a Methane Vapor-Solid Equilibrium System
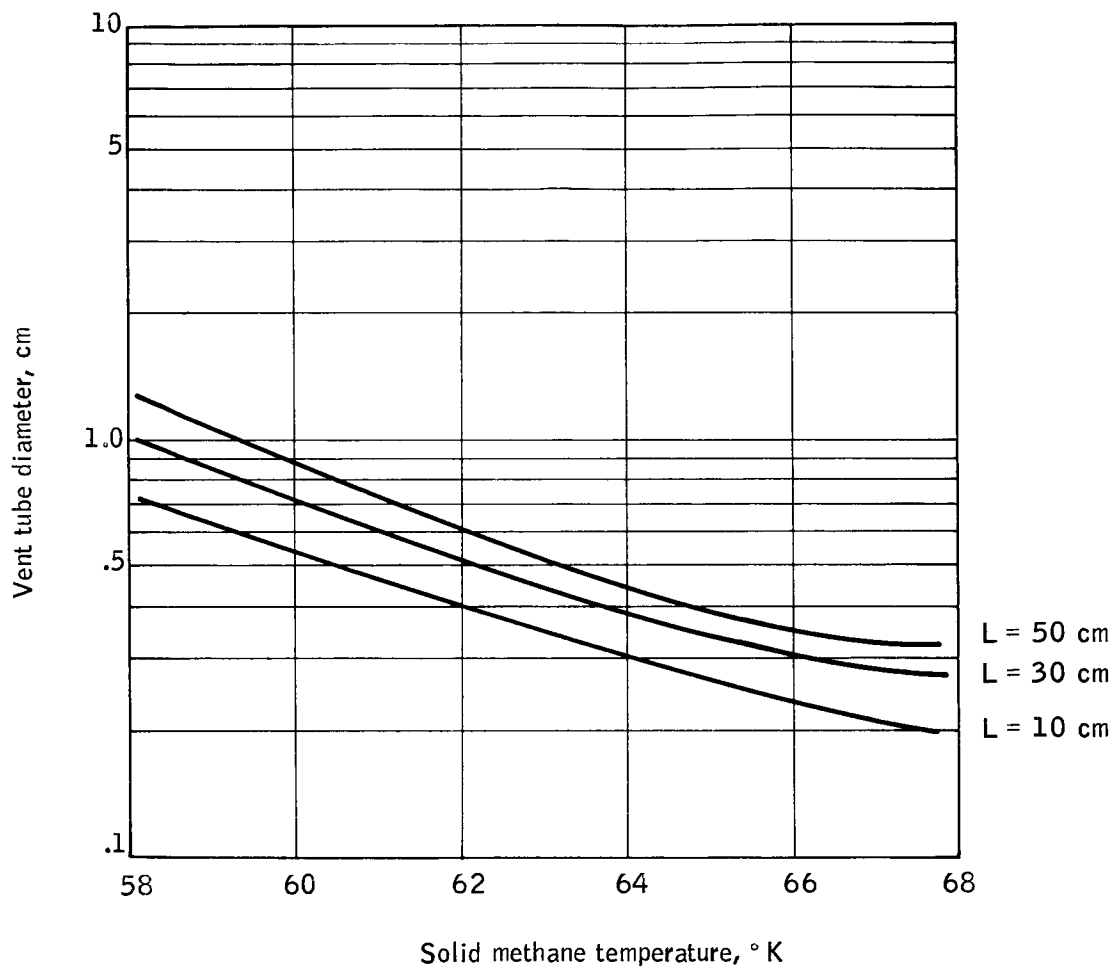
Figure 87.   Tube Sizing for Methane Venting

TABLE 19.- PRELIMINARY SIZING OF A 10mW, 15°K REFRIGERATOR[a]

Sensor requirements

T, °K	15 to 20
Duration, years	1
Total heat load, m	6.4

Refrigerator requirements

	Neon	Methane
Refrigerants density, g/cm^3	1.495	0.49
latent heat, joules/g	105.2	615
Containers volume, cm^3	2200	3600
dimensions, cm	11.2 o.d. x 22.4 high	14.9 i.d. x 20.1 o.d. x 25 high
mass, grams refrigerants	3000	1600

Heat rates, milliwatts

	Neon	Methane
Heat exchanger lines	< 0.6	< 0.3
Insulation	< --	< 8.0
Radiation	< 1.0	< 2.8
Supports	< 2.0	< 14.0
Detector	< 6.4	< --
	< 10.0	< 25.0

Estimated Weight:

Neon and methane	11.1 lbs
Vacuum container	8.0
Insulation	2.0
Containers	2.5
Heat exchanger	0.5
Support	0.5
Miscellanes	2.0
Total weight	26.6 lbs.

[a]Total heat load is 10 mW on neon; actual total detector heat load is 6.4 mW including provision for 5 mW of detector bias current heating.

► Calculation of Detector Heat Loads

Heat loads were quoted previously for radiation and conduction to the detector and for radiation to the copper detector rod. These quantities are justified below.

● Radiation to detector: -

The top of the detector will be assumed to be at 15°K, to view 200°K surroundings, to have an emittance of 0.5, an area of 0.2 cm^2 and a view factor of unity. This will give a very conservative estimate. Radiation to the sides and bottom of the detector will be ignored since they view lower temperature surroundings and will be given a very low emissivity coating. The above values give

$$q_{rad} = 0.91 \text{ mW}$$

● Conduction to detector through supports:-

The design of the detector support system is discussed later. For the purposes of estimating heat leakage through this support system, a configuration of twelve titanium alloy wires is assumed, 0.005-cm diameter and 3.5-cm long. The thermal conductivity integral between 200°K and 15°K is 6.32 x 10^3 mW/cm. These values give

$$q_{cond} = 0.42 \text{ mW}$$

● Radiation to detector rod:-

Since the rod views the structural support which has a gradient from 200°K to 62°K it can be conservatively assumed that all the radiation is emitted from the top one third of the tube at 200°K If the tube has an emmissivity of 0.02 and the rod emissivity is 0.01, the rod is 10-cm long and 0.2 cm in diameter. The support tube is approximately 3-cm diameter.

Thus,
$$F_{12} = \frac{0.02 \times 0.01}{0.02 + \frac{0.2}{3.0}(1-.02).01}$$

$$\approx \quad 0.01$$

If a shape factor of 0.2 due to columnar offset is assumed

$$q_{rad} \approx 0.11 \text{ mW}$$

► Conduction Along Service Lines

Tubing for heat exchanger and vent lines has not been selected in this report. An estimate of the heat leak along these tubes can be made assuming a likely

size of Mylar tubing, 0.6-cm diam with 0.025-cm wall. The average thermal conductivity of Mylar is assumed to be 0.001 watt/cm-°K between 16°K and 200°K. The following estimates are made.

- Heat exchanger lines:-

    200°K environment to 15°K neon can ~ 0.0005 watt

    62°K methane can to 15°K neon can ~ 0.0001 watt

    200°K environment to 62°K methane can ~ 0.003 watt

- Vent lines (assuming no venting flow):-

    200°K environment to 15°K neon can ~ 0.0004 watt

    200°K environment to 62°K methane can ~ 0.0003 watt

Thermal design of solid-cryogen refrigerator for 60 to 70°K operation: In this case, the detector is to operate at 60 to 70°K having a thermal load of approximately seven mW for a duration of one year. This detector thermal load is discussed in detail in the analysis of the 15 to 25°K neon-methane refrigerator. There, it was found that the total detector heat load is 6.44 mW. For a 60 to 70°K methane refrigerator for the same detector support system, the detector heat load will be substantially the same as for the neon-methane system. As was indicated previously, methane is the best cryogen for cooling in the 60 to 70°K temperature range because of its high latent heat of sublimation and its low density. A thermal optimization of a methane refrigerator system is presented in Figure 88. This design is based on a methane container having an L/D ratio of unity. This particular L/D ratio is chosen to minimize the heat flow to the methane container through the surrounding multilayer insulation. One curve in Figure 88 indicates the methane mass as a function of the diameter of the methane container. The second curve indicates the total methane mass requirements for one-year operation, due to all the heat loads on the methane, as a function of the methane container dimensions. This total heat load is made up of two fixed heat loads, that due to the detector and that due to the main support column for the refrigerator, plus the heat load through the insulation system, which is a function of the container size. As previously indicated, the detector heat load is taken to be seven mW. The main support column is taken to be identical to that used for the neon-methane refrigerator. Conduction plus radiation heat load down this column is also identical since in both cases the column supports a 65°K methane container from a boundary at 200°K. The heat flow through the multilayer insulation is taken to that through a 5.08-cm (2-inch) layer of multilayer insulation. The area of this insulation layer is assumed to be the average of the area of the methane container and the outer area of the insulation blanket. Methane mass and container size requirements are defined by the intersection points of those curves i.e., 1850 g (4.08 lbs) and 17 cm (6.7 in.). Methane container dimensions would be oversized 10 percent as a safety factor.
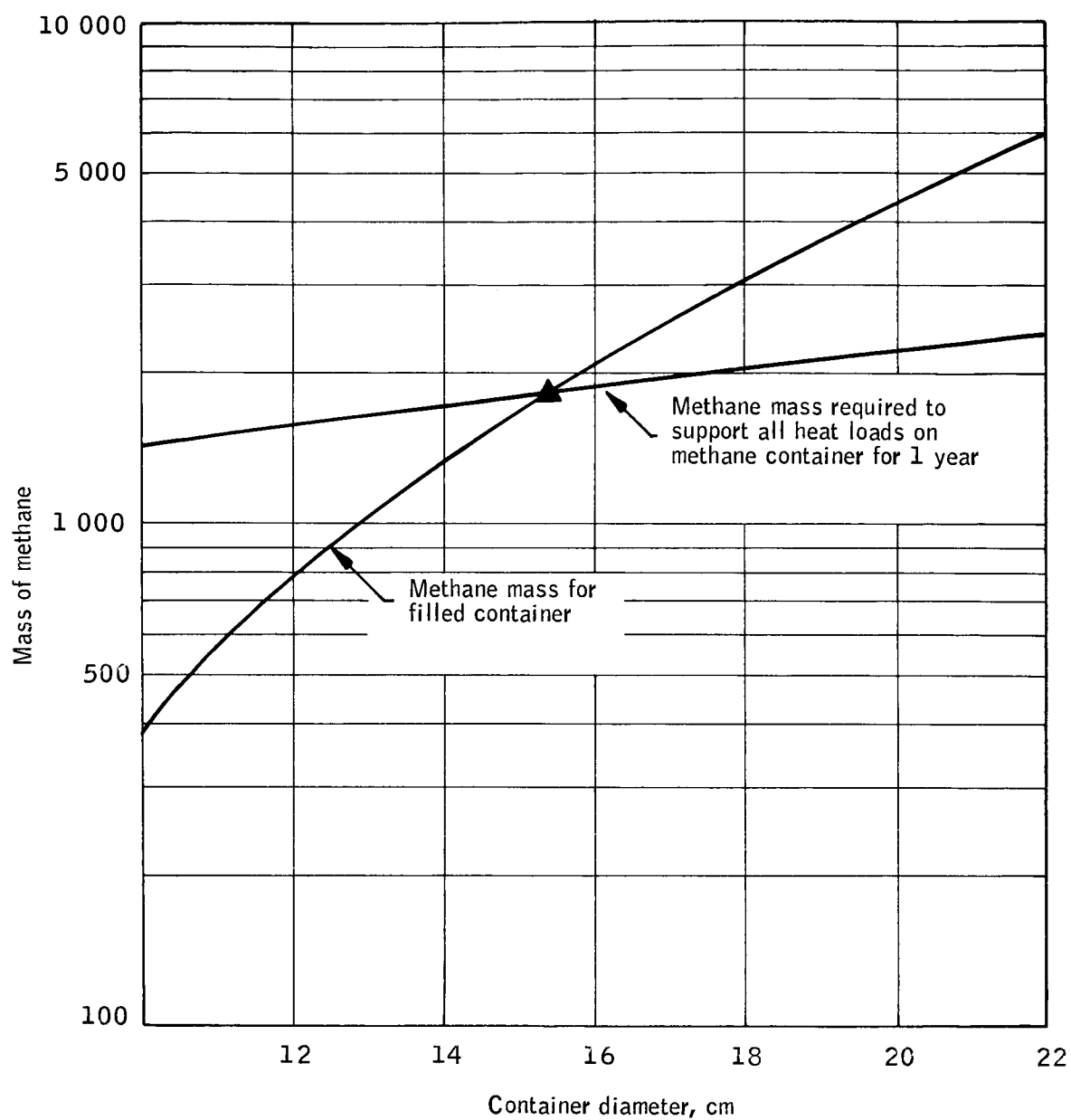
Figure 88. Methane Mass Requirements for 70°K Refrigerator

To size the methane venting tube for maintaining the methane temperature, it should first be noted that 1850 g of methane are to be vented in one year (3.17×10^7 sec). The resulting mass flow rate will be

$$\frac{1.85 \times 10^3 \text{ g}}{3.17 \times 10^7 \text{ sec}} = 5.84 \times 10^{-5} \text{ g/sec}$$

Equation (18) is used to determine the corresponding venting tube diameters required to fix the temperature operating point of this system; this results in

$$D^4 / L = \frac{2.68 \times 10^{-4}}{P^2} \text{ cm}^3 \qquad (21)$$

where P is the methane vapor pressure in Torr. For a venting tube length of 30 cm, which would be typical of that required for a methane refrigerator, this equation indicates that for a 60°K temperature operating point (0.1 Torr pressure) $D \approx 1$ cm. Larger venting tubes would not be too practical; thus, 60°K is taken to be the lowest operational temperature for a methane system. This system is shown schematically in Figure 89 and its characteristics are indicated in Table 20. Here the methane mass has been increased 300 g (approximately 15 percent) over the thermal optimization value to provide a conservative design.

Mechanical design of solid-cryogen refrigerator: -- As indicated previously, the structural and thermal design of a spacecraft-borne sublimating solid refrigerator are mutually dependent tasks. The aim of the present structural design is to devise elements that will maintain the positions of various refrigerator elements under the severe acceleration and vibrational loads associated with a spacecraft boost phase and, yet, provide low heat leak paths to and within the refrigerator. Thus, for structural members, emphasis will be placed on titanium or Dacron taut-wire suspension systems and the use of glass filament wound, epoxy-reinforced materials. This combination of structures and materials provides for support systems which possess high strength and low thermal conductivity. The cross-sectional areas of these members will be minimized and their lengths made long in order to decrease the heat leak along these members. At the same time, the cross-sectional areas must be sufficient to maintain the maximum stresses developed in these elements for the maximum acceleration and vibration loads experienced by the system.

Several components of the refrigerator system have been identified as key structural and thermal elements. These elements are analyzed in the present design; they are the:

- Main support column for the refrigerator

- Taut-wire suspension system for the neon container in the neon-methane refrigerator

- Taut-wire suspension system for the detector.

207
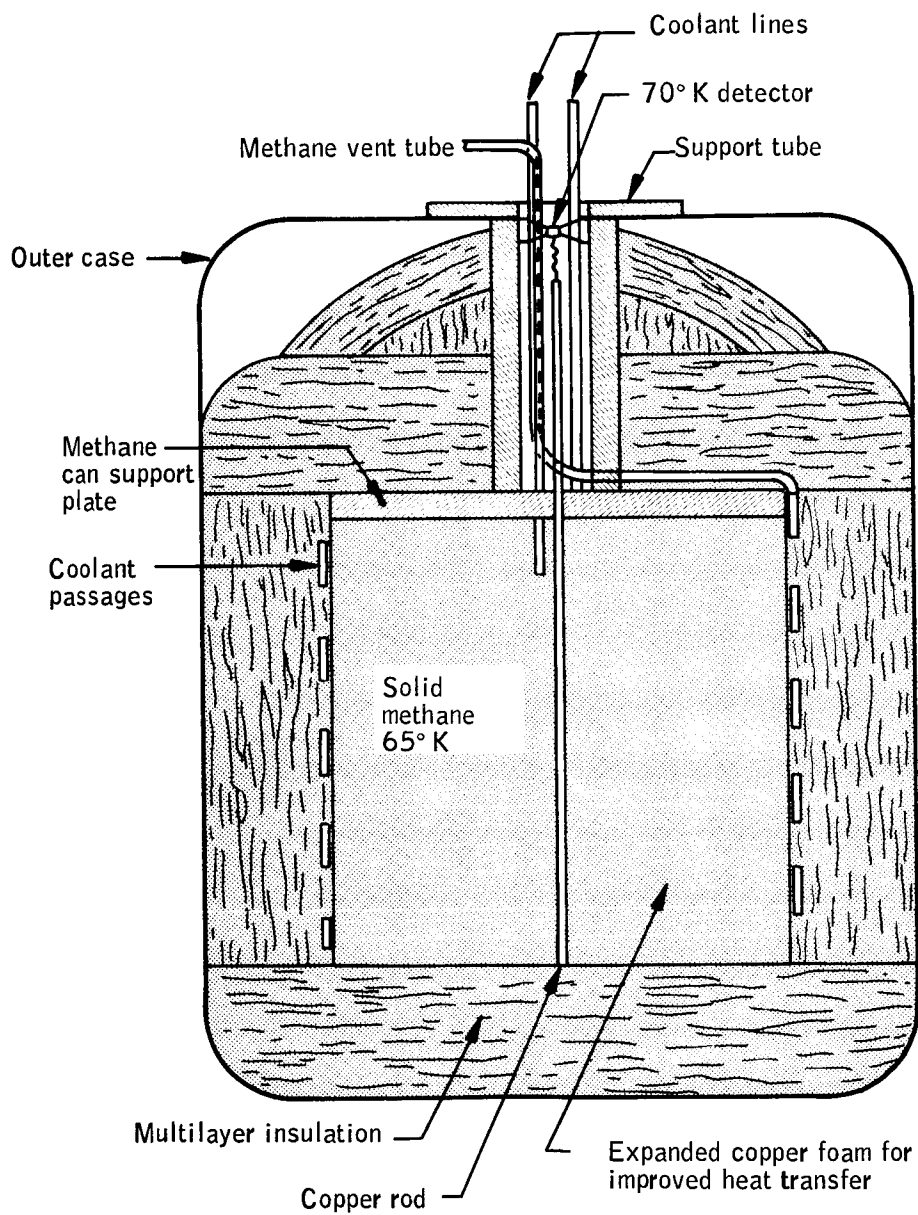
Figure 89. Schematic of Methane Refrigerator

TABLE 20. - PRELIMINARY SIZING OF A 60 to 70°K REFRIGERATOR

Sensor requirements

T, °K	60 to 70
Duration, years	1
Total head load, mW	7

Refrigeration requirements

Refrigerant	Methane
density, g/cm^3	0.49
latent heat, joules/g	615
Container	
volume, cm^3	4400
dimensions, cm	17.8 in diam x 17.8 high
mass, g	2150 (4.75 lbs)

Head loads on methane, mW

Insulation	13.0
Support column	16.8
Detector	7.0
	36.8

Estimated weight:

Methane	4.85 lbs
Vacuum container	5.10
Insulation	1.50
Methane container	1.50
Heat exchanger	0.50
Support column	0.50
Miscellaneous	2.00
Total weight	15.95 lbs

Emphasis will be placed on the neon-methane refrigerator system structural elements, as the taut-wire detector suspension system and the refrigerator support column are common to both refrigerator systems. A main support column designed for the neon-methane refrigerator (weight 26. 6 lbs) will support the methane refrigerator (weight 16 lbs) with an even larger safety factor. As has been indicated in the thermal design, the detector mount and refrigerator support column has been already assumed to be an indentical, common element in both systems.

Structural analysis of tubular support column: The tubular support column is the primary suspension member for the entire refrigerator primary structure. The outer methane container is attached directly to the lower mounting flange on this member. The structural dynamics model to be analyzed consists of a thin-walled, effectively weightless tubular beam which supports two flexibly connected rigid bodies. Since the primary transverse moments will act essentially through the center of gravity of the neon-methane systems, it is clear that the region of critical stress will be at the upper, flanged end of the support column. This critical stress will be reduced by enlarging the upper end of the column; this will be accomplished by using a conical tube. The structural analysis will indicate optimal parameters for this conical tube. Dimensional constraints have been dictated for the tube by the thermal analysis. Figure 90 shows the orientation of the conical tube and supported mass which will be subsequently analyzed. The tube will be constructed from glass filament wound reinforced epoxy. It has been shown for a similar refrigerator configuration (ref. 16) that this material possesses excellent mechanical energy absorbing characteristics such that acceleration levels of the supported mass did not exceed sinusoidal levels of the base forcing function for any excitation frequency. As such, the system may be considered very nearly or greater than critically damped (see Appendix E) Thus, it appears that a static analysis of the representative beam-mass system should lead to conservative structural specifications.

It may be noted here that the single-cryogen (methane) system may be analyzed as a tubular beam which supports just a single rigid body. Therefore, the single-cryogen system is structurally simpler than the two-cryogen system. With the exception of the analysis of the filament-supported inner mass (neon) of the neon-methane system, results of the analysis to follow are more conservative for, but apply to, the single-cryogen system.

▶ Vertical deflection and extensional stress in support column: Since rotational forces are considered to be small (ref. 17) only vertical F_v and horizontal F_h forces are germane to this analysis. The vertical deflections are given by

$$\delta_v = u(L) = \frac{F_v}{EAo}\left[1 - \left(\frac{\gamma}{2}\right)\left(\frac{L}{\gamma}\right)\ell n\left(\frac{1}{1-\gamma}\right)\right] \tag{22}$$

210.

and for the maximum extensional stress (All equations shown here are referenced to Appendix F where the derivations are shown.)

$$\sigma_{e_{max}} = E\left(\frac{du}{dx}\right)_{x=L} = \frac{F_v}{A_o} \cdot \frac{1 - \frac{\gamma}{2}}{1 - \gamma} \tag{23}$$

whereas pertinent structural parameters are defined in Figure 90 (i.e., δ, A_o).

► <u>Horizontal deflections and bending stresses in support column</u>: The relationship for horizontal deflection is obtained at the c.g. of the neon-methane mass as

$$\delta_h = \left(C_{11} + 2C_{12}d + C_{22}d^2\right) F_h \tag{24}$$

where

$$C_{11} = \frac{L^3}{EI_o}\left(1 - \frac{\gamma}{2}\right)^3 \left\{\left[1 + \frac{EI_o}{GkA_oL^2}\left(\frac{\gamma}{1-\frac{\gamma}{2}}\right)^2\right] \frac{1}{\gamma^3} \ln\left(\frac{1}{1-\gamma}\right) - \frac{2+\gamma}{2\gamma^2}\right\}$$

$$C_{12} = \frac{L^2}{2EI_o} \cdot \frac{\left(1 - \frac{\gamma}{2}\right)^3}{1 - \gamma} \tag{25}$$

$$C_{22} = \frac{L}{EI_o} \frac{\left(1 - \frac{\gamma}{2}\right)^4}{\left(1 - \gamma\right)^2}$$

and the maximum bending and shear stresses

$$\sigma_{max.} = \left|-\frac{Z}{I} \cdot M(x)\right|_{max.} = F_h\left[-\frac{aL}{I_o}\left(\frac{1-\frac{\gamma}{2}}{1 \quad \gamma \frac{x}{L}}\right)^2 \left(1 + \frac{d}{L} - \frac{x}{L}\right)\right]_{max.}$$

$$\tau_{max.} = \frac{F_h}{A} = \frac{F_h}{A_o} \frac{1 - \frac{\gamma}{2}}{1 - \gamma} \tag{26}$$

$A_0 = 2 \pi a t$

$I_0 = \pi a^3 t$

$A = A_0 \; \dfrac{1 - \gamma \frac{x}{L}}{1 - \gamma/2}$

$I = I_0 \; \dfrac{1 - \gamma \frac{x}{L}}{1 - \gamma/2}$
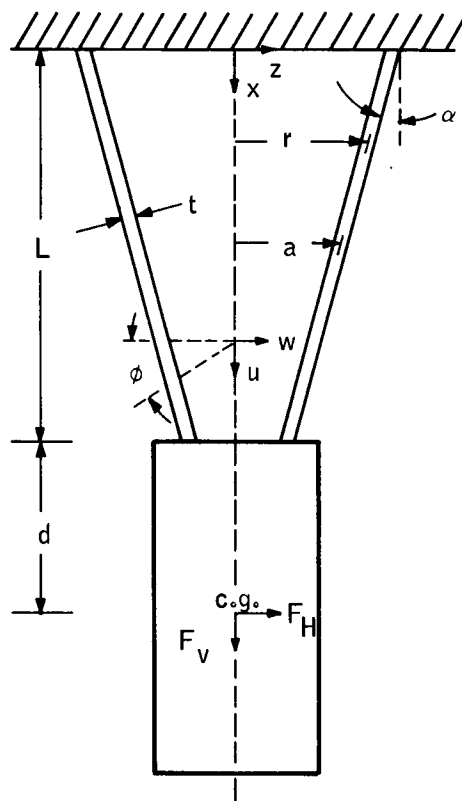
$r = a \; \dfrac{1 - \gamma \frac{x}{L}}{1 - \gamma/2}$

$\gamma = \dfrac{\frac{L}{a} - \tan \alpha}{1 + \frac{1}{2} \frac{L}{a} \tan \alpha}$

Figure 90. Schematic Cross Section of Neck Tube

A comparison of the maximum bending and shear stresses with the maximum extensional stress for $F_v = 2 \ F_h$ is presented below.

Since the maximum bending stress should occur near x = O

$$\sigma_{max.} \text{ bending} \approx \frac{1}{2} \left(1 - \frac{\gamma}{2}\right) \left(1 - \gamma\right) a \ L + d \ \frac{A_o}{I_o}$$

$$\left|\sigma_{max.}\right| \text{ extension} \approx \left(1 - \frac{\gamma}{2}\right) \left(1 - \gamma\right) \frac{L + d}{a}$$

$$\frac{\tau \text{ max.}}{\sigma \text{ max extension}} = \frac{1}{2} \tag{27}$$

Since L + d >> a, the tensile and compressive stresses due to bending are by far the largest. Thus, minimization of these stresses is required. When $\gamma > 1/2 \ (1 + d/L)$, the maximum bending stress occurs at x = O and is given by

$$\sigma_{max. \ bending} = \frac{F_H a L}{I_o} \cdot \left(1 - \frac{\gamma}{2}\right)^2 \left(1 + \frac{d}{L} \right) ; \ (x = o) \tag{28}$$

When $\gamma > 1/2 \ (1 + d/L$, however, the maximum bending stress occurs at $x/L = 2 \ (1 + d/L) - 1/\gamma$, and is given by

$$\sigma \text{ max bending} = \frac{F_H a L}{4 I_o} \frac{\frac{1}{\gamma} \left(1 - \frac{\gamma}{2}\right)^2}{1 - \gamma \left(1 + \frac{d}{L}\right)} ; \ (x = x_m) \tag{29}$$

Upon additional mathematical manipulation, it can be shown that γ optimum is

$$\frac{1}{2 \left(\frac{3}{4} + \frac{d}{L}\right)} \cong \frac{4}{15}$$

for the model presently considered. It is readily determinable from the definition of γ in Figure 90 that the upper diameter of the cone should be about 1-3/8".

► Values of critical stresses and displacements for the tubular support specifications (ref. Figure 90):

$$\gamma \; = \; \gamma \text{ optimum } = \; 4/15$$

$$L \; = \; 4.5 \text{ in.}$$

$$\sigma \; = \; 0.02 \text{ in.}$$

$$a \; = \; 0.59 \text{ in.}$$

$$\left. \begin{array}{l} A_o \; = \; 2\pi a t \; = \; 0.074 \text{ in.}^2 \\ I_o \; = \; \pi a^3 t \; = \; 0.012 \text{ in.}^4 \end{array} \right\} \quad \frac{I_o}{A_o} \; = \; \frac{1}{2} a^2 \; = \; 0.174 \text{ in.}^2$$

$$d \; = \; 5 \text{ in.}$$

$$F_V \; = \; m\ddot{X}_V \; = \; \eta_V W \; = \; 12(16) \; = \; 192 \text{ lbs}$$

$$F_H \; = \; m\ddot{X}_h \; = \; \eta_H W \; = \; 6(16) \; = \; 96 \text{ lbs}$$

$$E \; = \; 4.5 \times 10^6 \text{ psi (ref. 14)}$$

$$G \; = \; 2 \times 10^6 \text{ psi (ref. 14)}$$

From equations (22) and (23), the vertical deflection and maximum stress resulting from the vertical (longitudinal) inertial load of 12 g maximum (ref. 17) is calculated

$$\delta_r \; = \; \frac{F_V}{EA_o} \left(1 - \frac{\gamma}{2} \right) \left(\frac{L}{\gamma} \right) \ell n \left(\frac{1}{1-\gamma} \right)$$

$$= \; \frac{192 \left(1 - \frac{4}{30} \right)}{4.5 \, (0.074) \, 10^6} \quad \frac{(4.5)(15)}{4} \quad \ell n \left(\frac{1}{1 - \frac{4}{15}} \right)$$

$$= \; 0.0026 \text{ in.}$$

$$\sigma_{e_{max.}} \; = \; \frac{F_V}{A_\sigma} \left[\frac{1 - \frac{\gamma}{2}}{1-\gamma} \right]$$

$$= \; \frac{192}{0.074} \left[\frac{1 - \frac{4}{30}}{1 - \frac{4}{15}} \right]$$

$$= \; 3000 \text{ psi}$$

214

Similarly, the applications of equations (24), (25), and (29) yield the maximum horizontal deflection and the stress which occurs in the tube as a result of the horizontal maximum inertial forces of 6 g's.

$$\delta_n = \left[C_{11} + 2 C_{12}(5) + C_{22}(5)^2 \right] \; 96 \text{ in.}$$

$$C_{11} = 0.00062$$

$$C_{12} = 0.000167$$

$$C_{22} = 0.000087$$

$$\delta_n = 0.44 \text{ in.}$$

$$\delta_{b_{max.}} = \frac{F_H \, aL}{4 \, I_o} \; \frac{\frac{1}{\gamma}(1 - \gamma/2)^2}{1 - \gamma \left(1 + \frac{d}{L}\right)}$$

$$= \frac{96 \, (0.59) \, (4.5)}{4 \, (0.012)} \left[\frac{\frac{15}{4} \left(1 - \frac{4}{30}\right)^2}{1 - \frac{4}{15} (1 + 1.1)} \right]$$

$$\cong 36\,600 \text{ psi}$$

and $\sigma_{b_{max.}}$ is located midway up the column or about 2-1/4 in. from the end.

$$\tau_{max.} = \frac{F_H}{A_o} \cdot \frac{1 - \gamma/2}{1 - \gamma} = \frac{92}{0.074} \cdot \frac{13}{11}$$

$$= 1470 \text{ psi}$$

Structural model of the neon container support system: Thermal consi-
derations predominated in the selection of a taut filament support system for
the neon container in the place of more conventional supporting methods,
such as that of column supports between the methane and neon containers.
However, it will be shown that little if any penalty is accrued in structural
integrity and reliability by this choice. Since the neon and methane units
possess masses of the same order of magnitude, large damping of the methane
leads to large damping of the neon, and the system is closely coupled. Conse-
quently, a static analysis of the neon system at elevated inertial loading levels
is expected to provide a realistic evaluation of the maximum loading and dis-
placements the system will experience.

A suspension system consisting of eight sets of wire pairs is considered here.
The wires fasten along the upper and lower edges of the neon container and
connect to the internal edges of the methane container in an assembly as shown
in Figure 91.

►Stress displacement relationships

The derivations of the stress displacement relationships for this multifila-
ment support system is presented in Appendix G and summarized here.

The displacement in the vertical v or axial direction is given by

$$\delta_v = \frac{F_v \ell}{8EA \cos^2 \theta_w} \qquad (30)$$

where θ_w is the angle between the wire and the vertical axis and $\cos \theta_w = \cos \alpha \cos \gamma$ (Figure 92).

The expression for the stress in a single wire as a result of the vertical
force is

$$\sigma_v = \frac{F_v}{8A \cos \theta_w} \qquad (31)$$

The displacement and stress due to the horizontal inertial load is

$$\delta_H = \frac{F_H \ell}{2EA} \cdot \frac{1}{\sum\limits_{i=1}^{8} \left\langle \cos \psi_{i1} \right\rangle^2 + \left\langle \cos \psi_{i2} \right\rangle^2} \qquad (32)$$

216
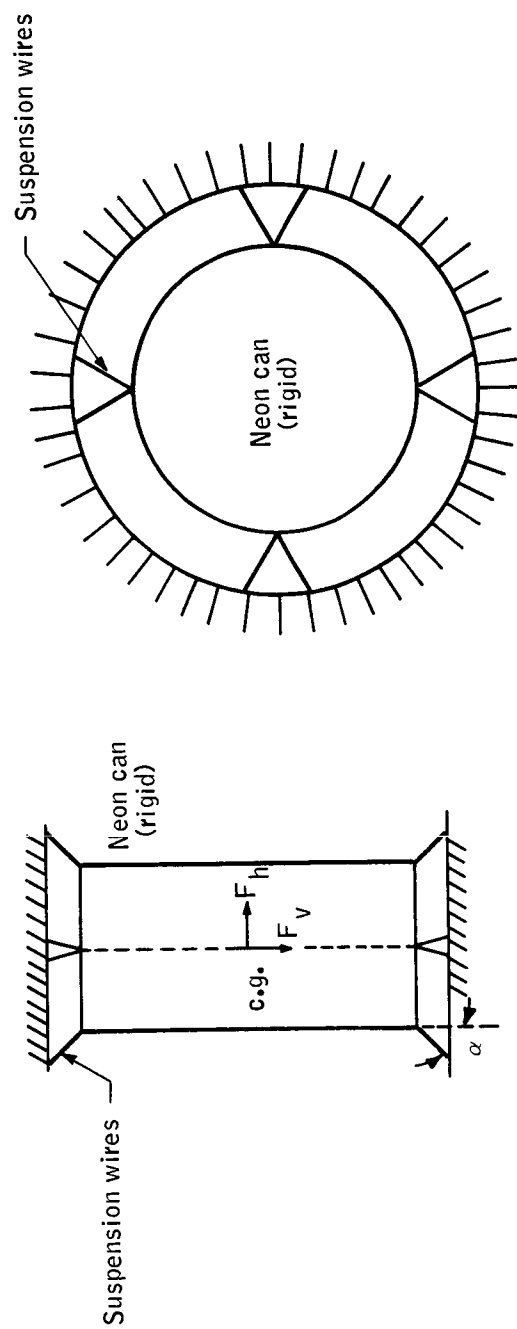
Figure 91. Vertical and Transverse View of Neon-Suspension System

217
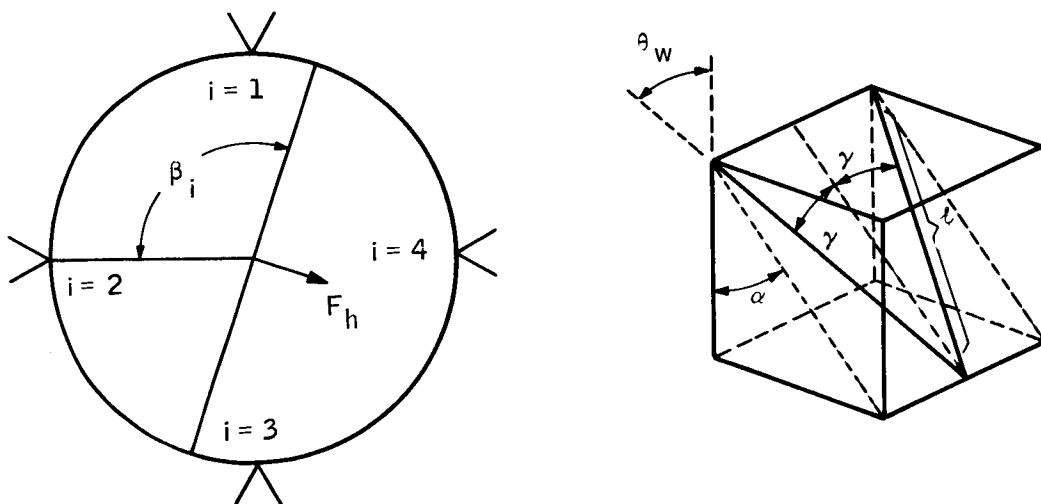
Figure 92. Representation of Angles α, β, γ, and θ_ω for the Filaments of the Neon Support System

$$\sigma_{H_{ij}} = \frac{F_H}{2A} \cdot \frac{\cos \psi_{ij}}{\displaystyle\sum_{i=1}^{8} \left\langle \cos \psi_{i1} \right\rangle^2 + \left\langle \cos \psi_{i2} \right\rangle^2} \qquad (33)$$

ψ is the included angle between the wire and horizontal inertial force vector,

where:

subscripts i and j do not denote tensor notation, but are indices which identify the jth of two wires in i^{th} of eight pairs of supporting filaments

$$\cos \psi_{i1} = \sin \gamma \ \cos \beta_i + \sin \alpha \ \cos \gamma \ \sin \beta_i$$

$$\cos \psi_{i2} = \sin \gamma \ \cos \beta_i + \sin \alpha \ \cos \gamma \ \sin \beta_i \qquad (34)$$

β_i represents the angle between the normal to the horizontal force vector and the ith wire pair.

$\langle \ \rangle$ in the summation refers to the convention whereby only positive values of $\cos \psi_{ij}$ are evaluated.

Values of critical stresses and displacements for the neon assembly multi-filament support system are as follows:

$$F_v = m\ddot{X}_v = n_v W = 12 \, (11.2) = 134 \text{ lbs}$$

$$E = 1.5 \times 10^6 \text{ psi (Dacron filaments)}$$

$$A = 4.53 \times 10^{-4} \text{ in.}^2$$

$$d = 0.024 \text{ in.}$$

$$\ell = 1.15 \text{ in.}$$

$$\alpha = 26.6°$$

$$\gamma = 45°$$

< > in the summation refers to the convention whereby only positive values of $\cos \psi_{ij}$ are evaluated.

Values of critical stresses and displacements for the neon assembly multi-filament support system are as follows:

$$F_V = mX_V = n_V W = 12(11.2) = 134 \text{ lbs}$$

$$E = 1.5 \times 10^6 \text{ psi (dacron filaments)}$$

$$A = 4.53 \times 10^{-4} \text{ in}^2$$

$$d = 0.024 \text{ in}$$

$$\ell = 1.15 \text{ in}$$

$$\alpha = 26.6°$$

$$\gamma = 45°$$

Thus, $\cos \theta_W = \cos \alpha \cos \gamma = (0.707)(0.894) \cong 0.632$ and the stress due to vertical forces equation (31) is

$$\sigma_V = \frac{F_V}{8A \cos \theta_W}$$

$$= \left[\frac{134}{8 (4.53 \times 10^{-4})(0.632)} \right] \text{ psi}$$

$$= 57\ 500 \text{ psi}$$

Application of equation (30) yields

$$\delta_V = \frac{F_V \ell}{8EA \cos^2 \theta_W}$$

$$= \frac{(132)(1.15)}{(8)(1.5 \times 10^6)(4.53 \times 10^{-4})(632)^2}$$

$$= 0.07 \text{ in.}$$

220

The stresses in the Dacron filaments and the displacement of the neon container will vary as the direction of the maximum horizontal force vector changes. The conditions which result from two particular force vectors are evaluated to obtain an indication of the maximum horizontal stress levels and displacements which may be experience by the system. The β_i function is used to evaluate $\cos \psi_{ij}$, equation (34).

Case 1 $\beta_1 = 0$
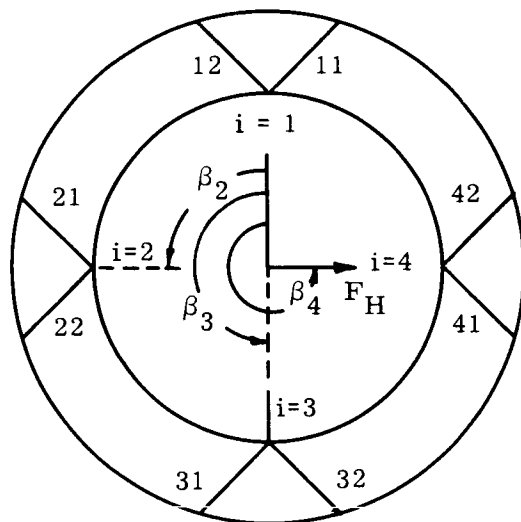
Case 2 $\beta_1 = \dfrac{\pi}{4}$

i =	1,	2,	3,	4
β_i =	0	$\dfrac{\pi}{2}$	π	$\dfrac{3\pi}{2}$

$\cos \beta_i$ = 1　0　-1　0

$\sin \beta_i$ = 0　1　0　-1

$\cos \psi_{12} = \sin \gamma$

$\cos \psi_{21} = \sin \alpha \cos \gamma$

$\cos \psi_{22} = \sin \alpha \cos \gamma$

$\cos \psi_{31} = \sin \gamma$
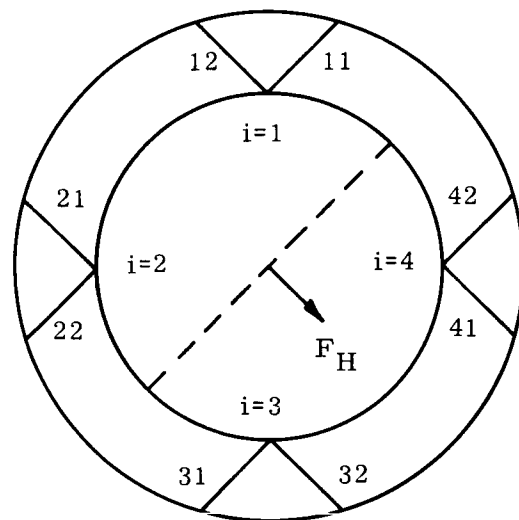
i =	1,	2,	3,	4
β_i =	$\dfrac{\pi}{4}$	$\dfrac{3\pi}{4}$	$\dfrac{5\pi}{4}$	$\dfrac{7\pi}{4}$

$\cos \beta_i$ = 0.707　-0.707　-0.707　0.707

$\sin \beta_i$ = 0.707　0.707　-0.707　-0.707

$\cos_{11}$ = 0.707 $(- \sin \gamma + \sin \alpha \cos \gamma)$

$\cos_{12}$ = 0.707 $(\sin \gamma + \sin \alpha \cos \gamma)$

$\cos_{21}$ = 0.707 $(\sin \gamma + \sin \alpha \cos \gamma)$

$\cos_{22}$ = 0.707 $(- \sin \gamma + \sin \alpha \cos \gamma)$

All other $\cos \psi_{ij}$s are negative and are, therefore, not evaluated.

221

(Case 1 - Cont.)

$\sum \cos \psi_{i1} = \sin \alpha \cos \gamma + \sin \gamma$

$\sum \cos \psi_{i2} = \sin \alpha \cos \gamma + \sin \gamma$

$\sum \cos \psi_{i1} = \cos \psi_{i2} = 0.707$

$(0.899 + 1.0) = \underline{1.34}$

(Case 2 - Cont.)

$\sum \cos \psi_{i.} = 0.707(\sin \gamma, 2 \sin \alpha \cos \gamma + \sin \gamma$

$\sum \cos \psi_{i2} = 0.707(\sin \gamma + 2 \sin \alpha \cos \gamma - \sin \gamma)$

$\sum \cos \psi_{i1} = \sum \cos \psi_{i2} = 1.414 (0.707) (0.899)$

$= \underline{0.90}$

The values of $\sum \cos \psi_{ij}$ indicates that δ_H for Case 2 would be greatest. Therefore for Case 2

$$\delta_H = \frac{F_H \ell}{2EA} \cdot \frac{1}{\displaystyle\sum_{i=1}^{8} \langle \cos \psi_{i1} \rangle^2 + \langle \cos \psi_{i2} \rangle^2}$$

$$= \frac{67.2 (1.15)}{2(1.5 \times 10^6) (4.53 \times 10^{-4})} \cdot \frac{1}{(0.90)^2 + (0.90)^2}$$

$$= 0.057 \text{ in.}$$

In addition, the maximum stress in the two cases analyzed, as the $\cos \psi_{ij}$ values show, occurs in filaments 12 and 21.

$$\sigma_{H_{ij}} = \frac{F_H}{2A} \frac{\cos \psi_{ij}}{\displaystyle\sum_{i=1}^{8} \langle \cos \psi_{i1} \rangle^2 + \langle \cos \psi_{i2} \rangle^2}$$

$$\sigma_{H_{12}} = \sigma_{H_{21}} = \frac{(67.2)}{2(4.53 \times 10^{-4})} \cdot \frac{0.707 \left[0.448 + 0.707 (0.894) \right]}{\langle 0.92 \rangle^2 + \langle 0.90 \rangle^2}$$

$$\sigma_{H_{12}} = \sigma_{H_{21}} = 35\ 000 \text{ psi}$$

222

Summary and conclusions: The highest stresses occurring in the refrigerator system compared to the limiting stresses of the materials and a brief resume of maximum deflection is presented in the following table.

Structural support column

σ bend max.	36 600 psi
σ ext max.	3 000 psi
τ max.	1 470 psi
σ resultant max.	40 000 psi
σ ultimate at 300°K	94 000 psi (min., ref. 14)
δ_V	0. 0026 in.
$\delta_{H\ max.}$ at c. g. (methane can)	0. 44 in.

Neon filament support system

σ_V	57 500 psi
σ_h	35 000 psi
σ resultant max.	92 500 psi
σ ultimate	135 000 psi at 300°K
δ_V	0. 070 in.
δ_H	0. 057 in.

The values of stress in the support column are apparently well within tolerable limits, and they indicate that a reduction in wall thickness may be possible. Until further analysis is done to determine an acceptable factor of safety consistent with the expected performance of the column and the minimum wall thickness needed to prevent buckling, no further recommendation is made. It may be worthwile to note that the conical column having end

223

of 1-3/8" and 1" is subjected to a maximum bending stress of σ_b cone

$= 1.6 \dfrac{F_H a L}{I_0}$. The stress in an equivalent 1-inch diameter cylindrical

column σ_b cyl $= 2.1 \dfrac{F_H a L}{I_0}$, and thus, a 24 percent reduction in the maximum stress is achieved by using a conical column.

The maximum undamped horizontal deflection could extend to about 0.44 inches, but no system liability is expected from this excursion. A reduction in d, the distance from the end of the support column to the c.g. of the methane-neon system, by a factor of two would, however, yield the twofold advantage of reducing the horizontal deflection to about 0.13 in. and the bending stress which acts on the column.

Although the stress levels in the dacron filament support system for the neon are relatively high, they are less than quoted values for the ultimate strength (reference 18). Additional reductions in stress may be considered without altering the thermal load by increasing the cross-sectional area and the length for a fixed filament A/1 ratio.

Although the rotational accelerations of the vehicle are small, asymmetrical or "off center" loads could develop on the neon-can suspension. A system of filament pair supports was used rather than that of a set of single wires in order to restrain torsional motin of the neon can about the vertical axis.

Also, an angle α = 45° was chosen for the plane of the filament pairs such that it would not project through the center of the container. Consequently, this design restrains container rotation about horizontal axis which passes through the center of gravity.

Thermal performance. -- Certain aspects of thermal performance will be discussed here. These aspects are distinguished from those covered previously by their noncritical nature, i. e., they do not involve satisfaction of basic design requirements. Thus, it is the purpose of the following paragraphs to give an indication by approximate quantitative analysis that the designs of the solid-cryogen refrigerator will perform adequately in certain instances of nondesign point operation. In some cases, it is not necessary to demonstrate adequacy of performance for both cryogens in the neon-methane unit and for the methane unit. In these cases, the point will be made with respect to the most stringent case.

Heat transfer within the cryogen cans: Consideration of the problem of heat transfer within the cryogen cans can be confined to the neon container in the neon-methane unit since the operational requirements are more stringent in this case.

Two heat transfer problems are encountered in the neon can. One is the removal of latent heat from solidifying gases by the helium refrigerant during cryogen formation. The other is removal of detector heat by subliming solid during normal operation. Both problems involve the conduction of heat in a direction perpendicular to the main can axis between the outer can cylindrical wall, 5. 6-cm radius, and the central copper rod, 0. 1-cm radius. When the can is filled with neon of conductivity about 0. 005 watts/cm°K, the conductance of this path is given by $\dfrac{2\pi \times 0.005 \times 22.4}{\ln\left(\dfrac{5.6}{0.1}\right)}$, = 0. 15 watts/°K. Since

200 watts have to transferred during cryogen formation, this conductance is too low. The can will, thus, be filled with expanded copper foam of 92-percent void fraction. An estimate of the geometrical parameters for this foam suggest a surface area of 5 cm^2/cm^3 and an effective thermal conductivity of about three percent of the equivalent solid. The lateral conductance with this foam in place will, thus, be raised by a factor of $\dfrac{10 \times 0.03}{0.005} = 60$

times. The new effective lateral conductance of 9 watts/°K is adequate when it is observed that few of the 200 watts of cooling do not have to be taken from the center of the can. Visual inspection of the copper foam suggests that the maximum thickness of solid neon through which heat must be removed is about 0. 1 cm. The conductance of this particular path for the whole can is

given by $\dfrac{\pi/4 \times (11.2)^2 \times 22.4 \times 5 \times 0.005}{0.1}$ = 552 watts/°K. This very high conductance suggests that a foam with greater conductivity and less surface area per unit volume would be more suitable if it can be obtained.

The 2-mm diameter copper rod between the neon can and detector has been sized for a heat load of 10 mW and a temperature drop of 0. 5°K, i. e., its conductance is 0. 02 watts/°K for a thermal conductivity of 20 watts/cm°K. A short copper wire will connect the end of the detector cooling rod to the detector itself. Possible dimensions for this wire are 1. 5-cm long and 0. 050-cm diam. These dimensions give a conductance of 0. 026 watts/°K.

Most of the thermal resistance between detector and solid neon will be in the rod and wire. The resistance of these items will be $\left[\dfrac{1}{0.026} + \dfrac{1}{0.02}\right] = 88°K/$ watt. For a 5 mW load plus about 1 mW in stray heat leaks, the difference between the detector and neon can temperatures will, thus, be about 0.53°K. These estimates assume good contact between the detector rod and the copper foam. This can be achieved by soldering the foam to the rod.

The latent heat of the neon will be removed by the helium refrigerant flowing through passages surrounding the outside of the can. These passages should have a large surface in common with the can so as to reduce the heat flux per unit area through the can wall and to eliminate the need for conduction in the direction of the can walls. Such passages would be wide and shallow. They could be formed by creating an annular space around the outside of the neon can, or a commercial sheet material could be used with coolant passages formed between two layers of sheet metal. Choice of a system would depend upon cost and availability considerations if construction is contemplated. For preliminary design consideration, the passages are assumed to be 1-cm wide by 0.2-cm high. The heat transfer coefficient that may be expected is estimated as follows for 40°K as an example:

Helium flow rate	W	= 50 liters liquid/hr
		= 3.47 gms/sec
Passage area	A	= 0.2 cm^2
Passage hydraulic diam.	D	= 0.33 cm
Viscosity	μ	= 30 x 10^{-6} poises (g-mass/sec-cm^2)
Specific heat	C_p	= 5.8 joules/g-°K
Thermal conductivity	K	= 0.0003 joules/sec-cm-°K

The heat transfer coefficient h is given by

$$\left(\frac{hd}{K}\right) = 0.023 \left(\frac{dW}{A\mu}\right)^{0.8} \cdot \left(\frac{C_p\mu}{K}\right)^{0.4}$$

Substitution of the above values in the equation gives h ~ 0.7 watts/cm^2-°K. Since 200 watts have to be transferred from the neon can, a reasonable passage length of 100 cm would result in a temperature difference of the order of a few degrees.

Although it would be advisable to flow helium over as much of the outer surface of the neon can as possible since the stainless steel can has a poor conductance, the copper foam will help even out circumferential heat flow. The foam should be cut so that it has a slight compression fit with the can. Since the contact between the foam and the wall is somewhat imperfect, heat will,

thus, be partly transferred from the foam to the can wall through a thin layer of solid neon.

The requirements of the methane systems are similar but less stringent, so no further remarks on those components are necessary. Thermal conductivity of solid methane is about one order of magnitude less than that of solid neon, but this is inconsequential if copper foam is used.

Operation with 300°K boundary temperature: The heat loads calculated in earlier paragraphs can be modified quite simply to account for a boundary temperature of 300°K rather than 200°K. The new figures for the neon-methane system are as follows, with the 200°K figures for comparison.

	Heat load, mW	
Boundary temperature	200°K	300°K
Methane can		
Supports	14	29
Insulation	8	32
Neck tube radiation	2.8	14
Heat exchanger and vent tubes	0.6	1.3
	25.4	76.3
Neon can		
Detector radiation	0.9	4.5
Detector wire support	0.4	0.7
Detector rod	0.1	0.5
Neon can support	2.0	2.0
Radiation from methane	1.0	1.0
Detector bias (zero if stored)	5.0	(0)
Heat exchanger	0.6	1.0
	10.0	(9.7)

The methane loss is the most critical and will sublime at roughly three times the design rate, which gives a unit lifetime of about one-third of a year with a 300°K outer boundary temperature.

A similar calculation can be made for the methane refrigerator using the applicable data given previously. The results are tabulated below.

| | Heat load, mW | |
Boundary temperature	200°K	300°K
Access tube and service lines conduction	14.0	29.0
Access tube radiation	2.8	14.0
Insulation	13.0	52.0
Detector	7	5
	36.8	100.0

The methane will, thus, sublime at about three times the normal rate if operated at 300°K boundary temperature, which gives a lifetime of about one-third of a year.

Effectiveness of the passive control system: The cryogen vent tubes were sized to provide a pressure over the solid consistent with the required operating temperature and heat load. A calculation can be made to determine the rate at which the cryogen temperature changes with change of heat load, assuming the given tube resistance.

The flow equation for the tubes may be written in a re-arranged form of equation 18

$$p^2 = R_F \cdot m \cdot T \tag{35}$$

where $R_F = \dfrac{256 \, R\mu\ell}{\pi \, Md^4}$, is the flow resistance and is assumed constant for small changes in temperature.

The relationship between mass flow m and heat load Q is

$$m = \frac{Q}{L}$$

where L is the latent heat.

The temperature/pressure relationship for a solid/gas equilibrium system is given by

$$T = f_{gs} \, (P) \tag{36}$$

The regulation effectiveness of the passive system will be given by an equation of the form

$$\frac{dT}{T} = f(T) \cdot \frac{dQ}{Q} \qquad (37)$$

This expression may be determined as follows:

$$\frac{dT}{dQ} = \frac{dT}{dP} \cdot \frac{dP}{dm} \cdot \frac{dm}{dQ} \qquad (38)$$

From equations (35), (36), (37), and (38)

$$\frac{dT}{dQ} = f'_{gs}(P) \cdot \left[\frac{R_F}{2P - R_F \, m \, \frac{dT}{dP}} \right] \cdot \frac{1}{L} \qquad (39)$$

so that

$$\frac{dT}{T} = \frac{f'_{gs}}{f_{gs}} \cdot \left[\frac{m \, R_F}{2P - R_F \, m \, \frac{dT}{dP}} \right] \frac{dQ}{Q} \qquad (40)$$

$$\frac{dT}{T} = \frac{f'_{gs}}{f_{gs}} \left[\frac{1}{2 \frac{f_{gs}}{P} - f'_{gs}} \right] \frac{dQ}{Q}$$

For methane (from Figure 86),

$$T = f_{gs}(P) = \frac{500}{7.4 - \log P} \qquad (41)$$

For neon (from Figure 84),

$$f_{gs} = T = \frac{114}{7.28 - \log P} \qquad (42)$$

From these last two equations, the following control expressions are obtained for design point operation of the cryogen containers.

Neon

$$f'_{gs} = \frac{T^2}{114 \, P} \qquad (43)$$

229

For   T   =   15°K
            P   =   0.4 Torr

$$f'_{gs} = 4.93 \tag{44}$$

$$\frac{dT}{T} = 0.0047 \cdot \frac{dQ}{Q}$$

Methane

$$f'_{gs} = \frac{T^2}{500\,P} \tag{45}$$

For   T   =   62°K

            P   =   0.2 Torr

$$f'_{gs} = 38.45 \tag{46}$$

$$\frac{dT}{T} = 0.0011 \frac{dQ}{Q}$$

Equations (45) and (46) show the fractional change in solid cryogen temperature for a given fractional change in heat load. In both cases, the temperature sensitivity is less than one percent of the heat load variation. This is considered to be quite satisfactory and would seem to indicate that active temperature control is unnecessary.

The regulation of the methane refrigerator is obviously identical to that of equation (46).

Subcooling: Since helium is to be used as the refrigerant, it should be possible to cool most of the unit to about 6°K. This would permit the system to be closed for a period of time while the pressures and temperatures of the cryogens build up to the design values. An estimate of the length of time that the neon-methane unit may be stored in the subcooled condition can be made as follows:

Neon can

Average specific heat between 6°K and 15°K   =   0.29 joules/g-°K

Thermal capacity of 3000 grams solid neon
between 6°K and 15°K   =   7740 joules

230

Estimated heat leak, assuming methane can
at 62°K, outer boundary at 300°K, and with
no detector load   ≈   7 mW

Days of storage possible $\dfrac{7740 \times 1000}{3600 \times 24 \times 7}$ ≈ 13 days

Methane can

Average specific heat between 6°K and 62°K   = 2 joules/g-°K

Thermal capacity of 1760 grams of methane
between 6°K and 62°K   = 179 000 joules

Estimated heat leak assuming a 300°K outer
boundary   ≈ 110 mW

Days of storage possible = $\dfrac{179\ 000 \times 1000}{110 \times 3600 \times 24}$ ≈ 19 days

The methane can estimate includes the extra heat leak from the environment
due to its lower temperature. This is compensated for by the neglect of the
thermal capacity of the structural members and insulation. It is suggested
that two weeks be considered to be the maximum length of storage with a
300°K outer-boundary temperature, until experimental data are available.

The appropriate figures for the methane unit will be nearly the same as those
for the methane can of the neon-methane unit. Here, the methane mass will
be slightly higher and the heat leak slightly less for a 300°K boundary. Since
the calculations are all approximate, a maximum storage period of two weeks
in the subcooled condition is suggested.

Thermal transient response of the refrigerator: This problem is essen-
tially very complex and can only be satisfactorily resolved by experiment.
A very simple analysis can be made by assuming that the cryogen containers
are the only heat sinks and that the heat leaks do not depend upon the sink
temperatures.

Neon

200°K boundary heat leak with no detector load   = 5.0 mW

300°K boundary heat leak with no detector load   = 9.7 mW

Thermal capacity of 3000 grams at 0.29 joules/g-°K   = 900 joules/°K

Rate of temperature rise with 200°K outer boundary   = 0.02°K/hr

Rate of temperature rise with 300°K outer boundary   = 0.039°K/hr

Methane

200°K boundary heat leak	= 25.4 mW
300°K boundary heat leak	= 76.3 mW
Thermal capacity of 1600 grams at 2 joules/gm°K	= 3200 joules/°K
Rate of temperature rise with 200°K outer boundary	= 0.029°K/hr
Rate of temperature rise with 300°K outer boundary	= 0.086°K/hr

For the methane unit the rate of temperature rise is slightly different. By scaling the above members, the appropriate figures will be 0.03°K/hr and 0.085°K/hr for the 200°K and 300°K boundary cases, respectively.

Servicing techniques. -- In order to make a quantitative assessment of refrigerator servicing requirements, it is necessary to neglect the effect of the space vehicle internal plumbing, etc. and to consider the refrigerator to end at the interface between it and the vehicle. The additional restrictions and requirements placed by the vehicle and the ground support system will have to be included after a study of the integrated system has been made.

The areas of refrigerator operation which may be included under servicing may be categorized as follows:

● Cool-down and solid-cryogen formation.

● Consideration of storage and shipping requirements.

Cool-down and solid-cryogen formation: Since the neon chamber operates at 15°K, and neon has a triple-point temperature of 24.6°K, only two refrigerants may be considered - liquid hydrogen and liquid helium. Both are relatively freely available. Liquid hydrogen is cheaper, has a higher volumetric heat capacity, but is hazardous. Its normal boiling point of 20.4°K is higher than the intended 15°K operational temperature for the neon and so a degree of sublimation cooling of the latter would be necessary to reach the operating temperature. This would reduce the amount of neon available for steady operation and prevent any subcooling of the neon to be obtained. Liquid helium is safe to use and would permit higher temperature gradients to be obtained in the neon chamber during solid formation. Its main disadvantages are its higher cost and the larger volume which would be needed for servicing.

The requirements for solid-methane formation do not place any further restrictions upon the choice of refrigerant.

Several ways of using the helium refrigerant may be envisaged. One very simple method would be to spray helium into the space between the neon and methane cans. This would require the use of only one extra tube from the outside which need not make contact with any of the internal components. Gas

would exit via the neck penetration. This method would introduce no additional heat leaks, but it has the disadvantage that the detector must be kept in a vacuum at all times, thus, requiring two vacuum areas rather than one. Another disadvantage would be the need to make the inner assembly leak tight with respect to the insulation so as to prevent temporary degradation of the latter during ground hold. This method has long-range advantages, but it is probable that more conservative techniques should be used at least until some flight experience with these devices has been obtained. Consequently, a system in which refrigerant is passed through passages of some sort in contact with the cryogen chambers will be used. Such an exchanger could be external or internal to the cryogen cans.

Internal coils would obviously bypass the thermal resistance of the container walls from the cans; however, they would take up too much valuable space and introduce too many complications into the construction of the cans. The cooling passages will, therefore, be built onto the outside of the cans.

One heat-exchange pass will be made in which cold liquid or gaseous helium will first cool the neon chamber and then the methane chamber. Connections will amount to one tube from the exterior to the neon can, one tube from the neon can to the methane can, and one tube from the methane can to the exterior. Thus, the solid-methane should be formed and considerably subcooled before the neon chamber is completely filled. This subcooling will be reduced somewhat because most of the sensible heat of the refrigerator structure will be removed via the methane chamber heat exchanger.

The amounts of heat to be removed from the neon-methane unit at 300°K are approximately as follows:

Neon

Sensible heat, 300°K to 15°K	302 joules/g
Latent heat of solidification from vapor	105
Sensible heat, 15°K to 6°K	26
Total	433 joules/g
For 3000 grams	1 299 000 joules

Methane

Sensible heat, 300°K to 62°K	502 joules/g
Latent heat of solidification from vapor	615
Sensible heat, 62°K to 6°K	112
Total	1230 joules/g
For 1600 grams	1 970 000 joules

233

Structural members, insulation, etc.

Assume that all components are stainless steel and that they are all cooled to 6°K

Sensible heat, 300°K to 6°K	75 joules/g
For 2630 grams	197 000 joules

It will be assumed that it should be possible to cool the unit and form the cryogen in two hours at the most. The cooling requirements may be restated thus:

Neon container	~ 200 watts
Methane container plus structural items	~ 300 watts

The liquid-helium refrigerant requirement may be estimated by assuming that the equivalent of all latent heat plus sensible heat up to 70°K (est) is removed from all the flowing helium. Thus,

$$3\ 466\ 000 \text{ joules } = \text{ (helium-mass flow) } x \left[h_{g_{70}} - h_{4.2} \right]$$

$$\text{Helium-mass flow } = \frac{3\ 466\ 000}{(382 - 9)}$$

$$= 9060 \text{ gms}$$

$$\text{or 73 liters}$$

This total does not include the amount of helium needed for cooling the transfer line and space vehicle plumbing, of course. Exactly how much helium will be needed can only be determined by experiment. The problem is highly time dependent in nature and is not amenable to theoretical analysis. Apparently a liquid-helium supply of 100 liters should be adequate.

Within the refrigerator, mylar tubes will be used for carrying the coolant to the cans. The exact dimensions and positions of the tubes will not be selected until construction is contemplated because of the numerous secondary considerations which will appear in that phase, such as availability of material and ease of assembly. Mylar tubes of 0.25-in. diam. with 0.010-in. wall thickness is suggested. A possible routing of lines so as to provide long thermal conduction paths would be as follows: exterior to bottom of neon can; top of neon can to top of methane can via bottom, to increase the path length; bottom of methane can to exterior.

The problem of heat conduction within the neon can was discussed previously.

The neon and methane cans will be filled via their vent lines. Layout of these lines in the space vehicle will present some problems. The flow resistance of these lines must be preserved at the value calculated previously, but gases must be dumped in a manner that does not affect the vehicle attitude control.

Similar remarks to the foregoing can be made concerning the methane refrigerator. A simple scaling of the numbers shows that in this case about 65 liters of liquid helium would be necessary.

There is little doubt that the helium requirement could be very greatly reduced by careful study of the overall space vehicle system and programming of flow rates to make best use of the sensible heat of the helium gas.

Storage and shipping considerations: It may be necessary to ship or store a refrigerator in cold condition. Previous calculations show that the unit can be stored in a 300°K environment, evacuated, for about two weeks. This requires that the cryogen vent lines be closed off or equipped with some kind of regulated valves which will open when the cryogen pressures reach design values.

Launch considerations. -- There are three launch phases of interest. They are ground hold, ascent, and adjustment to equilibrium operating conditions. A quantitative assessment of the behavior of the refrigerator under these circumstances is impossible at the present time since the refrigerator is but a part of a complete system. However, potential problem areas can be identified and an indication can be given of how they can be solved quantitatively.

Ground hold is somewhat similar to general storage, and the remarks made previously apply. If, after ascent, the refrigerator must be able to reach equilibrium quickly, the system must not be subcooled by more than a degree before ascent. This will require that a small amount of cold helium be circulated through the refrigerator under ground hold conditions, and its flow should be carefully monitored to retain this fine control. The circulation of coolant will solve the problem of higher environmental temperatures at this stage, 300° exterior instead of 200°K. A vacuum environment will be required at all times for protection of the detector as well as to minimize heat leaks.

Calculation of ground-hold helium coolant requirements will be straightforward but will depend upon the overall system configuration and scheduling. The vent lines can be closed off under all subcooled storage conditions.

Ascent conditions will place severe structural loads on the refrigerator, as was previously considered in detail. A decision will have to be made concerning the transient thermal behavior of the refrigerator. Since the detector must be kept in a vacuum, the whole unit can be kept evacuated during ascent.

When orbit is reached, the vacuum chamber can be opened to space, and the vent lines can be opened. The speed with which thermal equilibrium and operational conditions are obtained will depend entirely upon the adequacy of the thermal control during ground hold and ascent. This should be a relatively simple problem to solve during the design of the vehicle.

Summary. -- The main parameters of both refrigerators are given in Tables 19 and 20. Inspection of these parameters shows that the principal heat load upon the solid neon is due to the detector, and that upon the methane can in both units is due to conduction along the support tube. The size of the neon container is, therefore, set mainly by the detector load. Thus, only minor reductions in the amount of neon needed can be obtained by improvements in design. The design of the support or neck tube connecting the methane can to the exterior is, however, of primary importance. It may be anticipated that the major portion of further development work upon these and future solid cryogen refrigerators will concentrate upon refining the design of this neck tube. The following areas of study may be defined:

- Optimization of neck tube and container geometry

- Selection of materials with a higher strength to thermal conductivity ratio

- Utilization of the cold vent gases in cooling the neck tube

- Better definition of structural requirements, in the form of better information on inertial loading during launch.

The data which were used to perform this study are all subject to critical scrutiny. As has been pointed out above, however, the reliability of data is not critical in any area except for the support tube material.

The analyses which were used to predict certain heat loads could well be improved by refining the models used. This is particularly true in the case of radiative heat loads, where view factors and emissivity data are relatively poorly defined at this state.

The precoolant system must be studied further. It appears wasteful to build in tubing for brief usage whereafter it merely serves to degrade performance. Sizing and positioning of heat exchanger tubes will require more study at the design stage. Mylar tubing is very stiff and is, thus, not amenable to intricate layouts which require bending. Both the heat exchanger and vent tubes as sized in this report would appear to take up too much room in the neck tube. Some design rearrangement will be necessary here, also.

Detector Mounting

Introduction. -- Principal heat loads on the primary solid refrigerant (neon in the case of the 16°K refrigerator) are from the detector and its mounting system, as previously discussed. These heat loads are generated by: detector bias dissipation, detector lead and support wire conduction, and radiant heat transfer from the vacuum enclosure surrounding the detector. Controlling and minimizing these heat loads is one of the key elements toward the design and construction of a solid-cryogen detector refrigerator of minimum size and weight.

236

During the detector discussion, several detector mounting schemes were presented for the Ge: Cd and Hg: Cd: Te detectors. Concern here will be given only to the Ge: Cd detector mounting as it is the first choice and presents a greater problem in achieving the required conditions. Of the two mounting methods shown for the Ge: Cd detector, i. e., the integrating chamber approach and the total internally reflecting crystal (TIR), the latter method is most promising from a thermal design standpoint as it can be implemented within a smaller volume than the integrating chamber method.

Mounting requirements for the selected detector involve factors other than the physical placement of the detectors on a substrate. Figure 93 is a conceptual sketch of a complete detector mount. To provide optimum detector operation, the detector must be shielded from all radiant energy outside of the desired field of view (FOV) and outside of the desired spectral band. To accomplish these requirements, a FOV-limiting cold shield is placed in front of the detectors with a baffle between the two detectors to reduce optical "crosstalk". In front of the cold shield a passband filter is mounted to allow only radiant energy in the desired spectral band to enter. The filter and cold shield assembly are cooled to the same temperature as the detector; thus, these elements will not provide self-emission signal inputs to the detector.

Optical alignment requirements dictate that the detectors be placed in a precise position when mounted in the refrigerator and maintain their positioning throughout the subsequent thermal excursions and launch environments. The detector mounting substrate must, therefore, be spatially restrained independently of the 16°K thermal conduction rod that transports the detector heat loads to the neon primary refrigerant. Figure 93 illustrates a system of six titanium-alloy wires arranged into two opposed conical arrays of three wires each. These wires are pre-tensioned, to provide rigid restraint of the detector substrate, and attached to the refrigerator enclosure at their outer ends. Detector positioning is made by adjusting the length and tensile stress of the six taut support wires.

Electrical leads for the two detectors and a temperature sensor will require an additional six leads, also of titanium alloy, but these leads will be essentially slack and not provide support. Conceptually, and a point that needs further investigation, the taut support wires could also function as the required electrical leads. However, the reduced heat leakage obtained by this concept, as will be seen in the following paragraphs is not significant and is of only a small thermal advantage.

A thermal connection must be provided between the rigidly supported detector substrate and the copper conduction rod leading to the primary refrigerant. This thermal connection must be flexible so as to avoid perturbations on the detector substrate position by the motions of the primary refrigerant vessel and its conduction rod. It will be shown that a few small copper wires can provide this thermal connection, the wires being soldered to both the detector substrate and the conduction rod.

237
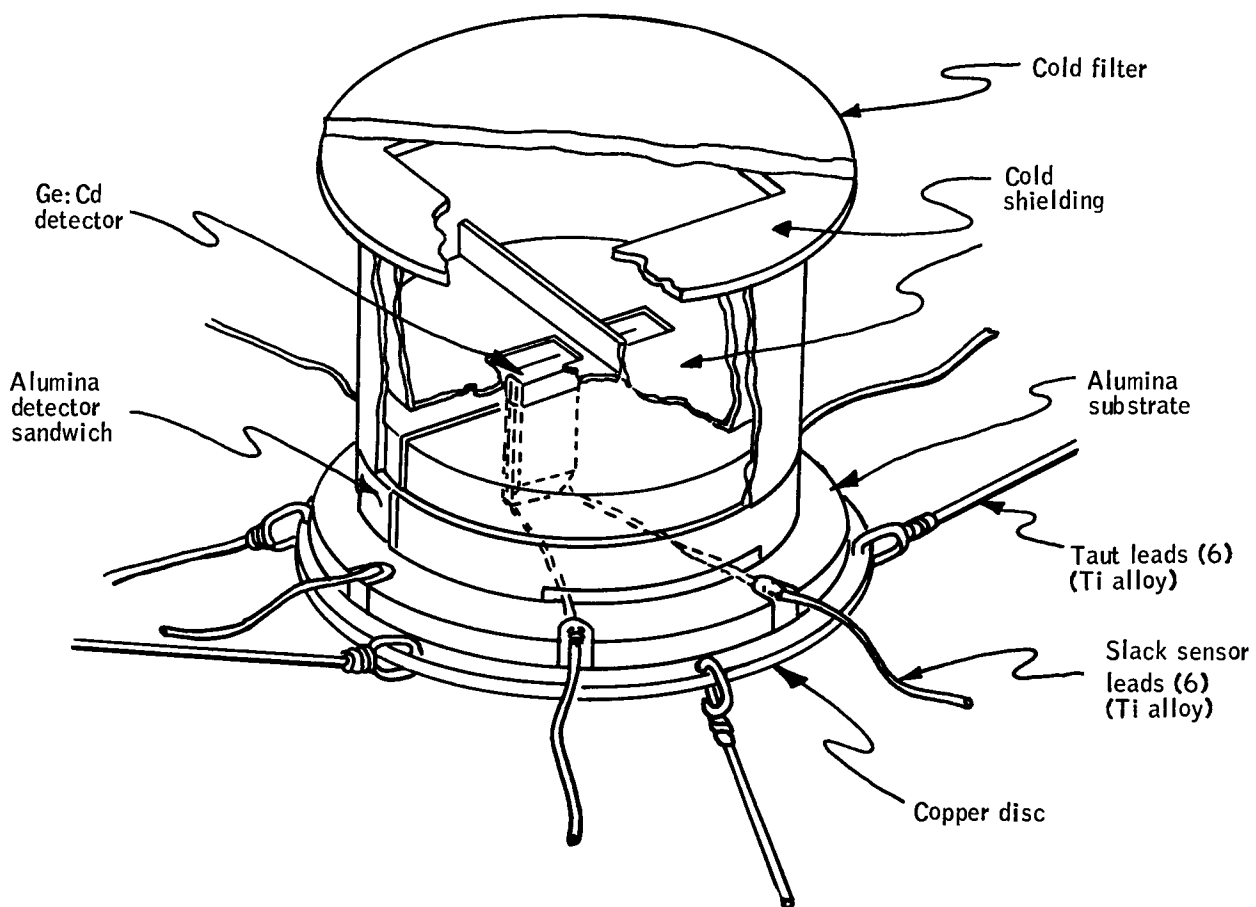
Figure 93.   Detector Mount Conceptual Design

Thermal design. --

Detector dissipation: The bias dissipation for each Ge:Cd detector can be limited to 2.5 milliwatts as noted during the detector discussion. For this study, a detector bias level of 5.0 milliwatts will be assumed to avoid undue constraints of the optimum bias selection. It remains, therefore, to determine the thermal conduction and radiation parameters to define the total detector heat loading. Since the refrigerator will be operated with shell temperatures near 200°K in orbit and near 300°K for ground-based tests, the detector heat loads will be determined for both conditions.

Detector lead conduction: Titanium alloys exhibit the lowest thermal conductivity properties of all metals founds in the literature. One such alloy consisting of 90 percent Ti, 6 percent Al, and 4 percent V has been previously used in wire form for cryogenic applications. Preliminary indications are that the alloy is weldable and can be plated. When suitably plated with gold, the wire can be considered to be solderable. Despite their low thermal conductivity characteristics, these titanium alloys exhibit acceptably low electrical resistivities.

Data for the thermal conductivity as a function temperature for the selected alloy is presented in reference 19. Computing the thermal conductivity integral Σk, for the two outer boundary temperatures yields:

$$\sum_{16}^{200} k = 7 \ 13 \ watt/cm$$

$$\sum_{16}^{300} k = 13 \ 93 \ watt/cm$$

The conducted heat leakage of the leads is

$$Q_c = (\Sigma k) \frac{NA}{L} \ watt$$

where:

N = number of leads = 12

A = lead cross-sectional area = $20.3 \times 10^{-6} \ cm^2$ (with 0.002 in. diam)

L = lead length = 1.5 inches = 3.8 cm

Therefore:

$$Q_c = (\Sigma k) \ (64 \times 10^{-3}) \ \text{milliwatt}$$

$$Q_{c \ 200} = 0.46 \ \text{milliwatt}$$

$$Q_{c \ 300} = 0.89 \ \text{milliwatt}$$

Detector radiant heat loading: Aside from the detector bias dissipation, radiant transfer to the detector substrate assembly is the most significant heat load. This radiant heat transfer from the vacuum enclosure to the substrate fits a classical total enclosure problem where

$$Q_R = A_D \left[F_e \ F_a \right] D \ \sigma \left(T_E^4 - T_D^4 \right)$$

where:

A_D = detector substrate area

σ = Stefan - Boltzman constant

T_E = enclosure temperature, 200°K or 300°K

T_D = detector temperature, 16°K

A_E = enclosure area $\approx$ 10.0 A_D

The detector temperature T_D is so low that it is insignificant in the above heat transfer equation and will be ignored. The complex emittance/geometry term will be evaluated:

$$\left[F_e \ F_a \right] \ D = \cfrac{1}{\cfrac{1}{F_a} + \cfrac{1}{\varepsilon_D} - 1 + \cfrac{A_D}{A_E} \left(\cfrac{1}{\varepsilon_E} - 1 \right)}$$

With a total enclosure the geometric view factor F_a = 1.0 and the area ratio A_D/A_E is physically very small, i.e., the emittance of the enclosure ε_E will have very little impact on the radiant heat transfer to the detector substrate.

Therefore,

240

$$\left[F_e \ F_a \right] D = \epsilon_D$$

and

$$Q_R = \Sigma \left[A_D \ \epsilon_D \right] \sigma T_E^4$$

Referring again to Figure 93, some characteristic dimensions can be projected:

  o.d. of cold shield = 0.5 cm

  Height of cold shield = 0.6 cm

  o.d. of cold filter = 0.6 cm

  Thickness of cold filter = 0.05 cm

  o.d. of alumina substrate = 0.64 cm

  Thickness of alumina substrate = 0.10 cm

  o.d of copper mounting disc = 0.75 cm

  Thickness of copper mounting disc = 0.75 cm

  Emittance of copper cold shield and mounting plate = 0.02

  Emittance of alumina substrate = 0.6

Total exposed area of low emittance components = 2.15 cm^2, and for high emittance components = 0.201 cm^2.

Therefore

$$\Sigma A_D \ \epsilon_D = 0.164 \ cm^2$$

and

$$Q_{R \ 200} = 1.49 \ milliwatts$$
$$Q_{R \ 300} = 7.52 \ milliwatts$$

Summary of detector heat loads: The summation of the detector heat loads previously generated is:

$$Q = Q_D + Q_C + Q_R$$

$$Q_{200} = 5.00 + 0.46 + 1.49 = 6.95 \text{ milliwatts}$$

$$Q_{300} = 5.00 + 0.89 + 7.52 = 13.41 \text{ milliwatts}$$

These detector heat load figures emphasize the signicant importance of two factors: first, the detector substrate assembly must be kept as small as possible to minimize the radiant heat loading, and second, the advantages of obtaining a 200°K, or lower, outer-shell ambient for the solid refrigerator. Both of these factors contribute measurably to the reduction of the primary cryogen refrigeration capacity requirements.

Detector - refrigerator coupling requirements: It is desirable to maintain the detector temperature as close as is practical to the refrigerant temperature. There will be a small gradient along the copper conduction rod from the primary refrigerant container to the end of the rod. If an allowable gradient for the flexible thermal linkage between the conduction rod to the detector substrate assembly is set,

$$\Delta T = 0.25°K$$

then the required thermal resistance is defined as

$$R = \frac{\Delta T}{Q_{200}} = 31.5°K/\text{watt}$$

Thermal resistance can also be defined as a function of material properties:

$$R = \frac{L}{RA}$$

where: L = path length = 1.0 cm

A = cross-sectional area

R = thermal conductivity of copper = 12 watt/cm - °K,

and the required area of the linkage is:

$$A = \frac{L \ Q_{200}}{k(\Delta T)} = 0.0023 \text{ cm}^2$$

Wire diameter = 0.054 cm, which is equivalent to one #23 AWG wire or four #29 AWG wires.

With a linkage designed for 200°K shell temperature operation, the temperature gradient during 300°K operation is:

$$\Delta T = \frac{L \ Q_{300}}{kA} = 0.49°K$$

Mechanical design. -- Figure 94 illustrates schematically the arrangement of the six taut titanium-alloy suspension wires alternately inclined ±30° from a horizontal plane and spaced equally about the circumference of the detector substrate. The mechanical system, which is a good approximation to a simple concentrated mass spring case, has the following characteristic:

W = weight of detector substrate assembly = 0.50×10^{-3} lb

M = mass of assembly = $\frac{W}{g}$ = 1.3×10^{-6} lb-sec^2/in.

A = cross-sectional area of each wire = 3.14×10^{-6} in.^{2}

L = length of each lead = 1.5 inch

S = pre-tensioned wire stress = 0.8×10^5 lb/in.^{2} at 300°K

U.T.S. = 1.3×10^5 lb/in.^{2} at 300°K

= 2.2×10^5 lb/in.^{2} at 77°K

E.L. = 1.2×10^5 lb/in.^{2} at 300°K

= 2.0×10^5 lb/in.^{2} at 77°K

E = modulus of elasticity of titanium = 1.65×10^7 lb/in.^{2}

The vertical, and balanced forces for $N = 3$ wires are:
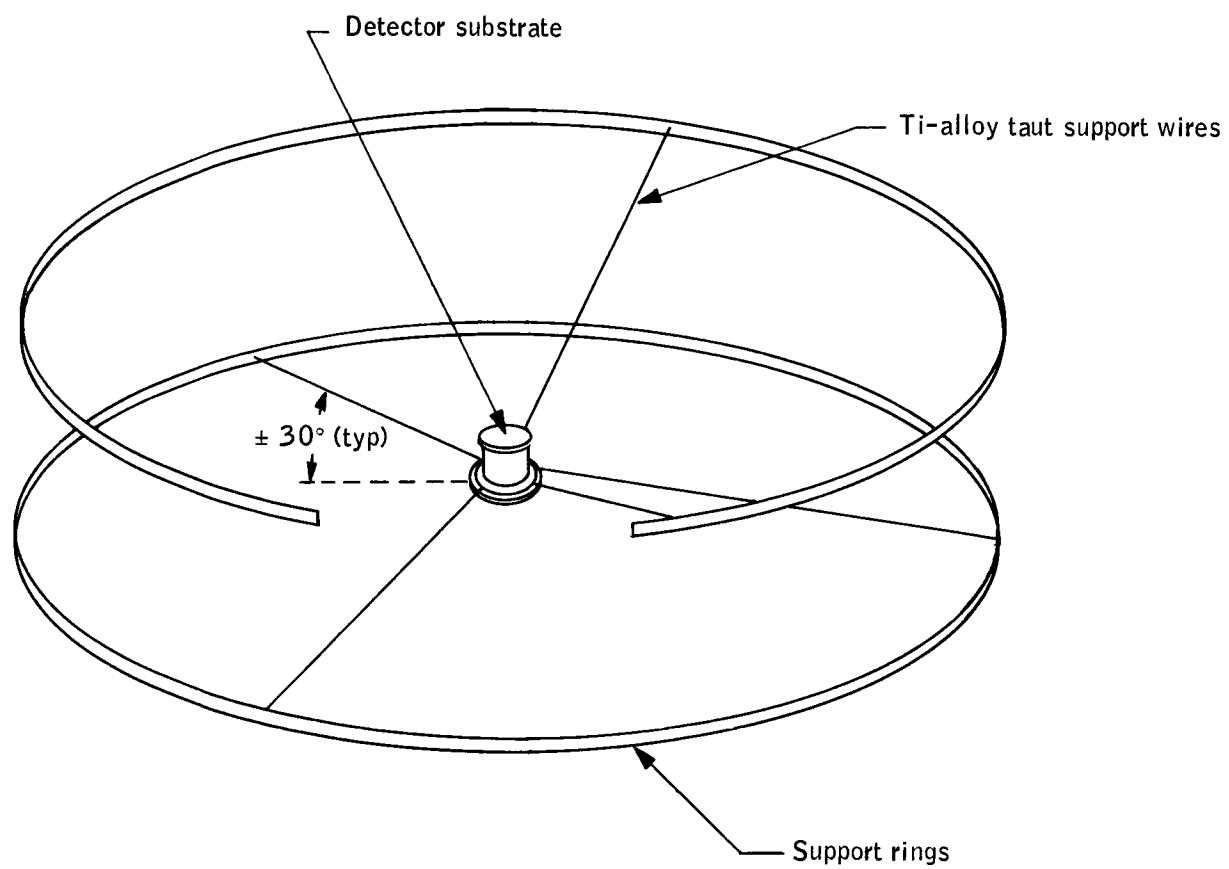
Figure 94. Detector Substrate Support Schematic

244

$$F_V = (\sin 30°) \text{ NSA}$$

$$F_V = 0.38 \text{ lb}$$

Vertical stiffness is a function of the effective spring constant:

$$K_V (\sin 30°) \frac{\text{NEA}}{\text{L}} = 52 \text{ lb/in.}$$

and the vertical resonant frequency is

$$f_V = \frac{\sqrt{2K/M}}{2\pi} = 1420 \text{ Hz}$$

For launch acceleration fields the vertical deflection of the detector substrate is

$$\delta_V = \frac{W_a a}{K}$$

where $a = 10$

$$\delta_V = 96 \times 10^{-6} \text{ in.}$$

In a similar fashion the lateral mechanical characteristics can be found:

$$F_L = \left[\cos 30° + 2 (\cos 60°) (\cos 30°) \right] \text{SA}$$

$$F_L = 2 (\cos 30°) \text{ SA} = 0.44 \text{ lb}$$

$$K_L = 2 (\cos 30°) \frac{\text{EA}}{\text{L}} = 60 \text{ lb/in.}$$

$$f_L = 1530 \text{ Hz}$$

For a lateral acceleration of 10 g's the deflection is

$$\delta_L = 83 \times 10^{-6} \text{ in.}$$

These launch induced mechanical motions, limited to 10 g accelerations in the case presented, will create an added stress level on the titanium-alloy wires. To determine this effect, a computation of the initial wire deflection δ_o, caused by the 0.8×10^5 psi initial stress is made:

$$\delta_o = \frac{SL}{E} = 7.3 \times 10^{-3} \text{ in.}$$

If a combined 10 g acceleration, both vertical and lateral, were to occur simultaneously, the increased wire deflection is

$$\Delta\delta = \frac{\delta_V}{\sin 30°} + \frac{\delta_L}{2\cos 30°} = 0.24 \times 10^{-3} \text{ in.}$$

The increased wire stress is therefore

$$\Delta S = \left(\frac{\Delta\delta}{\delta_o}\right) S = 2,630 \text{ lb/in.}^2$$

Arbitrary values of maximum acceleration have been chosen for these computations; it remains to be demonstrated that these values are reasonable. The detector support system could form a high "Q" resonant mount that may need structural damping applied if the titanium support wires do not exhibit sufficient non-linearity and/or damping characteristics. For the values shown, there certainly appears to be no undue displacements, low frequency resonances, or dangerous stress levels. Titanium-alloy wires stressed to

0.8×10^5 psi are safely rated even at 300°K.

One area not examined here, but which will have to be dealt with in a detailed design, are the variations in the taut support wire stresses as the detector mount is exercised through its several temperature environments. The alignment is initially made at room temperature, nominally 300°K; it will then be chilled during the formation of the solid cryogen refrigerant, and finally, the refrigerator outer shell will be cooled to 200°K in orbit. A taut-wire stress thermal compensation method may have to be employed into the design.

Proof of these detector support concepts will only come with a suitable program designed to model and evaluate the suspension system, both thermally and mechanically.

CALIBRATION REQUIREMENTS

Primary Calibration

A primary requirement of the radiometer is its ability to measure the horizon radiance with the maximum possible accuracy. Since the accuracy of measurement can be no greater than the accuracy of the primary calibration, the source and calibration method is extremely critical. The following conditions of calibration must be met to assure that this accuracy is achieved:

246

1)   The radiance of the source within the calibration apparatus in the 14-to 16-micron band must be known within one percent of its actual value, and its radiance must not vary in excess of 0.1 percent.

2)   The calibration source must appear to be at infinity so that it simulates the conditions of horizon measurement and no error is introduced by an uncertainty in the field of view of the radiometer.

3)   A means of attenuation of the source radiance must be provided so that the radiometer may be calibrated at radiance values equivalent to the radiance range of the horizon.

4)   The radiometer must be calibrated at a sufficient number of points to define completely the calibration curve of the instrument. The exact number of points should be determined empirically after the radiometer is constructed.

5)   A known zero reference for calibration must be provided so that the effect of thermally emitted radiation by the optical components of the radiometer may be eliminated.

In-Flight Calibration

Since the radiometer will be measuring the radiance of the earth's horizon over a one-year period, a means of in-flight calibration must be provided. This calibration will detect any changes which occur in the radiometer transfer function so that the basic calibration data may be adjusted. The following conditions must, however, be satisfied to assure an acceptable in-flight calibration system:

1)   The source must include a means of attenuation such that the radiant power in the 14-to 16-micron band which impinges on the detector surface equals the power which the detector would receive when measuring the horizon radiance.

2)   The source must have a sufficient number of radiant power levels to check the entire radiance range of the horizon. These attenuation levels are necessary for the detection of nonlinear variations of the system as shown in the Figure 95.

Typical sources of these variations are as follows:

    Figure 95 (a)   Detector responsivity
                    Optics transmission
                    Electronic amplifier gain
    Figure 95 (b)   Detector responsivity changes
                    Partial overloading of an electronic amplifier
    Figure 95 (c)   Electronics zero drift
                    Stray radiation
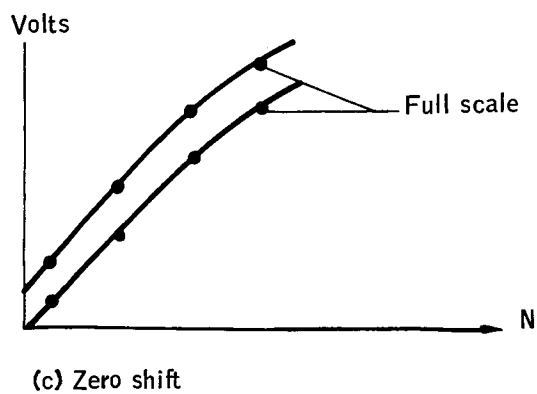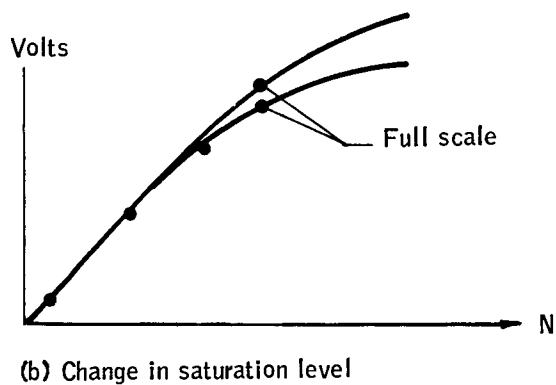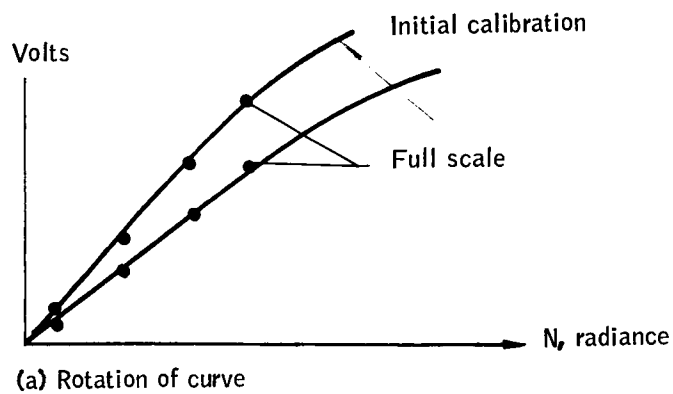
Figure 95. Types of Variations in the Radiometer Transfer Characteristics

3) The source must be situated within the system such that at least one radiant power level will traverse the entire radiometer system. This requirement will assure detection of any changes which occur in the optical system as well as changes in the more complex elements such as the detector and electronics.

4) The radiance of the source must be sufficiently stable over the one-year period to assure that calibration errors due to variations in the radiometer system do not exceed one percent.

5) The temperature of the calibration source must not impose an excessive heat dissipation requirement on the thermal design of the spacecraft.

6) A method of calibration at a zero level must be included so that the effect of thermally emitted radiations by the optical elements of the system may be eliminated.

PRIMARY CALIBRATION SYSTEM

Introduction

Two methods of calibration have been studied and analyzed. The first uses a diffuser at the focal point of a collimator, and its radiance is varied by the distance between it and the radiation source. The second method uses the blackbody source whose radiance is varied by adjusting its temperature. Both of these methods are an extended source at infinity calibration which simulates the actual horizon-measurement situation. The basic configuration of the calibration components for either method is shown in Figure 97.

Both methods are recommended for primary calibration to not only provide a method of confirmation but also to cross check the radiometer's spectral sensitivity. This is possible since the variable temperature source varies its spectral power distribution with radiance variation, whereas the spectral power distribution of the fixed temperature source will not change. Figure 96 shows the spectral power distribution of the variable temperature source at the minimum and maximum radiance temperature. The graph also shows the spectral power distribution of the fixed temperature source.

If the spectral response of the radiometer $S(\lambda)$ is an ideal rectangular function, the output of the detector will be equal for each source at an equal radiance. Since the spectral response function will have been measured, its relative output may be predicted by

$$R = \int_{0}^{\infty} P(\lambda)\, S(\lambda)\, d\lambda$$
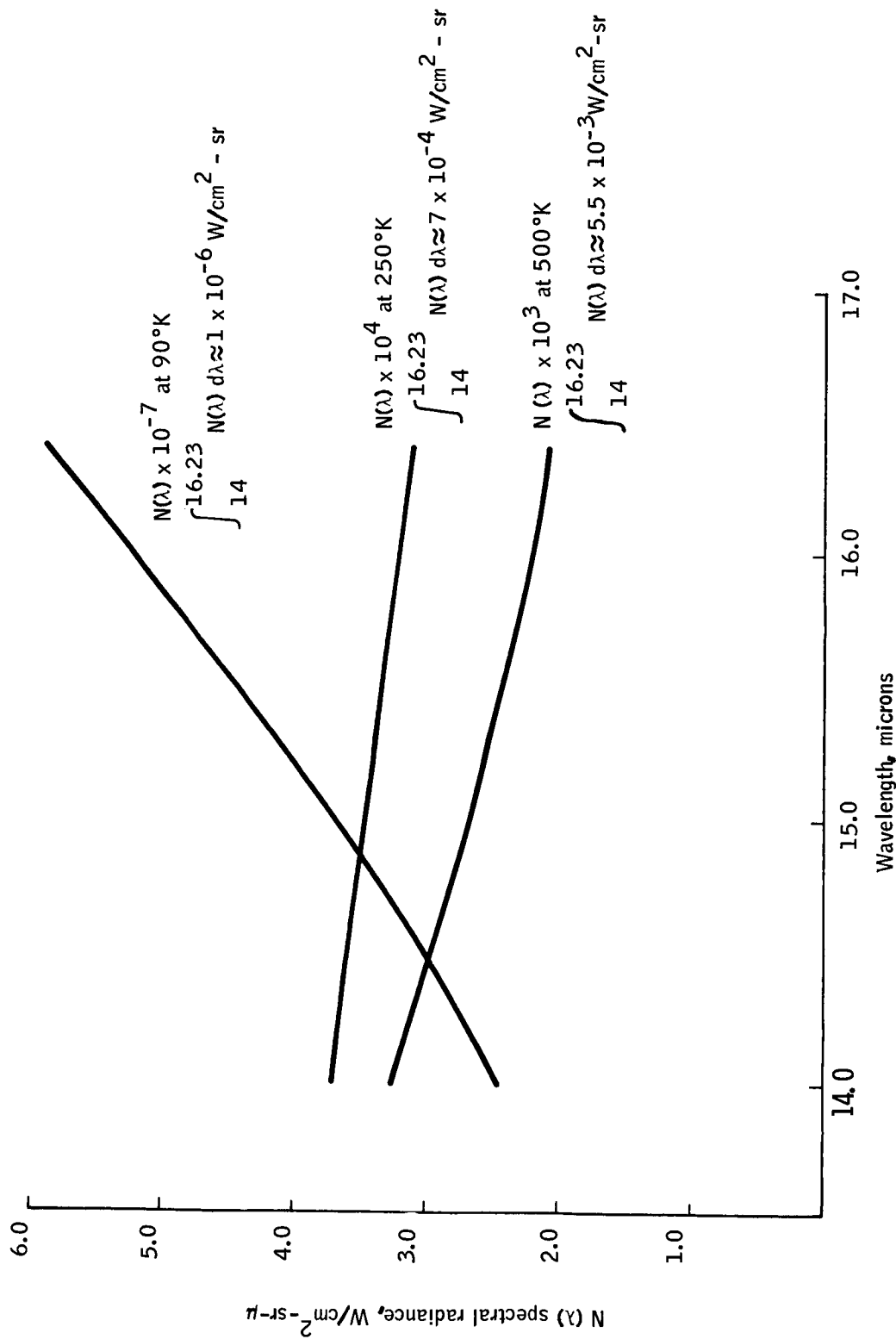
Figure 96. Spectral Radiance Distribution of Variable Temperature Source at Maximum and Minimum Temperatures and 500° Fixed Temperature Source

The figure contains the following labels:

$N(\lambda) \times 10^{-7}$ at 90°K
$\int_{14}^{16.23} N(\lambda)\, d\lambda \approx 1 \times 10^{-6}\ W/cm^2 - sr$

$N(\lambda) \times 10^4$ at 250°K
$\int_{14}^{16.23} N(\lambda)\, d\lambda \approx 7 \times 10^{-4}\ W/cm^2 - sr$

$N(\lambda) \times 10^3$ at 500°K
$\int_{14}^{16.23} N(\lambda)\, d\lambda \approx 5.5 \times 10^{-3}\ W/cm^2 - sr$

Wavelength, microns

$N(\lambda)$ spectral radiance, W/cm^2-sr-μ
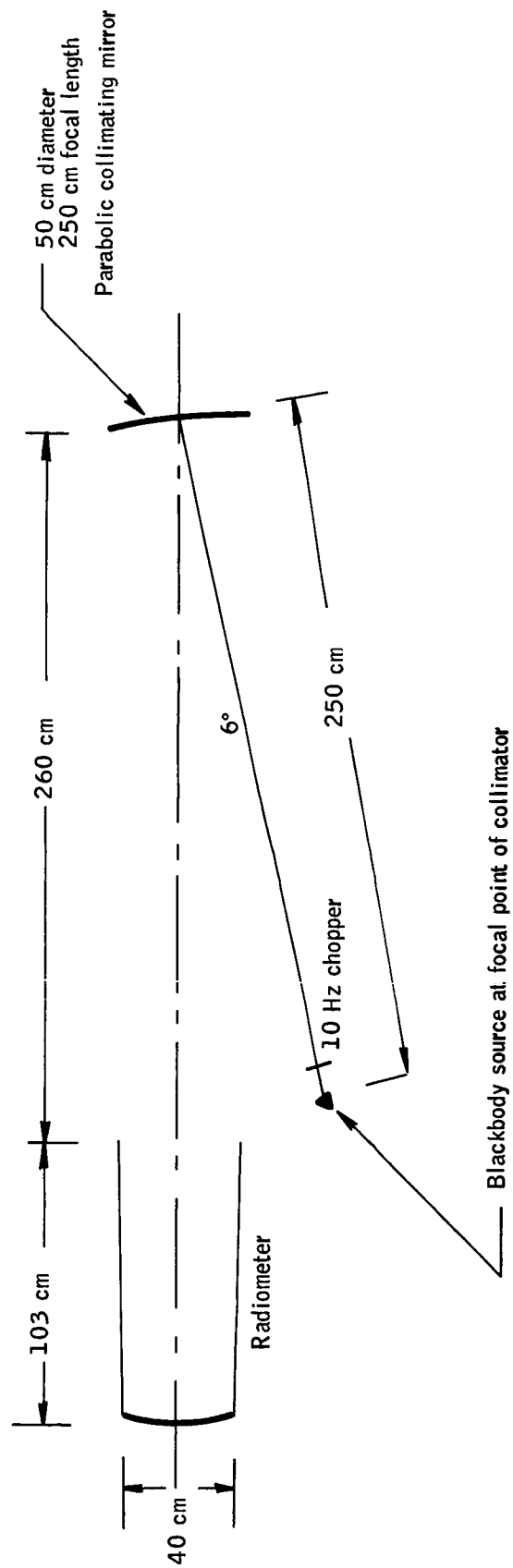
Figure 97. Configuration of Optical Components for Primary Calibration

50 cm diameter
250 cm focal length
Parabolic collimating mirror

260 cm

6°

250 cm

10 Hz chopper

Blackbody source at focal point of collimator

103 cm

40 cm

Radiometer

251

assuming $\int_0^\infty P(\lambda)\ S(\lambda)\ d\lambda$ is equal for each source.

The ratio of these predicted values for each type source to the actual value which is measured will indicate the error in the measurement of the spectral response function.

Fixed Temperature Source with the Diffuser Method

Apparatus. -- Figure 98 is a schematic diagram of the calibration equipment as it would be assembled with a fixed temperature source. All of the equipment is contained within a vacuum chamber within which is a liquid-nitrogen shroud. All of the calibration components are then radiatively cooled to approximately 80°K. The radiometer, itself, is insulated from the cold environment and heated to 200°K, its nominal operating temperature in the spacecraft. The field of view of the radiometer is entirely filled by the 50-centimeter diameter, f/5 parabolic collimator. This mirror is gold coated and has been stored in an inert nitrogen atmosphere to deter aging of the mirror surface. The collimator is used 6° off axis so that the radiometer and the source are separated by approximately 12°.

The diffuser is located at the focal point of the parabolic collimator. This diffuser could be one of three materials;

1. An infrared transmitting material such as germanium whose surface has been made diffuse.

2. An opaque plate which contains small holes of random size and spacing to achieve diffusion by diffraction.

3. A fine, mesh wire screen which diffuses by a combination of diffraction and reflection.

The optimum material will be chosen by laboratory testing such as gonioradiometric measurements. Figure 99 shows the diffuser, chopper, and radiation source in an enlarged scale. The angles indicated at the right show the longest dimension of the field of view of the radiometer and the overall angular size of the diffuser. It may be seen that the diffuser will be made three times larger than the field of view to eliminate the errors that could be caused by diffraction or aberration of the collimator. The source-to-diffuser distance, which is shown, is that which is used at the highest radiance level, and the angle subtended by the diffuser, which is shown, is used for the calculation of the worst case $\cos^4$ error. The mirror chopper which is directly in front of the blackbody source will be operated at approximately 10 cycles/second which will eliminate most of the stray-light errors. The source itself will be discussed in greater detail in the following paragraphs. Since the source will be operating at 500°K, it will be contained within a well-insulated container so that the temperature of other components will not be effected.
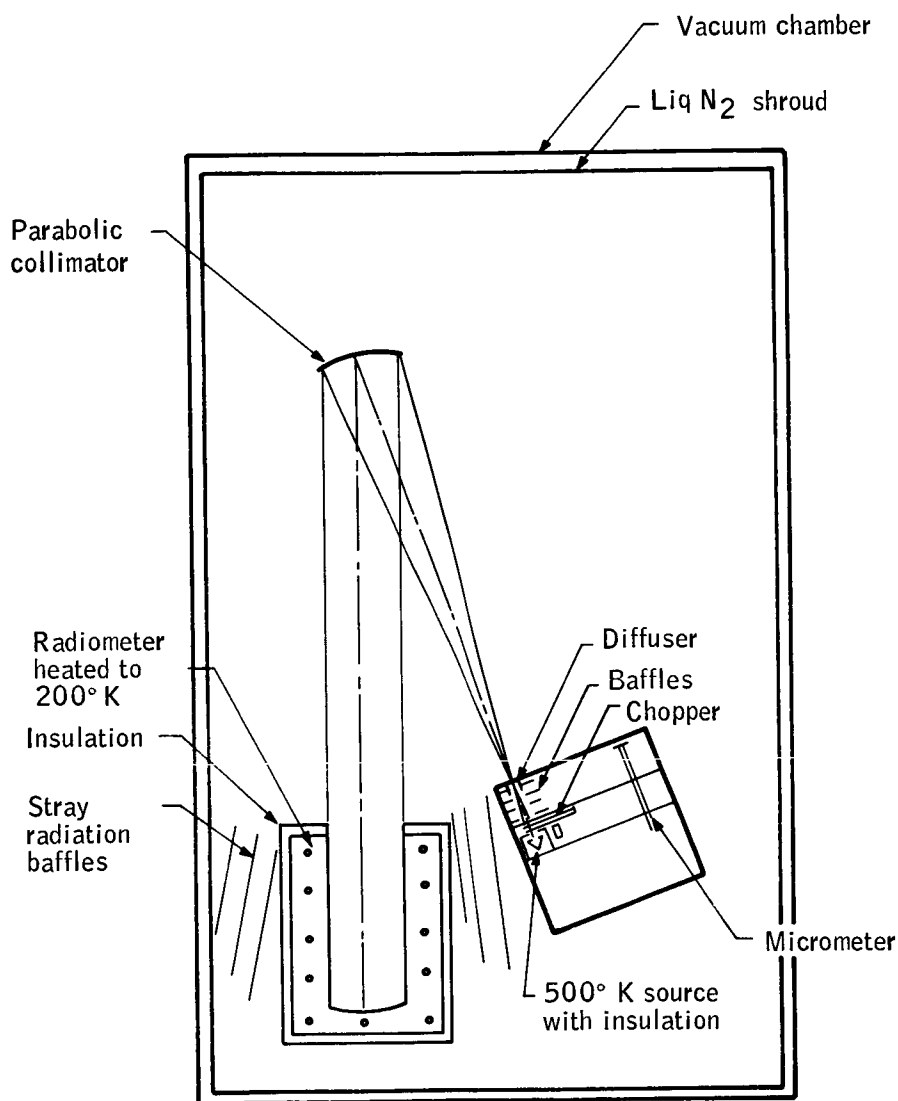
Figure 98. Apparatus for Primary Calibration Using Fixed
Temperature Source with a Diffuser
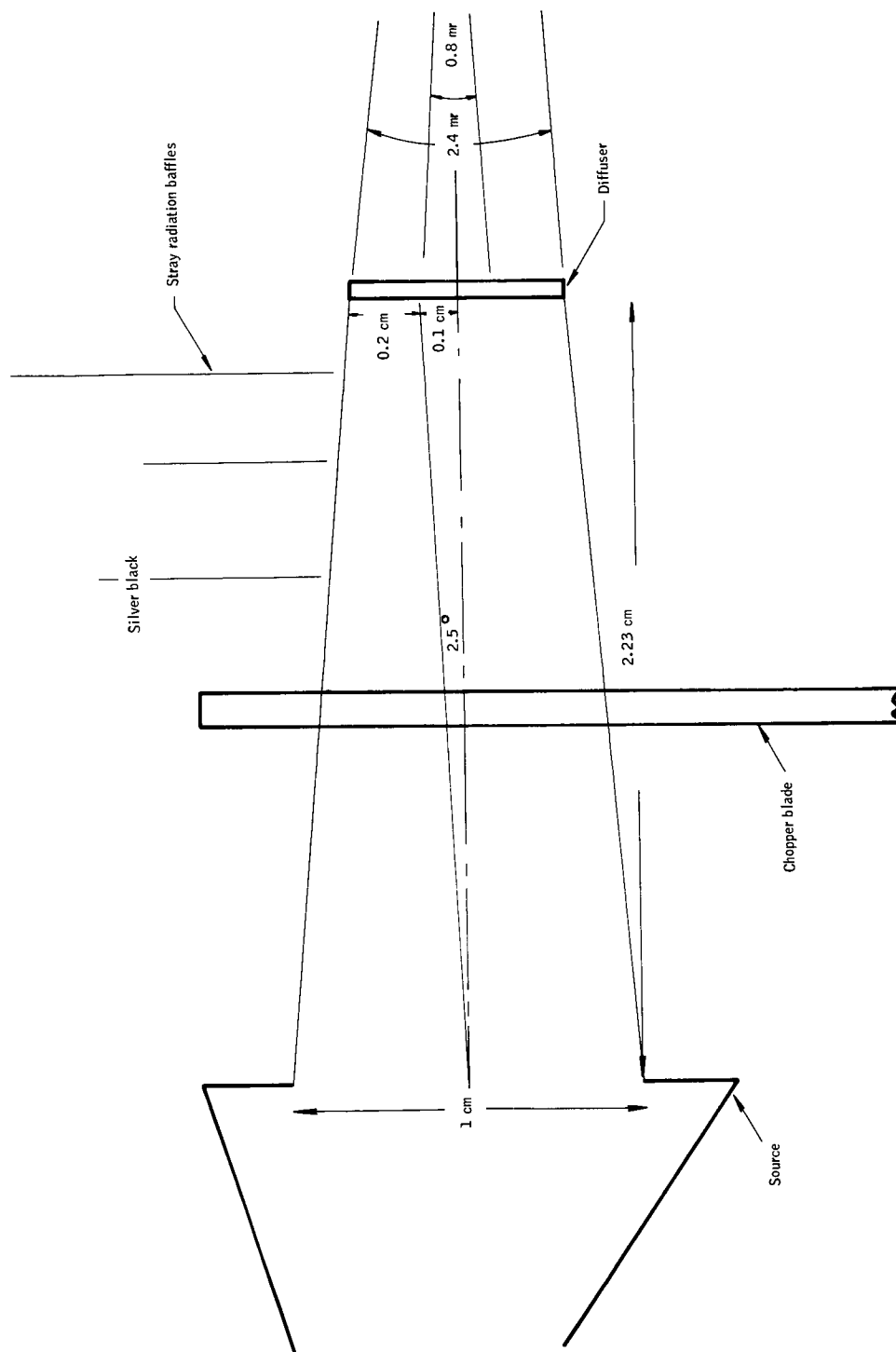
Figure 99. Source, Diffuser, and Chopper - 10x Scale

The micrometer shown in Figure 98 will measure the source-to-diffuser distance. If sufficient accuracy cannot be achieved with a micrometer or calibrated screw, it could easily be replaced with a Michelson interferometer with a detector and counter. This apparatus would be capable of measuring the source-to-diffuser distance to a half wavelength of the coherent source (laser) used, nominally 0.5μ.

Fixed temperature source. -- The 500°K, fixed temperature source, which is shown in Figure 100, is one which is presently under development at the National Bureau of Standards (NBS) as a primary standard of black-body radiation. The source is a cylinder which is made of a high-purity graphite. In the center of the cylinder is the blackbody cavity which has a one cm. aperture and contains stops to limit the radiation to a 20-degree cone. The chamber which is between the blackbody cavity and the outer shell is filled with freezing tin which will, of course, maintain the temperature of the blackbody source during the freezing process.

The source is filled with liquid tin from a ceramic crucible which is wound with a nichrome-wire heating element to maintain the molten state. The crucible is contained in an argon atmosphere, and the blackbody chamber is purged with argon before filling. This assures that there will be no oxidation of the tin which would alter the freezing temperature.

When the chamber is completely filled with liquid tin, the cooling process is monitored by a thermalcouple which is inserted in the chamber and indicates when the temperature remains stable at the freezing point. With no additional heat input the tin will require approximately one hour to freeze completely; however, a nichrome-wire heating element may be wound around the outer shell of the source to maintain the freezing point for any time desired.

Members of the National Bureau of Standards who are engaged in development of this source have stated that the purity of the tin and previous thermophysical performance indicate that the source temperature will be accurate within 0.001°K as determined on the International Practical Temperature Scale and within 0.01°K on the thermodynamic scale.

The preliminary dimensions of the cavity have been chosen using the Gouffe' method of calculating the emissivity of the cavity.

$$\epsilon_0 = \epsilon_0^1 \ (1 + k)$$

$$\epsilon_0^1 = \frac{\epsilon}{\epsilon \ [1 - (s/S)] + (s/S)}$$

$$k = (1 - \epsilon) \ [(s/S - (s/S_0)]$$

1.00-mm or 0.5-mm wall

1.4mm
diam hole

1200 g   Sn

Cavity brace
graphite
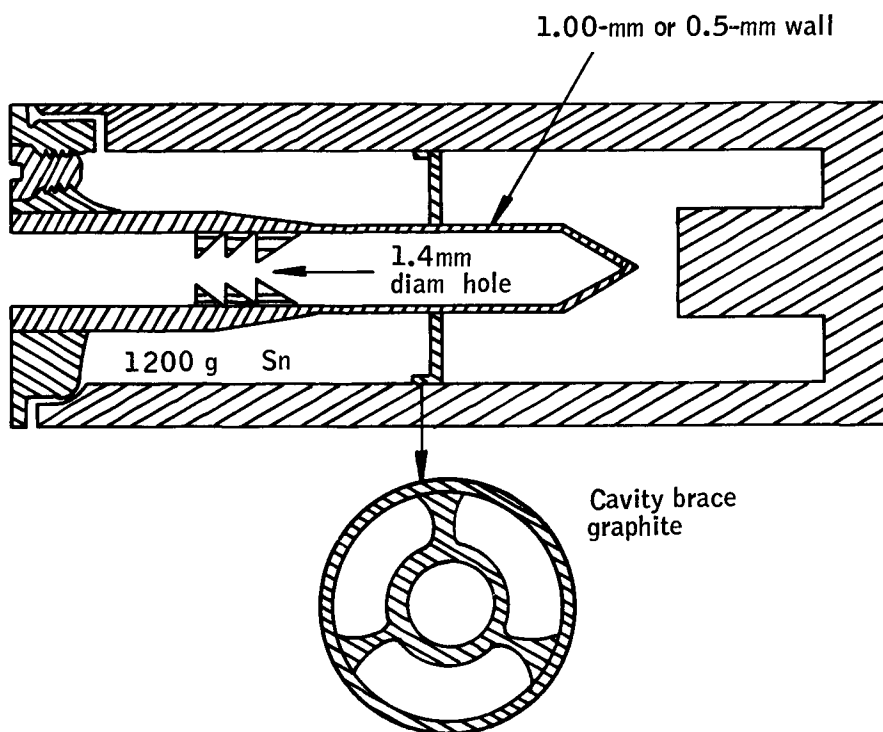
Figure 100.   NBS Freezing Tin Blackbody Source

where:

    ϵ = the emissivity of the material forming the body surface

    s = area of the aperture

    S = area of the interior surface

    S_o = the surface of sphere of the same depth of the cavity in the direction normal to the aperture

Assuming that the surface emissivity of graphite (λ = 14 to 16μ) is 0.38 and that a 1.0-cm aperture is required, an iterative solution to this equation was used to find the minimum source dimension which would give a cavity emissivity of no less than 0.999.

The resulting cavity dimensions for the source are shown in Figure 101; solution of the Gouffé equation for this cavity gives ϵ_o = 0.9991.

The final design of this source will, of course, be completed in a much more rigorous manner. The cavity emissivity can be found by the methods of De Vos and Sparrow as well as Gouffé to confirm these results. Also, other geometric designs can be investigated to achieve a high emissivity with a smaller cavity.

The second fixed temperature source, whose use is explained in the section on radiance calibration procedure, is similar to the source above, except that the freezing point of mercury is used. A diagram of this source is shown in Figure 102. The blackbody cavity is made alumina (Al_2O_3)

which has been painted with a high-emissivity black paint on the inside. The cavity is surrounded by a glass cell which contains one ppm maximum impurity, freezing mercury. A silicon-oil thermal buffer surrounds the glass cell. The thermal guard shown is wound with the nichrome-ribbon heater which maintains the mercury at its freezing point. Surface temperature sensors are placed on the guard and are used to control the temperature by a closed-looped control system. The outer liquid-nitrogen shroud insulates this source from the other components and cools the mercury to approach the freezing point.

Preliminary dimensions of this source are shown in Figure 103. The Gouffé equation which has been discussed above was used to determine these dimensions. It was assumed that the emissivity of the epoxy black paint on the cavity is 0.9 (λ = 14 to 16μ) since such paints are presently in existance and have been tested at cryogenic temperatures. The aperture size of 0.6 cm was chosen since the radiometer is viewing the source directly, and 0.6 cm is the diameter of the diffuser with the freezing-tin source - diffuser method as is shown in Figure 99. These values give a cavity emissivity of ϵ_0 = 0.99996.

If, however, these high emissivity paints cannot be used, a cavity emissivity of 0.9993 may be achieved with the following source characteristics:

ϵ = 0.38
ϵ_o = 0.9991
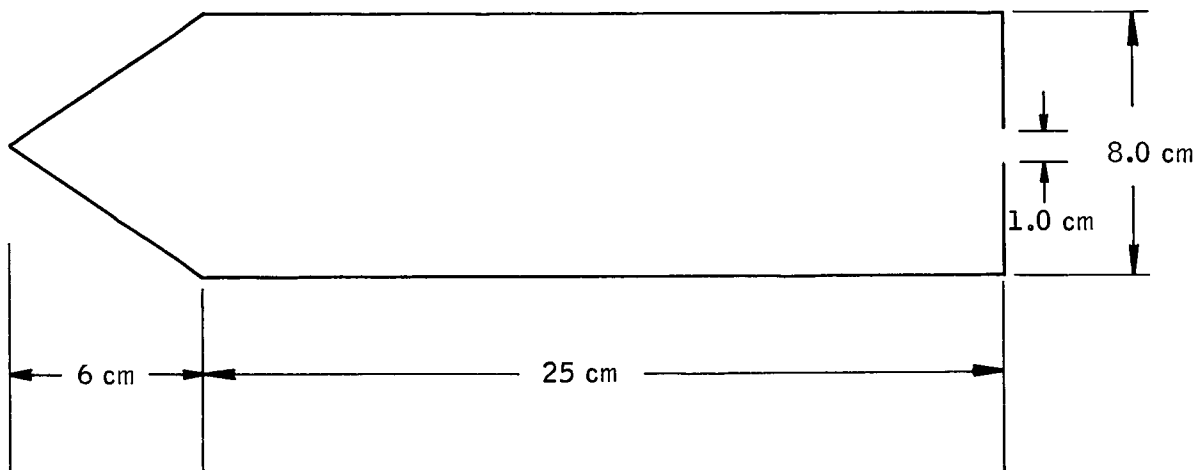
Figure 101.   Freezing Tin Blackbody Cavity Dimensions as
Derived by Gouffe' Method

Blackbody cavity

AL_2O_3 shell

Glass cell filled with Hg

Silicon oil buffer

Thermal guard wound with heater ribbon

Liq N_2 container
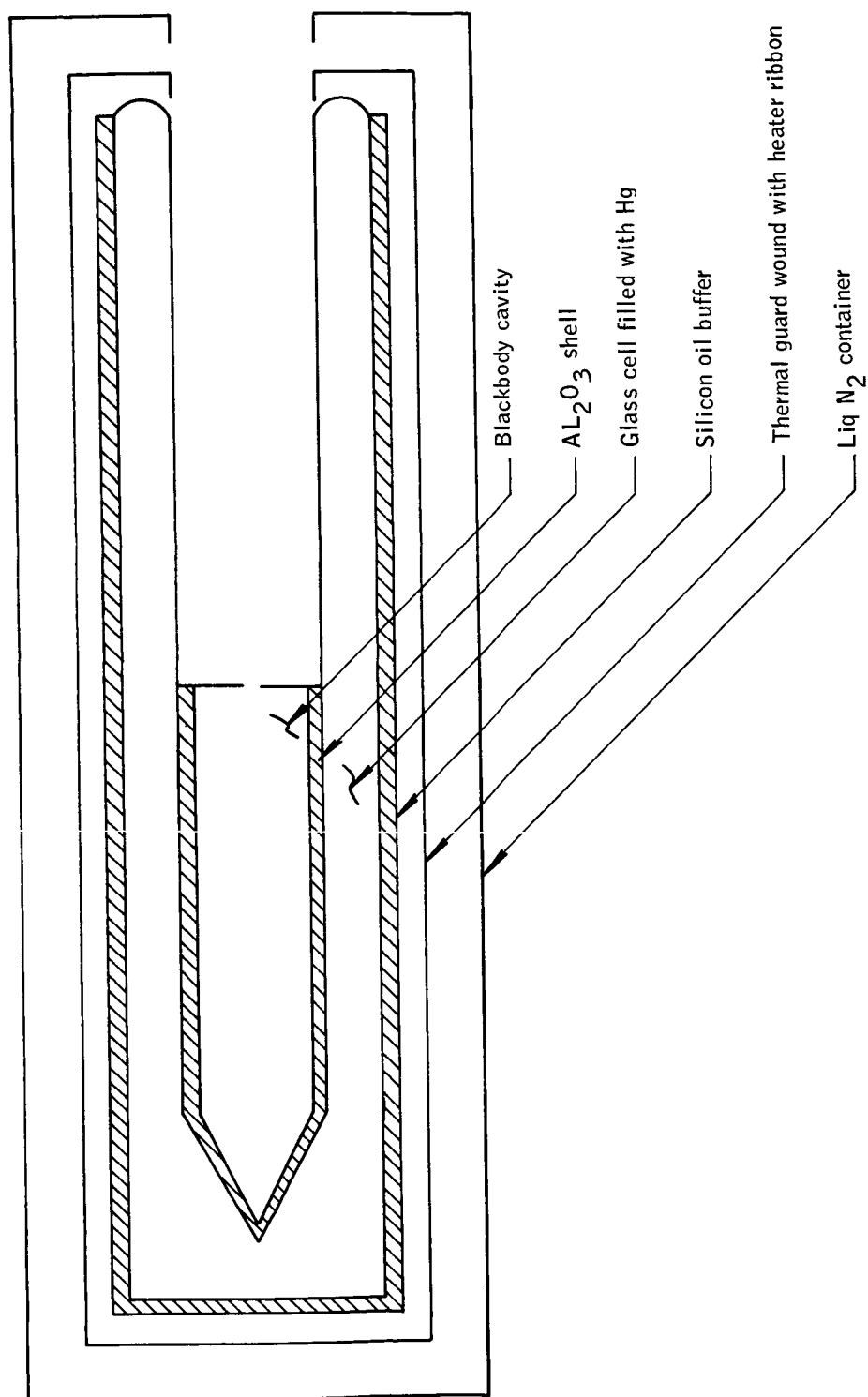
Figure 102. Mercury Freezing Point Fixed Temperature Source

259

ε = 0.9
ε₀ = 0.99996

4 cm

0.6

15 cm

4 cm
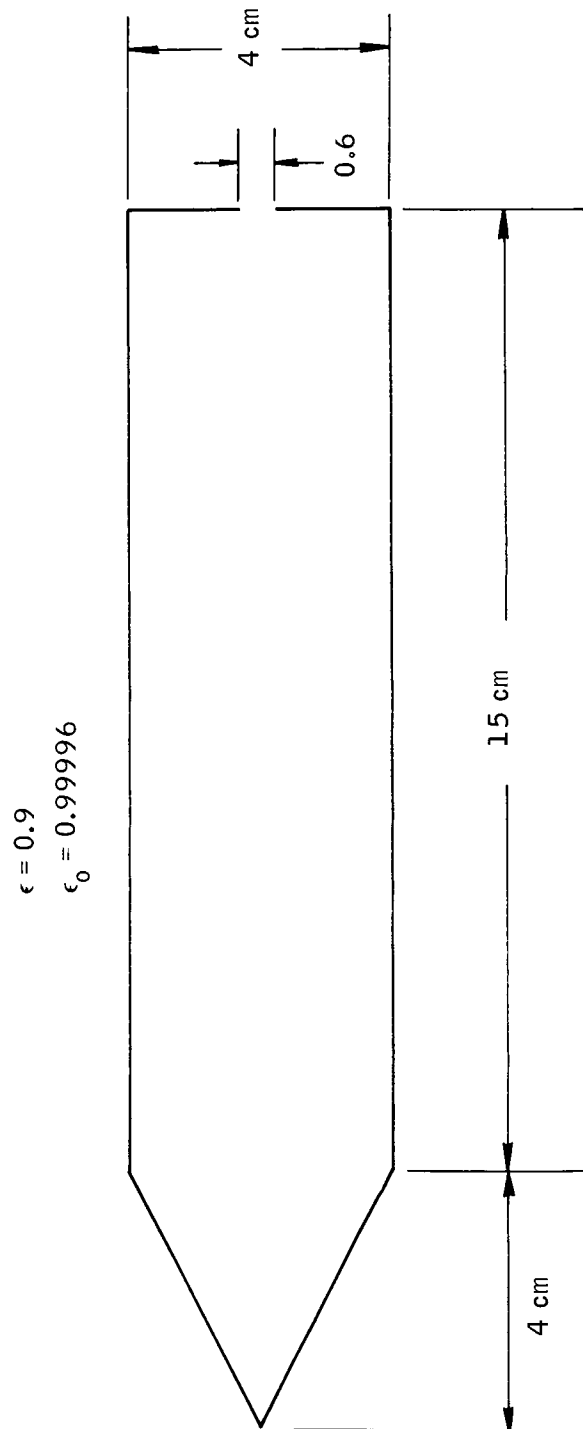
Figure 103.   Freezing Mercury Blackbody Cavity Dimensions as
Derived by Gouffe' Method, $\epsilon = 0.9$, $\epsilon_O = 0.99996$

this collimator. Radiation is transmitted by a nonselective beam splitter. This beam splitter will be fabricated from smaller half-silvered germanium mirrors which are cemented together to give the required full aperture size. Direction of radiation is reversed 180° by the flat mirror, reflected by the beam splitter, and focused onto the detector. Effective area of the detector will be increased by housing it within an integrating chamber. The spectral filter on the window of the chamber will be similar to that of the radiometer and will transmit only that radiation which is within the 14-to 16-μ band. An exact spectral match between this filter and the one in the radiometer is not necessary since all of the components are gold-coated elements whose reflectance is very insensitive to small spectral shifts.

Detector output from this measurement represents the 100 percent level in the reflectance tests. The flat mirror is now replaced by the collimator which is to be measured. The collimator is rotated off axis the same amount as will be used in the actual calibration test, nominally 6 degrees. The flat mirror is placed at the focal point of the collimator so that an autocollimation system results. Radiation is now focused by the test collimator onto the flat mirror which reflects the radiation back onto the collimator; radiation is then reflected by the beamsplitter and focused onto the detector. The reflectance of the collimator may now be calculated as follows:

$$\rho = \frac{\sqrt{V_1}}{V_o}$$

where V_o is the detector output with the test collimator not in the system and V_1 is the detector output when the test collimator is used.

The principal of this reflectance measurement is that all of the radiation which is collimated by the first collimating mirror with the exception of reflectance or transmittance losses is focused onto the detector. Therefore, all of the components of this system must be larger than the "beam" of the radiation. To assure that this is the case two initial alignment tests may be made:

1. After the components are aligned within the chamber, a visible light test may be made. In this test the freezing-tin source is replaced by a visible light source of the same size, and the beam splitter is replaced by a visible-light transmitting beam splitter of approximately the same optical path. Each of the elements of the system may then be visually inspected to see that beam diameter is smaller than the element.

2. After replacing the freezing-tin source and the germanium beam-splitter, the vacuum chamber is evacuated. With the components arranged as in Figure 100, the output of the detector is monitored while the source is moved toward the collimator. As the source approaches the collimator, the angle of divergence of the radiation will increase; however, there should be very little or no change in the detector output if all the components are indeed larger than the radiation beam. Eventually, of course, the output

261

material emissivity = 0.38

length of cylinder   = 20 cm

length of cone   =   5 cm

diameter of cylinder =   5 cm

diameter of aperture = 0.6 cm

As with the freezing-tin source, these emissivity values will be confirmed by the solution of the other two methods of emissivity calculation.

   Calibration procedure. -- Several preliminary tests will be necessary prior to calibration of the radiometer. Among these are the following:

1.   The cavity of the blackbody will be scanned with a test radiometer having a very small field of view. This will assure that temperature or emissivity gradiants do not exist within the source.

2.   A gonioradiometric measurement of both the blackbody source and the diffuser will be made. This will be accomplished by rotating the source or diffuser while monitoring its relative radiance with the test radiometer. This test will assure that the blackbody and diffuser are Lambert radiators over the necessary range of angles. Figure 99 demonstrates that the blackbody source should be a Lambert radiator over ±2.5° and that the diffuser should be Lambertian over the angle subtended by the collimator or about 10°.

3.   The blackbody radiation source shown in Figure 98 should be cooled well below the equivalent noise level of the radiometer (liquid He_2) and the measured zero level of the radiometer. This test will determine if the stray radiation which is modulated by the source chopper is below the noise level of the radiometer.

4.   The reflectance of the parabolic collimator shown in Figure 98 will be measured. This if, of course, necessary since the radiance of the diffuser as it is seen by the radiometer is equal to the produce of the inherent radiance of the diffuser and the reflectance of the collimator.

   Measurement of the collimator reflectance: Figure 104 is a schematic diagram of the apparatus for measuring the collimator reflectance. These components are assembled in a vacuum chamber which is cooled with a liquid-nitrogen shroud in the same way as radiometer calibration. The freezing-tin, chopped source is placed at the focal point of a collimating mirror. Assuming the dimensions shown in Figure 104 and first-order optical theory, the radiation is diverging at a ±1 milliradian angle from

262
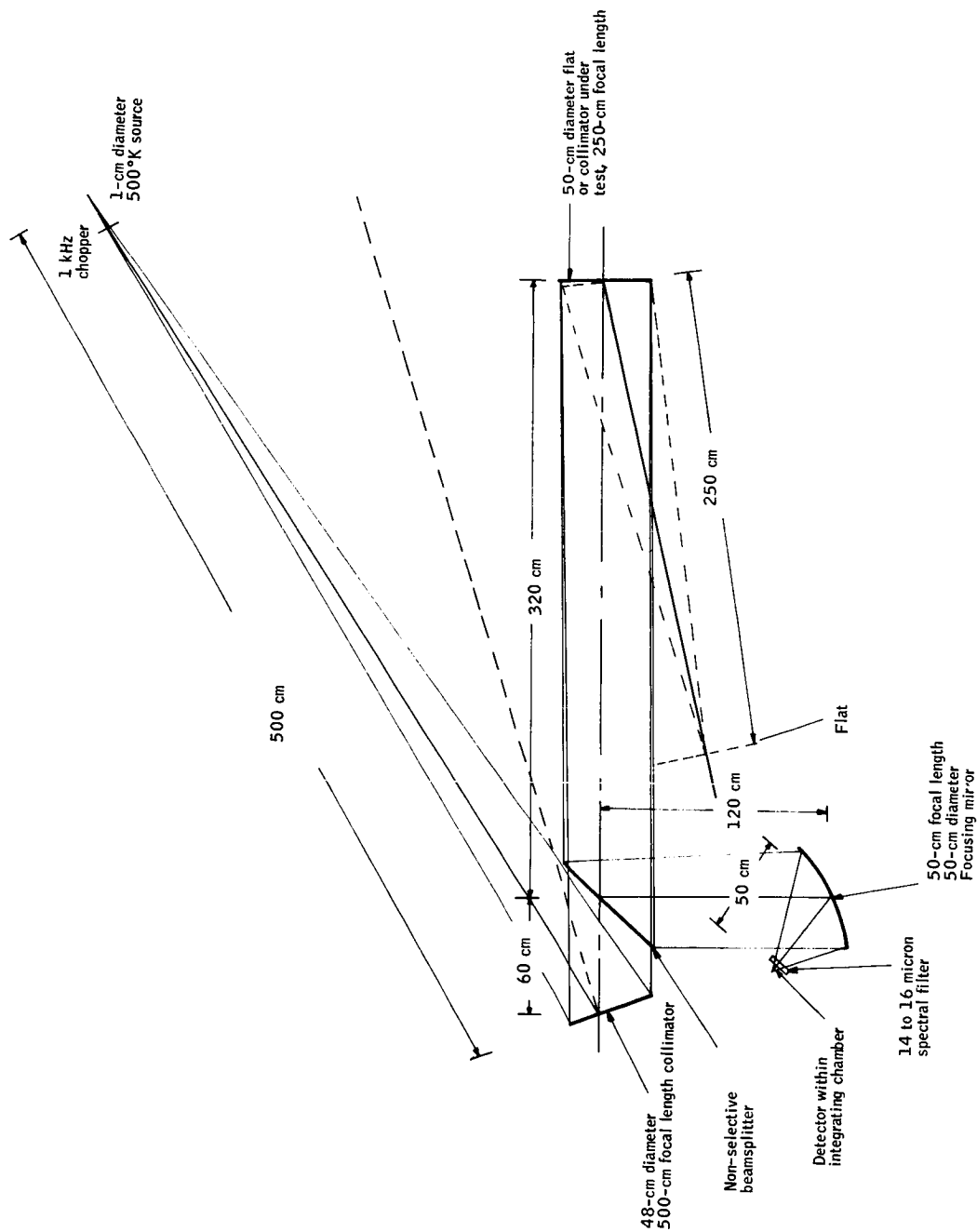
Figure 104. Layout for Collimator Reflectivity Measurement

1 kHz chopper

1-cm diameter 500°K source

500 cm

60 cm

320 cm

50 cm

120 cm

250 cm

50-cm diameter flat or collimator under test, 250-cm focal length

Flat

50-cm focal length 50-cm diameter Focusing mirror

14 to 16 micron spectral filter

Detector within integrating chamber

Non-selective beamsplitter

48-cm diameter 500-cm focal length collimator

will start to drop rapidly when the beam diameter exceeds the diameter of the components. After this test is completed the source is returned to the focal point of the collimator.

Measurement of the modulated stray radiation: A source of bias error can occur from stray radiation or radiation emitted from the various components of the system which is modulated by the source chopper. The calculation shown in the error analysis indicates that this radiation is less than the noise level of the system; however, this will have to be proven by measurement. The apparatus will be assembled in the vacuum chamber as shown in Figure 98 except that a liquid-helium shroud is used to cool the blackbody cavity. The output of the radiometer is recorded as the source is moved through its full excursion. The radiometer should indicate no modulated radiation since it should be less than the noise level of the instrument. If a modulated signal is seen, the baffles within the chamber will be rearranged and the 200°K temperature of the components verified to reduce this source of error.

Radiance calibration: After all of the preliminary tests have been completed the radiance calibration procedures are initiated. The components are aligned within the vacuum chamber as is shown in Figure 98 except that the mercury freezing-point source is placed directly at the focal point of the collimator instead of the diffuser. The thermalcouples, which are placed throughout the chambers and on all components, are measured as they are throughout the entire calibration process. When the mercury source thermalcouple indicates that the mercury has started to freeze, the radiometer measurement of the source is made. The radiance of this source is, of course, well known from its freezing-point temperature and the emissivity of the blackbody cavity. Figure 105 shows that the radiance of this source falls within the radiance range at which the radiometer is to be calibrated. Having calibrated this single point, the mercury source is replaced by the diffuser and the tin freezing-point source.

After this source has started its freezing process as is indicated by the source thermalcouple, the radiometer measurement of the diffuser is started. The distance between the source and the diffuser is adjusted until the radiometer output equals that which was obtained when measuring the mercury source. When this equality is achieved, the radiance of the diffuser will equal that of the mercury source. Figure 105 indicates that the radiance of the freezing mercury source is approximately 5.5×10^{-4} watts/cm^2-sr.

Figure 106 shows the source-to-diffuser distance required to obtain the radiance range of calibration. When a diffuser is approximately 2.8 cm from the source, its radiance is equal to that of the mercury source. After the diffuser has been adjusted so that its radiance is equal to that of the mercury source, the exact source-to-diffuser distance is measured with the micrometer shown in Figure 98.

The entire radiance response function of the radiometer may now be measured by changing the distance from the source to the diffuser, calculating the radiance of the diffuser by the inverse square law, and measuring the radiomenter output. Figure 99 shows that the freezing-tin blackbody is an extended source so that the point-source, inverse square law cannot be applied in the

264
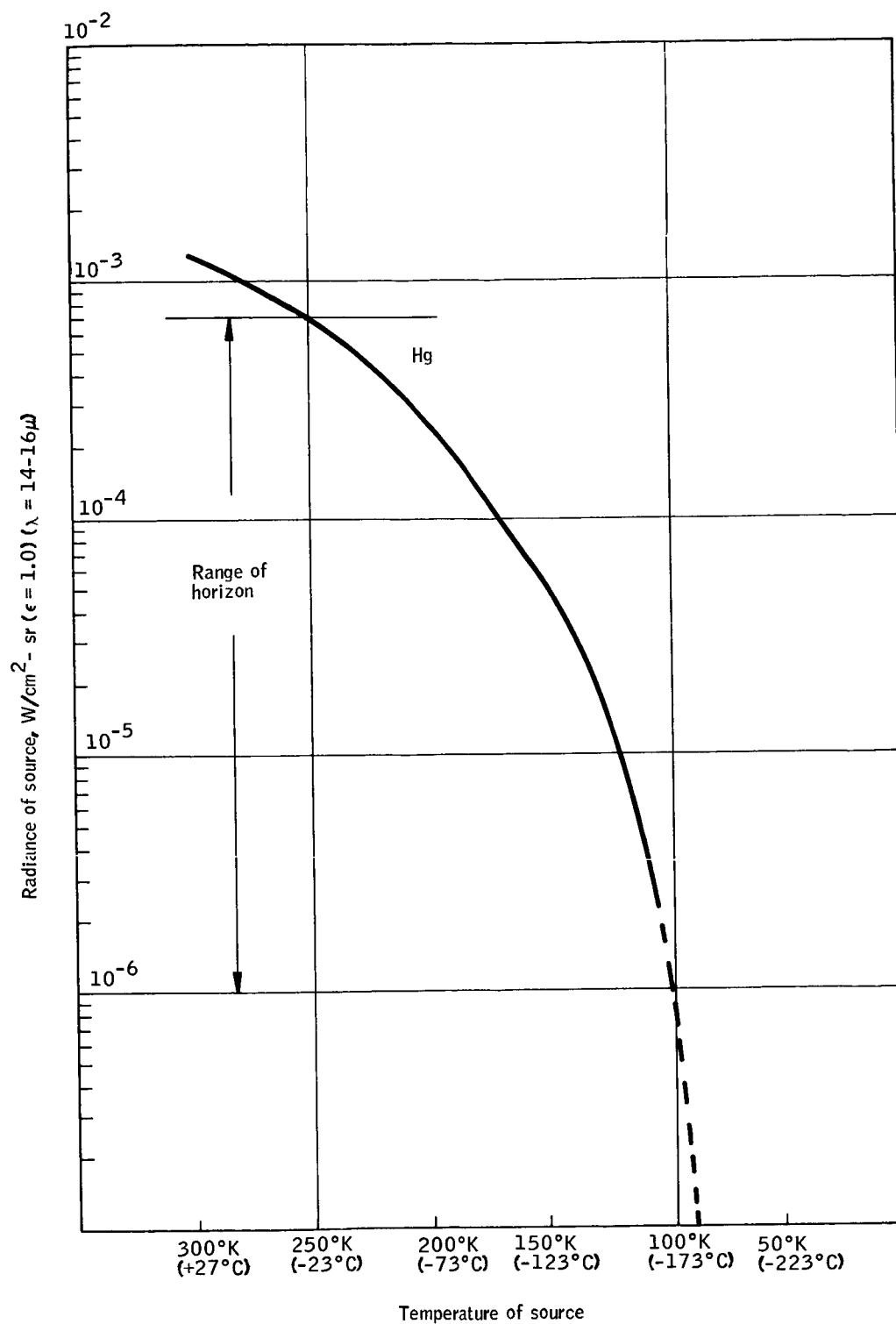
Figure 105. Radiance of Blackbodies, λ = 14 to 16.28μ, as a Function of Temperature
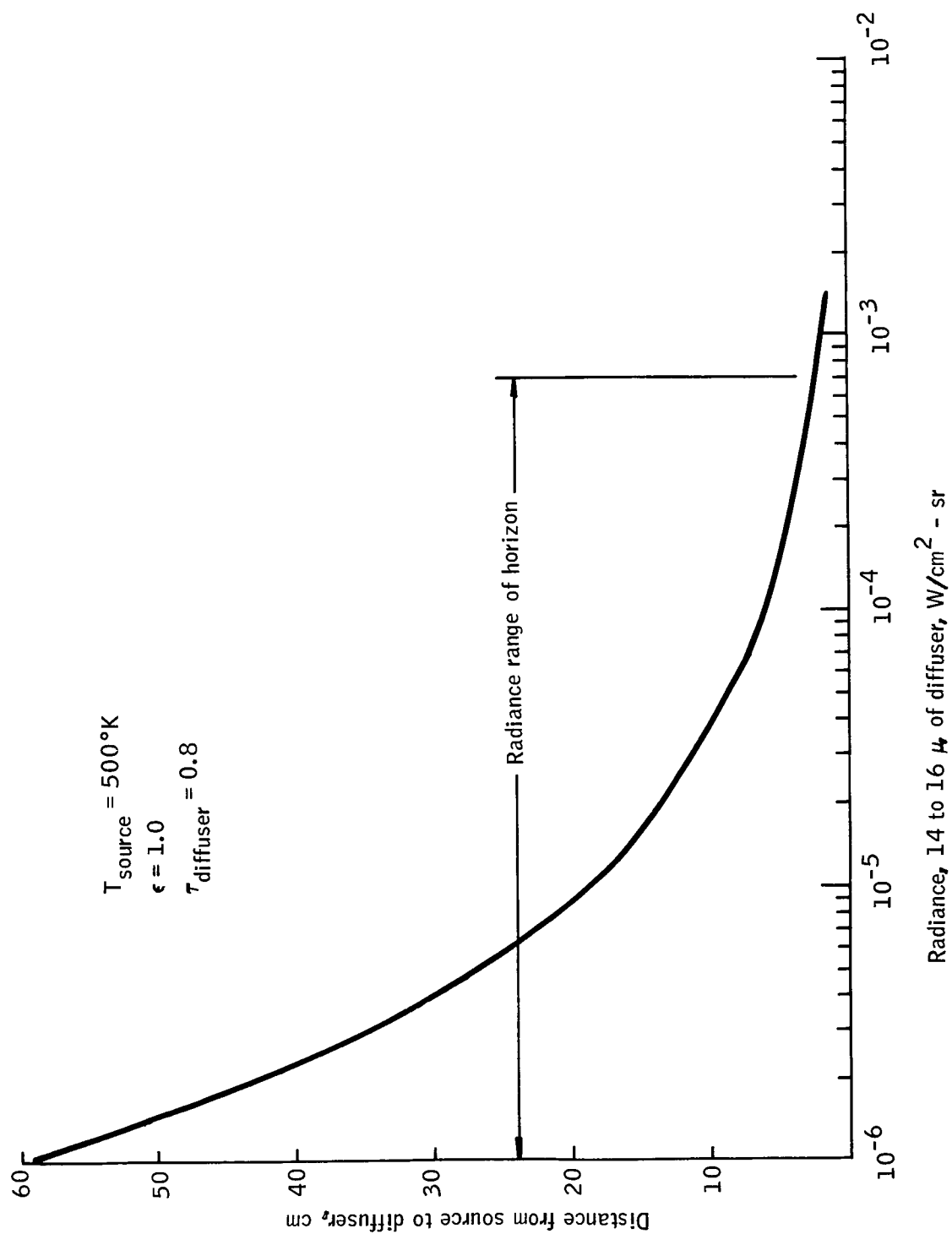
Figure 106. Source to Diffuser Distance Required to Obtain Radiance Levels

$T_{source} = 500°K$

$\epsilon = 1.0$

$\tau_{diffuser} = 0.8$

Distance from source to diffuser, cm

Radiance, 14 to 16 μ of diffuser, W/cm^2 - sr

Radiance range of horizon

usual way. The radiance of the diffuser is a function of the irradiance from the blackbody and the geometric characteristics of the diffuser. Since the latter remains constant throughout the calibration, an expression for the irradiance in terms of the source-to-diffuser difference must be derived. Figure 107 represents the circular blackbody source at some distance x from a small area of the diffuser dσ. If the source is divided into sufficiently small circular zones of radius r and width dr, the irradiance at dσ can be calculated with the inverse square law. Thus

$$dH = \frac{dJ}{X^2 \sec^2 \theta} \cos \theta$$

where dJ is the radiant intensity (w/sr) of the elementry zone in the direction of dσ.

The area dS of the elementry zone is $2\pi r \, dr$, and its effective area as seen from dσ is $2\pi r \cos \theta \, dr$. The irradiance produced by this zone of radiance N at dσ is then

$$dH = \frac{N 2\pi r \cos^2 \theta}{X^2 \sec^2 \theta} \, dr$$

since $r = x \tan \theta$ and $dr = x \sec^2 s\theta \, d\theta$, the irradiance from this zone may be rewritten as

$$dH = 2\pi N \sin \theta \cos \theta \, / \, d\theta$$

Integrating this expression gives the well-known equation for the irradiance from an extended source

$$H = \int_0^\theta 2\pi N \sin \theta \cos \theta / \, d\theta$$

$$H = \pi N \sin^2 \theta \tag{47}$$

Applying equation (47) to the calibration system which has been described gives

$$N = \frac{(N_o)(r^2 + x_o{}^2)}{r^2 + x^2}$$
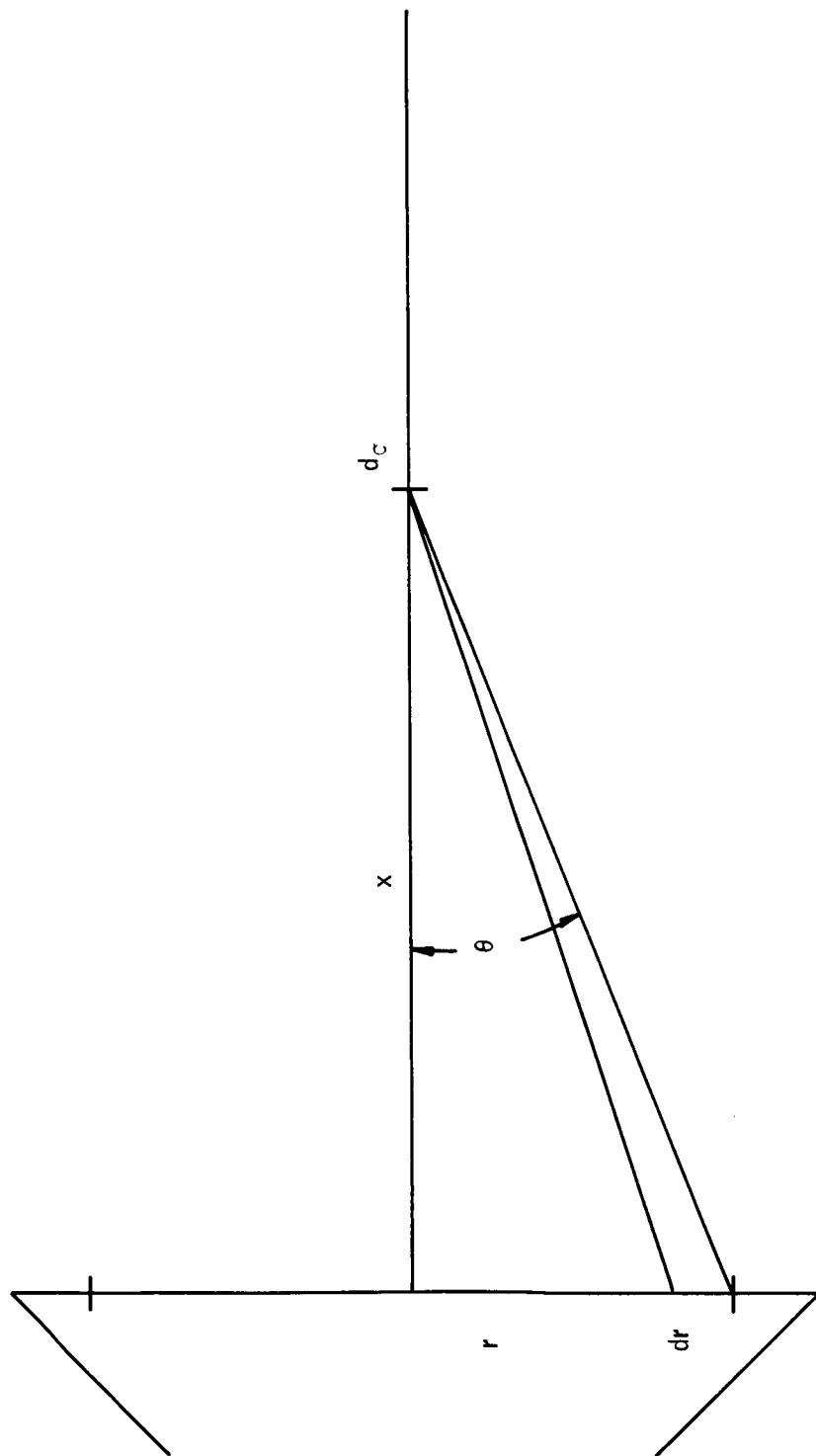
Figure 107. Diagram for Calculating the Irradiance at the Diffuser
from the Extended Blackbody Source

268

where:

N_o = radiance of mercury source

= radiance of the diffuser when the radiometer output was matched.

r = radius of the freezing-tin source aperture.

x_o = source-to-diffuser distance when the radiometer output match was obtained.

x = source-to-diffuser distance at any position.

Adjustable Temperature Source Method

The second calibration method which is recommended as part of the primary calibration procedure uses an adjustable temperature source to achieve the required radiance range. Figure 108 is a schematic diagram of the calibration apparatus as it would be assembled in the vacuum chamber. This apparatus is the same as is used in the diffuser method except that the variable temperature source replaces the diffuser - freezing-tin source.

Description of the source. -- Figure 109 is a schematic diagram of the adjustable temperature source. The blackbody cavity is cut into a solid copper or aluminim block. Cavity temperature is a function of heat balance created by heat transfer to the liquid nitrogen cold shield and the ribbon heater which is wound around the metal block. Surface temperature sensors are also attached to the surface of the metal block. These are connected to a closed-loop temperature-control system so that the temperature of the source may be held constant at any value during the calibration procedures. Radiance of the blackbody cavity is calculated from the source temperature which is measured with the platinum resistance thermometer. The thermometer is fitted into the well which is filled with silicone oil as is shown in Figure 109.

The electrical leads of the thermometer are heat stationed within the well to minimize heat-leakage error on the thermometer readings. Techniques for the use of capsule platinum thermometers have been well defined by Powell and Sparks (Ref. 20).

Platinum resistance thermometer calibration will be achieved through the use of fixed points on the International Practical Temperature Scale. Attention must be made to the fine points of thermometer calibration such as the temperature gradient effect of the current flowing in the platinum thermometers. This effect can be as high as 0.005°C, but is a function of repeatable thermometer conditions, and can be eliminated by extrapolating the thermometer resistance to a zero-current flow. In addition, precise calibration of the Mueller Bridge, which is used to determine the thermometer resistance, must be conducted. Methods for bridge calibration are
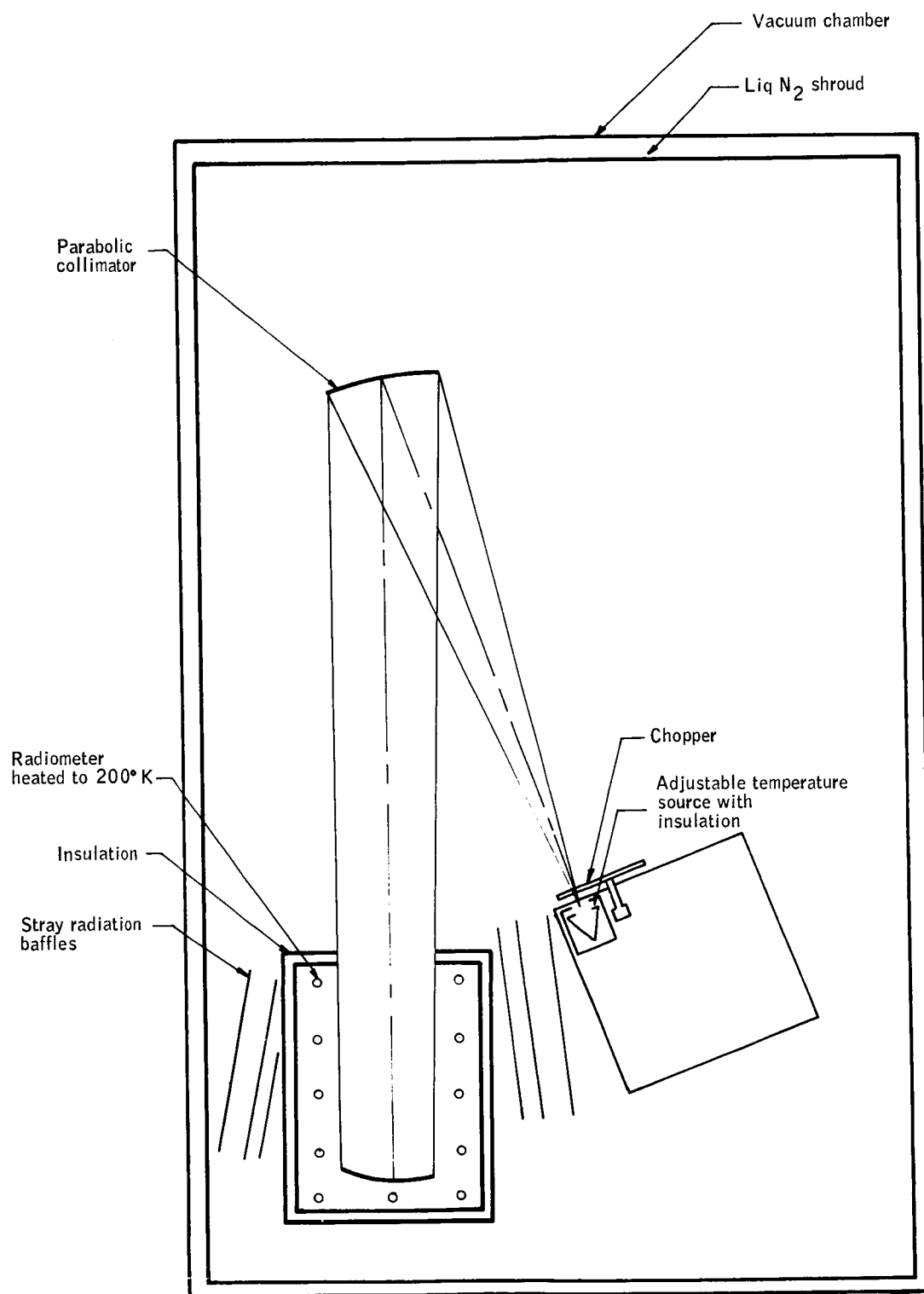
Figure 108. Apparatus for Primary Calibration Using the Adjustable
Temperature Source
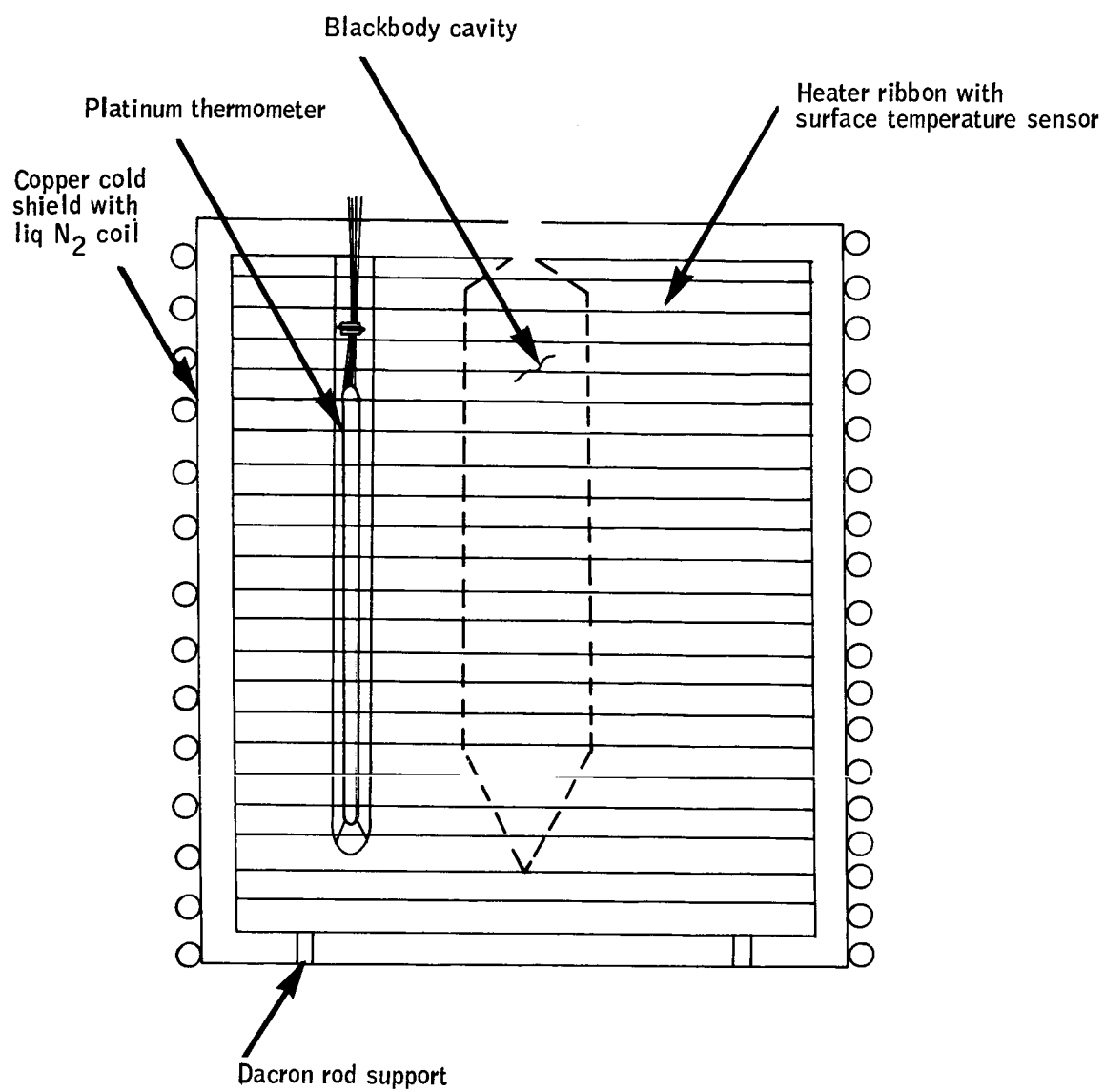
Figure 109.   Adjustable Temperature Source

given by Brooks (Ref. 21). The most precise platinum thermometry is conducted when the bridge and thermometer are calibrated in the same laboratory where used. Insitu calibrations avoid the long time constants associated with stabilizing equipment after moving and also the possible shipping, shock calibration errors. Careful use of platinum resistance thermometers and auxiliary equipment can achieve temperature measurement accuracies to better than 0.003°C

A preliminary analysis of temperature gradients along an aluminum cavity showed that an axial gradient of only 0.01°K would exist if there was 0.041 watt of thermal power flow through the block. Heat transfer from each end of the metal block to the enclosure is only 0.021 watt, and the radiated energy from the cavity through a one-cm aperture is only 0.017 watt.

The results of this investigation, therefore, show that if careful design practices are followed temperature gradients cannot exceed 0.01°K in the block and most probably would not exceed 0.002°K If it should be found after a more rigorous thermal analysis that excessive gradients do exist, they may be minimized by the use of a thermal guard which is placed between the cold shield and the copper or aluminum block. This would be supported from the cold shield by Dacron rods and would be similar to the thermal guard which is shown in the freezing-mercury source in Figure 102. The gradients could also be further reduced by black coating an area equal to that of the aperture on the opposite end of the metal block. This would emit energy at same rate as it is emitting from the aperture, thus balancing the axial heat flow and reducing thermal asymmetrics.

Preliminary dimensions and cavity emissivity are the same as was indicated for the freezing-mercury source in Figure 103 because the aperture size and material emissivity are the same. As was previously discussed with this mercury source, if the required emissivity cannot be achieved with black epoxy paint, the dimensions of the source can be increased slightly and a cavity emissivity of 0.9993 achieved with a material emissivity of only 0.38. These results, it will be remembered, are based upon the Gouffé method of calculating the emissivity of a cavity and must be confirmed by the other two methods.

Calibration procedure. -- As in the fixed temperature source calibration method, several preliminary tests must be conducted. Among these are the following:

1. Scan the blackbody cavity with a small field-of-view radiometer to discover temperature or emissivity gradiants.

2. A gonioradiometric measurement of the source to assure that it is a Lambert radiator over the field of view of the radiometer.

3. The measurement of modulated stray radiation.

4. The previously measured reflectance of the collimator.

272

After these tests have been completed as discussed in the fixed temperature source calibration method, the components are aligned within the vacuum chamber as is shown schematically in Figure 108. The vacuum chamber is evacuated, and the chamber and source are cooled with the liquid nitrogen. When the temperature sensors, which are located throughout the chamber, indicate that the chamber has reached an equilibrium at approximately 80°K, the calibration is initiated.

Source temperature is increased to approximately 90°K, stabilized at this point, and the temperature of the platinum resistance thermometer is recorded. While measuring this source the output of the radiometer is recorded. When sufficient measurement time has elapsed, the source temperature is increased by some small amount, say 5°, allowed to stabilize and the platinum thermometer and the radiometer measurements are recorded. This procedure is repeated until the full radiance range has been calibrated; as shown in Figure 105, this radiance range represents a source temperature range from 90°K to 250°K. Source radiance is calculated at each level from the source temperature and emissivity and the reflectance of the collimator so the radiance response of the radiometer may be recorded. Exact temperature increments which are used will be determined emperically from the linearity of the radiometer response function.

Calibration of the In-Flight Calibration Sources

After the primary calibration has been completed and the results of both methods agree, the in-flight sources are calibrated.

Neither the parabolic collimator or the source optical bench are required for this calibration. The field of view of the radiometer is completely filled with a very low radiance surface to simulate the cold space that is viewed during the in-flight calibration. This surface is a high-attenuation black baffle which is cooled with liquid helium and is placed at approximately the same position as was the parabolic collimator during calibration. The configuration of this apparatus is shown in Figure 110. If it is assumed that the baffle can be cooled to 10°K by the liquid helium, its radiance is approximately 10^{-40} W/cm^2-sr, which may be ignored; the noise equivalent radiance of the radiometer is 3 x 10^{-7} W/cm^2-sr.

To calculate the required attenuation by the baffles, three sources which irradiate the baffle must be considered:

1. Emission of the radiometer.

2. Emission of the chamber.

3. Emission of the in-flight source which is located at the field stop.

273
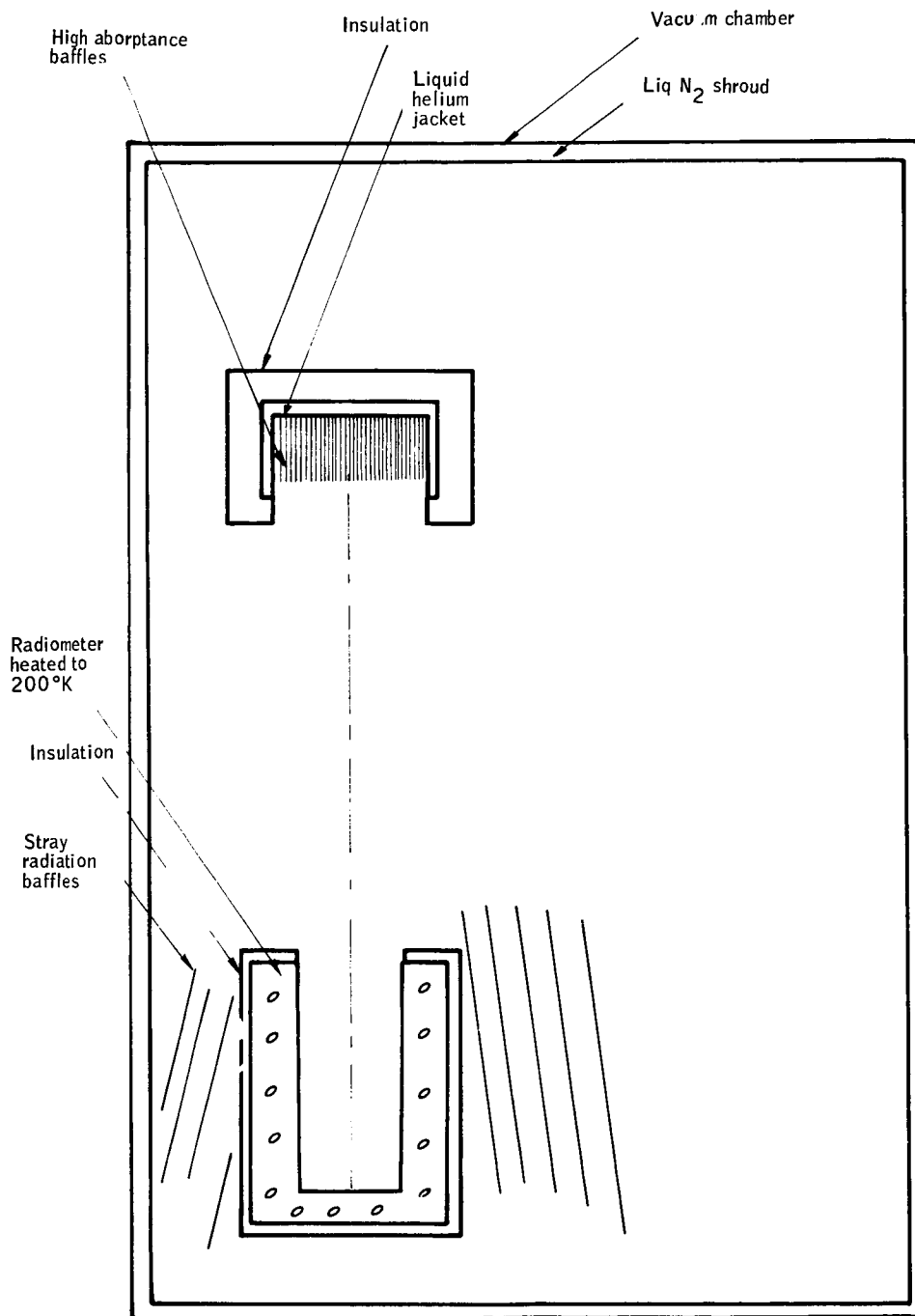
Figure 110. Apparatus Configuration to Simulate Cold Space
During In-Flight Source Calibration

If it is assumed that the radiometer is at its highest temperature of 240°K, that the emissivity of the radiometer is 1.0, and that is a Lambert radiator. The radiance of the radiometer cavity is 6×10^{-4} W/cm^2-sr.

The approximate irradiance on the plane of the baffle may be calculated as follows:

$$H = N \Omega$$

where:

N = radiance of the radiometer cavity

Ω = solid angle subtended by the radiometer cavity from the baffles.

Assuming that the baffles are 250 cm from the radiometer,

$$H = 1.2 \times 10^{-5} \text{ W/cm}^2$$

If the baffles are Lambert diffusers of reflectance ρ, then

$$N_{baffle} = 3.8 \times 10^{-6} \rho \text{ W/cm}^2\text{-sr}$$

The vacuum chamber is maintained at 77°K and its emissivity is 1.0, yielding

$$N_{chamber} = 8.3 \times 10^{-7} \text{ W/cm}^2\text{-sr}$$

Radiance of the baffle due to the chamber is then

$$N_{baffle} = 8.3 \times 10^{-7} \text{ W/cm}^2\text{-sr}$$

The 300°K, 0.1 cm^2 in-flight calibration source which is located near the field stop can also irradiate the baffle. The radiant power on the plane of the primary mirror from this source is 2.65×10^{-5} watts if the source has a radiance of 1.35×10^{-3} W/cm^2-sr. The irradiance on the baffle is then 6.63×10^{-8} W/cm^2 which gives the baffle a radiance of

$$N_{baffle} = 2.11 \times 10^{-8} \text{ W/cm}^2\text{-sr}$$

The radiance of the baffle from all three sources of radiation is then $4.7 \times 10^{-6} \rho$ W/cm^2-sr.

Since the radiance of this baffle must be less than the noise equivalent radiance of the radiometer,

$$\rho \leq \frac{3 \times 10^{-7}}{4.7 \times 10^{-6}}$$

$$\leq 6.4\%$$

This reflectance value corresponds to an attenuation factor of only 15.6, which may easily be achieved with a black baffle. The radiometer and baffle are aligned within the vacuum chamber; the vacuum chamber is evacuated and the components cooled until the thermocouples within the chamber indicate that the thermal equilibrium has been reached. Calibration is then initiated in the same sequence as will be used in flight. Each of the four radiant power levels are introduced into the field of view of the radiometer whose detector output is recorded. These four levels will be used as the basis of determining if any variation in the response function of the radiometer has occurred.

Error Analysis of the Primary Calibration

There are two types of errors which will cause inaccuracies in the calibrated radiometer response function. Bias errors are caused by an unwanted, constant, effective radiance; this type of error would raise or lower the calibration response function from its true value. Scale errors are a function of source radiance and are expressed as a percentage of radiance, these errors multiply the response curve by a constant which rotates the calibrated response function from its true value.

Bias errors. -- Bias errors are caused in the calibration system by radiation from a source other than the blackbody which is chopped by the source chopper. The radiometer cannot, of course, differentiate between this radiation and the source radiation, thus resulting in an error.

Figure 111 diagramatically demonstrates the nature of this error. This figure is an example of the radiance wave form as it is chopped by the source chopper. If it is imagined that during the calibration the blackbody source is cooled so that it contributes no energy to the radiometer, a wave form such as the solid line in the figure would result. Level A in the figure is due to radiation emitted from the various components of the chamber which impinges on the radiometer detector but is not chopped by the source chopper. Level B is radiation which is emitted by the various components of the chamber but is modulated by the source chopper. If it is now imagined that the blackbody source is heated to some temperature, the dotted waveform would result. Because the chopped, stray radiation is adding to the radiometer output when the chopper is covering the blackbody source, the real zero level, A, is not measured.

This analysis assumes that there is no measurement of A, and that B is assumed to be equal to A. The value of B then becomes the bias error. If the blackbody source is lowered to liquid-helium temperature and the measurement is made as is described in the section on the measurement of modulated stray radiation, the value of B can then be measured and a correction made to reduce the error. The contributors to the bias error B when the fixed temperature with the diffuser method is used were calculated by making the following assumptions:

1. All components except the radiometer are at 77°K.
2. The temperature of the radiometer is between 200°K and 240°K.

276
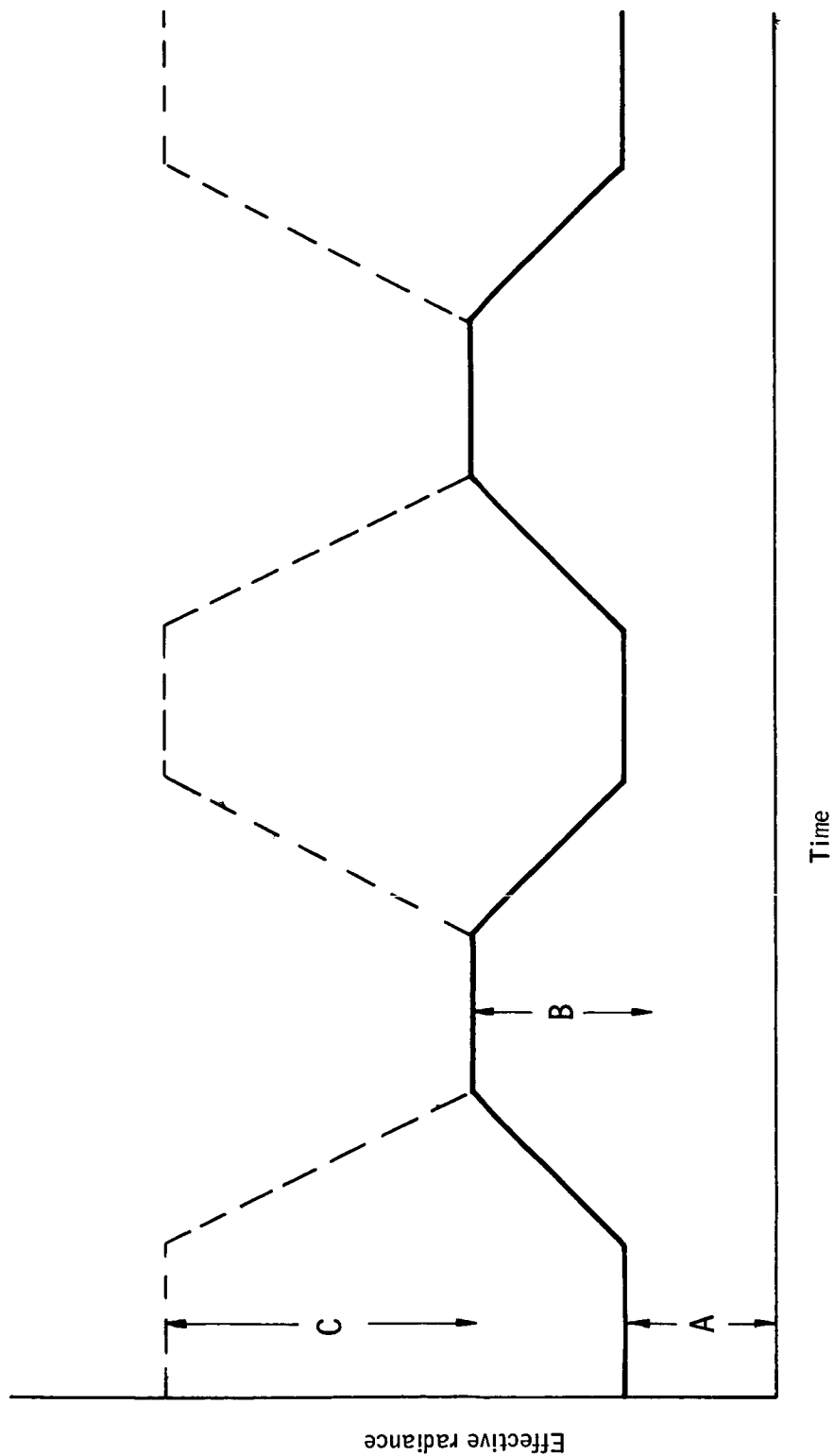
Figure 111. Example of Calibration Bias Errors

Time

Effective radiance

3. The chopper blade is a Lambert reflector and radiator whose reflectance is 0.02 and whose emissivity is 0.98.

4. The effective radiating area of the chopper is 0.3 cm^2 and is placed 1.0 cm, from the diffuser.

5. The transmittance of the Lambert diffuser is 0.8; its emissivity is 0.2, and, although it is inconsistant with the preceding values, its reflectance is assumed to be 0.3. This inconsistent assumption is used since it increases the calculated errors.

6. The emissivity of the baffles which are between the chopper and the diffuser is 0.2 on the side facing the chopper and 0.98 on the side facing the diffuser. This is shown in Figure 99. Both sides are assumed to be Lambert radiators.

7. The average distance of the diffuser baffles is 0.3 cm from both the chopper and diffuser. These baffles have an emitting area of 0.3 cm^2 to both the diffuser and the chopper.

8. The vacuum chamber is a Lambert radiator with an emissivity of 1.0.

9. The collimator is a Lambert radiator with an emissivity of 0.02 and a reflectance of 0.98. It has a diameter of 50 cm and a focal length of 250 cm.

10. The collimator is the only element which can radiate directly into the radiometer since it completely fills the field of view. Emission from other components only affects the radiometer if it impinges on the diffuser.

The bias error components with the diffuser have been calculated to be the following:

1. Emission of the chopper which irradiates the diffuser

$$N = 6.23 \times 10^{-8} \text{ W/cm}^2\text{-sr}$$

2. Emission of the diffuser which is reflected by the chopper in the diffuser

$$N = 3.04 \times 10^{-11} \text{ W/cm}^2\text{-sr}$$

3. Emission of the baffles which is reflected by the chopper onto the diffuser

$$N = 3.37 \times 10^{-11} \text{ W/cm}^2\text{-sr}$$

4. Emmission of the radiometer which is transmitted by the diffuser and reflected by the chopper onto the diffuser

at $T_{radiometer} = 200°K$

$$N = 3.04 \times 10^{-10} \text{ W/cm}^2\text{-sr}$$

278

at $\quad T_{radiometer} = 240°K$

$$N = 7.82 \times 10^{-10} W/cm^2\text{-}sr$$

5. Radiation from the vacuum chamber which is transmitted by the diffuser and reflected from the chopper onto the diffuser

$$N = 9.7 \times 10^{-11} W/cm^2\text{-}sr$$

The sum of the bias error components is then $6.3 \times 10^{-8} W/cm^2\text{-}sr$ which is significantly less than the noise equivalent radiance of the radiometer which is $3 \times 10^{-7} W/cm^2\text{-}sr$

Using these same assumptions which are listed above, the level of A in Figure 111 was calculated. This does not cause an error in itself but it should be minimized as much as possible to avoid second-order effects.

The calculated components of this level are as follows:

1. Collimator emmission into the radiometer

$$N = 1.66 \times 10^{-8} W/cm^2\text{-}sr$$

2. Radiometer emmission which is reflected by the diffuser

at $\quad T_{radiometer} = 200°K$
$$N = 7.84 \times 10^{-7} W/cm^2\text{-}sr$$

at $\quad T_{radiometer} = 240°K$
$$N = 1.8 \times 10^{-6} W/cm^2\text{-}sr$$

3. Emission of the diffuser

$$N = 1.66 \times 10^{-7} W/cm^2\text{-}sr$$

4. Emission of the baffles which is transmitted by the diffuser

$$N = 6.92 \times 10^{-7} W/cm^2\text{-}sr$$

5. Radiation from the chamber which is reflected by the diffuser

$$N = 2.49 \times 10^{-7} W/cm^2\text{-}sr$$

The sum of these values if a 200°K radiometer is assumed is 1.91×10^{-6} W/cm^2-sr or 2.97×10^{-6} W/cm^2-sr if 240°K radiometer is assumed. Although this value is significantly larger than the noise equivalent of the radiometer, it does not introduce an error as was discussed with Figure 111.

When the adjustable temperature source method is used, there is a change in the bias errors since the diffuser is not in place. Bias errors with this method are due to radiation which is directly reflected from the chopper blade when it is in the field of view of the radiometer. Because of the change in apparatus, the assumptions upon which the bias error was calculated are somewhat changed:

1. All components except the radiometer are at 77°K.

2. The temperature of the radiometer is between 200°K and 240°K.

3. The chopper blade is a Lambert reflector and radiator whose reflectance is 0.02 and whose emmissivity is 0.98.

4. The vacuum chamber is a Lambert radiator with an emmissivity of 1.0.

5. The collimator is a Lambert radiator with an emmissivity of 0.02 and a reflectance of 0.98. It has a diameter of 50 cm and a focal length of 250 cm.

6. The collimator is the only element which can radiate directly into the radiometer since it completely fills the field of view.

The calculated bias error component with the adjustable temperature source and no diffuser are as follows:

1. Emmission of the chopper

$$N = 8.15 \times 10^{-7} \, W/cm^2\text{-sr}$$

2. Emmission of the radiometer cavity which is reflected by the chopper

at $T_{radiometer} = 200°K$

$$N = 5.22 \times 10^{-8} \, W/cm^2\text{-sr}$$

at $T_{radiometer} = 240°K$

$$N = 1.2 \times 10^{-7} \, W/cm^2\text{-sr}$$

3. Radiation from the chamber which is reflected by the chopper

$$N = 1.66 \times 10^{-8} \, w/cm^2\text{-sr}$$

The sum of these bias error components is $8.84 \times 10^{-7} \, W/cm^2$-sr If the temperature of the radiometer is assumed to be 200°K and is $9.52 \times 10^{-7} \, W/cm^2$-sr if the temperature is 240°K. These values may be compared with the noise equivalent radiance of the radiometer which is $3 \times 10^{-7} \, W/cm^2$-sr.

Since the sum of the modulated, stray radiation exceeds the noise equivalent radiance of the radiometer, a correction is required. Two possible methods could be used to accomplish this correction:

1. The blackbody source may be cooled with liquid helium and the stray radiation measured. This value could then be subtracted from the radiometer output during calibration. This method is outlined in the section concerning the measurement of modulated stray radiation.

2. A low emmissivity mirror chopper could be used instead of the black diffuse chopper. The blade of this chopper would be rotated from normal to the optical axis so that the radiometer's cavity emmission is not reflected back into the field of view. The emission of the chopper blade, assuming an emmissivity of 0.02, would produce a radiance of only $1.6 \times 10^{-8} \text{W}/\text{cm}^2$-sr. The only other source of modulated stray radiation would be due to the virtual image of a section of the chamber which is formed by the mirror surface of the chopper. This section of the chamber could be a baffle cooled by liquid helium so that it would contribute an insignificant bias error.

Since the diffuser is not used with the adjustable source, the only contributor to the zero level (A in Figure 111) is the emmission of the collimator into the radiometer. This is an equivalent radiance of $1.66 \times 10^{-8} \text{W}/\text{cm}^2$-sr if the collimator is at 77°K and has an emmissivity of 0.02.

Scale errors. -- Scale errors are a function of the radiance of the calibration source and are expressed as a percentage of that radiance. The assumptions upon which each of the errors was calculated are described with each contributor. The contributors to scale errors during primary calibration with the fixed temperature source and diffuser are as follows:

1. Stray radiation from the source which is reflected by the chamber onto the diffuser. Assuming the chamber walls are Lambert reflectors with a reflectance of 10 percent, a 9×10^{-5} percent error would result from this reflected radiance.

2. Figure 112 demonstrates an error which would result from a variation in the radiance on the diffuser at off-axis points. The ratio of $\omega''/\omega' = \cos 2\theta$; the effective area of the source as seen from y' is reduced by $\cos \theta$; and the effective area of the diffuser at y' is also reduced by $\cos \theta$. Therefore, the irradiance at y' is less than at y by a factor of $\cos^4 \theta$.

When the diffuser is placed at its original position, where the radiometer output equals that which was obtained when

281
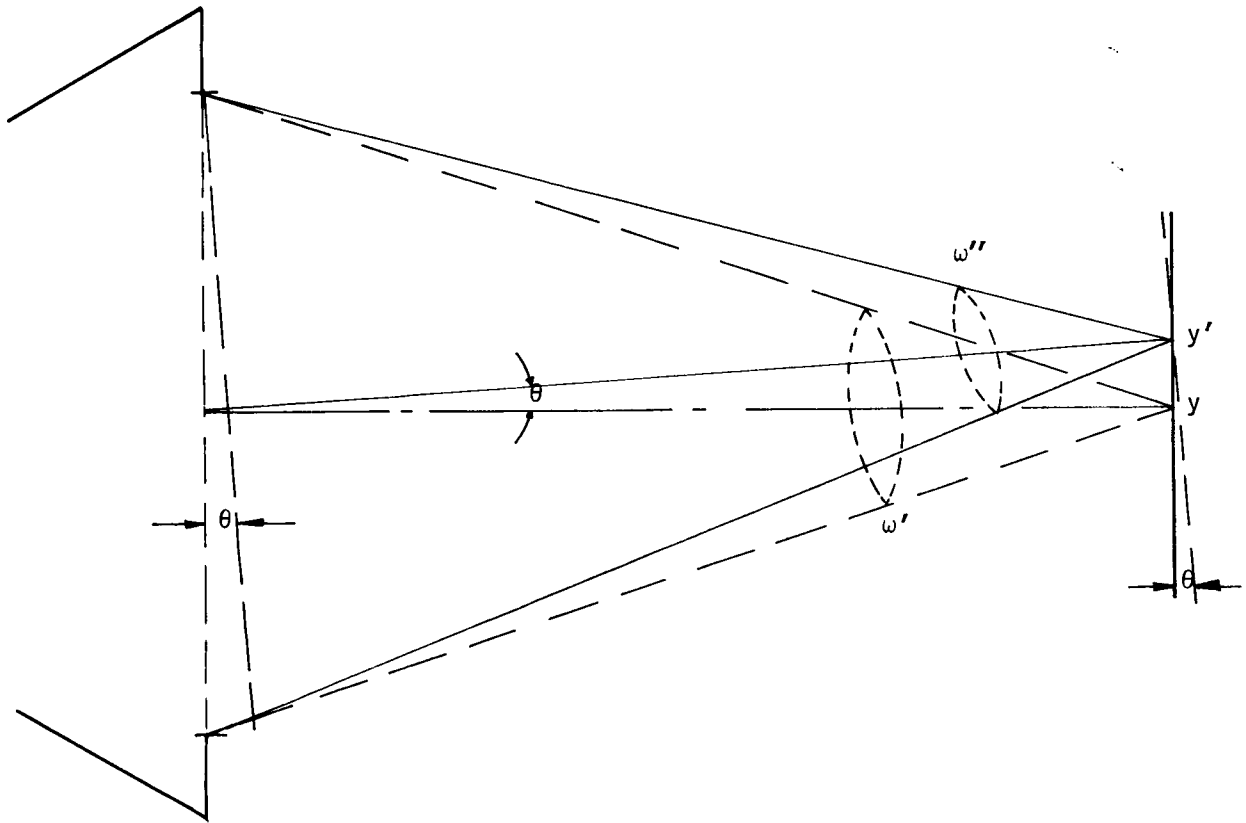
Figure 112. Derivation of $\text{Cos}^4 \theta$ Error

measuring the freezing-mercury source, there is, by definition, no $\cos^4 \theta$ error. However, when the source is moved from this position the $\cos^4 \theta$ effect causes an additional attenuation. From Figures 105 and 106, the radiance of the freezing-mercury source is approximately $5.3 \times 10^{-4}\,W/cm^2$-sr. This same radiance is achieved when the diffuser is approximately 2.8 cm from the freezing-tin source. Figure 106 also shows that the closest position of the diffuser is 2.2 cm and the furthest position is 59 cm from the source. The $\cos^4 \theta$ error may then be calculated at these two extreme positions. Results of such a calculation shows that a 0.11 percent error will occur at the highest radiance level (at a distance of 2.2 cm) and a 0.13 percent error will occur at the lowest radiance level (at a distance of 59 cm).

3. Variation of source-to-diffuser distance can cause an error if the source should rotate. This error would also be in the form of a $\cos^4 \theta$ attenuation. If it is assumed that the source will be held stable (such that it can rotate by no more than two arc min), a 0.02 percent error can result from this rotation. The two arc min rotation stability is, of course, a conservative estimate of what actually may be achieved with optical benches.

4. Since the radiance of the diffuser is calculated from knowledge of source-to-diffuser distance, an error can occur by an inaccuracy in this measurement. Using the equation which was derived in the section on radiance calibration, this error may be analyzed.

$$N = \frac{(\bar{N}_o)(r^2 + x^2_o)}{r^2 + x^2}$$

Assuming the radius of the source is 0.5 cm, that x_o is 2.8 cm (the source-to-diffuser distance which equals the radiance of freezing-mercury source), and that the source-to-diffuser distance may be measured within 0.001 inches, the error may be calculated at the extreme positions, $x = 2.2$ cm and $x = 59$ cm. Results of this calculation show that an error of 0.22 percent could exist at the high radiance level when the source-to-diffuser distance is at the minimum and 0.086 percent at the low radiance level. Interferametric means could be used to measure this distance within a half-wave length of visual radiation if the error must be reduced.

5. As is shown in the equation above, the radius of the blackbody source must also be measured; an inaccuracy in this measurement will result in a calibration scale error. If it is assumed that the diameter of the source is nominally 1.0 cm and that it can be measured within 0.0001 inch, an error of 0.005 percent will result at the highest radiance level. At lower radiance levels (greater source-to-diffuser distance), the error is insignificant since the source radius is small compared to this distance.

283

6. An error in the knowledge of the source temperature will cause an error in calibration. If it is assumed that the source is known within 0.01°K as is stated by the National Bureau of Standards, a 0.008 percent error would result.

7. An inaccuracy in the knowledge of blackbody emissivity will also cause an error in calibration. According to the Gouffe equation which was discussed in the section describing the freezing-tin source, the emissivity of the blackbody cavity is 0.9991. Assuming that it will be no less than 0.999 and that the radiance calculations are performed using an emissivity of 1.0, a 0.1 percent error will result.

8. An error in the measurement of collimator reflectance will cause a calibration error since the apparent radiance of the source is equal to the product of its inherent radiance and the collimator reflectance. Assuming the procedure outlined in Figure 104, the various components which will lead to this error are as follows:

    a. During the 100 percent level measurement, the entire surface of the flat mirror is used; however, when the collimator is inserted only a 0.5-cm diameter portion will be used. An error will then result if the reflectance of this small spot is not typical of the entire surface. To reduce this error, the flat mirror will be shifted to permit averaging the reflectivity variations over its surface. A residual integration error will result, and this is estimated to be 0.02 percent.

    b. An error can occur in this measurement by absorption or scattering in the optical path since the path increases when the collimator is inserted and the flat mirror placed at its focal point. Path attenuation in the vacuum chamber is assumed to be 1 percent/100 meters. Since the path increase is 500 cm, a 0.05 percent error could result.

    c. As was previously discussed describing the method of measuring the reflectance of the collimator, the radiation "beam" will be smaller than the optical components to assure that no radiation is lost. If it is assumed that this safety margin is a 3-mm wide rim of a collimator and that the reflectance of this rim varies from that of the remainder of the mirror, an error will result. When calculating this error, reflectance was assumed to be 96 percent for the 3-mm rim and 98 percent for the remainder of the mirror. This calculation results in a 0.083 percent error.

    d. Nonuniformities in the optical component will not cause an error unless they align with a nonuniformity in the collimator or flat mirror. This error will be virtually eliminated

by rotating the flat mirror and the collimator so that these nonuniformities are averaged over the surface. A residual integration error may be present which is estimated to be no greater than 0.02 percent.

e. If the flat mirror is not located exactly at the focal point of the collimator, the radiation will be diverging at a greater angle as it is reflected from the collimator. A larger portion of the beam splitter and focusing element than was used at the 100 percent level measurement will be utilized as a result.

An error will result if the reflectance of this larger portion of these two elements is not typical of the remainder of their surface. It was assumed that the flat mirror was displaced two mm from the focal plane, the reflectance of the outer edge of the beamsplitter was 49 percent whereas the reflectance of the remainder of the beamsplitter was 50 percent, and the reflectance of the outer edge of the focusing element was 96 percent whereas the reflectance of the remainder of this element was 98 percent. This calculation results in a 0.004 percent error from the beamsplitter reflectance variation and 0.01 percent error from the focusing element reflectance variation.

The sum of all of the errors in the collimator reflectance measurement is then 0.187 percent.

The total scale error from all sources discussed is shown in the table below:

	Highest radiance level	Lowest radiance level
Sum of errors, percent	0.65	0.53
Rss of errors, percent	0.33	0.26

The contributors to scale errors when the calibration is performed with the adjustable temperature source have been calculated as follows:

1. An error in the knowledge in the temperature of the adjustable temperature source will cause a calibration error. It is assumed that the temperature may be maintained and measured within the 0.01°K at any temperature within the range which is required. At the lowest radiance level, which corresponds to a temperature of 90°K, a 0.01°K inaccuracy would cause a 0.44 percent radiance calibration error. At the highest radiance level, which corresponds to a temperature of 250°K, this error will be 0.016 percent.

2. An error in the knowledge of the emissivity of the blackbody source will also cause a calibration error. According to the Gouffe' equation which was discussed in the section on variable temperature source, the emissivity of the cavity will be 0.9993 even if the black epoxy paint is not used in the cavity. Assuming that the emissivity will be no less than 0.999 and that the radiance calculations are performed using a value of 1.0, a 0.1 percent error will result.

3. The same error for the reflectance of the collimator, which was calculated in the previous section, will be present with the variable temperature source. It will be remembered that the sum of all components of this error was 0.187 percent.

The other scale errors which were mentioned as contributors with the fixed temperature source-diffuser method would not affect the variable temperatures source because of the following assumptions:

1. Stray radiation from the source which is reflected from the chamber into the source would be absorbed within the blackbody cavity.

2. The source is a Lambert radiator within an angular range at least that subtended by the collimator or about 10°.

3. Since the adjustable temperatures source is extended as compared to the radiometers field of view and it is not moved during the calibration, no distance measurements are necessary.

The sum of the scale errors with the variable temperature source is then 0.303 percent at the highest radiance level and 0.331 percent at the lowest radiance level.

IN-FLIGHT CALIBRATION

Description of System

Two separate calibration sources will be used to achieve calibration at no fewer than four points over the 700:1 radiance range of the horizon. The three lower radiant power points of calibration will be provided by a wire filament mounted above the primary optical tube. Radiation from this source will be collimated and directed into the primary mirror by an off-axis parabola which is mounted within the tube. Radiant power attenuation for the three levels will be accomplished by a rotating aperture plate which will decrease the effective area of the collecting aperture. These three levels of radiant power will be directed through all of the optical elements of the system so that the changes in these components will be detected.

The highest radiant power level will be calibrated by a second wire filament source which may be injected into the optical system directly in front of the field stop. This source will be maintained at 300°K so that it will not impose a significant heat load but will be well above the ambient temperature. A final calibration point will be achieved by a measurement of cold space. This will provide a zero reference so that the effect of thermal emission by the optical components may be determined. The components of this system as shown in Figure 113 are:

1. Two sources controlled to 300°K and 400°K.
2. Temperature control circuits.
3. Zero-reference monitoring circuits.
4. Calibration control circuits.
5. Mechanical actuators to insert radiometric signals into the radiometer field of view.
6. An aperture plate which attenuates one of the sources. This plate has two apertures, of different sizes, which attenuate the radiance of one of the sources to attain different irradiance levels.
7. A shutter which opens to allow radiance inputs to be inserted into the FOV during calibration, and shields against stray radiation from the calibration source at other times.
8. An off-axis, paraboloic mirror which collimates the light from one of the sources into the FOV. This is necessary to obtain the desired radiance levels.

Calibration Source

For preliminary design, calibration levels were chosen which will irradiate the detector at a power level which is equivalent to that which results from a measurement of the horizon at radiance levels of 7.0, 1.0, 0.1, and 0.01 W/m^2 - sr.
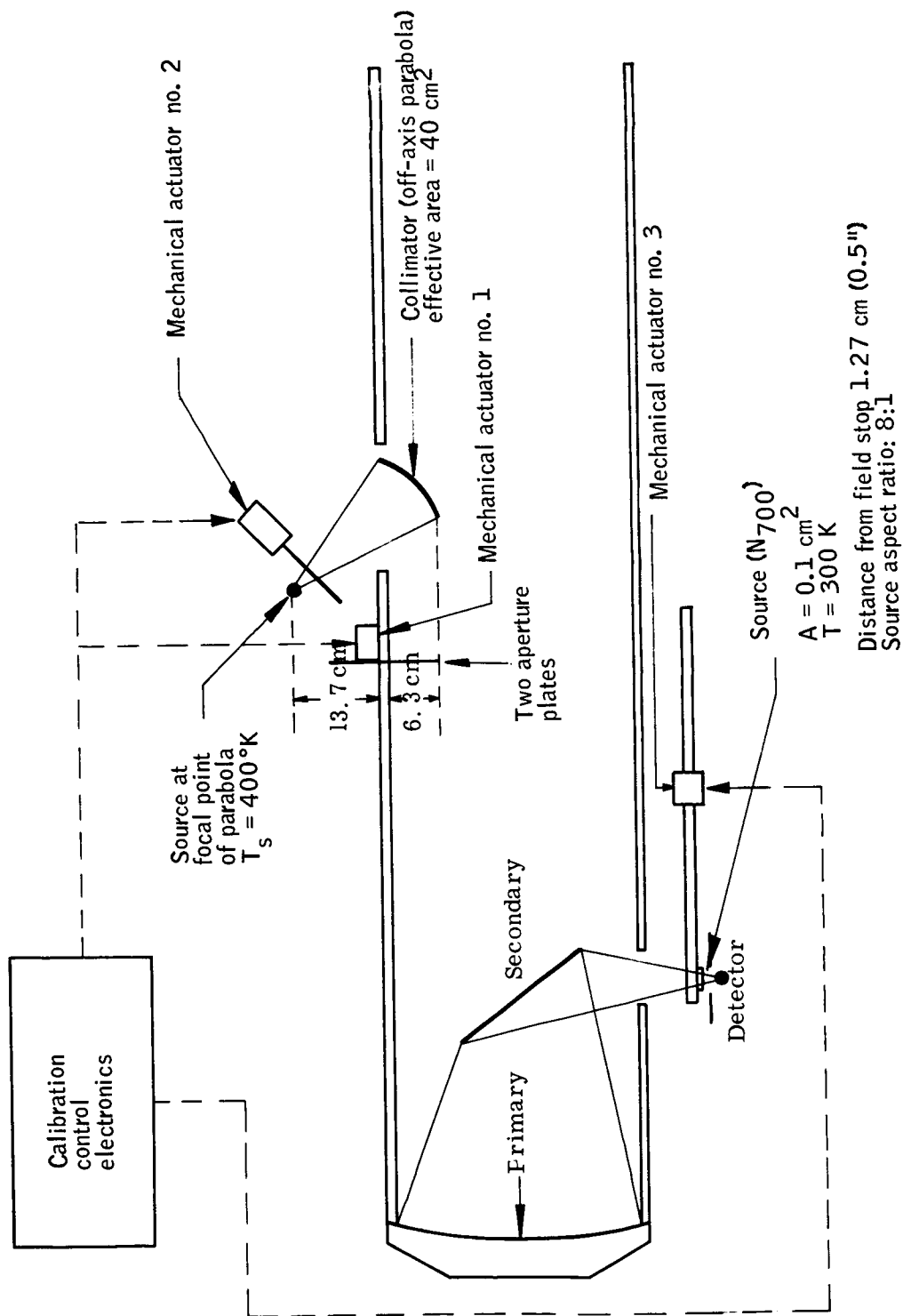
Figure 113. In-Flight Calibration System Schematic Diagram

The minimum and maximum radiance values above are set by the horizon radiance itself; the other two values are arbitrary and can actually be chosen only after the linearity characteristics of the particular detector are determined. The design approach chosen permits increasing the number of levels by introducing additional aperture plates, each having three levels.

The radiant power at the three lower levels is achieved by irradiating an off-axis parabola with a source of a suitable temperature. Placement of the off-axis parabola in the field of view supplies collimated energy to the primary mirror which is focused on the detector. The required source temperature is determined as discussed below.

The power reaching the detector for a given value of earth radiance is

$$P_o = N_H \, A_p \, \Omega$$

where

N_H = horizon radiance,

A_p = area of primary collecting mirror, and

Ω = solid angular field of view of the radiometer.

The power reaching the detector during the calibration cycle is

$$P_s = N_s \, A_o \, \Omega$$

where

N_s = source radiance,

A_o = effective radiation area, and

Ω = field of view of the radiometer.

Equating P_s and P_d the source irradiance is found to be

$$N_s = \frac{A_p \, N_H}{A_o} \tag{48}$$

A source temperature of 400°K was chosen as a convenient temperature which will not impose a difficult perturbation on the thermal design of the spacecraft.

The radiance of this source N_s may be found to be 3.14×10^{-3} W/cm^2 - sr if an emmissivity of 1.0 is assumed. Solving equation (48) for the required area of the paraboloid gives

$$A_O = \frac{N_H A_p}{N_S} \tag{48a}$$

The area of the primary mirror has been chosen as 1255 cm^2; thus equation (48a) may be solved for the effective area of the calibration paraboloid for a horizon radiance of 1×10^{-4} W/cm^2 - sr. Then, $A_O = 40$ cm^2 is the area of the full calibration paraboloid. Insertion of apertures in front of the paraboloid permits the two lower levels of calibration in Figure 113. The areas of these apertures are proportional to the projected area of the paraboloid (31 cm^2) and are as listed below.

Equivalent horizon radiance, W/cm^2-sr	Attenuation aperture area, cm^2
1×10^{-5}	3.1
1×10^{-6}	0.31

Achievement of a radiant power level equal to the maximum horizon radiance (7×10^{-4} W/cm^2-sr) can be easily shown to involve the use of either an excessively large calibration parabola or a 700°K source. Therefore, this level will be calibrated by the insertion of a source directly in front of the field stop shown in Figure 113. Calculation of the source temperature which is required to achieve the desired radiant power level is now necessary. If it assumed that the source is equal to or larger than the field stop, the radiant emittance of the source in the 14- to 16- micron range should equal the irradiance at the field stop when the radiometer is measuring the maximum horizon radiance. The required emittance is

$$W_S = H_H = \frac{N \Omega A_O}{A_{Fs}} \tag{49}$$

where:

W_S = emittance of the calibration source in the 14-to 16-micron range,

N_H = irradiance on the plane of the field stop when measuring the maximum horizon radiance,

N = maximum horizon radiance = 7×10^{-4} W/cm^2-sr,

Ω = solid angular field of view of the radiometer,

A_O = area of the primary mirror = 1255 cm^2, and

A_{Fs} = area of the field stop = 1.02×10^{-3} cm^2.

Solving equation (49) with these values gives $W_s = 1.4 \times 10^{-3} \ W/cm^2$.

Reference to blackbody tables demonstrates that a source temperature which is less than the ambient spacecraft temperature is necessary to achieve this level. Therefore, the area of the source must be decreased to enable calibration at this level. The power which irradiates the detector when measuring the maximum horizon radiance is given by

$$P = \frac{N_H \ A_{Fs} \ A_o}{f^2} \tag{50}$$

where f = the focal length of the primary mirror = 80 cm, and all other symbols have the same meaning as above.

The power which irradiates the field stop by the small calibration source is

$$P = \frac{N_s \ A_s \ A_{Fs}}{r^2} \tag{51}$$

where:

N_s = radiance of the calibration source,

A_s = area of the source, and

r = distance from source to field stop.

Solving equations (50) and (51) for the area of the source gives

$$A_s = \frac{N_H \ A_o \ r^2}{N_s \ f^2}$$

If it is assumed that a 300°K source ($N_s = 1.35 \times 10^{-3} \ W/cm^2$ - sr) is desirable, that it is placed 1.27 cm from the field stop, and that the optical system has a 60 percent collection efficiency; the area of the source may be calculated to be 0.1 cm^2. This is a reasonable source area and can be built with the same aspect ratio as the field stop (0.158 cm x 0.632 cm). The tangent of the angle which is subtended by the primary mirror from the field stop is 0.5 for a f/2 cone; the angle subtended by the longest source dimension from the field stop is 0.632/1.27 = 0.498. The source would then truly act as a nonextended source as was calculated. A typical design of a source which could be used at either of the two calibration positions is shown in Figure 114.

Windings of nichrome resistance wire are chosen as the heating element because of its low temperature coefficient of resistance. These windings are used to form two arms of a resistance bridge which measures the temperature of the element. The complete element is coated with silicon monoxide

0.003-inch diameter (no. 40), 130
turns nichrome resistance wire,
1 coil (thermal input) R = 100 Ω

0.0005-inch diameter
platinum resistance wire,
2 coils bifilar wound,
300 turns (temperature
sensing), R = 5.0 K each
winding

Silicon monoxide
coating

Ceramic substrate
(bobbin)

0.1cm

1.0
cm
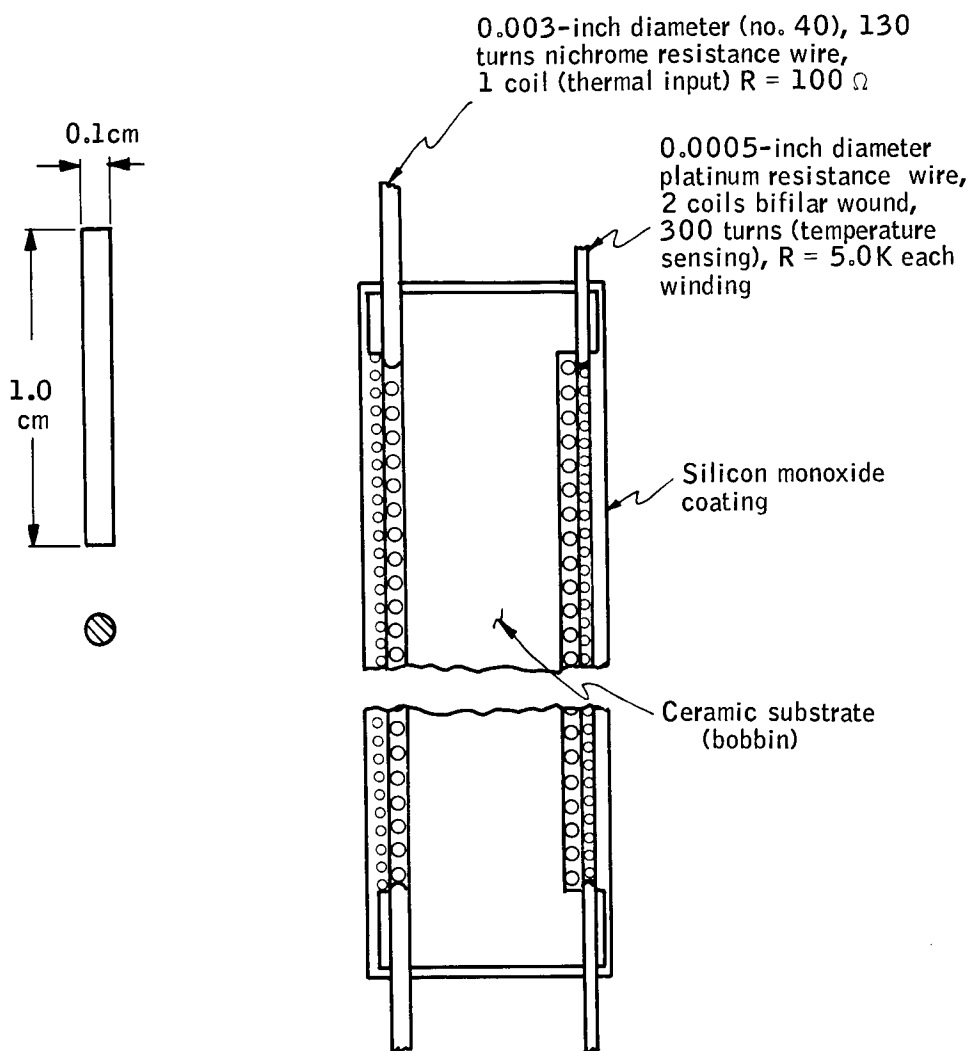
Figure 114.   Source Detail Design

to provide a high emissivity surface of high stability; radiation efficiency is thus maximized and temperature variations thus reduced across the element.

Source Temperature Control

Radiated source power must be constant for a period of one year in space. The fundamental expression for the source input power is

$$P_{in} = P_{cond} + P_{rad}$$

For this expression, the conducted power is

$$P_{cond} = K(T_s - T_o) = KT$$

where:

K = conductivity constant,

T_s = source temperature, and

T_o = sink temperature;

and the radiated power is

$$P_{rad} = \epsilon \sigma (T_s - T_o)^4 = \epsilon \sigma T^4$$

where:

ϵ = surface emissivity, and

σ = Stefan-Boltzmann constant.

If relatively small changes and a value for T_o are assumed, differentials can be taken.

If the conducted losses are "m" times the radiated losses

$$P_{cond} = mP_{rad} = KT = m\sigma \epsilon T^4$$

which may be reduced to

$$\frac{\Delta P_{in}}{P_{in}} = \left(\frac{m + 4}{m + 1} \right) \frac{\Delta T}{T}$$

if conducted and radiated losses are to the same sink temperature T_o.

The temperature stability required to maintain the radiated power to within ±0.1 percent is

$$\frac{\Delta T}{T} = \frac{1}{4} \frac{\Delta P_{rad}}{P_{rad}} = 0.25 \times 10^{-3}$$

At T = 200°K (400°K source)

$$\Delta T = 0.25 \times 10^{-3} \times 200 = \pm 0.05°K$$

The regulation of source input power required to achieve this stability for m = 2 is

$$\frac{\Delta P_{in}}{P_{in}} = \left(\frac{2 + 4}{2 + 1}\right) \frac{\Delta T}{T} = 2 \frac{\Delta T}{T}$$

and since $\frac{\Delta T}{T} = 0.25 \times 10^{-3}$

$$\frac{\Delta P_{in}}{P_{in}} = 0.5 \times 10^{-3}$$

Therefore, if conduction losses are assumed to be twice the radiation losses the source input power must be regulated to better than ±0.05 percent in order to maintain the radiated power to within ±0.1 percent.

Methods of Source Control

It is necessary to control voltage, current, power, or temperature. Because of the stringent temperature stability or measurement required (±0.05°K), a closed-loop temperature control has been chosen (Figure 115). In this circuit, the temperature is sensed in a resistive bridge. Two of the bridge elements, the platinum resistance wires, are wound around the resistance heater element so as to sense surface temperature. The other arms of the bridge are nichrome wires which are bonded to a thermally stable area in the instrument. Since nichrome has a very low temperature coefficient (TC) of resistance, the effects of any temperature variations in their mounting area is minimized. Their TC will be approximately 20 ppm/°C, consequently a ±10°C change will contribute approximately ±0.02 percent change in the temperature measurement signal.

The temperature coefficient of the platinum resistance wire is approximately 0.3×10^{-3}/°C which may be compared to 2×10^{-5}/°C for the nichrome resistance. Thus, the output signal of the bridge will primarily be a function of the source temperature.
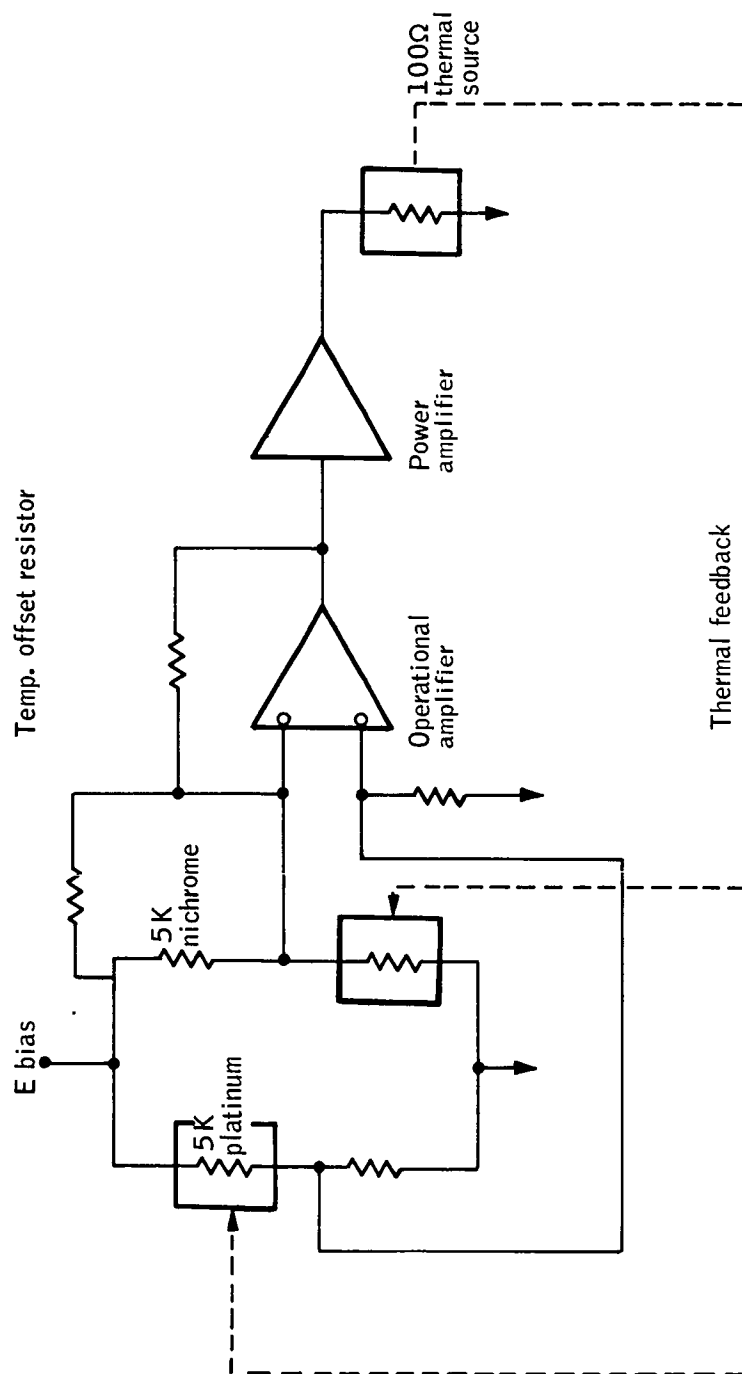
Figure 115. Closed-Loop Temperature Control System

The source temperature setting will be accomplished through the adjustment of a temperature offset resistor. This circuit applies an input to the operational amplifier which causes the thermal bridge to become unbalanced; therefore, the temperature of the source will be that at which the input offset current is balanced by the bridge output current caused by bridge unbalance.

Calibration Control

Calibration will be generated and controlled by digital logic circuits. The total estimated time of calibration will be 2.0 seconds (Figure 116) and the duration of the calibration input will be approximately 250 milliseconds at each level. A time of 200 milliseconds will be available to the data acquisition circuits for calibration of a given input level, and the remainder of the time will be required for control of the various calibration system elements. The principal contributor to these delays is the time constant of the mechanical actuators which is expected to be approximately 100 milliseconds. A logic design diagram of the calibration control circuits is shown in Figure 117. Operation of these circuits is described below.

The cal start/stop input gates a clock into a shift register which counts down the clock frequency. Output signals are taken at appropriate points in the shift register for logic sequencing.

The output of the input gate also sets an R-S flip-flop which opens the shutter for the first calibration level. Approximately 400 milliseconds later, output one is gated through to the aperture control amplifier, and the second is calibrated. This signal lasts for 250 milliseconds. At $t=900$ milliseconds output is gated through to the aperture control amplifier, and the third level is calibrated. At $t=1400$ milliseconds, the flip-flop is reset by output, and the shutter is closed.

Calibration Errors

The three-level, in-flight calibration system as shown in Figure 113 has two optical elements that, by self-emission, radiate into the optical system of the radiometer thus adding to the "dc" radiation of the primary optics.

The radiation from the calibration optics may be different for each calibration point because the calibration optics are physically different for each point. Reference to cold space for each calibration level thus becomes necessary to negate this radiation during the calibration process. The shutter, which covers the source while making a cold-space reference, cannot be negated in the same manner because it is not in place both during calibration and during the zero reference of cold space. Therefore, the shutter must be considered as part of the source and will require thermal control or measurement to some degree of accuracy.
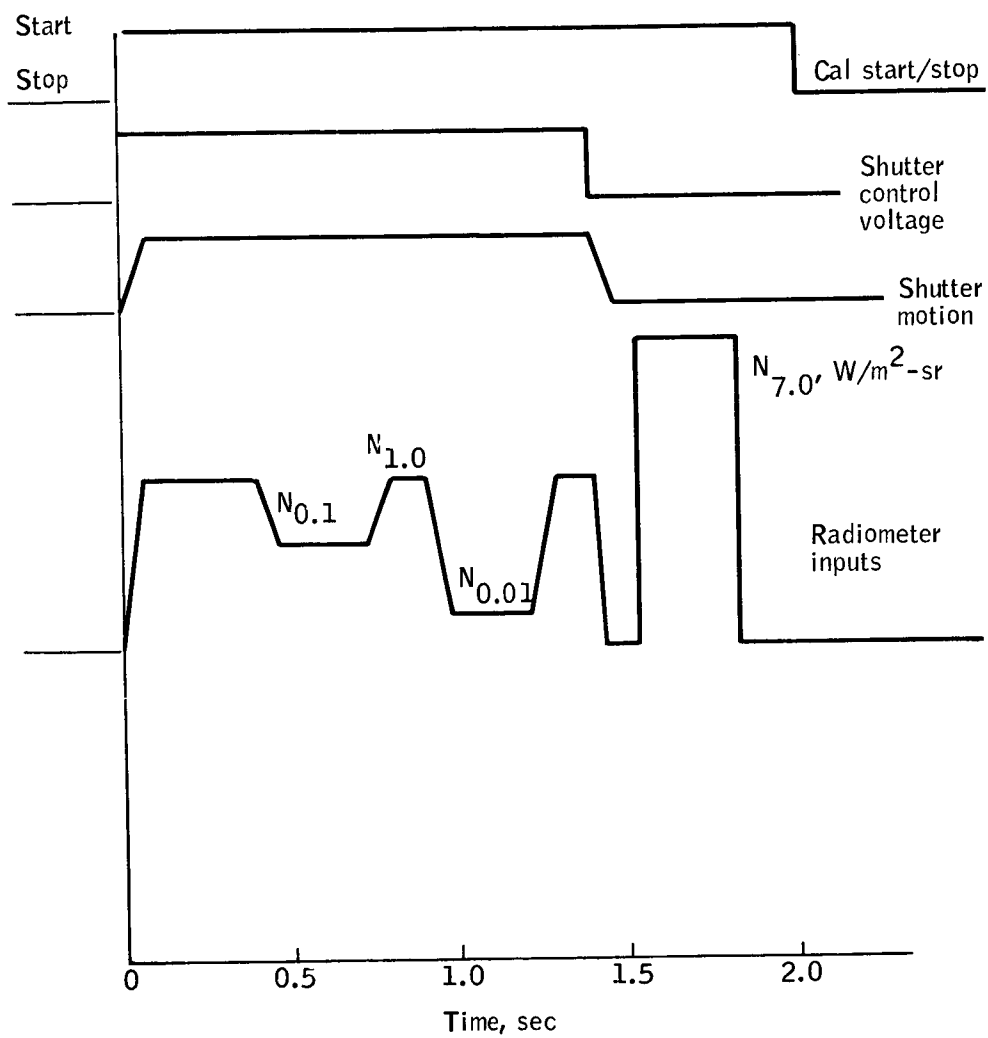
Figure 116. Calibration Control Waveforms
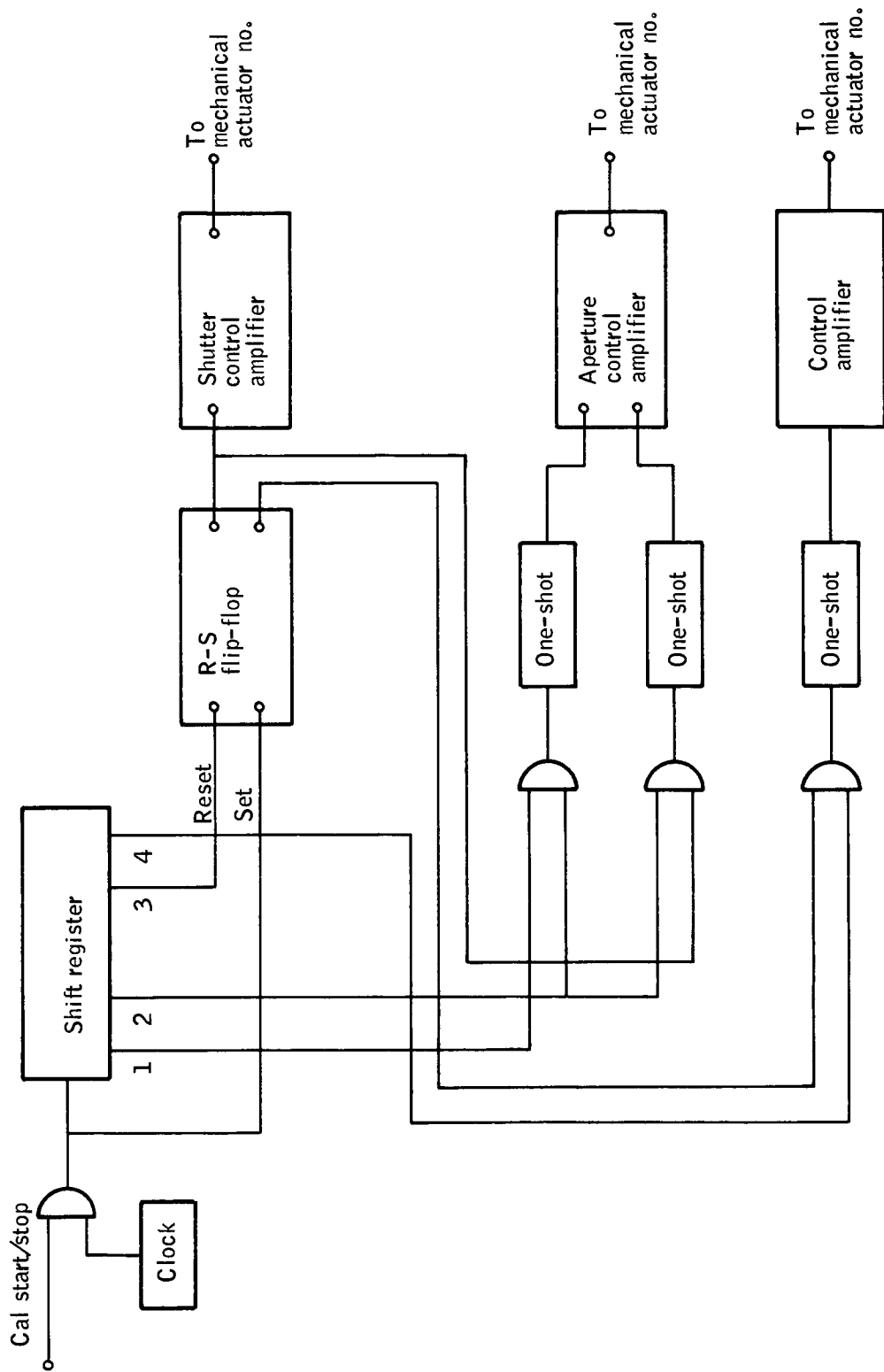
Figure 117. Logic Design Diagram of Calibration Control Circuits

Figure 118 illustrates the contributing sources of radiation during the in-flight calibration process. These levels as given in terms of radiant intensity are

1. Aperture No. 1 calibration level (low) $= 7.6 \times 10^{-4}$ W/sr

2. Aperture No. 2 calibration level (middle) $= 7.6 \times 10^{-3}$ W/sr

3. Full aperture calibration level (high) $= 7.6 \times 10^{-2}$ W/sr

4. Primary optics (200°K) $= 1 \times 10^{-2}$ W/sr

5. Calibration system optics (200°K) $= 1.6 \times 10^{-4}$ W/sr

6. Shutter (200°K) $= 7.6 \times 10^{-5}$ W/sr

The above values are based on the following assumptions:

1. Primary optical effective area $= 760 \text{ cm}^2$

2. Primary optic emissivity $= 0.02$

3. Calibration collimator effective area $= 31 \text{ cm}^2$

4. Calibration collimator emissivity $= 0.02$

5. Aperture plate emissivity $= 0.02$

6. Shutter emissivity $= 1.0$

7. Source emissivity $= 1.0$

8. Source temperature $= 400°K$

9. Ambient temperature for all elements except source 200°K

Error sources contributed by the in-flight calibration system are

1. Temperature stability of the source (discussed earlier) - scale error.

2. Reflectivity changes of the in-flight collimating mirror - scale error.

3. Reflectivity changes of the radiometer primary optics which occur in such a manner that the portion of the primary mirror used by the in-flight calibration system changes differently than the rest of the primary - scale error.

4. Temperature drift of the collimating mirror, aperture plate, and primary optics, between calibration and measurement - bias error.

5. Temperature changes of the shutter between primary calibration and in-flight calibration - scale error.
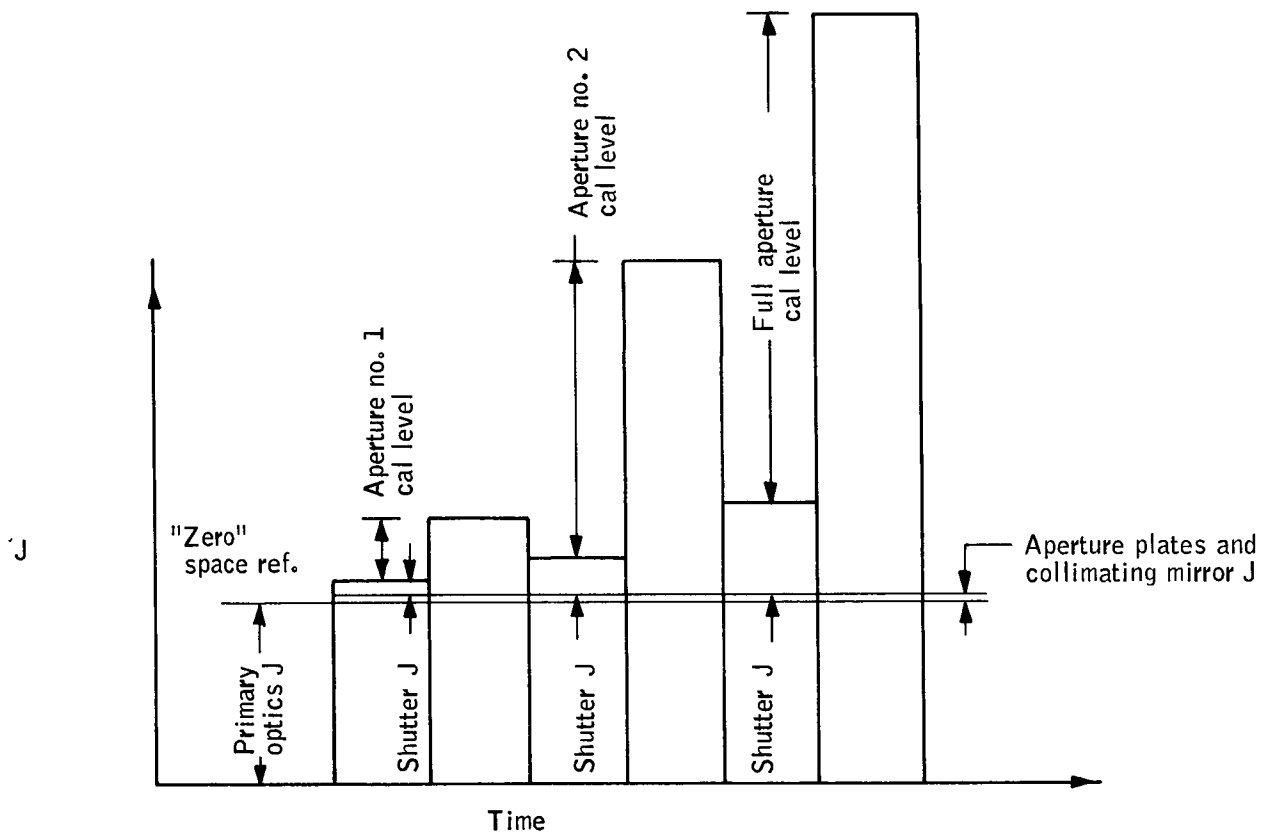
Figure 118. Sources of Radiant Intensity During the In-Flight Calibrating Process

6. Position shifts of the in-flight calibration system components - scale error.

Of the scale error contributors listed above, the temperature stability of the source is the most critical; this stability has previously been shown to be manageable. The error sources of items 2 and 3 above cannot be evaluated analytically, but literature shows that high-quality reflective coatings have a high degree of stability in a space environment and will change less than 0.2 percent for a period of one year. The scale error contributors, items 4, 5, and 6 above, are discussed in the following paragraphs.

Item 4, temperature drift of the optics which contributes chopped radiation by self-emission, will cause a bias error if its temperature changes between in-flight calibration and horizon measurement. For this analysis a permissible error is assumed; then, the temperature change during the five-second interval between calibration and measurement required to get this assumed error is shown to be much higher than can be expected during in-flight operation.

First, the primary optics which contribute a level of radiance conservatively estimated to be 60 times NER is considered. If it is assumed that a bias contribution of 1/10 NER is tolerable, then the mirror emission can change by 1/600, or 0.17 percent.

By the expression

$$\frac{\Delta T}{T} = \frac{4 \Delta N}{N}$$

where

$$\frac{\Delta N}{N} = 0.0017 \text{ and}$$

$$\frac{\Delta T}{T} = \frac{0.0017}{4} ,$$

$$\Delta T = 0.09°K$$

if $T = 200°K$. This ΔT is certainly an excessive temperature shift to expect for the primary optics during a five-second interval (1.08°/min).

The optics of the in-flight calibration system can be handled in the same manner. However, analysis as above is not required since the calibration optics have only five percent the emitting area of the primary optics and thus can undergo a temperature drift 20 times greater than the primary optics to create the same error. The calibration optics will have a higher temperature drift rate because of their relatively low mass, but a drift rate of 1.08°K per minute, is an unreasonably high rate for any portion of the radiometer.

This error is negligible even for angular shifts of several minutes of arc and can be disregarded.

The in-flight calibration scale and bias errors are summarized in Table 21.

TABLE 21.- IN-FLIGHT CALIBRATION ERRORS

Error Source	Error	
	Type	Magnitude
Instability of calibration source	Scale	0. 1%
Emissivity changes of calibration optics	Scale	0. 2%
Angular tilt of aperture plate	Scale	0. 1%
Uncertainty of shutter temperature	Scale	0. 1%
Angular tilt of the collimator-source	Scale	0. 005%
Total		0. 505%
Temperature drift of calibration optics between calibration and measurement	Bias	0. 001 W/cm^2-sr
Total		0. 001 W/cm^2-sr

Alternative In-Flight Calibration Systems Considered

The in-flight blackbody calibration source must be extremely stable in radiance for at least one year and be self-regulating in the variable thermal environment to be encountered during the mission. The central problem of stability of the in-flight source is one of maintaining the blackbody core temperature as constant as possible in the presence of variations in source shell temperature, power fluctuations, and aging of the heater windings of the core. An initial design was completed which draws on the design philosophy of the fixed temperature primary calibration standard. This standard uses the high stability of the melting point and excellent thermal conductivity of a solid-liquid equilibrium of a pure metallic element to set the source temperature. As long as solid and liquid coexist in equilibrium, the

temperature will remain at the melting point. In the design to be discussed the melting temperature is the vacuum melting point of, for example, tin or lead.

The radiance source is a shallow conical cavity which simulates an ideal blackbody source by the effects of multiple reflections in the core which increases the effective absorption and emissivity of the cone wall coating. The blackbody cone is in intimate thermal contact with a solid-liquid equilibrium of pure elemental tin. The expansion or contraction of the tin by virtue of the difference in density between the solid and liquid phase causes an elongation or contraction of the bellows. In filling the core, it is important that all the compressible gas be removed so that the bellows is terminated by a ferrite cylinder which acts as the core of a position-sensing solenoid. The solenoid and bellows are within an evacuated chamber to prevent changes in atmospheric pressure effecting the position of the bellows. Heat input to the tin is controlled by the heater current which is proportionally controlled by the position of the ferrite core of the solenoid. The exterior of the source is surrounded by thermal insulation.

In operation, the heater power is set at a value which maintains the solid-liquid equilibrium at, for example, 50 percent solid. The motion of the solenoid core in response to changes in the ratio of solid to liquid demands more or less heater power independent of the power supply terminal voltage or heater winding resistance. Any tendency to "hunt" on the part of the electromechanical servo loop can be made quite small by adjusting the proportionality constant between bellow translation and heater power change and the thermal conductivity of the wall between the heater and the tin bath.

This source design did not receive further consideration, however, because its complexity and impact on system thermal control are greater than is necessary or should be considered during a feasibility study.

The use of an electrically heated wire filament source with a thermal feedback control system was then considered. If variations in all components of the radiometer system are to be detected, the radiant energy from at least one calibration level must be directed through the entire optical system. Therefore, the insertion of a wire filament source directly into the radiometer tube was studied. It is easily shown that this is not a practical configuration. In the recommended system, a small 400° K source is placed at the focal point of a collimator which is located within the collimator tube and has a 40cm^2 area. If the source, however, was inserted directly into the path with no collimator, the source itself would then be required to have an area of 40cm^2. Thermal gradients in the source, a very large shutter and shutter mechanism, and heating of the radiometer components render the direct insertion of an uncollimated source impractical. Therefore, the collimated source configuration, which is described, was selected as the recommended system.

Because of the limited time during a rotation of the spacecraft for in-flight calibration an adjustable temperature source would not reach a thermal equilibrium, so it cannot be used. Therefore, a fixed temperature source

was selected with the various effective radiance levels achieved by the insertion of apertures. These apertures may be inserted either between the source and the collimator, or between the collimator and the primary. The latter method was chosen for the following two reasons:

1. The apertures should be placed as far as possible from the source to reduce the heating of the aperture by the source.

2. The required mechanical stability of the aperture is much less if it is placed in the collimated radiation rather than in the diverging radiation from the source.

Calibration Actuation Devices

The calibration system requires three actuators to operate sequentially during the in-flight calibration process. One actuator will be required to insert the two attenuation apertures in front of the calibration paraboloid; a second will close a shutter to isolate the calibration source from the radiometer; and the third actuator will move a second small calibration source directly over the field stop. The selection criteria for the actuator were an angular motion of 60° in a vacuum greater than 10^{-7} Torr for more than 15 000 hours and a minimum expenditure of energy during the actuation period. Size, weight, and the operating temperature range were also considered.

The temperature uncertainty of the source shutter appears to be the largest potential error contributor of the in-flight calibration system. Calibration radiance is the difference between the source radiance and the shutter radiance (Figure 118); thus, any unmonitored temperature change of the shutter after primary calibration causes a direct scale error. A simple way to analyze the error magnitude is to recognize that the total effective radiance of the shutter (at 200°K) is 1/10 that of the source; therefore, the temperature measurement of the shutter is 1/10 as critical as that of the source. For a shutter temperature uncertainty of 0. 5°K, an error of ±0. 1 percent will result. Shutter temperature must, then, be known or controlled to 0. 25 percent, or to ±0. 5°K. This is a manageable task when considering that the ±0. 5°K temperature measurement is not an absolute determination, but a relative determination.

Scale errors contributed by axial shifting of the critical components of the three-level calibration system are considered to be negligible because the subject system is small and compact, a condition amenable to physical stability. Also, proper design eliminates errors caused by nominal mechanical shifting of components. For instance, the distance between the source and collimating mirror can be made noncritical if the source is extended or sufficiently large. The position of the aperture plate is not critical axially; however, the angular position of both the aperture plates and the calibration system axis must be considered. The projected area of the aperture plate is a direct function of the sine of the angle with the normal to the optical axis. The resultant scale error is also directly proportional to the sine of this angle; so if an angular tolerance of ±3 minutes of arc is assumed, the error is 0. 1 percent.

304

An axial shift of the calibration system which is assumed to be the source and collimator (telescope) will cause an error proportional to the cosine of the angular shift. The error ratio for a telescope angular shift of ϕ for an f/3.0 collimator and an extended source is

$$\frac{2 \int_{\alpha}^{o} \cos \alpha - \int_{\alpha + \phi}^{\phi} \cos \alpha}{\int_{\alpha}^{o} \cos \alpha} = E \qquad (52)$$

where α is half angle of f 3.0 cone.

Solving equation (52) for a shift ϕ of 0.02° (1.2 minutes) gives

$$2 \frac{(0.1650476 - 0.1650438)}{0.1650476} = \frac{7.6 \times 10^{-6}}{1.6 \times 10^{-1}} = 4.8 \times 10^{-5}$$

Three devices which could be used for the calibration actuation were investigated. These particular devices were manufactured by IMC. Their actuators are similar to their stepper motors but are detented by the use of premanent magnets to return to their initial position when the power is terminated. Two of the devices were originally manufactured for a space environment. The third was manufactured to pass MIL-E-52723 and MIL-E-5400 and can be modified for the space environment. The actuators equipped to operate in the space environment utilize Barden precision ball bearings with duroid (a molybdenum disulphide impregnated, teflon, epoxy glass composite) ball retainers which provide a teflon, molybdenum disulphide coating on the balls. This acts as a lubricant and also keeps the balls from cold welding to the races. The coil windings are coated with a vacuum-degassed lacquer which has a low vapor pressure which does not tend to sublimate or outgas in a vacuum of 10^{-9} Torr. Operating temperatures of the devices vary, but the manufacturer states that they can all be conditioned for operating at 200°K. The magnetic paths in each device are sufficiently efficient so that the permanent magnets (alnico V) will not be demagnetized at low temperatures. They operate well above the knee of the demagnetization curve of the material, and will not lose remanence from low temperature saturation.

IMC has also manufactured flag indicators using sleeve bearings made from artificial sapphire. The shaft is made of stainless steel hardened to 47 Rockwell-C and passivated. This combination has operated in a hard vacuum for more than 10^7 cycles without failure or significant wear. Bearings of this type may be used if duroid retainers for the ball bearings prove to be inapplicable for intermittent motion.

The three actuators and their characteristics are listed below.

1. Two-position actuator No. 011-913

Housing	1.062" diameter x 1.600" long
Weight	5 oz
Electrical characteristics	45 Ω, 28 Vdc
Temperature range	-55°C to 125°C (MIL-E-5400, 5272)
Excursion	90°
Detent torque	2 oz-in.

This actuator can be pulsed in either direction and will return to center by the use of a magnetic detent when the power is removed. A torque of 1.5 oz-in. is provided when power is applied.

2. Two-position actuator (for space environment) No. 011-906-3

Housing	1.062" diameter x 1.670" long
Weight	150 g
Electrical characteristics	150 Ω, 28 Vdc
Temperature range	-55°C to 125°C
Pressure excursion range	760 to 7.6 x 10^{-7} Torr
Torque	0.7 oz-in. when energized
Detent torque	0.2 oz-in. at each stop position

This actuator can be pulsed for 70 milliseconds and will move +90° and remain in position. Another, opposite, pulse is required to move -90° back to starting position.

3. Two-position actuator (for space environment) No. 008-912

Housing	0.750" diameter x 1.135" long
Weight	50 g
Electrical characteristics	60 Ω, 19 Vdc
Temperature range	-10°C to +60°C
Pressure range	760 to 10^{-9} Torr
Excursion	22.5°
Detent torque	0.2 oz-in. at each stop position
Torque	7 oz-in. when energized

This actuator can be pulsed for 70 milliseconds and will move +22.5° and remain in that position; an opposite pulse will move it back to starting position. The excursion may be increased, by the manufacturer, to 60°.

The manufacturer can vary these units to be detented in a central position or elsewhere, change the angular excursions of up to ±90°, and increase the detenting torque. Once the operating parameters of the calibration system are specified, the basic actuators could be manufactured to perform each calibration function.

The operating and holding torque will be a function of the inertia loads of the shutters, the actuation speed, and a rotational coupling due to the stabilization spin of the spacecraft.

Power Consumption

The power consumption by the components of the in-flight calibration system are as follows.

Source power	0. 2 W total
Temperature control (2)	1. 0 W total
Mechanical actuators (3)	6. 0 W each
Calibration control (1)	0. 5 W

Figure 119 shows the frequency distribution of this power consumption. The large peak power requirements are due to the presence of unstabilized centrifugal forces generated by spacecraft spin. Were it not for these forces the peak power would be a factor of five less.

Radiometric Analysis of Space

A zero reference point of calibration will be made by a measurement of cold space to allow correction for the thermal emission of radiation by the optical components of the radiometer. A possible source of error in such a calibration would occur from the radiant power emitted by celestial objects. A study of this effect has been completed.

1. A comparison has been made between temperature and visible star magnitudes for objects having outputs matching the radiometer radiance threshold. These visible radiance levels have been compared to the star population characteristics.

2. The irradiance levels produced by known stars in the radiometer spectral interval have been calculated and compared with spectral measurements when this data was available.

3. The self-emission of the planets has been calculated for the spectral interval of the radiometer and compared to measurements of the planets. The irradiance levels produced by reflected sunlight from the planets has been calculated for the radiometer spectral interval.
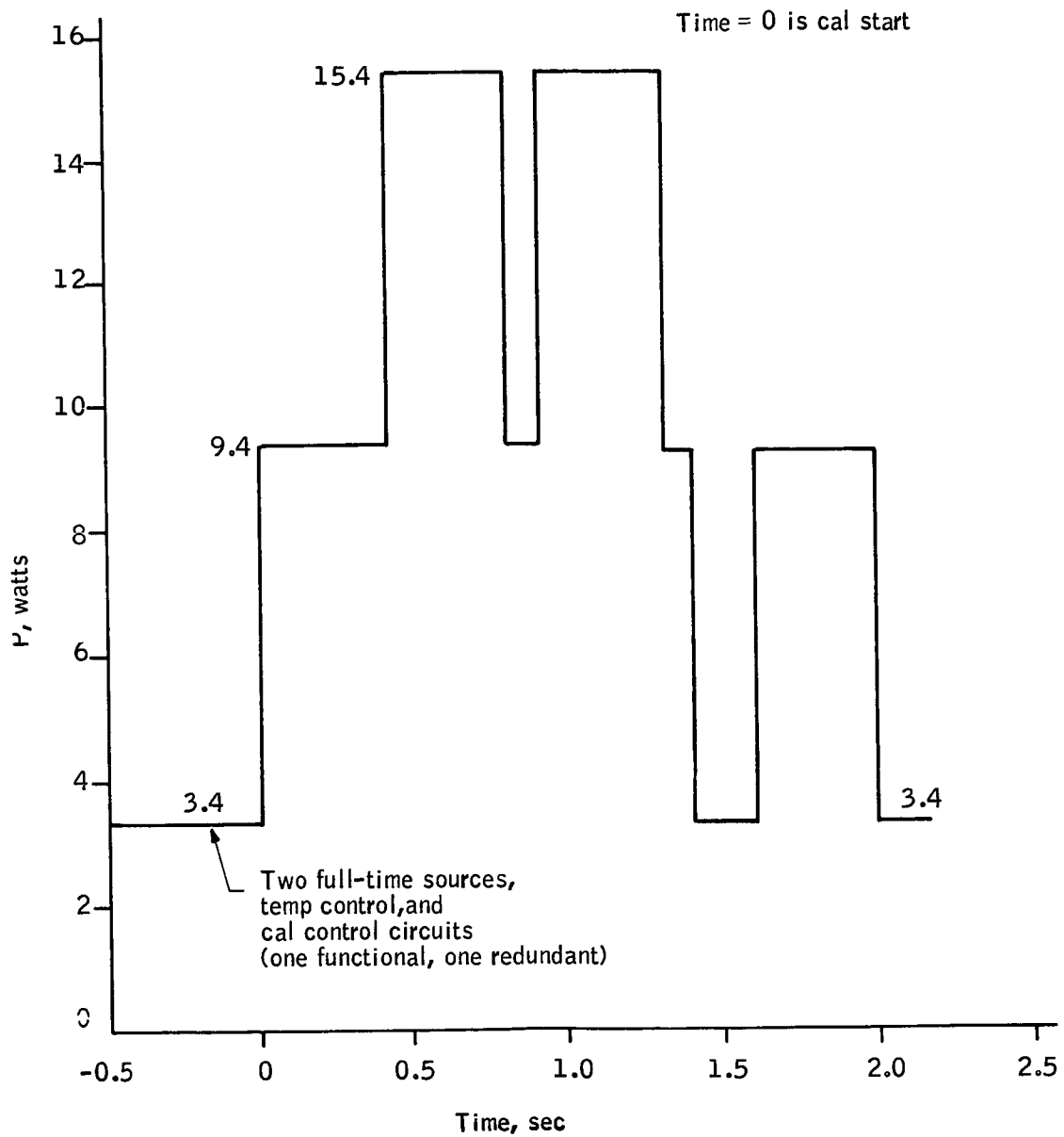
Figure 119. In-Flight Calibration Circuits Power Profile

4. The spectral radiance in the radiometer spectral interval and the radiant power which is detected by the radiometer from these objects has been computed.

5. The threshold radiance level of the radiometer has been compared with known space objects to find which targets will be detected.

6. An analysis of the possibilities of presently undetected space targets with large infrared outputs has been made, and the probability of detecting previously unknown objects has been estimated.

Summary of results. -- It appears that only Mercury, Venus, Mars, Jupiter, earth and the moon and sun will be detectable by their self-emission. With the exception of possibly the moon, sunlight reflected by celestial objects is not sufficient to produce a detectable signal. The probability of detecting previously unknown space objects is extremely small.

Radiometer threshold and visible radiance. -- The radiometer threshold as defined by the minimum horizon radiance is

$$N_{min.} = 1 \times 10^{-6} \text{ W/cm}^2\text{-sr}$$

with a spectral interval of

$$\Delta \lambda = \lambda_1 - \lambda_2 = 16 \text{ microns} - 14 \text{ microns} = 2 \text{ microns}$$

and a solid-angle field of view of

$$\omega = \theta_1 \times \theta_2 = 0.2 \times 10^{-3} \text{ radian} \times 0.8 \times 10^{-3} \text{ radian}$$

$$\omega = 1.6 \times 10^{-7} \text{ sr}$$

The resulting minimum spectral radiance is

$$N_{\lambda \text{ min.}} = N_{min.} \Big/ 2 \text{ microns} = 5 \times 10^{-7} \text{ W/cm}^2\text{-sr-}\mu$$

and the spectral irradiance level for objects equal to or smaller than the field of view is

$$H_{\lambda \text{ min.}} = \omega N_{\lambda \text{ min.}} = (1.6 \times 10^{-7} \text{ sr}) \, 5 \times 10^{-7} \text{ W/cm}^2\text{-sr-}\mu$$

or approximately

$$H_{(15\mu \text{ min.})} = 8.0 \times 10^{-14} \text{ W/cm}^2\text{-sr-}\mu$$

An equation can be developed comparing visible spectral irradiance with source temperature of a constant infrared level. Analysis of the standard star irradiance with the blackbody equations shows

$$H_{\lambda \text{ max.}} = H_o \frac{\omega_{\lambda \text{ max.}}}{\omega}$$

where:

H_o = 2.27×10^{-12} W/cm^2, the irradiance of a zero bolometric magnitude star (blackbody total),

ω = $5.669 \times 10^{-12} \, T^4$ W/cm^2 - °K^4,

ω_λ = $1.29 \times 10^{-15} \, T^5$ W/cm^2 - °K^5 - μ, and

$H_{\lambda \text{ max.}}$ = $2.28 \times 10^{-4} \, H_o \, KT$ W/cm^2 - μ

where:

t = temperature (°K)

K = multiple of standard irradiance

$$H_{15\mu} = [H_{\lambda \text{ max.}} \, (T)] \, [H_{15\mu}/H_{\lambda \text{ max.}} \, (T)]$$

Since the ratio $H_{15\mu}/H_{\lambda \text{ max.}}$ (T) may be found on a blackbody slide rule or can be calculated, the temperature is the only variable.

310

$$H_{15\mu} = 8 \times 10^{-14} \text{ W/cm}^2 \text{ (threshold value)}$$

$$H_{\lambda \text{ max.}}(T) - 2.28 \times 10^{-4} H_o T \text{ W/cm}^2\text{-}\mu$$

$$H_o = 2.27 \times 10^{-12} \text{ W/cm}^2 \text{ standard}$$

$$\frac{H_\lambda}{H_{\lambda \text{ max.}}} = \frac{C_1 \lambda^{-5}}{e^{C_2/\lambda T} - 1} \left(1.2875 \times 10^{-11} T^5 \right)^{-1}$$

$$8.0 \times 10^{-14} = \frac{\left(2.28 \times 10^{-4} \right) \left(2.27 \times 10^{-12} \right) T K C_1 \lambda^{-5}}{\left(e^{C_2/\lambda T} - 1 \right) \left(1.2875 \times 10^{-11} T^5 \right)}$$

where the subterms are

$$C_1 \lambda^{-5} = 3.74 \times 10^{-12} \times (1.5 \times 10^{-3})^{-5}$$

$$= 492$$

$$\frac{C_2}{\lambda t} = \frac{1.43848}{1.5 \times 10^{-3} T} = \frac{960}{T}$$

$$\frac{\left(8.0 \times 10^{-4} \right) \left(1.2875 \times 10^{-11} \right)}{\left(2.28 \times 10^{-4} \right) \left(2.27 \times 10^{-12} \right)} = 1.995 \times 10^{-9}$$

$$1.995 \times 10^{-9} T^4 (e^{960/T} - 1) + 492 K$$

$$K = 4.05 \times 10^{-12} T^4 (e^{960/T} - 1)$$

This equation may be plotted in terms of K by substitution of a series of T values to give the necessary irradiance to reach the system threshold as a function of temperature; this substitution gives the values listed in the table below.

Temperature, T, °K	K
960	5.92
9600	3.62×10^3
96	7.57
200	0.784
2000	40
20 000	6.38×10^4
150	1.2
1500	18.4
50 000	1.35×10^4
300	0.770
3000	123.6
600	2.06
6000	910.0
250	0.725

The factor K can be converted to bolometric magnitudes by

$$m_b = -2.5 \log K$$

The bolometric magnitudes may be converted to equivalent visual magnitudes by using the bolometric correction factor which is a function of temperature

$$M_v = m_b + BC$$

312

The BC values have been taken from reference 22 for the temperature interval from 30 000°K and extrapolated down to 800°K.

Star background analysis. -- The field of view of the radiometer is 0.2 x 10^{-3} rad x 0.8 x 10^{-3} rad or 5.25 x 10^{-4} degrees^2.

On the basis of star magnitudes and distribution from ref. 22 as plotted in ref. 23, there would be (mean) one star in the radiometer field of view which is +17, the visual magnitude, or brighter of which 0.0525 star is the 12th magnitude or brighter. Those stars whose magnitude is +12 or less would only be detectable if their temperature was less than 800°K.

The required visual magnitude for detection by the radiometer increases with increasing star temperature for the same radiometer threshold. There are very few M-type stars; they represent 2.7 percent of all stars brighter than M_v = 8.5.

The MO-type star has a temperature of 3600°K and the M5 type has a temperature of 2800°K; however, cooler objects with temperatures as low as 700°K have been detected (ref. 24).

Tables 22, 23, and 24 (ref. 23) show that there is a very small probability of detecting stars with the radiometer because there are very few red stars of high radiant intensity. The following stars from these tables are shown in the table below.

No.	Name	Type	Visual magnitude	Bolometric
1	Betelguese	M2	+0.7	-0.7
2	Sirius	A1	-1.43	-1.94
3	Canopus	FO	-0.77	-0.77
4	Arcturus	KO	+0.03	-0.14
5	Rigil Kent	G2-K3	-0.27	-0.36
6	Mira	M6	+1.9	-0.5
7	ν Cru.	M3	+1.6	-0.2

TABLE 22. - BOLOMETRIC CORRECTIONS FOR MAIN SEQUENCE STARS

Type star	Effective temp., °K	Bolometric correction
O5	35 000	5. 0
B0	22 000	2. 8
B5	14 000	1. 4
A0	10 700	0. 6
A5	8 500	0. 2
F0	7 400	0. 0
F5	6 500	0. 0
G0	5 900	0. 05
G5	5 500	0. 1
K0	4 900	0. 17
K5	4 200	0. 6
M0	3 600	1. 2
M5	2 800	2. 4

TABLE 23. - TARGET STAR DISTRIBUTION BY TYPE

	O	B	A	F	G	K	M	Other
Average Distribution, $M_v < +8.5$	<1%	10.5%	22.3%	18.6%	14.3%	31.9%	2.7%	1%
The 20 brightest stars, $M_v < +1.50$	--	6 / 30%	5 / 25%	2 / 10%	3 / 15%	2 / 10%	2 / 10%	--
The 40 brightest stars, $M_v < +2.00$	--	15 / 38%	10 / 25%	4 / 10%	2 / 5%	6 / 15%	3 / 7%	--
The 100 brightest visual stars, $M_v < +2.65$	4	32	23	9	7	17	7	1[a]

[a] WC7, very hot

TABLE 24. - DISTRIBUTION OF 100 BRIGHTEST STARS
BY TYPE

Type	00-4	05-9	B0-4	B5-9	A0-4	A5-9
Count	--	4	19	13	20	3
Type	F0-4	F5-9	G0-4	G5-9	K0-4	K5-9
Count	4	5	2	5	13	4
Type	M0-4	M4-9		WC-7		
Count	6	1		1		

Only Betelgeuse of the first 20 bright visual stars approximately equals radiometer threshold in terms of temperature and magnitude. A search of the hundred brightest stars, however, yields two at longer wavelengths.

The star Mira (θ Cet.) has the greatest radiant intensity in the spectral range of the radiometer; however, this intensity is approximately a factor of 40 below the radiometer threshold.

Since the redder stars most closely approach the radiometer threshold, it is necessary to search for these stars. A measurement program extending into the infrared has been conducted and reported in references 24 and 25. Reference 24 reports measurements made up to 20 microns, but no magnitude information is given. The data of reference 25 extends up to 0.9 microns and can be used to select very red stars. The very red objects do not show as much difference in their visual and 0.9 micron magnitude as the M type stars and this partially negates a search through the list of 1325 stars which are listed in reference 25.

Only two stars were noted that approached the I magnitude (0.9 micron) of Betelgeuse; these stars are listed below.

Name	Type	M_v	M (J)
α Ori	M2	+0.69	-2.3 Betelgeuse
α Her	M5	+3.06	-1.17
β Gru	M3	+2.10	-1.58
X Cyg	S10.1e	+10.31	+1.15 2300°K

One object having a very large increase in I magnitude was noted (see last item in table above).

No stars in the list exceeded, however, the radiometer threshold. A further extension of measurements to 3.4 microns is contained in reference 26. The star X Cyg and several other stars were noted whose infrared output was increasing; however, these were M5 to M8 stars of low intensity whose bolometric magnitudes were below the radiometer threshold.

A further source of information on very red objects was found in reference 27, however, no sources had sufficient energy to approach the radiometer threshold. The object "R Mon" is considered a protostar with a hot core and a cooler, less dense shell, but "R Mon" has a bolometric magnitude of approximately 9.2 which is well below threshold. Simple correction from the 12.4 visual magnitude based on temperature and blackbody radiation law would give a bolometric magnitude of -0.6 which would be very close to the radiometric threshold. Thus, the one known cool object is not detectable even though simple extrapolation would place it in the probable detection area.

<u>Related star data</u>. -- Project Defender (reference 28) was a measurement program to verify various blackbody models of infrared stellar radiation. Only one star was measured in the 7.8-to 13.2-micron band; this was Alpha Hercules whose observed power was 2.75×10^{-14} W/cm^2. Calculations based on measurements made in the visible spectrum, 2.0 to 2.4 microns and 3.4 to 4.0 microns, would predict a power level range of 1.5 to 1.32×10^{-14} W/cm^2 in the 7.8 to 13.2 micron band. Alpha Hercules is an M5-II star with a temperature of 2550°K to 2680°K having a visual magnitude of +3.5. This is approximately 2.6×10^{-15} W/cm$^2\mu$ and the radiometer at 15 microns would receive only about 0.7×10^{-16} W/cm$^2\mu$. As the radiometer threshold is 8×10^{-14} W/cm$^2\mu$, the star will not be detected.

A measurement was made on Betelgeuse (α Ori) under a program conducted by the California Institute of Technology. The measured value was 3.90×10^{-15} W/cm$^2\mu$ at 9.7 microns with a probable error of 0.09×10^{-15} W/cm$^2\mu$ with systematic errors of 20 percent possible in the blackbody calibration. The theoretical calculation based on visual measurements predicted 1.3×10^{-14} W/cm$^2\mu$. Irradiance at 15 microns is approximately 1/3 of irradiance at 9.7 microns, which places Betelgeuse at about 1/70 of threshold or about 4.5 bolometric magnitudes below threshold.

<u>Planetary irradiance</u>. -- Sunlight from the planets was the initial source investigation. The field of view of the radiometer is 0.2×10^{-3} by 0.8×10^{-3} radians or 41 arc seconds by 164 arc seconds. Jupiter subtends an angle of 32 to 50 arc seconds, and Venus subtends an angle of 10 to 62 arc seconds. At times, these two planets will have a larger diameter than the narrow dimension of the radiometer field of view; however, all other planets are smaller than the field of view. Venus is complicated by the illuminated crescent since its orbit radius is less than the earth's orbital radius.

Planet	Bolometric magnitude	Effective temperature, K reflected sunlight
Venus	-4.4	5900
Mars	-2.8	5900
Jupiter	-2.5	5900
Mercury	-1.2	5900
Saturn	-0.4	5900

Reference to the listed bolometric magnitudes of the planets (based on reflected sunlight) shown above illustrates that none of the planets exceed the radiometer threshold by reflected sunlight.

A convenient check of the initial calculations can be made for the planet Venus. A totally reflecting star-like object having the appearance of a zero-magnitude star and a temperature of less than 5900°K produces a flux level of 2.3×10^{-12} W/cm^2 at the edge of the earth's atmosphere; however, only 0.92×10^{-16} W/cm^{2}μ are received in the interval at 15 microns. Venus is almost -4.4 magnitudes or 57 times brighter yielding 0.53×10^{-14} W/cm^{2}μ at 15 microns.

As previously calculated, the radiometer threshold is 8.0×10^{-14} W/cm^{2}μ at 15 microns or 15 times greater than the signal from Venus' reflected sunlight.

Reference 29 predicts slightly lower values for sunlight as shown below.

Planet	Irradiance at 15 microns W/cm^{2}μ
Mercury	4.5×10^{-16}
Venus	4.5×10^{-15}
Mars	6.0×10^{-16}
Jupiter	6.0×10^{-16}
Saturn	3.6×10^{-16}

Planetary self-emission. -- The planets emit energy as a function of their temperature. Their output in the radiometer spectral region can be calculated to determine if they are detectable.

The equation used to calculate the irradiance is

$$h_{15\mu} = \left(\frac{H_{15}}{H_{\lambda\ max.}}\right)\left(\frac{H_{\lambda\ max.}}{\pi}\right)\left(\frac{\pi d^2}{4D^2}\right)\ (1 - A)$$

where:

  d = planet diameter,

  D = mean closest approach, and

  A = visual albedo.

Values for these various parameters are listed in Table 25. The table shows that Saturn is slightly below the threshold of the radiometer whereas Jupiter, Mars, Venus, and Mercury are progressively above threshold. The values are calculated for the closest distance between the earth's mean orbit and the mean orbit of the planet. For the inner planets, this indicates that they will be near the earth-sun line. The data of reference 29 for self-emission, shifted to 15 microns, is tabulated below.

Name	Irradiance at 15 microns $W/cm^2\mu$
Mercury	480.0×10^{-15} (greatest elongation)
Venus	342.0×10^{-14} (greatest elongation)
Mars	274.0×10^{-14} (opposition)
Mars	56.5×10^{-14} (quadrature)
Jupiter	24.4×10^{-14}
Saturn	1.63×10^{-14}

This is identical with the previous table except for the planet position in orbit for the first three planets.

Moon radiance. -- The moon is sufficiently large to always fill the radiometer field of view. The radiometer will see direct reflected sunlight and the emitted radiance of the moon.

The moon has a bolometric magnitude of -12.7 and a color temperature of 5900°K.

The brightness of the full moon compared to a zero magnitude star would be

$$\frac{B_1}{B_2} = \log^{-1}\left(\frac{-12.7}{-2.5}\right) = \log^{-1}(5.08) = 1.2 \times 10^5$$

The subtended angle of the moon from near earth is

$$\omega = \frac{\pi}{4}\left(\frac{3.44 \times 10^3}{0.384 \times 10^6}\right)^2 = 63.2 \times 10^{-6} \text{ sr} .$$

320

TABLE 25. - INFRARED RADIANT CHARACTERISTICS

Planet	Albedo	Temp, °K	Diameter, x 10^3 km	Distance, x 10^6 km	Irradiance x 10^{-14} W/cm^2 μ
Mercury	0.06	690	4.842	91.6	1017.0
Venus	0.76	330	12.332	41.4	1462.0
Mars	0.15	285	6.664	78.3	280.0
Jupiter	0.50	135	139.800	628.3	25.0
Saturn	0.50	120	115.100	1276.6	1.7
Uranus	0.66	<100	47.400	2720.0	0.006

while the radiometer sees only

$$\omega' = 1.6 \times 10^{-7} \text{ sr}$$

Then,

$$\frac{B_1}{B_2} \frac{\omega'}{\omega} = 1.2 \times 10^5 \left(\frac{1.6 \times 10^{-7} \text{ sr}}{63 \times 10^{-6} \text{ sr}} \right) = 3.05 \times 10^2$$

$B_2 = 0.92 \times 10^{-15}$ W/cm$^2\mu$ at 15 microns for a zero-magnitude star at 5900°K.

Therefore, the radiometer will be irradiated by

$$B_1 = (3.05 \times 10^2)(0.92 \times 10^{-16})$$

$$B_1 = 2.82 \times 10^{-14} \text{ W/cm}^2\mu$$

which agrees with reference 29 when corrected for the field of view.

Self-emission from the moon can be calculated from its temperature. The dark moon has a temperature of approximately t - 120°K and a sunlit value of t - 380°K. Since the lowest moon temperature is 120°K, the signal calculation based on this temperature is

$$h_{15\mu} = \left(\frac{H_{15\mu}}{H_{\lambda \text{ max.}}} \right) \left(\frac{H_{\lambda \text{ max.}}}{\pi} \right) \left(1.6 \times 10^{-7} \text{ sr} \right)$$

$$h_{15\mu} = \left(3.8 \times 10^{-2} \right) \left(\frac{3.3}{\pi} \times 10^{-1} \times 10^{-4} \right) \left(1.6 \times 10^{-7} \right) \text{ W/cm}^2\mu$$

$$h_{15\mu} = 6.4 \times 10^{-14} \text{ W at 15 } \mu \text{ from 120°K.}$$

The 10-micron wavelength temperature as reported in reference 22 is 260°K, however, no mention is made of the sun phase. The spectral irradiance is:

322

$$h_{15\mu} = \left(\frac{H_{15\mu}}{H_{\lambda\ max.}}\right) \left(\frac{H_{\lambda\ max.}}{\pi}\right) \left(1.6 \times 10^{-7}\ sr\right)$$

$$h_{15\mu} = (0.46) \left(\frac{1.5}{\pi} \times 10^{1} \times 10^{-4}\right)\left(1.6 \times 10^{-7}\ sr\right)$$

$$h_{15\mu} = 3.52 \times 10^{-11}\ W/cm^{2}\mu \text{ at 15 microns from } 260°K.$$

The visual albedo of the moon is very low (0.07), so that the visual emissivity should be 0.93. If the emissivity remains constant at 15 microns, the calculated spectral irradiance values would decrease approximately seven percent.

At 120°K, the moon self-emission would equal the radiometer threshold (within the accuracy of these calculations). At the higher temperature, 260°K, the signal would be well above threshold. Therefore, the moon would be detected by its self-emission. The reflected sunlight signal is approximately 1/3 of the threshold, and therefore detection would be marginal and dependent on whether the local surface was dark or light.

ATTITUDE DETERMINATION SUBSYSTEM

INTRODUCTION

Basic Requirements

The requirements on the attitude determination subsystem are derived from the requirement to fix the position of a point on the measured radiance profile within an error compatible with the radiometer radiance measurement requirements. This error has been established as one-quarter of a kilometer, one sigma. Translation of this error to an equivalent angular error in determination of the direction of the optical axis of the radiometer yields an angular error of 20 arc seconds. This requirement has been allocated as shown in Table 26.

TABLE 26. - ATTITUDE DETERMINATION ERROR ALLOCATION

Item	Allocation, arc seconds
Attitude of attitude determination subsystem with respect to the celestial sphere	± 14
Orbit determination	± 10
Spacecraft data processing	± 3
Time correlation	± 3
Ground data reduction and star ephemeris	± 3
Alignment of radiometer with respect to to the attitude determination subsystem	± 8.6

Error Allocation with Attitude Determination Subsystem

The basic constraint of a rotating spacecraft with passive scanning implies sampling of the celestial sphere, as distinguished from a continuous-attitude information input. The impact of this discontinuous input is a strong feedback into vehicle dynamics, much stronger than would be implied by a tracking system. Either stringent requirements must be placed upon vehicle angular rates and acceleration or a precise model of the vehicle motion must be available to allow interpolation across those intervals where attitude data is unavailable. The error allocated to the attitude of the subsystem with respect to the celestial sphere is then attributable to two sources: (1) the measurement of the line of sight itself and (2) the error in the model of vehicle motion. It is

324

assumed that these are small, independent errors and add as variances of independent distributions. The error is then divided equally between the two sources, yielding an allocation of 10 arc seconds for measurement error and 10 arc seconds for model error. This section of this report treats only these errors.

System Design

General instrument selection. -- The data requirements dictate a sun-synchronous polar orbit, which places the vehicle in the sunlight for approximately 65 percent of the orbit. One of the major problem areas in starmapper design is the design and testing of baffles for operation in sunlight. If a solution can be found to the attitude determination problem using the sun alone during the daylit portion of the orbit, this problem can be completely avoided. The solution clearly depends upon the predictability of the vehicle dynamics. An analytical study of the dynamics, a modeling of the vehicle, and a modeling of a data reduction system indicates that the sun alone is adequate for solution of the attitude determination problem if sufficient information is gained from the data on the dark side. Accordingly, a mechanization using an unbaffled star-mapper and sun sensor was selected.

Starmapper Design

The basic parameters in starmapper design are field of view, resolution and sensitivity. Field of view and sensitivity are directly related in a tradeoff defining sample rate with resolution defining the instrument accuracy.

Sample Rate

A critical parameter in starmapper design is the number of stars required per unit time; this is related to the vehicle model and is essentially the sample rate on vehicle position. It can be demonstrated that, for the general case of an untorqued vehicle, three stellar observations are adequate for a solution. For a torqued vehicle, where there is no general analytical solution, the required sample rate cannot be determined without a numerical solution. Since, for this study, the numerical investigation of the equations of motion was concurrent with sensor design, the required sample rate could not be precisely determined before proceeding with instrument design. Accordingly, a conservative position was taken and the number of stars was fixed at four. Since each star observation yields two independent equations, this number allows an eight-variable fix on attitude for each vehicle revolution. The number of variables required to fix a solution is presently estimated to be 15 with several of these variables having periods of the order of several vehicle revolutions; hence, with 4 stars per revolution, the solution is over determined and the excess data can be used in an error reduction system.

Having defined, somewhat arbitrarily, a requirement for four stars per vehicle revolution, a strong tradeoff between instrument field of view and sensitivity exists. The basic mechanical parameters of an optical system are aperture and f/number, aperture controlling sensitivity, and f/number controlling

achievable resolution. It is desirable to hold aperture within reasonable limits. The sensitivity of a device, for fixed f/number, is directly proportional to aperture diameter. Establishing a base point for illustration, the requirement for 4 stars per revolution, at a sensitivity equivalent to +3.2 visual magnitude, yields a 3 inch aperture for approximately 10 to 1 signal-noise ratio at a field of view of 20 degrees.

Instrument resolution is defined as the variance of the distribution of output timing errors from a discrimination system, these time errors referenced to an attitude error through the vehicle spin rate. At a spin rate of 3 rpm, the time error equivalent to 10 arc seconds is 154 microseconds.

The three parameters affecting resolution (to first order) are optical resolution (blur circle), slit width, and amplifier-detector bandwidth. The simplest system has a transfer characteristic such that the output has a time resolution less than 154 microseconds. Since this implies narrow slit width and wide bandwidth, this system is a limiting system from aperture diameter (i.e., this system has largest possible aperture) and optical resolution. It is of interest to determine whether a more complex system has significant impact upon these optical parameters. From the results reported below, a system which relies upon pulse interpolation has significant advantages and allows reduction in aperture, increase in optical resolution, increase in slit width, and decrease in amplifier bandwidth.

A basic requirement of the system is data storage. With the bandwidth required to handle time resolutions of the order cited above, an on-board discrimination technique is a necessity.

To ensure that resolution is not lost, a system which does not introduce errors of the order of the required time resolution must be designed. The simplest system for noise discrimination is amplitude thresholding. Simple thresholding, however, requires multiple-sample output to hold resolution. The minimum number of samples required per unit reciprocal bandwidth is of the order of 4 if a data interpolation system is used on the ground and 9 to 10 otherwise. To relieve storage requirements, it is of interest to go to the next level of complication and determine whether on-board interpolation is feasible.

A simple system, utilizing division between two threshold excessions, was found by simulation to yield an interpolation factor of the order of 9, referenced to the optical blur circle at the minimum signal-noise ratio.

The instrument design described below is a wide-field system with narrow-band output and on-board interpolation and discrimination.

Sun Sensor Design

The basic requirements for the sun sensor are wide field to accommodate possible variations in orbital position relative to the sun and accuracy of 10 arc seconds. Since sensitivity is not a factor here, optical aperture (and hence output bandwidth) is not an important parameter. Solar characteristics were investigated in the literature and it appears that the solar limb is sufficiently

well defined and stable to provide a reference to 10 arc seconds. The conceptual instrument design is a 35-degree system with photo-diode detection and wide band output with amplitude difference detection.

Estimation Model

Given discontinuous data derived from attitude sensors, the vehicle attitude must be determined during the horizon crossing, which clearly implies an interpolation technique. The use of continuous smoothing with the Kalman-Bucey optimization theory was investigated. This approach has the advantage of a continuous computation of the covariance matrix, giving a continuous estimate of the error. Since the system of equations governing the motion is nonlinear and the noise model is highly correlated over long-time intervals, this approach was discarded in favor of a discontinuous least-squares solution. A program incorporating this solution was developed and tested against simulated star transits, derived from a deliberately perturbed model of the vehicle motion.

INSTRUMENT DESIGN

The function of the attitude determination instrument system is to determine the attitude of the radiometer within accuracy requirements for any time during the one-year operational life of the vehicle. The following paragraphs describes the evaluation of the various design parameters which must be considered to establish the system's overall design.

Starmapper

A starmapper is an optical system which scans a band of the nighttime sky by means of the rotational motion of the vehicle. When a star image crosses a reticle slit pattern located at the focal plane of the optical system, the transit is noted by a photodetector. This signal triggers a clock circuit which then records the time of the star transit in the data storage memory. Thus, the starmapper system consists of the optical system, the slit reticle, the photodetector, and the necessary electronics such as power supplies, amplifiers, filters, level detectors, counters, and switching circuits to control the various functions. A schematic diagram of these component parts is shown in Figure 120 to show the overall relationship.

Location of starmapper optical axis. -- To provide sufficient data for the attitude determination algorithm with some redundancy, a requirement was established for detection of at least four stars each scanning revolution of the space vehicle. The means by which this may be accomplished is a function of the following:

- Limiting star magnitude or instrument sensitivity
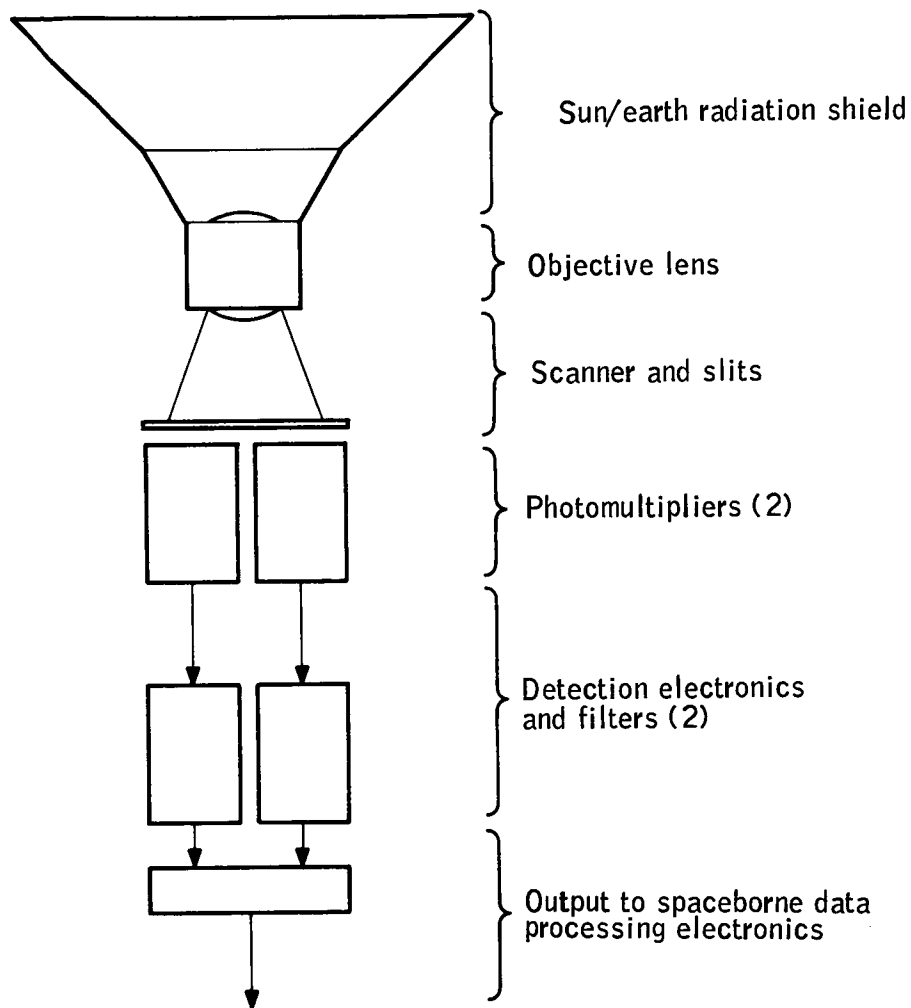
Figure 120. Component Parts of Sensor, Schematic Only

- Instantaneous field of view

- Length of scanned path (i. e., total solid angle)

Establishment of these parameters must start with a calibrated stellar catalog. Table 27 shows the number of stars in the celestial sphere as a function of visual magnitude.

TABLE 27. - NUMBER OF AVAILABLE STARS

Visual magnitude	Number of stars
- 2 to 0	2
0 to 1	9
1 to 2	28
2 to 3	106
3 to 4	307
Total	452

There are 41 253 square degrees in the celestial sphere and approximately 365 square degrees must be scanned to allow detection of 4 stars of 4th magnitude or brighter, if stars were uniformly distributed. Because of nonuniformities in the area near the galactic poles, approximately 1000 square degrees must be scanned to detect 4 stars of 4th magnitude or brighter. Because of this large difference between viewing directions, studies were made of computer simulated scans of a catalog of real stars, rather than relying upon an assumption of uniform distribution.

The angle between the spin axis of the vehicle and the optical axis of the star-mapper (cant angle) defines the scanned solid angle of the starmapper. Figure 121 shows the relationship between the required instantaneous field of view and the cant angle required to detect four stars on the dark side of the earth. These data were obtained from worst-case conditions obtained from computer runs of the Control Data Corporation (CDC) star catalog. A simulated scan was made in each of four orbital positions for each orbit with a precession increment of one degree between each orbit. These curves were then made from the worst conditions of the 1440 positions checked for each cant angle and field of view.

Another effect of cant angle is shown in Figure 122 which shows the starmapper error required to achieve 10 arc seconds of accuracy in the pitch axis. This is due to the functional form of the transformation from an oblique axis to the pitch (radiometer) axis.
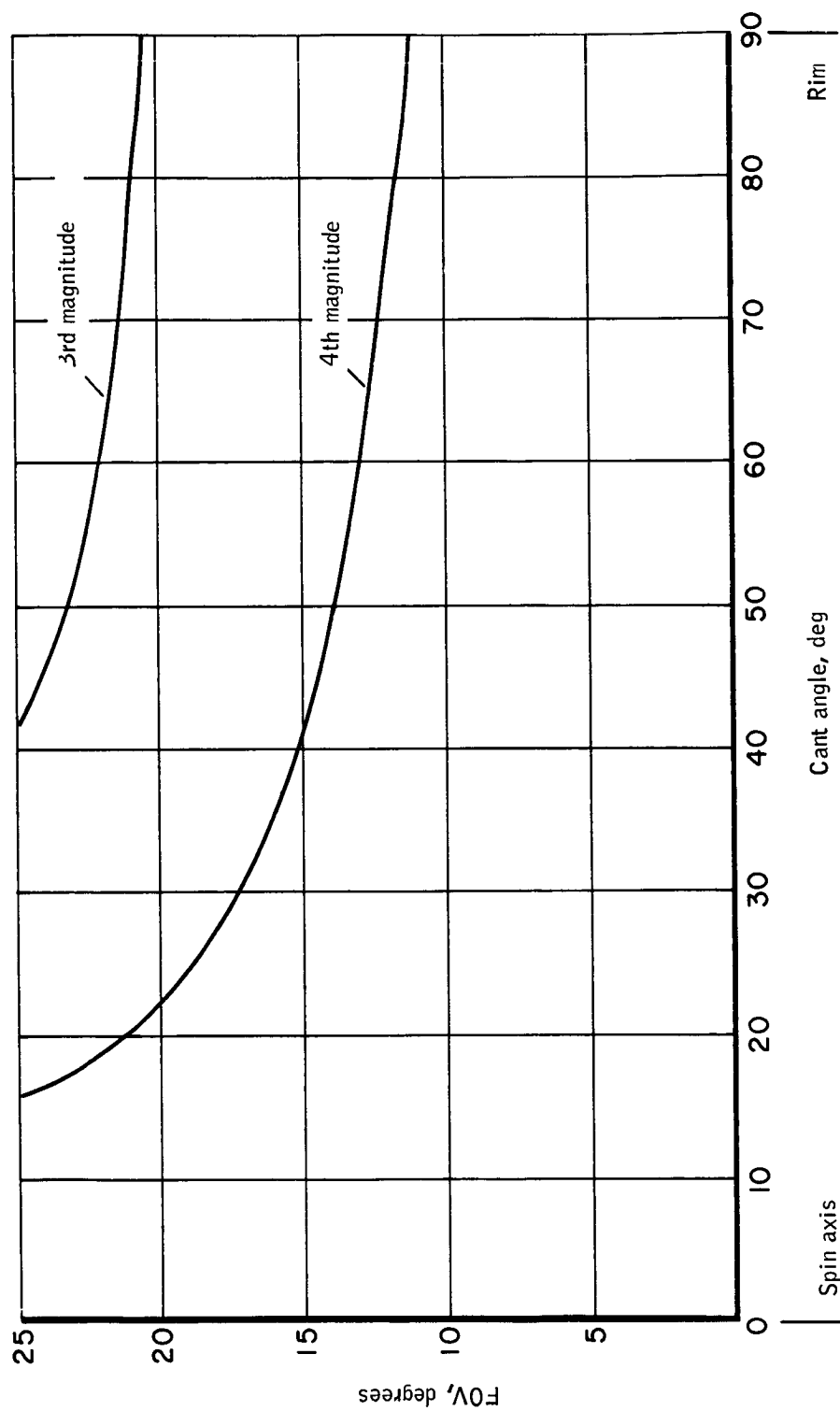
Figure 121. Cant Angle and Field of View Required to Detect Four Stars on Night Side
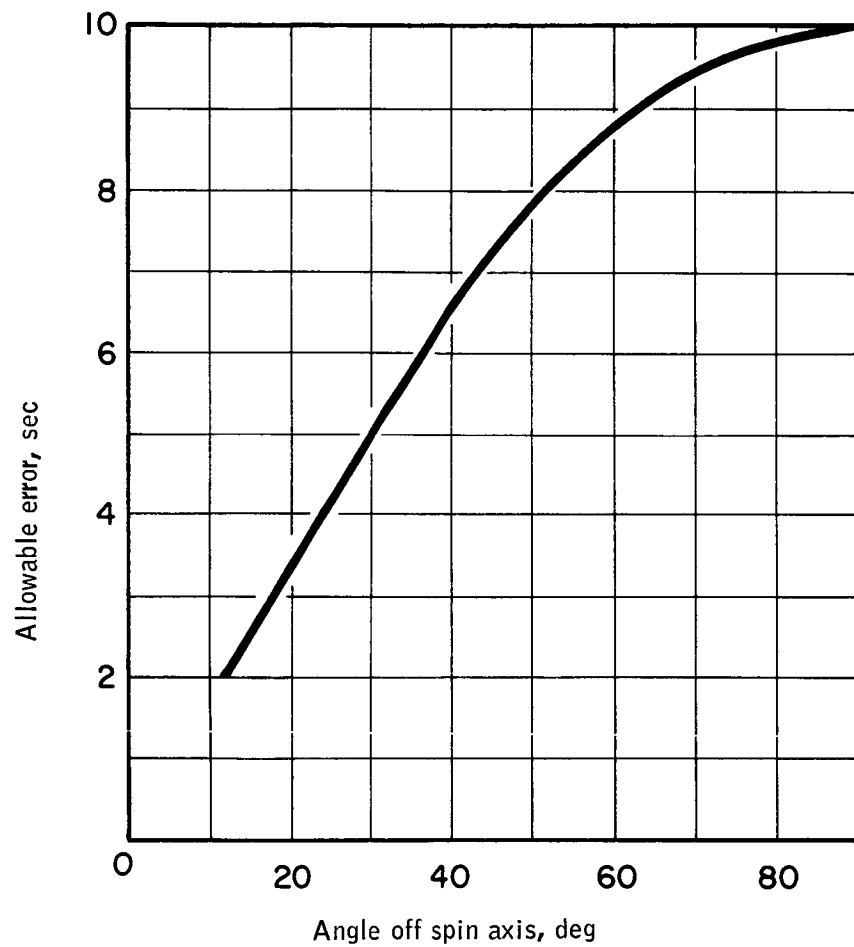
Figure 122. Allowable System Error for Various Optical
Axis Directions

It may be seen from Figures 121 and 122 that from considerations of instrument accuracy and minimum field of view required for a given limiting magnitude star, locating the starmapper in the same axis as the radiometer is the optimum position if stars are only to be scanned on the dark side of the earth. If the system were to be used for viewing stars on the daylight side, it would be necessary to locate the system closer to the spin axis in order to get it farther from the sun and to provide an extremely good light baffle to prevent the sunlight from entering the optical system. For daylight use, an angle of 50 degrees off the spin axis is an optimum compromise.

Sensitivity and field of view. -- From Figure 121, a clear tradeoff exists between the field of view and sensitivity. With an optical axis at 90 degrees. The choice lies between a sensitivity capable of detecting stars at approximately third magnitude with a 20-degree field or detecting stars at fourth magnitude with a 12-degree field. In general, resolution at wide field is more easily obtained than sensitivity. For feasibility design, the 20-degree field with sensitivity equivalent to +3.2 visual magnitude is chosen.

Nonuniformities in star count. -- The nonuniformities in the star count in an orbit are shown in Figures 123 and 124. These data were obtained from computer simulated scans. Parameters were 20-degree field of view, optical axis located 90 degrees from the spin axis, and earth blocking assumed below 25 degrees above the horizon. A simulated scan was made each five degrees along the orbit with the satellite spin axis in the direction 0 degree declination and 238 degrees right ascension. This orbit was chosen because it contains the widest variation in both magnitude and numbers of stars. Note that during this one orbit the limiting magnitude of the 4th brightest star varies from 1.8 to 3.2 and the number of stars brighter than 3.3 photographic magnitude varies from 4 to 24. Since it is desired to limit to six the number of stars detected during each scan because of memory capacity, it is obvious that the system must contain an on-board, automatic bias-level control to regulate the number of stars detected.

Since there is such an uneven distribution of stars in the celestial sphere, the question arises about the frequency of clustered stars and their effect on the proper operation of the system. A computer run was made simulating the satellite in orbits spaced 20 degrees apart in right ascension. Scans were made at 90-degree intervals in each orbit. The 6 brightest stars, which are also greater than 3.2 photographic magnitude, were determined with the printout identifying the stars and showing the angular separation in the spin plane.

On these scans, six stars brighter than the limiting magnitude were found in each case, except twice when there were only five stars and once with four stars. If clustering is defined as a group of two or more stars with individual separations of three degrees or less, the following star clusters were determined:

- Seven sets of doublets seen on separate scans

- One pair of doublets seen on the same scan
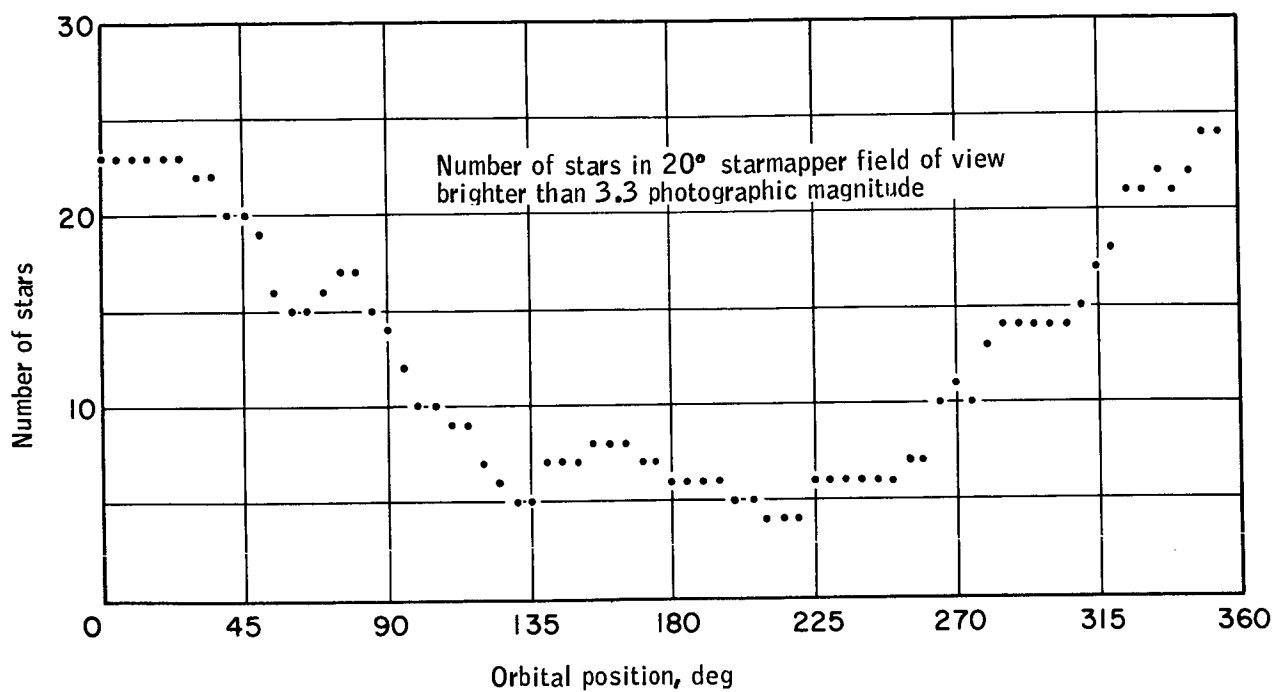
Figure 123. Variation in Number of Stars Detected During One Orbit
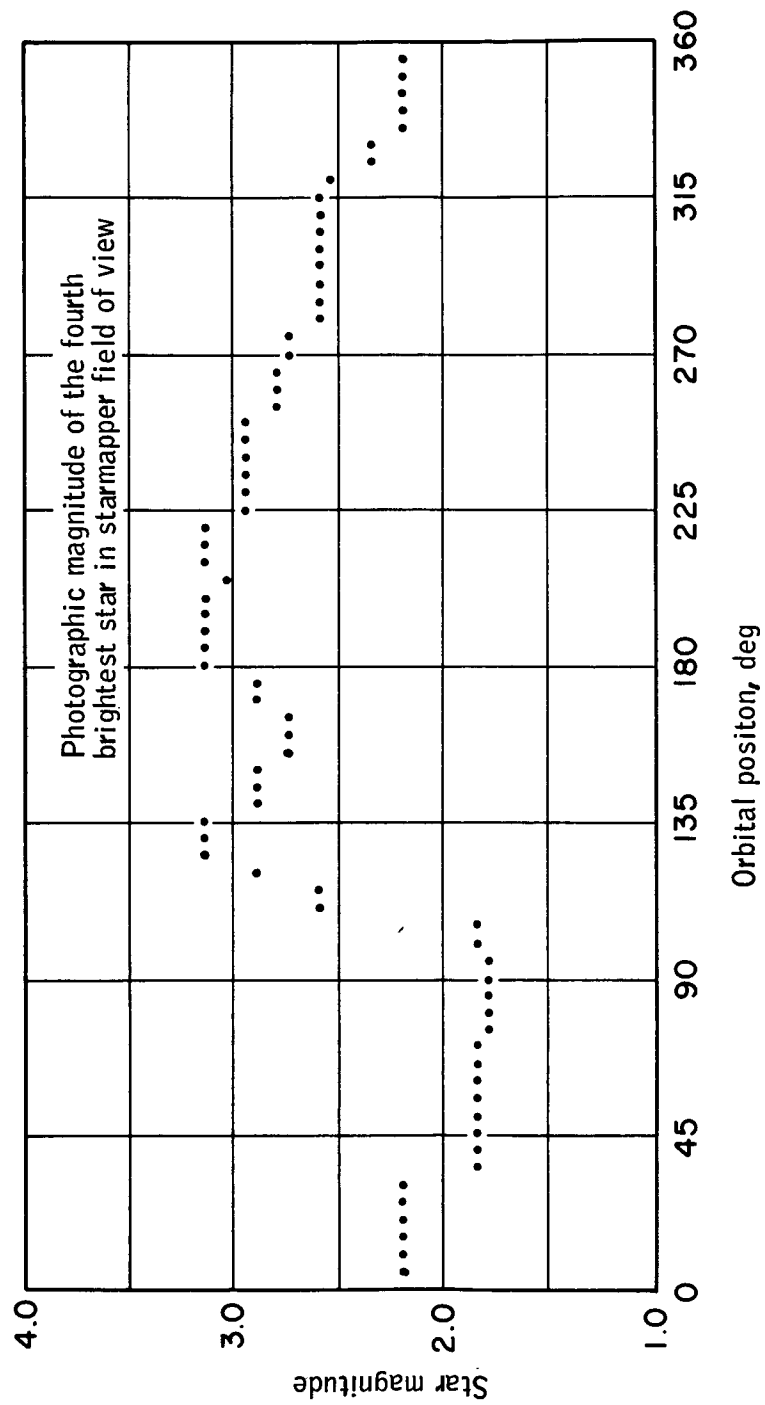
Figure 124. Variation in Detection Level Required During One Orbit

334

- Six sets of triplets seen on separate scans

- One set of quadruplets seen on the same scan

These clusters have the effect of reducing the number of usable stars per scan, but normally can be used as the equivalent of at least one star. None of these cases occurred when the total star count was already limited to four or five, so the usable star count remains at four or more stars per scan, except in the case of the quadruple cluster. However, two of these stars are an astronomical doublet with an angular separation of less than 0.001 degree and therefore will be seen by the reticle slit as a single star. This case then degenerates into a triplet, an additional star transit can be stored, so again there will always be at least four usable star transits per scan.

An equally important consideration for the accuracy of the system is the over-all spacing of the detected stars. Obviously, if all the stars are grouped in a short space along the spin plane the attitude determination of the vehicle will not be as accurate as for the case when the stars are scattered along the total scanning field of view. Due to the fact that the stars tend to be grouped into the Milky Way, which also contains the majority of the bright stars, it was found that a considerable degree of this type of grouping existed between the six brightest stars of each scan. Out of the available scan path of 170 degrees, practically all of the overall spacings were between 60 and 120 degrees, but this is considered to be very adequate for accurate attitude determination. In only one specific orbit is there a case where the total separation is as small as 30 degrees and this condition exists for only 40 degrees along the orbit. The exact effects of this relatively poor geometry must be determined by the computer-attitude accuracy study. Figure 125 shows the right ascension and declination of the vehicle along the polar orbit paths where these conditions exist. The number of degrees shown within the shaded area is the overall spacing of the star group, and the length of the area in declination is the duration of this condition.

Summary of basic parameters. -- The basic parameters that have been established are as follows:

- Optical axis -- 90 degrees away from the spin axis

- Field of view -- 20 degrees

- Limiting magnitude -- 3.2 photographic magnitude

- Automatic bias -- level control required

Basic system design. -- The optical aperture that is required to detect a 3.2 magnitude star is determined by the signal-to-noise ratio that will give a suitably small probability of false target detections. Factors that enter into this consideration are optical efficiency, quantum efficiency of the photodetector, image quality, slit reticle design, and data processing system design.
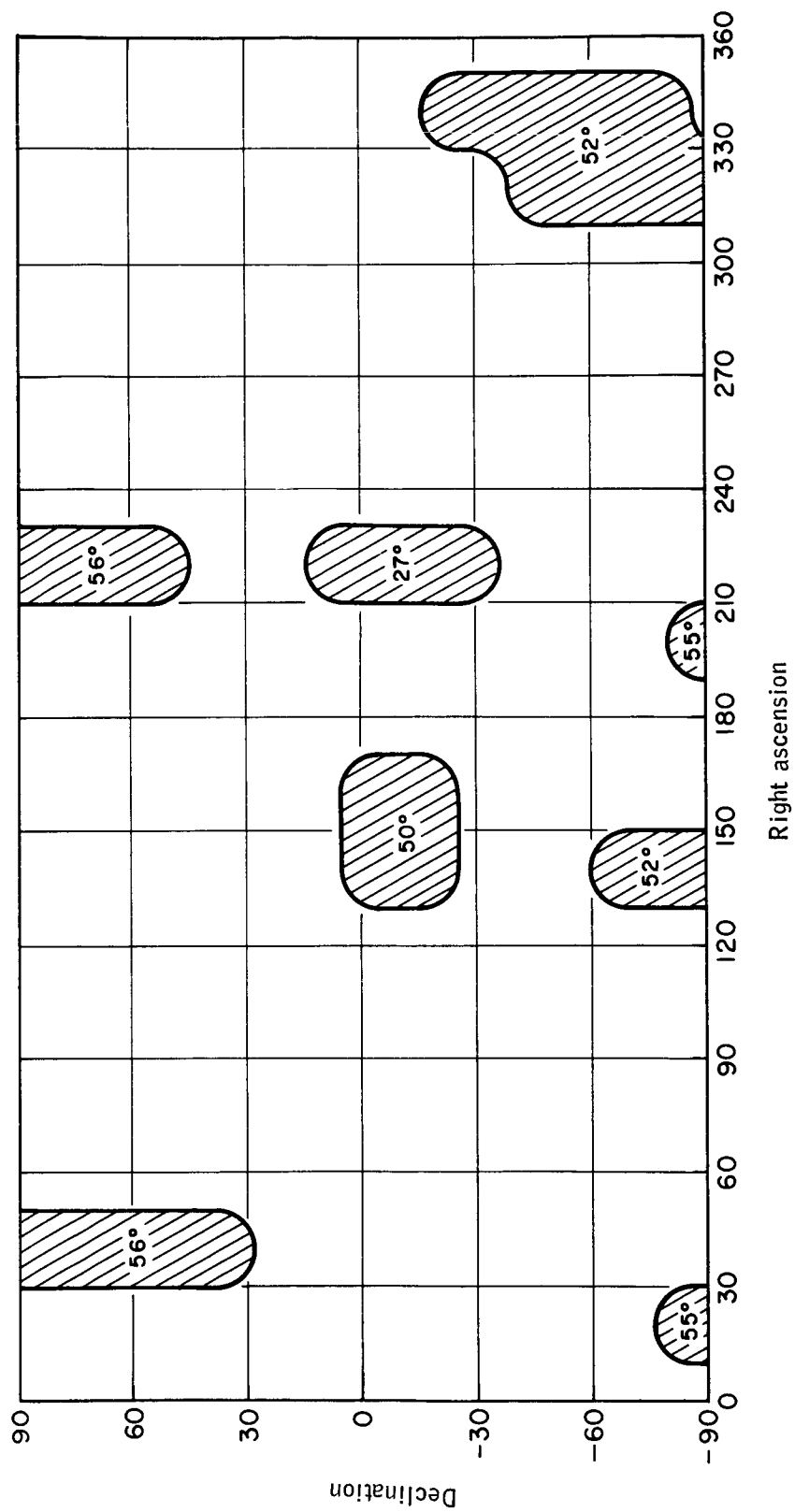
Figure 125. Starmapper Scanning Geometry

These factors are discussed in detail in a later section where an aperture diameter of three inches is shown to be adequate.

The overall characteristics of the optical design are dependent upon the geometrical relationships which exist between the reticle diameter, the objective lens diameter, the focal length, the field of view, and the f/number of the lens. The relationship between these quantities is completely established by the following expression:

$$D \times f/no \bullet FL = \frac{d}{2 \tan \frac{FOV}{2}}$$

which is most easily evaluated by use of the lens calculation nomogram shown in Figure 126.

There are two quantities of interest which are related through the simple geometry. The first is the reticle diameter, which must, by definition, subtend the required field of view at the focal surface. The second is the mechanical width of the slit, which must subtend the design resolution at the focal surface. It is desirable to limit the length of the starmapper to minimize mounting problems. It clearly is of interest to determine whether the required reticle is sufficiently large to require re-collecting optics to operate with available photomultipliers. It is also of interest to show that the design slit width is well within the range of allowable mechanical tolerances.

The resolution requirements of the system can be met by an f/4 system, while an f/2 system requires substantial effort to meet requirements. Focal length is then 12 inches (3 - inch aperture) and reticle diameter is 4.26 inches. The selected photomultiplier for this system has a one-inch diameter. Hence, re-collecting optics are required for this reason alone, although lack of surface uniformity in photomultipliers implies this solution also. The slit width requirement is to be approximately 60 arc seconds. Since the slit is in the focal surface, the above equation can be used directly, and the slit width is approximately 0.003 inch, well within the limits of mechanical tolerances.

Reticle design. --

Optical effects: Many different slit configurations have been investigated and used for starmapping systems. The most promising are the oblique V type and the radial X type which both provide the same information, namely, transit time, and angle off-axis. However, accurate measurement of these quantities is dependent upon the image quality, or blur circle size, and shape at the reticle plane. Aberrations are a monotone increasing function of axis. The aberrations most strongly affected by the off axis angle of the image are astigmatism, curvature of field, and distortion. Curvature of field can be reduced by using a curved focal surface.
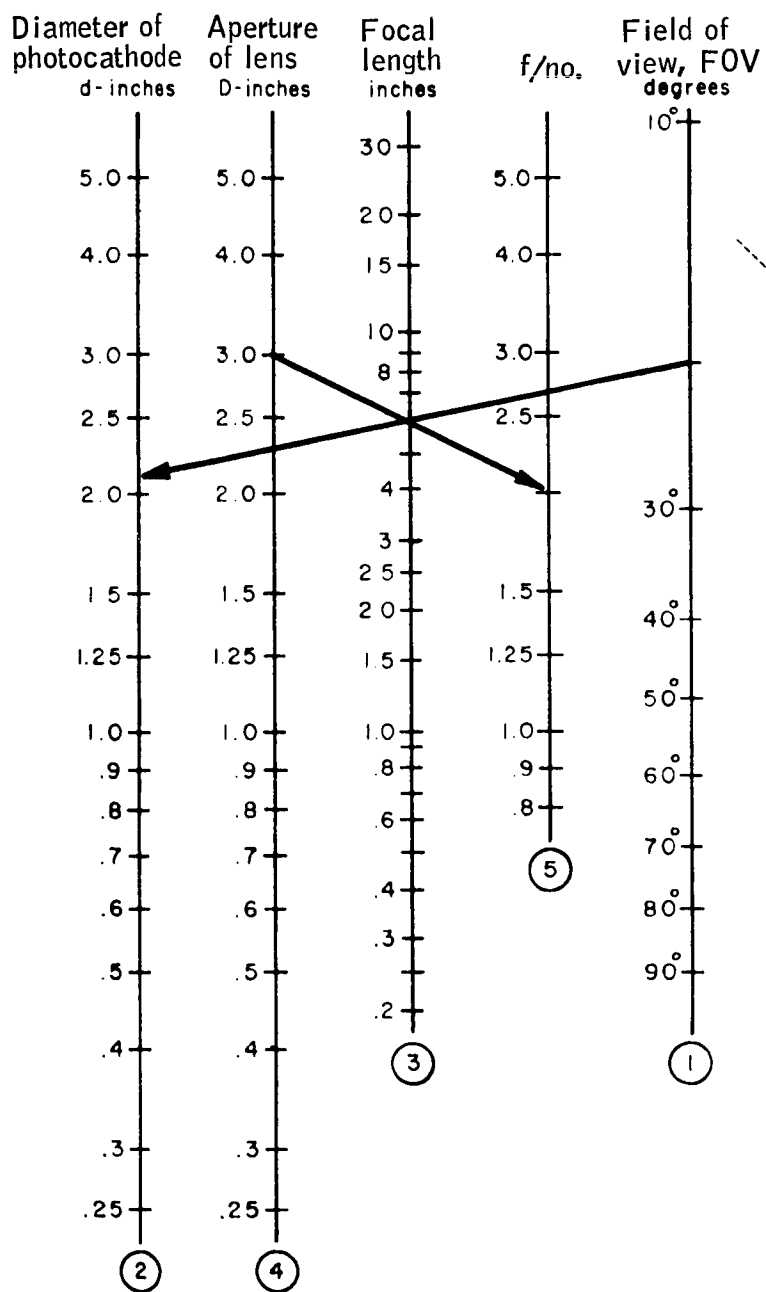
Figure 126. Lens Calculation Nomogram

With the system of data processing proposed here, i. e., image interpolation, the effect of symmetric aberrations is significantly reduced. Since astigmatism and distortion are radially symmetric aberrations, radial slits are not as strongly affected by these aberrations as oblique v slits. (See Table 28).

Chromatic aberrations are not severe for wavelengths greater than 3800 angstroms. Although the photomultiplier response permits the use of shorter wavelengths, it does not appear necessary for the following reasons:

- Optical filtering -- the attenuation of most optical glasses builds up sharply below 3800 angstroms and creates a need for more exotic materials and design techniques.

- Balmer limit -- even for very hot stars (B and O type) the radiation is severely attenuated in the stellar atmosphere for wavelengths below 4000 angstroms. The Balmer limit exists at 3646 angstroms. The Balmer discontinuity as a function of spectral class is not known exactly, but the following values may be taken as approximate:
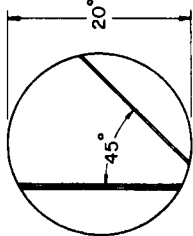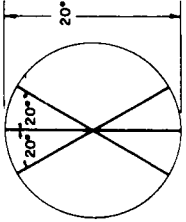
Spectral class	Discontinuity $(E\lambda+/E\lambda-$, $\lambda = 3646$ Å)
B0	1.15
B5	1.78
A0	3.09
A5	2.63
F0	1.82
F5	1.52

- Dispersion -- the dispersion of most optical glasses increases very rapidly below 4000 angstroms; thus, the problem of achromatism becomes large at shorter wavelengths.

Two other aberrations deserve mention; spherical aberration and coma. For the present design, a conservative approach using an f/4 optical system is recommended. Since spherical aberration is proportional to D^2 (Table 28), the f/4 design will reduce this effect by a factor of 16 from an f/1 system. Spherical aberration is not dependent on the off-axis angle. When using radial X-type slits, coma merely increases the size of the blur circle but does not introduce systematic errors. The oblique V-type slits are asymmetrically affected by coma; thus, this design approach cannot tolerate this aberration if any image interpolation technique which relies upon symmetry is to be used.

Data reduction effects: Two points which must be considered before the final choice of slit configuration are data reduction and star identification. The effects of the two basic slit configurations on the data processing problem in general and the slit matching problem in particular are considerably

339

TABLE 28. – IMAGE QUALITY REQUIRED BY TWO SLIT DESIGNS

	Spherical aberration, (t^0, D^2)	Coma, (t^1, D^2)	Astigmatism, (t^2, D^0)	Curvature of field, (t^2, D^0)	Distortion, (t^3, D^0)	Longitudinal chromatism, (t^0, D^0)	Lateral chromatism, (t^1, D^0)	Optical system alignment
1. Oblique V-type slits	Same	Must be accurately controlled, since coma can produce systematic errors (because slits are not radially symmetric) maximum interpolation of comatic image is not more than 1/4 blur circle size.	Combination of nonradial slits and t^2 dependence makes this configuration extremely dependent on amount of astigmatism. Will create a factor of 2 to 4 degradation in accuracy, typically.	Same	Nonradial slits produce difficult design problem since this aberration is proportional to t^3. If no distortion calibration is used, distortion must be kept below .01 percent.	Same	Same	Both centering and rotational alignment very difficult because of lack of axial aperture point and lack of radial symmetry.
2. Radial X-type slits	Since this aberration varies as t^0, it leads to a more or less symmetrical enlargement of the image diameter. Probably not a major source of design difficulty.	With this design coma has the effect of increasing the diameter of the blur circle, but only in proportion to the off axis angle (t^1). It does not produce a systematic error.	Strong off axis dependence (t^2). Focusing at sagittal image focus merely spreads image out along slit, but does not widen image. Therefore, astigmatism produces no degradation of accuracy.	Either scanner surface must be curved or field flattener must be not imposed during optical design, if flat field constraint is need cause no image degradation. With proper design this aberration	Radial slits make optical system measurement invariant with respect to distortion. This eases optical design problem.	This is not a major design problem since the spectral region lies within the limits: $3800 \leq \lambda \leq 6200$ angstroms.	This is not a major design problem since the spectral region lies within the limits: $3800 \leq \lambda \leq 6200$ angstroms.	Very easy since intersection of three slits coincide with optical axis: rotational alignment achieved by rotating sensor and maintaining movement of collimated star image along middle slit.

1. Oblique V-type slits — 20°, 45°

2. Radial X-type slits — 20° 20° 20°

t = off-axis angle

D = diameter of objective (for fixed focal length)

(t^0, D^2): this symbolism means that the aberration in question is proportional to t^0 and to D^2

different (slit matching means the recognition and association of all pulses from a given star on a given scan). This process must precede the actual identification of stars and is critical in terms of the total accuracy of the data processing problem. The two reticles discussed here are shown in Figure 127.

Figure 128 was drawn from a computer simulation of real stars transiting each of the two reticles using a 12-second spin period, a 5-degree cone angle, a precession rate of - 14.9 degrees per second, and a spin rate of 44.9 degrees per second, with the angular momentum vector on the celestial equator 90 degrees east of the first point of Aries. All stars of magnitude three and brighter were considered. The optical field of view in both cases was taken as 20 degrees centered about the optical axis which, in turn, was set 45 degrees off the spin axis. Other spin periods and off-axis angles will produce similar results. The first and tenth scans were chosen as representative and are the scans shown.

In Figure 128, time is the independent variable and the pulse heights are purposely made different for ease of visual matching. For the three radial slits, the pulses drawn above the line are from the upper three slit segments, and the lower segment pulses are drawn below the line. Similarly, for the vertical-canted configuration, the pulse from the vertical slit is drawn above the line, and the canted slit pulse is shown below the line. Pulses which transited only one of the two slits are marked with an X. These occurred due to the differing optical lengths of the slits and/or the effects of coning. In this figure, it is quite easy to determine the star transit sets, but actually the way the data reduction and star identification computer would see these same scans is shown in Figure 129 where all the pulses are identical. With three radial slits, the computer will sort for three equally-spaced pulses which then are stored as star transit signals. With the vertical-canted slit configuration in this star field, it becomes difficult if not impossible to correctly identify the matching transit pairs due to the differing time spacing and overlap. This problem has been encountered in operational use of starmappers and the primary advantage of the X-slit configuration is relief in this area.

The X-slit configuration has, however, a disadvantage in that the upper and lower halves of the field are indistinguishable. There are three ways of coping with this problem:

- By suitable coding of either upper or lower slits. The obvious, simplest code is doubling of the slits in one-half of the field. This technique has the disadvantage of requiring larger aperture for the same signal-to-background noise ratio as an uncoded system. The increase in aperture area required is approximately the square root of 1.5 or an aperture diameter increase of 20 percent. An additional disadvantage is incurred in that either data handling complexity or storage is increased by this technique.

341
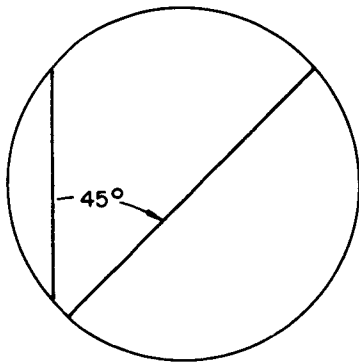
Vertical-Canted Configuration
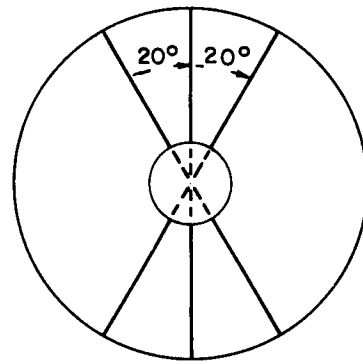
Three Radial Configuration

Figure 127. The Two Types of Reticles Considered
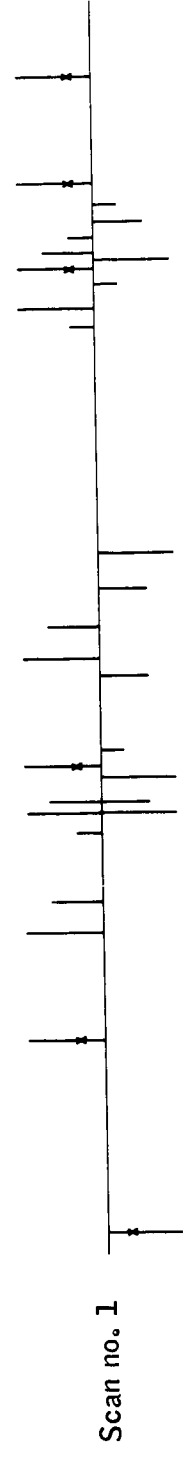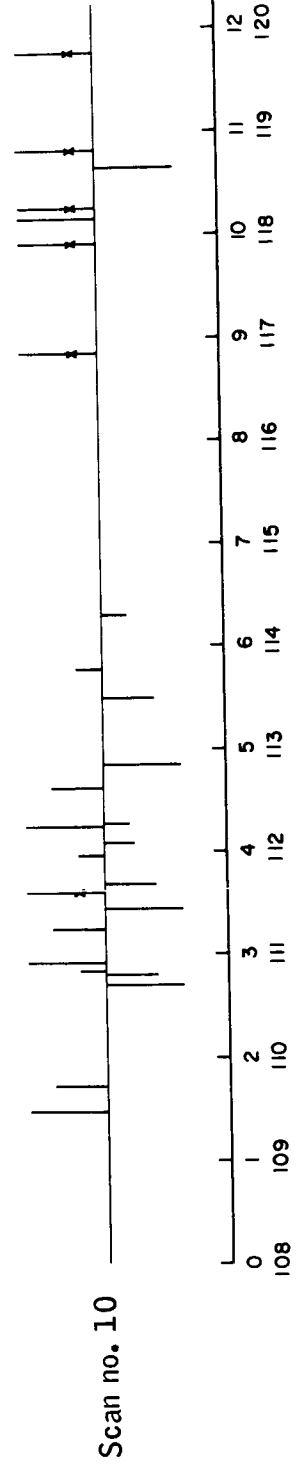
Figure 128. Simulated Star Pulses from the Two Reticles

Scan no. 1

Three radial

Scan no. 10

Scan no. 1

Vertical – canted

Scan no. 10

343
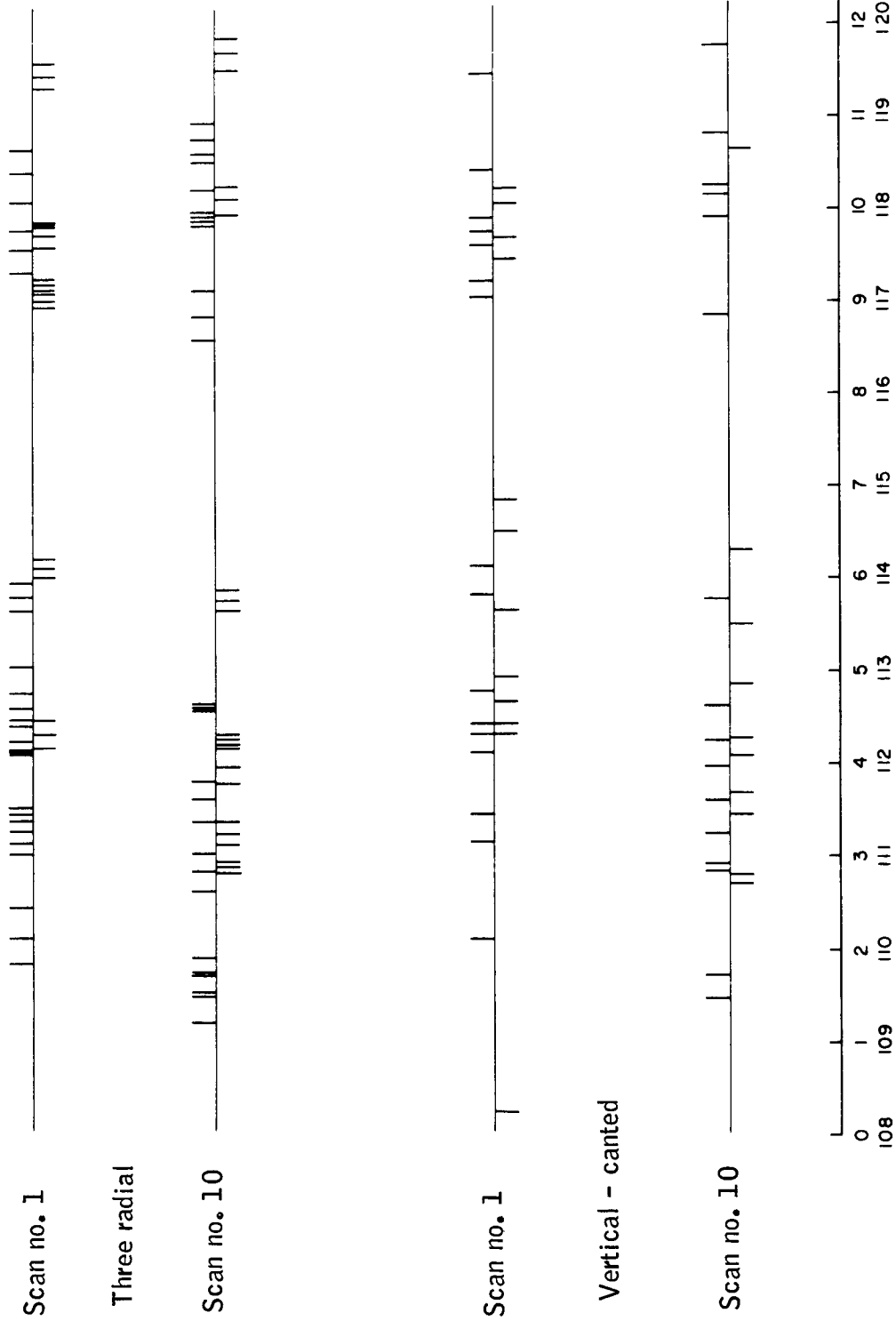
Figure 129. Simulated Pulses as Seen by Data Processing

Scan no. 1

Three radial

Scan no. 10

Scan no. 1

Vertical – canted

Scan no. 10

344

- By use of multiple detector systems, simply separating upper and lower slit systems until data reduction. The disadvantage is clearly the requirement for two photo-multipliers and associated electronics.

- By doubling the field of view to 40 degrees and using half the field, since the optical system is not a trivial design problem at 20-degree field, this does not appear to be a feasible approach.

For feasibility design, the multiple-detector system approach was selected, since it is relatively straightforward and allows some redundancy in the case of single p. m. factor, and requires minimum on-board data handling complexity, and/or storage.

Multiple-slit coding for noise rejection: Slit width and angle accuracy are directly related. However, as the slit width is decreased, the optical aperture must be increased for constant scan period to ensure that a sufficient number of photons are obtained.

An alternate approach to obtain high-angle accuracy is to use multiple slits with a correlation technique. In this way, one can obtain high-angle accuracy with a reasonable aperture and scan period. The basic technique is to correlate the output of the photodetector with an electrical replica of the multiple slit pattern. If the peak output of the correlator exceeds a preassigned detection threshold, a star is assumed to be present at the time corresponding to the peak output.

Autocorrelation coding requires complication in the sensor electronics and introduces cross-correlation noise. Shot noise is not eliminated, although the star signal is enhanced, the background noise is increased. An equally spaced two or three slit code is a special case and would appear to be subject to the same disadvantages.

The general topic of multiple-slit codes is treated in Appendix H. From these results and because of the complexity introduced, the recommended slit design does not use multiple slits.

345

Signal-to-noise ratio:

Calibration of star flux

Code (ref. 30) gives for the monochromatic flux from a star of visual magnitude zero and color index B-V = 0 a value

$$f = 3.8 \times 10^{-9} \text{ erg/cm}^2\text{/sec/Å} \tag{54}$$

at 5560 angstroms. This value was adopted.

The usual spectral responses of photomultipliers (S-4, S-11, S-9, etc.) correspond roughly in band pass and band-pass location to the Johnson "B" filter widely used to determine blue magnitudes. This induces the use of blue magnitudes in the calculations of star signals.

If blue magnitudes are used, the flux calibration needed is at 4300 angstroms (center of Johnson B filter). Code (ref. 30) gives a magnitude difference for Vega (type A_o visual magnitude 0.00 and color index 0.00) between 5560 and 4300 angstroms of

$$\Delta M\left(\frac{1}{\lambda}\right) = -0.20 \tag{55}$$

It is preferred to work in terms of $M(\lambda)$ the magnitude as a function of wavelength rather than reciprocal wavelength. The two are related by

$$M(\lambda) = M(1/\lambda) + 5 \log(\lambda/\lambda_o) \tag{56}$$

From the definition of magnitude in terms of intensity,

$$\frac{f(\lambda)}{f(\lambda_o)} = \left(\frac{\lambda_o}{\lambda}\right)^2 10^{-.4 \Delta M(1/\lambda)} \tag{57}$$

Using equations(57)and(54), it is found that the monochromatic flux from a star of visual magnitude zero and color index zero at 4300 angstroms

$$f_{4300\text{Å}} = 7.64 \times 10^{-12} \frac{\text{watts}}{\text{cm}^2\text{-micron}}$$

or in terms of incident photons

$$f_O = 1.66 \times 10^7 / \text{sec-cm}^2 \qquad (58)$$

This is taken as the number of photons incident on the earth's atmosphere from Vega per square centimeter per micron bandwidth.

Signal due to star and background

To calculate the resulting photocathode current, the stellar energy distribution, optical transmission, and photocathode response must be taken into account. The latter two quantities must necessarily be taken from the manufacturer's specifications. The former quantity is approximated by a blackbody.

Thus,

$$n_O = \frac{f_O}{B(\lambda_O T)} \int E_{opt}(\lambda) \, E_{quant}(\lambda) \, B(\lambda T) \, d\lambda \qquad (59)$$

where

λ = wavelength

E = efficiency

$B(\lambda T)$ = Planck function for photon flux

Having n_O, the number of photoelectrons per star transit for the star signal from a star of blue magnitude M_B and the sky background are

$$S = n_O \, 10^{-.4 \, M_B} \frac{\pi}{4} \, D^2 \frac{\alpha}{\omega} \qquad (60)$$

$$B = n_O \, N \, 10^{-4} \, \frac{\pi}{4} \, D^2 \, \frac{\alpha}{\omega} \, A \qquad (61)$$

where

S = star signal $\dfrac{\text{photoelectrons}}{\text{star transit}}$

B = sky background signal

D = diameter of optics in centimeters

α = slit width in degrees

ω = rotation speed of scanner in degrees per second

N = sky background in number of tenth magnitude stars per square degree

A = total slit area projected on the celestial sphere in square degrees

Noise calculations

The photomultiplier noise is commonly available from manufacturer's specifications in number of dark current photoelectrons per second γ. The number of dark current photoelectrons per star transit is then

$$m = \gamma \frac{\alpha}{\omega} \qquad (62)$$

It is desirable to detect stars of some magnitude M_B with a certain probability and to reject weaker stars with largest possible probability. Equations (60), (61), and (62) are used to determine a detection threshold which will assure this. If it is assumed that the numbers involved are large enough (larger than about 32), the normal distribution can be used.

If the mean number is

$$N = S + B + m \qquad (63)$$

and the threshold is x, the detection probability p is the probability that the actual number n exceeds x or

$$p(n \geq x \mid N) = 1/2 \text{ erfc} \left(\frac{x - N_o}{\sqrt{2 N_o}} \right) \qquad (64)$$

where

$$\text{erfc}(x) = \frac{2}{\sqrt{\pi}} \int_x^\infty e^{-\alpha^2} \, d\alpha$$

If the electrical filter used in the signal processing is matched in bandwidth to the star signal, write the signal-to-noise C as

$$C = \frac{S_t}{\sqrt{2(S_t + B + m)}} \qquad (65)$$

where $S_t = x - B - m$ is the star signal at the threshold.

Also,

$$C = \frac{x - B - m}{\sqrt{2x}} \tag{65a}$$

More generally the star signal and filter bandwidth may not be matched. In this case, the use of photon rates is preferred; change these to electrical currents and use Schottky's theorem.

Then, the currents at the photocathode due to star, background, and "tube noise" are

$$i_s = e \, n_o \, 10^{-.4 \, M_B} \frac{\pi}{4} D^2 \tag{66}$$

$$i_b = e \, n_o \, N \, 10^{-4} \frac{\pi}{4} D^2 \tag{67}$$

$$i_\gamma = e \, \gamma \tag{68}$$

The mean square fluctuation in the cathode current at the threshold will be

$$\sqrt{\overline{i^2}} = \sqrt{2e \left[\frac{x}{N} i_s + i_b + i_\gamma \right] \Delta f} \tag{69}$$

where Δf is the filter bandwidth.

Another method is simply to scale the result of (65) by the square root of the ratio of actual bandwidth to that of a matched filter.

Application to starmapper

The calculations are presented here pertaining to the proposed starmapper. Take,

α = 1/60 degree

ω = 18°/second

$M_B = 3.50^m$

Assume for simplicity that E_{opt} and E_{quant} may be taken as constant and that the EMR 541N which is used has peak quantum efficiency of about 20 percent. At 5200 angstroms, the response has fallen to about 10 percent but over the band 3600 to 5200 angstroms it averages about 17.5 percent. Assume γ is given as 125/second. Also, arbitrarily assume 50 percent optical efficiency and 3600 Å $\leq \lambda \leq$ 5200 Å.

Equations (60) and (61) have become

$$S = f_o \, 10^{-.4 M_B} \, E_{opt} \, E_{quant} \, \frac{\pi}{4} D^2 \frac{\alpha}{\omega} \, \Delta\lambda \tag{60a}$$

$$B = f_o \, N \, 10^{-4} \, E_{opt} \, E_{quant} \, \frac{\pi}{4} D^2 \frac{\alpha}{\omega} A \, \Delta\lambda \tag{61a}$$

where

$$\Delta\lambda = \frac{\int B(\lambda T) \, d\lambda}{B(\lambda_o T)} \tag{70}$$

Equation (70) can be evaluated from the blackbody tables in Allen (ref. 31). However, the variation of the integrand in 3600 to 5200 angstroms is slow enough to take it as constant and equal to that at 4300 angstroms. Thus, $\Delta\lambda \approx 0.16$ micron. Finally, take D = 3.0 inches and N = 200 and 3 slits, one arc minute wide and 25° FOV. Then,

$$S = 1.66 \times 10^7 \times 10^{-.4 \times 3.5} \times 0.5 \times 0.175 \times (1.27 \times 3.0)^2 \, \pi$$

$$\times \frac{1}{60 \times 18} \times 0.16/\text{transit}$$

$$= 391/\text{transit}$$

$$B = 1.66 \times 10^7 \times 2 \times 10^2 \times 10^{-4} \times 0.5 \times 0.175 \times (1.27 \times 3.0)^2 \, \pi$$

$$\times \frac{1}{60 \times 18} \times \frac{3 \times 25}{60} \times 0.16/\text{transit}$$

$$= 245/\text{transit}$$

$$m = \frac{125}{60 \times 18} = 0.115 \approx 0$$

is neglected altogether.

For 95 percent detection probability, the threshold from 64 is found as $x = 595$ and with a matched filter the signal-to-noise ratio at detection threshold is 10 to 1.

False star detections

Using equation (64) with $N_o = B + m$, that is, with no star in the slit, what is the probability one is found? Now the argument of the complementary error function is large and using the approximation

$$\text{erfc } y \sim \frac{e^{-y^2}}{y\sqrt{\pi}} \left[1 - \frac{1}{2 y^2} + \frac{1.3}{(2 y2)^2} - .. \right]$$

The number of false star detections per scan would be N_1 where

$$N_1 = \frac{360 \, n}{\alpha} \frac{e^{-y^2}}{2 y \sqrt{\pi}}$$

where n is number of slits and

$$y = \frac{x - B - m}{\sqrt{2(B + m)}} \quad .$$

For this case $y = 15.8$, $n = 3$, and

$$N_1 = \frac{360 \times 3 \times 60 \times e^{-15.9^2}}{2 \times 15.9 \sqrt{\pi}}$$

$$\approx \frac{360 \times 3 \times 60 \times 10^{-108.57}}{2 \times 15.9 \sqrt{\pi}}$$

It is hardly necessary to go further with this example.

Strictly speaking, the secondary emission multiplication noise should be included. However, this can be expected to add no more than 20 percent to the noise (ref. 32).

Interpolation factor by Monte Carlo technique

The one remaining question pertains to how well can interpolating the optical blur circle be done while doing threshold detection at the output of a filter.

It is assumed the star energy density in the focal plane to be gaussian, i. e.,

$$j(x, y) = \frac{e^{-\frac{x^2 + y^2}{2\sigma^2}}}{2\pi\sigma^2} \tag{71}$$

If this distribution is scanned with a slit and if T_S is the time the star center takes to cross the slit, the time variation of the photodetector output will be

$$G(t) = \phi(t/\sigma + T_S/2\sigma) - \phi(t/\sigma - T_S/2\sigma) \tag{72}$$

where

$$\phi(t) = \frac{1}{\sqrt{2\pi}} \int_{-\infty}^{x} e^{-\lambda^2/2} \, d\lambda \tag{73}$$

Let the maximum photoelectron rate from a limiting magnitude star be $n_0/\sec$ and that from the faint star background plus tube dark durrent be N_0. Let the filter impulse response be $h(t)$. Then, the filter output signal will be,

$$i(t) = e \Gamma \int_{-\infty}^{t} s(\tau) \, h(t - \tau) \, d\tau \tag{74}$$

where

e = electron charge,

Γ = photomultiplier gain, and

$$s(t) = n_0 G(t) + N_0 \tag{75}$$

352

The signal s is really the result of several Poisson processes and is, thus, a random variable. Realistically, the evaluation of equation(74)should contain this fact.

This may be done in the following way. Equation(74)is first approximated by,

$$\frac{i(t)}{e\Gamma} = I(t) = \sum_{i=0}^{M} a_i \, s(\tau_i) \, h(t - \tau_i) \, \Delta\tau_i \tag{76}$$

where a_i, τ_i, and $\Delta\tau_i$ depend on the chosen quadrature rule.

Next, the mean number m_i of photoelectrons in the time $\Delta\tau_i$ is calculated as,

$$m_i = s(\tau_i) \, \Delta\tau_i \tag{77}$$

The number actually occurring is then found from a Poisson distribution having mean m_i.

To do this, take advantage of the fact that if $p(n)$ is the probability of n_i, then,

$$\sum_{j=0}^{\infty} p(n_i) = 1 \tag{78}$$

Thus, the $p(n)$ are set on the real number interval between zero and one so as to delineate a set of "bins" of which the n_i^{th} one is $p(n_i)$ in length. A random number between zero and one is generated. If it falls in the n_i^{th} "bin", we take $s(\tau_i) = n_i$.

The actual generation is as follows:

(1) Find m_i.

(2) Generate random number R_i.

(3) Sum the series

$$C(N) = \sum_{n=1}^{N} \frac{m_i^{n} \, e^{-m_i}}{n!} \quad \text{until,}$$

$$C(N) \geq R_i.$$

(4) Set $n_i = N$.

In practice, the number $m_i \lesssim 5$ and since

$$\sum_{n=1}^{22} \frac{5^n e^{-5}}{n!} \approx 1 - 10^{-8}$$

N is set ≤ 22. In this way, a distribution of $I(t)$ is generated by

$$I(t) = \sum_{i=0}^{M} a_i \, n_i \, h(t - \tau_i) \, \Delta\tau_i \qquad (79)$$

A threshold is set at say I^* and the solutions t_1^*, t_2^* of

$$I^* = \sum_{i=0}^{M} a_i \, n_i \, h(t^* - \tau_i) \, \Delta\tau_i \qquad (80)$$

are determined.

After sufficient repetitions of the preceding the variances

$$\sigma(t_1^*), \ \sigma\left(\frac{t_1^* + t_2^*}{2}\right), \ \sigma(t_2^*)$$

are calculated.

Then, take the interpolation factor as

$$K = T_s/\sigma \left(\frac{t_1^* + t_2^*}{2}\right) \qquad (81)$$

The following case was considered.

$$n_o/T_s = 391$$

$$N_o/T_s = 245$$

One arc minute slit and 18° per second rotation period.

(These numbers correspond to a 3.5 magnitude type A0 star, 3-inch diameter optics, optical band 3600 to 5200 Å, optical efficiency 50 percent, quantum efficiency 17.5 percent, 3 slits, 25° field of view, and 200 tenth magnitude stars per square degree of background.)

A linear phase shift, sixth order Paynter filter was assumed. This has transfer function

$$T(s) = \frac{1}{\prod\limits_{i=1}^{3} \left[a_i \left(\frac{s}{\omega_c} \right)^2 + b_i \frac{s}{\omega_c} + 1 \right]} \quad (82)$$

with,

$$a_1 = 1.866, \quad b_1 = 2.3860$$

$$a_2 = 0.6579, \quad b_2 = 0.6204$$

$$a_3 = 0.2310, \quad b_3 = 0.1224$$

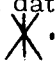Thus, the impulse response is,

$$h(t) = \sum_{i=1}^{3} \left\{ 2 a_i \, \omega_c \, e^{-\alpha_i \, \omega_c t} \cos(\beta_i \, \omega_c t) + 2 \, b_i \, \omega_c \, e^{-\alpha_i \, \omega_c t} \sin(\beta_i \, \omega_c t) \right\} \quad (83)$$

355

$$\alpha_1 = 0.6393, \qquad \beta_1 = 0.3566, \qquad a_1 = 0.0440, \qquad b_1 = 0.2691$$

$$\alpha_2 = 0.4715, \qquad \beta_2 = 1.1391, \qquad a_2 = 0.0555, \qquad b_2 = 0.1067$$

$$\alpha_3 = 0.2641, \qquad \beta_3 = 2.0604, \qquad a_3 = 0.0114, \qquad b_3 = 0.0143$$

A total of 873 star-crossing times were computed. It was found,

$$\left.
\begin{aligned}
\sigma(t_1^*) &= 1.492 \times 10^{-4} \text{ sec} \\[1em]
\sigma(t_2^*) &= 1.444 \times 10^{-4} \text{ sec} \\[1em]
\sigma\left(\frac{t_1^* + t_2^*}{2}\right) &= 1.020 \times 10^{-4} \text{ sec}
\end{aligned}
\right\}
\tag{84}$$

Since in this case $T_s = 9.26 \times 10^{-4}$ second, it was found that $K = 9.1$. That is, the blur circle for this case may be interpolated by a factor of nine; thus, the factor of six used in earlier computations is conservative.

Summary of reticle design: The above discussions and conclusions lead to the following reticle design. An optical field of view of 20 degrees is required to ensure that four or more stars of 3.2 magnitude or brighter, will be scanned 100 percent of the time. This field of view coupled with a long focal length (12-20 inches) yields an image or reticle diameter of greater than 4 inches. The effects of optical aberrations are minimized if the slit pattern used is radial, and data reduction is facilitated by the use of a triple slit configuration such as ⋉ .

Satisfactory signal-to-noise ratio minimum false star detections, and interpolation accuracy to 10 arc seconds may all be achieved with a blur circle equal to the slit width of 60 arc seconds. A blur circle of this size to the edge of the field of view of 20 degrees is within the state of the art for an f/4 optical system, and for a 12-inch focal length lens the numerical width of each slit will then be 0.0035 inch, which is well within the state of the art. The resultant slit reticle design will then be as shown in Figure 130.

The angle of 20 degrees between adjacent slits is somewhat arbitrary. The greater this angle, the more accurately the off-axis star angle may be determined, but the effective scanning field of view for transitting all three slits will be reduced. However, the extreme ends of these 20 degree slits only subtends a total angle of 7 degrees on the celestial sphere which means that more stars near the horizon will be detected without being washed out by earth glow or turning off of the starmapper.
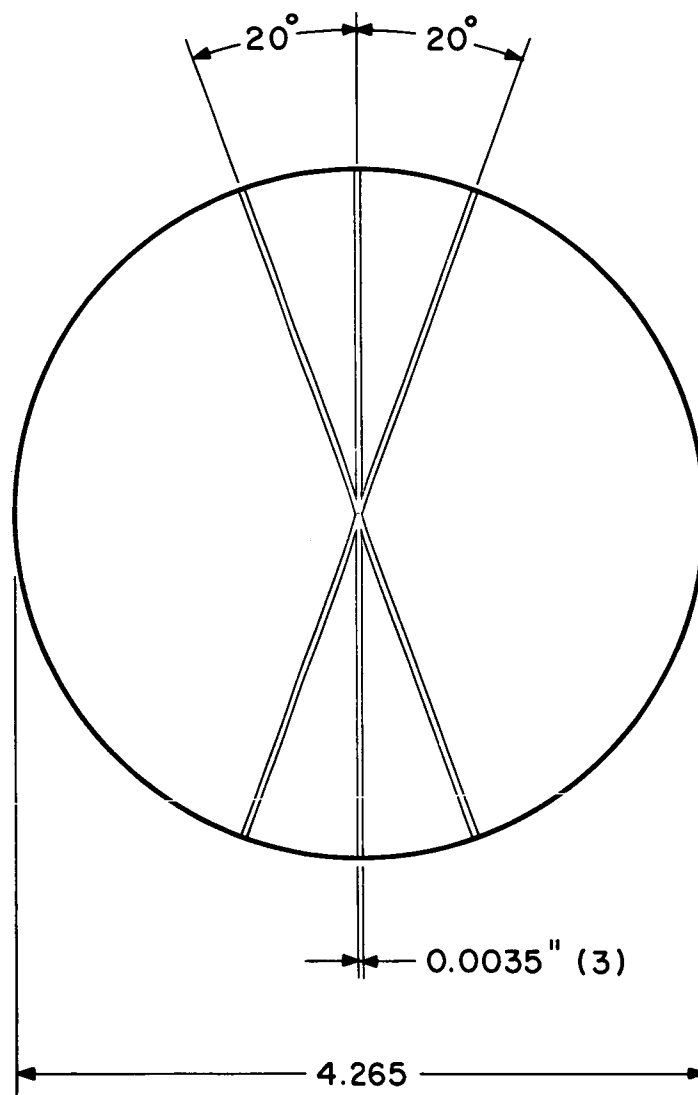
Figure 130. Reticle Design Layout

357

The crossover portion at the center of the reticle will not yield useful data from a star which may cross this area since it will only trigger a single pulse rather than the required three pulses and, therefore, could be blanked out. However, this point must be located precisely on the optical axis, and, therefore, it is extremely useful to leave it clear for both internal alignment and alignment to the radiometer.

One more factor of this reticle design remains to be discussed; the differentiation between the two sides of the reticle pattern. As discussed previously, autocorrelation coding, in general, allows the entrance of at least as much noise as it eliminates. An equally spaced two or three slit code is merely a special case and would be subject to the same disadvantages of allowing the entrance of more background noise without increasing the amplitude of the signal. Therefore, the proposed method of determining the set of slits transited by the star image is the use of two sets of optical fibers, with each set leading to a separate detection system. This will allow tagging the transit data in the memory with an indicator of the originating slit set. Other benefits of the use of this method are lighter weight and improved operational mission success as will be discussed later.

Optical design of the sensor. -- The physical and optical properties of the sensor lens are crucial elements in the design of the sensor. Many lens prescriptions have been considered and evaluated in the search for a feasible lens for this system. The method of evaluation of a lens from the prescription of curvatures, spacings, and indices of refraction has been the use of a computer calculated, ray-trace program of sufficient versatility to describe the performance of the lens at any selected aperture and field of view with automatically plotted spot diagrams, modulation transfer functions, and detailed surface-by-surface ray position and direction identification. The automatically plotted spot diagrams present the configuration of the image of a star on a preselected plane perpendicular to the optical axis. The spot diagrams can be obtained for any wavelength of light and any position of the image plane. Spot diagrams for several wavelengths of light, image plane positions, and apertures were obtained for the lenses considered for this sensor. An important property of the ray-trace evaluation is that it assumes only geometric optics i.e., that the effect of diffraction on each ray is negligible compared to the effect of the geometrical aberrations in producing the spot diagram configuration. As the lens aberrations are reduced, the effect of diffraction becomes more important in the prediction of effective image size. To estimate the relative approach to the diffraction limit of a given lens, a modulation transfer function was computed and plotted. The modulation transfer function is an estimate of the fineness of detail which an optical system can detect. Its particular utility in this application was based more on the fact that its results came from optical path length and diffraction considerations than the interpretation of the modulation transfer function.

The degree of approach to the diffraction-limited (aberration-free) lens was evaluated by plotting the modulation transfer function of the diffraction limited lens on the same graph as the modulation transfer function of the lens under consideration.

358

Sensor lens: As the result of these evaluation procedures, a lens design was selected on the following qualifications: (1) at least 80 percent of the energy of the composite image made up of the individual images formed at 5893, 4358, and 4047 angstroms wavelength shall be within a one minute of arc slit width, (2) the lens formula should be of physically realizable glass, (3) all lens surfaces should be spherical if possible, to avoid the use of aspheric surfaces whose physical realization might be questionable without extensive investigation. The lens selected on the basis of these qualifications was chosen as a demonstration of feasibility of the design of the sensor, not necessarily the final lens to be fabricated.

The lens found to be capable to meeting the three requirements stated above is a seven element double gauss construction using rare earth glass as well as conventional glass in its construction. It was found to meet the spot-size requirements when stopped down to an aperture of f/7. The field of view of the lens is 20 degrees total. Spot diagrams for the lens at various fields of view are shown in Figures 131 through 145. The coordinates of the spot diagrams are shown as seconds of arc for both axes. The rays traced are positioned in the entrance pupil so that each ray represents approximately the same area of the pupil. Since the entrance pupil is to be uniformly illuminated in this application, each ray represents an equal fraction of the incident light energy.

Spot diagrams were computed for three wavelengths of light by inserting the appropriate indices of refraction for the glass used in the prescription.

Spot diagrams for equal field angles and positions on the image plane were effectively superimposed and evaluated in comparison to a one minute of arc slit. A graph of the distance from the reference position to the edge of the spot is shown for the chosen lens in Figure 146 for three wavelengths of light chosen in the color region where the stars of interest are most intense and where the photomultiplier chosen is the most sensitive. Note that the spot radii for 4047 and 5893 angstroms fall completely within a 30 arc-second radius. This means that all of the energy in these wavelengths would fall completely within a one minute of arc slit scanning in the direction of the spot diagram ordinate. To evaluate the effect of the 4358 angstrom spot on the total energy available for a one minute of arc slit, the area of the spot diagram, 30 arc seconds either side of the reference position on the image plane, was measured. This area was compared with the total area of the spot and expressed as a percent of the total energy available at this color. The average energy based on the three wavelengths is shown in Figure 147 as a function of field angle.

The approach of this lens to a diffraction limited lens is shown by the modulation transfer function graph in Figure 148. The fact that the modulation transfer function of this lens is less than that of the ideal lens can be used as an indication that: (1) the geometric ray trace spot diagrams shown above closely represent the appearance of the image of a star in the image plane chosen, since the geometric lens aberrations dominate the performance of the lens, and (2) that by further refinement of the lens design such as adjusting curvatures, spaces, types of glass, and the use of aspheric surfaces, the lens could be made to approach the diffraction limit more closely.

Figure 131. Spot Diagram, f/7 Starmapper Lens, 0.5893–Micron Wavelength, 0° Half-Field Angle

Figure 132. Spot Diagram, f/7 Starmapper Lens, 0.5893-Micron
Wavelength, 2.5° Half-Field Angle

361

Figure 133. Spot Diagram, f/7 Starmapper Lens, 0.5893-Micron
Wavelength, 5.0° Half-Field Angle

X-AXIS
ARC SEC

1.774+001
1.670+001
1.565+001
1.461+001
1.357+001
1.252+001
1.148+001
1.044+001
9.393+000
8.349+000
7.305+000
6.262+000
5.218+000
4.174+000
3.131+000
2.087+000
1.044+000
0.000+000
-1.044+000
-2.087+000
-3.131+000
-4.174+000
-5.218+000
-6.262+000
-7.305+000
-8.349+000
-9.393+000
-1.044+001
-1.148+001
-1.252+001
-1.357+001
-1.461+001
-1.565+001
-1.670+001
-1.774+001
-1.879+001

FIELD ANGLE MULTIPLIER K = 0.7500000

1.710183-003
U

Y-AXIS

-1.781699-005
M

Figure 134. Spot Diagram, f/7 Starmapper Lens, 0.5893-Micron
Wavelength, 7.5° Half-Field Angle

363

FIELD ANGLE MULTIPLIER K = 1.0000000

X-AXIS
ARC SEC

2.957+001
2.783+001
2.609+001
2.435+001
2.261+001
2.087+001
1.913+001
1.739+001
1.565+001
1.391+001
1.218+001
1.044+001
8.697+000
6.957+000
5.218+000
3.479+000
1.739+000
0.000+000
-1.739+000
-3.479+000
-5.218+000
-6.957+000
-8.697+000
-1.044+001
-1.218+001
-1.391+001
-1.565+001
-1.739+001
-1.913+001
-2.087+001
-2.261+001
-2.435+001
-2.609+001
-2.783+001
-2.957+001
-3.131+001

Y-AXIS

U
2.834894-003

M
-4.510584-005

Figure 135.   Spot Diagram, f/7 Starmapper Lens, 0.5893-Micron
Wavelength, 10.0° Half-Field Angle

Figure 136. Spot Diagram, f/7 Starmapper Lens, 0.4358-Micron Wavelength, 0° Half-Field Angle

365

Figure 137. Spot Diagram, f/7 Starmapper Lens, 0.4358-Micron Wavelength, 2.5° Half-Field Angle
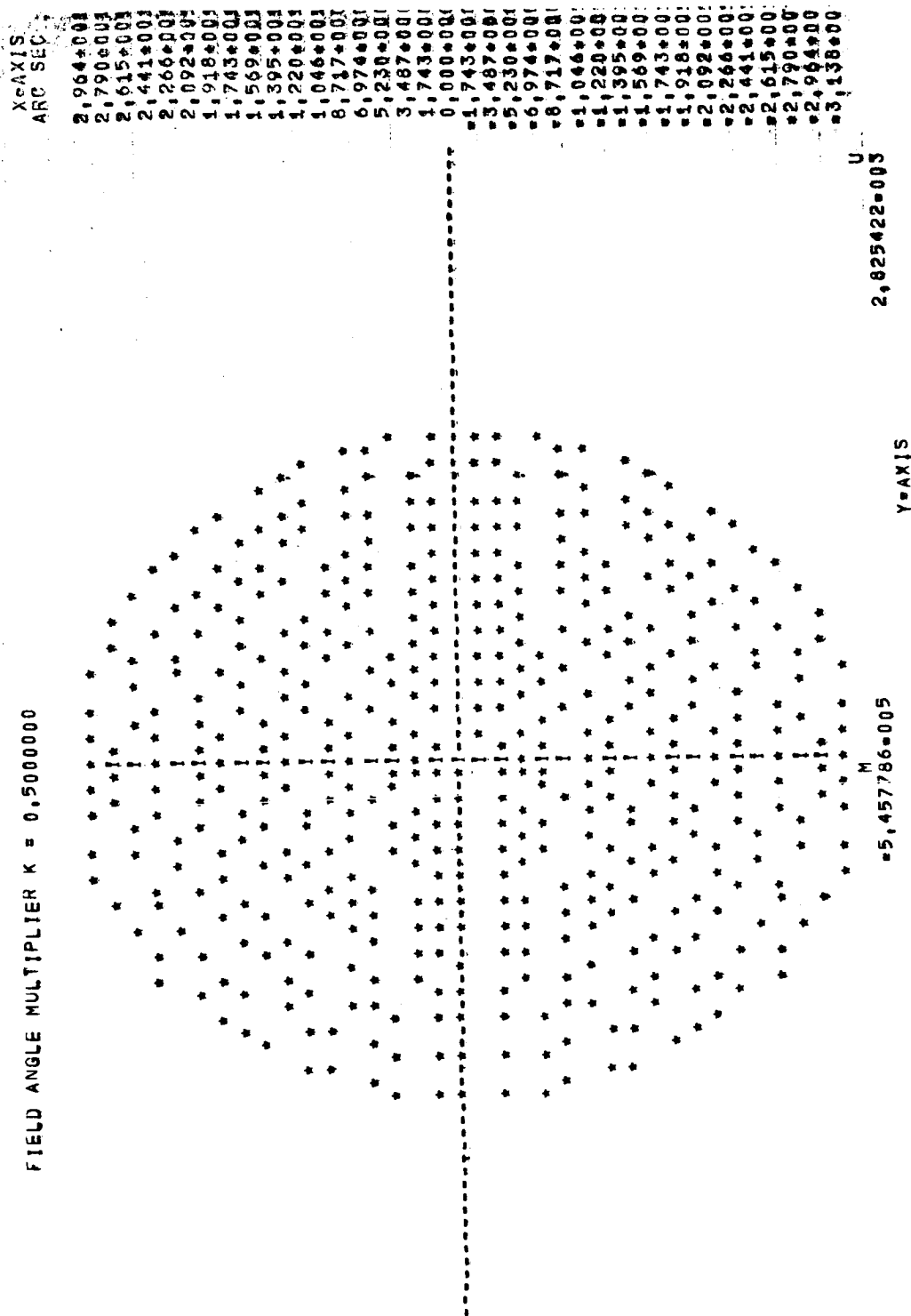
Figure 138. Spot Diagram, f/7 Starmapper Lens, 0.4358-Micron
Wavelength, 5.0° Half-Field Angle

367

X-AXIS
ARC SEC

5.928+001
5.579+001
5.230+001
4.882+001
4.533+001
4.184+001
3.836+001
3.487+001
3.138+001
2.790+001
2.441+001
2.092+001
1.743+001
1.395+001
1.046+001
6.974+000
3.487+000
0.000+000
-3.487+000
-6.974+000
-1.046+001
-1.395+001
-1.743+001
-2.092+001
-2.441+001
-2.790+001
-3.138+001
-3.487+001
-3.836+001
-4.184+001
-4.533+001
-4.882+001
-5.230+001
-5.579+001
-5.928+001
-6.276+001

FIELD ANGLE MULTIPLIER K = 0.7500000

Y-AXIS

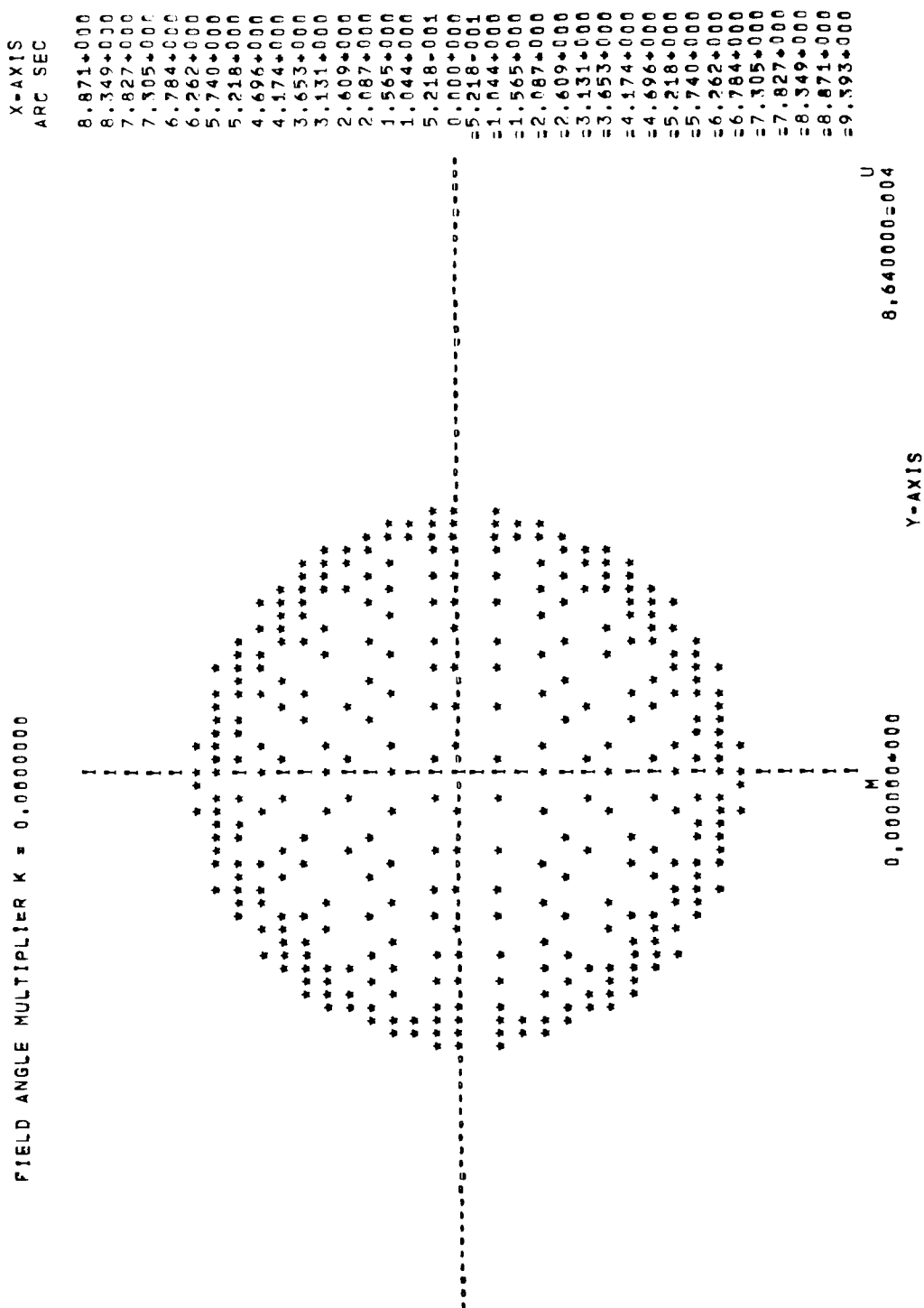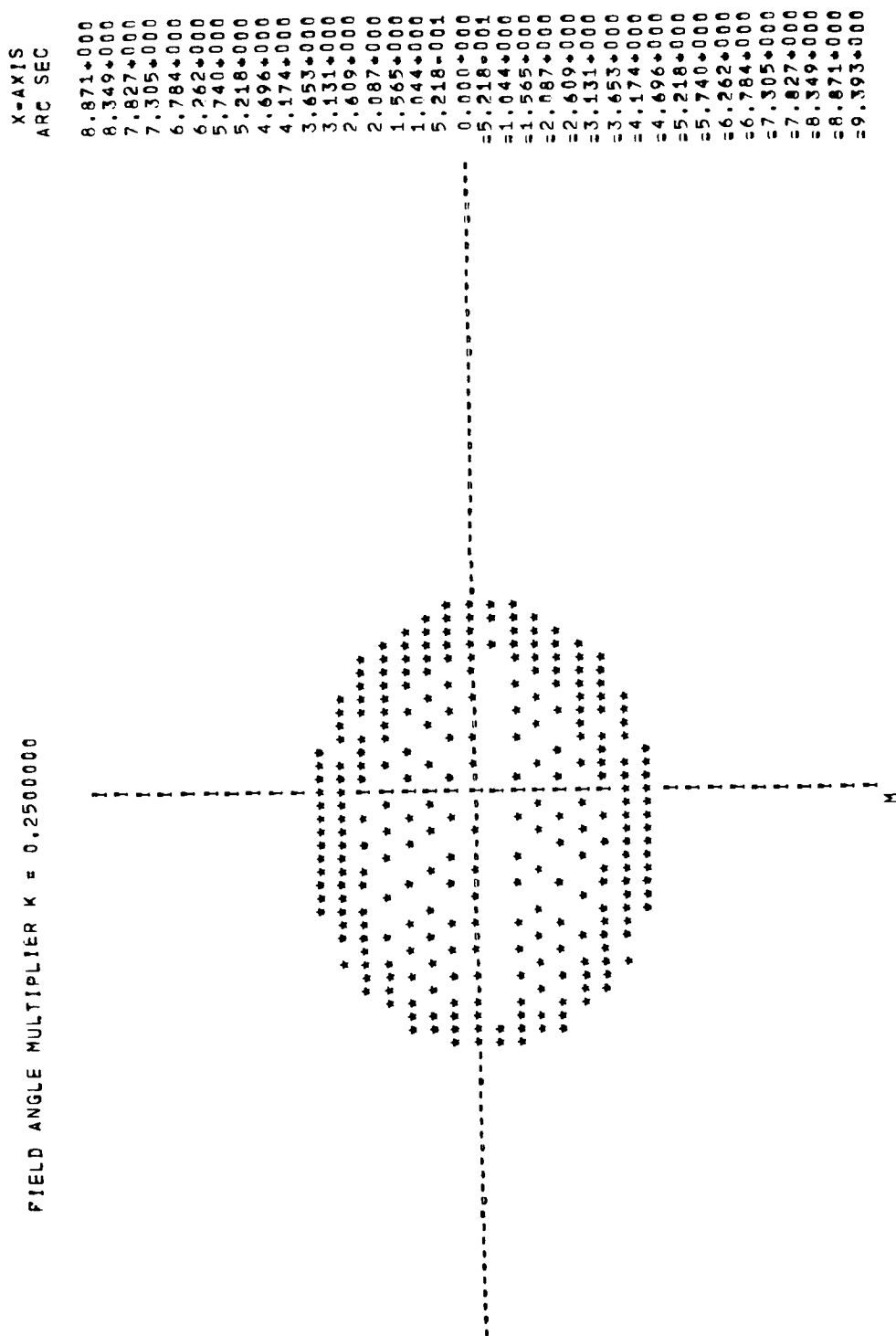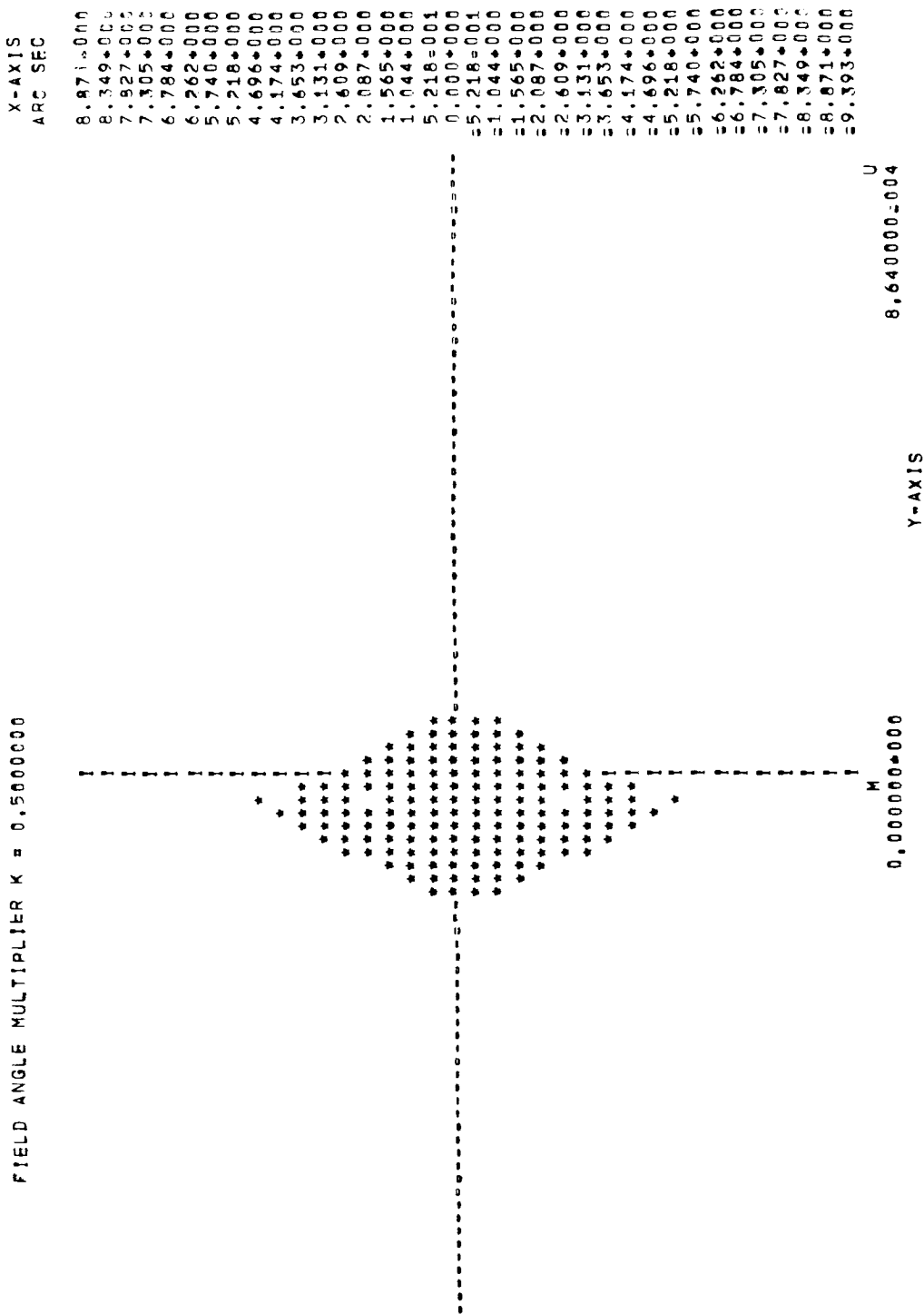U
5.734567-003

M
-2.543279-005

Figure 139.   Spot Diagram, f/7 Starmapper Lens, 0.4358-Micron
Wavelength, 7.5° Half-Field Angle

Figure 140. Spot Diagram, f/7 Starmapper Lens, 0.4358-Micron Wavelength, 10.0° Half-Field Angle

Figure 141. Spot Diagram, f/7 Starmapper Lens, 0.4077-Micron Wavelength, 0° Half-Field Angle

X-AXIS
ARC SEC

2.953+001
2.779+001
2.605+001
2.432+001
2.258+001
2.084+001
1.911+001
1.737+001
1.563+001
1.379+001
1.216+001
1.042+001
8.685+000
6.947+000
5.211+000
3.474+000
1.737+000
0.000+000
-1.737+000
-3.474+000
-5.211+000
-6.947+000
-8.685+000
-1.216+001
-1.390+001
-1.563+001
-1.737+001
-1.911+001
-2.084+001
-2.258+001
-2.432+001
-2.605+001
-2.779+001
-2.953+001
-3.126+001

FIELD ANGLE MULTIPLIER K = 0.7550000

0.00000+000

2.68000-003

Y-AXIS

Figure 142. Spot Diagram, f/7 Starmapper Lens, 0.4077-Micron
Wavelength, 2.5° Half-Field Angle

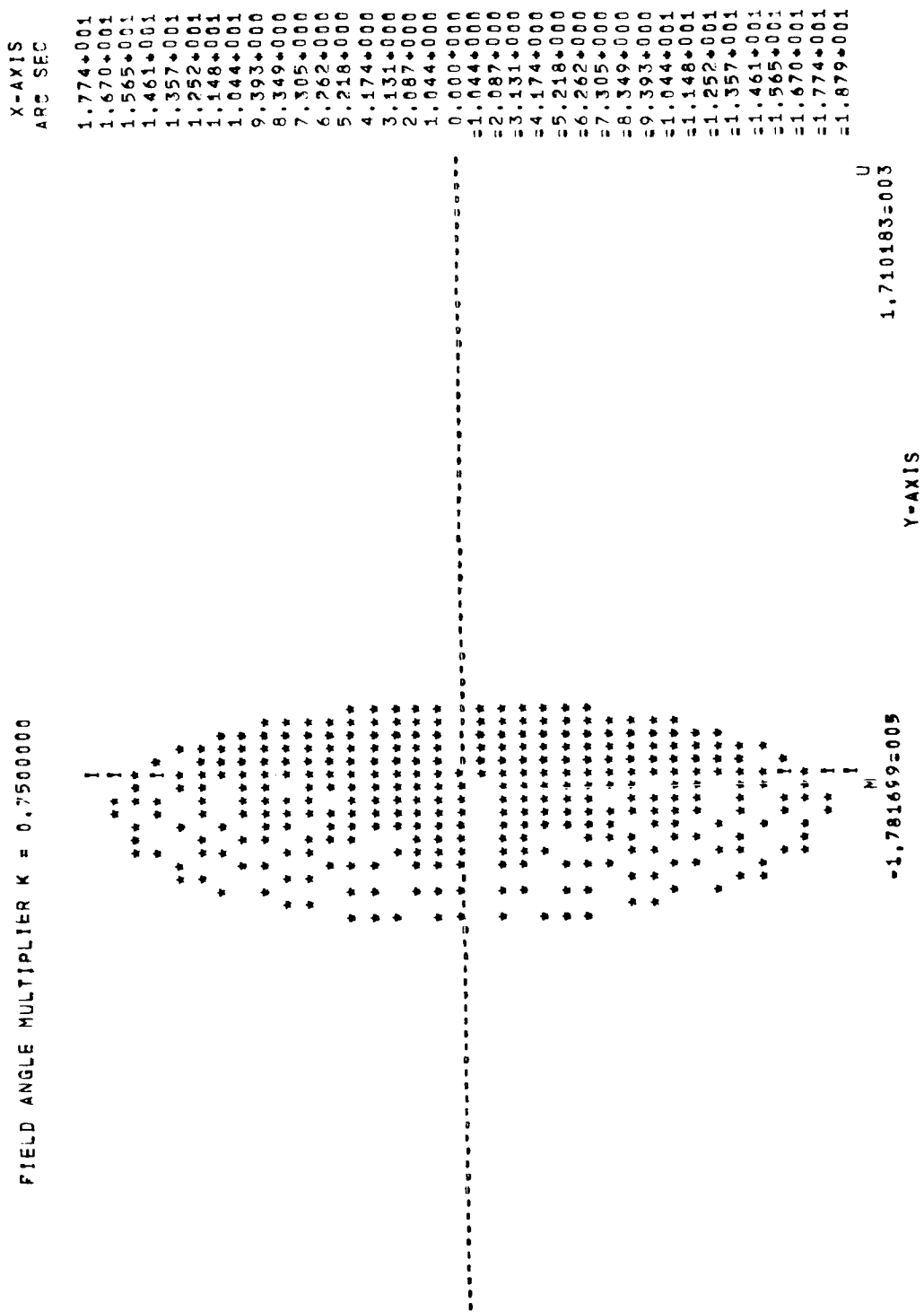Figure 143. Spot Diagram, f/7 Starmapper Lens, 0.4077–Micron Wavelength, 5.0° Half–Field Angle
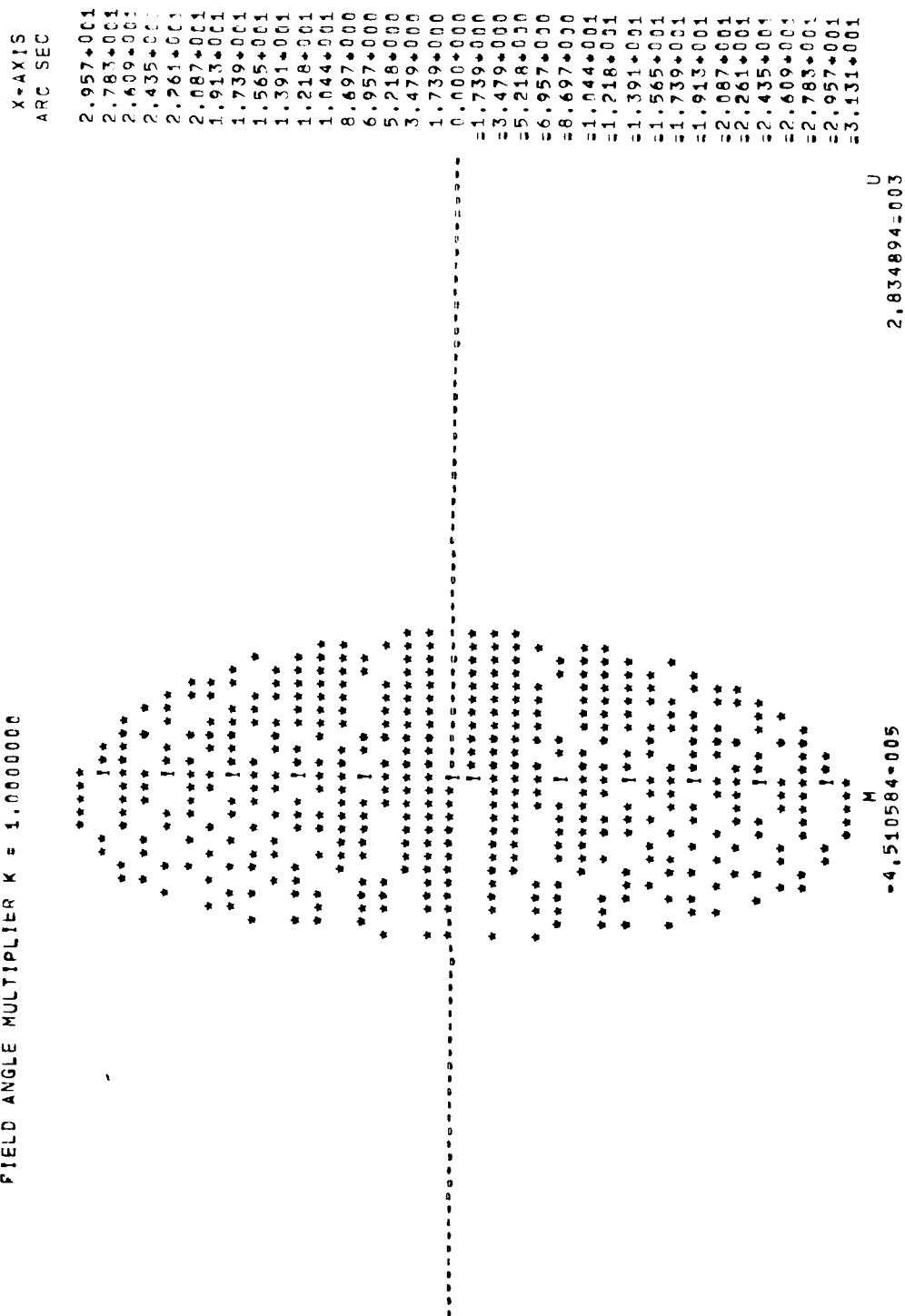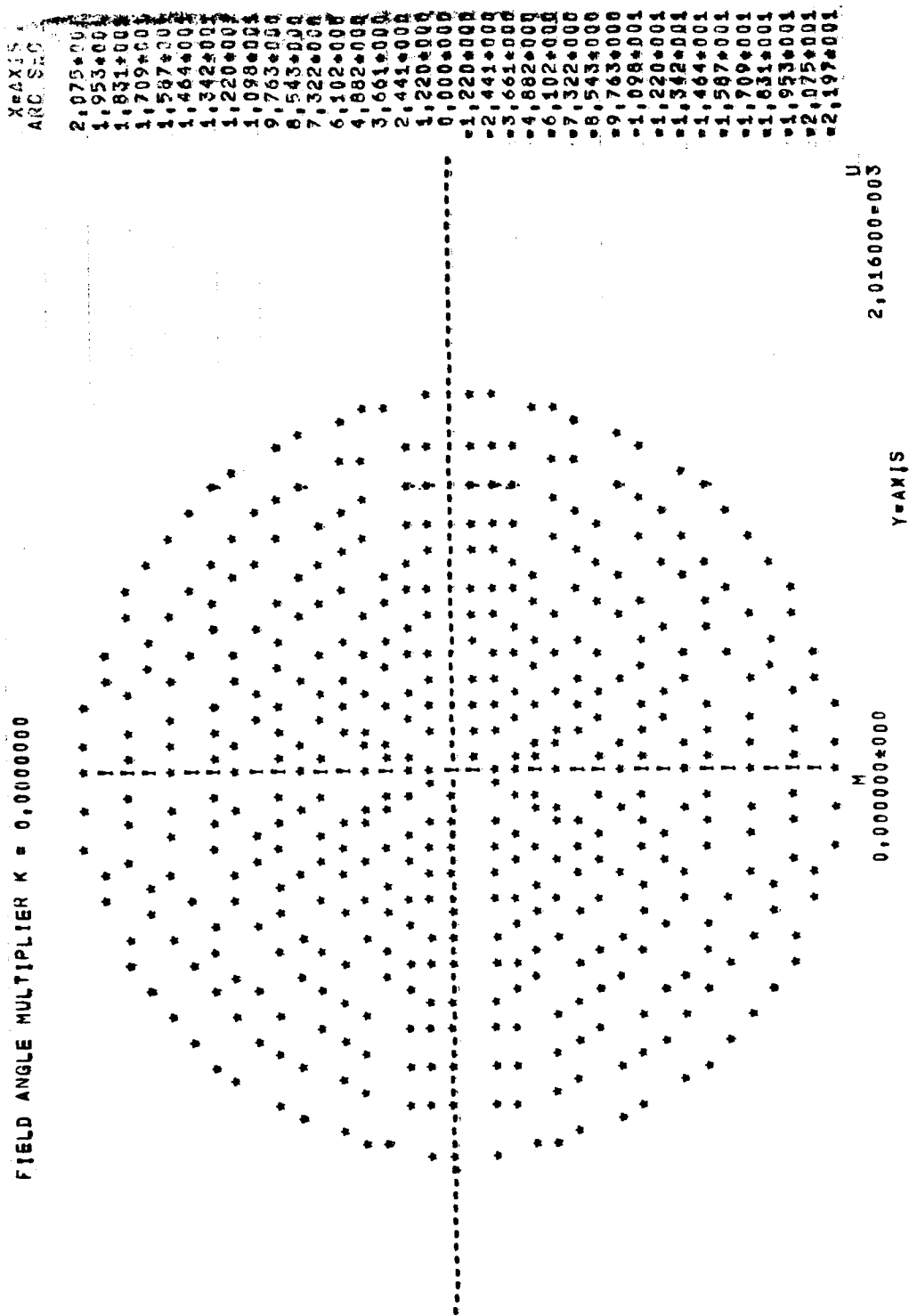
Figure 144. Spot Diagram, f/7 Starmapper Lens, 0.4077-Micron Wavelength, 7.5° Half-Field Angle

Figure 145. Spot Diagram, f/7 Starmapper Lens, 0.4077-Micron
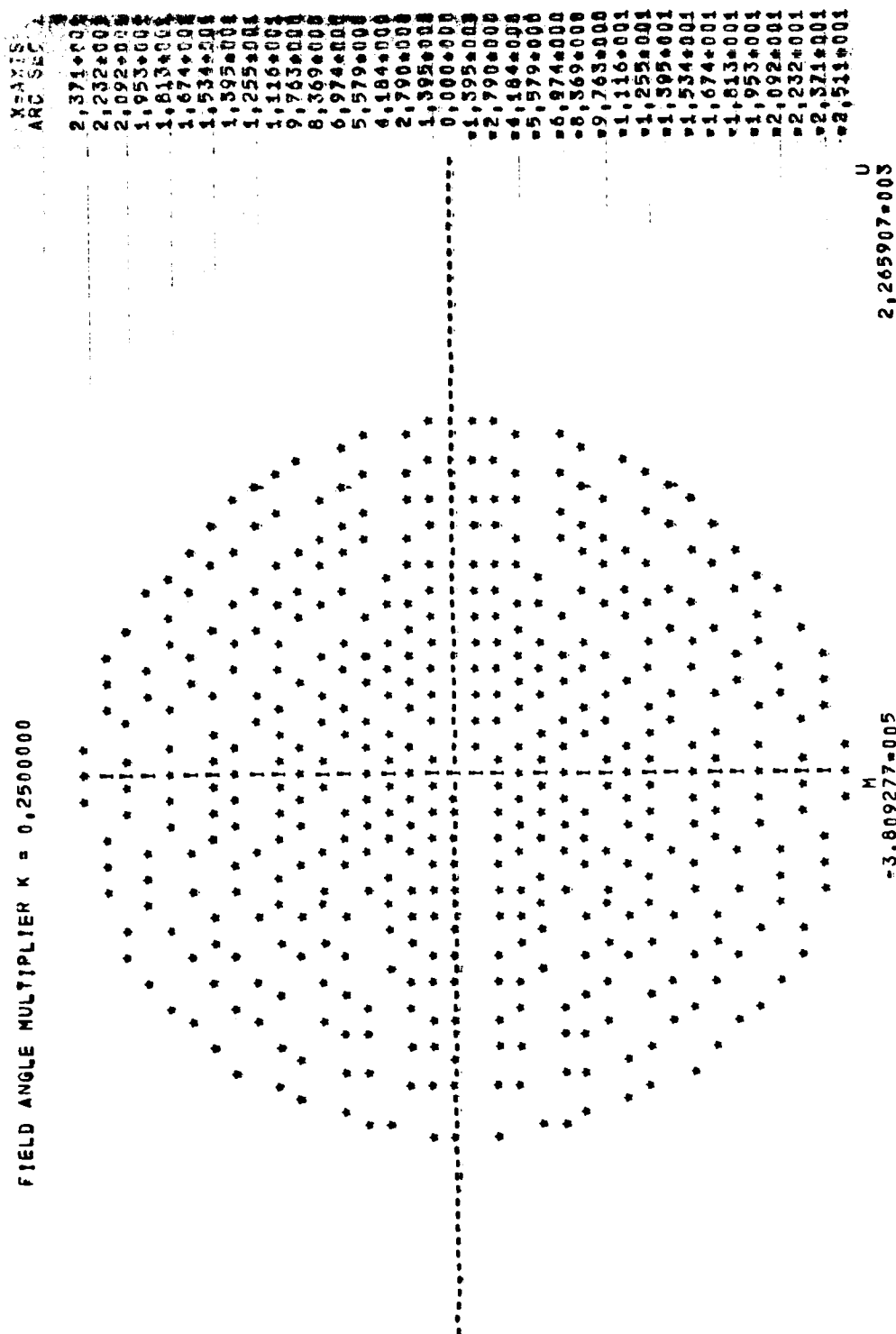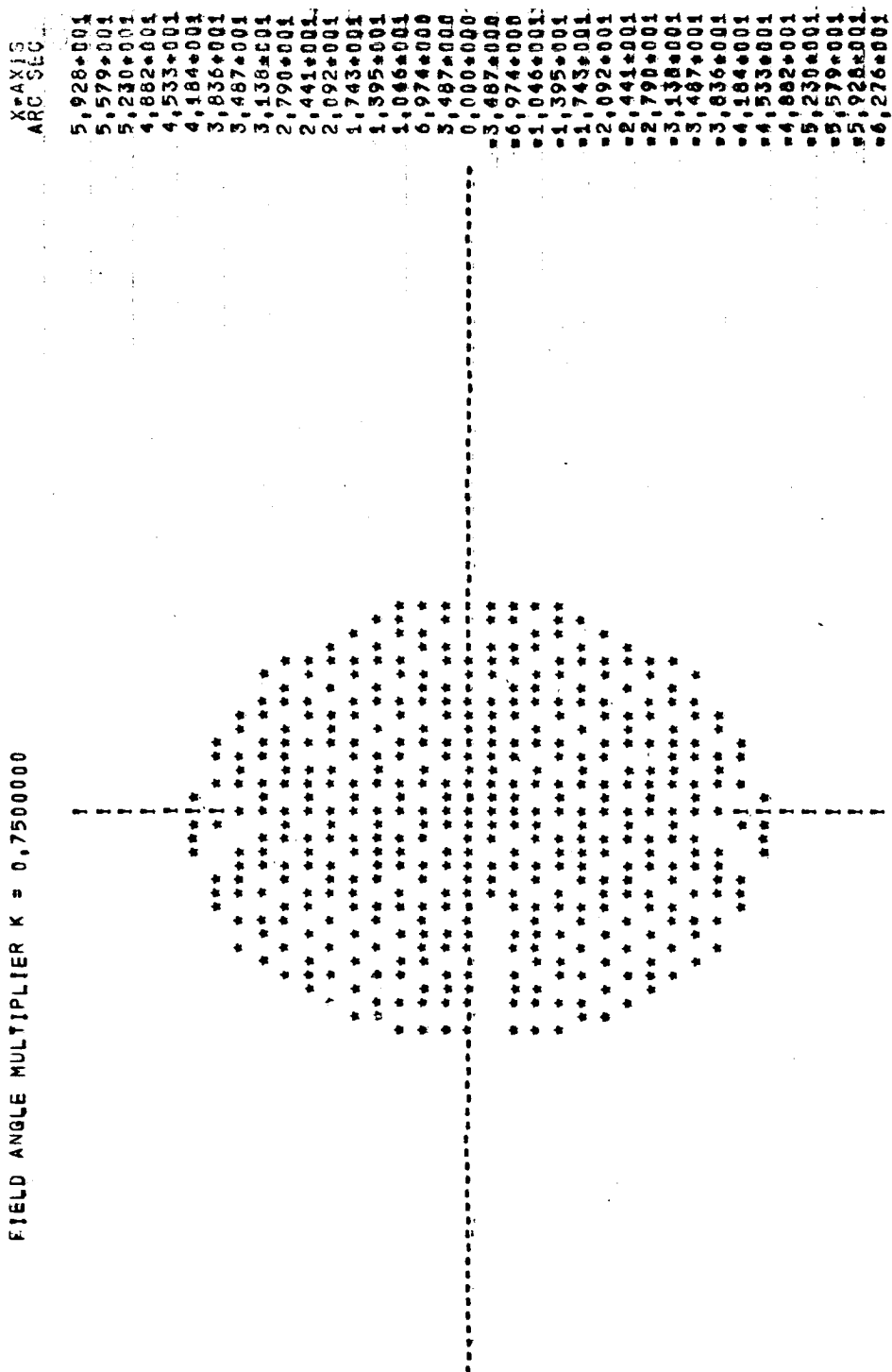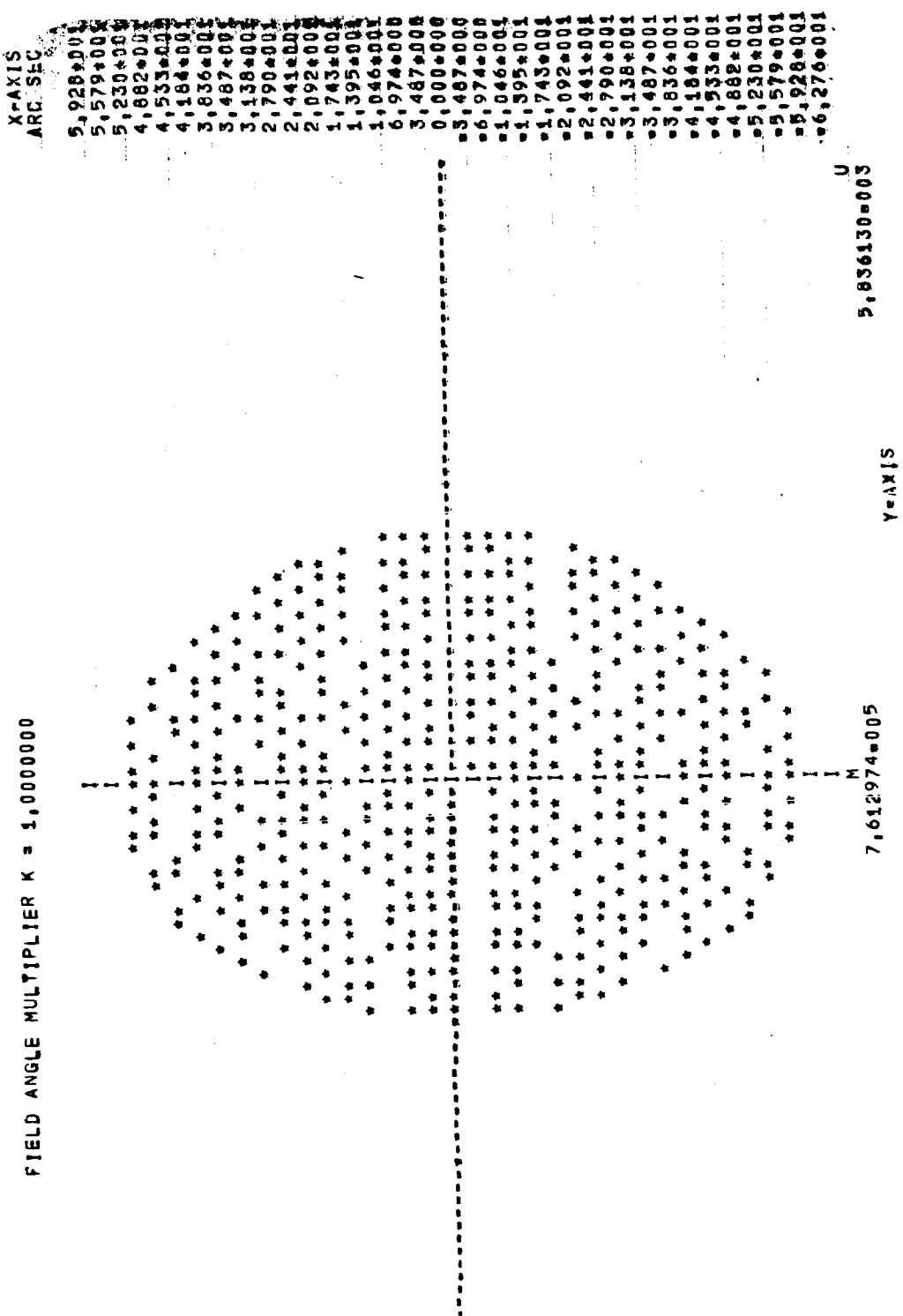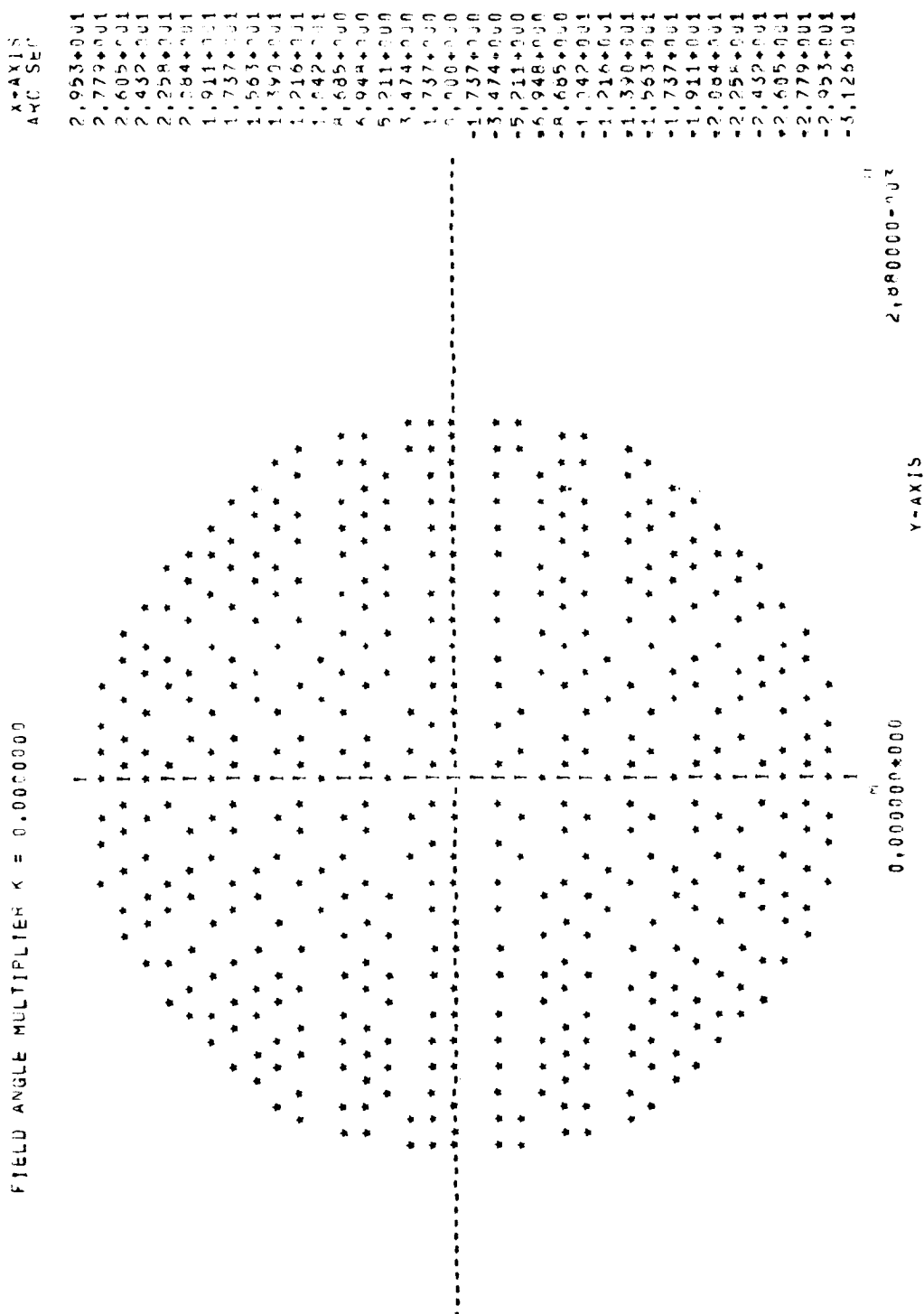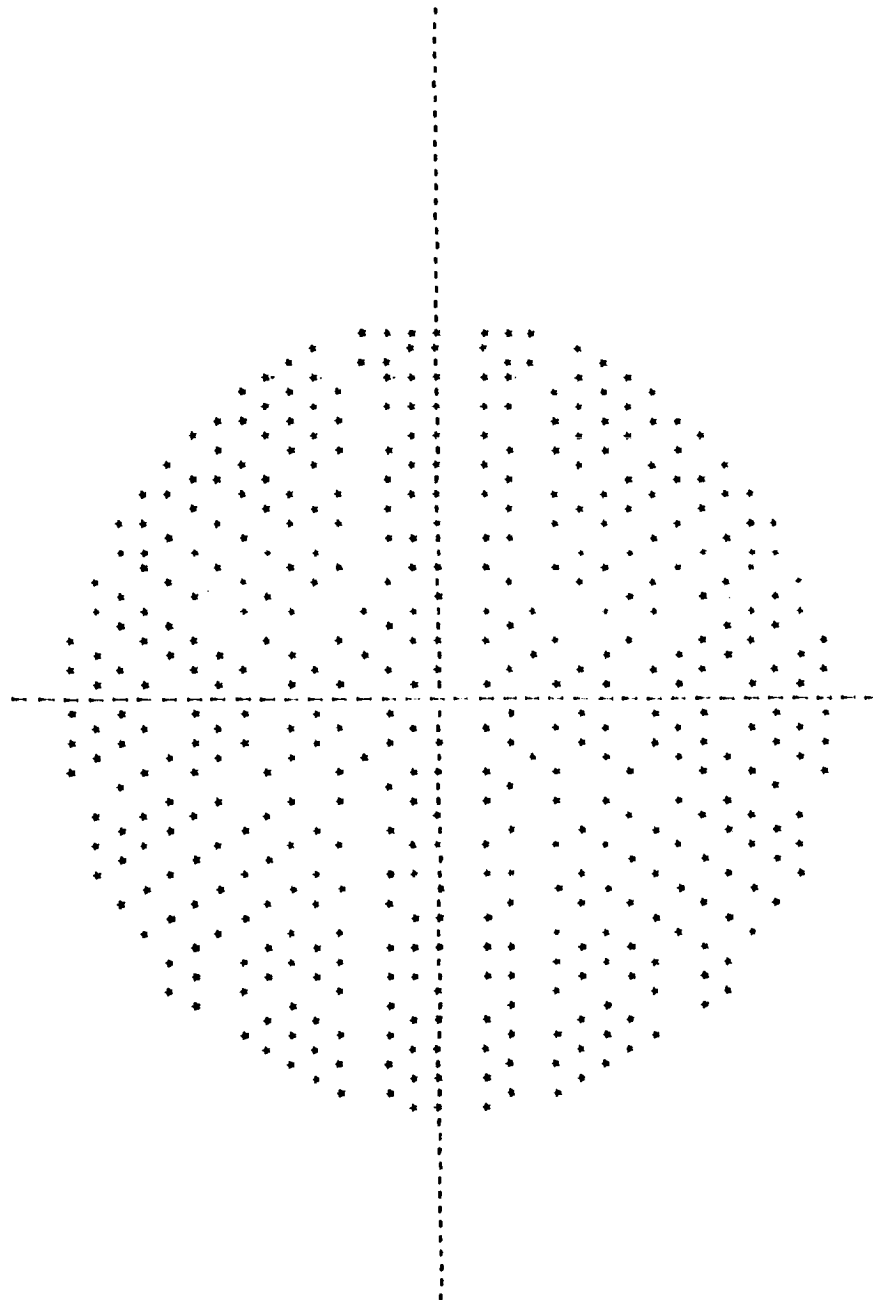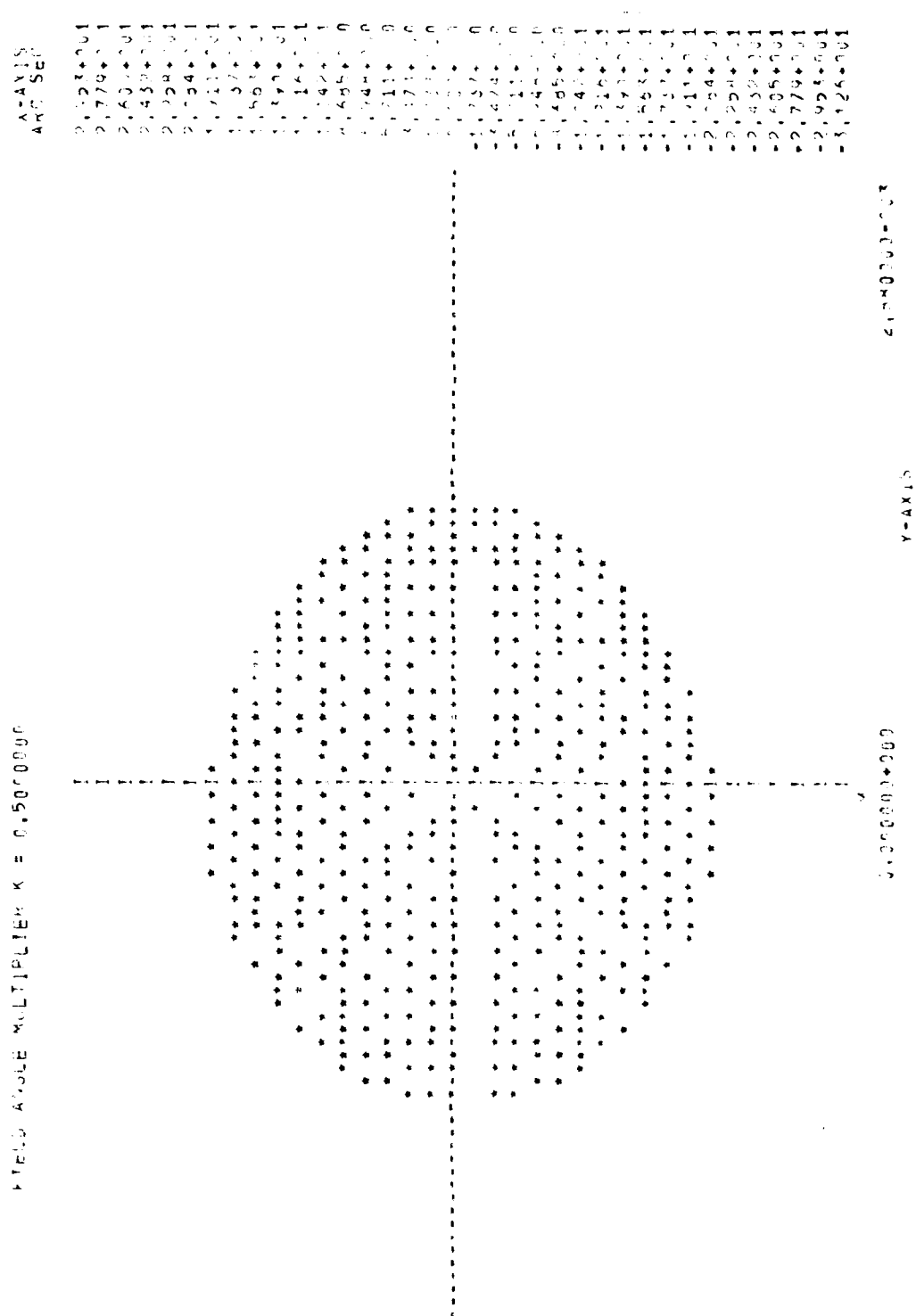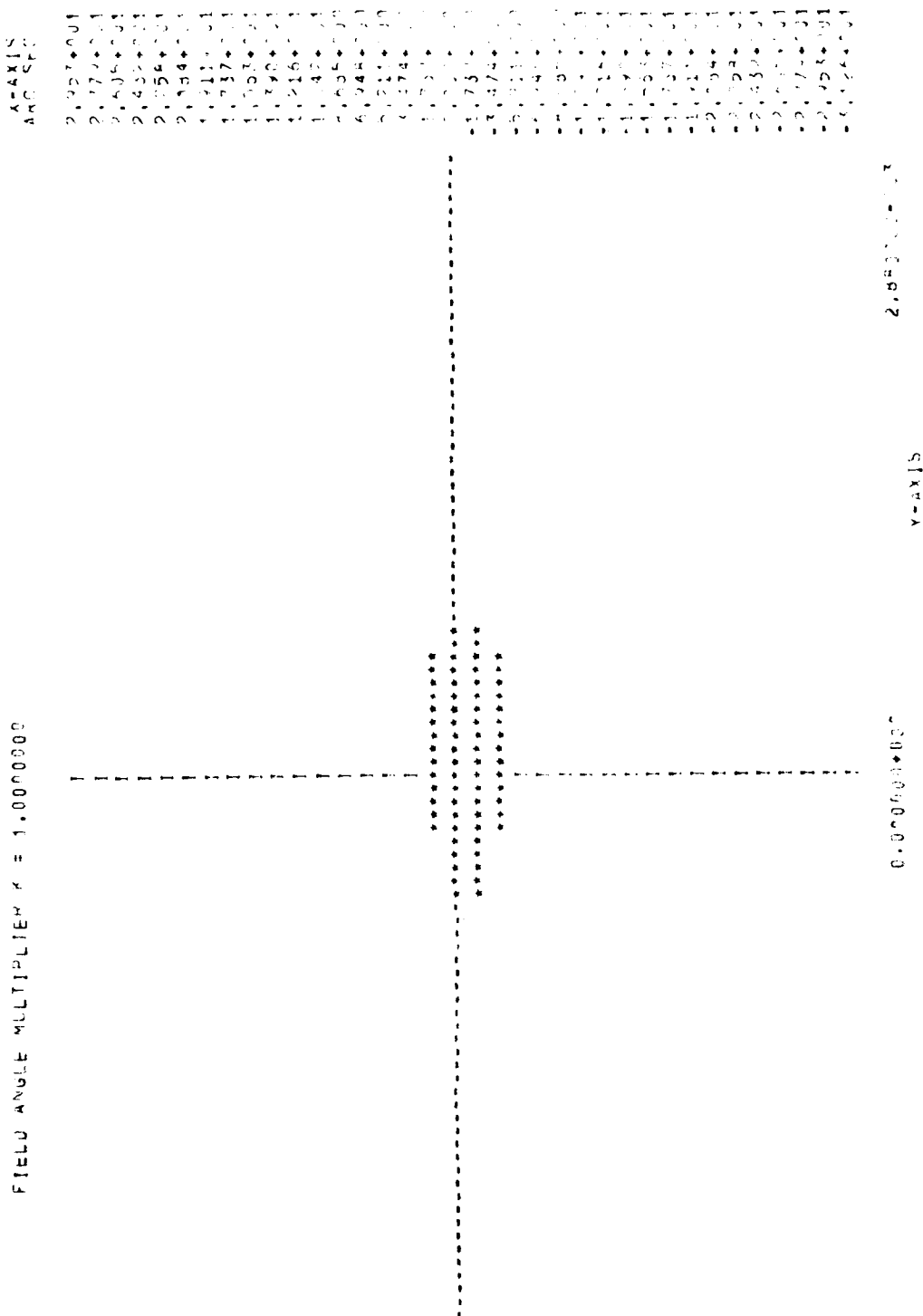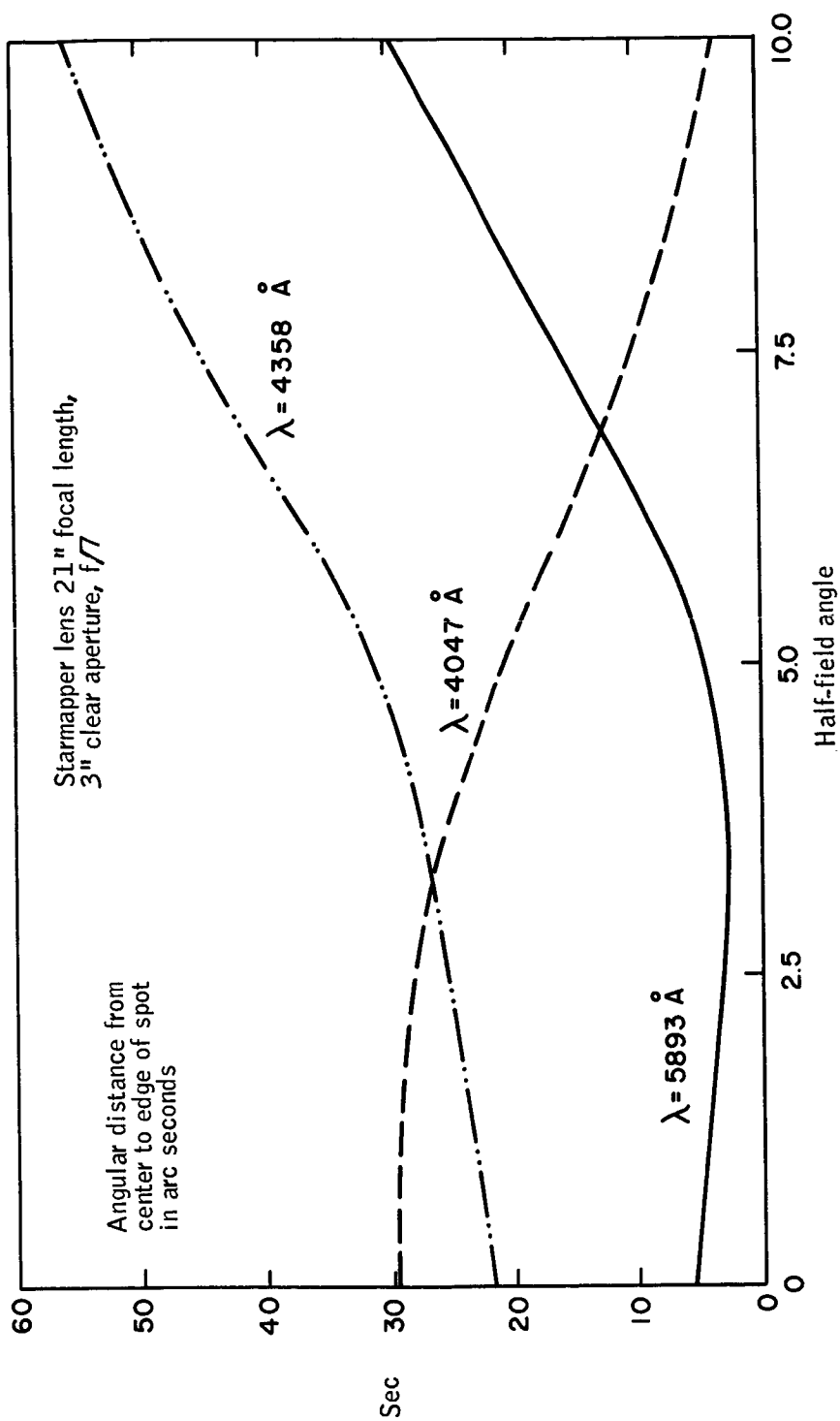Wavelength, 10.0° Half-Field Angle
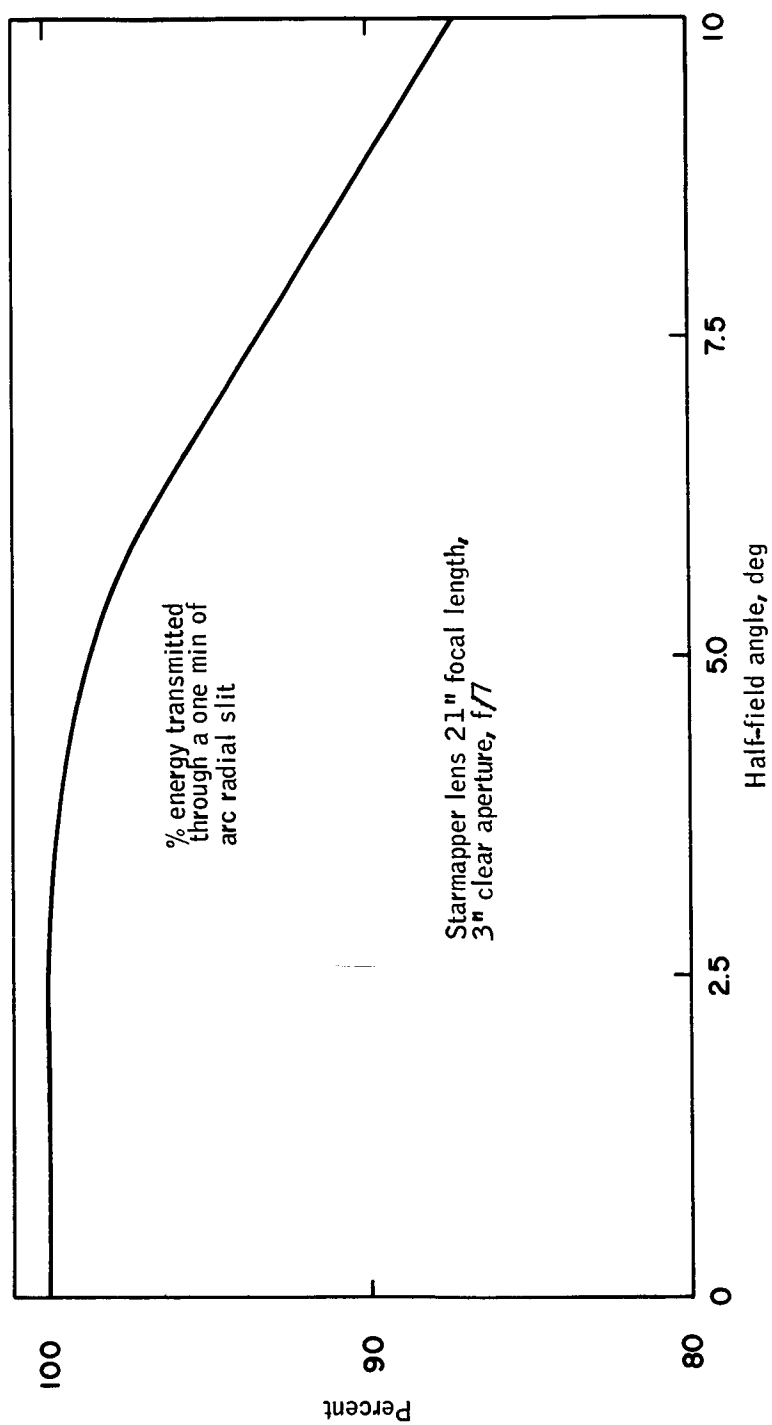
374

Figure 146. Effective Field of View

Figure 147. Average Effective Field of View

376
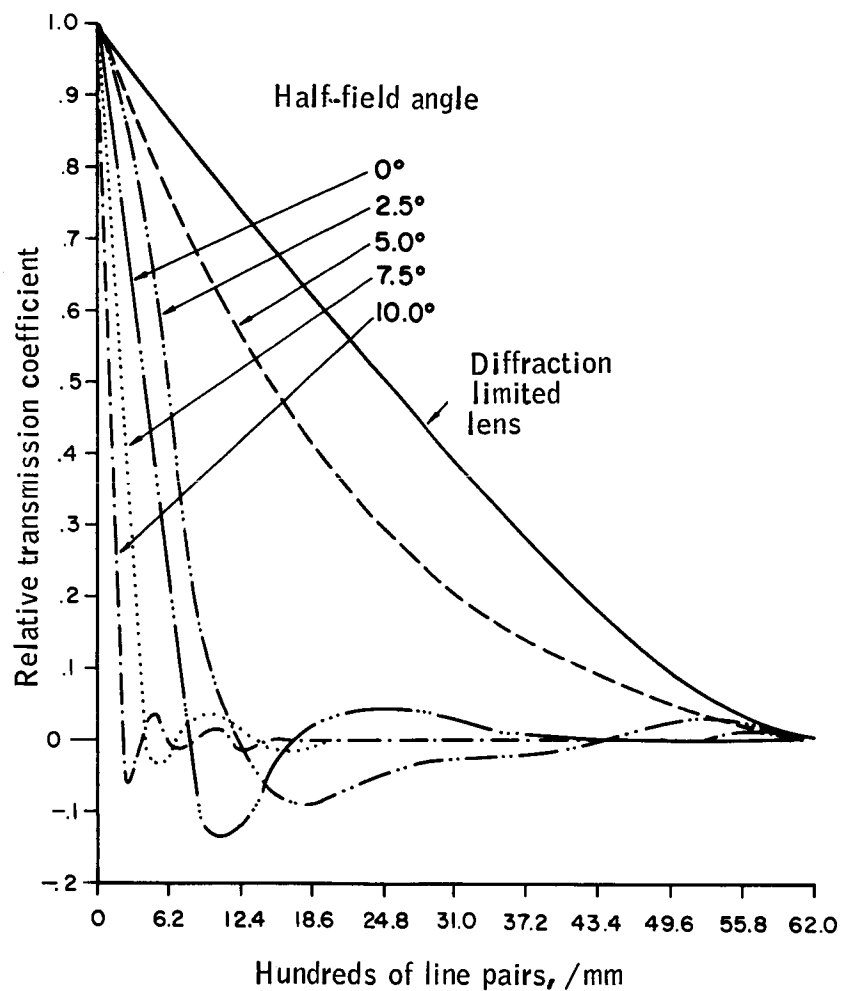
Figure 148.   Modulation Transfer Function of Starmapper Lens at
0.5893-Micron Wavelength

Light collection systems: Light from the star images passing through the scanning slits can be collected on the photocathode in three ways: (1) directly impinging on the photocathode, (2) collected by a system of collecting lenses which spread the light from the slits over the whole photocathode, (3) collected at the slits by fiber optics, then formed into a circular bundle spaced far enough from the photocathode to distribute the light widely over the sensitive surface.

► Direct collection of light from the slits:

This method implies two major design parameters: (1) a space-qualified photomultiplier of photocathode diameter sufficient to cover the complete focal plane of the sensor, and (2) that the sensitivity of each area of the photocathode is identical with that of all other areas within an appropriate tolerance determined by the detectability and false target discrimination appropriate to the design goal of accuracy.

An additional property associated with the first parameter mentioned above is that the photocathode must have sufficient durability to withstand the concentrated energy of bright objects focused in a small area by the lens.

Examination of available photomultipliers showed that direct light collection was not practical for the focal lengths and fields of view of the systems considered. No space-qualified photomultipliers of that diameter, bright spot resistance, and sufficiently uniform photocathode sensitivity are available.

► Condenser lens system:

A second method of collecting light on the photomultiplier photocathode utilizes convex (usually plano-convex) lenses placed very close to the slits to converge the light passing through the slits on the photocathode of the photomultiplier. In this system the photocathode can be smaller diameter than the focal plane of the scanning system. The basic optical design of the condensing system is to place a pair of plano-convex lenses with their plane sides outward immediately behind the focal plane of the scanning system with a combined focal length such that the image of the exit pupil of the scanning lens is formed on the photocathode with a diameter no greater than the photocathode.

The physical diameter of the condensing lenses must be enough larger than the focal plane to collect all the light passing through the slits. Thus for a 21-inch focal length lens, the pair of condensing lenses would need to be at least 7.5 inches in diameter. If a one-inch diameter photocathode is used, in order to reduce the three-inch clear aperture of the exit pupil to the photocathode size, about nine-inch clearance between photocathode and reticle will be needed to provide sufficient size reduction; the photomultiplier would extend about five inches beyond its photocathode.

378

The use of condensing lenses avoids the two difficulties cited in the analysis of the previous system:

(1) Availability of space-qualified photomultipliers: space-qualified photomultipliers of 1-to 1.5-inch photocathode diameter are available,

(2) Uniform sensitivity of photocathode: the condenser system provides uniform illumination of the photocathode from the light of the star image passing through the slit at any point in the focal plane. This property of the condenser system also prevents localized burning of the photosensitive surface when bright sources are viewed by the lens.

However, two difficulties are noted in this system. They are: (1) should it prove desirable to use separate condenser systems for the two sets of radial slits, the total length of the system could become much greater, and (2) the overall length of the system even with a single photomultiplier is large from image plane to end of the photomultiplier compared to the length needed for the fiber optics collection system described in the next section.

▶ Fiber optics light collection system

In this system, optical fibers are arranged in a close packing arrangement behind each of the six slits. The fibers thus arranged are grouped into separate bundles and conveyed to two separate photomultipliers. This line-to-circle conversion makes the most efficient use of the glass and of the photomultipliers, since the only glass needed at the slit plane is a line of fibers about three times the width of the slits. At the other end of the fiber optics, the ends of the two fiber bundles would be placed a sufficient distance above the photocathode to allow most of the photocathode to receive energy from the fiber ends, thus avoiding area sensitivity variations and minimizing the damage to the photocathode from bright images.

Evaluation of the collection efficiency of a fiber optics system depends principally on the transmission characteristics of a single fiber and the packing arrangement of the fiber ends.

The usual method of considering the arrangement of the fibers, is shown in Figure 149, where the lines joining the centers form a square of sides 2R in length. The area of the square = $4R^2$. Each corner of the square includes one quarter circle; the total circular area encompassed by the square is one circle or πR^2. The area between the fibers is the difference between the two or

$$(4 - \pi) R^2 \tag{85}$$

A measure of the efficiency is the ratio between the area of the space between the fibers to the area of the circle, or:
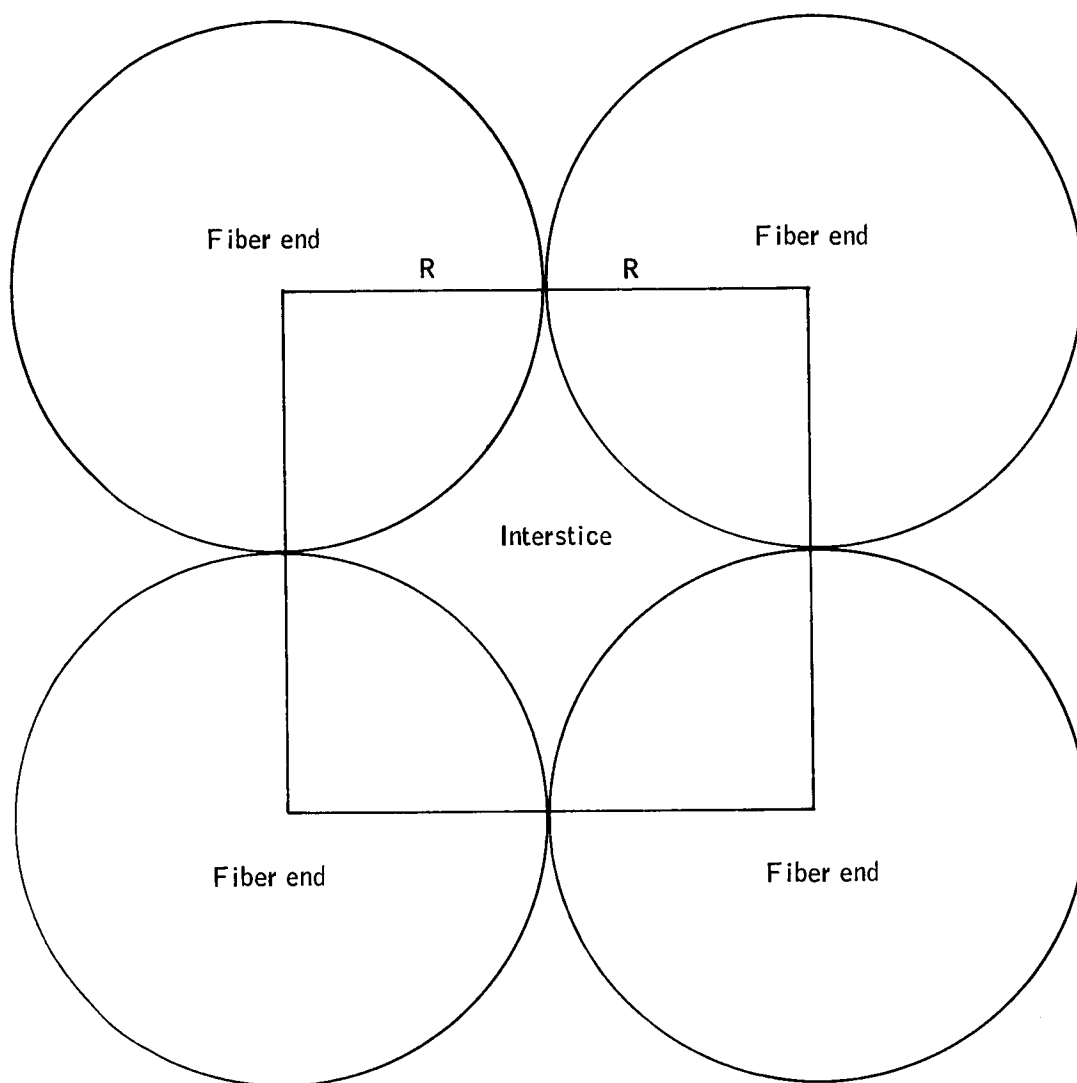
Figure 149. Fiber Ends Arranged in a Square Configuration

$$E = \left[1 - \frac{4 - \pi)\ R^2}{\pi\ R^2}\right] \times 100\% = \frac{4}{\pi} \times 100 = 72.68\% \tag{86}$$

A more efficient method of arranging the fibers is shown in Figure 150. Here the line joining three centers forms an equilateral triangle of sides 2R.

The area of the triangle is given by

$$A_T = R\sqrt{(2R)}^2 - R^2 = R^2\sqrt{3} \tag{87}$$

The lines joining centers enclose a total of a half circle, whose area

$$A_{HC} = \frac{\pi R^2}{2} \tag{88}$$

The efficiency is then

$$1 - \frac{R^2\sqrt{3} - \frac{\pi R^2}{2}}{\frac{\pi R^2}{2}} = \frac{2\sqrt{3}}{\pi} = 90.69\% \tag{89}$$

The effectiveness of this method of packing is shown in Figure 151. Here is shown a four layer assembly potted in epoxy and polished. Note that even though the assembly was cured with the fibers under pressure in a jig, the ideal packing configuration was approached but not attained. The two efficiencies cited above can be considered to be upper and lower bounds for the efficiency of a given packing configuration.

The overall transmission efficiency of randomly oriented fibers in a fiber bundle is shown in Figure 152 for various lengths of fiber bundles. Note that the transmission in the short wavelength region is greater than 60 percent for a 12-inch fiber bundle. The length of the fiber bundles needed for this line to circle conversion is of the order of three inches or less. This would indicate that the geometric packing configuration will be a more important factor in determining the attenuation than will the attenuation along the length of the fiber.

The fiber optics configuration of light collection was selected for the light collection system for the following reasons: (1) ease with which the light from upper and lower slit sets may be divided and coupled to separate photo-multipliers, (2) transmission efficiency of the system is comparable to the condensing lens system, (3) mounting flexibility provides for adjusting the con-figuration of the light collection system with a minimum of angular and radial constraints. Further, once firmly positioned, the light input to the photo-multiplier would be insensitive to temperature and accelerations acting on the fiber bundle.
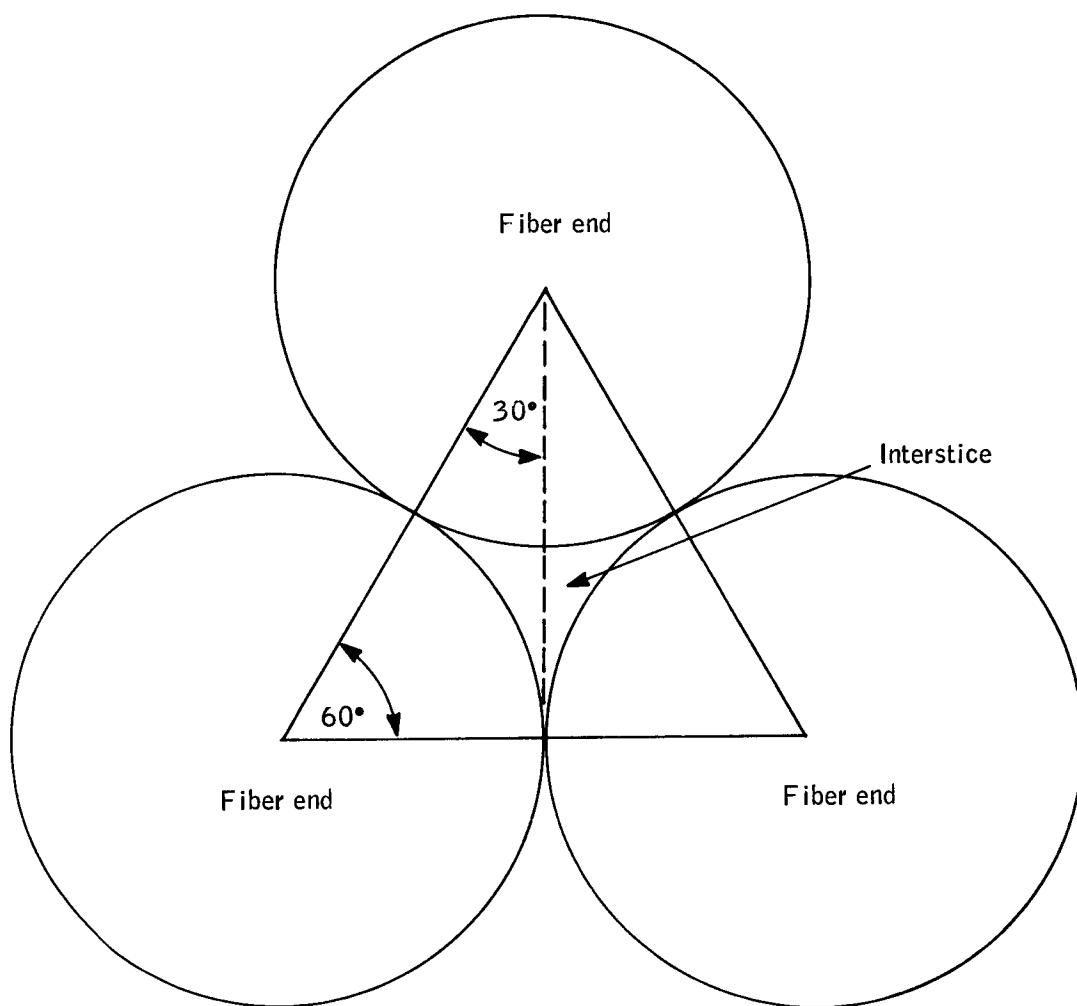
Figure 150. Fiber Ends Arranged in a Triangular Configuration
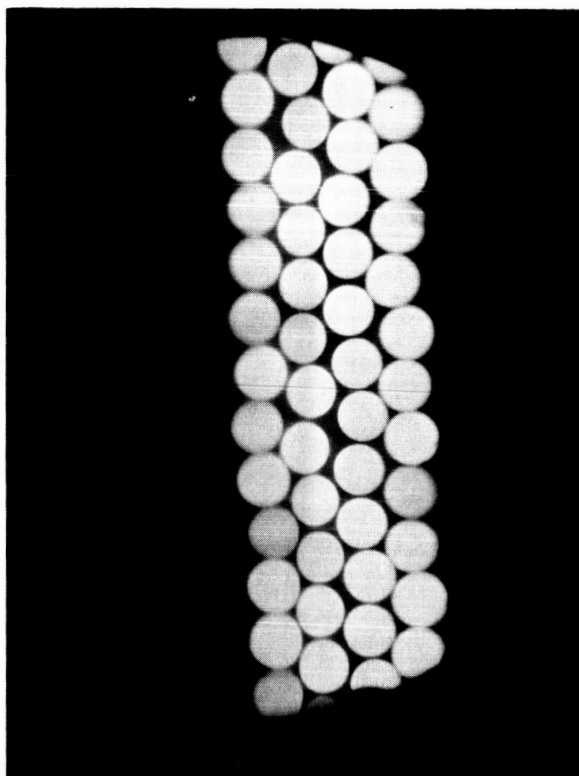
Figure 151. Photomicrograph of Four Layers of Fiber Ends Potted in Epoxy, Ground, and Polished
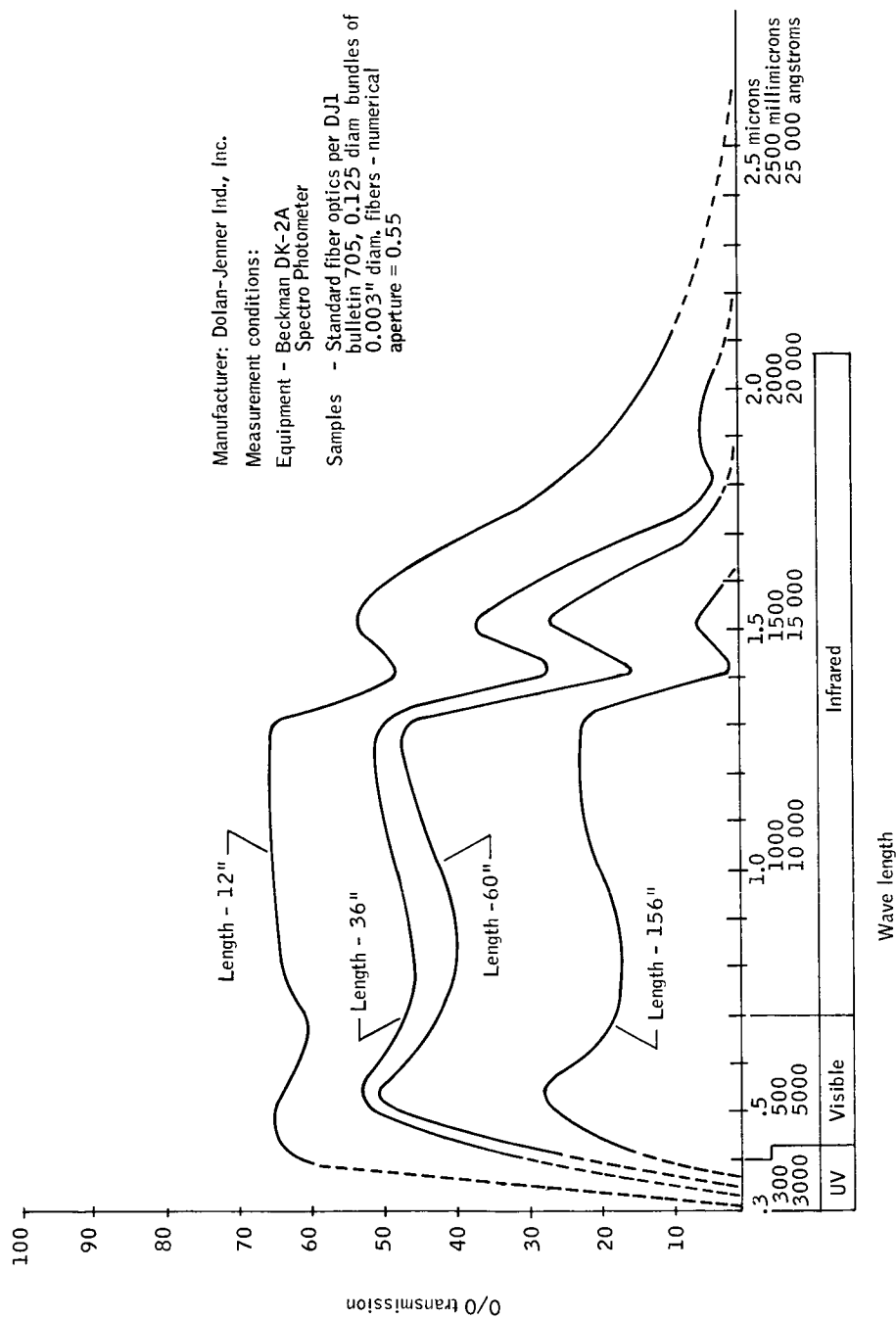
Figure 152. Light Transmission Characteristics for Flexible Fiber Optics

The effect of the choices of lens parameters and light collection systems is shown in an assembly drawing in Figure 153. The flare of the baffle is adjusted to give a 20-degree field of view.

Electronic Design. --

System considerations: The following paragraphs will explain the method of signal processing starting with the light output of the slit configuration and eventual determination of star transit times. Three optical systems which have been discussed elsewhere in this report will be considered as the "light gathering" elements. The three systems are:

(1) f/2.0, 3-inch aperture, 6-inch focal length

(2) f/4.0, 3-inch aperture, 12-inch focal length,

(3) f/6.0, 4-inch aperture, 24-inch focal length.

Each one of the optical systems above has the capability of covering a 20-degree field of view. The first two optical systems have the same light gathering capability from the standpoint of aperture size; the third system will gather more light due to its bigger aperture. There are also other tradeoff factors in the optical elements which will effect the electronics. The prime factor is that of blur circle size. Each of the three optical systems has different blur circle sizes and these blur circle patterns have different shapes (aberrations) and are also wavelength dependent. The prime factor which affects the electronics system is the resultant light pattern from the slit which will be converted into electrical impulses in the photomultiplier. If a diffraction-limited system is assumed (the f/7 system approaches this condition); then, in order to detect 80 percent of the blur circle when it is centered in the slit, the star transit time must be defined as $T_s = 2.56 \; \sigma_t = 9.25 \times 10^{-4}$ seconds. This calculation assumes a one minute of arc blur circle and three revolutions per minute spin rate, thus

$T_s = 2.56 \; \sigma_t$ is derived from the fact that the optical system is considered to be diffraction limited and that $84 \cong 80$ percent of the energy is within the blur circle. Using the Airy Disc function, it can be shown how the 84 percent figure is derived.

$$y = \left(\frac{2 \; J_1(x)}{x} \right)^2 \tag{90}$$

where $J_1(x)$ is a Bessel function.

It is shown that $J_1(x)$ has its first minimum at $x = 3.832 = 1.22 \pi$.

Consequently, equation (90) goes to zero at that point.

The energy within the radius 1.22π is
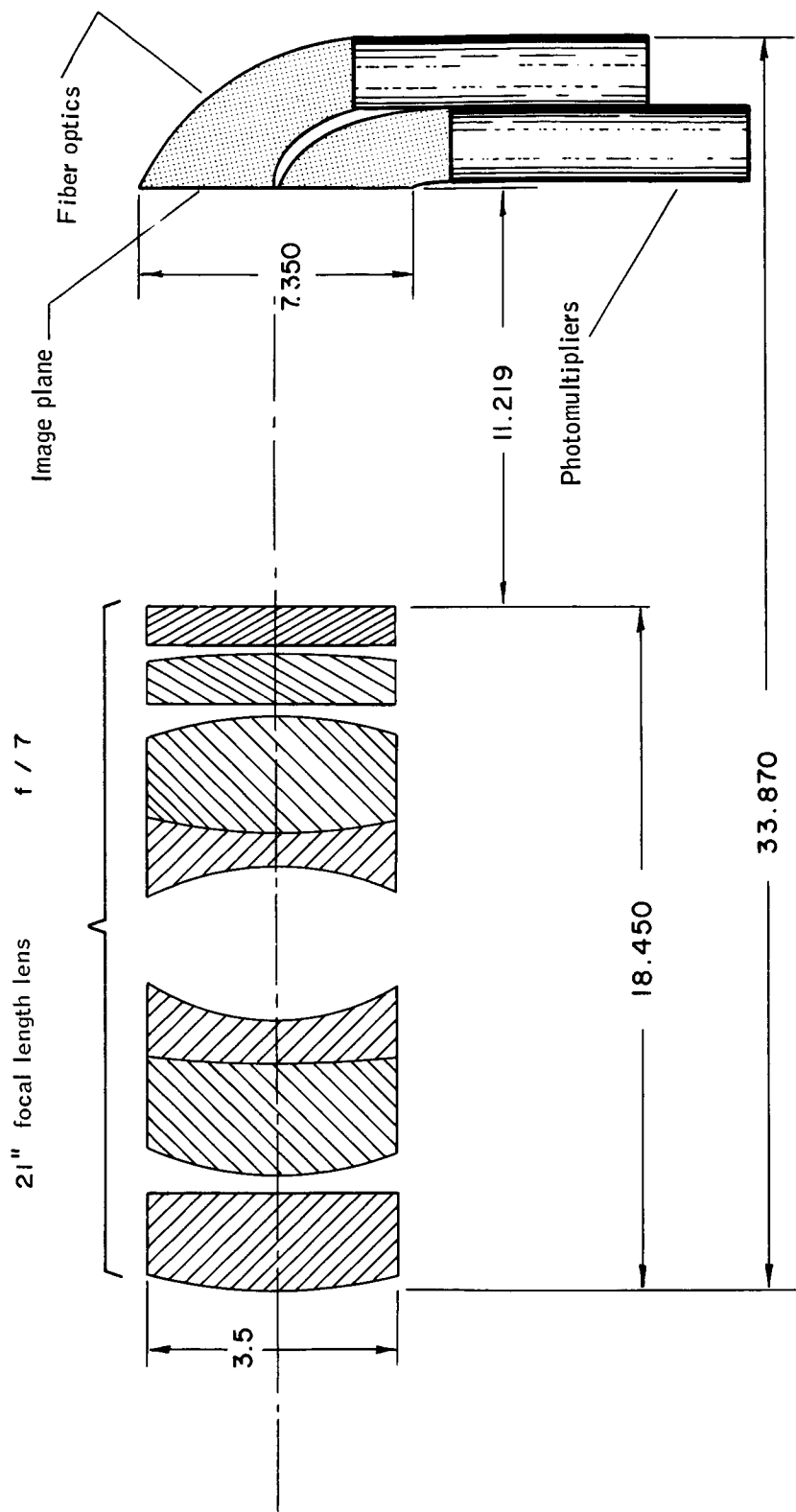
Figure 153. Starmapper Sensor Optical System

Fiber optics

Image plane

Photomultipliers

7.350

11.219

33.870

18.450

3.5

21" focal length lens

f / 7

$$L(r) = 1 - J_o^2 (Kr) - J_1^2 (Kr)$$

$$= 1 (0.4)^2 - (0)^2$$

$$= 1 - 0.16 = 0.84 \approx 0.8.$$

A signal at the input to the photomultiplier is now defined (approximated by a normal distribution),

$$G(t) = \phi \left(\frac{t}{\sigma} + \frac{T_s}{2\sigma_t} \right) - \phi \left(\frac{t}{\sigma} - \frac{T_s}{2\sigma_t} \right) \qquad (91)$$

where

$$\phi(t) = \frac{1}{\sqrt{2\pi}} \int_{-\infty}^{t} e^{-x^2/2} \, dx$$

At $t = 0$, $G(t) = G(0) = 0.8$

$$G(0) = \phi \left(\frac{T_s}{2\sigma_t} \right) - \phi \left(\frac{-T_s}{2\sigma_t} \right) = 0.8.$$

Let

$$\phi \left(\frac{T_s}{2\sigma_t} \right) = \phi(\tau)$$

or

$$\phi(\tau) - \phi(-\tau) = 0.8$$

$$\phi(\tau) = \frac{1}{\sqrt{2\pi}} \int_{-\infty}^{\tau} e^{-x^2/2} \, dx$$

$$\phi(-\tau) = \frac{1}{\sqrt{2\pi}} \int_{-\infty}^{\tau} e^{-x^2/2} \, dx$$

$$\phi(\tau) - \phi(-\tau) = \frac{1}{\sqrt{2\pi}} \int_{-\infty}^{\tau} e^{-x^2/2} \, dx - \int_{-\infty}^{\tau} d^{-x^2/2} \, dx - \int_{\tau}^{\tau} e^{-x^2/2} \, dx$$

$$\phi(\tau) = \frac{1}{\sqrt{2\pi}} \left[-\int_{\tau}^{-\tau} e^{-x^2/2} \, dx \right] = \frac{1}{\sqrt{2\pi}} \int_{-\tau}^{\tau} e^{-x^2/2} \, dx$$

$$\phi(\tau) = \frac{2}{\sqrt{2\pi}} \int_{0}^{\tau} e^{-x^2/2} \, dx$$

$$0.8 = \frac{2}{\sqrt{2\pi}} \int_{0}^{\tau} e^{-x^2/2} \, dx$$

Substituting $y^2 = \frac{x^2}{2}$; $y = \frac{x}{\sqrt{2}}$; $\sqrt{2} \, dy = dx$

then,

$$0.8 = \frac{2}{\sqrt{\pi}} \int_{0}^{\tau/\sqrt{2}} e^{-y^2} \, dy = \text{erf} \, \frac{\tau}{\sqrt{2}} \tag{92}$$

Using tables for $\text{erf}(x) = \text{erf} \, \frac{\tau}{\sqrt{2}}$

$$\frac{\tau}{\sqrt{2}} = 0.906$$

$$\tau = 1.28$$

$$\frac{T_s}{\sqrt{2} \, \sigma_t} = 1.28; \quad T_s = 2.56 \, \sigma_t \tag{93}$$

It has been shown that an interpolation factor of 9.1 is justified. If a slit width of one minute of arc is assumed so as to match the slit to the blur circle (assuming that the blur circle is uniform over the field of view) then, an angular accuracy of 60 seconds of arc/9 = 6.67 seconds of arc exists. In reality, however, the blur circle will not be uniform over the entire field of view so it is assumed that as a worst case the blur circle will be no larger than one minute of arc. Thus, 80 percent

388

of the light or better will be centered in the slit.

Having now defined the slit width (one minute of arc) some statements can be made about signal-to-noise ratios for the three systems. Many factors must be taken into account for calculating S/N ratio. From Figure 154, the light flux is seen as a function of wavelength which is available from the star Vega which is a 0.04 magnitude type A0 star. This curve has been well established. On the same figure is superimposed the spectral response curve of the proposed photomultiplier tube (discussed later). By multiplying the two curves together into a composite curve, a curve is noted of photomultiplier response in terms of amps/cm²/micron as a function of wavelength (in microns). Then, integrate (numerically) to find the total current per square centimeter out of the photomultiplier tube. The expression $m_x = m_{known}[10^{-.4(m_x - M_{known})}]$ can "scale" the amount of current for any given star magnitude (of the same spectral class, of course).

The area under the composite curve is computed to be 7.92×10^{-14} amperes per square centimeter (cathode current) for the star Vega. This assumes an optical efficiency of 100 percent which shall be corrected for later.

Now, the signal available from a 3.5 magnitude star shall be calculated:

$$I_{3.5} = I_{0.04} \cdot 10^{-.4(3.5-0.04)} \times E_{opt} \times A \times K_1 \qquad (94)$$

where

$I_{3.5}$ = current (cathode) due to 3.5 magnitude star

$I_{0.04}$ = current (cathode) due to 0.04 magnitude star

E_{opt} = optical efficiency

A = area of objective lens in square centimeters

K_1 = constant = 80 percent of total energy in slit

The noise due to the background can also be calculated in terms of equivalent tenth magnitude stars per square degree.

$$I_{200-10}th = I_{0.04} \cdot 10^{-.4(10 - 0.04)} \times E_{opt} \times A \times N \times SA \qquad (95)$$

where
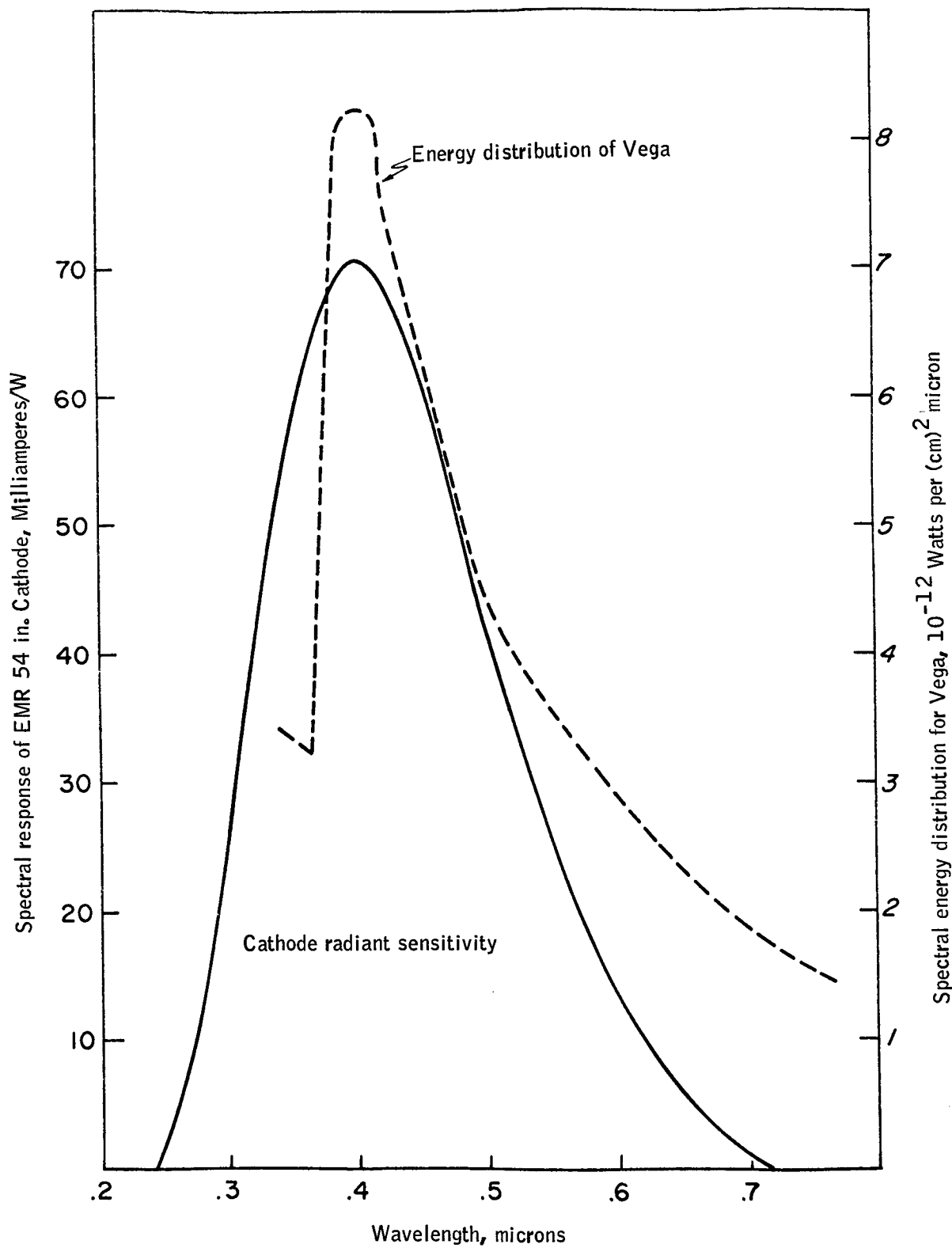
Figure 154. Cathode Radiant Sensitivity Spectral Energy Distribution of Vega

390

Several alternatives are available for shutting off the photomultiplier supply:

- External sensors mounted around the periphery of the starmappers

- Ground command

- Monitoring of peak anode current from the photomultiplier tube

The first alternative is not as desirable for physical reasons. It may be hard to establish the geometry of how many and where these sensors would be located.

The second alternative should be used when it is known, for example, that the moon will be in the field of view (approximately two days per month). By far the best alternative is that of monitoring the peak anode current from the photomultiplier output. This limit can be set such that any bright target can be discriminated against.

The peak anode current monitoring circuit can be made so that the tube is shut off permanently and can only be restarted by command from ground, or the circuit could be made to attempt turn on after some period of time.

A supply such as EMR's remote power supply, in conjunction with a quick shut-off circuit, is more desirable. The EMR circuit would have to be modified, however, to allow quick discharge of the bleeder chain if that criteria is necessary. The Consolidated Avionics supply appears to be capable of quick shutdown when supplied an external shutdown signal. It is also recommended that the power to the photomultiplier be reinitiated by both ground command and automatic turn on. In fact, the turning off of the starmappers may initiate the sun sensor operation. Once the starmapper is turned off the sun sensor can be turned on. When the sun sensor stops generating pulses, the starmapper may be turned back on. If enough earth or sun light is present, the starmapper will turn itself off and wait for a fixed delay period before attempting reinitiation.

High input impedance amplifiers

A high input impedance amplifier with moderate gain ($A \approx 10$) can be built easily. Some operational amplifiers are available which will work adequately or a field effect amplifier stage may be used.

Low pass filter design

Much investigation has been done at Control Data on the design and optimization of linear phase shift low pass filter designs. Active networks have allowed the builting of filters without the use of inductors. The filter which is recommended for this application is the Paynter filter whose transfer function for a sixth-order filter is given as

391

$$A(s) = \cfrac{1}{\left[1+2.386\left(\dfrac{s}{\omega_c}\right)+1.866\left(\dfrac{s}{\omega_c}\right)^2\right]\left[1+.6204\left(\dfrac{s}{\omega_c}\right)+.6579\left(\dfrac{s}{\omega_c}\right)^2\right]\left[1+.1224\left(\dfrac{s}{\omega_c}\right)+.23175\left(\dfrac{s}{\omega_c}\right)^2\right]}$$

The sixth order filter was picked because of its better roll-off capabilities and because its approximation to linear phase is very good. The higher order Paynter filter has a nearly gaussian transient response (which matches our input signal model) and has a dispersion time of

$$\tau = \frac{1}{\sqrt{n-1}}\ \frac{2}{\omega_c}$$

and a delay time of π/ω_c. The dispersion to delay time ratio is therefore

$$\frac{2}{\pi}\frac{1}{\sqrt{n-1}}$$

The dispersion time $\tau = 0.895/\omega_c$ for a sixth-order filter and the delay time is π/ω_c. Therefore, the dispersion to delay time ratio is 0.285.

A gaussian input response from a Paynter filter has been simulated and the optimum ω_c for maximum S/N ratio has been determined. Since $2.56\ \sigma_t = T_s$, $\sigma_t = 3.617 \times 10^4$ seconds, $\sigma_t\ \omega_c = 0.7$ (determined as maximum S/N ratio by computer program simulating Paynter filter response to a near gaussian pulse).

$$\omega_c = \frac{0.7}{3.617 \times 10^4} = 1.935 \times 10^3$$

$$f_c = 308\ \text{Hz}$$

S/N ratios calculated earlier in this section were for f_c = 308 Hz (Δf = 1.02 f_c = 314 Hz.

It should be noted before leaving the subject of filters that the amplitude response filters (Butterworth, etc.) give better S/N ratios -- this is fine for radar work where detection is the only concern. The concern here is for both S/N ratio and preserving the fidelity of the input signal. An implementation of the active filter is given in Appendix K.

Differential Amplifiers

There are many differential amplifiers available today in a single package (TO-5 can or flat pack). The Fairchild μA702 or μA709 will easily work in this application.

392

- Level Detectors

Once more, level detector circuits are standard. The Fairchild μA710 is quite applicable to the situation.

- Logic

It is suggested that integrated circuits be used for the logic for obvious power, weight, and reliability reasons. More attention can be given to redundancy if desired since the volume of electronics should be small.

- Sun Detectors

The integrating sphere design presented elsewhere in the text is adequate. Once more, there is a wide variety of photodetectors available. A silicon photodiode with a large sensitive area is desirable. The remainder of the sun sensor electronics is similar, and in some cases, shared with the star-mapper.

Reliability

A reliability prediction was made based upon a similar system which was built for NASA GSFC on the ATS-SCNS program. In evaluation of the ATS system, it was found that the weakest link (highest failure rate component) was the photomultiplier tube. In fact, the failure rate for the photomultiplier and power supply were estimated (and verified by EMR) to be 3.6 percent per 1000 hours. The sum total of electronics accompanying this tube had a failure rate of 0.44 percent per 1000 hours.

Our system is defined in a similar manner (one photomultiplier, one set of electronics); a total failure rate would be computed of 4.04×10^{-5} per hour or a probability for operating one year without failure of 70 percent. Actually, it is much better than if a completely redundant starmapper were considered. The probability of success for a one-year mission would be $1 - (0.3)^2 = 91\%$.

The system reliability may still be improved by considering the two photo-multipliers in each starmapper. If one of the two photomultipliers failed the other photomultiplier tube could operate but in a downgraded mode of operation (loss of one half of the total field of view).

Another factor which can enhance the starmapper probability of success is that of duty cycle. It is anticipated that the photomultiplier tubes may have a duty cycle of about 35 percent. Advantages gained in turning the high voltage supplies on and off must be assured by careful circuit design since transient conditions could degrade both the photomultiplier and its supply.

Another factor to be considered in the reliability model is that of getting sufficient data to ensure success of the attitude determination. Therefore, the system reliability should also be calculated to include the sun sensors, since both the starmappers and sun sensors will be providing the transient time information.

I_{200-10}th = current (cathode) due to 200-10th magnitude stars

N = number of 10th magnitude stars per square degree

SA = total slit area in square degrees.

The signal-to-noise ratio can now be defined as peak signal-to-rms noise at the output of the filter or

$$S_{peak}/N = \frac{K_2 \, K_3 I_{SS}}{\sqrt{2e(I_{SS} + I_{BC} + I_{DC}) \, \Delta f}} \tag{96}$$

where

Δf = noise equivalent bandwidth

I_{SS} = star signal current, average

I_{BC} = sky background current, average ⎫ Both are essentially

I_{DC} = dark current of tube, average ⎭ dc currents

e = 1.6 x 10^{-19} coulombs

K_2 = dynode chain signal degradation factor

K_3 = attenuation of peak amplitude due to filter

Given enough S/N ratio for the limiting magnitude star, from probability theory detection may be defined based upon the chances of detecting false signals. A new signal-to-noise ratio will now be defined as the signal at the threshold to the rms noise. It is found that these two methods of calculations have accurately approached physical measurements. In the calculations matched filtering was also assumed.

It is the intention to design a system which will have sufficient S/N ratio to assure detection of a 3.5 magnitude star and maintain accuracy (time, angle) at this limiting magnitude. A calculation of S/N ratios at a limiting magnitude of 3.5, an optical efficiency of 50 percent, Δf = 314 Hz for the three proposed optical systems results in the following:

System 1 - 10:1 (threshold level set for 95 percent probability of detection)

System 2 - 10:1 (threshold level set for 95 percent probability of detection)

System 3:- 13:1 (threshold level set for 95 percent probability of detection).

Note that Systems 1 and 2 are equal due to the fact that the apertures are both three inches. The accuracies of the two systems are different, however.

It must again be emphasized what the results above mean. If the threshold is set for 95 percent detection probability and the detection is with a matched filter, the above S/N ratios hold true. The values of the threshold setting will be lower for weak stars and higher for bright stars. In terms of threshold settings with respect to the star signal, however, the threshold setting will approach the peak value of the star for dim stars, and will be lower for the bright star.

Electronics subsystems:

Functional block diagram

The functional block diagrams shown in Figures 155 and 156 are methods of processing data from a two-photomultiplier starmapper and a one-photo-multiplier starmapper. Note that little difference in the electronics pro-cessing exists between the two functional diagrams. In terms of actual hardware, however, a more substantial difference exists. Table 29 shows a comparison of the one and two photomultiplier schemes as far as advan-tages and disadvantages.

In Figure 155, the outputs of the two photomultipliers are sent through similar analog circuitry; the analog outputs are fed into an "or" circuit which will combine in an analog fashion the pulse from the two photomulti-pliers. A photomultiplier identification circuit preceding the "or" gate will allow tagging of the transit time word with the proper code.

Figure 156 shows the output of the one photomultiplier scheme fed into the same analog circuitry of the two photomultiplier system. The prime differ-ence between the two systems lies in the complexity of the identification cir-cuitry.

The transit times will be made up of several words of information. The first word will be the leading edge time of 20 bits and the second word will be an n bit word which gives the duration of the pulse. In addition, a coding bit for the upper or lower half of the slit plane (for the one photomultiplier case) or a coding bit for photomultiplier 1 or photomultiplier 2 (two-photomultiplier case) will be added to the two words which are stored.

Signal processing method

The signal processing method for the one or two photomultiplier methods is essentially the same. This discussion will assume two photomultipliers and point out differences as they occur in the discussion.

The raw output pulses from each cathode are multiplied by a factor of 10^6 to 10^7 and fed into a high impedance load. An amplifier with high input

TABLE 29. - ADVANTAGES AND DISADVANTAGES OF TWO SIGNAL PROCESSING METHODS

Two-photomultiplier scheme		One-photomultiplier scheme	
Advantages	Disadvantages	Advantages	Disadvantages
Coding of upper, lower slits automatic.	Two photomultipliers • Reliability • Size • Weight • Power	Only one photomultiplier (high voltage problem less; more reliability).	Upper and lower half identity scheme more complex.
Signal-to-noise may be better due to less background noise.	Fiber optics may be difficult to implement depending upon structure.	Weight	More possibilities of bad data due to decoding scheme.
Mechanical system more flexible.	Overall, more electronics.	Power	More sky background, thereby lowering S/N ratio by a factor of 20 % (now 8:1); requires increase in aperture to increase signal at expense of added weight; size.
Somewhat less electronics as far as encoding scheme.	May require more commands.	Size	
May be reliability advantage if photomultipliers are somehow isolated and 10° FOV sufficient to do attitude detection.	Coding scheme does not suffer from variations in slit width, satellite spin speed.	Less complex system structure-wise.	
Storage requirements same as one photomultiplier.	Total attenuation of optical system may be more, depending upon implementation.	Can consider two inch (1.7") photomultiplier to reduce condenser sizes.	
		Condenser system easier to implement than fiber optics (at expense of weight and size).	

Figure 155. Two-Photomultiplier Starma

Note:
n, (n+1), are derived from spacecraft clock
correlating to time/revolution.
(odd, even revolutions)

1(n+1) + 5(n+1)

2 (n+1)

8

3 (n+1)

4 (n+1)

Leading edge detector — 6

Trailing edge detector — 7

Divide by 3

Stars per revolution counter no. 1 (max. count = 3)

Overflow detector one — S / C

1

Divide by 3

Stars per revolution counter no. 2 (max. count = 3)

Overflow detector two — S / C

2

Divide by 3

Stars per revolution counter no. 3 (max. count = 3)

Overflow detector three — S / C

3

Divide by 3

Stars per revolution counter no. 4 (max. count = 3)

Overflow detector four — S / C

4

Clear beginning revolution (n)

5

per Functional Block Diagram

398

Figure 156. One Photomultiplier Starm

1 (n+1) + 5(n+1)

2(n+1)

9

3(n+1)

4(n+1)

Leading edge detector   6

Trailing edge detector   7

D — Divide by 3 — Stars per revolution counter no. 1 (max. count = 3) — Overflow detector one   S   C
8

D — Divide by 3 — Stars per revolution counter no. 2 (max. count = 3) — Overflow detector two   S   C
8

D — Divide by 3 — Stars per revolution counter no. 3 (max. count = 3) — Overflow detector three   S   C
8

D — Divide by 3 — Stars per revolution counter no. 4 (max. count = 3) — Overflow detector four   S   C
8

Clear beginning revolution (n)

1
2
3
4
5

impedance amplifies the voltage signal (about a 0.1 volt for a bright star, 10^6 ohms load and 10^6 photomultiplier gain). This voltage is amplified without distortion to a reasonable working level and then transmitted to a low pass filter. The low pass filter is matched to the signal for optimum processing and is of the linear phase shift type. The output of the filter is fed to two circuits -- another low pass filter and to one of two inputs of an operational amplifier. The second low pass filter is also of the linear phase shift type; however, its cutoff frequency is so low that only slowly varying signals are allowed through it. This slowly varying signal is predominately star background noise (and dark current). The star background is subtracted from the original filtered star pulse by feeding the slowly varying pulse into the other input of the differential amplifier. The output of the differential amplifier will appear then as a star pulse without dc to ≈ 1 cps components of frequency which is then "or"ed with the other photomultiplier loop circuitry. These "or"ed signals are then sent to a number of level detectors, in this instance we have shown four. Each level detector is set for different threshold values which are optimized for best detection at a given star magnitude. Since the slope of the signal is fairly constant over a given portion of the gaussian signal, each level detector will process its information in a near optimum manner. The diagram shows that the level detectors have been set to detect stars greater than 3.5, 3.2, 2.7, and 2.0 in magnitude. These magnitudes have been determined from a computer printout of simulated detected stars for the starmapper as it sweeps through an orbit so that it includes approximately the same number of stars in each group.

Each level detector feeds a counter which can count to four star detections. The fourth count, however, is not a legitimate count but rather a means for denoting overflow of a count-three counter. For multiple slits, this count is three or four stars times the number of slits one star will cross.

Each count-three counter then will be counting the number of stars which its associated level detector has detected. Overflow in any counter must proceed from top to bottom in the diagram. This suggests that a given number of detected stars within limits can be determined and only that number which is desired is recorded.

If only the top counter (stars greater than 3.5 magnitude) overflows, it is known for example that between three and six stars were detected during one revolution of the spacecraft. If the two top counters overflow, it is known that between six and nine stars have been detected and so on. The results of the logic shown in the figure will allow the criteria to be developed for choosing between three and six stars per orbit for storage. If, for example, the first three counters overflow, it would allow stars detected from the third counter to be recorded with their transit times. Therefore, in this case, all stars detected by level detector three (3 stars) plus those seen by level detector four ($0 \leq n \leq 3$) be gated to the transit time determinator.

Other logical outputs derived from the overflow detector outputs can be used. If no overflow counters have been "set", the situation can be changed by changing gain at the photomultiplier. Changing gain at the photomultiplier is

most desirable since the noise added to the signal does not increase linearly with the amplitude of the signal. If, however, the gain at the photomultiplier already is maximum, electronic circuitry could be included which would change the gain in amplifiers after the tube. This method of course, amplifies the noise as much as the signal.

Another logical output derived from the output of the overflow detectors would be that where all overflow detectors are "set." This indicates that too many stars per revolution have been detected and could soon "flood" the memory. Then, based upon this logical decision, the photomultiplier gain or amplifier gain can be lowered in discrete gain adjust steps.

After the number of stars is determined (and from which level detector they should be sent) the information is sent to the transit time register. First, the assumption is made that the data will not change appreciably over two revolutions (40 seconds) of the spacecraft. This appears to be valid since the simulated transit times which have been computed (including the effects of torques) have shown that the data will not change appreciably over two revolutions.

The output of the chosen level detector will send sharp rectangular pulses to two one shot circuits. These one shot circuits will generate a pulse (very narrow) which will correspond to level detection of the leading and trailing edges of the detected star.

The leading edge pulse will cause the contents of the real time clock to be enabled to a holding register. At the same time, a width counter is started. When the trailing edge pulse appears, the width counter will stop, thus providing sufficient information to derive transit times (star in the center of the slit). The leading time word plus the width word will be sent to storage along with two automatic tag bits which will tell which photomultiplier and which starmapper yielded the transit time information. The tag bit which identifies the photomultiplier (or which field of view) is derived from each independent photomultiplier loop.

All of the above discussion has assumed that there is only one slit, i. e. , one transit time per star. In reality, three slits or three transit times per star will be generated and, therefore, the counters must take this into account (count once for every three pulses). Errors may occur but generally the number obtained will be accurate enough that between three and six stars (three transits each) will be stored. It should be emphasized that this technique is used only to obtain a number which is used solely for gating purposes.

The size of the real time clock should be determined by overall system accuracy which must be achieved. It would appear here that a 100 kHz counter (10 microseconds per count) would be adequate since 10 seconds of arc accuracy is equivalent to about 155 microseconds. Since a counter is aboard to provide number of revolutions, the size of the real time clock need be only twenty bits.

402

The real time clock also is used to provide the same transit information from the sun detectors. At the time when the starmapper(s) are not operating the sun detector(s) will be sending pulses to the real time clock register. Information will be recorded in the same manner as the star information. Another bit should be provided for identifying the fact that the information is sun information.

Thus far, the two photomultiplier system has been discussed. If the one-photomultiplier system is used, then the tag identifying circuitry is more complex, i. e., it must do more control functions.

To inspect this system more, consider that the slits for the one-photomultiplier case are coded as ✳, that is, one half of the field of view has double slits. The dead zone between these double slits is made small (approximately one minute of arc). As the star sweeps across the top or bottom the top or bottom must be identified. Thus, whenever a leading pulse is detected a flip-flop gate is set. If within some time interval later (approximately the time corresponding to two minutes of arc) another leading pulse occurs, it is known to some degree of confidence that the star crossed the coded half of the ✳ slits. Then the information is coded accordingly. In addition, this flip-flop gate is used to disable our counting circuitry for the second pulse, that is, the second pulse is not counted in the coded slit area. In addition, the transit information is not recorded from the second pulse. The second pulse is used only to identify upper or lower field of view.

This scheme is not foolproof. False targets can interfere with the scheme. Two or more stars transiting at the same time but in different fields of view can also provide false coding. In addition, S/N ratio will be lowered due to an increase of sky background (increased by a factor of 1.5). This increase in sky background will cause a 20 percent degradation in S/N ratio. This can be overcome by increased aperture, of course, but at the expense of weight, size of structure, etc.

Other control circuitry will be necessary to issue commands to various parts of the starmapper. Commands which may be necessary are as follows:

        Turn on starmapper one
        Turn on starmapper two
        Turn off starmapper one
        Turn off starmapper two
        Turn on sun sensor one
        Turn on sun sensor two
        Turn off sun sensor one
        Turn off sun sensor two
        Enable starmapper one
        Enable starmapper two
        Enable sun sensor one
        Enable sun sensor two
        Disable starmapper one
        Disable starmapper two
        Disable sun sensor one
        Disable sun sensor two

Raise photomultiplier gain (discrete steps)
Change bias (discrete steps)
Raise amplifier gain (discrete steps)
Eject optical cover(s)
Reset clock

There may be status points which will need monitoring within the system:

High voltage--system 1
High voltage--system 2
Low voltage--system 1
Low voltage--system 2
Clock reading output
Raw analog signal output photomultiplier 1 } System one
Raw analog signal output photomultiplier 2
Raw analog signal output photomultiplier 1 } System two
Raw analog signal output photomultiplier 2

All of these commands would be desirable to have, but in the form listed would require much information transfer. A central matrix in the spacecraft could provide commands to the starmapper and sun sensor subsystems as programmed and required.

Another way to minimize the number of command signals is to use sequencers in the satellite so that a number of sequential input pulses would perform the desired function. Suppose it is desirable to raise the gain of photomultiplier #2 in starmapper one. Further assume that both starmappers are on as well as both sun sensors. The procedure would be to execute an enable starmapper one command followed by a raise photomultiplier gain. The gain of the photomultiplier would be raised one discrete step. For more gain the raise photomultiplier gain command would be issued again. The gain of the photo-multiplier, is determined by a stepping device (counter) in the satellite. The counter would have the property of recycling automatically after maximum gain gain had been reached.

Component parts

For completeness, discussion about the more important electronic component parts used in the starmappers and sun sensors is included in the following paragraphs.

Photomultiplier tubes

Control Data Corporation (CDC) has done extensive investigation in this department and has had both spaceborne and ground applications of photo-multiplier tubes. The small miniature version of the RCA 1P21 was flown in a "photometer" aboard the Gemini 10 mission. This tube, because of its low gain, high noise, and small sensitive cathode area is not applicable here. The venetian blind tubes are optimum for many reasons; the rugged structure of the tube, the large cathode faces, and high gain.

CDC has used the ASCOP series photomultiplier in optical scanning systems. The Electro-Mechanical Research, Inc. EMR 541A and 541E series tubes have

been used extensively, the former in a ground test setup, SCADS, and the latter in ATS Self-Contained Naviagation System Experiment. The 541E was chosen for its broad range of spectral response, plus the fact that its peak sensitivity correlates closely with radiance of "blue" stars. The 541E tube has about the highest overall sensitivity of any tube on the market. (Some models have had quantum efficiencies greater than 25 percent).

More recently, the 541N series tube was released. Built in the same fashion as the other 541 tubes, the 541N tube does not have as great a quantum efficiency as does the 541E tube; however, the 541N offers one great advantage -- operation over a greater temperature range. The 541N can withstand tempera- ture ranges of -73°C ± 10°C to 150°C, whereas the 541E series tube can with- stand a range of -73°C ±10°C to 85°C. Since the quantum efficiency is close to that of the 541E tube (and greater than that of the 541A tube) the 541N tube primarily on that basis is chosen, but in addition, the 541N tube is also quieter as far as dark current is concerned.

Another manufacturer who has built some ruggedized type photomultipliers is EMI Electronics. These tubes were also considered.

The 541N photomultiplier has a one-inch diameter photocathode which means that the image from systems such as the f/6 optical unit must be condensed appreciably. Two-inch and larger photocathode tubes are available and the 543N (1.7-inch diameter) has recently been announced. At this time, the 541N0114 EMR tube is recommended. Specifications are given in Appendix I.

The photomultiplier tube requires high voltage in order to provide high gain. The typical high voltage supply includes an input voltage regulator, dc-dc inverter, quintupler and filter. Several alternatives appear in the way of supplies. A wrap-around supply can be obtained for the 541 series photo- multiplier tubes. The photomultiplier tube-power supply combination is contained in a hardened cylindrical shell 1.75 inches in diameter by 5.5 inches in length. All that need by supplied to the tube is the 28 volts dc (or 24 volts dc) and the tailoring resistors which regulate the gain of the photo- multiplier tube. The wrap-around unit dissipates about 1.5 watts of power. A schematic of the supply is shown in Figure 157. Specifications are given in Appendix J.

Since it is undesirable to locate the supply with the photomultiplier for thermal considerations the supply should be located elsewhere. EMR makes the same supply in its own self-contained unit for remote applications. Another possi- bility for a power supply is one being developed by Consolidated Avionics (who are subcontractors to a manufacturer who is building equipment for NASA GSFC). This power supply has more restricted specifications than the EMR supply, but has the capability of sweeping 200 000 volts per second. This means that the power to the photomultiplier could be dropped in a matter of some ten milliseconds.

It will be necessary to design some circuitry which will turn the photomultiplier off in a very short time. Whenever the tube sees a bright target such as the sun, earth, or moon, it is desirable to turn the voltage to the tube off as soon as possible.
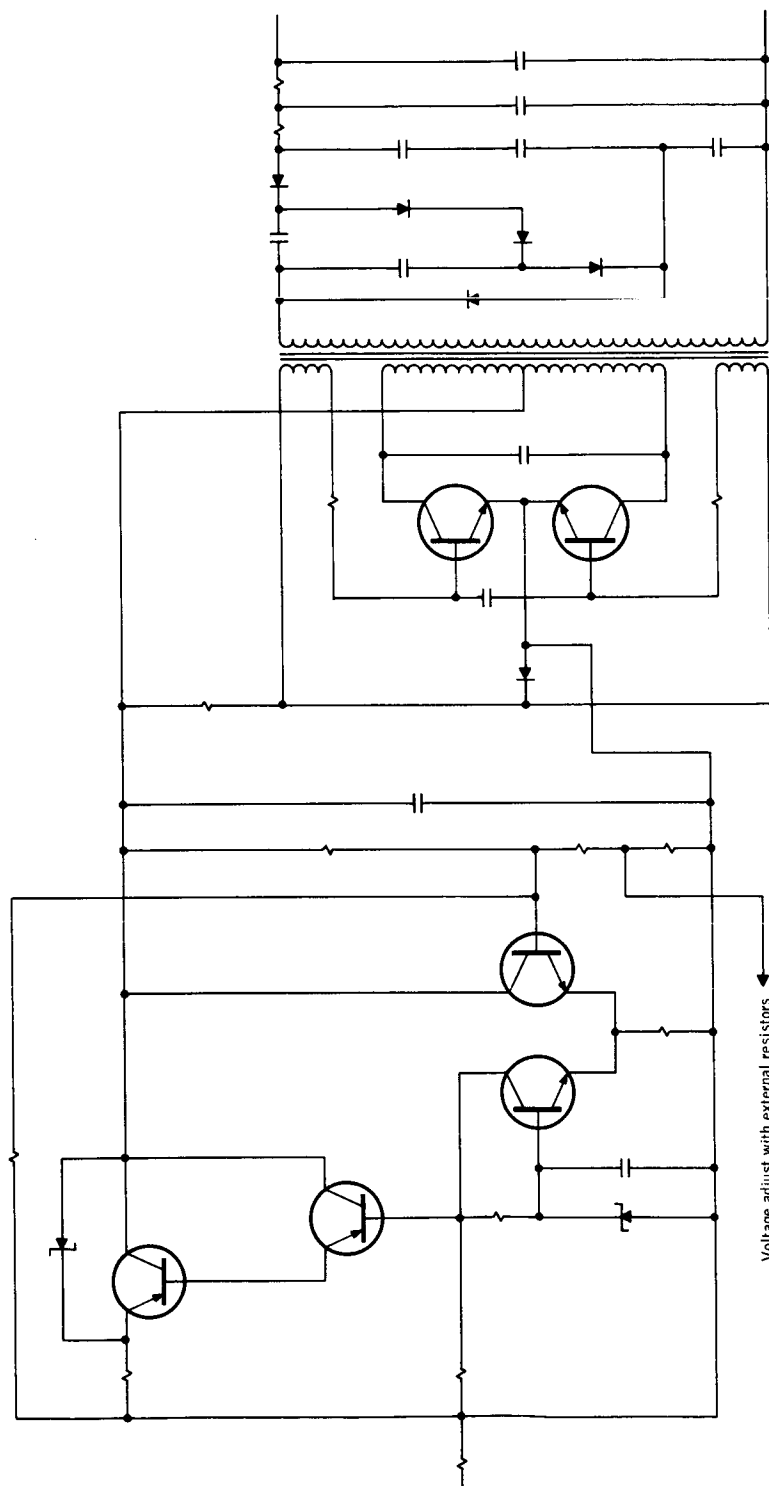
Figure 157. EMR 652-M1 Power Supply

Voltage adjust with external resistors

<u>Light shield design</u>

Even though the starmapper will be operated only on the dark side of the earth, some protection must be given to the optics to prevent direct and reflected light from the moon from entering the system when it is some distance off the optical axis. The following discussion shows that protection from the moon is afforded if incident light does not strike the shield interior closer than approximately one aperture diameter from the lens.

The situation analyzed is portrayed in Figure 158. Parallel light flux of value $\vec{F}$ falls on the interior of a shielding cone and is diffusely reflected according to Lambert's law. Some of the reflected radiation is scattered into the objective. Let the angle $\vec{F}$ makes with a normal to the cone be θ_o and the element of cone area be $d\vec{A}_1$, the element of lens area be $d\vec{A}_2$, and let the angles a radius vector $\vec{r}_{12}$ from $d\vec{A}_1$ to $d\vec{A}_2$ makes with $d\vec{A}_1$ and $d\vec{A}_2$ be Θ and θ, respectively. If the scattering albedo is λ_o the diffuse light onto $d\vec{A}_1$ is,

$$i_1 = \frac{\lambda_o F \cos \theta_o}{\pi} \quad \text{watts/cm}^2/\text{steradian} \tag{97}$$

The portion of this reflected into the direction of $d\vec{A}_2$ is,

$$i_2 = \frac{\lambda_o F \cos \theta_o}{\pi} \cos \Theta \, dA_1 \quad \text{watts/steradian} \tag{98}$$

and the total amount of diffuse light into the lens from the element of cone area dA_1 is,

$$dI = \frac{\lambda_o F}{\pi} \cos \theta_o \, dA_1 \int_{\text{lens}} \cos \Theta \, d\Omega \quad \text{watts} \tag{99}$$

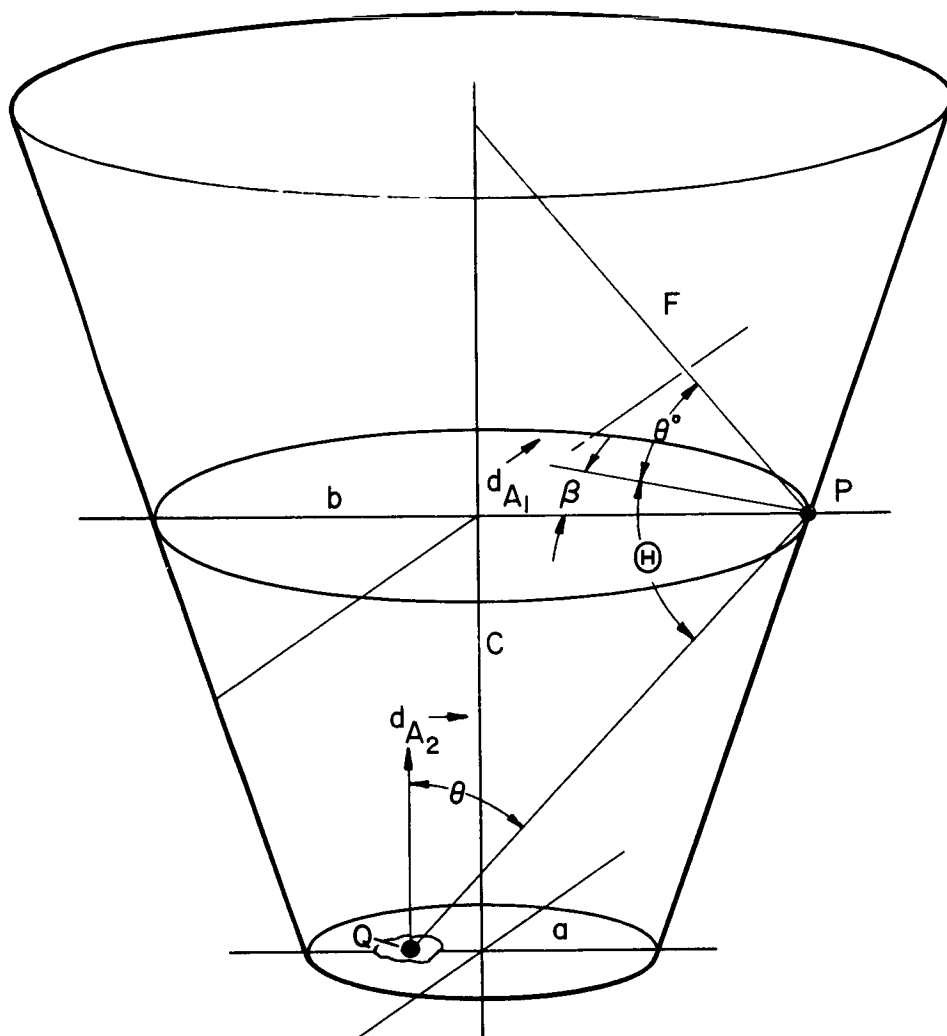The integration over the lens can be carried out with the result that,

Figure 158. Geometry of Light Striking Baffle

$$\int_{lens} \cos \Theta \ d\Omega = \frac{\pi C}{2b} \cos \beta \left(\frac{d^2}{\sqrt{d^4 - 4a^2 b^2}} - 1 \right)$$

(100)

$$= \frac{\pi}{2} \sin \beta \left(\frac{d^2 - 2a^2}{\sqrt{d^4 - 4a^2 b^2}} - 1 \right)$$

The behavior of equation (100) for $a = 1$ and $\beta = 10°$ as a function of C is shown in Figure 159.

From Figure 159 it is concluded that as long as stray light does not fall closer than about one lens diameter $(C = 2)$ from the optics the scattering into the lens should be minimal. For example, if rays making an angle of 35° to the axis strike one lens diameter up, $\theta_o = 45°$. Let the albedo be 10^{-3} ("Parsons Black"). Then, per unit area from this point on the cone the proportion P of incident light flux which is scattered onto the optics is,

$$P = \frac{10^{-3}}{\pi} \cos 45° \times 0.27 = 6.07 \times 10^{-5}$$

Some idea of the moonlight striking the lens may be approximated from Figure 160. This moon brightness curve was plotted from photometric measurements made by Rougier (ref. 33) and has a peak value for a full moon of 0.34 lux. These values have been converted to watts/cm^2 for comparison convenience.

At this point, it must be noted that from the geometry of the actual vehicle orbit the full moon will occur 45 degrees from the starmapper optical axis, and then as may be seen from Figure 160, the radiance of the moon rapidly decreases as it becomes gibbous. However, as was noted in Figure 159, the light scattered into the optics rapidly increases as the light rays penetrate deeper into the cone. The question then arises as to the total effects of the decreasing moonlight intensity and the increasing percentage of scattered light. Appendix L derives the total percent of light scattered from the illumination of the cone that will be seen by the photodetector at various off-axis angles.

Combining this relationship with the reflected moonlight for the proper moon phase gives the curve shown in Figure 161 which shows the light energy actually passing through the slits. For comparison, starlight into the lens
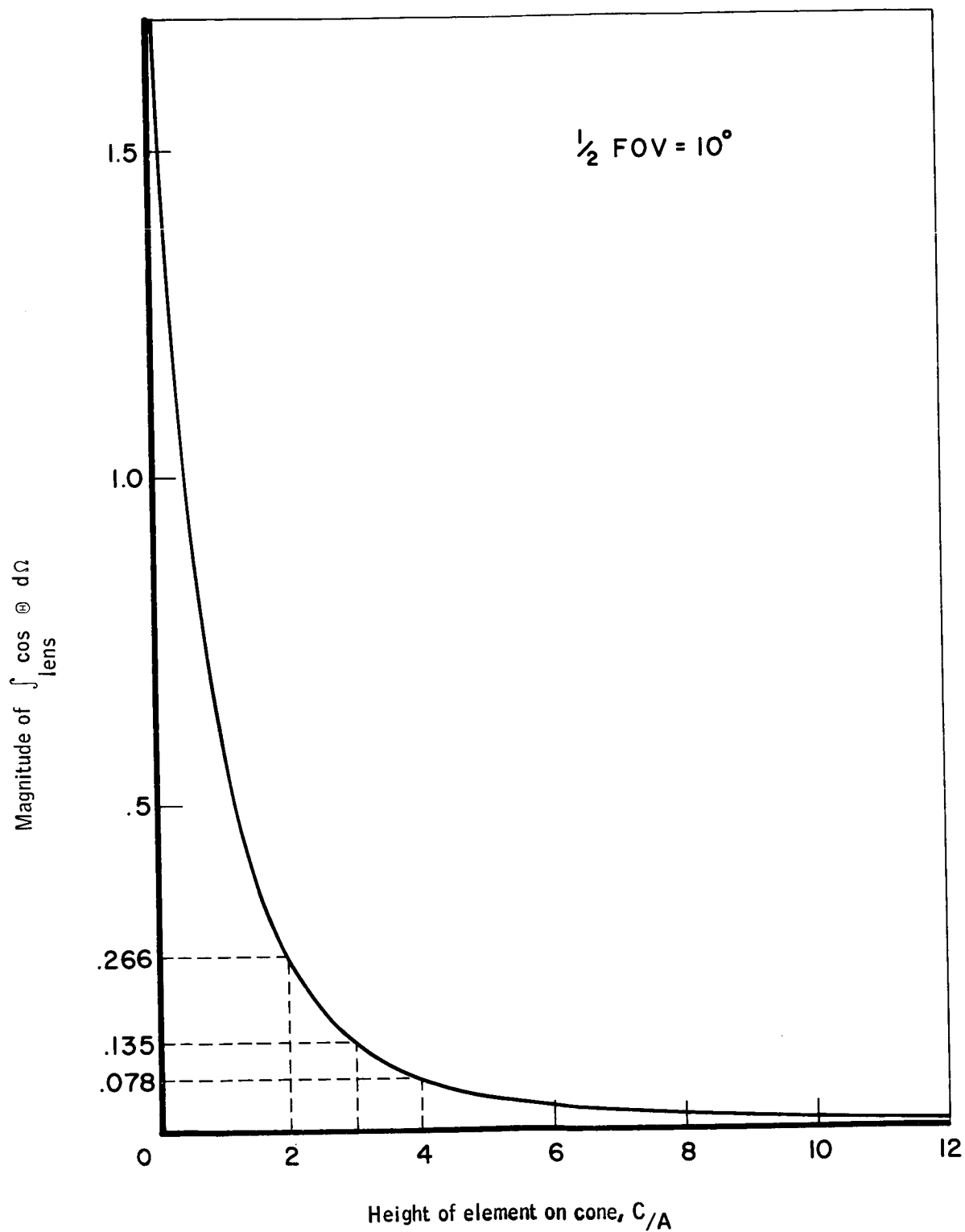
Figure 159.   Light Scattered Diffusely from Element of Cone Area
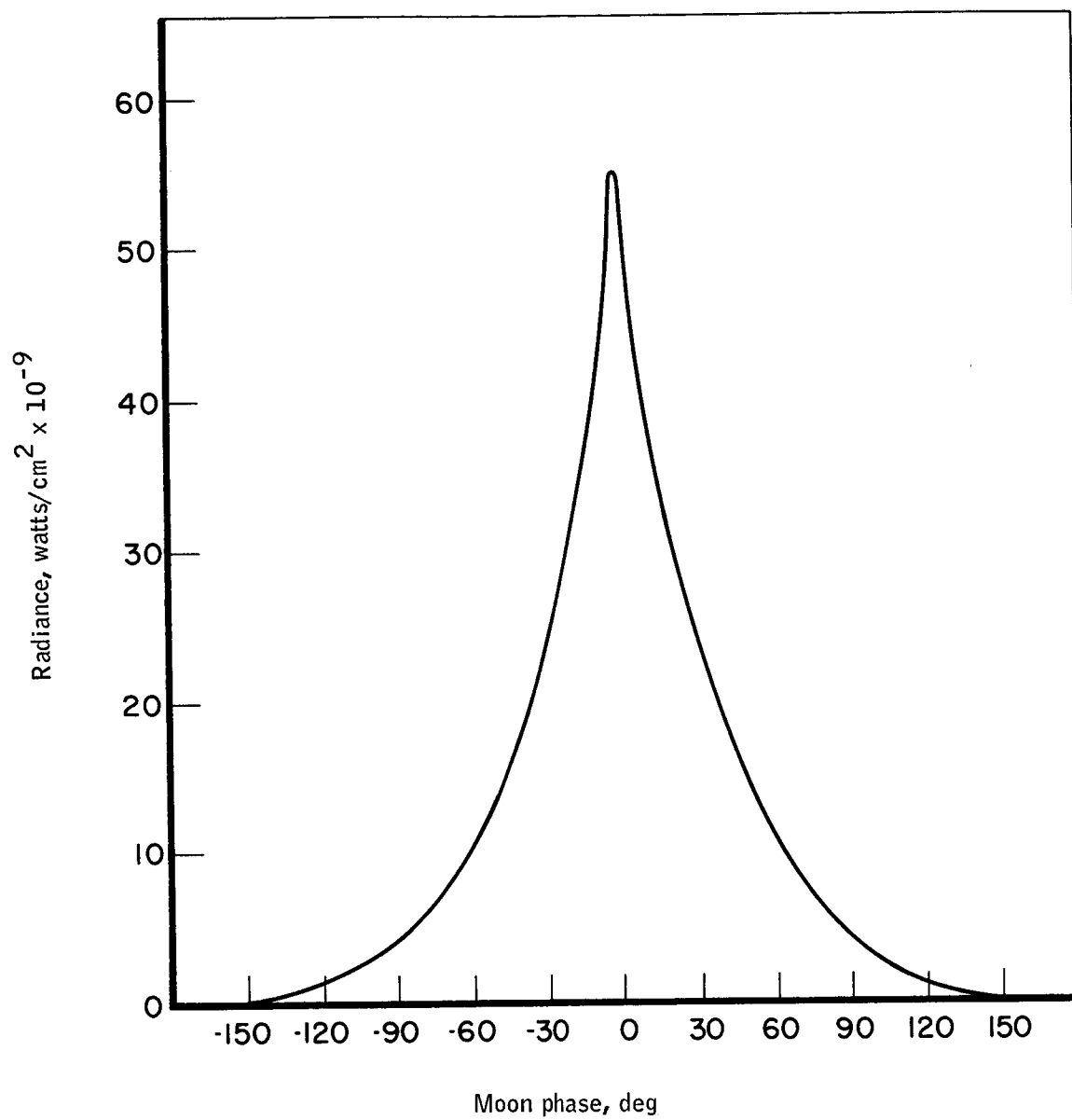into Optics
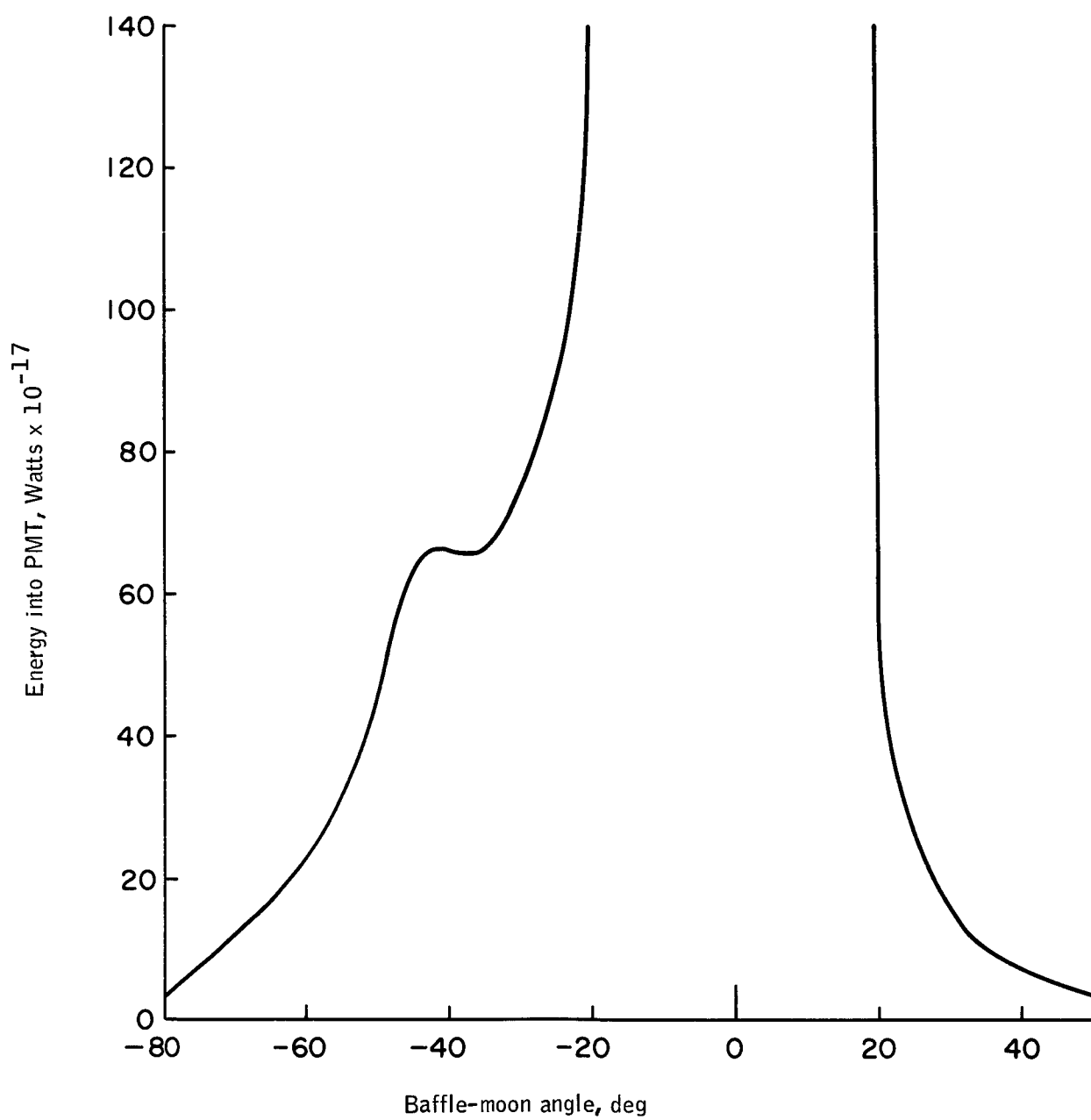
410

Figure 160. Radiance of Various Moon Phases

Figure 161. Moonlight Energy Profile

412

from a type AO, 3.5 magnitude star would be 3.05×10^{-12} watt. The peak intensity of the full moon at -45 degrees creates a point of reflex in the curve, but not to the extent that one would expect.

The asymtotes at ±20 degrees are the points at which direct moonlight will strike the lens itself without being scattered by the cone. This interval of 40 degrees is then the period during which the system will be shut down due to excessive noise. The moon travels in orbit at approximately 15 degrees per day and, therefore, the system would require shutdown for approximately 2-2/3 days or 43 orbits once each month. An automatic shutdown is incorpor-ated into the electronics to turn off the system in case the moon is inadver-tantly viewed and the photomultiplier is overloaded.

Effects of nighttime light inputs on photomultiplier

The question of photocathode and/or dynode damage or high noise conditions caused by sources visible at night has been examined. Those sources identi-fied and investigated are:

- Aurora
- Airglow
- Earth-reflected moonlight

Earth-reflected moonlight has an intensity corresponding to the light from a $0^m 0$ star. Since data from the system is accepted during an earth transit, this does not cause a system noise problem. None of these sources is suffi-ciently intense to damage the photomultiplier.

Brightness of aurora

Estimates of brightness of the aurora (ref. 34) as viewed from the surface range from 1.47×10^{-14} to 1.47×10^{-8} watt per square centimeter at a wave-length of 0.555 micron. Aurora occurs from a minimum altitude of 5 kilo-meters to a maximum altitude of 1100 kilometers.

Airglow

Airglow intensity at earth's surface is estimated to be 4.75×10^{-11} watt per square centimeter at 0.555 micron (ref. 34).

Earth-reflected moonlight

Meisenholder (ref. 35) has calculated the reflected light from the moon, earth, and other planets with account of spectral variations in albedo. His results are summarized in Figure 162. At zero phase, illuminance is 8×10^{-10} watt per square centimeter. From Figure 163, range correction factor at 250 000 statute miles is 1.04×10^3. Then, use Figure 164 at zero phase with
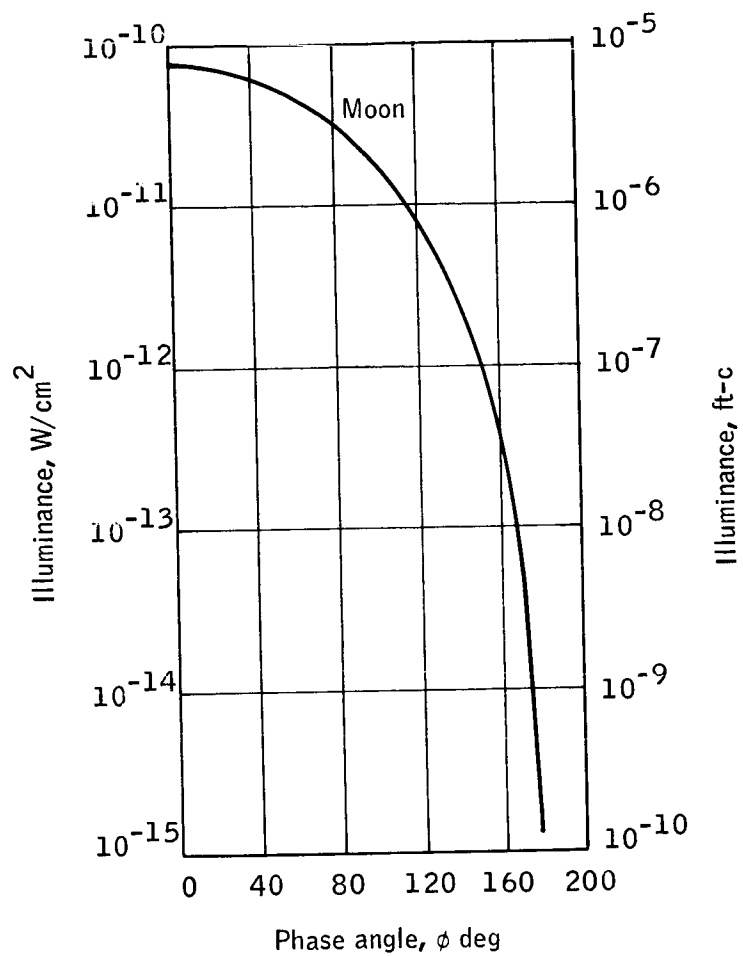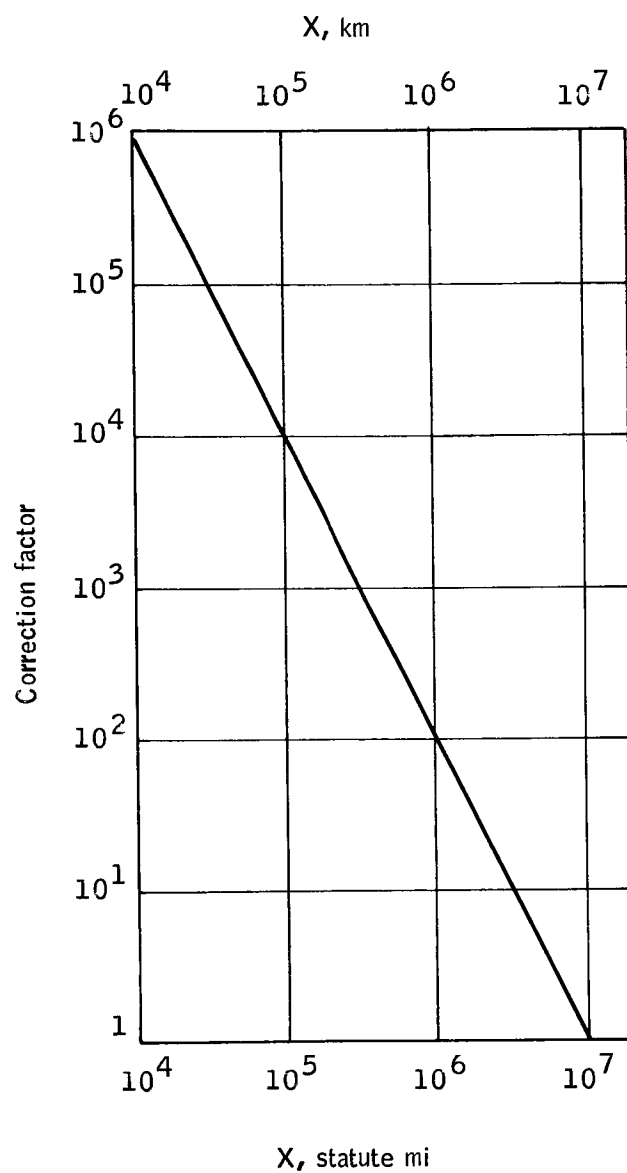
Figure 162. Illuminance versus Phase Angle, Moon

Figure 163. Correction Factor versus Range
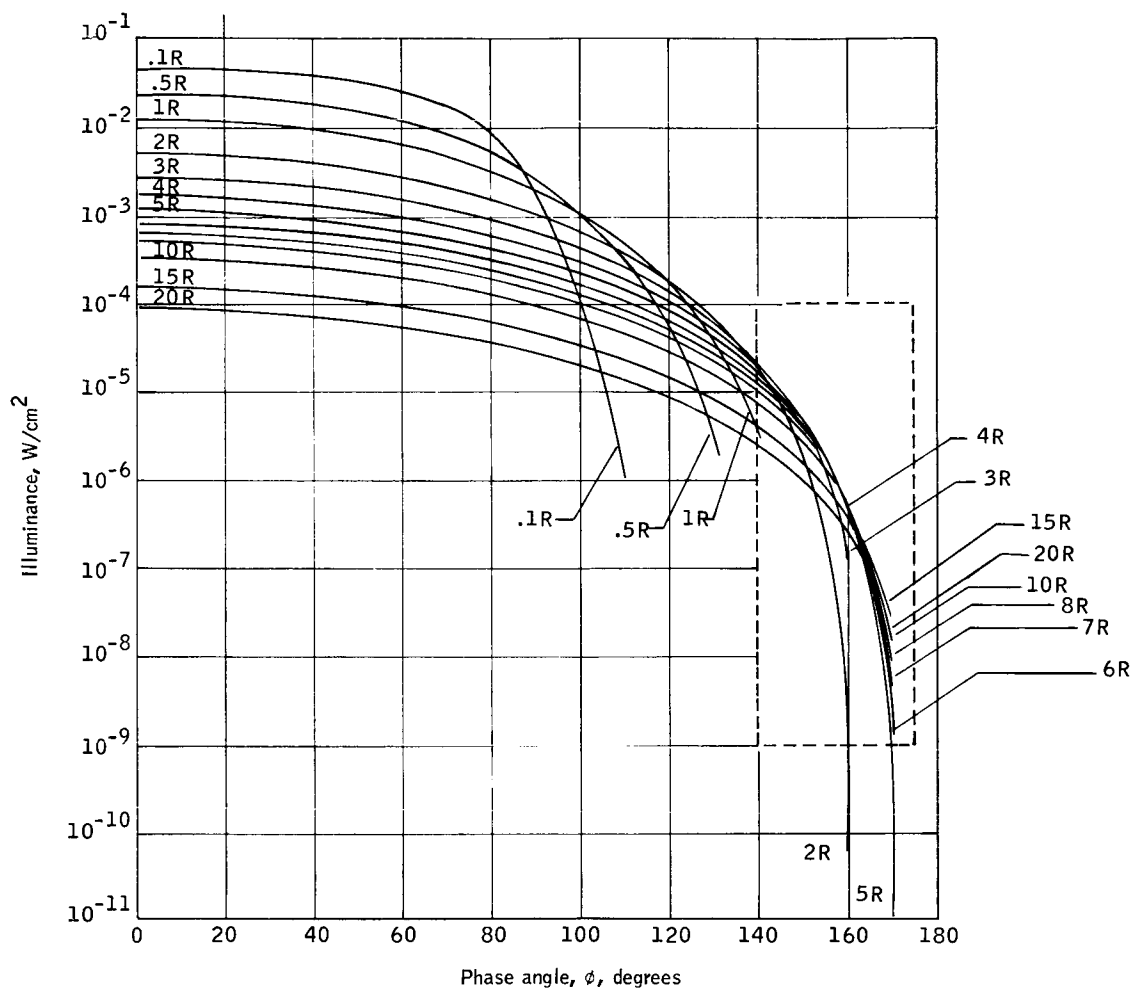
Figure 164. Light Intensity versus Phase Angle for Various Distances
from the Surface of the Earth

8.32×10^{-7} watt per square centimeter incident rather than 0.136 watt per square centimeter (solar constant). At 0.1 earth radii and zero phase, Figure 164 gives an illuminance of 5×10^{-2} watt per square centimeter.

Due to moon shine, the earth illuminance will be

$$I = \frac{8.32 \times 10^{-7}}{1.36 \times 10^{-1}} \times 5 \times 10^{-2}$$

$$= 3.06 \times 10^{-7} \text{ watt per square centimeter.}$$

However, this is total energy in the spectrum. Percent of the solar energy in the optic band pass (0.4 to 0.6 micron) is 28.2 percent. Thus,

$$I_{earth} = 8.60 \times 10^{-8} \text{ watt per square centimeter.}$$

Summary

The total earth shine plus aurora is then:

4.5×10^{-12} watt per square centimeter -- reflected moonlight

1.47×10^{-8} watt per square centimeter -- aurora

0.005×10^{-8} watt per square centimeter -- airglow

$\approx 10^{-7}$ watt per square centimeter.

Thus, the intensity in the field of view will vary from about 10^{-7} watts per square centimeter near the poles to about 8.6×10^{-8} watts per square centimeter at the equator.

The entire earth is not in the field of view, however. At 500 kilometers, the earth subtends about 168 degrees. This 10^{-7} watt should be reduced by the ratio of the slit area to that of the area subtended by the earth, a factor

$$\frac{3 \times 1/60 \times 20}{\pi/4 \, (168)^2} = 4.51 \times 10^{-5}$$

Therefore, the effective earth illumination on the night side, neglecting city lights, is

$$I_{eff} \lesssim 4.5 \times 10^{-12} \text{ watt per square centimeter.}$$

417

Sun Sensor

The sun sensor is an optical system similar to the starmapper; however, the function of the sun sensor is to detect sun transits on the daylight portion of the orbit. Since this portion represents approximately 65 percent of the total orbit, observations are necessary to update and maintain the required attitude accuracy. Of primary concern to a sun sensor is the uniformity and roundness of the sun's disk and whether the edge or limb is sharply enough defined to provide 10-arc-second system accuracy. The following paragraphs are devoted primarily to the determination of this accuracy, followed by a description of a proposed sun-sensor design.

Sun parameters. -- Since the limb darkening of the sun is an important astrophysical quantity, much data of this kind, both experimental and theoretical, appear in the literature. The more recent results of several investigators are summarized by Allen (ref. 36) whose data are plotted in Figure 165. These indicate that the fall-off in radiant intensity across the sun's disk is less at the longer wavelengths, a fact physically understandable since the longer wavelength radiation has its origin in the topmost layers.

Limb darkening at the extreme edge: A sun-sensing device will operate by sensing the extreme limb of the sun as is done with a sextant on earth in determination of latitude. Primary interest, then, is on data on darkening at the extreme edge. This is available in the data of Kopal (ref. 37), Degroot (ref. 38), and Pagel (ref. 39), among others.

Kopal (ref. 37) has estimated the sun's brightness distribution just inside the extreme edge of the disk. His data, reproduced in Table 30 and Figure 166, are derived from Dutch measurements of the brightness of the uneclipsed crescent of the sun at a wavelength of 4540 angstroms in the moments before totality during the 1936 total eclipse.

TABLE 30. - LIMB DARKENING OF THE SUN AT THE EXTREME EDGE

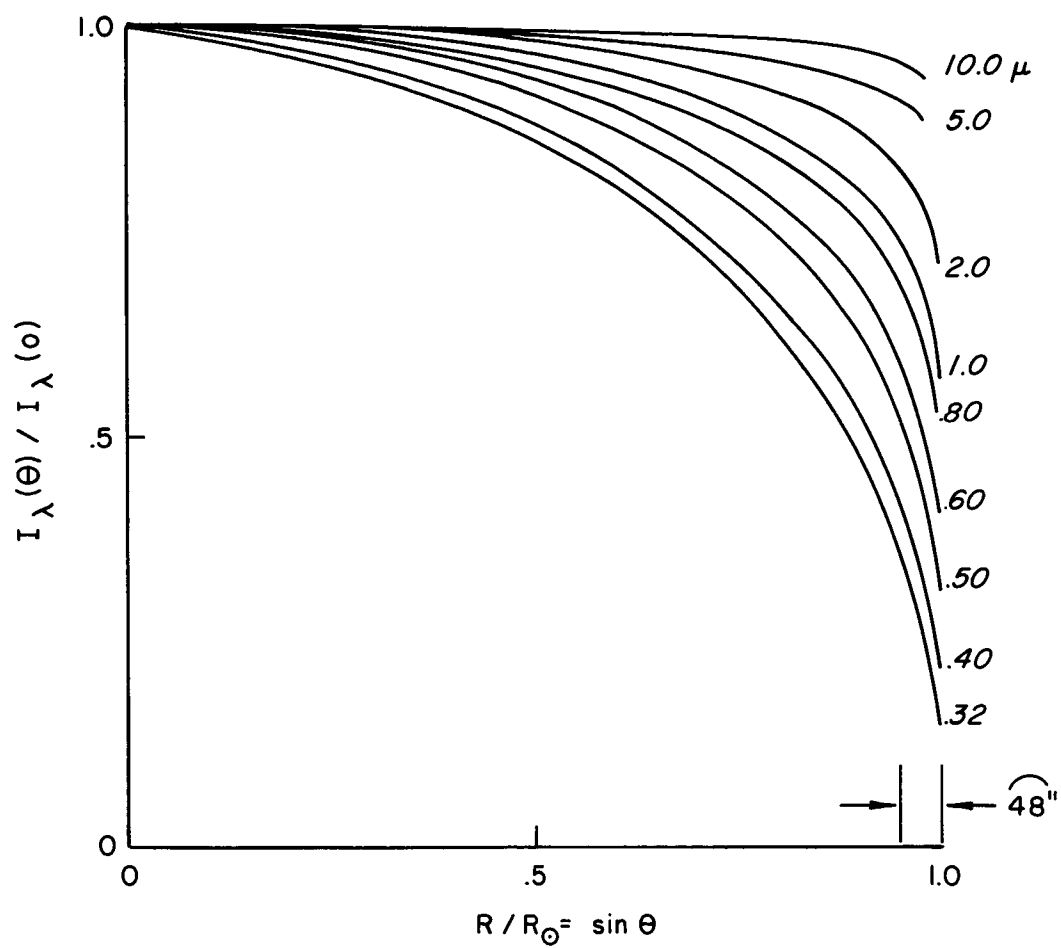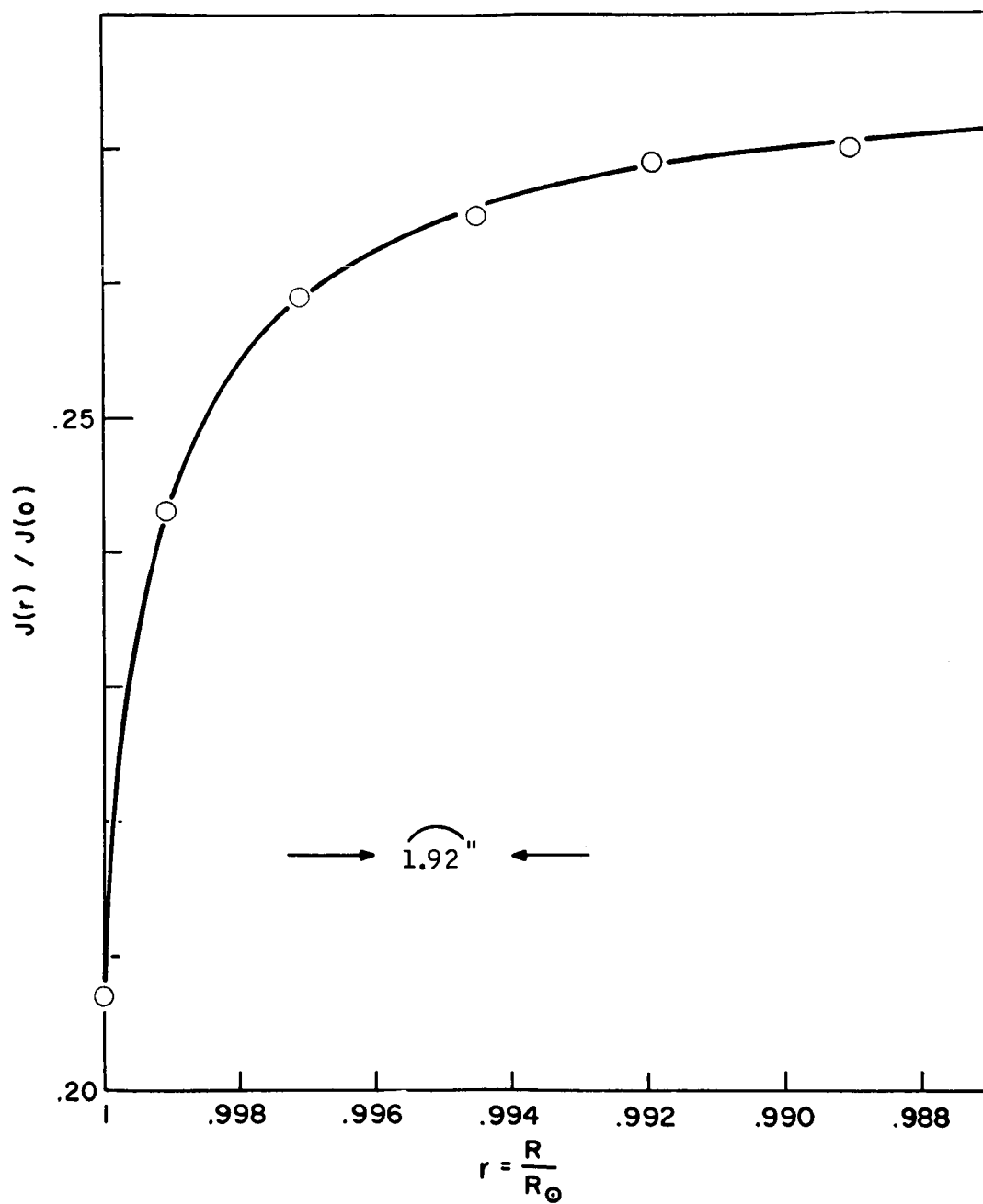| r/R	J(r) / J(0)
1.000	.207 ± .006
0.99906	.243 ± .003
0.99707	.259 ± .002
0.99448	.265 ± .001
0.99189	.269 ± .003
0.98990	.275 ± .005
0.98897	(.27)

418

Figure 165. Sun's Limb Darkening

419

Figure 166.   Solar Limb Darkening at Extreme Edge

Kopal summarizes these results, "In light of the effective wavelength of 4540 angstroms, the solar brightness remains finite and equal to approximately 21 percent of central intensity up to the very limb of the sun. Second, the rate with which this surface brightness falls off between 99 and 99.8 percent of the solar semi-diameter turns out to be considerably less than the average decrease over the central parts of the apparent solar disk".

The method of Julius (ref. 40) used by Kopal (ref. 37) has been objected to (Evans, ref. 41) on the grounds that it breaks down at the extreme limb due to irregularities in the lunar profile. Thus, DeGroot (ref. 38) uses only a narrow slit which bisects the crescent at a right angle to it. His results appear in Figure 167.

Pagel (ref. 39) is preoccupied with the temperature distribution in the layers near the limb. Nonetheless, in his discourse, the results of a number of other workers are summarized and unified so that it appears worthwhile to examine these, too. These are reproduced in Figure 168.

Collectively, these results establish that at least at wavelengths of 4540, 5465, 6560, and 5400 angstroms the sun's edge is extremely well defined, the intensity falling by an order of magnitude in about a second of arc.

Brightness outside the solar disk: The question remains as to what extent the chromosphere can be expected to interfere with a photometric measurement of limb position. Kopal (ref. 37) comments on this part of the problem stating: "Strictly speaking, we ought to add to the right hand side of Equation (1) a constant representing light of the solar corona and such outer layers as are not eclipsed by the moon. The amount of this light is, however, so small in comparison with that of the solar crescent at almost any phase that we may safely ignore it," (phrases have been underlined for emphasis).

Allen (ref. 36) gives a "smoothed and averaged" number distribution of atoms and atomic ions, electrons, and temperature in the chromosphere. The portion of this table to 1.01 solar radii is reproduced in Table 31. Strictly speaking, determination of a chromospheric radiance profile from these data requires a detailed knowledge of the various radiative processes occurring and the scattering and absorption coefficients which characterize these. However, some deductions can be made using judicious approximations.

First, the temperature is about constant in $R < r < 1.0029\ R$. Thermodynamic equilibrium can perhaps be assumed here. If it is also assumed that Beer's law holds, the equation for the radiance profile becomes (ref. 42)

$$I(h) = \int_{\Delta\lambda} \int_{S} \sum_{i} K_i\ \rho_i\ B(\lambda T)\ e^{-\int_{S'}^{S} \sum_{i} K_i\ \rho_i\ dS''}\ dS'\ d\lambda \qquad (101)$$
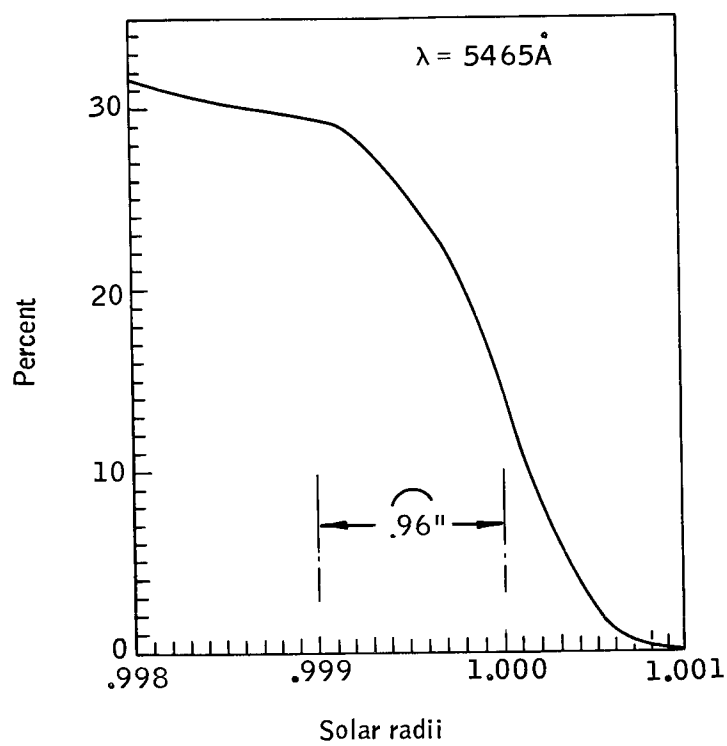
Figure 167. Limb Darkening at Extreme Edge
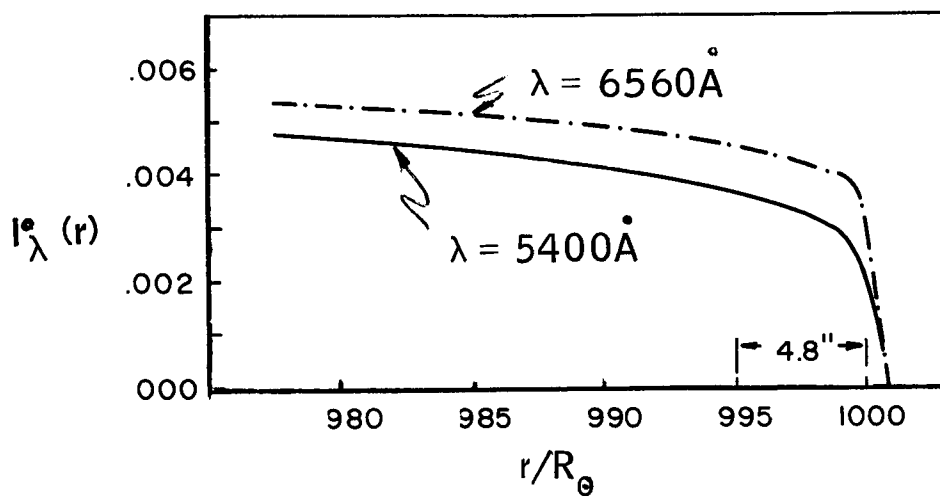
Figure 168. Limb Darkening Curves at Extreme Edge

TABLE 31. - CHROMOSPHERE DATA

R	T, °K (a)	N/cm^3	N$_e$/cm^3
1.0	4.4^3	7.94^{15}	1.26^{12}
1.0003	4.7^3	2.0^{15}	6.31^{11}
1.0007	4.9^3	3.16^{14}	3.16^{11}
1.0014	5.2^3	3.99^{13}	1.26^{11}
1.0029	5.8^3	3.99^{12}	5.02^{10}
1.0043	6.3^3	7.94^{11}	2.52^{10}
1.0057	7.4^3	2.0^{11}	2.0^{10}
1.0072	13^3	5.02^{10}	1.59^{10}
1.0086	30^3	1.59^{10}	1.0^{10}
1.0101	75^3	6.31^9	5.02^9
1.0115	160^3	2.52^9	2.52^9
1.0144	400^3	7.94^8	7.94^8

a $\quad 4.4^3 = 4.4 \times 10^3$

where K_i = absorption coefficient of ith species,

   ρ_i = density of ith species,

   $B(\lambda T)$ = Plank function, and

   S is the "sight line" through the sun's atmosphere.

If the absorption coefficients are frequency independent, the integration over wave length can be carried out with the result that

$$I(h) = \text{const } T^4 \int_S \sum_i K_i \, \rho_i \, e^{-\int_{S'}^{S} \sum_i K_i \, \rho_i \, dS''} \, dS' \tag{102}$$

Allen's data also indicates that the density of atoms is approximately exponential with height. Thus, the principal contribution to the radiance is likely from the deepest lying levels on the sight line, and further approximation of the radiance gives

$$I(h) = \text{const } T^4 \sum_i K_i \, \rho_{i_{av}}$$

Since the absorption coefficients are not known, they are assumed to be equal (near the sun's limb the atoms are most numerous). The estimated chromospheric radiance profile is plotted in Figure 169 as proportional to density of atoms, ions, and electrons.

Also in the same figure, again from Allen, photometric data from the coronal brightness at $r = 1.01$ R is plotted. The sum of the continuous spectrum (K component) and the Fraunhofer spectrum modified by interplanetary dust scattering (F component) at sunspot maximum and minimum are plotted. The chromosphere is expected to merge smoothly into the corona. Despite the crude approximations, the smoothed density data come close to the coronal-brightness data and thus probably are a good match to the average brightness of the chromosphere.

These data indicate that the brightness of the chromosphere falls by a factor 10^5 in the first $1/100$ sun radius (or ten arc seconds) outward.
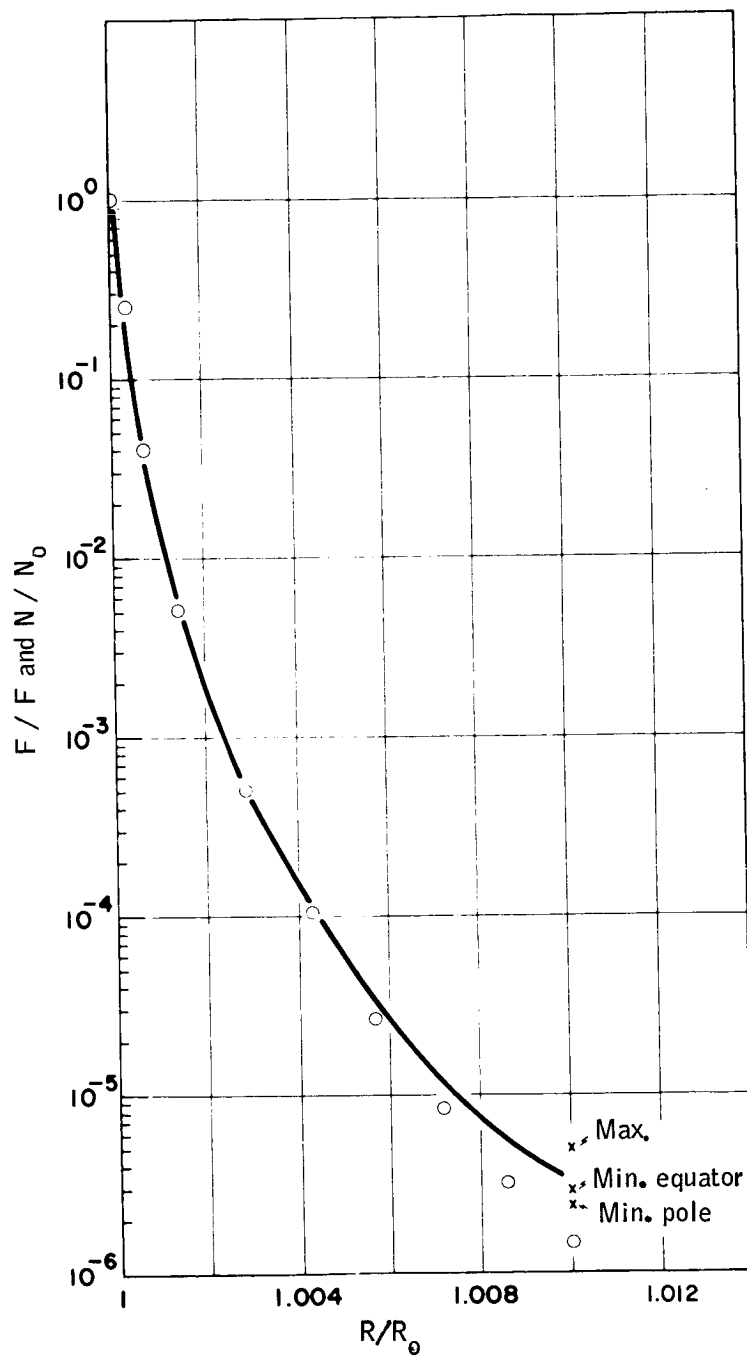
Figure 169. Estimated Chromospheric Radiance Profile

It is possible to improve on the preceding. Let R be the sun's radius, h be the height of closest approach of the sight line to the sun's surface, and r be generic height of sight line above the sun. Let the absorption coefficient K vary exponentially with scale height $1/k_1$. This is equivalent to the assumption of an exponential density.

Put,

$$J_o(h) = \sqrt{\frac{\pi R}{2k_1}} \; e^{-k_1 h} \tag{104}$$

$$J_1(r) = J_o(h) \; \text{erf} \sqrt{k_1 (r - h)} \tag{105}$$

$$K(r) = K_o \, e^{-k_1 r} \tag{106}$$

Then for a sight line which does not intersect the photosphere equation (101) can be written

$$I(h) = e^{-K_o J_o(h)} \int_h^\infty \frac{j(r) \left[e^{K_o J_1(r)} + e^{-K_o J_1(r)} \right]}{\sqrt{(R + r)^2 - (R + h)^2}} (R + r) \, dr \tag{107}$$

where $j(r)$ is the source function at height r.

We have $R \gg h$ and in the region where significant contribution to the integrand of (107) occurs $R \gg r$. Thus,

$$I(h) = \sqrt{2R} \; e^{-K_o J_o(h)} \int_h^\infty j(r) \cosh \left[K_o J_1(r) \right] \frac{dr}{\sqrt{r - h}} \tag{108}$$

Since an exponential density has already been assumed,

$$j(r) = j_o \, e^{-k_2 h} \tag{109}$$

With this (108) becomes

$$I(h) = 2\sqrt{\frac{2R}{k_1}}\ j_o\ e^{-k_2 h - K_o J_o(h)} \int_{-\infty}^{\infty} e^{-\frac{k_2}{k_1} x^2 - K_o J_o(h)\ \text{erf}\ x}\ dx \quad (110)$$

In the absence of thermal equilibrium $k_1 \neq k_2$, and no further analytical progress is possible. If attention is confined to the region very close to the limb, local thermodynamic equilibrium will prevail $k_1 = k_2$. Equation (109) becomes an elementary integral, and

$$K(h) = \frac{j_o}{2 K_o}\left(1 - e^{-K_o \sqrt{2\pi R H}\ e^{-h/H}}\right) \quad (111)$$

where $k_1 = k_2 = 1/H$. K_o is evaluated from the condition that the limb ($h = 0$) occurs at unit transverse optical depth and j_o is found from the value of I at $h = 0$. Then

$$I(h) = I(0)\ \frac{1 - e^{-e^{-h/H}}}{1 - e^{-1}} \quad (112)$$

Function (112) is plotted in Figure 170. The ordinate is in units of $I(0)$ and the abscissa in scale heights. Page 1 (ref. 39) asserts that a reasonable H is 200 kilometers. In the region, $1.00 \leq r/R_\odot \leq 1.0014$, Allen's data (ref. 36) has the scale height in the range 140 km $\leq H \leq$ 310 km. If $H = 200$ kilometers, 5H occurs at $r/R_\odot = 1.0014$. At these heights, the temperature is in the range $4400°K \leq T \leq 5200°K$, so that local thermodynamic equilibrium is also a fair assumption. Thus, in the first 1.38 seconds of arc off the limb, the brightness of the chromosphere falls by two orders of magnitude from its value at the limb. Thus on the average, the sun's edge appears to be defined to at least a second of arc.

Effects of flares, sunspots, and prominences: It remains to consider to what extent solar flares, prominences, and sunspots will effect a photometric determination of the sun's limb.
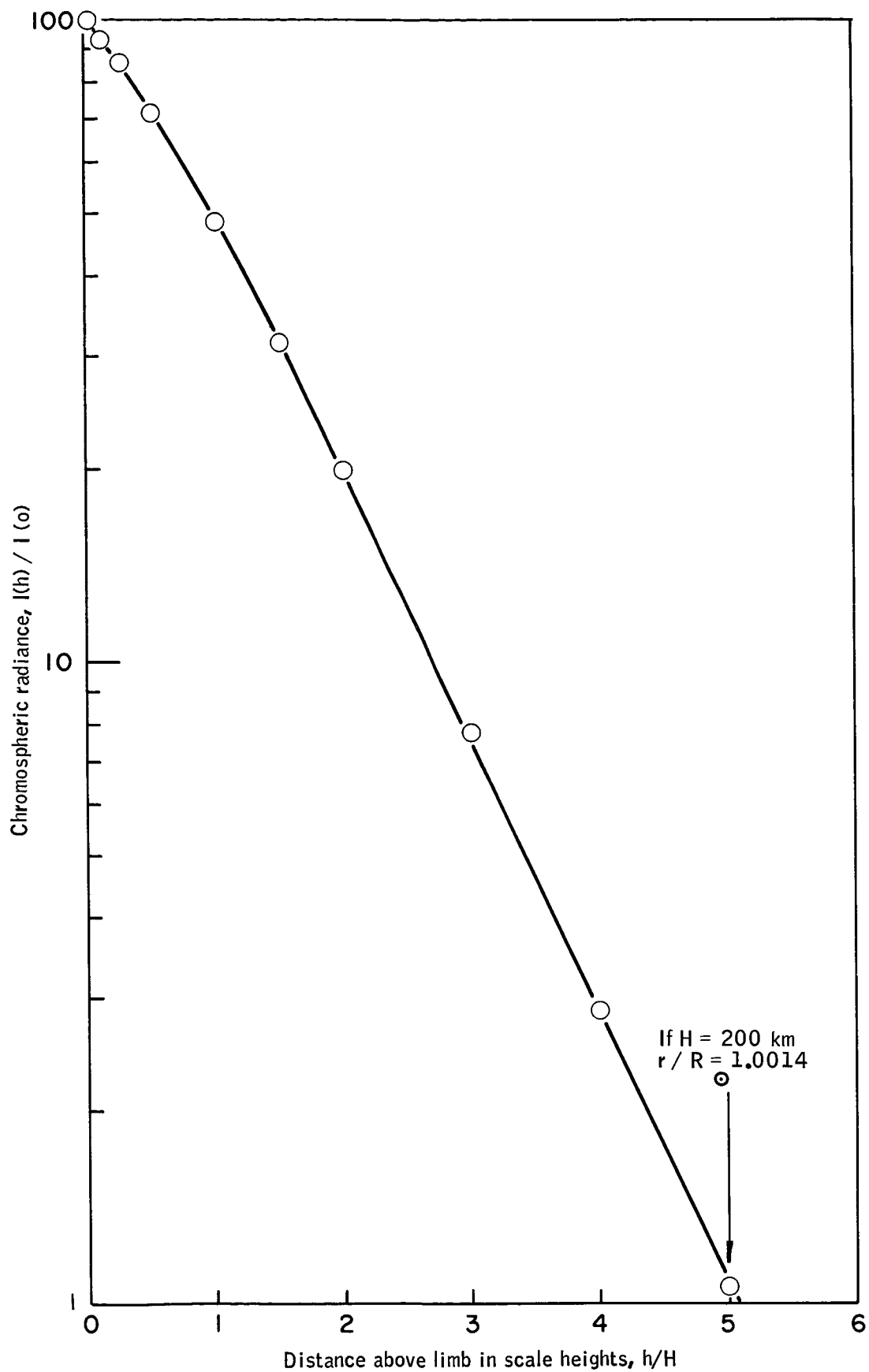
428

Figure 170.   Chromospheric Radiance Profile

It has been observed[a] that during sunset when virtually only the longer wavelength red of the visible spectrum penetrates the then existing, long optical path through the atmosphere to observer, solar prominences (which are brightest in the red) are not seen visually. Therefore, they cannot be as bright as 10^{-2} of the mean solar disk (ref. 43) and are probably no brighter than 10^{-3} and may be faint as 10^{-4} of the radiance of the mean solar disk.

Solar flares are bright enough to be seen visually (ref. 44) against the sun's surface. Occurring on the portion of the sun's limb being scanned, they could effect the result of a photometric limb-position determination. However, no photometric data on their intensity appears to be available, possibly because they are rare and short lived (15 to 30 minutes). They occur in active sunspot regions.

Sunspots can be as large as a minute of arc in size; typically, the intensity at the center (ref. 44) is 20 percent that of the photosphere. Thus, a sunspot on a portion of the limb might be expected to cause significant error in a photometric limb determination. Fortunately, on the limb, sunspots are foreshortened to the extent they are almost, if not entirely, invisible. Additionally, sunspots never occur north of +40° solar latitude or south of -40° solar latitude, whereas the sun sensor will scan the sun through the poles. This last applies with equal force to the flares which occur with the sunspots.

The sunspots and prominences will effect the sensor output when the scanning slit is well within the sun's disk. But if triggered on the limb, the light input at instant of triggering would be a factor 20 to 50 below that in the disk, as will be subsequently shown. Therefore, sunspot effects severe enough to cause false triggering signals can hardly be expected when the slit is well in the sun's disk.

Nothing has been said about the choice of a wavelength band. The curves of Figure 165 indicate a more even distribution of light intensity in the photosphere at the longer wavelengths and suggests that these may be preferred. A limited library research has not turned up data at the extreme edge for these wavelength bands. The part of the previous discussion dealing with the chromosphere is not wavelength dependent and can be taken directly. It is then necessary to interpolate from the limb to one-half percent of a solar radius within, where Allen's data leaves off. If this is done the longer wavelengths appear equally acceptable. It should be mentioned, however, that longer wavelength involves a loss of resolution.

    Conclusions: It may be, therefore, concluded that the sun's limb is extremely well-defined (Allen, ref. 39) gives it as circular to 0.01 arc second. Additionally, the effects of prominences will be nil, and since the scanning is through the sun's poles, sunspots and flares will cause no significant limb measurement error. Measurement of the position of the sun's limb to much

---

[a]This was reported via private communication by W. Luyten, Professor of Astronomy, University of Minnesota.

less than ten arc seconds should be possible. This is at least possible in the visible, and probably well into the infrared.

Sun measurement error. --

Diffraction limited optics: In detecting the sun's limb with a scanning optical system it is desirable to trigger the output at a point where the detector response has as steep a slope as possible, yet the triggering is not to be at such a low level as to be vulnerable to presence of flares and prominences. Thus, triggering should occur when about 10 to 15 arc seconds of the limb are in the scanning slit. The analysis will first assume diffraction-limited optics.

A slit is shown (Figure 171) occulting the solar disc and is immersed in the sun's limb to a depth η. The area of the sun's disc exposed to the detector is

$$A = \frac{R^2}{2} (\theta - \sin \theta) \tag{113}$$

with

$$\cos \frac{\theta}{2} = 1 - \frac{\eta}{R} \tag{114}$$

Now, typically, $\eta < 1$ arc minute, $R \approx 16$ arc minutes, $\eta/R \approx 1/16$. From equation (114),

$$\frac{\eta}{R} \approx \frac{\theta^2}{8} - \frac{\theta^4}{384} \tag{115}$$

If the 4th-order term is dropped,

$$\theta \approx 2\sqrt{\frac{2\eta}{R}} \tag{116}$$

With this approximation, the 4th-order term would be about 1/1736 justifying its neglect.

Use of equation (116) in equation (113) gives,

$$A = \frac{4}{3}\sqrt{2R \eta^3} \tag{117}$$

Radiance of the solar disk increases by only a few percent in about the first 10 seconds of arc near the edge (Figures 166 to 168). This radiance can be assumed uniform. Then, the relative error in both detector response and area of sun's disc exposed are equal. From equation (117)
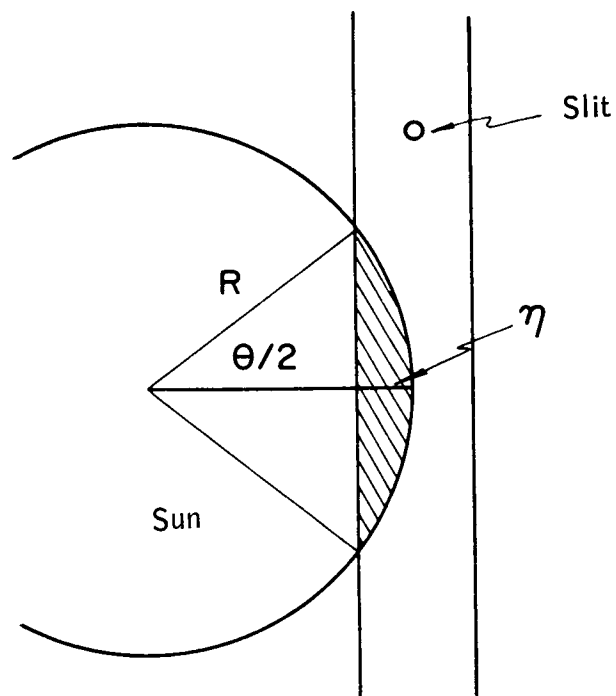
Figure 171. Measurement Geometry

$$\frac{\Delta A}{A} = \left(1 + \frac{\Delta \eta}{\eta}\right)^{3/2} - 1 \qquad (118)$$

If $\Delta\eta \ll \eta$, equation (118) becomes

$$\frac{\Delta A}{A} = \frac{3}{2}\frac{\Delta\eta}{\eta} \qquad (119)$$

Equation (119) may be safely used for most calculations even though $\Delta\eta$ approaches η in size, e.g. if $\Delta\eta = 10$, $\eta = 15$; equation (118) gives $\Delta A/A = 1.15$, whereas (119) gives $\Delta A/A = 1.0$ and is in error by only 15 percent.

An optical aperture of at least one-half inch is needed to obtain ten arc-seconds resolution according to the Rayleigh criterion. The energy in sunlight is enough that some attenuation will be necessary. The required field of view (FOV) is about 35 degrees so that refracting optics seem called for. Attenuation may take the form of a band-pass evaporated-film filter deposited on the lens surface, thus avoiding much heating of the interior of the sensor. A 200-angstrom band will be assumed centered at 5500 angstroms. This choice is not critical, but it should be within the response of a silicon photodiode.

There is 1.93×10^{-3} watt per square centimeter of sunlight incident on the earth's atmosphere in the tentatively chosen band. If ΔF is the total sunlight per square centimeter incident on the optics in the chosen band, and $A_\odot$ is the area of the sun's disc. Then,

$$\Delta F = \frac{F_\odot}{A_\odot} \Delta A = \frac{F}{\pi}\sqrt{\frac{\eta}{2R^3}} \Delta\eta \qquad (120)$$

for $\eta = 15''$, $\Delta\eta = 10''$

$$\Delta F = 8.01 \times 10^{-6} \Delta\eta \text{ watt/square centimeter} \qquad (121)$$

Silicon diodes with noise equivalent power (NEP) of 10^{-12} watt per $\text{cps}^{1/2}$ are readily available. Thus, there is little question of obtaining the required angle accuracy with diffraction-limited optics.

Effect of optical aberrations: It has been shown that the position of the sun's edge can be precisely measured with diffraction-limited optics. However, approximately a 35° FOV is required if the sun is to be continually in the scanned FOV throughout the year. Diffraction-limited optics with this size FOV are difficult to obtain. One minute of arc "blur circle" over the FOV is more within the optical state of the art.

If this limitation is accepted, the optics itself will smear out the sun's limb and introduce a further inaccuracy.

If the edge of the sun's disc is assumed to be "smeared out" due to imperfect optics and the smearing is assumed to be gaussian with variance σ^2. Then, the brightness is represented by

$$I(r) = \begin{cases} I_o, & , \quad r \leq R \\[2em] I_o e^{-\dfrac{(r - R)^2}{2\sigma^2}} & , \quad r > R \end{cases} \tag{122}$$

Light through a "wide" slit (wide with respect to $\sqrt{2}\,\sigma$) at the sun's edge will be about

$$\frac{F}{I_o} = f = \int_{r_o}^{\infty} \int_{-\theta_o}^{\theta_o} e^{-\dfrac{(r - R)^2}{2\sigma^2}} r \, dr \, d\theta \tag{123}$$

with $\theta_o = \cos^{-1} r_o/r$, where $r_o \geq R$ is the minimum distance of the slit edge from the sun's center.

Of course,

$$f = 2 \int_{r_o}^{\infty} e^{-\dfrac{(r - R)^2}{2\sigma^2}} \cos^{-1}\left(\frac{r_o}{R}\right) r \, dr \tag{124}$$

In the region where significant contribution to the integral (124) occurs,

$$r = r_o + \epsilon, \quad \epsilon \ll r_o$$

Therefore, a good approximation is

$$\theta_o = \cos^{-1} \frac{r_o}{r} \approx \sqrt{2} \sqrt{\frac{r - r_o}{r}} \tag{125}$$

whence,

$$f \approx 2\sqrt{2} \int_{r_o}^{\infty} e^{-\dfrac{(r - R)^2}{2\sigma^2}} \sqrt{r - r_o}\sqrt{r} \, dr \tag{126}$$

If $X = \dfrac{r - R}{\sqrt{2}\,\sigma}$

434

$$f = 4\sqrt{2}\ \sigma^2 \int_{\frac{r_o - R}{\sqrt{2}\ \sigma}}^{\infty} e^{-X^2} \sqrt{X - \frac{r_o - R}{\sqrt{2}\ \sigma}}\ \sqrt{X + \frac{R}{\sqrt{2}\ \sigma}}\ \ dX \tag{127}$$

Now $\sqrt{2}\ \sigma \approx 30$ seconds of arc, $R = 960$ seconds of arc, $R/\sqrt{2}\ \sigma \approx 16$, whereas $(r_o - R/\sqrt{2}\ \sigma$ is of the order of one or less; thus, the second radical in (127) varies relatively slowly compared to the rest of the integrand and by further approximation,

$$f = 4 \cdot 2^{1/4} \sqrt{r_o\ \sigma^3} \int_{p/2}^{\infty} e^{-X^2} \sqrt{X - p/2}\ \ dX$$

$$= 4 \cdot 2^{1/4} \sqrt{r_o\ \sigma^3}\ e^{-p^2/4} \int_{0}^{\infty} e^{-pX}\ e^{-X^2} \sqrt{X}\ \ dX \tag{128}$$

with $\quad p = 2\ \dfrac{r_o - R}{\sqrt{2}\ \sigma}$

From a table of Laplace transforms, the integral of (128) is evaluated with the result that,

$$f = \sqrt{2\pi\ r_o\ \sigma^3}\ e^{\frac{(r_o - R)^2}{4\sigma^2}}\ D_{-3/2}\left(\frac{r_o - R}{\sigma}\right), \tag{129}$$

for $r_o \geq R$ only and,

where $D_{-3/2}$ is a parabolic cylinder function.

To estimate the error in the slit position Δr_o in terms of the error in intensity measurement Δf, df/dr_o is formed and evaluated at $r_o = R$ since triggering near this point is desired. Consequently

$$\left.\frac{df}{f}\right|_{r_o = R} = \sqrt{2\pi\ \sigma^3}\ \left\{\frac{1}{2R} + \frac{D'_{-3/2}(0)}{\sigma\ D_{-3/2}(0)}\right\} dr_o \tag{130}$$

This expression is evaluated in terms of known end-point values of the parabolic cylinder functions,

$$D_\nu(0) = \frac{\Gamma\left(\frac{1}{2}\right) 2^{\frac{\nu}{2}}}{\Gamma\left(\frac{1-\nu}{2}\right)}$$

$$D'_\nu(0) = \frac{\Gamma\left(-\frac{1}{2}\right)}{\Gamma\left(-\frac{\nu}{2}\right)} 2^{\frac{\nu-1}{2}} \qquad (131)$$

Using (131) in (130) and the fact that $2R \gg \sigma$, angle error is

$$(\Delta r_o)_{r_o} = R \approx \frac{2\sqrt{2}\,\sigma}{3} \frac{\Delta f}{f_o} \qquad (132)$$

Equation (132) represents the error at the instant the slit edge touches the true edge of the sun.

Also

$$f_o = \frac{\pi \sqrt{\sigma^3}\, R}{\frac{9}{4}\Gamma\left(\frac{5}{4}\right)} \qquad (133)$$

Equations (132) and (133) are the equations of primary interest.

If the slit edge is allowed to intersect the sun's edge,

$$f = 2\sqrt{\sqrt{2}\,R\,\sigma^3}\left[\frac{4}{3}\eta^{3/2} + \frac{\sqrt{2}\,\pi}{\Gamma(5/4)}\left(\frac{1}{4} + \frac{\eta^2}{8} - \frac{\eta^4}{32}\right) + \Gamma(5/4)\left(\frac{\eta}{2} + \frac{\eta^3}{3}\right)\right] \qquad (134)$$

where

$$\eta = \frac{R - r_o}{\sqrt{2}\,\sigma} \ll 1 \quad \text{and} \quad r_o \le R$$

The first term in braces is from the direct light of the solar disc; the remaining terms are from the gaussian blurring of the sun's edge by the optics. These latter terms dominate the term in $\eta^{3/2}$, and, thus, most of the light is from the gaussian tail.

Allowable intensity error may now be found for a ten arc-second limb determination for optics with one arc-minute diameter (or any other diameter for that matter) blur circle. In the Airy-diffraction pattern 84 percent of the energy occurs in the central peak. If the blur circle for the gaussian distribution herein used contains 84 percent of the energy, this blur circle is 2.5 σ in diameter, and one minute of arc blur circle has $\sqrt{2}\,\sigma = 33$ seconds of arc.

436

If $\sqrt{2}\,\sigma$ = 30 seconds of arc, and Δr_o is not to exceed ten seconds of arc

$$\frac{\Delta f}{f_o} = \frac{1}{4} \qquad (135)$$

Thus the error in the intensity measurement at the moment of sensor triggering must not exceed 25 percent.

Equation (133) is utilized to translate this error into absolute measure. Light intensity through the slit is given by

$$F = \frac{F_\odot}{A_\odot}\, f_o = \frac{1}{\frac{9}{4}\,\Gamma(5/4)}\,\sqrt{\frac{\sigma^3}{R^3}}\, F_\odot \qquad (136)$$

With the previously used values,

$$F = 1.665 \times 10^{-5} \text{ watt/cm}^2$$

which must be measured to an accuracy 4.16×10^{-6} watt/cm^2. Thus, there is little question of obtaining the required angle accuracy with optics having one minute of arc resolution, and this accuracy can probably be obtained with worse optics.

Instrument design. --

Refractive optical design: The sun's position with respect to the satellite varies by about 34 degrees in the 3 o'clock orbit. Thus, approximately a 35-degree FOV is chosen so that position measurements may be made throughout the year. With this FOV, diffraction-limited optics are out, but as previously noted the required angle accuracy can be obtained with a one minute of arc blur circle. This is within the state of the optical art, especially since no achromatization is necessary. The Rayleigh limit at one-half inch aperture is ten arc seconds. Thus, a one-inch aperture at about an f/number of two is probably adequate. A dielectric film filter to isolate a 200-angstrom band centered at 5500-angstroms would be deposited on a lens surface. Thus, a tentative lens specification for refracting optics is:

- Aperture: 1 inch

- f/2

- One minute of arc blur circle, or better

- Coated with evaporated-film band-pass filter (5400 to 5600 angstroms).

One single diametrical slit on the focal plane could be used. It need only be so narrow as to prevent excessive sunlight from entering the detector when the full sun's disc is viewed. Slit width did not enter into the previous error analysis.

On the other hand, the use of two slits in the shape of a V would locate the sun's image with respect to the optical axis and should be considered, i.e., the extra slit would provide a measure of both sun elevation and azimuth.

A silicon photodiode would be used. At f/2 and 35° FOV the image plane of the optics is about 1.25 inch. The diode probably cannot be large enough to cover the image plane. Moreover, the responsivity of photodiodes is not uniform across the active area. The sufficiency of light signal suggests the use of an integrating sphere.

It is assumed that the slits cover negligible area, the area of sphere interior and diode active area are, respectively, A_1 and A_2, the sphere interior is diffusely reflecting with reflectivity ω, and the diode reflectivity is zero. Then it can be shown that the light into the diode for light flux F through the slits is approximately

$$I_{diode} = \frac{\omega A_2}{A_1} F \Big/ \left(1 - \frac{\omega A_2}{A_1}\right) \qquad (137)$$

A typical diode sensitive area has a diameter of about 0.444 inch (ref. 45). For a 1-1/4 inch slit plane, a sphere diameter of about 1-9/16 inches is convenient. Flat, white paint with reflectivity of 90 percent is available. Inserting these numbers in equation (137) gives

$$I_{diode} = 8.78 \times 10^{-2} F \qquad (138)$$

For one-inch optics at the instant of triggering, F would be 8.44×10^{-5} watt. Thus, the energy on the diode is 7.41 microwatts. For the diode in this example, the sensitivity at 0.9 micron and NEP are given as 0.4 microamp per microwatt and 5.5×10^{-13} watt second $^{1/2}$ at 1 kHz. At 0.55 micron the spectral response is down 40 percent from the value at 0.9 micron. Thus, the diode signal would be 2.7 microamps, a very adequate signal.

For a blur circle of $\sqrt{2}\,\sigma = 60$ arc seconds, the response is down by 36.7 percent, 34 arc seconds from the sun's limb. This corresponds to a bandwidth of about 1.9 kHz at three rpm satellite rotation speed. Thus, the diode noise exclusive of 1/f noise would be

$$5.5 \times 10^{-13} \times \sqrt{1900} \text{ watts} = 2.40 \times 10^{-12} \text{ watt}$$

which is more than a factor 10^6 below the signal. The 1/f noise is eliminated by cutting off the electrical band pass at about 100 cps. It is scarcely necessary to consider other sources of noise, at the signal level attained.

A slit width must be chosen which should be at least the blur circle size. At a width of two arc minutes, the signal when the sun's image is fully in the slit is

$$1.93 \times 10^{-3} \frac{\text{watts}}{\text{cm}^2} \times (1.27)^2 \pi \text{cm}^2 \times 8.78 \times 10^{-2} \times \frac{2 \times 32 \text{ min}^2}{16^2 \pi \text{ min}^2} = 68.3 \text{ microwatts}$$

This input will not saturate the diode.

438

A tentative specification for the slits can now be given. There would be two tapered slits subtending two arc minutes on the celestial sphere. They would be placed in the form of a V placed symmetrically about an image plane diagonal with a vertex angle of about 30 degrees.

A crude schematic of the proposed design appears in Figure 172.

The optical design shown in Figure 172 is conceptual only. To accomplish the alignment requirements, the sun sensor optical system and reticle will be combined in a quartz structure with an optical flat ground on one side for use with a miniature autocollimator mounted on the radiometer.

<div align="center">Interface Requirements</div>

The interface requirements for both the starmappers and the sun sensors are discussed in this section because they both have similar requirements, share much of the same electronics, and together constitute the required instrumentation for the attitude determination system.

Photomultiplier tube protection. -- The electronics section discussed proposed means of manually by ground command, and automatically in space, shutting off the high voltage to the photomultipliers to protect them from being damaged by overload from excess light. However, means should also be provided for additional protection during prelaunch and pre-orbital conditions.

A shield should be placed on the ground over the starmappers at all times since the sun or other bright lights shining into the system could cause intense heating and possible permanent damage to the tube. A shroud will be placed over the vehicle, but there probably will be times when the shroud is not on. In addition, when the shroud is removed in space, the vehicle may initially be misaligned such that a starmapper may be looking into the sun for periods longer than, say, seconds of time. If this is to be expected, a "pop-off" type cover should be designed for each starmapper. The pop-off cover can be actuated by ground command. The circuitry used to release the pop-off cover could be a simple solenoid and a solenoid "one shot" driver, or a simple dimple motor (squib) may be used to release the cover. Standard circuitry exists for these types of devices. The solenoid may be required to deliver a large peak-current surge; thus, any power supply feeding these devices must be capable of delivering these peak loads for short time periods.

Mounting geometry. -- The sun sensors and the starmappers should both be mounted to the supports of the radiometer since they must all be initially aligned and maintain their alignment relative to each other. To achieve this, they should all be mounted in the same cold-temperature area of the vehicle.

The optical axis of the starmappers must lie in a plane perpendicular to the spin axis and also parallel to the radiometer axis with an accuracy of 0.1 degree. The pitch-axis rotation angle between the starmappers and the radiometer may be established at any angle which is structurally convenient but must be measured and maintained within seconds of arc as specified by the error allocation.
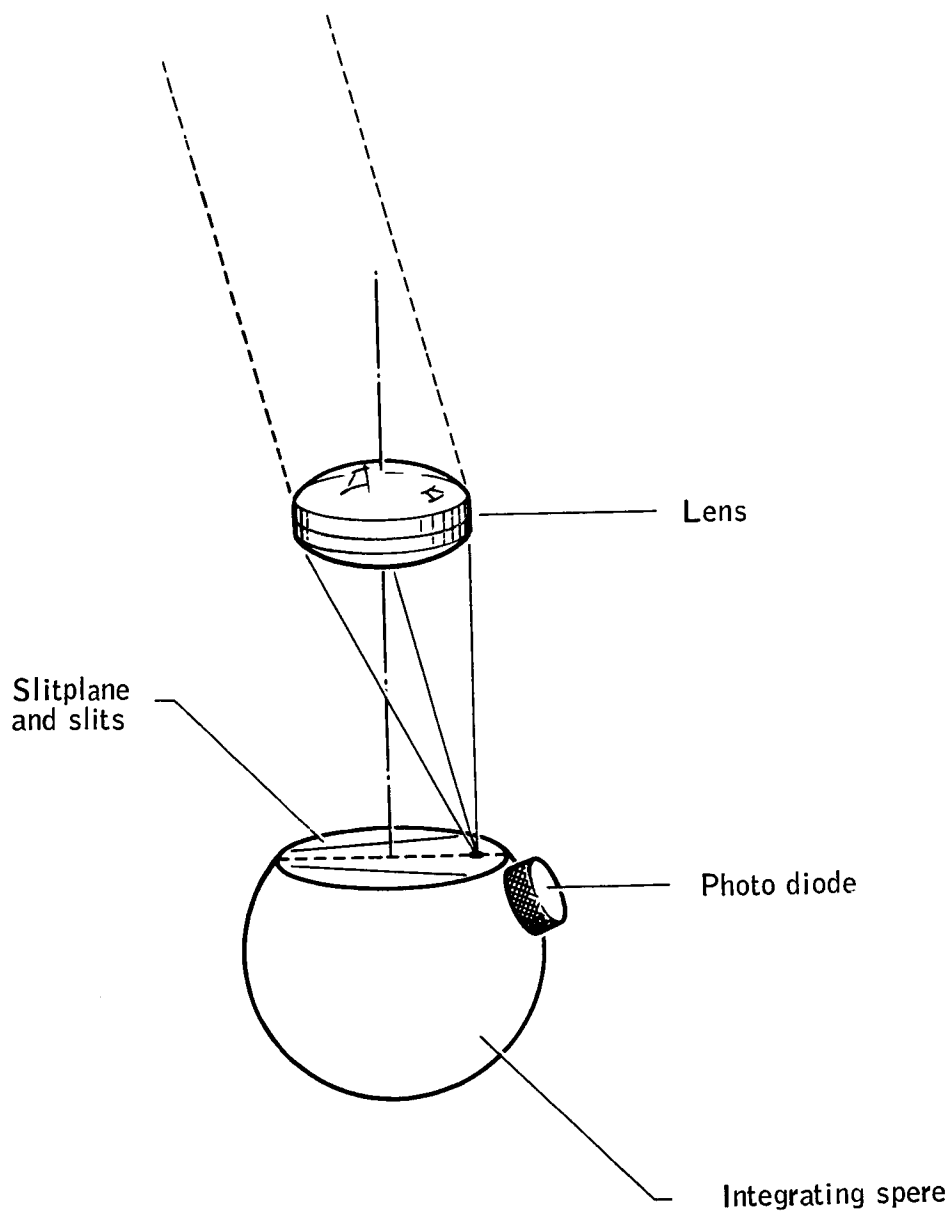
Lens

Slitplane
and slits

Photo diode

Integrating spere

Figure 172. Schematic of Sun Sensor

440

The sun sensors, however, must be mounted at an angle of 45 degrees off the spin axis since this is the nominal direction to the sun for a 3 a. m. /3 p. m. sun-synchronous type orbit. The field of view of the sun sensor is designed to accommodate the excursions of the sun from this position. The exact, aligned position of the sun sensors with regard to the radiometer must then also be carefully measured to the same degree of accuracy in the pitch rotational plane as is required of the starmappers in order to maintain equal operational accuracy.

To avoid extraneous signals into the sun sensors or starmappers, it is absolutely mandatory that no objects such as antennas or solar panels be anywhere within the fields of view of 35 degrees for the sun sensors and 20 degrees for the starmappers. In addition, for the starmapper it is highly undesirable to have any reflective surface any closer than at least 35 degrees off the optical axis. It is true that there is a light shield on the starmapper. However, it is only a minimum type, and reflective surfaces could catch the light of a full moon and reflect it into the light shield, greatly increasing the background noise of the system.

Starmapper and sun sensor electrical power requirements. -- Power to the sun sensors and starmappers can be handled in two ways. Preferred is a 24 - to 28-volt dc input which is necessary to drive the photomultiplier power supply. This same dc voltage can be converted to ± dc levels for use in the analog/digital circuitry. If central sources of well-regulated voltages are available for use, these voltages would be considered for use rather than generating additional voltage levels.

Each starmapper will consume about 7 watts, and each sun sensor should consume about 0.25 watt of power. The prime power consumption area is the photomultiplier-power supply combination which consumes 1.5 watts each. Therefore, two photomultiplier units consume three watts of the seven watts in each starmapper. Four watts of power is necessary to drive all electronics of the system with the exception of the oscillator, real-time clock, and half-speed counters.

Weight and volume. -- The estimated weight and volume of the starmapper and sun sensor components are shown in Table 32.

TABLE 32. -DETECTION SYSTEM WEIGHT AND VOLUME

	Weight, lbs.	Volume, cu.in.
Starmapper		
Optical system	8	730
Light shield	2	280
Photomultiplier power supplies	3	32
Sun sensor	2	20
Electronics	6	150
Total per system	21	1212
Total per vehicle	42	2424

Design Analysis

Preceding sections have discussed the parametric effects of each of the subsystems of the starmapper and sun sensor designs. This section contains a resume of these design decisions which, assembled, results in a workable system which meets the design requirements.

Starmapper. -- A computer-assisted study of actual stars available on the orbital path of the vehicle throughout the year showed that there will always be four or more stars of photographic magnitude of 3.2 or brighter for an optical system field of view of 20 degrees. Optically, an f/4 twelve-inch focal length system with an effective aperture of three inches is within the state of the art to provide a blur circle of one minute of arc or less to the edge of the 20-degree field of view.

Signal-to-noise ratio analysis shows that, for a 3.5-magnitude star with reticle slit width equal to the blur circle of one minute of arc and the proposed optical system, the signal-to-noise ratio will be 10:1 for a 95-percent detection probability and practically zero false star detections. The theoretical interpolation factor for these same conditions was shown to be nine. Therefore, the design is actually conservative since it assumes a limiting magnitude of 3.2 and an interpolation factor of six to give an accuracy of 10 seconds of arc across a one minute of arc slit.

The reticle design is three crossed slits, each one minute of arc wide, which for this focal length is 0.0035 inch on the reticle plane. This slit width is well within the state of the art. The X slit pattern has been found very effective for use in ground data reduction, especially if the upper and lower transits are identified. This identification is done by means of separate bundles of optical fibers leading to separate photomultiplier tubes. For this application, optical fibers are as efficient with less weight and volume than a condensing lens system.

From a reliability standpoint, the system is actually better. The photomultiplier tubes do have a relatively high failure rate, but if one tube fails in one starmapper, data from a 10-degree field of view will still be gathered. A second look at the star availability data shows that even with only a 10-degree field of view, four or more stars of 3.5 magnitude or brighter can be detected 93 percent of the time, three or more stars 98 percent of the time, and two or more 100 percent of the time. In addition, the coning effects of precession will effectively increase this field of view and the probability of detecting additional stars. Since it is proposed to have two complete starmappers aboard the vehicle, each with two photomultipliers, it will require failure of all four photomultipliers to abort the mission. The probability of this not happening is 99 percent for the one-year mission duration.

Sun sensor. -- Investigation of data on the definition of the sun's limb shows that it is defined to better than one second of arc. An optical system of one-inch aperture, with a two-inch focal length, and field of view of 35 degrees is proposed. It is within the state of the art for this system to have a blur circle

of one minute of arc for the band pass of 5400 to 5600 angstroms which will be provided by an evaporative-film coating on the objective. The reticle slits for the sun sensor will be in the form of a V with each slit two arc minutes in width. For this focal length, the slits will then be 0.0006-inch wide, which is also within the state of the art. The light is then gathered by an internally reflecting integrating sphere and detected by a photodiode. The error analysis showed that this system used in the high intensity light from the sun will provide the required accuracy. Since there is no photomultiplier in this system, the probability of success for a one-year mission is approximately 99 percent. However, to ensure against a catastrophic failure, it is proposed that the two sun sensors be installed in the vehicle.

SYSTEM INTEGRATION

The research package consists of three independent (in the sense of being designed for different functions) instruments which are tied together mechanically and thermally because of a critical alignment requirement. They also share a common data memory. Primary emphasis of this section is upon the alignment problem. There are, however, other obvious interfaces and, in addition, there are some fairly subtle points to be considered in the integration. The research package interfaces are discussed below

THERMAL

The radiometer and attitude sensors are soaked in the same thermal environment. Critical thermal requirements are:

- Temperature stability of the detector

- Effects on alignment of shifting thermal gradients

- Required operating temperature for the starmapper

- Temperature stability and gradient structure of the radiometer optics and housing.

The problem here then is to define the time history of the detector temperature as influenced by varying external inputs and thermal gradients in the radiometer housing and to specify thermal inputs to hold them within acceptable limits.

Consultation with the manufacturer (EMR) has determined that operation of a photomultiplier at 200°K presents no problem. Also, dissipation of the tube represents a heat input the order of 250 milliwatts, an insignificant effect. The sun sensors present an obvious problem, since by definition the sun is viewed with these devices in daylight and there is no heat input in the dark. The total input to these devices is of the order of one watt. Proper reflective coating on the sun sensor lens will reduce this input to less than one milliwatt. Direct thermal coupling by a copper strap to the radiative backplate, which is dissipating tens of watts, allows these devices to remain at essentially the same temperature throughout the orbit. The electronic packages are located outside the cooled region, and thus present no significant thermal load to the research package. The thermal design of the system is covered in the radiometer section where a detailed analysis of thermal and gradient histories is included.

444

ELECTRICAL

The research package and its elements each require isolation from ground loops and power-supply noise. This problem is met by using separate power supplies for each element. Standard design practices should be adequate to prevent instrument crosstalk. Each subsystem has special power requirements, which are met by separate buses for each instrument.

There does not appear to be any significant problem in electrical interfaces, either within the package (completely isolated subsystems) or external to the package.

MECHANICAL

The obvious mechanical interface is alignment between the attitude determination instruments and the radiometer and between the attitude determination instruments themselves. This subject is analyzed in detail below. There have been mechanical problems in simply fitting the starmapper into the experiment package, and problems were encountered in spacecraft balance with certain configurations. A configuration has been obtained which meets the attitude control subsystem (ACS), starmapper, and radiometer requirements.

The General Alignment Problem

The internal alignment of an instrument (e.g., radiometer) is distinguished from the instrument-to-instrument alignment. In the devices included in the research package, the internal alignment elements are tabulated in Table 33.

TABLE 33. - INTERNAL ALIGNMENT ELEMENTS

Device	Elements affecting alignment
Radiometer	**Primary mirror** Displacement normal to optical axis Mirror tilt **Secondary mirror** Displacement normal to and along optical axis Mirror tilt **Field stop** Displacement (Shifts of elements behind field stop affect focus, not alignment)
Starmapper and sun sensor	Lens tilt **Reticle** Displacement normal to optical axis **Folding elements (between object space and reticle)** Displacement normal and along optical axis Tilt

As an illustration of the magnitude of the problem, the internal alignment of the starmapper is examined. The focal length of the device is approximately one foot. The total alignment error budget is roughly eight arc seconds. Assuming independent errors, the allocation to the starmapper can be assumed to be four arc seconds.

Using the standard relation for lengths on a focal surface (reticle is assumed to be at a focus), the displacement corresponding to four arc seconds referenced to the focal surface is roughly 0.2 thousandths of an inch, i.e., if the starmapper bends from reticle to lens system by more than 0.2 mil, that device is beyond alignment tolerance. With the numbers obtained here, it would appear that, as a first principle, no folding elements can be allowed in the starmapper.

A first-order approach to an alignment analysis is made as follows: A total error (1 sigma) of 8 arc seconds is allocated to misalignment. Observing the system externally, assuming that alignment errors for each subsystem are independent, and allocating errors equally, the allocation to each subsystem is:

446

Ground measurement (total)	4 arc sec
Radiometer (internal change from measurement through flight)	4
Starmapper/sun sensor (same condition as radiometer)	4
Integrating structure	4

Note that the starmapper and sun sensor are independent instruments, and alignment assignment is for each instrument.

Within the instruments, a first-order analysis yields the following elements as critical in alignment:

Radiometer (all numbers refer to resultant alignment shift, not element motion)

Tilt of primary mirror	0.8 arc sec
Tilt of secondary mirror	0.8
Displacement of primary	0.8
Displacement of secondary	0.8
Displacement of field stop with respect to nominal	0.8

Starmapper/sun sensor

Tilt of reticle	2.0 arc sec
Displacement of reticle	2.0

Integrating structure (holds starmapper reference with respect to radiometer reference).

Starmapper or sun sensor with respect to radiometer	4 arc sec

No assumption of independence has been made; internal errors are assumed to be directly additive (unity correlation).

There are two approaches to meeting these alignment requirements. The first relies upon structural rigidity and minimization of thermal gradient changes in the system. The second relies upon devices which are capable of sensing misalignments tied together in such a fashion as to measure the attitude sensor optical axis with respect to the radiometer optical axis. In reality, as will be discussed below, there does not appear to be any feasible system which does not rely upon structural rigidity of at least portions of the system.

Structural Considerations

There are several basic error-inducing parameters that must be considered in designing an integrated supporting structure within the alignment constraints of the HDS experiment. The more critical of these are the following:

- Basic dimensional stability of candidate materials relative to metallurgical instability and plastic deformation.

- Design, fabrication, and finish treatment techniques and processes to control or remove residual stress properties in finished parts.

- Isolation, as much as possible, from transient heat sources.

- Variations in thermal conductivity characteristics between materials.

- Maintaining an isothermal integrated structural environment by controlling cross-sectional areas and providing required thermal paths either through the structure or external straps.

Careful consideration of these problem areas and a thoroughly planned and integrated program covering the design, analyses, fabrication, and testing could produce an experiment supporting structure that would meet alignment criteria of the proposed HDS experiment. Honeywell's background with gyros, accelerometers, and floated instruments and the thermal distortion studies and tests by Republic Aviation Corporation on the Advanced Orbiting Solar Observatory for GSFC show that dimensional control and alignment within the two to four arc-second range can be achieved if the thermal gradients can be maintained at the 1 or 2°F level (references 46 through 49).

An experiment package incorporating this alignment control approach is a finely balanced system from a thermal standpoint, and any degradation in the thermal control system or other subsystems that could induce thermal transients would affect this balance and hence the alignment accuracy. Because of the unknowns in the space environment, a package that would incorporate the above structural design accuracies and requirements plus an in-flight alignment checking system that could read out any variations caused by system degradation or spatial environmental variations would seem most desirable.

Other Techniques

Use of celestial references for alignment. -- An ideal solution to the problem of alignment between the attitude determination subsystem and the radiometer is viewing by the radiometer of a celestial body. This, then, permits referencing of the radiometer data to the same (celestial) coordinate system as the attitude determination subsystem.

The radiometer does not have significant response in the spectral region where the majority of stars have output. Direct readout of stars with the

448

radiometer does not appear feasible. Use of a visible-light detector in the focal surface was then considered.

A calculation was made of the performance of a photodiode at the field stop of the radiometer in detecting stars. Stars of approximately visual magnitude 2.5 can be detected with this system; approximately 50 stars are available at this visual magnitude.

Two major problems are encountered in a mechanization of this concept. In order to obtain sufficient resolution to permit the use of a star for solution of the problem to the order of 5 to 10 arc seconds, re-collecting optics behind the focal surface are required, since with an f/2 16-inch system the length on the focal surface which subtends 5 arc seconds is of the order of 10^{-3} mm, which is considerably smaller than the state of the art in detector manufacturing. Placing collecting optics for visible light here may interfere with the primary measurement, although fiber optics techniques may allow operation. Also, the output must have a wide information bandwidth, must be accurately timed so that the earth does not generate output, and is subject to stray light inputs from the sun and the moon. The extremely narrow field of view of the radiometer and the vehicle motion make a prediction of time of appearance of a star extremely difficult. Although feasible, these difficulties indicate that this solution should be held in abeyance pending the investigation of other techniques.

The moon was then examined as a celestial source which could, with some difficulty in data processing (edge tracking), be used for alignment. The self-emission from the moon is adequate to obtain radiometer response, eliminating any requirement for a visual-wavelength detector in the radiometer.

The operational problem of viewing the moon is formidable. The moon subtends 30 arc minutes, and the radiometer field of view is of the order of 164 arc seconds normal to the scan direction. The precession in one orbit is equivalent to approximately 220 arc seconds. Hence, for a vehicle with no attitude perturbations, the moon will be seen once each 28 days. If, however, it is possible for the vehicle to change in attitude by 1/2 degree in an orbit, the moon can be missed. For this reason alone, it is not feasible to rely upon the moon for an in-flight alignment check. As is obvious, even more formidable difficulties are encountered in attempting to use the brighter planets for this purpose. In addition, it is doubtful that information with a 28-day period is useful, particularly since this will coincide with the starmapper shut-down period.

Alternate systems. -- Having ascertained that holding the mechanical alignment of two separate instruments to the tolerances required is an extremely difficult task, it is of interest to determine if there are other instrument system configurations capable of meeting the requirements.

An obvious candidate is the merger of the two instruments in a single optical system. Consider the optical requirements of the two systems: a wide-angle (certainly greater than 5 degrees) system operating in the visible wavelength (0.4 to 0.6 micron) and a narrow-field device operating in the long-wavelength

449

(14 to 16 microns) infrared. Dioptric systems for the radiometer are ruled out by the size of the required aperture (of the order of 16 inches) and the bandspread required (0.4 to 16 microns). Classical catoptric systems, while meeting the radiometer requirements, cannot meet the field-of-view requirements of the starmapper. (See the blur diagrams for a classical Newtonian telescope in Figure 173, where two milliradians is considered a difficult requirement). Catadioptric systems require a transmission element and are subject to the same objections as dioptric systems.

A new development (ref. 50) is the use of aspheric correcting, reflecting elements to obtain wide-field operation in a catoptric system using Schmidt corrections. The system, manufactured by Davidson Optronics, is designed for wide-field spectroscopy and is proposed for the Apollo Applications Program (AAP). The primary is 12 inches in diameter with a 6-inch correction mirror. Field of view is five degrees with a Hartmann number of 1.6 ± 2.3 seconds of arc. Because of the recent development of this device, no analysis has been performed, but further investigation into the mechanization of a dual radiometer-starmapper using such a system appears worthwhile from the standpoint of alignment. However, the obvious difficulties in mechanization may render such an approach unfeasible.

Because of the late publication date of the reflective Schmidt system, the studies included here are confined to an examination of separate optical systems.

Auxiliary Measurement Devices

At least two concerns, Exotech and Barnes, manufacture small autocollimators capable of measurement to the accuracy required. These devices offer considerable promise for tying the set of instruments together. The starmapper and radiometer lend themselves to the mechanization of internal autocollimators. The radiometer, for example, can accommodate a source behind the primary and/or secondary. Similarly, the starmapper has an already unused center section in the reticle, and the lens system can serve as a flat.

The devices examined have, typically, 0.5 second of arc absolute accuracy and a useful range of approximately 30 arc seconds. Analog output is available, and obvious summing techniques can yield a signal which is directly proportional to total misalignment. A detailed analysis of this approach is discussed below.

   Assessment of in-flight measurement problem. -- Alignment errors between sensors and the radiometer and within the individual optical subsystems may be divided into two categories, those induced by vibration and motion of mating surfaces and those caused by thermal changes and gradients. In order to ascertain the requirements for an in-flight alignment system it will be useful to discuss the sources of alignment error in greater detail.

   Mechanical: Mechanical considerations involve the physics of the interface between two objects which are fastened together mechanically (e.g.,
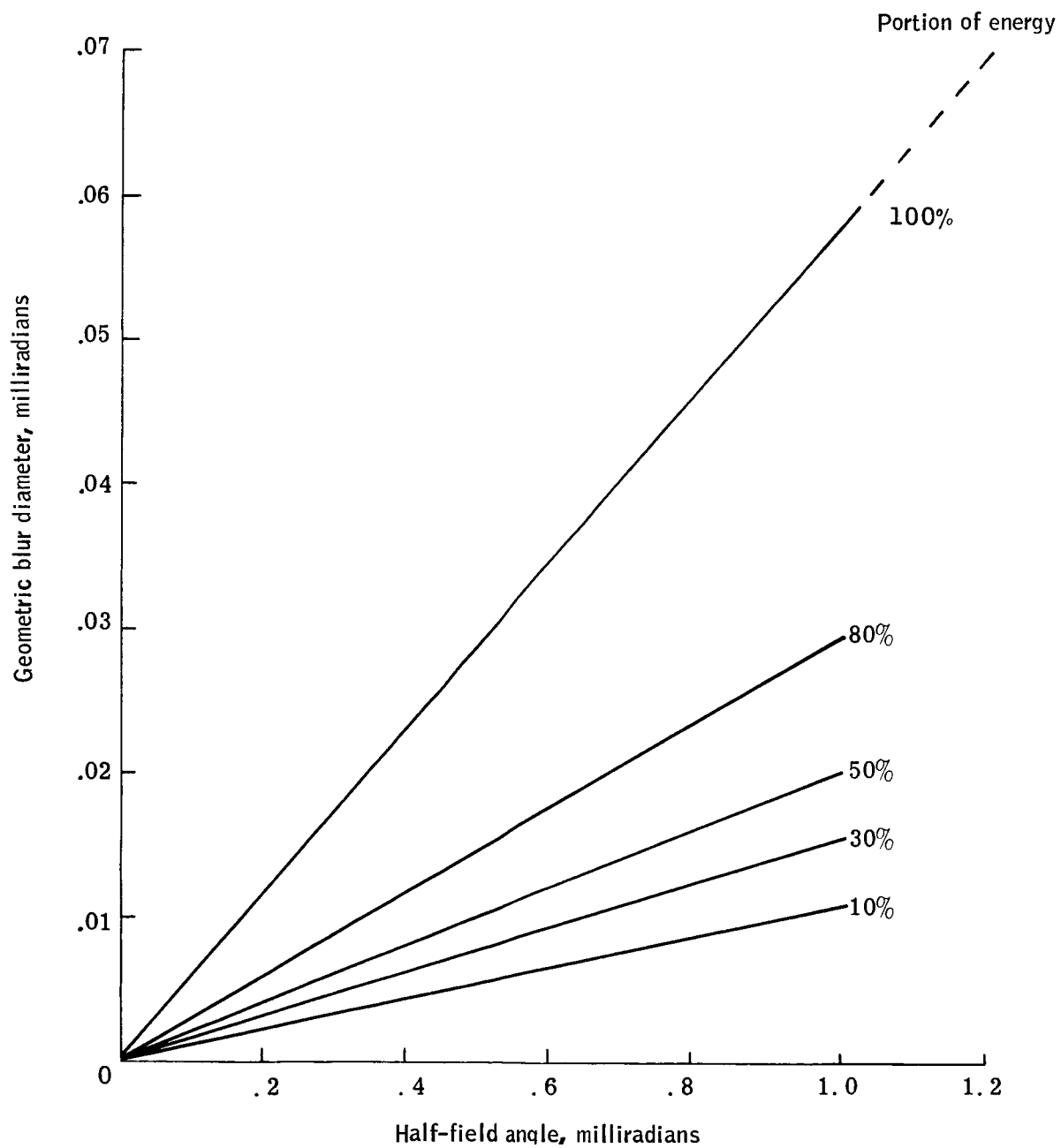
Figure 173. Geometric Blur Diameter for an f/2.0 Classical
Newtonian Design

bolted structures). As the surfaces of two objects are forced against each other, contact is initially made at the high points of surface irregularities. Since these areas are very small, high stress concentrations arise, and plastic yielding occurs until the contact areas are sufficiently large to support the applied load. If the objects are subsequently subjected to shock and vibration, local stress concentrations may cause further plastic yielding in particular areas, resulting in permanent alignment changes. Other phenomena such as creep and fatigue may contribute to the problem.

If the surfaces are of optical quality the surface irregularities will be so small that relatively large areas will be in contact. This would minimize the shock and vibration problems providing no distortions were introduced by the fasteners.

Fastening techniques incorporating removable components, e.g., bolts, introduce distortions adjacent to the fastener which largely offset the advantages of optical polishing.

These problems arise whenever two components are to be attached such as in mirror or lens mounts, reticle mounts, or in mounting complete instruments to a base or each other.

The severity of the problem is illustrated by a few isolated tests which indicate that optical instruments designed for Aerobee rockets will typically undergo misalignments of 10 to 20 arc seconds after being subjected to the acceptance tests for sounding-rocket payloads.

Typically, some degree of burnishing is usually evident on mounting surfaces after subjecting the mounted article to shock and vibration tests. When it is realized that one arc-second alignment change represents only ten millionths of an inch change over a two-inch distance between mounting pads, and that visible burnishing may represent the removal of several tens of microinches (one optical "fringe" is roughly 10 microinches), it is easy to visualize the reasons for the above test results and to see the difficulty in preventing alignment changes in demountable systems.

Thermal: Thermal problems are of two types:

(1) Changes in alignment due to absolute temperature changes from the original alignment temperature.

(2) Changes in alignment due to temperature gradients.

The first may arise as a result of using materials with different coefficients of thermal expansion in a structure, although this can usually be avoided. However, if angular misalignment or defocusing can arise from linear expansion of a single element, then absolute temperature changes are important. Consider the 16-inch, f/2.0 Newtonian reflecting telescope used in the radiometer. One arc second corresponds approximately to

$$32 \times 5 \times 10^{-6} = 160 \times 10^{-6} \text{ inches}$$

in the focal plane. If the folding mirror moves due to expansion in the length of the telescope tube, an image centered in the focal plane will become defocused and shifted by an amount equal to the linear expansion. For a 24-inch aluminum tube the expansion E would be

$$E = 24 \times 24 \times 10^{-6} = 576 \times 10^{-6} \text{ inches/°C}$$

which corresponds to 3.6 arc seconds/°C. If the focal plane reticle moves the same amount as the folding mirror, no angular shifts will be apparent although the image will be defocused.

Thermal gradients within a structure can cause alignment problems. This is simply illustrated by considering the primary lens or mirror of a simple telescope. If the lens is rigidly mounted in a tube of length L and a temperature gradient of $\Delta T/W$ °C/inch is established across the tube, unequal expansion will cause the tube to become curved. The apparent angular change in the optical axis is given by

$$\phi e = \frac{12 \times 24 \times 10^{-6}}{10^{-5}} \times 1 \approx 28.7 \frac{\text{arc sec}}{\text{°C-inch}}$$

It is apparent from these results that while it may not be impossible to maintain the angular alignment of many elements in a sizable structure to within 10 arc seconds it will be very difficult, requiring the use of materials such as quartz and invar which may be undesirable from an economic, structural, or magnetic viewpoint. Very elaborate handling and assembly procedures must be invoked to ensure proper system performance. Furthermore, to detect and isolate a single unstable element in a complex system could be very time consuming and expensive.

In-flight alignment sensors. -- An alternate approach is to use simpler and more economical structures and mounting techniques which will result in moderate alignment shifts through a space flight environment and to monitor these shifts using a small precise instrument of lower overall cost and complexity.

One possible approach with great flexibility would utilize a device being developed by Exotech which consists of a pair of angular sensors fabricated within a monolithic quartz structure, or within several quartz blocks cemented together. Because of their small size and low coefficient of thermal expansion, mechanical and thermal problems are minimized; extensive tests and analysis show that the optical axes of the two sensors will maintain their relative alignment within a fraction of an arc second over a wide range of thermal and mechanical environments. These sensors may be solar sensors, autocollimators, collimated light sensors, or any combination of these with very stable axes relative to each other. Such devices could be employed in the following manner.

If a light source is placed at the focal points of both the starmapper and radiometer, each instrument would act as a collimator whose output light beam is parallel to its optical axis. (If a collimated light sensor were placed in the beam, it would measure the angle between the collimated light and its own optical axis). If a pair of collimated light sensors rigidly attached to each other were placed in both beams simultaneously, it would be possible to measure the alignment error between radiometer and starmapper axes. The measurement accuracy would be in the order of one second for a misalignment of 20 to 40 arc seconds, which is well within system requirements. There is no need to know the absolute alignment of the sensors, so they can move small amounts without affecting measurement accuracy. They could even be moved in and out of the beam if necessary.

The light source located in the center of the focal plane of each instrument would have to be small and, in the case of the radiometer, dissipate little heat. Possibilities here include fiber optics or very small "pinlights" (0.016" to 0.040" in diameter). Since scattered and reflected light could cause problems it would be preferable to monitor the alignments on a periodic basis, which is compatible with slowly changing thermal inputs.

If the sensors cannot be tied together mechanically due to mounting or space considerations, each sensor can be paired with an autocollimator with each autocollimator aligned to a common reference mirror so that the sensor axes can also be monitored. Also, a solar sensor could be paired with a collimated light sensor to give direct comparisons between the solar vector and radiometer axis. In short, there are many possibilities.

Another application of the sensors described is in the recheck of system alignment during system test, where it is simply necessary to monitor the sensor outputs while positioning the radiometer and starmapper.

A slightly more complex version of the system can be used to measure defocusing of the radiometer. As the light source moves forward or backward from the focal plane, the rays on opposite sides of the collimated beam diverge or converge, respectively. If two sensors which are optically tied together using integral autocollimators are placed on opposite sides of the beam they can be used to monitor defocusing. With a suitable feedback system the sensors can be used to maintain system resolution changes to within two to four arc seconds. Defocusing information would be readily separable from alignment information since the sensor pair would provide equal and opposite signals for focus errors but would provide equal signals of common sign for an alignment error.

Instrumentation. --

Attitude sensors: The general class of optical attitude sensors which perform energy splitting between pairs of light detectors provides a useful means of determining the angular relationship between the sensor axis and the line of sight to a collimated source of light. Typically, these sensors consist of an objective lens which forms an image of the source (star, sun, pin-hole in a collimator, etc.) on a knife-edge type reticle. The reticle divides the power

454

in the focal plane onto detector pairs which are connected to yield equal and opposite outputs when the light is evenly divided. Simple electronic addition of the signals produces a sensor output signal which is proportional to the deviation between the sensor axis and the line of sight to the source over some field of view, depending on the optical parameters and the angular subtense (decollimation) of the source.

These sensors are susceptible to all of the sources of error discussed previously, and in order to avoid alignment changes associated with vibration and thermal cycling, sensors have been developed which include the lens, reticle, and supporting structure in a monolithic quartz block. Knife-edge patterns may be vacuum deposited directly onto the focal plane (rear surface) and a lens ground into the front surface of a single rod or block of material.

When two or more such sensors are included in one block, possibly looking in more than one direction, relative misalignment between their respective lines of sight becomes a virtual impossibility. Mechanical stresses during the launch environment will either shatter the device or will cause no permanent deformation. The very low thermal expansion of fuzed quartz (1/50 of the expansion of aluminum) ensures relative invulnerability to thermal variations and gradients.

Excellent results have been obtained through the use of silicon photovoltaic detectors operated in a short-circuit current mode for use in the optical sensors. They exhibit extremely low thermal sensitivity, especially when used in conjunction with spectral filters to select a wavelength region which minimizes thermal effects. Electronic amplifier techniques have been developed and demonstrated which yield sensitivites with silicon detectors only slightly less than those obtainable with photomultipliers.

For the purposes of the current study, these quartz-block type sensors are capable of fractional arc-second, absolute accuracies including all thermal, mechanical, and electronic errors.

However, this accuracy is meaningless if an attempt is made to mount rigidly the quartz block to a baseplate or experiment since it has already been established that errors greater than 10 arc seconds may be encountered due to mounting problems alone.

Electronic autocollimators: The basic quartz sensor, with some modification, may be converted into an autocollimator to provide a means of measuring the mounting error, in real time, relative to any flat optical surface. The special form of knife-edge reticle being employed permits placement of a light source behind the reticle plane. The central portion of the reticle is transparent and when suitably illuminated is projected outward by the objective lens in the form of a collimated light beam. When this beam strikes a reflecting surface the beam re-enters the optical system and is detected in the same manner as if it emanated from a distant source external to the system.

Since no beam splitters are used, the entrance and exit reticles are one element, and all components are part of one block of quartz; the autocollimator errors are comparable to or less than those obtained when observing external light sources. In addition, the reticle design is 100 percent efficient as compared to the 10 percent efficiency commonly obtained with a beam-splitter type autocollimator. This latter feature permits the use of very low light-level sources requiring low input powers.

Radiometer alignment instrumentation: Assuming that the final radiometer will have a dual field of view subtending 0.2 milliradian each with a separation of 0.8 milliradian between centers, the reticle pattern comprising the field stop will consist of a pair of 0.0064-inch diameter holes having centers 0.0256 inch apart. Thus, a space of 0.0192 inch exists between the apertures and is available for placement of a small light source. While reliable tungsten-filament light sources are available which are smaller than this dimension, it may be better to move the small amount of power dissipated by the lamp to a less sensitive location (in terms of the radiometer) by utilizing a fiber-optics light pipe. Sufficient space exists behind the field stop to permit a reasonable radius bend in the fiber optics without interfering with the radiometric beams in any manner.

To further avoid any possibility of thermal loading due to the light source, it is possible to operate the unit only occasionally as a check on alignment. The small amount of back-scattered visible and near-infrared radiation from the lamp which may return to the field stop will be rejected by the radiometer spectral filter. Any longer wavelength radiations from the envelope (at 15 microns) may be removed by using a glass filter and/or permitting the self-calibrating radiometric system to measure the lamp effects.

Other light sources such as gallium-arsenide emitting diodes and various solid-state devices based on similar principles have been analyzed and tested. These may provide good alternative candidate sources for special purposes.

It is a good practice to modulate the light source at a low frequency to enable the sensor to distinguish between the desired source and other, spurious sources of light such as sun glint, other internal lamps, etc.

One or more (a pair of sensors will also yield highly sensitive information on radiometer focus errors as well as providing a degree of sensor redundancy) quartz-block sensors may be placed in the rim of the radiometer, blocking less than 1.0 inch^2 each of the incoming infrared radiation. These sensors will provide highly accurate, two-axis information concerning bore-sight alignment of the radiometer. Any deviation from the initial radiometer line of sight may be accurately monitored in this manner regardless of the optical element or elements which have contributed to that error. Integral, quartz-block type autocollimators with each sensor will enable the sensors to measure accurately deviations from initial settings to a reference flat on the starmapper or to an optical surface common to the starmapper alignment devices.

456

It is believed that the system alignment requirements may be readily met using this optical approach.

Starmapper alignment instrumentation: The instrumentation used to align the starmapper may be very similar to the method discussed above since unused area exists in the center of the starmapper reticle. Another method which might provide tighter alignment possibilities in a simpler system would utilize a quartz-block optical system for the starmapper which would utilize three passes through the block length and involve one refracting and two reflecting surfaces. The field plane may also be curved for further optical correction, if required. It may be possible to obtain excellent optical performance over the required field of view through the use of a three-inch long, three - or four-inch-diameter quartz block.

A flat ground and polished into the quartz block would provide an excellent reference surface for aligning the radiometer sensors which would maintain a constant angular relationship to the starmapper axis within a fraction of an arc second under any conceivable flight conditions.

The concept of a combined autocollimator and sensor in a monolithic quartz structure was first used in solar sensors with considerable advantages over other methods. Practical accuracies better than 0.5 arc seconds absolute (to an external, optical surface) are expected under Aerobee flight conditions where high thermal transients follow rather severe launch environments.

Conclusion. --An overall system consisting of the radiometer alignment sensors, sensors incorporated into the starmappers, and the current approach to sun sensors can be combined to meet overall alignment requirements and will afford additional advantages as well.

Initial alignment problems will be greatly reduced, and the fabrication and installation of the individual components may be performed to reasonable tolerances since their internal and mounting errors will be subsequently monitored, both prior to flight and during experimental data gathering.

System alignment:

- System layout -- Figure 174 illustrates the final layout of the experiment package. Two starmappers are mounted offset below the radiometer on the central radiometer support structure, which also carries the secondary mirror and field stop. Two sun sensors are mounted on the support structure for the radiometer primary mirror. The starmapper aperture openings are 180 degrees away from the radiometer entrance aperture, since, with their baffles, the starmappers protrude into the radiometer field of view if mounted with entrance apertures in the plane of the radiometer entrance aperture. The sun sensor optical system, lens to reticle, is a monolithic quartz block with the reticle mounted in the manner described above.
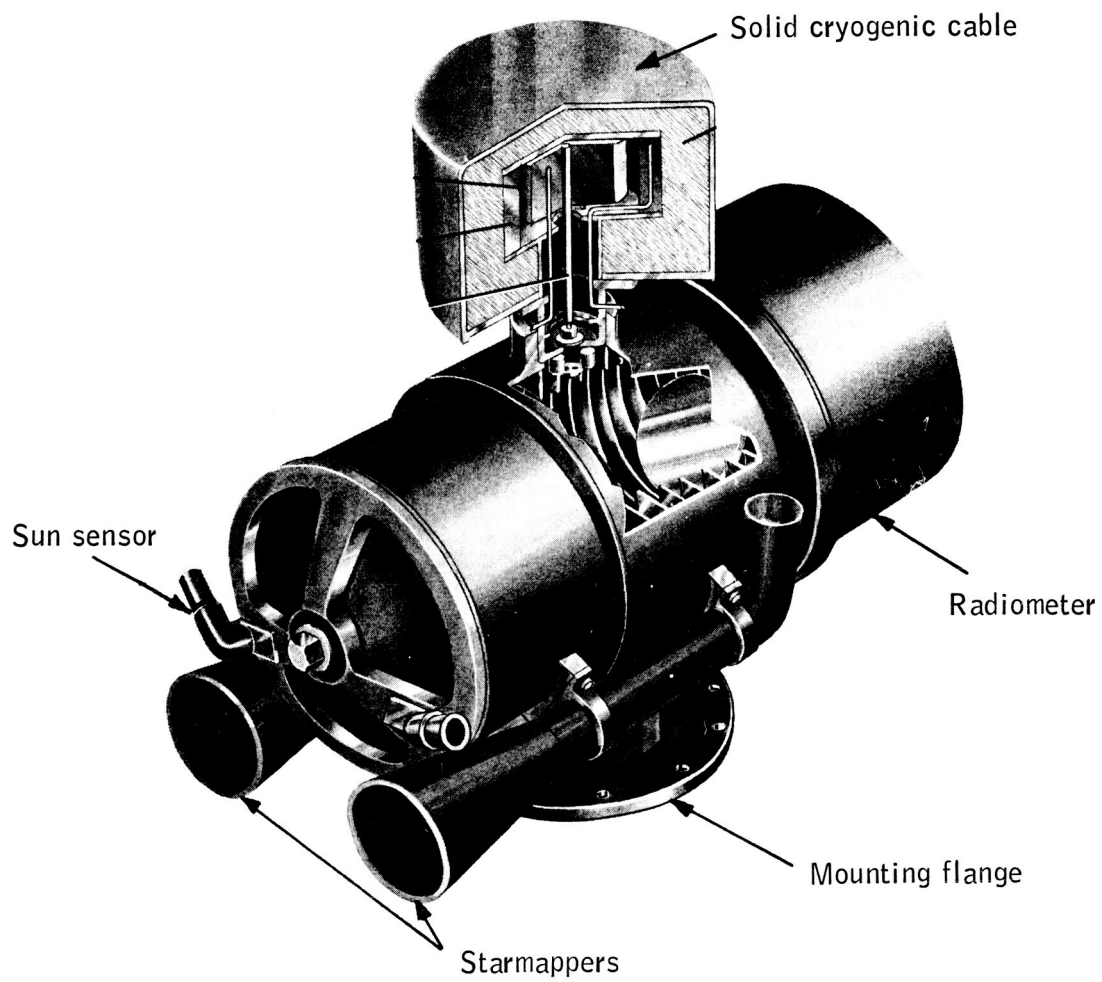
Figure 174. HDS Measurement System Concept

- Alignment instrumentation -- The placement and use of the alignment instrumentation is dictated by the requirement to tie together the three systems described above. Because of instrument placement, it appears that dual systems are required. Figure 175 shows the selected design.

A source is placed at the radiometer focus. This source is collimated, and deviations are measured by a sensor on the radiometer barrel. The sensor is tied to an autocollimator observing a reference flat, placed such that it is visible from the starmapper forward of the lens mount. A second autocollimator is mounted on the starmapper barrel and also tied to a sensor. A light source is mounted in the reticle center and collimated by the starmapper lens. Motion of the sensor mounts is then obtained from the autocollimators and can be compenstated in the derivation of instrument-to-instrument alignment. It may be noted that motion of the reference flat is noncritical.

To tie the sun sensor to the radiometer, essentially the same technique is utilized, excepting that the sun sensor and autocollimator are contained within a single, monolithic block.

TESTING

System Alignment

Testing of system alignment is a major interface area. Of the possible choices for testing system alignment, significant advantages are offered with a system whereby the subsystem supplier aligns his instrument to external references (optical flats) and system alignment is obtained by measuring the relative position of these references. A discussion of this area is given below.

The major problem is the cold chamber required to obtain response from the radiometer. Room-temperature surroundings preclude accurate measurement. In order to obtain noise-level response from the instrument, the surroundings must be cooled to temperatures of the order of liquid nitrogen, although a warmer environment will suffice for alignment. In addition, a special collimated point source must be provided which will yield a reasonable level of response in the 14- to 16- micron region. These requirements appear to be most easily met at the calibration facility. In all cases, it will be necessary to cold-soak the assembled system to reach stable, orbital operating temperature and to provide the required radiometer detector cooling. A special controlled (dry) atmosphere must be supplied to prevent damage to the optics.

Measurements must be made over a range of temperatures corresponding to the expected orbital temperature range plus a safety factor.

Three possible conceptual systems for assembly and alignment are apparent and are outlined in Figure 176. These are:
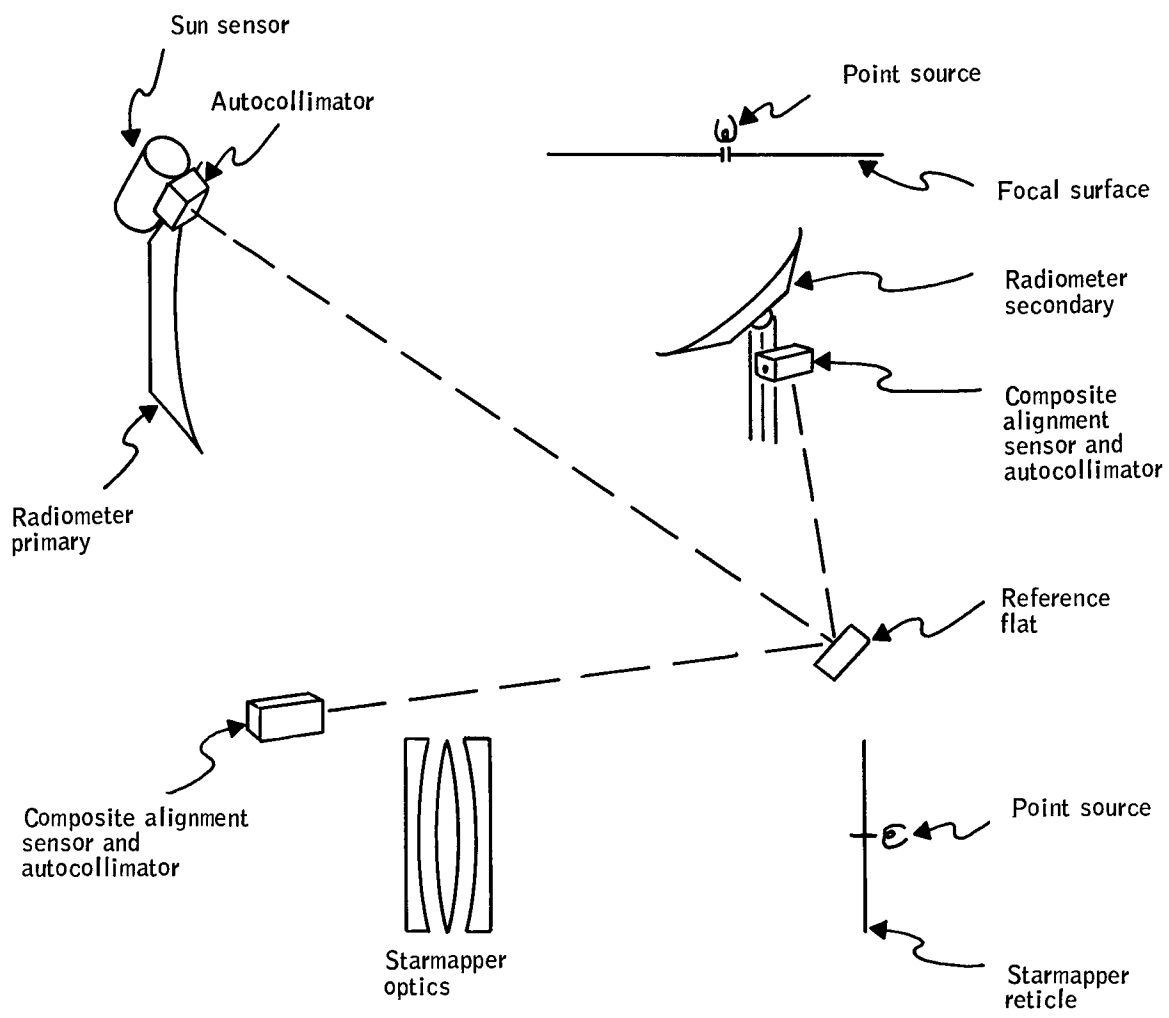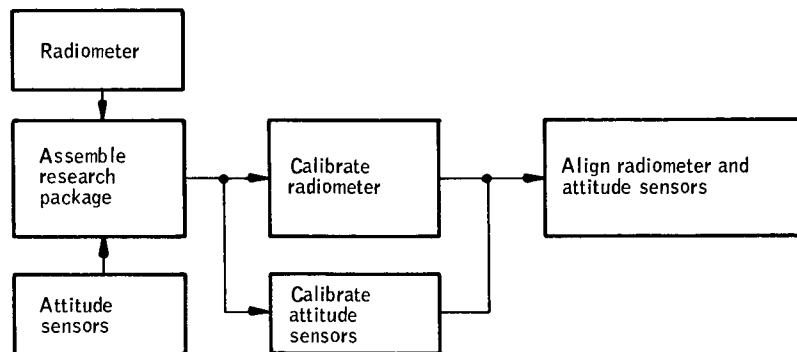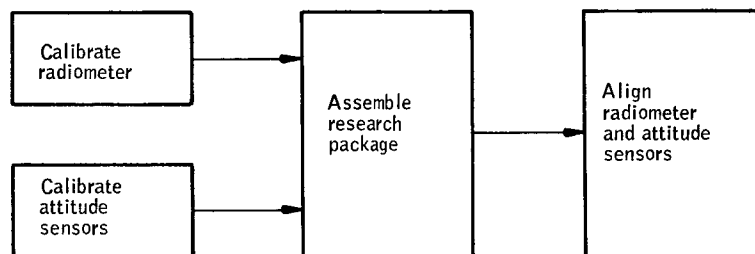
Figure 175. Conceptual Alignment Monitoring System

1. Assembly before radiometer calibration

2. Assembly after radiometer calibration (radiometer and starmapper internal alignment established in system test)
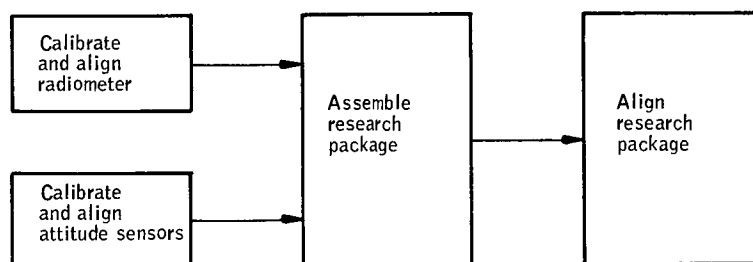

3. Assembly after radiometer alignment

Figure 176. Conceptual Systems for Assembly and Alignment

461

1) Assemble before and align during or immediately following cold-chamber calibration of radiometer. Use the radiometer detector directly with the ir source and the starmapper and sun sensor with the visible source for system alignment.

2) Mount a visible detector in the radiometer focal plane and establish angular position of the visible detector with respect to field stop(s). Assemble system after calibration and use a visible light system for system alignment measurement. This method has the advantage of using the optical systems of all three instruments during the system alignment.

   The second system described has a major difficulty in that it imposes a requirement on the design of the radiometer which may compromise the measurement itself. This system will not be pursued unless there is no other solution or the visible detector is required for other reasons, e.g., in-flight check of alignment.

3) Align radiometer, starmapper, and sun sensor to references on instrument (optical flat). Assemble after calibration and individual instrument alignment and measure system alignment with optical flats and theodolite system.

Of the three systems described above, the third appears to be the most desirable. It allows initial internal measurements to be made at a point where elaborate facilities are or will be available, i.e., at the suppliers in the case of the starmappers and sun sensor and at the calibration facility in the case of the radiometer, and requires minimum duplication of facilities at the system assembly and test level. It has the disadvantage of not easily permitting a meaningful, composite operating test of the entire system with external inputs. The first system separates the starmapper and sun sensor from the supplier's facilities for a critical measurement and would probably require assembly at the radiometer supplier's or at a special system assembly facility. There is an obvious handling interface here which would be desirable to avoid.

Performance Testing

General. -- There are strong reasons for having the capability of experiment-package performance testing at the system level. Capability of testing the entire experiment package to performance specifications is desirable since those tests required to qualify the package (e.g., vibration and thermal) may have amplification factors in the experiment package that are not shown in individual unit test and may degrade the system. Mere assembly of the system may cause degradation.

The performance items that will be specified may be generally categorized as

- Focus
- Internal alignment

462

- Detectivity
- Responsivity

The requirements for testing these items are discussed below. The system and also the detector, where infrared measurements are involved, are assumed to be at operating temperatures. Tests described below would be designed to determine that the system is performing properly, and wide deviations from test results obtained at the suppliers, even though within specification, would imply re-testing at the subsystem level.

Focus. --

Radiometer: A complete check of radiometer focus requires a 14- to 16-micron calibrated and collimated point source and cold external environment. In-flight calibration does not appear capable of checking focus since it is not a point source. However a visible point source off-axis against a scribed reticle on the focal surface, or an on-axis source against the field stop itself does appear to be possible for use if focus only to the focal surface (field stop) is a verification of system focus, since the reflective portion of the system is achromatic. Use of a visible light source implies a collimator and a dark facility only. If an off-axis reticle is used, the relationship between focus at this point (in visible) and focus at the field-stop (in ir) must be established during the primary calibration. There are some obvious problems in checking optical system performance with a visible source since the system has roughly a 36 arc-second blur circle at 16 microns and if the system is diffraction limited in the visible approximately a one arc-second blur circle in the visible, implying a very good collimator and definitely requiring a scribed reticle. If the system is aberration limited in the visible, the correlation between ir focus and visible focus may prove extremely difficult. Use of such a system is strongly dependent upon the mechanical rigidity of the re-collecting optical system, the depth of field of this system, the mechanical rigidity of the detector mount, and the surface responsivity variation of the detector-filter assembly (i.e., the sensitivity of the system to changes in focus beyond the focal surface).

Starmapper: A check of starmapper focus requires a dark facility and an 0.4 to 0.6 micron calibrated and collimated point source with precision movement capability because of the wide field of the system. This is not a difficult facility requirement, and a focus measurement of this order shall be made.

Sun sensor: A check of sun sensor focus requires a high-intensity collimated point source with precision movement capability. No dark facility is required. This measurement shall be made.

Internal alignment. --

Radiometer: Since elements behind the focal surface do not significantly affect alignment, which is defined completely by the position of the field stop(s) in the image surface relative to a reference in this surface, visible sources can measure alignment with no errors due to the transmission elements behind the field stop(s). Two techniques are available. One utilizes a source

placed behind the field stop, a beam splitter to put the source through the field stop, and then uses the radiometer optics as a collimator imaging the source on a detector outside the radiometer. Theodolite sightings on a flat detector on the mount and the radiometer reference flat(s) will then measure alignment. An alternate method is the use of the scribed reticle described above. The reticle (or field stop) would be mapped by a theodolite and referenced through a second measurement to the reference flat. Either method appears feasible and neither generates any substantial facilities requirements.

Starmapper: Identical approaches to those described above are applicable to the starmapper. The internal source position is suitable in the starmapper in that the central portion of the reticle is unusable and no device is required to remove the source from the active field of view of the instrument.

Sun sensor: Sun sensor alignment measurement apparently requires external inputs, either the point source used for focus check or mapping of the reference surface with a theodolite. The proposed design does not lend itself to use of internal sources.

Detectivity. --

Radiometer: Radiometer detectivity checks can be made with the in-flight calibration system and a dark-aperture noise analysis, i.e., establish responsivity with an in-flight calibration, measure noise voltage with a dark aperture, and determine the noise-equivalent radiance statistics. Dark-aperture noise must be measured with respect to noise, implying a cold-plate over the aperture.

Starmapper: Since the conceptual design does not call for an in-flight starmapper amplitude calibration, a calibrated reference source must be provided to define system responsivity, without which noise measurements are meaningless. Once the responsivity is established, a measurement of noise requires only a light-tight aperture plate, in the same manner as the radiometer.

Sun sensor: Detectivity is not a critical item in the sun sensor. Low noise output from the source required for focus check should be adequate.

Responsivity. --

Radiometer: Responsivity checks can be made with the in-flight calibration system and a dark aperture. Implicit in this measurement is the assumption that there is no system impact upon the in-flight calibration source. A procedure whereby test results similar to the results obtained at primary calibration indicates no impact, and widely different results imply recalibration will be instituted.

Starmapper: Responsivity checks on the starmapper imply a calibrated, collimated point source with the capability of precision movement. A dark facility is required.

464

Sun sensor: Responsivity checks on the sun sensor require a calibrated, high-intensity source with the capability of precision movement. No dark facility is required.

Data handling. -- A major interface exists between the data-handling area (including commands) and the experiment package. A radiometer data sequence has been defined for each vehicle revolution which includes in-flight calibration, measurement of zero reference from space, and data taking. Starmapper and sun sensor data handling is independent of radiometer data to the data handling interface. There are no shared commands.

APPENDIX A

QUANTUM IRRADIANCE AT DETECTOR
FROM SPHERICAL MIRROR

467

QUANTUM IRRADIANCE AT DETECTOR FROM SPHERICAL MIRROR

$$|dA_M| \;=\; 2\pi R^2 \sin 6 \, d\theta$$

$$\overrightarrow{dA_M} \;=\; |dA_M|\, \hat{U}_R$$
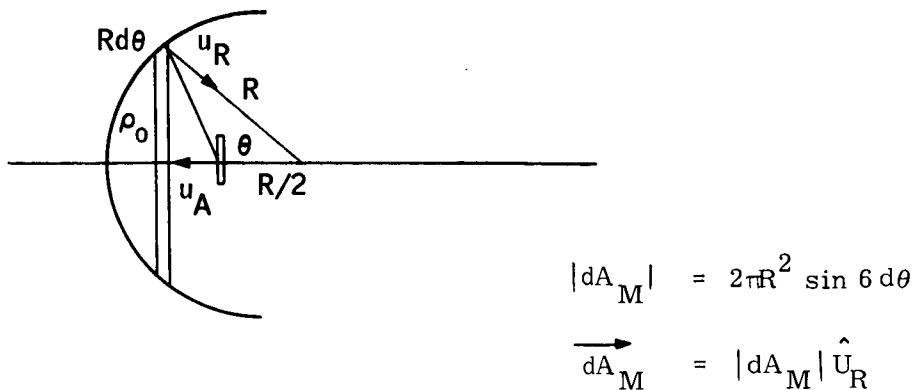
Figure A1. Assumed Mirror Geometry

Calculation:

$$dI_Q = \frac{\epsilon' \sigma' T^3 \left(\Delta_{\lambda_1} - \lambda_2\right)}{\pi} \; \frac{\overrightarrow{dA_M} \cdot \hat{U}_A}{R^2}$$

$$\therefore \quad I_Q = \epsilon' \sigma' T^3 \left(\Delta_{\lambda_1} - \lambda_2\right) \int_0^{\theta_0} \frac{2 \sin\theta \cos\theta \, d\theta}{(5/4 - \cos\theta)}$$

where $\theta_0 = \sin^{-1}$ and $\rho_0 / R = \sin^{-1} \dfrac{1}{4 \, f/\text{no.}}$

Then, $I_Q = 2 \, \epsilon' \sigma' T^3 \left(\Delta_{\lambda_1} - \lambda_2\right) \left[+ \cos\theta + 5/4 \ln(5/4 - \cos\theta) \right]_{\theta_0}^0$

469

Now,

For $f_{/no} = 1$, $I_Q = (\underline{0.166})\ \epsilon'\sigma'T^3 \left(\Delta_{\lambda_1} - \lambda_2\right)$

where for comparison the approximate formula gives

$$I_Q = -\frac{\epsilon'\sigma'T_M^{\ 3}}{4\left(f_{/no}\right)^2}\ \left(\Delta_{\lambda_1} - \lambda_2\right) = (\underline{0.250})\ \epsilon'\sigma'\ T^3\left(\Delta_{\lambda_1} - \lambda_2\right)$$

470

APPENDIX B

IRTRAN 6
KODAK INFRARED   OPTICAL MATERIAL
(POLYCRYSTALLINE CADMIUM TELLURIDE)

APPENDIX B

IRTRAN 6
KODAK INFRARED OPTICAL MATERIAL
(POLYCRYSTALLINE CADMIUM TELLURIDE)

OPTICAL PROPERTIES

Transmittance

Range: 0.9 to 31 microns (10 percent transmittance points for 0.080" thickness). The curves of Figures B1, B2, and B3 show transmittance of a typical sample. Because of manufacturing tolerances, transmittance variations of several percent in other samples should be allowed from curves shown, particularly in spectral regions where transmittance changes markedly with thickness.

Refractive

Wavelength microns	Refractive index at 25°C	Wavelength microns	Refractive index at 25°C
1.5	2.742	5.0	2.684
2.0	2.713	6.0	2.681
2.5	2.702	7.0	2.679
3.0	2.695	8.0	2.677
3.5	2.691	9.0	2.674
4.0	2.688	10.0	2.672

(Existing equipment is limited to measurements only up to 10 microns)

Anti-Reflection Coatings

Coatings can be applied to provide peak transmittance of approximately 90 percent at wavelengths over selected spectral regions up to about 20 microns.

PHYSICAL PROPERTIES

Hardness:	45 Knoop (about as hard as hard coal)
Density:	5.85 g/cm^3

Expansion coefficient:

Temperature range, °C	Coefficient, length/length/°C
25 - 100	5.5 x 10^{-6}
25 - 200	5.9 x 10^{-6}
25 - 250	6.2 x 10^{-6}
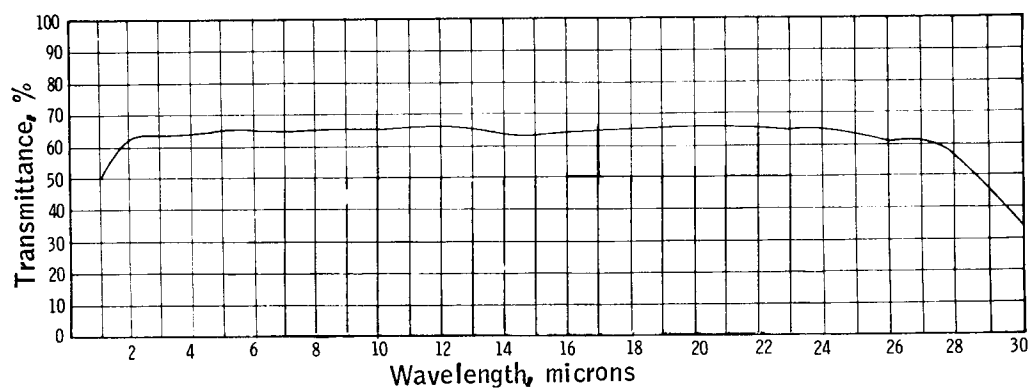
Figure B1. State-of-the-Art Transmittance of Hot-Pressed
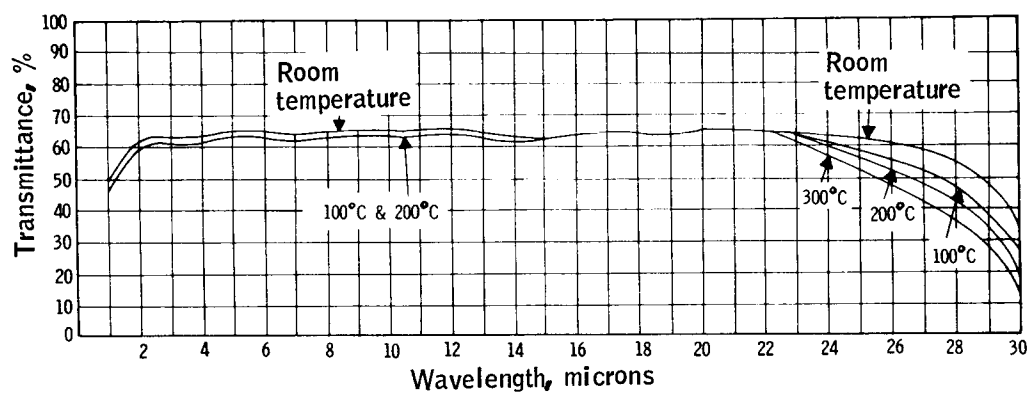Cadmium Telluride; Specimen Thickness = 0.125 inch

Figure B2. Transmittance of Hot-Pressed Cd:Te at Elevated
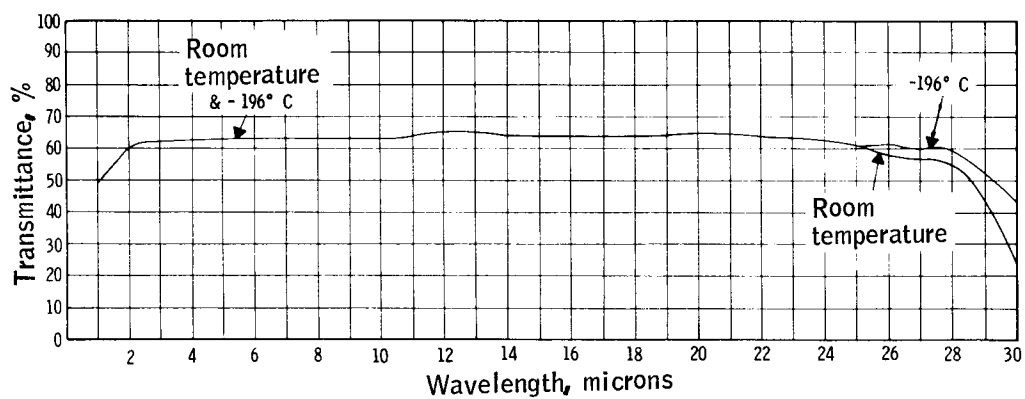Temperatures; Specimen Thickness = 0.125 inch

Figure B3.   Transmittance of Hot-Pressed Cd:Te at Liquid-Nitrogen
Temperature, -196°C; Specimen Thickness = 0.125 inch

476

Modulus of rupture: 4 590 psi at liquid-nitrogen temperature (-196°C)
4 540 psi at room temperature (25°C)
5 880 psi at 100°C

Modulus of elasticity: 5.2×10^6 psi at liquid-nitrogen temperature (-196°C)

5.3×10^6 psi at room temperature (25°C)

4.5×10^6 psi at 100°C

Thermal conductivity:	Temperature, °C	Thermal conductivity (Cal. sec.$^{-1}$ cm^{-2} °c^{-1} cm)
	-40	.013
	-20	.012
	0	.010
	20	.0098
	60	.0092
	100	.0088
	140	.0085

ENVIRONMENTAL RESISTANCE

Useful Temperature Range

Melting point of Irtran 6 is 1090°C. Actual maximum useful temperature limit is determined by length of exposure, type of atmosphere, mounting and sealing, required transmission, allowable emissivity, mechanical conditions, etc.

Thermal Shock

(Sample size: 2.0" diameter x 0.145" thick)

1. Quenched from room temperature (25°C) to liquid-nitrogen temperature (-196°C)

1. No cracks or other effects.

2. Quenched from 170°C to water at room temperature (25°C)

2. No cracks or other effects.

3. Quenched from 180°C to water at room temperature (25°C)

3. Axial cracks.

Environmental Properties

1. Exposure to 96 percent relative humidity at 90°F temperature.

   1. No change in transmittance after 11 days exposure.

2. Exposure to air at elevated temperature.

   2. No change in transmittance after 16 hours at 300°C. After 16 hours at 350°C, a light gray oxidation coating developed on the specimen surfaces.

3. Exposure to vacuum of approximately 100 microns at elevated temperature.

   3. No change in transmittance after seven hours at 300°C. At 400°C, thermal etching was observed after approximately five minutes.

Water Immersion

1. Direct water immersion at room temperature for 11 days.

   1. No change in weight or transmittance.

APPENDIX C

COMPARISON STUDY OF VARIOUS BANDPASS FILTER TYPES

APPENDIX C

COMPARISON STUDY OF VARIOUS BANDPASS FILTER TYPES
(Ref. 8)

The characteristics of some of the presently used narrow bandpass filters are shown in Figure C1. Indicated are the design, the number of layers, and the degree of manufacturing difficulty.

Type 1 in Figure C1 is the familiar metal-dielectric-metal filter which has the advantages of simplicity of design and requires essentially no auxiliary blocking filters. However, it has the serious limitation of low transmission (30 to 35 percent). Additionally, this filter type is not usable in the infrared because there is no metal which has optical properties in the infrared equivalent to the optical properties of silver or aluminum in the visible portion of the spectrum.

Type 2 in Figure C1 is the all-dielectric spike filter (The metal of Type 1 has been replaced with dielectric reflecting stacks.) This design can be used in the infrared. Its advantages include high transmission and ease of production. Such filters still require blocking filters, generally on both the short- and the long-wavelength sides of the pass band, because the rejection of the spike extends over a very limited spectral region. Filters of this design have the very serious limitation of having the bandwidth related to the rejection, i.e., the only way to achieve higher rejection and more rapid transition from transmission to rejection is to decrease the bandwidth. In practice, this means the signal as well as the noise is reduced, resulting in an improved performance.

Type 3 the all-dielectric, square-bandpass filters are characterized by very rapid transition from the transmitting band to the rejection bands, uniformly high transmittance over the pass band, and no inter-relationship between bandwidth and rejection. Even though no inter-relationship exists between bandwidth and the amount of rejection, in practice, the variation in bandwidth is limited. Square bandpass filters still require the assistance of reflecting stacks to give short- and long-wavelength rejection range. The performance advantages of this type of filter are obtained at a sacrifice in production ease. As can be seen from Figure C1, manufacturing tolerances are extremely rigid, requiring very accurate control. Figures C2 and C3 show the computed transmittance of nominal two percent and four percent square-bandpass designs.

Illustrated in Figures C4 and C5 are the improved characteristics of the square band filter over the spike filter. In the case of the nominal four percent bandpass at 2.72 microns, the transition from five percent transmission to 50 percent of maximum transmission occurs in approximately one fourth the wavelength interval for the square band filter as compared to the spike filter. Furthermore, the rejection in the off-band region of the square band filter is improved by a factor of 65. Both of these improvements are achieved with no significant loss in peak transmission in the region of interest. The results are similar for the nominal two percent bandpass filter at 4.29 microns.

Filter type	1. Metal spike	2. All dielectric spike	3. Square bandpass
Typical transmittance curves	100% ——— 0%		
Design	Metal | Dielectric Spacer | Metal	Quarter-wave stack | Half-wave spacer | Quarter-wave stack	Quarter-wave stack | Half-wave spacer | Quarter-wave stack ⋯⋯ Quarter-wave stack | Half-wave spacer | Quarter-wave stack ⋯
Number of layers	3	10 - 20	20 - 50
Layer tolerance	Metal layers of equal transmittance ± 2%	Match all layers to ± 3%	Match all layers to ± 1%

Figure C1. Characteristics of Various Bandpass Filter Types
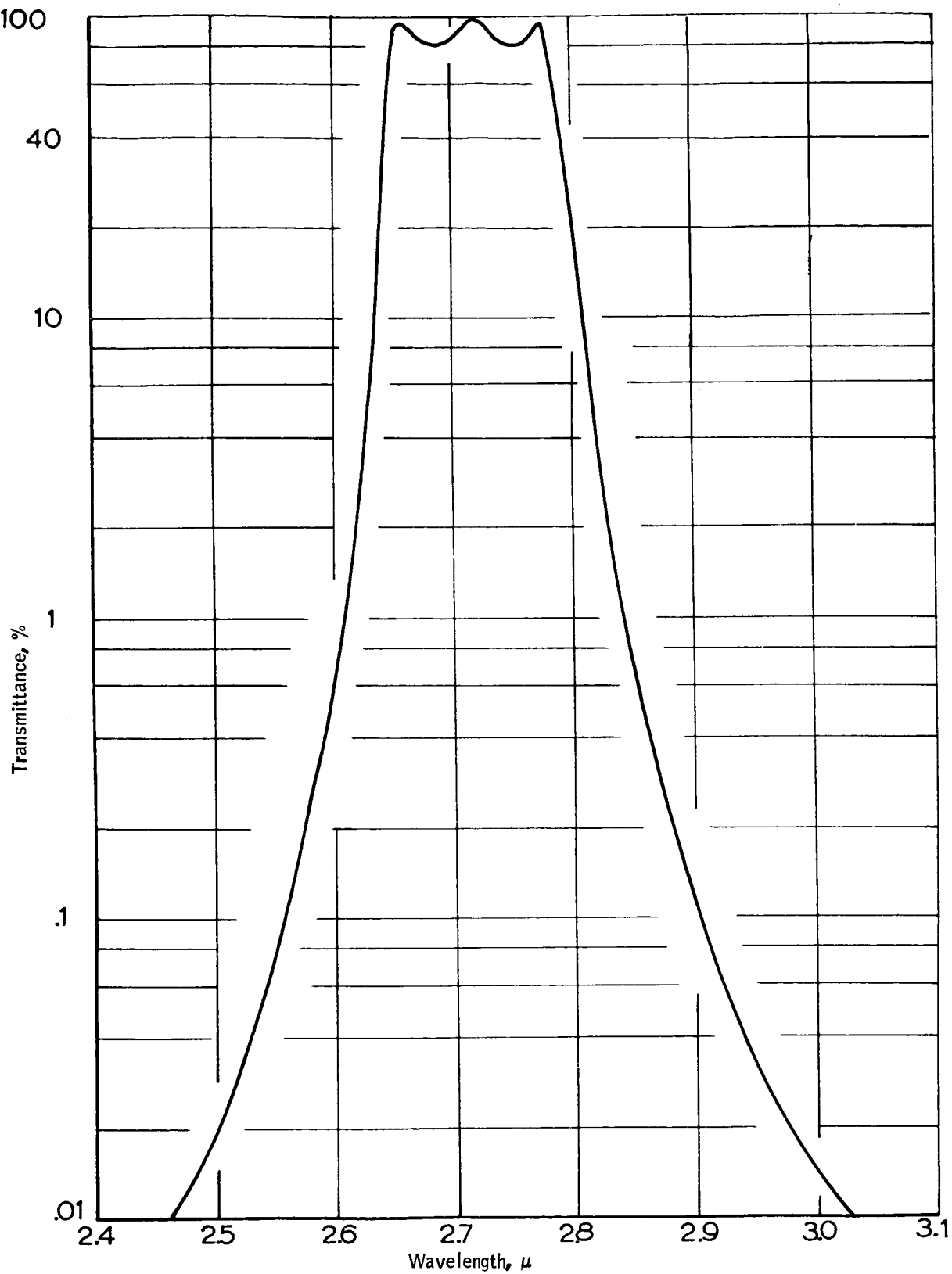
Figure C2.   Computed Transmittance of a Square Band Filter with
Nominal Bandwidth of 4 percent at 2.72μ
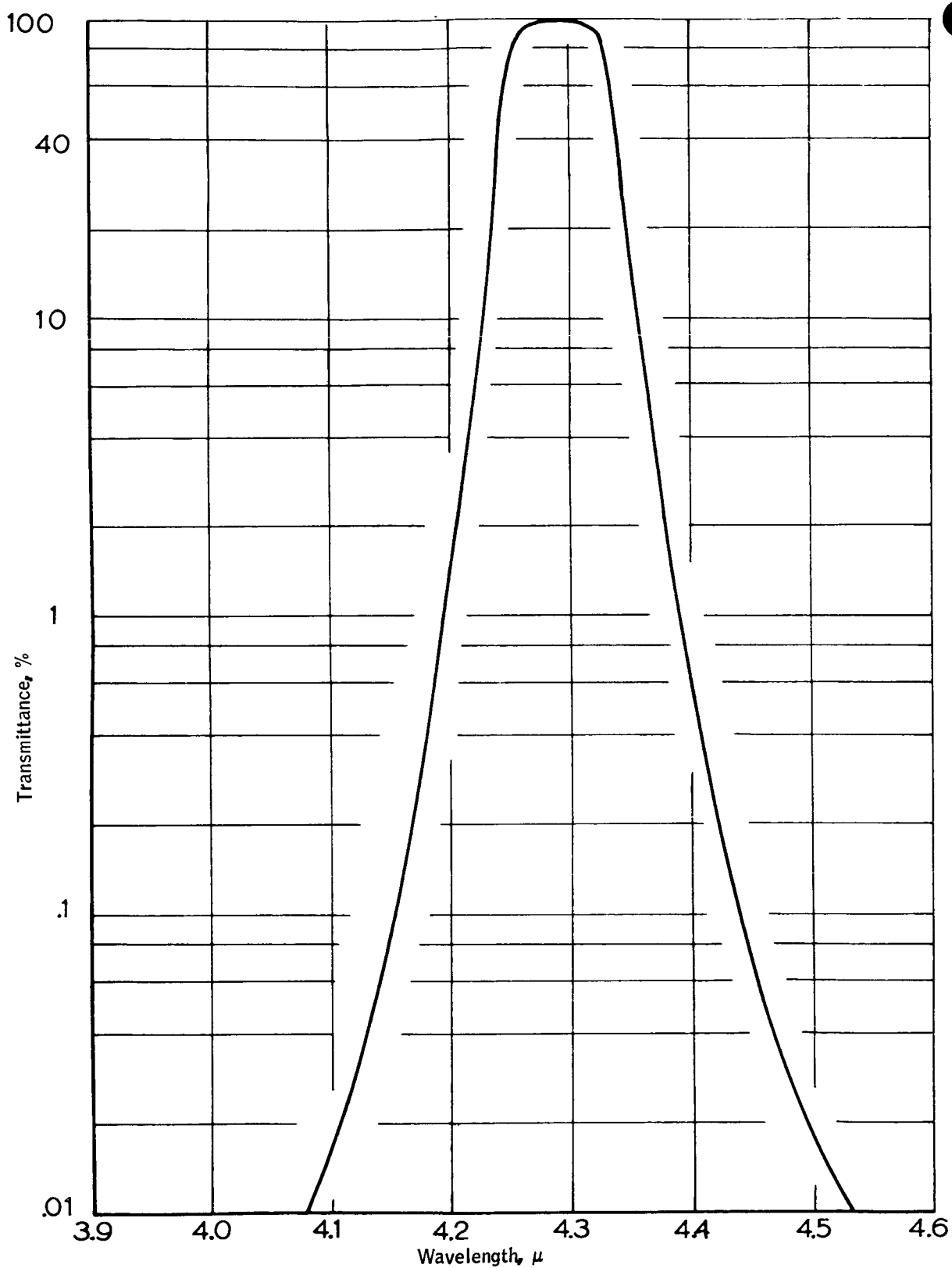
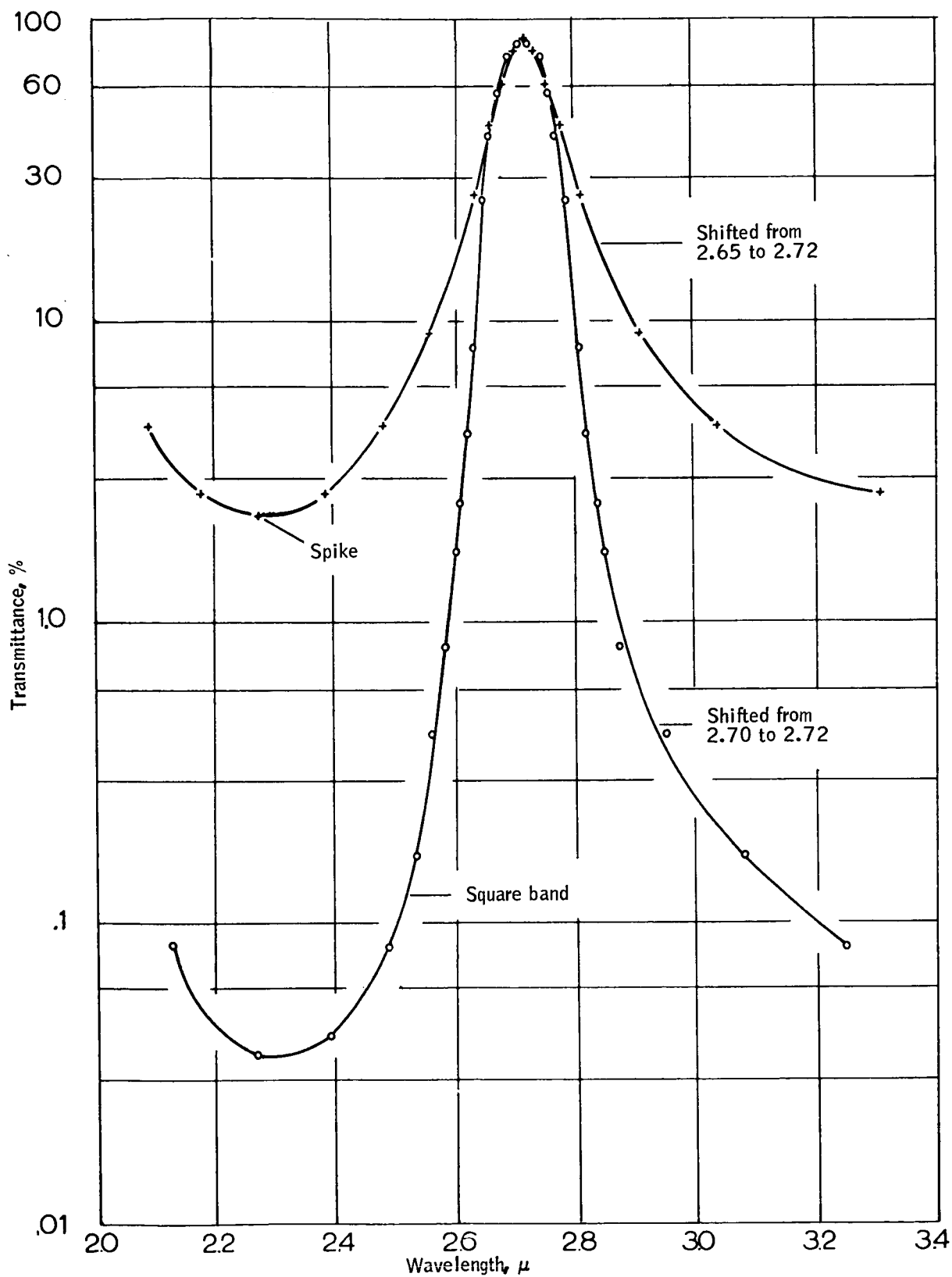Figure C3. Computed Transmittance of a Square Band Filter with Nominal Bandwidth of 2 percent at 4.29μ

Figure C4.   Measured Transmittance of Two Bandpass Filters with
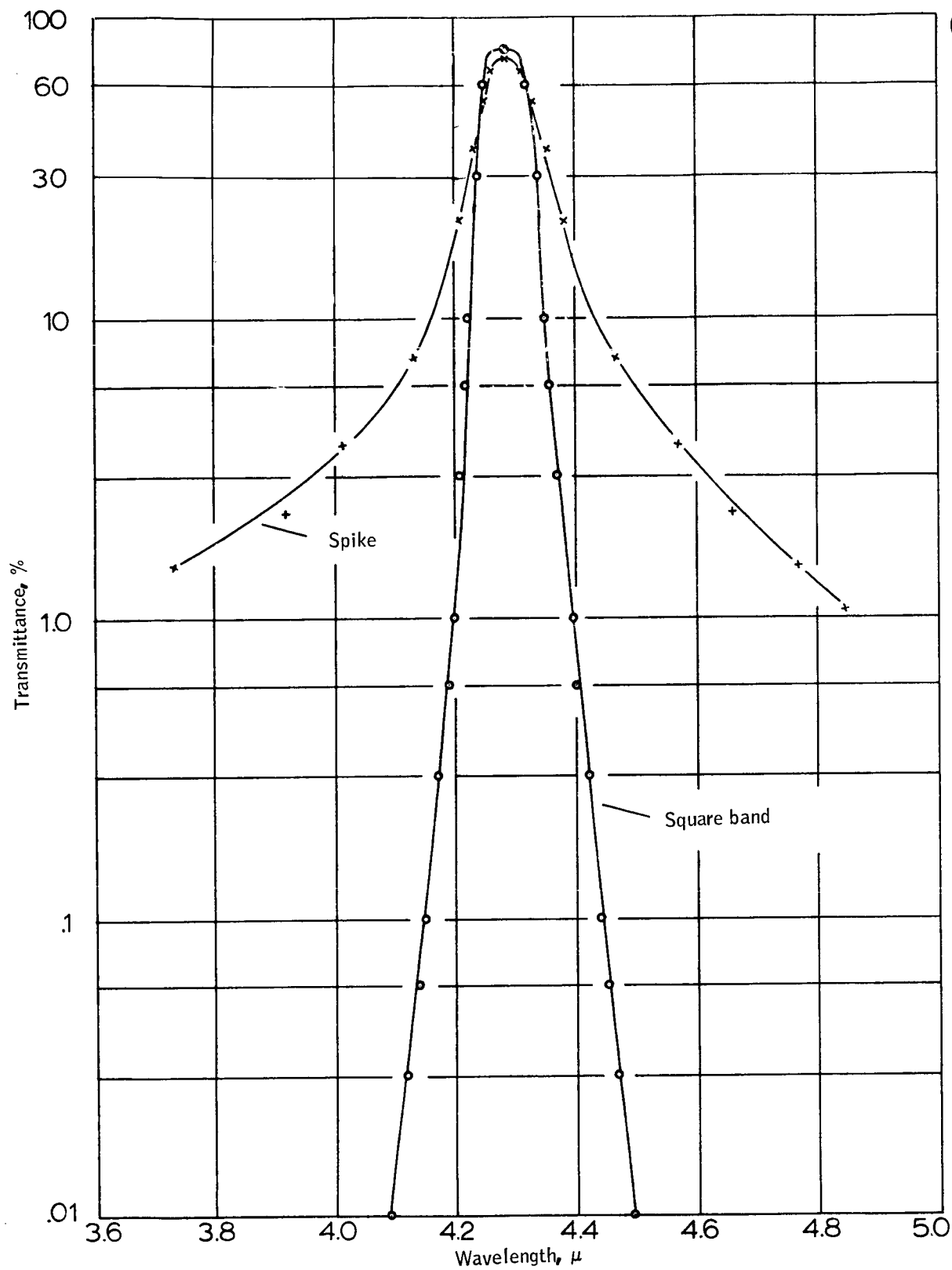Nominal 4 percent Half-Width at 2.72μ

Figure C5. Measured Transmittance of Two Unattenuated Bandpass Filters with Nominal 2 percent Half-Width at 4.29

486

As indicated before, filters of this type require additional interference coat-
ings to attenuate energy at all wavelengths outside the pass band. Figure C6
illustrates the effect of applying such coatings to the square band filter of
Figure C4. Transmission levels of under 0.01 percent outside the bandpass
region have been achieved on a consistent basis.

The term "shifted" on Figures C4 through C6 means that the actual measured
results were ratioed to center about two arbitrary wavelengths. The purpose
of this was to allow more rapid visual comparison between the spike and
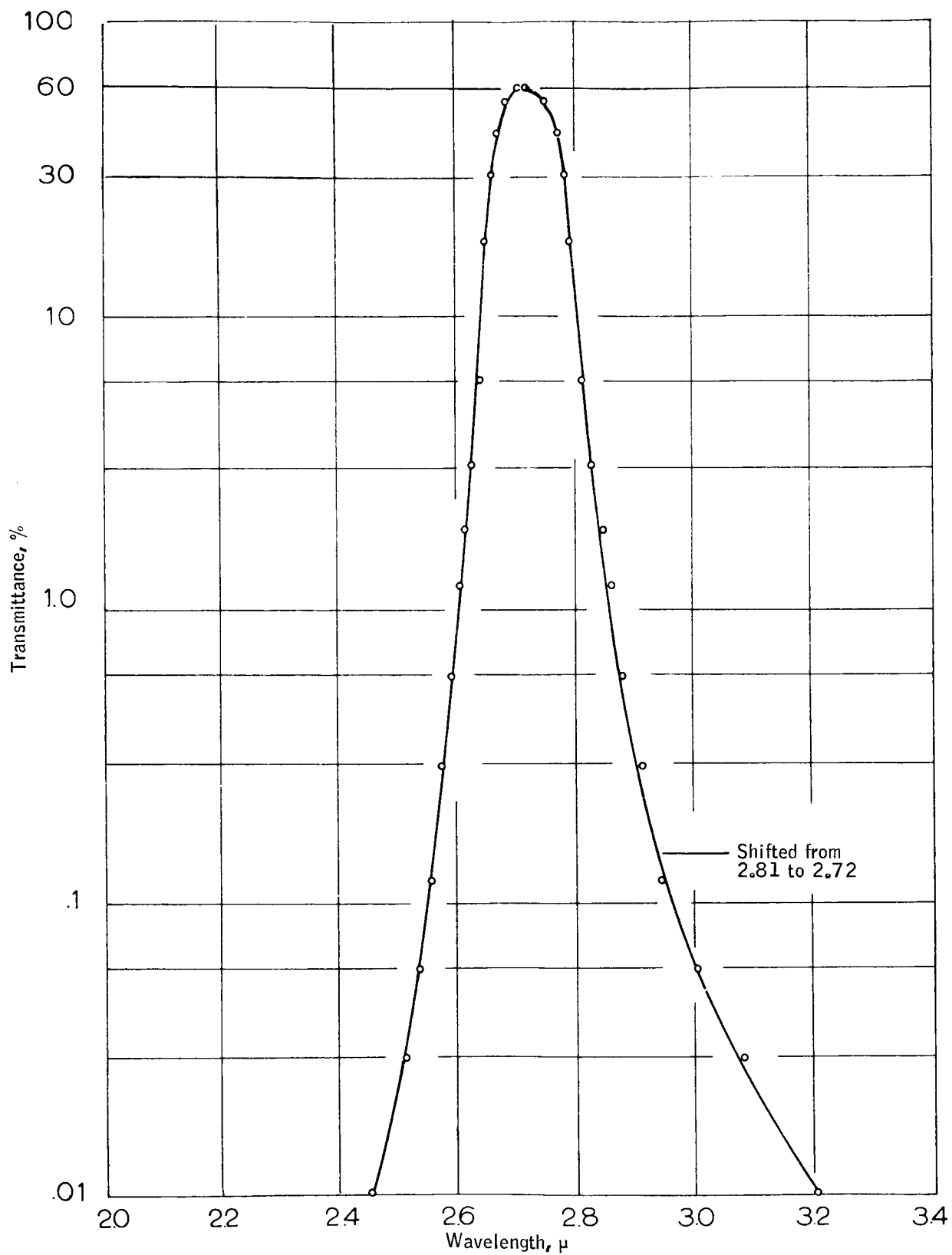square bandpass filters.

Figure C6. Measured Transmittance of the Square Band Filter of
Figure C4 with Blocking Filters Added

APPENDIX D

EFFECTS OF THE VARIATION OF ANGLE OF
INCIDENCE AND TEMPERATURE ON INFRARED
FILTERS

APPENDIX D

EFFECTS OF THE VARIATION OF ANGLE OF INCIDENCE AND TEMPERATURE ON INFRARED FILTERS

EFFECTS OF ANGLE SHIFT

The optical thickness of a thin film decreases as the angle of incidence is increased; consequently, a multilayer filter shifts towards shorter wavelengths as the angle of incidence is increased. The magnitude of the shift is dependent on the type of filter (narrow bandpass, long wavelength pass, etc), the filter design, the refractive indices of the coating materials used, and the precision with which the coating materials are deposited.

The angle of shift of a standard OCLI infrared filter is predicted by the crosshatched area of Figure D1, which represents a composite of theoretical and measured data. Figure D1 emphasizes the importance of including angle shift as a design consideration, particularly in systems in which the incident angle is in excess of 10°.

Figures D2, D3, and D4 show the measured incident angle effects on three typical OCLI infrared filters. For incident angles up to about 40° the shape of the filter is not appreciably altered, except for a slight decrease in transmittance. However, when the incident angles exceed 50°, shape changes begin to occur due to polarization effects and increased mismatch in the optical thickness of adjacent layers. These shape changes (Figures D2 and D3) are usually characterized by a flattening of the cut-on and cut-off slopes and a decrease in transmittance.

EFFECTS OF TEMPERATURE SHIFT

Standard multilayer infrared filters made by OCLI will shift to longer wavelengths when the film temperature is increased and to shorter wavelenths when the film temperature is decreased. More precisely, the wavelength shift of a multilayer filter is essentially a linear function of film temperature because the materials which form the various layers have indices of refraction which vary linearly with temperature. Therefore, the optical thicknesses of adjacent layers can be perfectly matched at only one temperature - the "design temperature." The crosshatched area of Figure D5 predicts the temperature shift of standard OCLI infrared filters with a design temperature of 20°C.

In general, OCLI infrared filters retain their transmittance and shape characteristics over a wide temperature range (Figures D6 and D7), but serious transmittance losses may occur at filter temperatures exceeding 50°C (Figure D8).
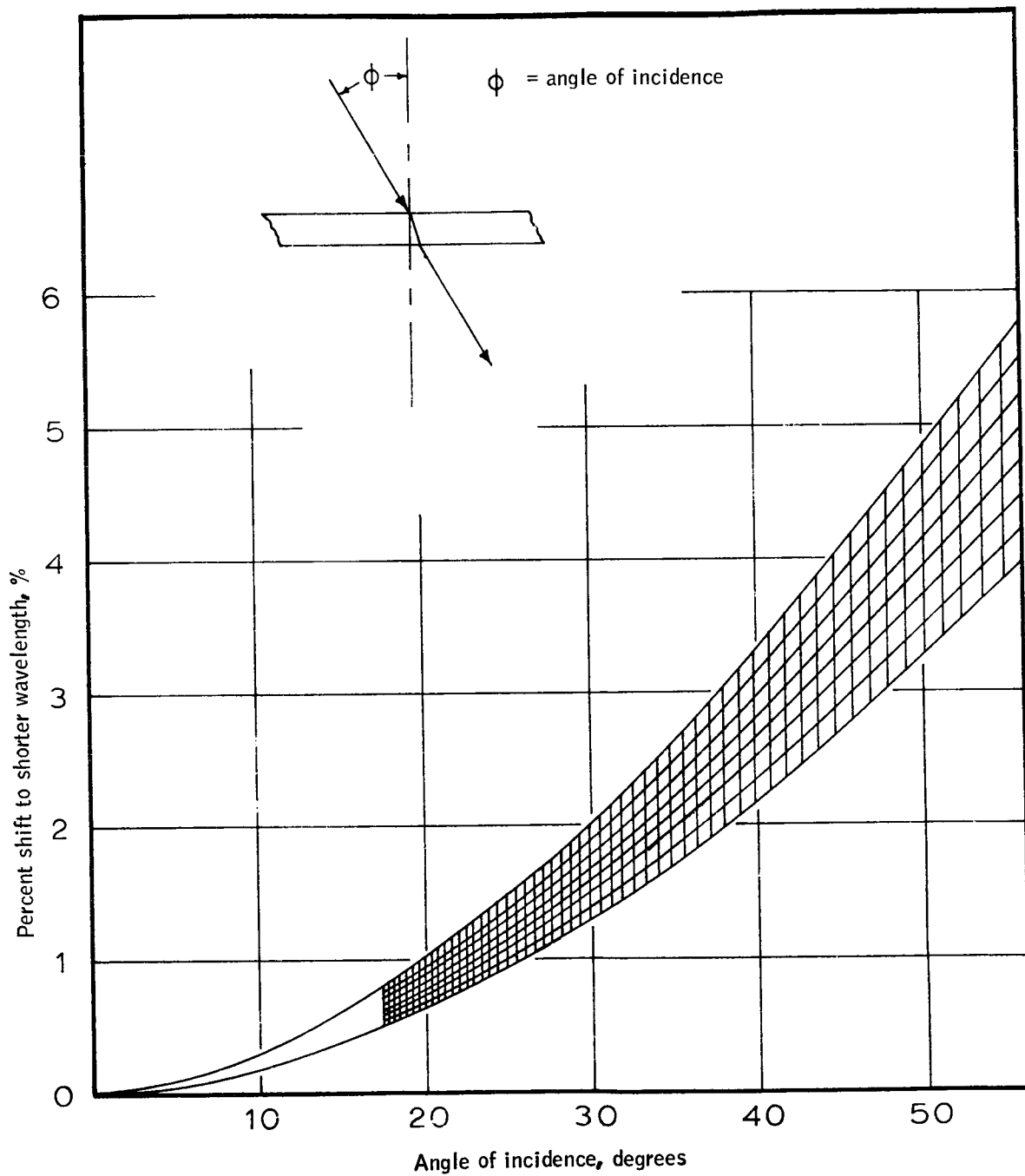
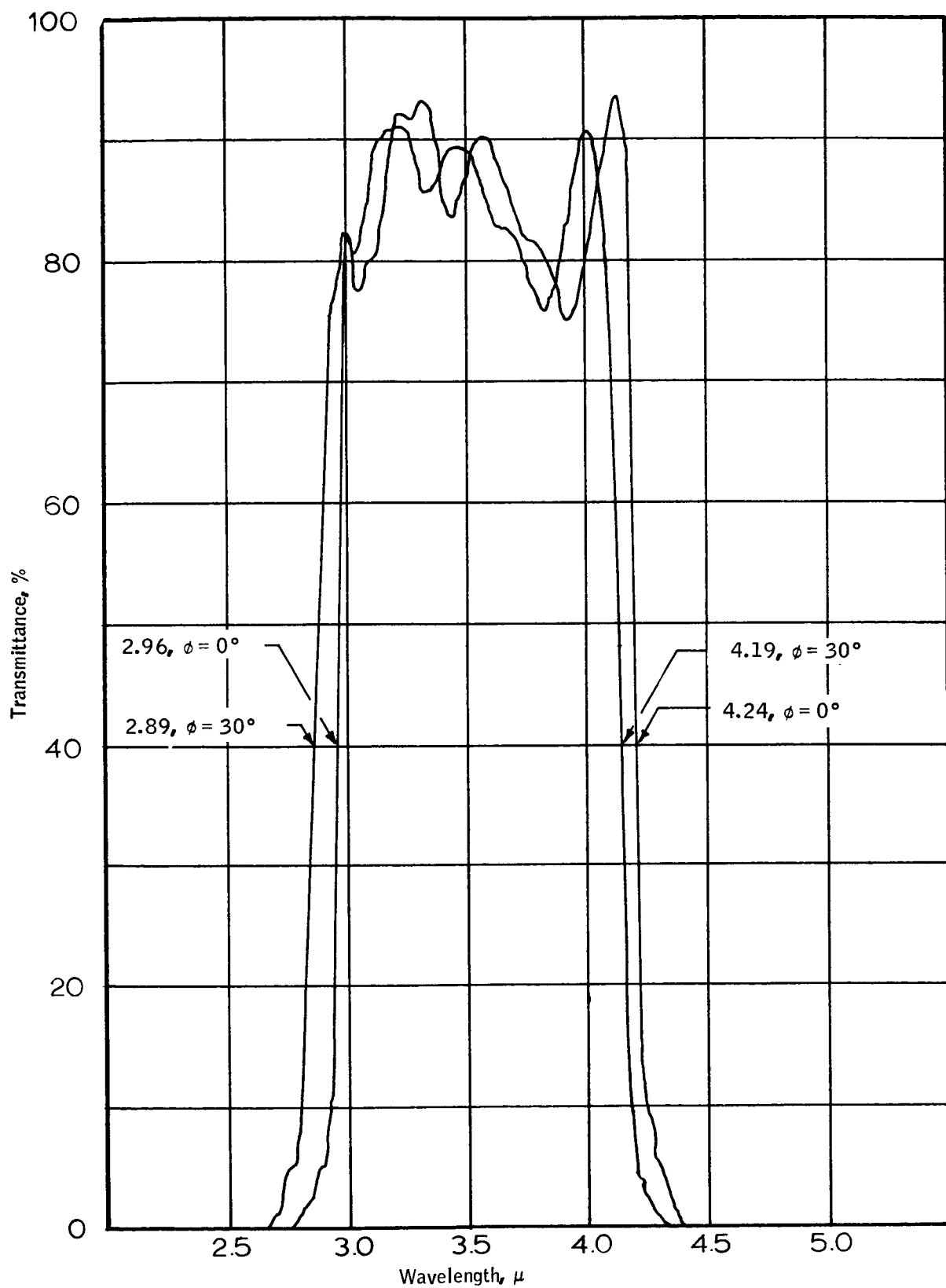Figure D1. Wavelength Shift as a Function of Angle

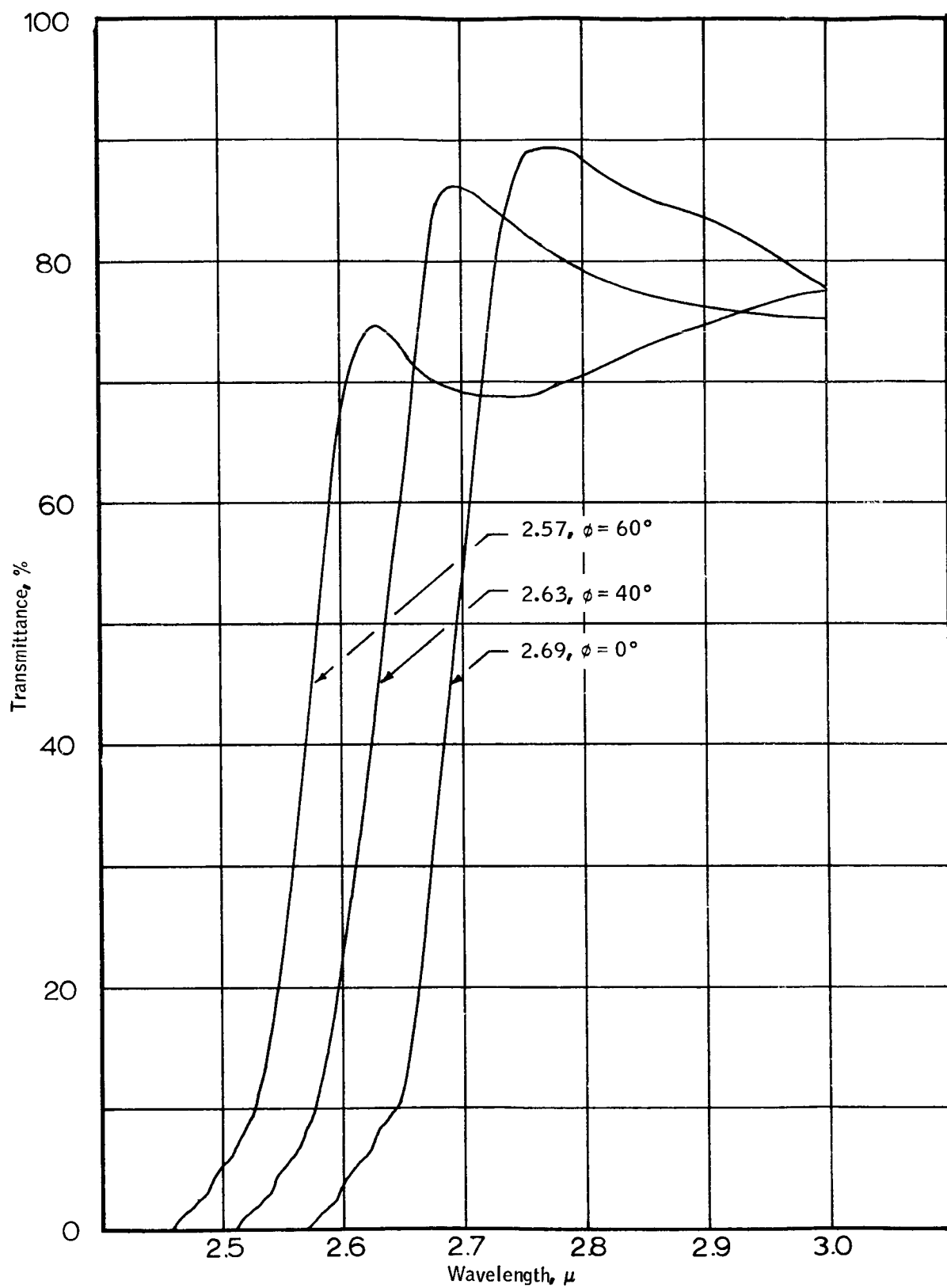Figure D2. Spectral Transmittance as a Function of Angle Incidence

Figure D3. Spectral Transmittance as a Function of Angle Incidence
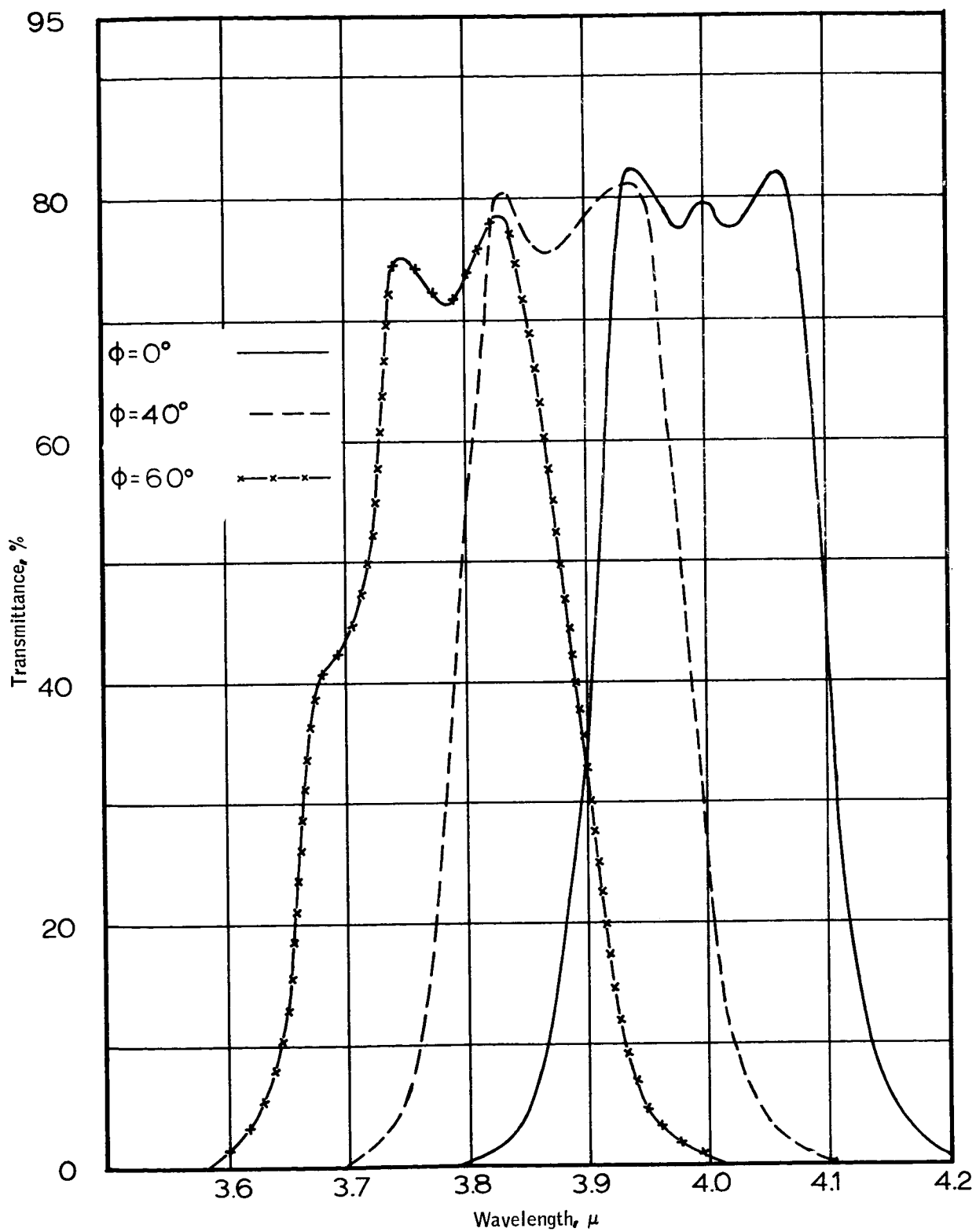
Figure D4. Spectral Transmittance as a Function of Angle Incidence
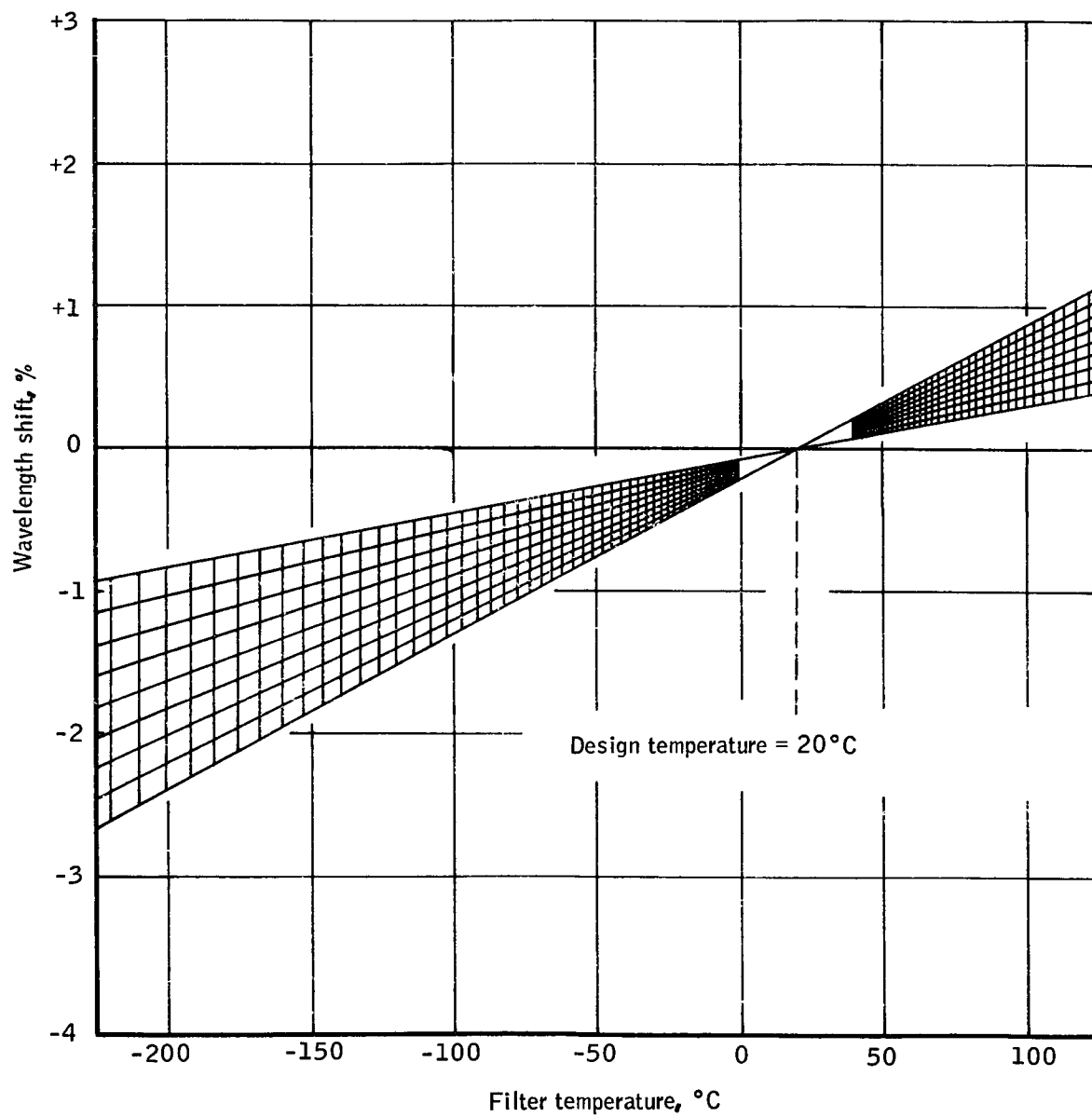
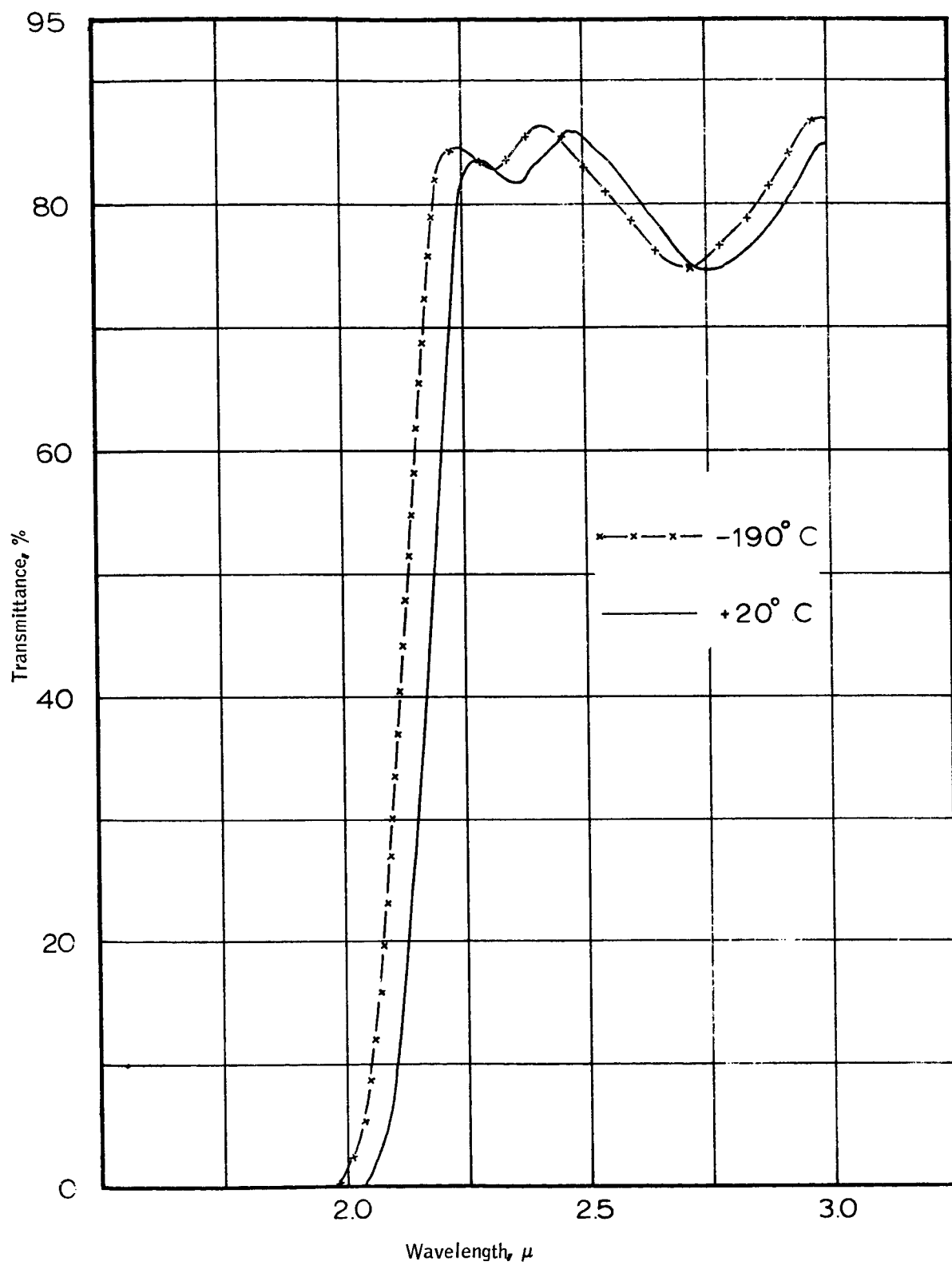Figure D5. Wavelength Shift as a Function of Temperature

Figure D6. Spectral Transmittance as a Function of Temperature
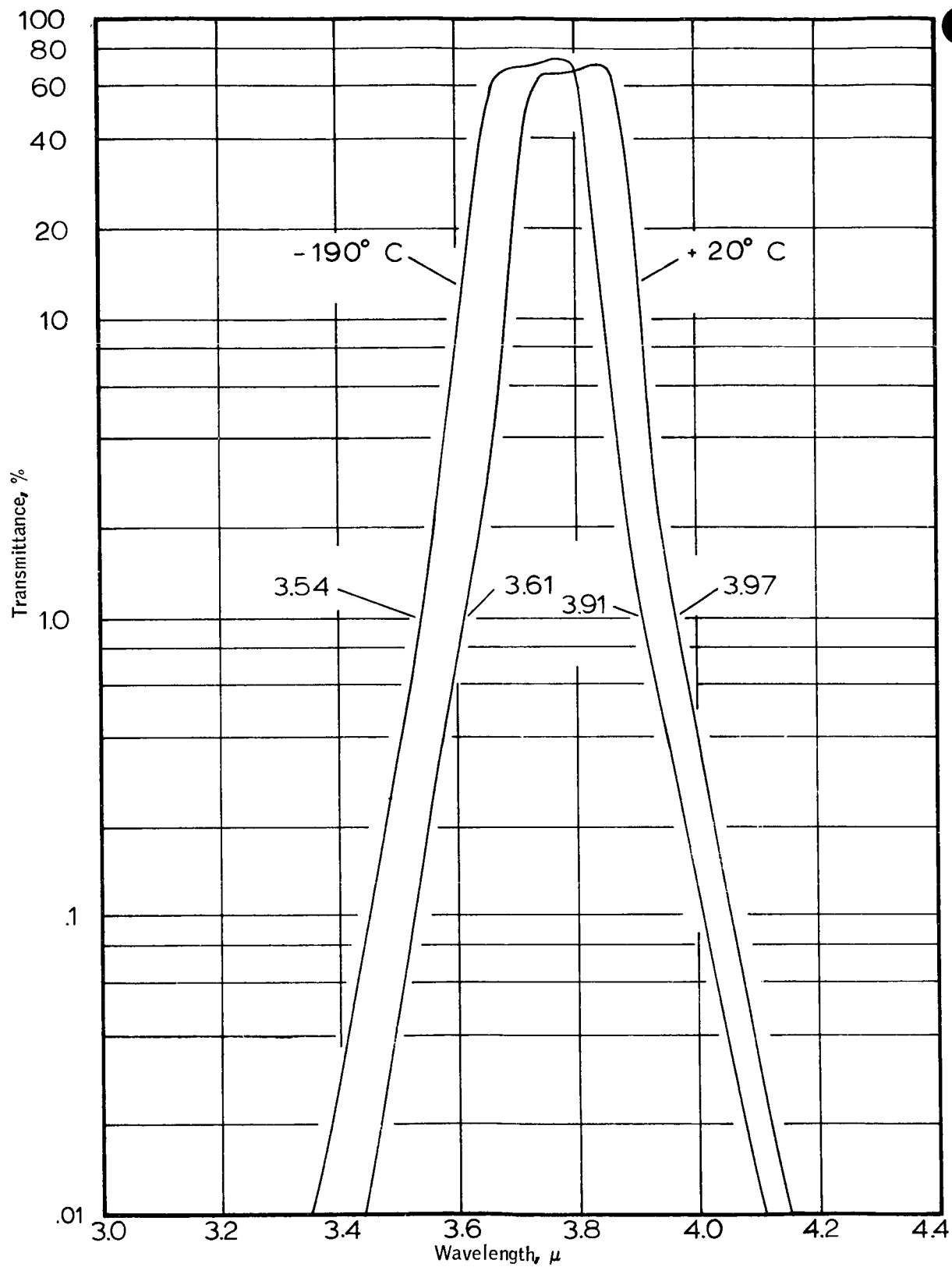
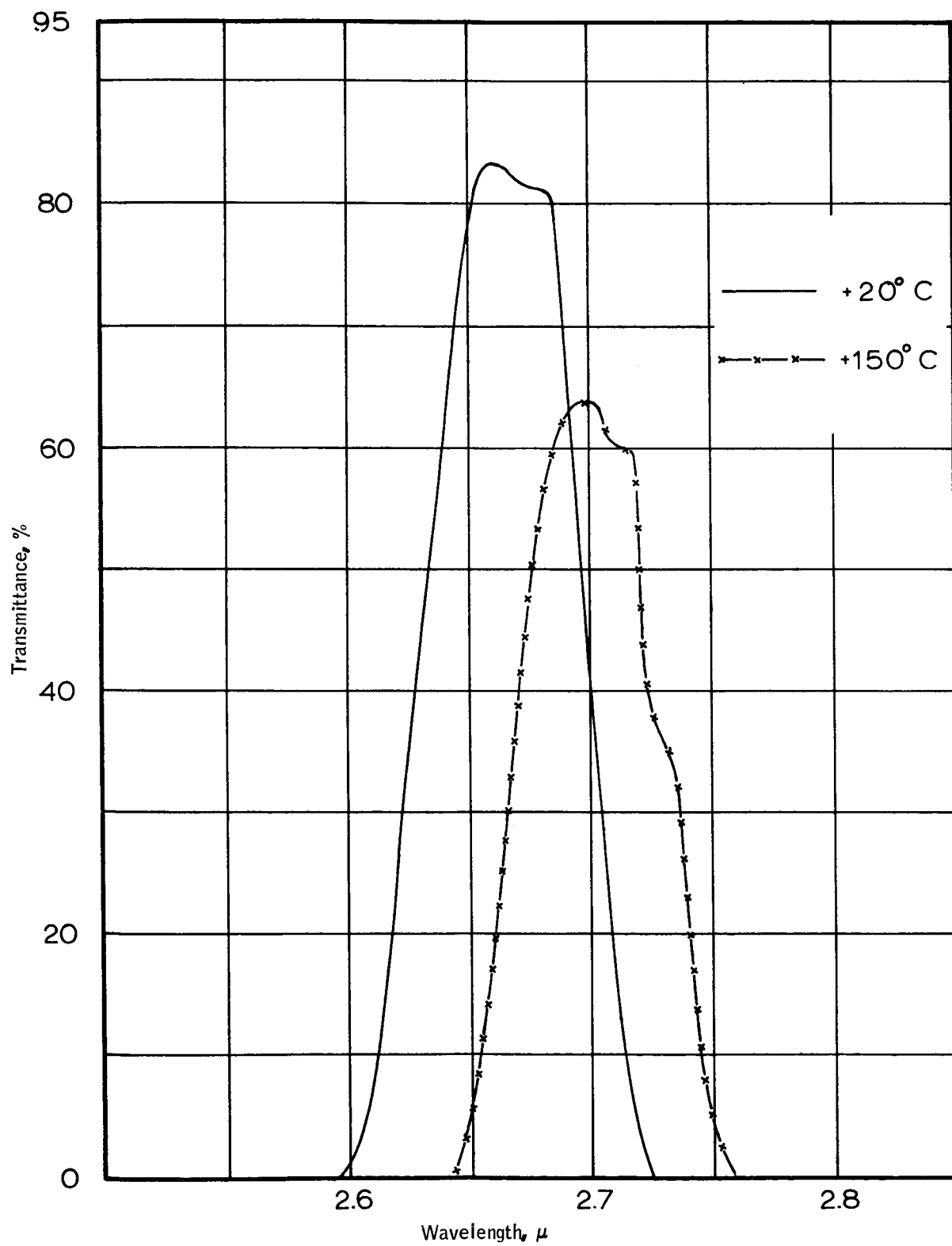Figure D7. Spectral Transmittance as a Function of Temperature

Figure D8. Spectral Transmittance as a Function of Temperature

Although the effects of angle shift and temperature shift are nearly identical,
the two effects can be superimposed on each other. For example, after
having been shifted to a shorter wavelength by a reduction in temperature
(Figure D5) a filter may be shifted to even shorter wavelengths by increasing
the angle of incidence (Figure D1). However, temperature shift and angle shift
are not completely independent of each other. Filters which are designed to
have minimum wavelength shift with increasing angles of incidence will
usually be very temperature sensitive. Conversely, filters which are designed
to have a minimum wavelength shift over a wide temperature range will usual-
ly be very angle sensitive.

APPENDIX E
DAMPED OSCILLATOR

APPENDIX E
DAMPED OSCILLATOR

It is desirable to examine the damped, linear, single degree-of-freedom system

$$m\ddot{x} + 2m\,\xi\omega_O\,(x-x_O) + m\omega_O^2\,(x-x_O) = o \qquad (E1)$$
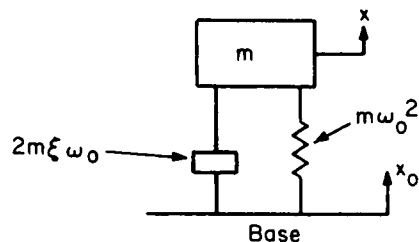
where ω_O is the undamped natural frequency ($\sqrt{\frac{K}{m}}$) of the oscillator and ξ is its critical damping ratio. Denoting the ralative displacement $x-x_O$ by x_r and taking

$$\left. \begin{array}{l} x_O \;=\; X_O \cos \omega t \;=\; Re\,(X_O e^{j\omega t}) \\[2mm] x \;\;=\; Re(Xe^{j\omega t}) \\[2mm] x_r \;=\; Re(Xre^{j\omega r}) \end{array} \right\} \qquad (E2)$$

From equation (E1)

$$\frac{X_r}{X_O} \;=\; \frac{\omega^2}{\left[(\omega_O^2 - \omega^2)^2 + 4\,\xi^2\,\omega_O^2\omega^2\right]^{1/2}}\, e^{-j\phi r} \qquad (E3)$$

where

$$\phi_r \;=\; \tan^{-1} \frac{2\xi\omega_O\omega}{\omega_O^2 - \omega^2} \qquad (E4)$$

Similarly,

$$\frac{X}{X_O} = \left[\frac{\omega_O^2\,(\omega_O^2 + 4\,\xi^2\,\omega^2)}{\omega_O^2(\omega_O^2 - \omega^2) + 4\xi^2\,\omega_O^2\omega^2}\right]\, e^{-j\phi} \qquad (E5)$$

where

$$\phi = \tan^{-1} \frac{2\xi\omega_0\omega^3}{\omega_0^2(\omega_0^2 - \omega^2) + 4\xi\omega_0^2\omega^2} \tag{E6}$$

Since expressions for $\left|\dfrac{X_r}{X_0}\right|_{max}$ and $\left|\dfrac{X}{X_0}\right|_{max}$ are sought equations (E3) and (E5) yield

$$\left|\frac{X_r}{X_0}\right|^2 = \frac{R^2}{(1-R^2)^2 + 4\xi^2 R} \tag{E7}$$

$$\left|\frac{X}{X_0}\right|^2 = \frac{1 + 4\xi^2 R}{(1-R^2)^2 + 4\xi^2 R} \tag{E8}$$

Equation (E7) has its maximum at $R = (1-2\xi^2)^{-1}$ if $2\xi^2 \leqslant 1$ and $R = \infty$ otherwise, while (E8) has its maximum at $R = (\sqrt{1+8\xi^2}-1)/4\xi^2$. Thus, when $\xi \geqslant \sqrt{2}/2$, $\left|\dfrac{X_r}{X_0}\right| \leqslant 1$ and when $\xi \geqslant 1$, $\left|\dfrac{X}{X_0}\right| \leqslant 1.15$. Therefore, if damping is near or greater than critical, the displacement, velocity , and acceleration levels for the oscillator mass are less or negligibly greater than the corresponding input levels, and the relative displacement level is less than the input displacement level.

504

APPENDIX F

TIMOSHENKO BEAM

APPENDIX F

TIMOSHENKO BEAM

Consider the longitudinal and transverse deformations of a Timoshenko beam
of variable cross section which is clamped at one end
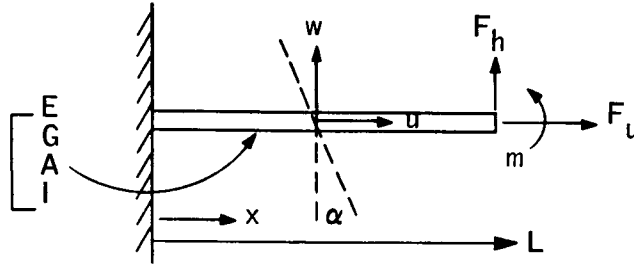
As we know, the total deformation is separable into two classes, the first
involving longitudinal extension only and the second involving only bending
and shear deformations. Let us first consider longitudinal extension and
then proceed to bending and shear deformation.

LONGITUDINAL EXTENSION

The strain energy in the beam due to longitudinal extension is given by

$$V = \frac{1}{2} \int_0^L EA \left(\frac{du}{dx}\right)^2 dx \tag{F1}$$

while the virtual work appropriate to F_v is

$$\delta W = F_v \, \delta u \Big|_{x = L} \tag{F2}$$

Applying the theorem of virtual work, we obtain

$$\int_0^L EA \frac{du}{dx} \delta \left(\frac{du}{dx}\right) dx = F_v \, \delta u \Big|_{x=L} \tag{F3}$$

which becomes, after integrating by parts

$$EA \frac{du}{dx} \delta u \Big|_0^L - \int_0^L \frac{d}{dx} \left(EA \frac{du}{dx} \right) \delta u \, dx = F_v \delta u \Big|_{x = L} \qquad (F4)$$

Since $u = 0$ at $x = 0$, we have as our governing equations, from equation (F4)

$$\left. \begin{aligned} \frac{d}{dx} \left(EA \frac{du}{dx} \right) &= 0 \qquad 0 < x < L \\ u &= 0 \quad \text{at} \quad x = 0 \\ EA \frac{du}{dx} &= 0 \quad \text{at} \quad x = L \end{aligned} \right\} \qquad (F5)$$

We now take E as constant, and $A = A_o \dfrac{1 - \gamma \frac{x}{L}}{1 - \gamma / 2}$, so that the first of equation (F5) becomes

$$\frac{d}{dx} \left(1 - \gamma \frac{x}{L} \right) \frac{du}{dx} = 0 \qquad 0 < x < L \qquad (F6)$$

Integrating this twice yields

$$u = -C_1 \frac{L}{\gamma} \ell n \left(1 - \gamma \frac{x}{L} \right) + L_o \qquad (F7)$$

and applying the last two of equations (F5) gives

$$u = -\frac{F_v}{EA_o} \left(1 - \frac{\gamma}{z} \right) \frac{L}{\gamma} \ell n \left(1 - \gamma \frac{x}{L} \right) \qquad (F8)$$

so that

$$\sigma_x = E \left(\frac{du}{dx} \right) = \frac{F_v}{EA_o} \frac{1 - \gamma/2}{1 - \gamma \frac{x}{L}} \qquad (F9)$$

508

HORIZONTAL RESPONSE

The strain energy in the beam due to bending and shear deformation is given by

$$V = \frac{1}{2}\int_0^L E1\left(\frac{d\psi}{dx}\right)^2 dx + \frac{K}{2}\int_0^L GA\left(\frac{dw}{dx} - P\right)^2 dx \qquad (F10)$$

where we take $K \approx \frac{1}{2}$, while the virtual work appropriate to F_h and M is

$$\delta W = F_h\, \delta w\Big|_{x=L} + M\,\delta\,\psi\Big|_{x=L} \qquad (F11)$$

We now define

$$\left.\begin{array}{l} w = w_b + w_s \\[2mm] P = \dfrac{d\,w_b}{dx} \end{array}\right\} \qquad (F12)$$

so that equations (F10) and (F11) become

$$\left.\begin{array}{l} V = \dfrac{1}{2}\displaystyle\int_0^L E1\left(\dfrac{d^2 w_b}{dx^2}\right)^2 dx + \dfrac{K}{2}\displaystyle\int_0^L GA\left(\dfrac{d\,w_s}{dx}\right)^2 dx \\[5mm] \delta W = F_h\,\delta\,w_b\Big|_{x=L} + F_h\,\delta\,w_s\Big|_{x=L} + M\delta\left(\dfrac{d\,w_b}{dx}\right)\Big|_{x=L} \end{array}\right\} \qquad (F13)$$

Applying the theorem of virtual work, we obtain

$$\left.\begin{array}{l} \displaystyle\int_0^L E1\,\dfrac{d^2 w_b}{dx^2}\,\delta\left(\dfrac{d^2 w_b}{dx^2}\right) dx + K\displaystyle\int_0^L GA\,\dfrac{dw_s}{dx}\,\delta\left(\dfrac{dw_s}{dx}\right) dx \\[5mm] = F_h\,\delta\,w_b\Big|_{x=L} + F_h\,\delta\,w_s\Big|_{x=L} + M\,\delta\left(\dfrac{dw_b}{dx}\right)\Big|_{x=L} \end{array}\right\} \qquad (F14)$$

Integrating the first term on the left by parts twice and integrating the second term on the left by parts once then gives

509

$$E1 \frac{d^2 w_b}{dx^2} \delta \left(\frac{d w_b}{dx}\right) \Bigg|_0^L - \frac{d}{dx}\left(E1 \frac{d^2 w_b}{dx^2}\right) \delta w_b \Bigg|_0^L + \int_0^L \frac{d^2}{dx^2}\left(E1 \frac{d^2 w_b}{dx^2}\right) \delta w_b \, dx$$

$$+ GAK \frac{dw_s}{dx} \delta w_s \Bigg|_0^L - K \int_0^L \frac{d}{dx}\left(GA \frac{dw_s}{dx}\right) \delta w_s \, dx \qquad (F15)$$

$$= F_h \delta w_b \Bigg|_{x=L} + F_h \delta w_s \Bigg|_{x=L} + M \delta \left(\frac{d w_b}{dx}\right)\Bigg|_{x=L}$$

Since $w = \frac{dw}{dx} = 0$ at $x = 0$, we have as our governing equations, from equation (F15)

$$\left. \begin{aligned}
\frac{d}{dx}\left(GA \frac{dw_s}{dx}\right) &= 0 & 0 < x < L \\
w_s &= 0 \quad \text{at} \quad x = 0 \\
GAK \frac{dw_s}{dx} &= F_h \quad \text{at} \quad x = L \\
\frac{d^2}{dx^2}\left(E1 \frac{d^2 w_b}{dx^2}\right) &= 0 & 0 < x < L \\
w_b = \frac{d w_b}{dx} &= 0 \quad \text{at} \quad x = 0 \\
\frac{d}{dx}\left(E1 \frac{d^2 w_b}{dx^2}\right) &= -F_h \quad \text{at} \quad x = L \\
E1 \frac{d^2 w_b}{dx^2} &= M \quad \text{at} \quad x = L
\end{aligned} \right\} \qquad (F16)$$

We now take E and w as constants and $A = A_0 \frac{1 - \gamma x/L}{1 - \gamma/2}$, so that the first of equation (F5) becomes

$$\frac{d}{dx}\left[\left(1 - \gamma \frac{x}{L}\right) \frac{d w_s}{dx}\right] = 0 \qquad (F17)$$

510

Integrating this twice yields

$$w_s = -\delta_1 \frac{L}{\gamma} \ln\left(1 - \gamma\frac{x}{L}\right) + \delta_o \tag{F18}$$

and applying the second and third of equations (F16) gives

$$w_s = \frac{-F_h}{GAK} \cdot \frac{L}{\gamma} \cdot \left(1 - \frac{\gamma}{2}\right) \ln\left(1 - \gamma\frac{x}{L}\right) \tag{F19}$$

Next, taking $I = I_o\left(\frac{1 - \gamma x/L}{1 - \gamma/2}\right)^3$, the fourth of equations (F16) becomes

$$\frac{d^2}{d_x^2}\left[\left(1 - \gamma\frac{x}{L}\right)^3 \frac{d^2 w_b}{dx^2}\right] = 0$$

Integrating this four times yields

$$w_b = \frac{1}{2}\left(\frac{L}{\gamma}\right)^2 \frac{b_2 + b_3 \, L/\gamma}{1 - \gamma\frac{x}{L}} + b_3\left(\frac{L}{\gamma}\right)^3 \ln\left(1 - \gamma\frac{x}{L}\right) + b_1 x + b_o \tag{F20}$$

and applying the fifth through the seventh of equations (F16) gives

$$\left.\begin{aligned}
w_b &= \frac{M}{2E1_o}\left(1 - \frac{\gamma}{z}\right)^3 \frac{x^3}{1 - \gamma\frac{x}{L}} + \frac{F_h\left(\frac{L}{\gamma}\right)}{2E1_0}\left(1 - \frac{\gamma}{2}\right)^3\left(1 + \gamma\right)\frac{x^2}{1 - \gamma\frac{x}{L}} \\[2mm]
&\quad - \frac{F_h}{E1_o}\left(1 - \frac{\gamma}{2}\right)^3\left(\frac{L}{\gamma}\right)^2 \frac{x}{1 - \gamma\frac{x}{L}} - \frac{F_h}{E1_o}\left(1 - \frac{\gamma}{2}\right)^3\left(\frac{L}{\gamma}\right)^3 \ln\left(1 - \gamma\frac{x}{L}\right) \\[2mm]
\frac{dw_b}{dx} &= \frac{\left(1 - \frac{\gamma}{2}\right)^3}{E1_o}\left[\left(1 - \frac{\gamma x}{2L}\right)M + \left[1 - \frac{1}{2}(1 + \gamma)\frac{x}{L}\right]F_h L\right]\frac{x}{\left(1 - \gamma\frac{x}{L}\right)^2}
\end{aligned}\right\} \tag{F21}$$

Equations (F19) and (F21) substituted in equations (F12) yield the desired solutions for $w(x_1)$ and $\psi(x_1)$ appropriate to an end load and an end moment.

Expressions for the stresses of interest are most easily obtained by noting that since bending and shear strains are separable

$$\sigma_x = -\frac{z}{I} M(x) = -\frac{z}{I_o} \left(\frac{1 - \gamma/2}{1 - \gamma \frac{x}{L}}\right)^3 \left[M + F_h (L - x)\right]$$

$$\tau_{xz} = \frac{F_h}{A} = \frac{F_h}{A_o} \left(\frac{1 - \gamma/2}{1 - \gamma \frac{x}{L}}\right)$$

(F22)

This is easily verified by using the constitutive (Hooke's Law) equations

$$\sigma_x = E \epsilon_x$$

$$\tau_{xz} = K G \epsilon_{xz}$$

(F23)

in conjunction with the strain-displacement relations

$$\epsilon_x = -z \frac{d\psi}{dx} = -z \frac{d^2 w_b}{dx^2}$$

$$\epsilon_{xz} = \frac{dw}{dx} - \psi = \frac{dw_s}{dx}$$

(F24)

and then making use of equations (F19) and (F21).

APPENDIX G
VERTICAL AND HORIZONTAL RESPONSE OF
MULTIFILAMENT SUPPORT SYSTEM

APPENDIX G

VERTICAL AND HORIZONTAL RESPONSE OF MULTIFILAMENT SUPPORT SYSTEM

VERTICAL RESPONSE

The strain energy in the eight wires resisting a vertical force F_v is, using symmetry,

$$V = \frac{1}{2} \frac{EA}{\ell} \sum_{i=1}^{8} \delta_i^2 = 4 \frac{EA}{\ell} \delta_w^2 \tag{G1}$$

where

$$\delta_w = \vec{\delta}_v \cdot \vec{U}_w = \delta_v \cos \omega_w \tag{G2}$$

In this expression $\vec{\delta}_v$ is a vector with magnitude δ_v in the direction of F_v, and $\vec{U}_w$ is a unit vector indicating the direction of any one of the wires ($\vec{U}_w$ always points toward the neon from the fixed base). Since $\delta_w = F_v \delta_v$, the theorem of virtual work yields

$$\delta_v = \frac{F_v \ell}{8 \, EA \cos^2 \theta_w} \tag{G3}$$

The stress in a single wire is then given by

$$\sigma_w = \frac{1}{A} \cdot \frac{EA \, \delta_w}{\ell} = \frac{F_v}{8A \cos \theta_w} \tag{G4}$$

Now relate θ_w to α and γ using Figure G1.
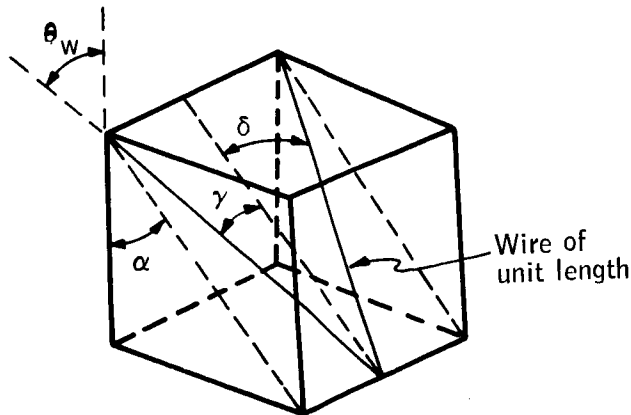
Figure G1. θ_w, α, and γ Relationships

We have:

$$a = \cos \theta_w$$

$$b = \cos \gamma \quad\quad\quad\quad (G5)$$

$$c = b \cos \alpha$$

Thus, the expected result is obtained

$$\cos \theta_w = \cos \alpha \cos \gamma \quad\quad\quad\quad (G6)$$

HORIZONTAL RESPONSE

To analyze this motion, consider two sets of n pairs of suspension wires arranged like the spokes of a wheel with a large-diameter axle; the pairs are arrayed symmetrically about the line of externally applied force as shown in Figure G2.
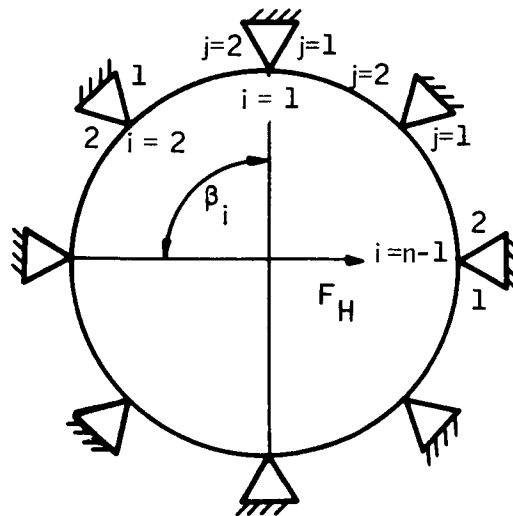

Figure G2. Suspension Wire Geometry

Now the strain energy in the two sets of wires is given by

$$V = 2 \left(\frac{1}{2} \frac{EA}{\ell} \right) \sum_{i=1}^{n} \left\langle \delta_{i_1} \right\rangle^2 + \left\langle \delta_{i_2} \right\rangle^2 \quad\quad\quad\quad (G7)$$

516

where $\langle \delta \rangle$ equals δ when $\delta > 0$ and equals 0 when $\delta < 0$. But

$$\delta_{ij} = \vec{\delta}_h \cdot \vec{u}_{ij} = \delta_h \cos \psi_{ij} \tag{G8}$$

where $\vec{\delta}_h$ is a vector with magnitude δ_h in the direction of F_h, and $\vec{u}_{ij}$ is a unit vector indicating the direction of the wire ij ($\vec{u}_{ij}$ always points toward the neon <u>from</u> the fixed base). Since $\delta_w = F_h \delta_h$, virtual work yields

$$\delta_h = \frac{F_h \ell}{2 \, EA \displaystyle\sum_{i=1}^{n} \left\langle \cos \psi_{i1} \right\rangle^2 + \left\langle \cos \psi_{i2} \right\rangle^2} \tag{G9}$$

so that the stress in a single wire is given by

$$\sigma_{ij} = \frac{1}{A} \cdot \frac{EA \left\langle \delta_{ij} \right\rangle}{\ell} = \frac{F_h \left\langle \cos \psi_{i1} \right\rangle}{2 \, A \displaystyle\sum_{i=1}^{n} \left\langle \cos \psi_{i1} \right\rangle^2 \left\langle \cos \psi_{i2} \right\rangle^2} \tag{G10}$$

Now relate ψ_{ij} to α, γ, and β_i using Figure G3.
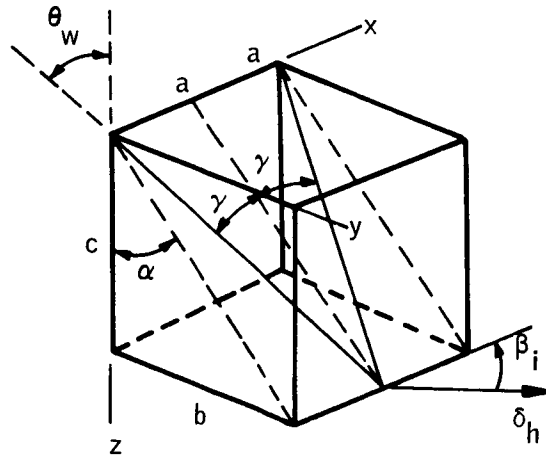
Figure G3. ψ_{ij}, α, γ. and β_i Relationships

Defining ϕ_{ij} and X_{ij} and Ω_{ij} as the angles the jth wire makes with the x, y, and z axes, respectively, and defining ϕ_j, X_j and Ω_j as the angles $\vec{\delta}_h$ makes with the x, y, and z axes respectively, we have for wires of unit length

$$\cos \phi_{i1} = -a \qquad\qquad \cos \phi_{i2} = a$$

$$\cos X_{i1} = b \qquad\qquad \cos X_{i2} = b \qquad\qquad \text{(G11)}$$

$$\cos \Omega_{i1} = c \qquad\qquad \cos \Omega_{i2} = c$$

$$\phi_i = \beta_i \qquad\qquad X_i = \frac{\pi}{2} = -\beta_i \qquad\qquad \Omega_i = \frac{\pi}{2}$$

But it can also be written

$$a = \sin \gamma, \qquad b = \sin \alpha \cos \gamma, \qquad c = \cos \alpha \cos \gamma \qquad \text{(G12)}$$

Thus, since

$$\cos \psi_{ij} = \cos \phi_{ij} \cos \phi_i + \cos X_{ij} \cos X_i + \cos \Omega_{ij} \cos \Omega_i \quad \text{(G13)}$$

and since $\cos \frac{\pi}{2} - \beta_i = \sin \beta_i$, the following equations are obtained

$$\cos \psi_{i1} = -\sin \gamma \cos \beta_i + \sin \alpha \cos \gamma \sin \beta_i$$

$$\cos \psi_{i2} = \sin \gamma \cos \beta_i + \sin \alpha \cos \gamma \sin \beta_i$$

$$\text{(G14)}$$

Now, for eight pairs of suspension wires, two cases are involved in which the wire pairs are arrayed symmetrically about the line of externally applied force F_h. The first case is characterized by $n = 1$ and $\beta_1 = \frac{\pi}{2}$, and the second case is characterized by $n = 2$, $\beta_1 = \frac{\pi}{4}$ and $\beta_2 = \frac{3\pi}{4}$. When F_h is not in the direction of a line of symmetry, however, the response is considerably more complicated, since it involves both translation perpendicular to the direction of F_h and torsional motion about the axes of the neon cylinder as

well as translational motion in the direction of F_h. The first two of these motions should be small if the stiffnesses $k_h = F_h/\alpha_h$ for the two cases above are roughly the same. Even so, it is wise to make γ significantly different from zero to control torsional motion about the axis of the neon cylinder.

Just as there exists translational-torsional coupling due to the asymmetries in the suspension system for the neon, there also exists coupling between translational inputs of arbitrary direction and rotational response of the neon about a horizontal axis passing through its center of gravity. To ensure that the suspension system adequately controls such motion, make α significantly different from β (see Figure G2).

APPENDIX H
MULTIPLE-SLIT CODED RETICLES

521

APPENDIX H
MULTIPLE-SLIT CODED RETICLES

A basic problem when designing a multiple-slit scanning system is the arrangement of the slit pattern. The number of slits is determined by the signal requirements and the slit widths are determined by the required angle accuracy. These problems are considered by Andreyev (ref. 51) and Jauregui (ref. 52).

A slit pattern is selected so that the autocorrelation function has a relatively simple form. Star pattern recognition is significantly complicated by a multiple-peaked correlation function. Desirable features of the autocorrelation function are

> Contidion 1. The autocorrelation function $R(t)$ should increase to its peak value and then decrease.

> Condition 2. The central peak should have the narrowest possible width and should resemble the correlation function of one slit with itself.

> Condition 3. The entire length of the pattern should be as short as possible. A tradeoff exists between low off-peak correlation values and short pattern length.

The task of finding a suitable slit pattern $f(t)$ having these autocorrelation properties is complicated by the fact that $f(t)$ must be non-negative. One example of a binary sequence with the above listed features is $f(t; m, n, k) =$ 1100101, with $n = 7$, $m = 4$, and $k = 1$. The parameter n signifies length of the sequence and m the number of 1's. The parameter k signifies the maximum off-peak correlation value. Figure H1 shows the autocorrelation function of this sequence when interpreted as a series of adjacent pulses of unit width.

The autocorrelation function shown in Figure H1 has all of the desirable features set forth earlier, i.e.,

> 1 It is monotonically decreasing as one proceeds from the peak value.

> 2. The central peak could be narrower only if $R(-1) = R(1)$ were equal to zero. For binary sequences $f(t; m, n, k)$ the factor of increase in the central peak width of $R(t)$ over what it would be for the autocorrelation function of a single pulse of unit width is $m/[m - R(1)]$. One way to remove this increased width is to make $R(1) = R(-1) = 0$. This precludes satisfying Condition 1.
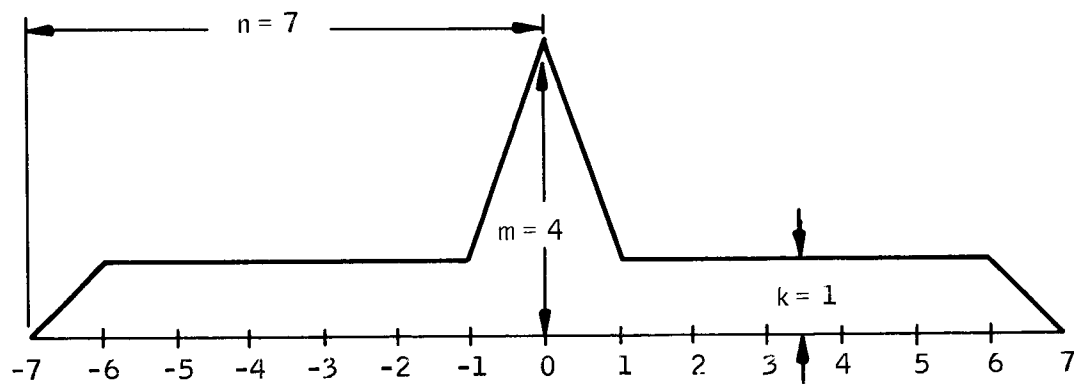
Figure H1. Auto-Correlation Function, R(t) of f(t, 4, 7, 1)

3. The length of the pattern shown in Figure H1 is the least possible for the given values of n, m, and k. A formula may be obtained which relates n, m, and k. This formula assumes that the autocorrelatio function has the form 0, 0, 0, 1, 2, 3, ... k-1, k, k ... k, m, k, k, ... k, k-1, ... 2, 1, 0, 0, 0. Under these restrictions

$$n = \frac{m(m - 1) + k(k + 1)}{2k} \qquad (H1)$$

Table H1 shows some results of equation (H1) for selected values of k and m. This formula may, however, represent binary sequences which do not exist. For example, it is impossible to achieve n = 11, m = 5, and k = 1 as a binary sequence. While n = 12, m = 5, and k = 1 does exist, it does not satisfy Condition 1 stated earlier. However, there may be a number of situations in which this condition can be relaxed.

Table H1 also shows the results of a construction algorithm which has been used to generate binary sequences. The resulting sequences do not satisfy Condition 1 in many cases but do satisfy Conditions 2 and 3. These sequences have a central peak in their respective autocorrelation functions which are wider by a factor of $m/(m - k)$ than the correlation function of a single unit pulse.

The algorithm begins with a pair of adjacent 1's. For example, if construction of a sequence which contains seven ones and whose maximum off-peak correlation value 2 is desired, start with

$$x_1 \ x_2 \ \cdots \cdots \cdots$$

$$1 \ \ 1 \ \ \cdots \cdots \cdots$$

The length of the sequence will be called ℓ which is two in this case. For the value of $t > 0$ at which $R(t)$ is for the first time less than the specified off-peak maximum, which in this case is two, make the following addition. Let $x_{t+1} = 1$. The new value of ℓ is now changed so that the new ℓ is the sum of the old value of ℓ and t. Following this approach the sequence 11101001100001 is produced. The process is terminated as soon as seven ones have been employed. According to equation (H1), the sequence might possibly have had a length of 11 instead of the length 14 which was obtained. Modifications to the above procedure can be made to produce shorter sequences. However, no systematic method of improving the process has yet been discovered. The greatest potential improvement exists in the range $100 < n < 400$ and $1 < k < 10$. Table H1 shows that the method described falls far short of what may be expected with respect to length of sequences for a specified off-peak maxima. Furthermore, these binary sequences almost invariably fail to have a monotonically decreasing autocorrelation function.

TABLE H1. -- AUTOCORRELATION CODES

Number of slits and autocorrelation peak, m	Specified autocorrelation noise, k	Actual code length, n	$n = \dfrac{m(m-1)+k(k+1)}{2k}$
1	0	1	---
2	1	2	2
3	1	4	4
4	1	7	7
5	1	12	11
6	1	21	16
7	2	14	12
7	1	31	21
8	2	23	16
8	1	45	29
10	2	39	24
10	1	81	46
20	4	99	50
30	5	196	90
50	10	358	128

Any attempt to use autocorrelation with scanning systems inevitably results in the generation of autocorrelation noise in side lobes about the detected signal. In addition, the noise on the star signal will also appear in the side lobes. The effect of this will be to drown out weaker stars occurring near the brighter ones.

In the argument which follows several assumptions will be made which are less confining than those imposed by physical constraints in a star scanning system. It will be shown that even with these more general assumptions a very difficult and apparently fundamental noise problem exists.

The "gedanken" experiment, illustrated in Figure H2, is performed to illustrate the above. A mask which consists of holes in a perfectly reflecting sheet is placed in the focal plane of an optical system, covering the entire field. Part of the signal passes through the holes to detector number 1 and the rest is reflected off the sheet to detector number 2. These detectors are assumed to have unit quantum yield and to be noiseless. The output of detector number 1 passes directly to an ideal adder (noiseless), that from number 2 is inverted and put into the adder.

Let there be 4k masks with 4k resolution elements (holes plus mirrors) and let these be placed successively into the focal plane. Thus 4k measurements of the light intensity in the focal plane are obtained. Note that 4k can be large enough to resolve the field arbitrarily well.

Analytically, the process may be described as follows. Distribution of light in the focal plane may be represented by a vector A in 4k dimensions. The 4k mask exposures is a 4k x 4k matrix whose elements are either plus one or minus one. From the adder the 4k outputs may be represented by a vector G in 4k dimensions. The experiment of forming the vector G from vector A is represented by

$$G = H A \qquad (H2)$$

Of course A the state of nature, is recovered by

$$A = H^{-1} G \qquad (H2a)$$

To make the measurement as well as possible, care must be taken in the choice of H or the code used. Any one resolution element should not be weighted more heavily than any of the others. H should be as nonsingular as possible. This will be true if H has the largest possible determinant. Thus, H will be a 4k x 4k "Hadamard" matrix (ref. 53).

These have the properties

1. Elements are ±1

2. Determinant is largest possible for a matrix with elements ±1
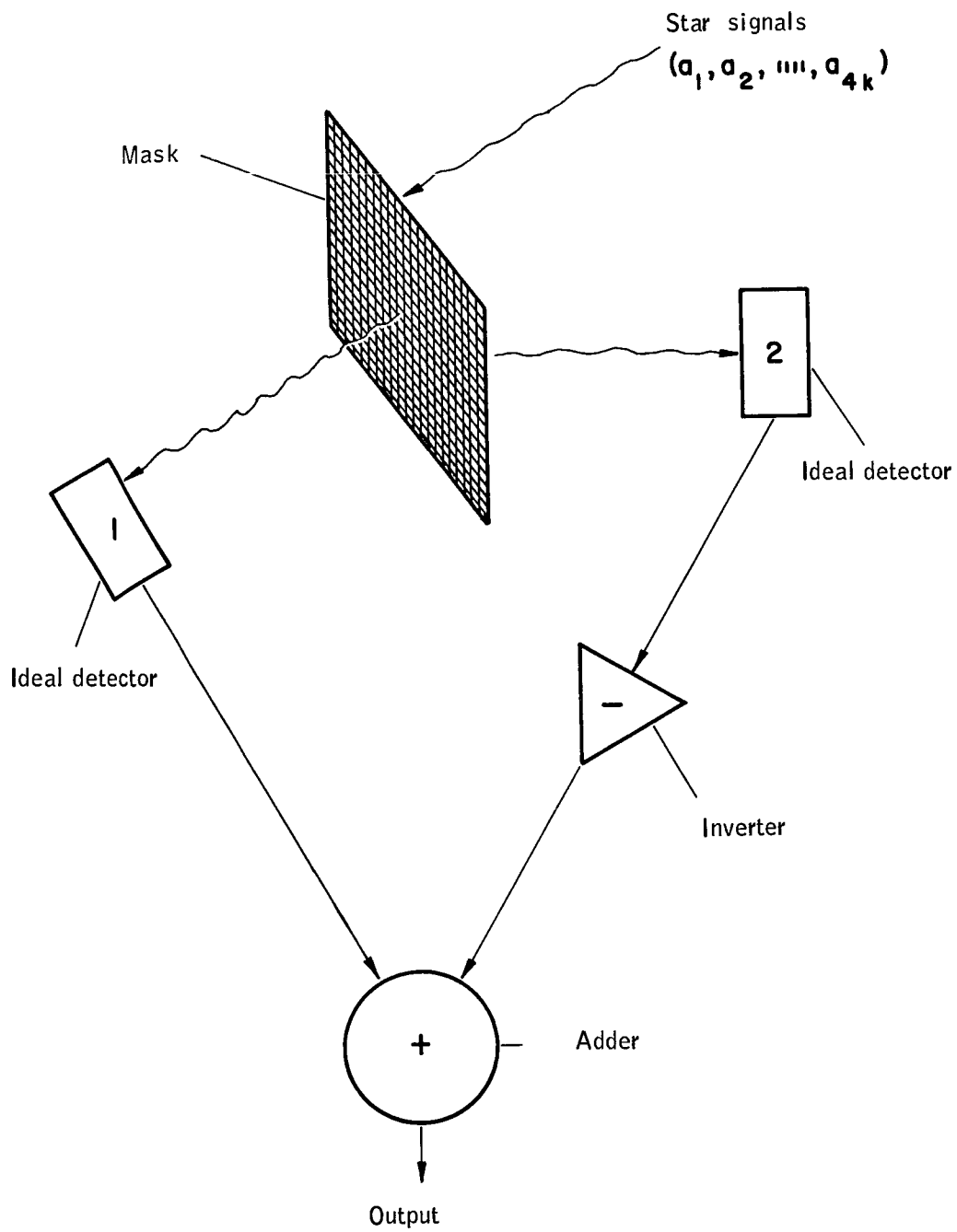
Figure H2. Ideal Auto-Correlator Setup

3. are orthogonal, and

4. If H_n is an $n \times n$ Hadamard matrix, then

$$H_{2n} = \begin{pmatrix} H & H \\ H & -H \end{pmatrix}$$

is a $2n \times 2n$ Hadamard matrix.

At this time, it may be noted, that scanning of a star field by a single slit in this context is represented by a unit matrix of order equal to the number of resolution elements in a single scan.

To illustrate the basic difficulty, consider a 4-element code represented by the matrix

$$H_4 = \begin{pmatrix} 1 & 1 & 1 & 1 \\ 1 & -1 & 1 & -1 \\ 1 & 1 & -1 & -1 \\ 1 & -1 & -1 & 1 \end{pmatrix} \tag{H3}$$

which incidently, is derived from the orthogonal matrix

$$H_2 = \begin{pmatrix} 1 & 1 \\ 1 & -1 \end{pmatrix}$$

Assume the state of nature is

$$A_4 = (0,\ 0,\ \lambda,\ 0) \tag{H4}$$

where the photon rate λ has variance λ.

Then

$$G_4 = H_4 A_4 = (\lambda,\ \lambda,\ -\lambda,\ -\lambda) \tag{H5}$$

and the measurement gives

$$B_4 = H_4 G_4 = (0,\ 0,\ 4\lambda,\ 0) \tag{H6}$$

However, the photon arrival rate is a Poisson process. Thus, the photon rates during successive exposures are uncorrelated, and the noise adds quadratically. As far as noise is concerned, the system is represented by a matrix with elements all plus one, and the result (H6) is really

529

$$B_4 = \begin{pmatrix} 0 & \text{with variance} & 4\lambda \\ 0 & " & " & " \\ 4\lambda & " & " & " \\ 0 & " & " & " \end{pmatrix} \qquad \text{(H7)}$$

That is, though the signal and its variance have been raised by a factor of four, noise has been introduced with the same variance into the side lobes against which stars with a signal of order $2\sqrt{\lambda}$ will be detected with difficulty if at all.

Note that all the signal is used, that this is an ideal code, and that multiple-slit coding is a special case of this code. In connection with this, the use of autocorrelation in "chirp" radar signals is done to avoid the necessity of high peak power transmitters in order to obtain an echo with sufficient time resolution and of sufficient magnitude to detect in the presence of amplifier noise.

It remains to consider the use of coded slits to differentiate star crossings in different areas of the field of view. By choosing several simple codes, no more than ten in length and cross correlating these with each other, cross-correlation noise is quickly seen to be possibly excessive with many of these simple codes.

For example, consider the codes 1101 and 11010001 with 3 and 4 slits, respectively. These are ideal "monopolar" codes, in that the autocorrelation function is the minimum possible off the peak. The autocorrelation functions are respectively, 1113111 and 110111141111011. However, the cross correlation is 11011113111. A signal of three in the presence of auto-correlation noise of 3 is clearly intolerable.

A better choide is the code 1100101 and its reverse 1010011. These are "maximum density" ideal codes, in that they are the shortest possible with peak correlation 4 and maximum off-peak correlation 1. The autocorrelation and cross correlation are now, respectively, 1111114111111 and 1210222210201. For sufficient signal through an individual slit, a correlation noise of 2 can readily be tolerated having peak signal of 4.

However, now stars of double the intensity readily pass through the wrong correlator, at least if the correlator is the usual matched delay line. It can be argued that this defect will not exist if the basic time delays in the delay lines or slit spacings in the slit code are incommensurable. However, even cross correlation noise of unit means starts of four times limiting intensity pass through the wrong correlator. The only solution is to clip all star pulses to the same height. However, if means are provided to reject codes of the wrong length in the correlator, these objections are overcome.

One further defect may be mentioned. Increasing the number of slits without simultaneously decreasing their width increases the noise from the faint star background. This noise in the usual case is already the largest single source of noise.

APPENDIX I

PRELIMINARY SPECIFICATIONS FOR EMR
541N-01-14 MULTIPLIER PHOTO TUBE

(ref. 54)

APPENDIX I
PRELIMINARY SPECIFICATIONS FOR EMR
541N-01-14 MULTIPLIER PHOTOTUBE

PHYSICAL CHARACTERISTICS

Number and type of dynodes: 14; venetian-blind; Ag: Mg
Maximum overall length (unpotted):   3.94 inch (100 mm)
Typical weight (unpotted):   71 grams
Window material: 7056 glass

Cathode sensitive area: 1-in. (25 mm) diameter, area = 0.786 in.^{2}
Cathode type: Semitransparent: bi-alkali

TABLE I1

Parameter	Note	Minimum	Typical	Maximum	Units
Photocathode characteristics	1				
Quantum efficiency Q at 4100 $\overset{o}{A}$		18	21.5		
Cathode luminous sensitivity S_k		55	72.0		$\mu A/lm$
Cathode peak radiant sensitivity σ_k		0.059	0.071		A/W
Typical quantum efficiency					See Fig. 11
Multiplier phototube characteristics, dc	1				
Voltage required for current amplification G of:					See Fig. 12
10^4			1690		V
10^5			2280		V
10^6			2950	3400	V
Dark current i_D at a current amplification of:					
10^5	1, 2		2.6×10^{-12}		A
10^6			2.5×10^{-11}	1×10^{-10}	A
10^7			2.5×10^{-10}		A
Anode luminous sensitivity S at a current amplification of 10^6		55	72.0		A/lm
Anode peak radiant sensitivity σ at a current amplification of 10^6		59 000	71 000		A/W
Equivalent anode dark current input at current amplification of 10^6	1				
Luminous E_D			3.5×10^{-13}	1.8×10^{-12}	lm
Radiant at 4200 $\overset{o}{A}$ ϵ_D			3.5×10^{-16}	1.7×10^{-15}	W
Equivalent noise input at current amplification of 10^6	1				
Luminous E_N			3.9×10^{-14}	1.0×10^{-13}	lm
Radiant at 4100 $\overset{o}{A}$ ϵ_D			4.0×10^{-17}	1.0×10^{-16}	W
Multiplier phototube characteristics, pulse	1				
Dark current counts at a current amplification of 10^6 at 20°C	2, 3		125		Pulses/sec
Pulse-height resolution (FWHM) for Cs^{137}, NaI (T1)	4		8.0		
Maximum ratings	5				
Supply voltage				3600	V
Anode current				0.3	mA
Ambient temperature				150	C

Table I1 - Concluded

Environmental

Shock	100 g, 11-millisecond duration
Vibration	30 g, 20 to 3000 cps
Temperature	-55°C to 150°C

Packaging

Potted weight (typical)	170 grams
	Normally packaged in a 1 - 3/8" o. d. x 4 - 1/4" length fiberglass housing. (Fig. I3)
Wiring diagram	See Figure I4.

Notes: 1. All data at room temperature = 20°C.
      2. Measured after dark-current stabilization.
      3. Discriminator bias at 1/4 of the average single electron pulse height.
      4. Harshaw scintillation crystal, NaI (T1) Type D, size: 1 in. x 1 in., S/N BY 591.
      5. Absolute maximum ratings, prolonged exposure at maximum ratings may result in permanent deterioration of tube performance.
      6. All dimensions in inches unless otherwise noted.
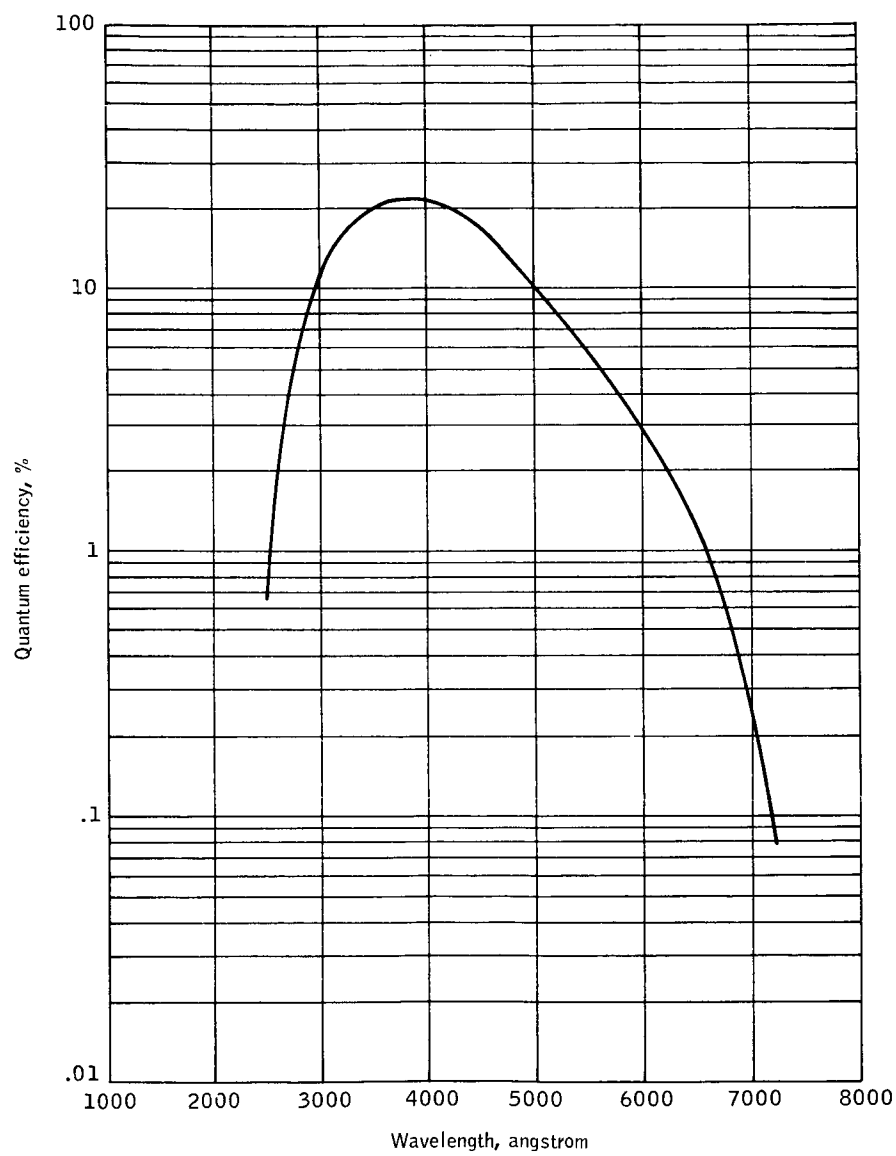
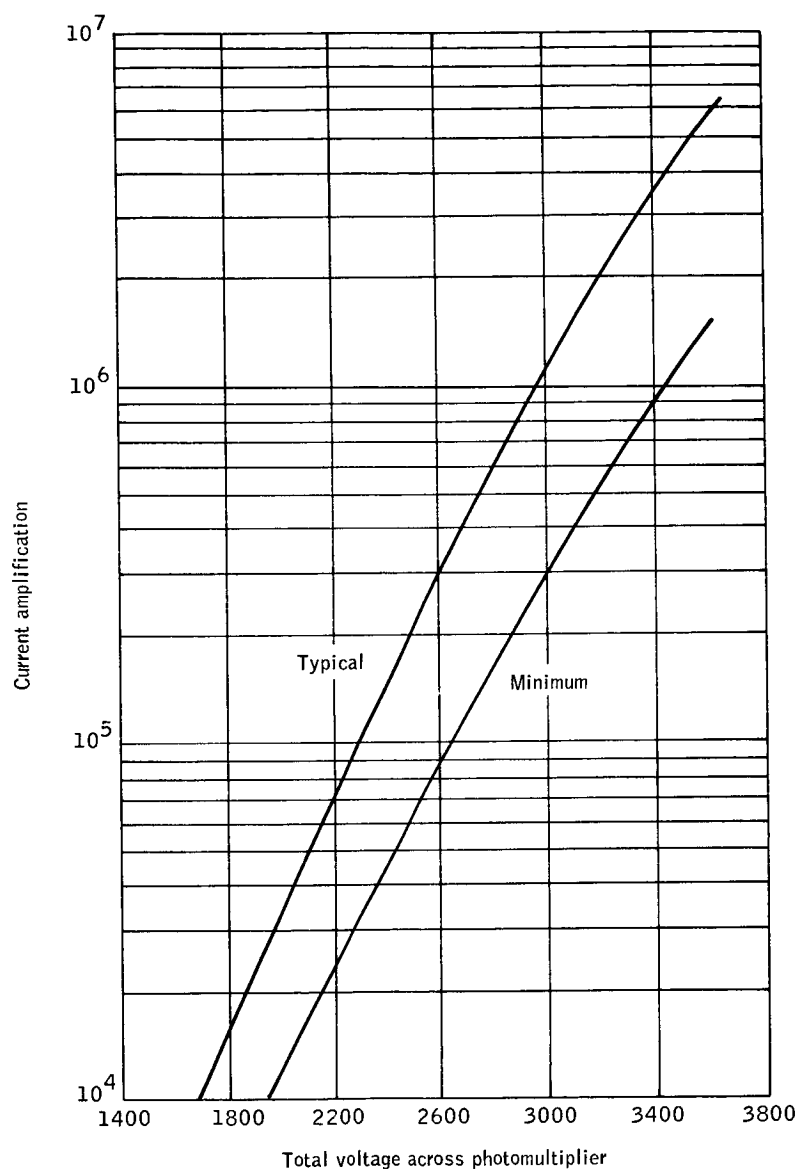Figure I1. Typical Spectral Response Characteristics

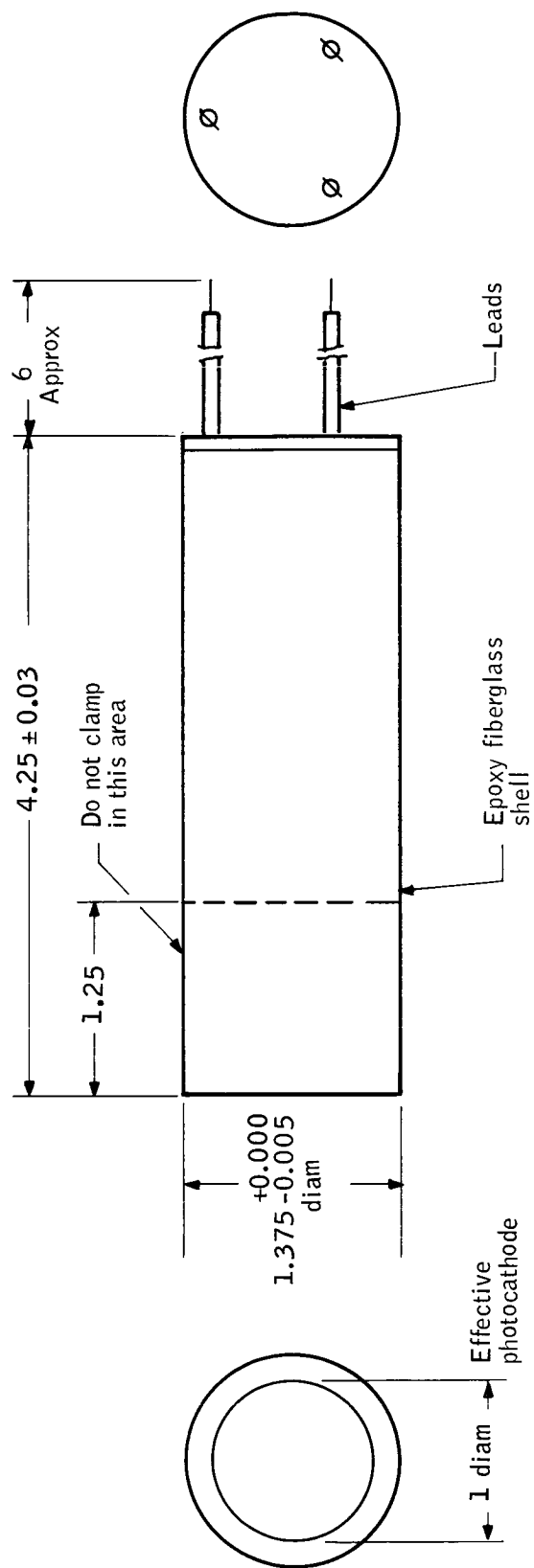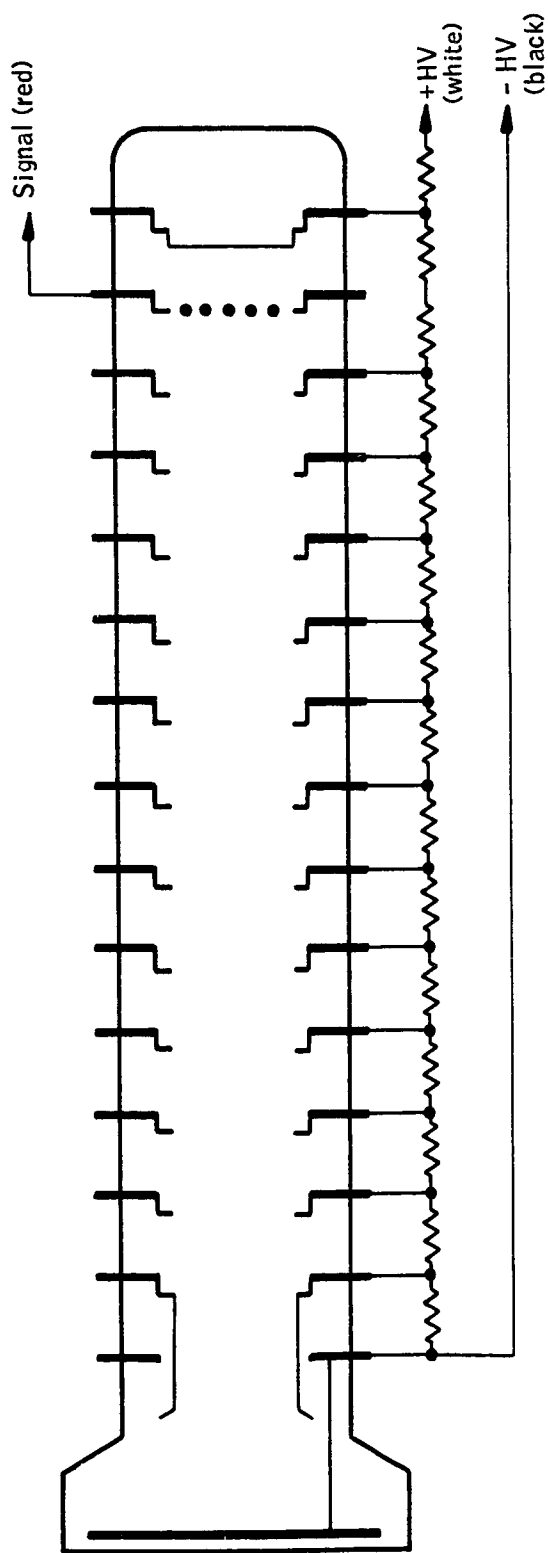Figure I2. Voltage Required versus Current Amplification

Figure 13. Mounting Diagram

Figure I4. Wiring Diagram

Notes:

Resistor values equal throughout unit

APPENDIX J

PRELIMINARY SPECIFICATIONS FOR
MODELS 651 AND 652 PHOTOTUBE-
POWER SUPPLY ASSEMBLY

APPENDIX J

PRELIMINARY SPECIFICATIONS FOR
MODELS 651 AND 652 PHOTOTUBE-
POWER SUPPLY ASSEMBLY

The EMR models 651 and 652 Power Supply units are designed to provide a highly regulated high-voltage supply for ASCOP Multiplier Phototubes of the Model 541 and 542 series. The power supply and phototube are potted together in one container to form an integrated photoelectric device.

The power supply circuit provides a voltage range from 1250 to 3500 volts in three configurations similar to the Model 640C, each capable of adjustment by approximately ± 17 percent from the nominal voltages of 1500, 2125, and 3000 volts respectively. Power input requirement is 28 volts dc.

The packaging of the power supply and phototube is in a housing one inch longer but of the same diameter as a standard potted Model 542 Multiplier Phototube. This standard package size applies to both 651 and 652 configurations. Specification of the phototube and power supply voltage range must be made prior to integration and potting as a complete unit. After potting, the Models 651 and 652 are lightweight, compact, and rugged units ideally suited for application in extreme environments such as found in space vehicles, satellites, or missiles.

Figure J1 is the power supply schematic.

ELECTRICAL SPECIFICATIONS

Input

Input voltage:	28 volts ±3 volts.
Input power:	580 milliwatts at nominal input, maximum output
Noise:	Maximum noise that will be placed on a one ohm source-impedance input voltage is 30 millivolts peak-to-peak.

Output

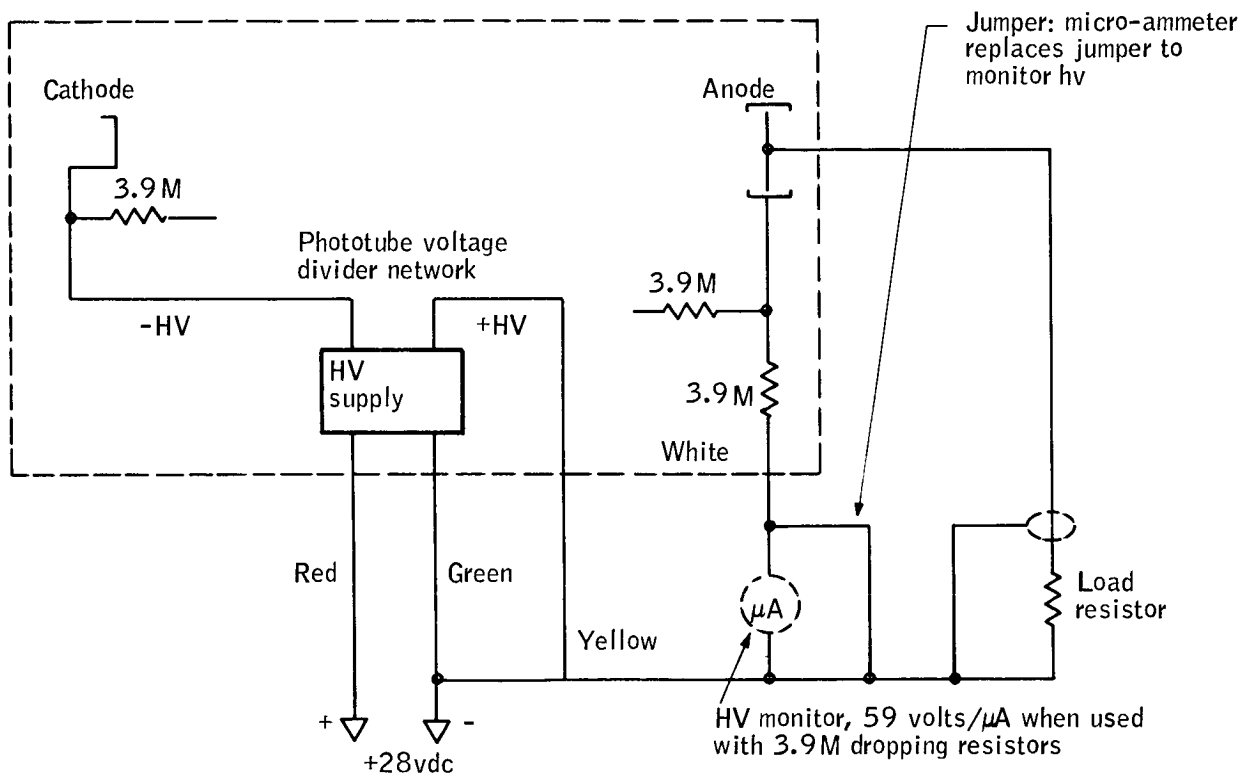|	
Voltage:	Three ranges are available:
	(a) 1250 to 1750 volts at 150 μA maximum
	(b) 1750 to 2500 volts at 105 μA maximum
	(c) 2500 to 3500 volts at 75 μA maximum

Figure J1. Power Supply Schematic

Line regulation: ±0.015% from 25 - 31 volts input

Temperature stability: ±0.015%/°C

Ripple: 500 millivolts peak-to-peak maximum

Grounding: Input and output isolated.
Power supply is designed for a negative high voltage.

MECHANICAL SPECIFICATION

Integrated package dimensions: 1.75-inch diameter;
651: 5 1/2" long (See Figure J2)
652: 5 3/4" long

Weight: Less than three ounces in addition to the standard 542 tube type package (approximately eight ounces)

Integrated package connections: Five leads: two input voltage leads, ground, anode, and high voltage monitoring point (last dynode)

Housing material: RTV silastic in an epoxy fiberglass or stainless-steel shell

ENVIRONMENTAL SPECIFICATIONS (OPERATIONAL)

Temperature: -30°C to +80°C

Vibration: 40g, up to 3000 cps

Shock: 100g, 11-milliseconds duration

ENVIRONMENTAL SPECIFICATIONS (NON-OPERATIONAL)

Temperature: -55°C to + 125°C

GENERAL ORDERING INFORMATION

For ordering purposes, the central voltages and ranges are:

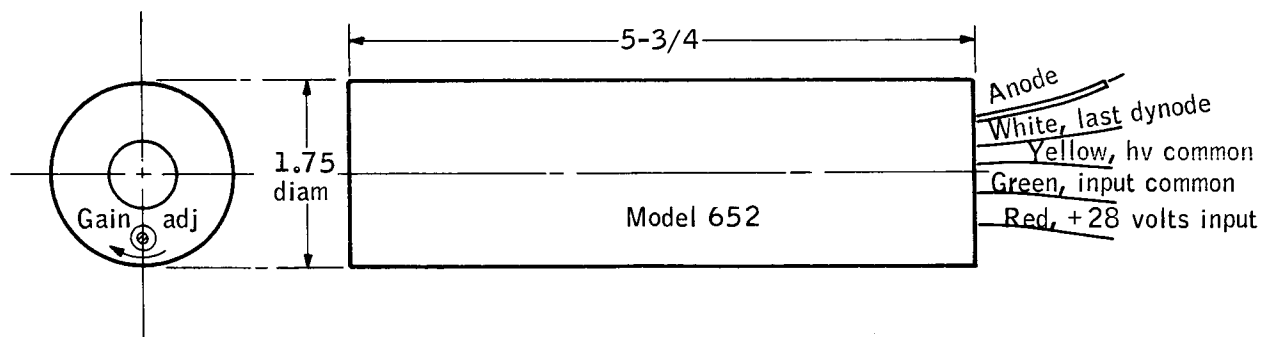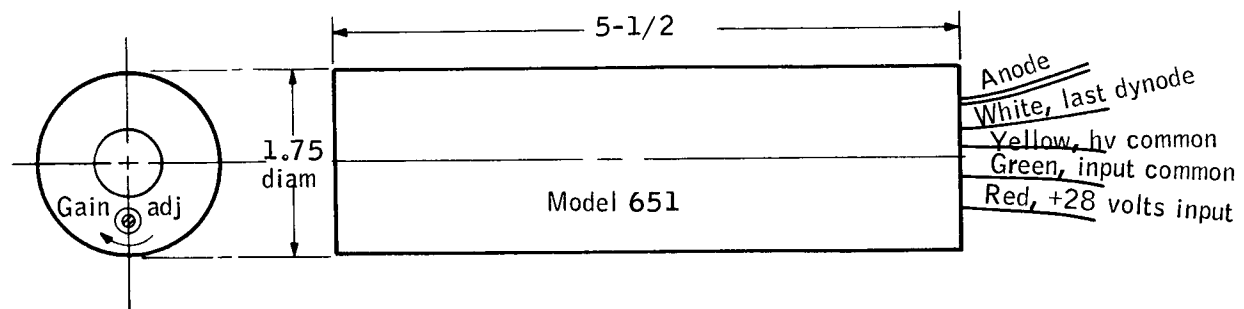| Center voltage	Nominal voltage range, volts
1500	1250-1750
2125	1750-2500
3000	2500-3500

Figure J2. Power Supply Outline

APPENDIX K
ELECTRONIC FILTER IMPLEMENTATION

APPENDIX K
ELECTRONIC FILTER IMPLEMENTATION

The transfer function for the linear phase versus filter mentioned in the low-pass filter design subsection is:

$$\frac{E_o(s)}{E_1(s)} = \frac{1}{\left[1.866\left(\frac{s}{\omega_c}\right)^2 + 2.386\left(\frac{s}{\omega_c}\right) + 1\right]\left[0.6579\left(\frac{s}{\omega_c}\right)^2 + 0.6204\left(\frac{s}{\omega_c}\right)^2\right] + 1\right]\left[0.23175\left(\frac{s}{\omega_c}\right)^2 + 0.122\left(\frac{s}{\omega_c}\right) + 1\right]}$$

(K1)

This transfer function may be implemented by cascading three quadratic stages. A practical circuit for implementing a quadratic stage is shown in Figure K1 (ref. 56). The design procedure for obtaining the values of R and C involves matching the poles of the desired filter transfer function with the poles of the circuit transfer function. If K = 1 in Figure K1, then for the first quadratic stage,
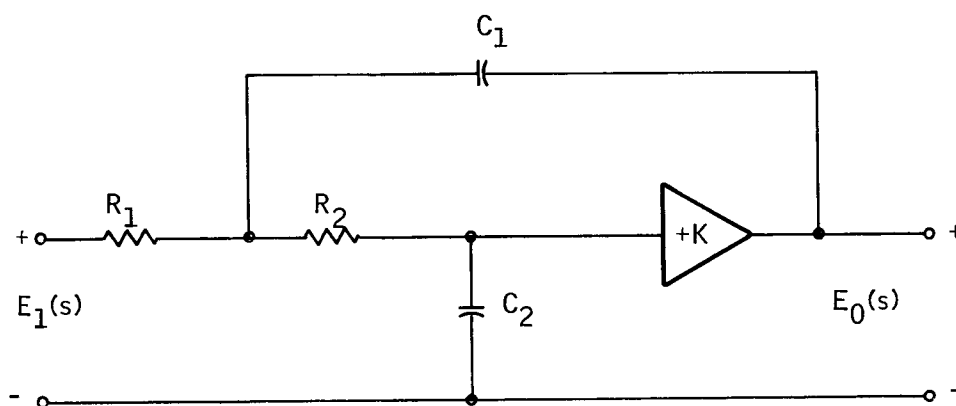
$$C_1 C_2 R_1 R_2 = \frac{1.866}{\omega_c^2}$$

and

$$C_2 (R_2 + R_1) = \frac{2.386}{\omega_c}$$

Now let $R_2 = R_1 = R$, so that $C_2 = \frac{2.386}{2R\omega_c}$ and $C_1 = \frac{2(1.866)}{2.386} \frac{1}{R\omega_c}$

The normalized filter amplitude and phase characteristics for the sixth-order linear-phase transfer function are shown in Figures K2 and K3 respectively.

Transfer function $= \dfrac{E_0(s)}{E_1(s)}$ $\dfrac{K}{S^2 C_1 C_2 R_1 R_2 + S\left[C_2 R_2 + C_2 R_1 + (1-K)\, C_1\, R_1\right] + 1}$
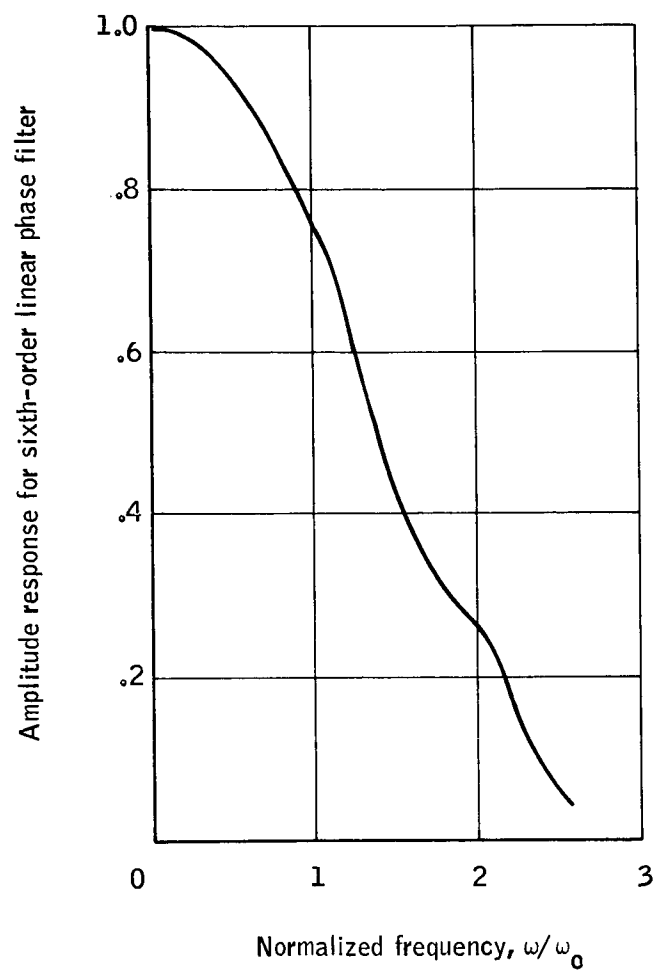
Figure K1. Practical Circuit

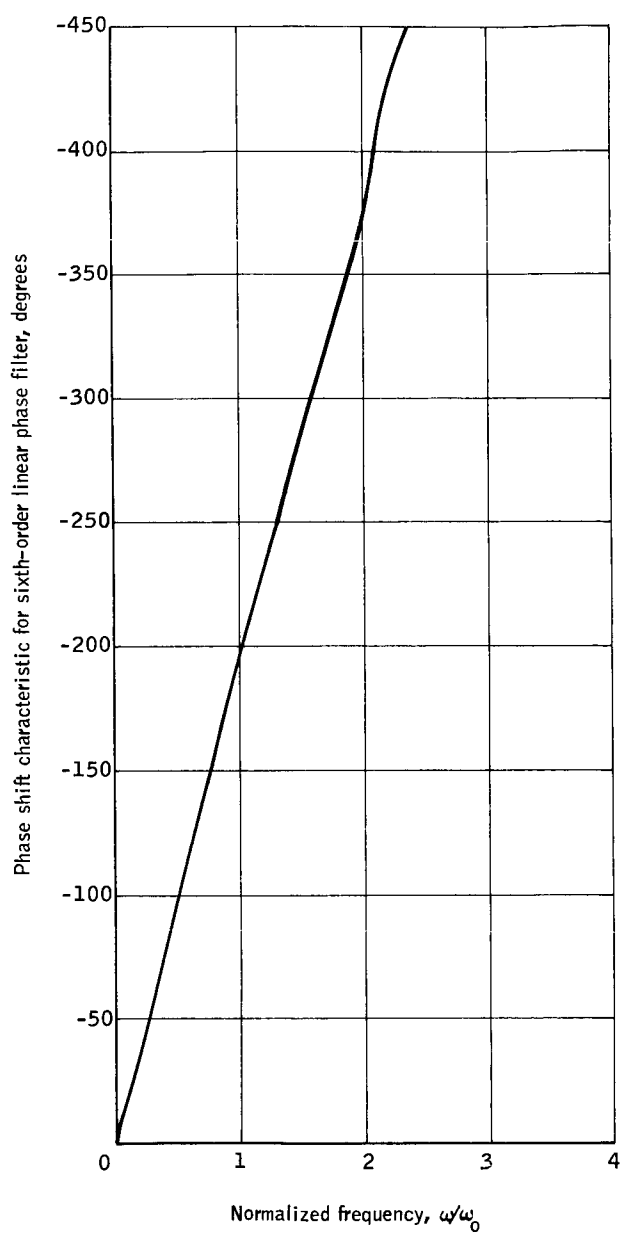Figure K2. Amplitude Characteristics for Linear Phase Filter

Figure K3. Phase Characteristics for Linear Phase Filter

APPENDIX L

SCATTERING OF STRAY LIGHT INTO AN OBJECTIVE
BY A SHIELDING CONE, NO. II

APPENDIX L

SCATTERING OF STRAY LIGHT INTO AN OBJECTIVE
BY A SHIELDING CONE, NO. II

If the lens diameter is a, the generic height of a point on the cone is c, the radius at that point is b, and the sun angle to the optic axis is β, the diffuse scattering into the optics is given by the quadruple integral

$$I = \frac{\lambda_0 F_0}{\pi} \int_{cone} \cos \theta_0 \, dA \int_{lens} \cos \vartheta \, d\Omega \qquad (L1)$$

It may be shown that

$$\int_{lens} \cos \vartheta \, d\Omega = \frac{\pi c}{2b} \cos \frac{\theta}{2} \left(\frac{d^2}{\sqrt{d^4 - 4a^2 b^2}} - 1 \right) - \frac{\pi}{2} \sin \frac{\theta}{2} \left(\frac{d^2 - 2a^2}{\sqrt{d^4 - 4a^2 b^2}} - 1 \right) \equiv F(a, b, c) \qquad (L2)$$

where $d^2 = a^2 + b^2 + c^2$, and θ is the cone angle.

The purpose of this discussion is to do the remaining integration over A_1, the sun illuminated inside cone area. To do this, we must first determine the extent of A_1. With reference to Figure L1, let the sun's flux F_0 make an angle β to the optic axis. Let the cone angle be θ, the radius of the cone edge be b_2, and ab be a line in the plane of the cone edge perpendicular to the plane of the optic axis and a sun ray passing through the optic axis. Then, let this line lie a distance

$$\ell = b_2 \tan \frac{\theta}{2} \cot \beta \qquad (L3)$$

from the optic axis. Let c_1 c_1' denote the sun's ray which goes deepest into the cone. Pass a plane through a, b, and c_1. The intersection of this plane with the cone defines the boundary of the shadowed and lit inner surface

Figure L1. Geometric Representation

of the cone, as will be shown

This plane makes an angle

$$\alpha = \tan^{-1} \frac{\sin^2\beta + \cos^2\beta \tan^2\theta/2}{2\sin\beta\cos\beta} \qquad (L4)$$

with the optic axis.

Expressed in the same set of coordinates (origin at lens center) as equation (L1), the equation of the plane z is

$$z = A - y\cot\alpha \qquad (L5)$$

where

$$A = c_2 - b_2 \cot\beta \tan\frac{\theta}{2}\cot\beta \qquad (L6)$$

Note that a z corresponds to c and y to b in equation (L1).

See Figure L2a for the definitions of symbols.

The equation of the cone is

$$\left. \begin{array}{l} z = (r - a)\cot\dfrac{\theta}{2} \\[2em] r^2 = x^2 + y^2 \end{array} \right\} \qquad (L7)$$

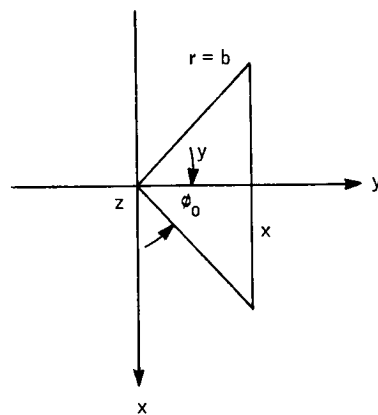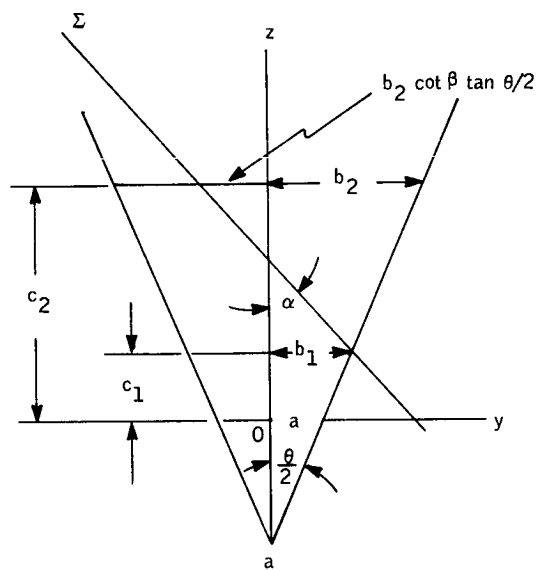Equations (L5) and (L7) give the projection of the intersection of plane and cone on the xy plane as,

$$r = m - ny \qquad (L8)$$

where

$$m = a + A\tan\frac{\theta}{2} \qquad (L9)$$

$$n = \cot\alpha \tan\frac{\theta}{2} \qquad (L10)$$

The integration will be effected using the element of cone area dA_1 as,

Figure L2.   Geometric Representation

$$dA_1 = \sec\frac{\theta}{2} \ r \ d\phi \ dz \tag{L11}$$

Using Figure L2 and equation (L8), the limit on the ϕ integration ρ_0, is found as

$$\phi_0 = \cos^{-1}\frac{m-r}{nr} \tag{L12}$$

A unit vector in the direction of the sun's rays is

$$\hat{f} = -\hat{k} \cos\beta + \hat{j}\sin\beta$$

The normal to the cone interior in terms of the angle variable ϕ is

$$\hat{n} = \hat{k} \ \sin\frac{\theta}{2} - \cos\frac{\theta}{2} \ (\hat{i} \ \sin\phi + \hat{j}\cos\phi)$$

and, thus,

$$\cos\theta = -\hat{f} \cdot \hat{n} = \cos\beta \ \sin\frac{\theta}{2} + \sin\beta \ \cos\frac{\theta}{2} \ \cos\phi \tag{L13}$$

The integral (L1) becomes

$$I = \frac{2\lambda_0 F_0}{\pi} \ \sec\frac{\theta}{2} \int_{c_1}^{c_2} (\cos\beta \ \sin\frac{\theta}{2} \ \phi_0 + \sin\beta \ \cos\frac{\theta}{2} \ \sin\phi_0) \ F \ (a, \ b, \ z) \ b \ dz \tag{L14}$$

where:

$$b = a + z \ \tan\frac{\theta}{2} \tag{L15}$$

$$c_1 = \frac{c_2 \ (1 - \cot\beta \ \tan\frac{\theta}{2}) - 2 \ a \ \cot\beta}{1 + \cot\beta \ \tan\frac{\theta}{2}} \tag{L16}$$

and

$$\phi_O = \cos^{-1} \frac{m-b}{nb} \qquad \text{(L17)}$$

Not much more can be done analytically with the remaining integration. However, this last one may be done numerically and has been carried out. Results for $\theta = 20°$, $a = 1\text{-}1/2$, and $c_2 = 19\text{-}7/8$ normalized to λF_o appear in Figure L3.

From the reference 34 in $3800 \text{ Å} \leq \lambda \leq 6000 \text{ Å}$ there is $4.181 \times 10^{-2} \text{ W/cm}^2$ in sunlight. Since the full moon is magnitude -12.70 and the sun is magnitude -26.78, the moonlight (assuming no wavelength dependence in the moon's albedo, which is not really true) is 2.34×10^{-6} that of sunlight. Assume further that the cone albedo is 10^{-3} and the cone dimensions are in inches. Then from Figure L3, the moonlight energy scattered into the lens with the moon 30° off axis is,

$$f'_{moon} = 2.195 \times 10^{-10} \text{ watts}$$

The amount of starlight from a type A_o, 3.5 magnitude star into the lens is

$$f_{3^m.5} = 3.051 \times 10^{-12} \text{ watts}$$

If this were the whole story the cone wouldn't do, but the scattering off the cone is not into the field of view. The light must be rescattered off the lens or interior walls to reach the slits. In the first instance, about 0.25 percent to 0.5 percent of the light is scattered (ref. 57).

In the second instance, two additional scattering events must occur. We, therefore, neglect the latter and consider only the former. Then, an amount of moonlight,

$$f_{moon} = 1.098 \times 10^{-12} \text{ watts}$$

is scattered into the field of view.

The amount reaching the photomultiplier is further attenuated by the ratio of the slit area to the field of view which is

$$R = \frac{3 \times 20 \times 1/60}{\frac{\pi}{4}(20)^2} = 3.14 \times 10^{-3}$$

Total moonlight to the photomultiplier in this example (HDS star scanner) is

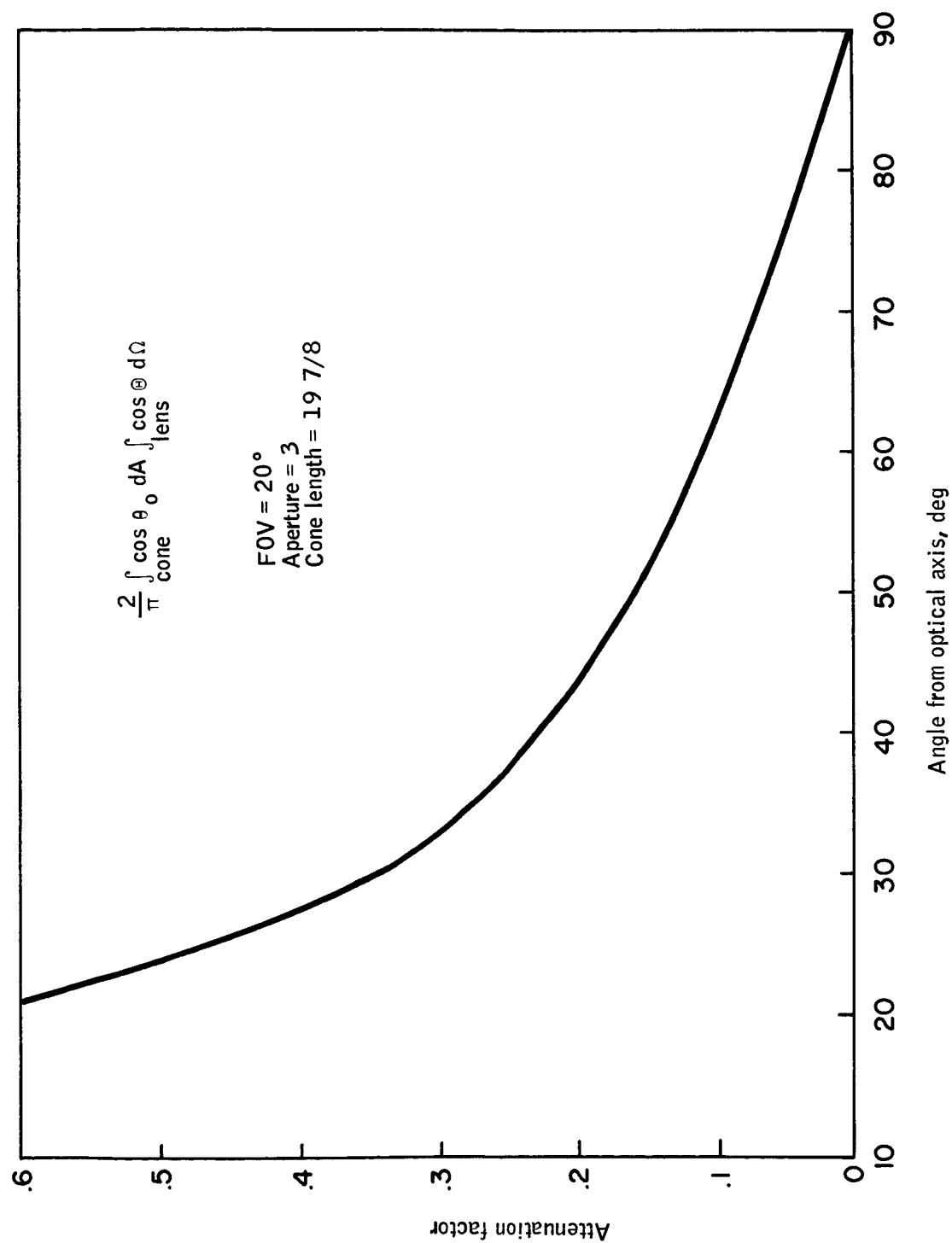$$F_{moon} = 1.098 \times 10^{-12} \times 3.14 \times 10^{-3}$$

562

Figure L3. Light Diffused from Shield into System

$$F_{moon} = 3.49 \times 10^{-15} \text{ watts}$$

Consider Figure L4. Let the surface Γ be generated by those rays which fall on the lip of the cone. Then Γ is an elliptic cylinder. Let the topmost ray of Γ intersect the cone (and cone extended) in c_2 and $c_2{}'$, respectively, and the lowest ray strike the cone in c_1 and $c_1{}'$. Pass a plane Σ through the points c_1 and $c_2{}'$ perpendicular to the plane determined by the cone axis and the ray $\overline{c_1 c_1{}'}$ (or $\overline{c_2 c_2{}'}$). This will intersect the lip of the cone in points a and b.

Now Σ intersects the elliptic cylinder in an ellipse σ_1 which passes through points a, b, c_1, and $c_2{}'$. It intersects the cone in an ellipse σ_1 which also passes through these same four points. (Actually if σ passes through a it must also pass through b.) Moreover, σ_1 and σ_2 have the same major axis. Thus, $\sigma_1 = \sigma_2$, and the shadowed area is defined by the intersection of Σ with the cone.

Equation (L3) is proved from equation (L13), for at the line a, b; $\cos \theta_o = 0$ and

$$\cos \phi_t = - \sin \alpha = - \cot \beta \tan \frac{\theta}{2} \tag{L18}$$

From Figure L5

$$\cot \alpha = \frac{c_2 - c_1}{b_1 + b_2 \sin \alpha} \tag{L19}$$

Using (L15) and (L16) with (L18),

$$\tan \alpha = \frac{1 + \cot^2 \beta \tan^2 \theta/2}{2 \cot \beta} \tag{L4a}$$
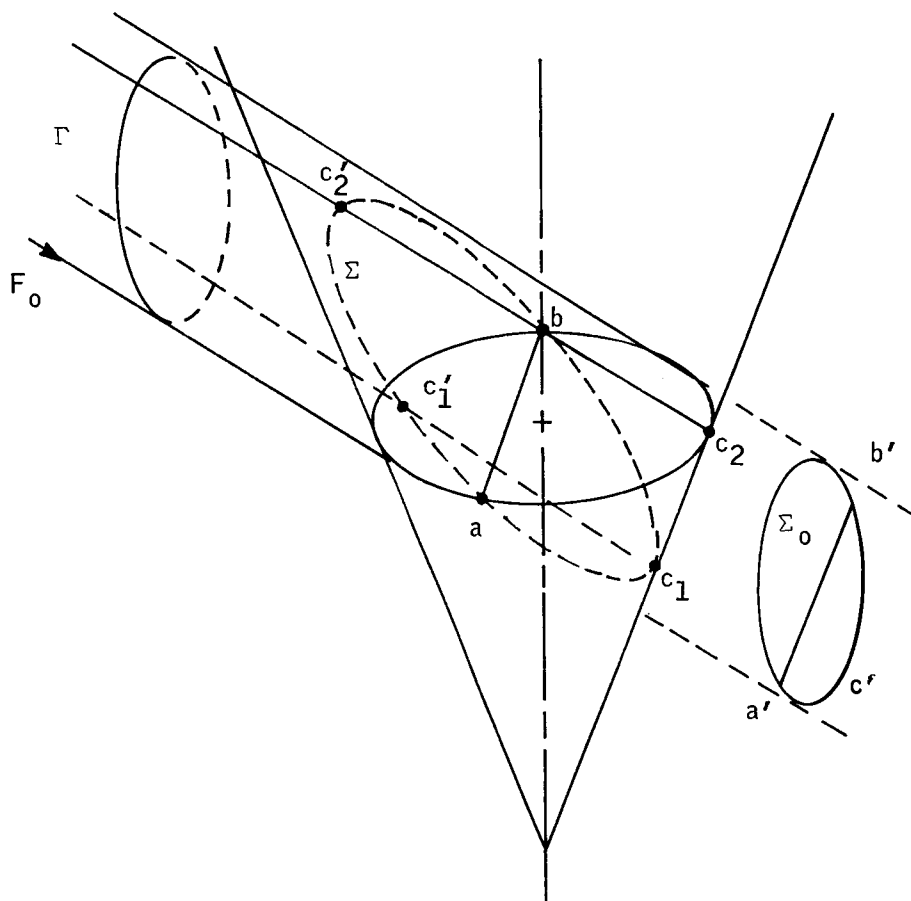
which is just equation L4.

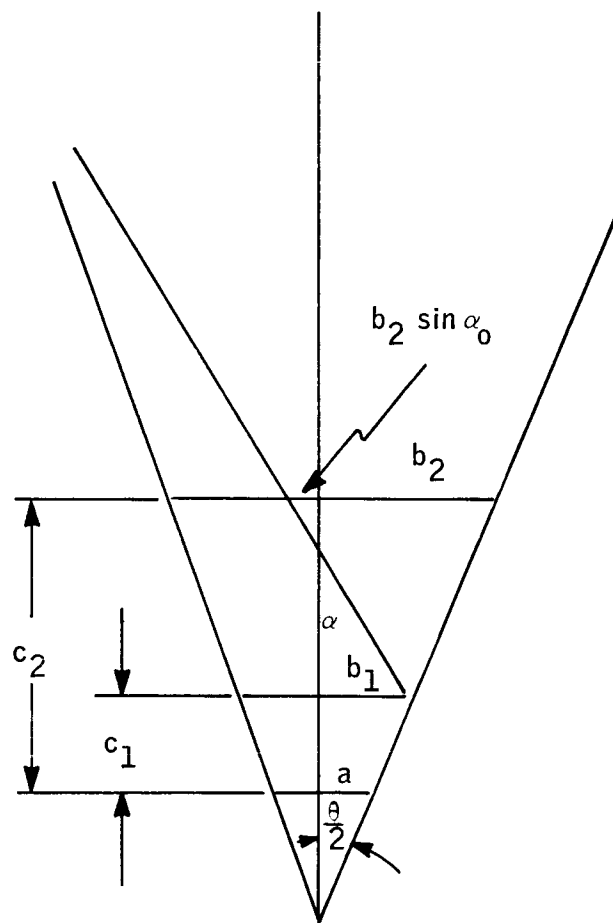Figure L4. Geometric Representation

Figure L5. Geometric Representation

REFERENCES

1. Morton, G. A.; et al.: RCA Review, vol. 20, Dec. 1959, pp. 599-634.

2. Kruse, P.W.; et al.: Elements of Infrared Technology. Wiley and Sons, 1962, p. 139.

3. Bennett, H.E.; Bennett, J.M.; and Ashley, E.S.: Infrared Reflectance of Evaporated Aluminum Films. J. Opt. Soc. Am., vol. 52, no. 11, Nov. 1962.

4. Bennett, J.M.; and Ashley, E.S.: Infrared Reflectance and Emittance of Silver and Gold Evaporated in Ultrahigh Vacuum. Applied Optics, vol. 4, no. 2, Feb. 1965.

5. Ladd, LeRoy L.: Cadmium Telluride Infrared Transmitting Material. Journal of Infrared Physics, vol. 6 no. 6, Sept. 1966.

6. Ballard, S.S.; McCarthy, K.A.; and Wolfe, W.L.: Optical Materials for Infrared Instrumentation. State of the Art Report, AD217367, Univ. of Michigan, Willow Run Laboratories, Jan. 1959.

7. Dalven, Richard: Germanium Semi-conductor Properties. Journal of Infrared Physics, vol. 6, no. 6, Sept. 1966.

8. Grant, James; Michel, Eugene; and Thelfn, Alfred: Recent Developments in Infrared Narrow Bandpass Filters. Paper presented at Sixth National Infrared Information Symposium, Nov. 7, 1961.

9. Anon.: A Compendium, the Properties of Materials at Low Temperatures. Phase A, Part I, WADD TR 60-56, Oct. 1960.

10. Ziegler, W T., et al.: Calculation of the Vapor Pressure and Heats of Vaporization and Sublimation of Liquids and Solids, Especially Below One Atmosphere Pressure: I Ethylene, II Argon, III Carbon Dioxide and Carbon Monoxide, IV Nitrogen, Fluorine. Technical Reports, Engineering Experiment Station, Georgia Institute of Technology, 1962-63.

11. Ziegler, W T.: The Vapor Pressures of Some Hydrocarbons in the Liquid and Solid State at Low Temperatures. NBS Technical Note No. 4, 1959.

12. Coblenz, W.W.: Investigation of Infrared Spectra. Carnegie Institute of Technology, 1962.

13. Caren, P.P.: Prog. Astronautics and Aeronautics, vol. 18, 1966, pp. 61-73.

14. Campbell, M.D.; and Associates: Thermophysical Properties of Plastic Materials and Composites to Liquid Hydrogen Temperatures (-423°F). ML-TDR-64-33 Part III, August 1965.

15. Anon.: Design of High-Performance Insulation Systems I. LMSC, A 742593-1, August 1965.

16. Anon.: Final Report. NAS 5-9549.

17. Goetzel; et al.: Space Materials Handbook. Addison-Wesley, 1965. Chapter 3.

18. Anon.: DuPont Fibers in Industry. Industrial - High Tenacity Grade, Dacron.

19. Anon.: Advances for Cryogenic Engineering. vol. 8, 1964, p. 268.

20. Powell, R L.; and Sparks, L.L.: NBS Report 9249.

21. Brooks, Paul P.B.: Calibration of Mueller Thermometer Bridges. NBS, 1965.

22. Allen, C.W.: Astrophysical Quantities. Second ed., Althone Press, 1963, p. 201.

23. Quasius, G.; and McCanless, F.: Star Trackers and System Design. Spartan Books, 1966. p. 16.

24. Johnson, Harold L.: Infrared Stars. Sky and Telescope, vol. 32, no. 2, August 1966, p. 73.

25. Iriarte, Braulio; Jonnson, Harold L.; Mitchell, Richard I.; and Wisniewski, Wieslaw Z.: Five Color Photometry of Bright Stars. Sky and Telescope, vol. 30, no. 1, July 1965.

26. Johnson, H.L.; Mitchell, R.I.; Iriarte, B ; and Wisnewski, W.Z.: Communications of the Lunar and Planetary Laboratory. Univ. of Arizona, UBVRIJKL Photometry of Bright Stars, vol. 4, part 3, Comm. 63, 15 April 1966.

27. Mendoza, Eugenio E.: Infrared Photometry of T Tauri Stars and Related Objects. The Astrophysical Journal, vol. 143, no. 3, March 1966.

28. Anon.: Final Report on a Space Background Study for Project Defender. Eastman Kodak, EK/ARD ED-1003, 19 April 1963.

29. Ramsey, R C.: Spectral Irradiance from Stars and Planets Above the Atmosphere from 0.1 to 100 microns. Applied Optics, vol. 1, no. 4, July 1962.

30.   Code, A.D.: Stellar Energy Distributions. Stellar Atmospheres, Chapter 2, University of Chicago Press, 1960, p. 50.

31.   Allen, C.W.: Astrophysical Quantities. Second ed., Athlone Press, London 1962.

32.   Van Der Ziel, A.: Noise. Prentice - Hall, Inc., 1954.

33.   Kuiper; and Middlehurst: Planets and Satellites. Univ. of Chicago, 1961, p. 214.

34.   Anon.: Handbook of Geophysics. Rev. ed., Macmillan Co., 1961.

35.   Meisenholder, G.W.: Planet Illuminance. Jet Propulsion Laboratory, Report 32-361, 10 Nov. 1962.

36.   Allen, C.W.: Astrophysical Quantities. First ed., Athlone Press, London, 1955.

37.   Kopal, Z.: Astrophy, J., vol. 105, Jan. 1947, pp. 60-74.

38.   DeGroot, T.: Bulletin of the Astronomical Institute of the Netherlands, vol. 16, 1962, p. 181.

39.   Pagel, B.E.J.: Astrophys, J., vol. 132, 1960, p. 790.

40.   Julius, W.H.: Astrophys, J., vol. 32, 1913, p. 225.

41.   Evan, D.S.: The Observatory, vol. 67, 1947, p. 138.

42.   Chandrasekhar, R.: Radiative Transfer. Dover Publications, 1960.

43.   Hardy, A.C.; and Perrin, F.H.: Principles of Optics. International Series in Pure and Applied Physics, 1932, p. 192.

44.   Rudaux, L.; and DeVaucouleurs, G.: Larousse Encyclopedia of Astronomy. Batchworth Press Limited, London, 1959.

45.   Anon.: Edgerton, Germeshausen and Greer Inc. Series SGD-444 Photodiode

46.   Saul, S.; and Cary, J.: Thermal Distortion Study for the Advanced Orbiting Solar Observatory. RAC 762-54, AOSO - R32-01, Republic Aviation Corp., 18 May 1964.

47.   Carri, R.; and Saul, S.: Thermal Distortion Analysis for the Advanced Orbiting Solar Observatory. RAC 762-98, AOSO - R252-01, Republic Aviation Corp., 25 June 1965.

48. Wein, D., Thermal Analysis for the Advanced Orbiting Solar Observatory. RAC 762-102, AOSO - R247-01, Republic Aviation Corp., 17 June 1965.

49. Anon.: Final Report for the Advanced Orbiting Solar Observatory. Vol. I, RAC 762-83-I, AOSO - R75-01, Republic Aviation Corp., 17 November 1965.

50. Epstein, Lewis C.: An All-Reflective Schmidt Telescope for Space Research, Sky and Telescope, April 1967.

51. Andreyev, V.D.: Transmission of a Useful Signal and a Background Signal through a Radial- lot Shutter System for Indication of Luminous Objects. Engineering Cybernetics, no. 3, pp. 30-40.

52. Jauregui, S.: A Theoretical Study of Complementary Binary Code Sequences and a Computer Search for New Kernels. Doctoral Thesis, United States Naval Postgraduate School, Monterey, California.

53. Peterson, W. Wesley,: Error Correction Codes. MIT Press and John Wiley and Sons, Inc., second printing, March 1962.

54. Anon.: 541N -01-014 Preliminary Specification. Electro-Mechanical Research, Inc., Photoelectric Division, March 1966.

55. Anon.: Preliminary Specifications Models 651 and 652 Phototube - Power Supply Assembly. Electro-Mechanical Research, Inc., Princeton Division, Jan. 1965.

56. Chabak, E. J.: Resistance-Capacitance Active Filters. United States Army Electronics Command, Fort Monmouth, New Jersey, Technical Report ECOM-2744, August 1966.

57. Kuwabara: J. Opt. Soc. Am., vol. 43, no. 2.

FEASIBILITY DESIGN OF AN INSTRUMENT SYSTEM

FOR MEASUREMENT OF HORIZON RADIANCE IN

THE CO_2 ABSORPTION BAND

By John C. Carson, Honeywell Inc.
    Joseph S. Titus, Honeywell Inc.
    Alden J. Mooers, Control Data Corp.
    Ralph W. Peterson, Control Data Corp.
    Charles N. West, Honeywell Inc.
    Richard M. Jansson, Honeywell Inc.

ABSTRACT

A feasibility design of an instrument system to collect data on the earth's horizon radiance profile in the 15-μ carbon dioxide absorption band is described. A radiometer, two star mappers, and two sun sensors constitute the primary elements of the experiment package. The radiometer utilizes a cooled Ge:Cd detector, in-flight calibration, and classical Newtonian optics. Radiometric requirements and constraints are analyzed in detail. Radiance profile data is referenced to a geocentric coordinate system and, thus, instantaneous attitude and position of the data-taking instrument must be known. While position information is obtainable from the ground, attitude must be measured from within the spacecraft. A passive starmapper, with a slit reticle and a photomultiplier detector, and a sun sensor, are the major components of the attitude determination system. Attitude determination is performed as a ground data processing task.

ERRATA

NASA CR-66429

FEASIBILITY DESIGN OF AN INSTRUMENT SYSTEM FOR
MEASUREMENT OF HORIZON RADIANCE IN THE CO_2
ABSORPTION BAND

By   John C. Carson
Joseph C. Titus
Alden J. Mooers
Ralph W. Peterson
Charles N. West
Richard M. Jansson

Page 61, Figure 25:   The lower curve label should read "Mercury
cadmium telluride with filter (theoretical)."

Issue date: 22 January 1968